RADIATION EFFECTS IN METAL-OXIDE-SEMICONDUCTOR CAPACITORS

John Lloyd Collins,BSc

A thesis submitted for the Degree of Doctor of Philosophy

The University of Aston in Birmingham

October, 1987

The University of Aston in Birmingham

RADIATION EFFECTS IN METAL-OXIDE-SEMICONDUCTOR CAPACITORS

John Lloyd Collins,BSc

A Thesis submitted for the degree of Doctor of Philosophy, 1987

SUMMARY

An investigation has been undertaken into the effects of various radiations on commercially made Al-SiO_2-Si Capacitors (MOSCs). Detailed studies of the electrical and physical nature of such devices have been used to characterise both virgin and irradiated devices.
In particular, an investigation of the nature and causes of dielectric breakdown in MOSCs has revealed that intrinsic breakdown is a two-stage process dominated by charge injection in a pre-breakdown stage; this is associated with localised high-field injection of carriers from the semiconductor substrate to interfacial and bulk charge traps which, it is proposed, leads to the formation of conducting channels through the dielectric with breakdown occurring as a result of the dissipation of the conduction band energy.
A study of radiation-induced dielectric breakdown has revealed the possibility of anomalous hot-electron injection to an excess of bulk oxide traps in the ionization channel produced by very heavily ionizing radiation, which leads to intrinsic breakdown in high-field stressed devices. These findings are interpreted in terms of a modification to the model for radiation-induced dielectric breakdown based upon the primary dependence of breakdown on charge injection rather than high-field mechanisms.
The results of a detailed investigation of charge trapping and interface state generation in such MOSCs due to various radiations has revealed evidence of neutron induced interface states, and of the generation of positive oxide charge in devices due to all of the radiations tested. In particular, the greater the linear energy transfer of the radiation, the greater the magnitude of charge trapped in the oxide and the greater the number of interface states generated. These findings are interpreted in terms of Si-H and Si-OH bond-breaking at the Si-SiO_2 interface which is enhanced by charge carrier transfer to the interface and by anomalous charge injection to compensate for the excess of charge carriers created by the radiation.

Key words: Metal-Oxide-Semiconductor Capacitor
Dielectric breakdown
Hot electron injection
Interface states
Oxide charge

DEDICATION.

This thesis is dedicated to my parents, without whose support and encouragement this would not have been possible.

ACKNOWLEDGEMENTS.

This work was financed by a SERC (CASE) award in collaboration with the CEGB Technology, Planning and Research Division based at Berkeley Nuclear Laboratories, Gloucester, UK; I am extremely grateful for their financial and technical support, without which this work would not have been possible.

In particular, I would like to thank my Supervisor, Dr P.N. Cooper, for his teaching, many helpful discussions and encouragement during the course of the work.

I would also like to thank:

John Harvey at the Berkeley Nuclear Laboratories: for suggesting the project, and his help and support throughout the project.

Plessey Semiconductors (UK) Ltd: for supplying the various materials and fabricating the MOS capacitors to my requirements.

The Rutherford Appleton Laboratories, Oxford, UK: for the use of their computing facilities.

Dave Langstaff of The Department of Electronics and Information Engineering in the University of Southampton, UK: for his help in using various CAD software.

Professor G.T. Wright and The Department of Electrical and Electronic Engineering in the University of Birmingham, UK: for the loan of their C-V and I-V apparatus.

Dr J. Hunt at The National Physical Laboratories, UK: for his assistance with the accelerator neutron irradiations.

Dr P. Fowles at The University of Birmingham, UK: for his assistance with the large-dose gamma irradiations.

Dr. M.R. Middleton at 3M, Swansea, UK: for the 3-d interferograms, i.e. those shown in Figures 105 to 108.

The Chelsea Dielectrics Group, KQC in The University of London, UK: for many useful discussions.

and finally, to Isabel: for her constant support, encouragement and understanding.

CONTENTS.

CONTENTS

CONTENTS

CONTENTS

CONTENTS

LIST OF FIGURES

LIST OF FIGURES

LIST OF FIGURES

LIST OF FIGURES

LIST OF FIGURES

LIST OF FIGURES

LIST OF FIGURES

LIST OF FIGURES

LIST OF FIGURES

LIST OF FIGURES

LIST OF FIGURES

LIST OF FIGURES

LIST OF FIGURES

LIST OF FIGURES

LIST OF FIGURES

LIST OF FIGURES

LIST OF TABLES

LIST OF TABLES

LIST OF TABLES

LIST OF APPENDICES

CHAPTER ONE.

INTRODUCTION

1.1 Historical Background

The field of semiconductor device physics has been heavily influenced by early studies of semiconductor surfaces. These early studies, such as those reviewed by FRANKL[1] and MANY,GOLDSTEIN and GROVER[2], were for many years regarded as of academic interest rather than of any practical importance. However, with the birth of planar technology in the early 1960's and the advent of the Metal-Insulator-Semiconductor (MIS) structure, the former academic view of surfaces and surface effects soon gave way to a more practical goal: that of understanding and controlling the surface-influenced behaviour of semiconductor devices.

The MIS system was first employed in the study of a thermally oxidised surface by TERMAN[3] and by LEHOVEC and SLOBODSKOY[4] in 1963. Since then, many research programmes have been devoted to the study of this Metal-Oxide-Semiconductor (MOS) system and a wealth of information covering most aspects of MOS device operation exists. The majority of research in this area of semiconductor device physics has been strongly influenced by the requirements of the semiconductor industry - in particular, the integrated circuit manufacturers.

1.2 Integrated Circuit Technology

Since their introduction, more than twenty years ago, monolithic integrated circuits (IC's) based upon the MOS system have become much smaller and far more complex. However, the basis of modern ICs is still the MOS system; the understanding of fundamental principles involved in the operation of this system is of paramount importance to the semiconductor industry. The understanding of this system is applicable not only to IC technology, but to other key areas of technological importance involving insulators and semiconductor-insulator interfaces.

This thesis is focussed on a fundamental study of various radiation effects on the MOS system and uses a particularly simple MOS structure - the MOS capacitor (MOSC) - as a research tool.

1.3 The MOSC as a research tool

The control of the electrical properties of the MOS system has been one of the major factors that has led to stable and high performance silicon ICs; the MOSC is used in both monitoring IC

fabrication and studying the electrical properties of the MOS system.

The advantages of the MOSC over other MOS systems (CCDs, MOSFETSs) lie in its simple structure, ease of fabrication and simplicity of analysis (because thermal equilibrium conditions may be assumed in the device and a one-dimensional analysis is accurate).

By far the most widely used MOSCs are silicon based with a silicon substrate, silicon dioxide (SiO_2) as the insulator (oxide) layer and an aluminium metal electrode overlaying the oxide in a planar configuration. This is the device structure used in this study.

Three regions of the MOS system are of major importance in IC technology: the bulk oxide, the Si-SiO_2 interface and the silicon itself. Charges in all three regions play a role in device operation. In the oxide and at the Si-SiO_2 interface, these charges are undesirables because they adversely affect device performance and stability. In the silicon, charges (such as dopant impurity atoms) are necessary for device operation.

One property or paramount importance is the dielectric breakdown strength of the oxide. Consequently there have been many research programmes (for examples, see the review articles by KLEIN[5] and SOLOMON[6]) directed towards understanding the fundamental physical processes that give rise to a breakdown event and the effects of processing (and other factors) upon these.

There are two major electrical properties of the Si-SiO_2 interface, both of which strongly influence device operating characteristics: oxide fixed charge and interface state level density. It is of great technological importance that the nature of such charge and traps be understood in order to control MOS system properties. Since such information is most easily extracted from study of the MOSC, it is an ideal test device to characterise MOS systems and to ascertain the nature of charge and traps in the three regions of interest.

In Chapter 2, the basic physical and electrical properties of MOSCs are described. This description is applied to the Al-SiO_2-Si MOSC structure and the role of various charges, both at the SiO_2-Si interface and in the bulk oxide, is discussed. This provides a basis for further investigations discussed in later chapters.

Chapter 3 considers the MOSC as a "field effect" device with high-field (of the order of MV cm^{-1}) dielectric breakdown and its relevance to current MOS research is shown. The models which have

been proposed for Al-SiO_2-Si MOSC breakdown under high-field stressing, based on impact ionization mechanisms, are discussed. A number of workers [7-9] strongly dispute these, believing that band-to-band impact ionisation is feasible in semiconductors (for example, breakdown of p-n junctions) but not in wide bandgap insulators such as SiO_2. These workers propose alternative breakdown models which are critically reviewed and compared with recent experimental findings.

1.4 The Use of MOSCs in Radiation Research

The use of semiconductor devices based on the MOS system in industrial, space and military environments has become so widespread that understanding the effects of radiation upon them is of great technological importance. To this end, many workers (for examples, see the December issues of the IEEE Transactions on Nuclear Science, reference 10) have directed their effort toward developing a framework for understanding radiation effects in MOS systems.

Ionizing radiation is known to deposit charge and introduce interface states (traps) in MOS devices[11]; non-directly-ionizing radiation is known to produce displacement damage which leads to oxide traps in MOS devices[12]. The MOSC is an ideal testbed device for investigating the behaviour of MOS systems in such radiation fields.

Comparatively little work has been directed towards the effects of radiation on the breakdown process in MOS systems, first reported by KLEIN and SOLOMON[13] in 1975. In Chapter 4, this work is reviewed and models for radiation induced dielectric breakdown (RIDB) are discussed.

It has been suggested by HARVEY[14] that such devices, because of their small size and portability, may prove invaluable as radiation detectors for research and industry; in particular, the use of radiation induced dielectric breakdown in MOSCs for recoil-proton detection has been proposed, the aim to detect neutrons in the 0.01 to 1MeV energy range via (n,p) reactions in a hydrogenous radiator placed in contact with the thin front electrode of an MOSC. At present, neutron dosimetry in this energy range is carried out using thermal neutron detectors inside large, rather cumbersome polyethylene moderating assemblies. A small, portable dosimeter based on such neutron-induced dielectric breakdown in an MOSC would prove to be an invaluable technique for neutron dosimetry, especially for measurements in confined areas.

It has been noted by several workers[13,231-234] that only very high linear energy transfer radiations (such as fission-fragments) have been found to induce breakdown. In order to understand more fully the direct interaction of these and other radiations with MOSCs, their effects on the electrical properties of such structures and the feasibility of MOSCs as such dosimetry tools, radiation induced dielectric breakdown is discussed considering the experimental evidence of other workers presented in Chapters **3** and **4**, in preparation for the new experimental evidence presented in Chapter **6**.

Experimental evidence for other radiation effects in MOS systems, and its relevance to the Al-SiO_2-Si MOSC in particular, is presented: popular models of radiation interactions are reviewed. The two main effects of radiation on the MOS system (radiation induced oxide charge and radiation induced interface states) are presented in the light of recent experimental findings and the models proposed to explain their generation are critically reviewed; the implications of these models are discussed with reference to MOS research and the development of future models.

1.5 Experimental Approaches

Since the materials and fabrication processes used to construct Al-SiO_2-Si MOSCs are the major factors influencing the device characteristics , these are described in detail at the beginning of Chapter **5** and a summary of the device parameters for the MOSCs used in this study is given to enable the reader to compare this work with that of other workers in the field on a quantitative basis.

As mentioned in section 1.2, charges in MOS systems are of great importance; MOS devices are sensitive to minute traces of charge, of order 10^{10} unit charges cm^{-2}. To detect such low charge densities very sensitive electrical measurements have been developed and elaborate models have evolved connecting the behaviour of charges to the measurements. One such technique is the high frequency Capacitance-Voltage method whereby the high frequency capacitance of a MOS device is measured as the bias across it is varied.

In Chapter **5**, this technique is described and a novel, simple method of calculating various parameters (for examples,density of interface states, flatband voltage shift and trapped charge density) from the C-V curves of the MOS system under test is presented.

Dielectric breakdown methods have been used in a thorough study of the properties of Al-SiO_2-Si MOSCs, both in and out of radiation fields. These methods and the information they afford are described, with appropriate theory, together with the other techniques used in this study to characterise MOSCs (Current-Voltage techniques, X-ray photoelectron and Auger spectroscopy, three-dimensional interferometry and scanning electron microscopy) before, during and after irradiation whilst under various electrical conditions. The techniques of irradiation, the radiation fields used, their source and energy spectra and the methods used to calibrate them are summarised.

In Chapter 6, the findings from a comprehensive investigation of MOSCs constructed for this study, using the techniques described in Chapter **5**, are presented along with the effects of various radiation fields on their electrical and physical characteristics, whilst the significance of the findings will be considered (and compared with the results of other workers in the field) in Chapter **7**.

1.6 Theoretical Considerations.

An important objective of this thesis is to indicate how existing theories, proposed to explain dielectric breakdown and radiation effects in MOSCs, need be modified, or changed, in order to account for the present experimental findings.

Accordingly, having presented a framework for discussion in previous chapters, Chapter **7** considers how the present data be best interpreted: the present-day interpretation of the nature of the Si-SiO_2 interface is amended to include various findings from this study; previously proposed models for intrinsic dielectric breakdown are modified in the light of new data on the structure of the two interfaces in Al-SiO_2-Si MOSCs; the KLEIN [234] model for radiation induced dielectric breakdown has been extended to account for various effects seen; and a basis for understanding radiation effects in MOSCs is proposed which quantitatively considers charge build-up in the oxide layer and interface trap generation and is an extension to the model proposed by MACLEAN[15].

Chapter **8** provides a summary of the principal experimental and theoretical findings presented in Chapters 6 and **7** , with suggestions for future work in the field of radiation effects in MOS devices.

CHAPTER TWO.

ELECTRICAL PROPERTIES OF MOSCs

In this chapter the basic electrical properties of ideal Metal-Oxide-Semiconductor capacitors (MOSCs) are described using appropriate theory: more extensive details can be found in the textbook by NICOLLIAN and BREWS[16]. This is applied to the Al-SiO_2-Si MOSC structure used in this study and some of the more important experimental findings that have recently emerged from other studies of this device structure are reviewed.

From the theory and review a near-complete electrical description of the Al-SiO_2-Si MOSC is given to provide a framework for understanding such devices under external influences (such as high-field stressing, dielectric breakdown and irradiation).

2.1 Ideal MOSCs

The simplest MOSC structure is shown in perspective in Figure1(a); by far the most commonly fabricated structure in the microelectronics industry is the Al-SiO_2-Si MOSC, which is schematically shown in Figure 1(b) with typical range for the thicknesses of the insulating (silicon dioxide) layer and top (aluminium) electrode. The distance T' is the thickness of the insulating layer covering the semiconductor and V is the bias voltage applied to the metal gate or field plate. (Throughout this and the following chapters the convention that the bias voltage , V, is positive when the gate is positively biased with respect to the Ohmic contact on the underside of the semiconductor, and V is negative when the metal gate is negatively biased with respect to the Ohmic contact, is taken).

The energy-band diagram of an ideal MIS structure for no applied bias voltage (V=0) is shown in Figure2, where Figures 2(a) and 2(b) are for n-type and p-type semiconductor devices, respectively.

An ideal MIS capacitor is defined[17] as follows:

(a) At zero applied bias, the energy difference between the metal work function, ϕ_m , and the semiconductor work function, ϕ_s , is zero or the work function difference , ϕ_{ms} , is zero such that:

$$\phi_{ms} = \phi_m - (\lambda + E_g/2q - \phi_B) \quad \text{For an n-type semiconductor} \quad \textbf{-1}$$

$$\phi_{ms} = \phi_m - (\lambda + E_g/2q + \phi_B) \quad \text{For a p-type semiconductor} \quad \textbf{-1a}$$

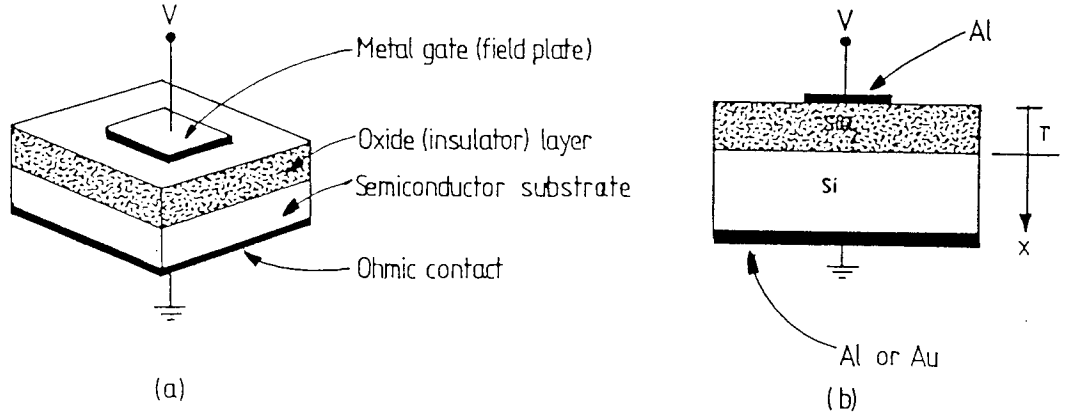

Figure 1: (a) A Metal-Insulator-Semiconductor capacitor shown in perspective.

(b) An Al-SiO_2-Si MOSC in cross-section; typical thicknesses, T', for the oxide layer range between 5nm and 3μm; typical thicknesses of top-gate Al electrode range between 15nm and 1μm.

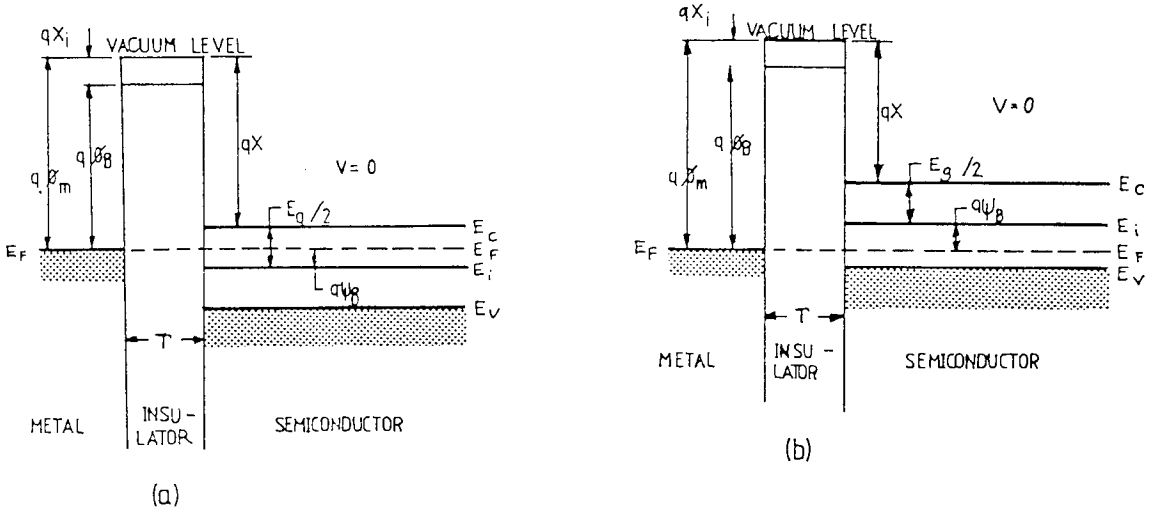

Figure 2: (a) An energy band diagram for an ideal n-type semiconductor MOSC under the zero bias condition.

(b) An energy band diagram for an ideal p-type semiconductor MOSC under the zero bias condition.

where λ is the semiconductor electron affinity, E_g is the bandgap, $\varnothing_B$ is the potential barrier between the metal and the insulator and q the electronic charge.

Thus, when there is no applied voltage the energy bands are flat; "flatband" conditions are said to exist.

(b) The only charges that exist in the structure under any biasing conditions are those in the semiconductor and those with equal, but opposite sign, on the metal surface adjacent to the insulator.

(c) There is no carrier transport through the insulator under d.c. biasing conditions; the resistivity of the insulator is infinite. Thus, the semiconductor Fermi level is unaffected by the bias applied to the MIS capacitor gate and remains invariant as a function of position.

The ideal-MOSC theory considered here serves as a foundation for understanding practical (non-ideal) MOS structures, such as the Al-SiO_2-Si MOSC used in this research.

2.2 Ideal MOSCs Under Bias Conditions

When an ideal MOSC is biased with positive (or negative) voltages the applied bias separates the Fermi energies at the two ends of the structure by an amount equal to qV; that is

$$-qV = E_{Fmetal} - E_{Fsemiconductor} \qquad -2$$

Since the barrier heights are fixed quantities, the movement of the metal Fermi level obviously leads to a distortion in other features of the band structure. Basically three cases may exist at the semiconductor surface: these are shown on energy-band diagrams in Figure 3(a) for a p-type device and Figure 3(b) for an n-type device.

Consider the MOSC with a p-type semiconductor substrate; when a negative voltage (V<0 case) is applied to the metal gate electrode,the band structure moves from the flatband condition so that

[An arrow pointing upwards denotes a negative potential]

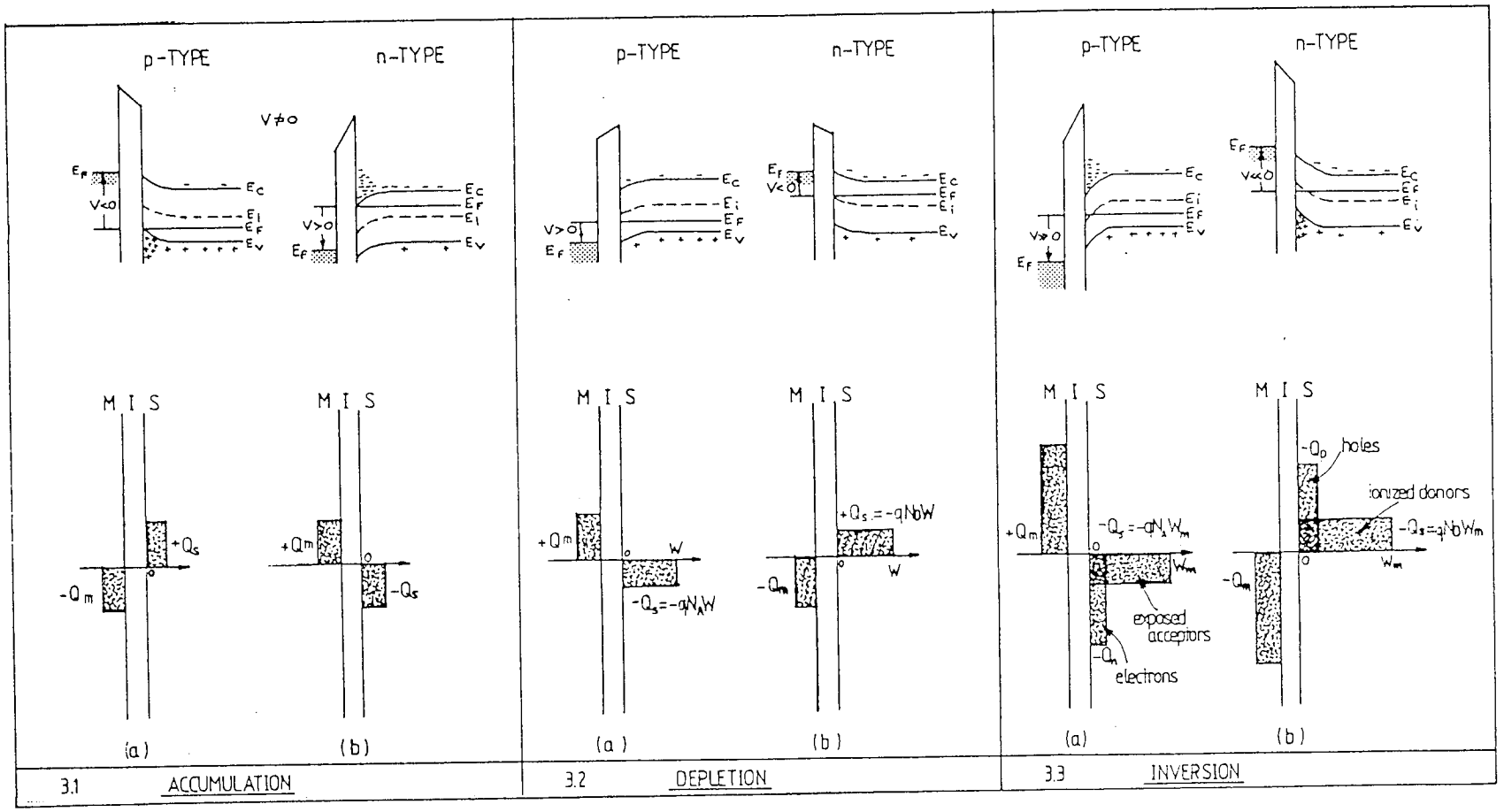

Figure 3: (a) Energy band and charge distribution diagrams for an ideal n-type semiconductor MOSC under the various conditions of bias. (b) Energy band and charge distribution diagrams for an ideal p-type semiconductor MOSC under the various conditions of bias.

Three cases can be seen to exist for both n-type and p-type MOSCs:
(3.1) Accumulation of the majority carriers
(3.2) Depletion of the majority carriers
and (3.3) Inversion of the semiconductor surface

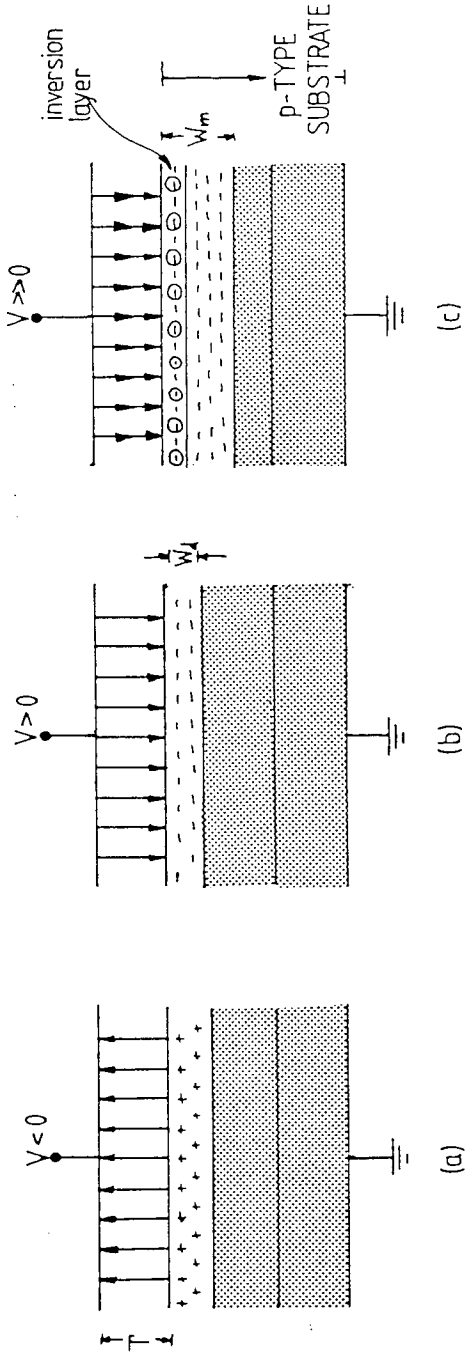

Figure 3: (c) Schematic diagrams illustrating the charge distribution in an ideal p-type MOSC (shown in cross-section) for the three cases shown in Figures 3.1 to 3.3.

the top of the valence band "bends" upward and becomes closer to the Fermi level (Figure3(a.1) No band bending occurs in the metal because it is an equipotential region. For an ideal MOSC, no current flows in the structure and so the Fermi level in the semiconductor remains constant.

Since, by Fermi-Dirac statistics, the carrier density level depends exponentially on the energy difference (E_i-E_F), that is;

$$p_p = n_i \; e^{(E_i - E_F)/kT} \qquad -3$$

where p_p and n_i are the density of holes and the intrinsic carrier density, respectively; this band bending causes an accumulation of majority carriers (holes in this case) near the semiconductor surface. This is the "accumulation" case. The corresponding charge distributions are shown on the right side of Figure 3(a).

When a small positive voltage (V>0 case) is applied the bands bend downward and the majority carriers are depleted (Figure 3(a.2) This is the "depletion" case. The space charge charge per unit area in the semiconductor , Q_{SC}, is given by the charge within the depletion region, thus

$$Q_{SC} = -qN_A W \qquad -4$$

where W is the width of the surface depleted depleted region and N_A is the acceptor impurity density.

When a larger positive voltage (V>>0 case) is applied, the bands bend even more downward so that the intrinsic Fermi level, E_i, at the surface crosses over the Fermi level , E_F (Figure 3(a.3) Since the electron concentration depends exponentially on the energy difference (E_F-E_i), the density of electrons, n_p, is given by

$$n_p = n_i \; e^{(E_F - E_i)/kT} \qquad -5$$

Thus, at this point the density of minority carriers, n_p , at the surface is larger than n_i, and that of the majority carriers (from Equation **3**) becomes less than n_i. The number of minority carriers (electrons) at the surface is greater than the number of majority carriers (holes); the surface is thus inverted. This is the "inversion" case; the surface of the p-type semiconductor is effectively n-type under these conditions.

As the bands are bent further, eventually the conduction band edge becomes very close to the Fermi level. At this point the electron concentration near the surface increases very rapidly.

After this point, most of the additional negative charges in the semiconductor consist of the charge Q_n (Figure 3(a.3)) due to the electrons in a very narrow n-type inversion layer, $0 \leq x \leq x_i$, where x_i is the width of the inversion region. Typically, the value of x_i ranges from 1 to 10nm and is always much smaller than the surface depletion layer width, W. Once the inversion layer is formed the surface depletion layer width reaches a maximum, W_m. This is because when the bands are bent downwards far enough for strong inversion to occur, even a very small increase in band bending (corresponding to a very small increase in depletion layer width) results in a large increase in the charge Q_n in the inversion layer. Thus, under such a strong inversion condition the charge per unit area in the semiconductor is given by

$$Q_s = Q_n + Q_{sc} \qquad -6$$

and

$$Q_{sc} = -q\, N_A\, W_m \qquad -7$$

where W_m is the maximum width of the surface depletion region.

If analogous biasing conditions are applied to an ideal n-type MOSC, the results will be as depicted in Figure 3(b.1) to 3(b.3). It is important to note from this figure that biasing regions in an n-type device are reversed in polarity relative to the voltage regions in a similar p-type device; that is, accumulation in an n-type device occurs for V>0 and so on. The charge distributions under these bias conditions are also shown in Figure 3(b) and are also seen to be analogous to the p-type device case.

2.2.1 The Surface Space-Charge Region

In this subsection the relations between the semiconductor surface potential, U_S, space charge, Q_S, and the electric field E are derived. These relations are then used to find the relationship between the applied gate voltage,V_g , and U_S and to determine the capacitance-voltage (C-V) characteristics of the ideal MOSC structure defined above.

Figure 4 shows a more detailed band diagram of the surface of a p-type semiconductor adjoining an

insulator layer in an MIS structure; at the semiconductor surface, U, (the electrostatic potential) is equal to U_S (the surface potential). The electron and hole concentrations, from Equations **3** and **5** , are given by

$$n_p = n_i \, e^{q(U - U_B)/kT} \qquad \text{- 8}$$

$$p_p = n_i \, e^{q(U_B - U)/kT} \qquad \text{- 9}$$

where U is positive when the band is bent downwards (as shown in Figure 4).

At equilibrium $U_B=0$ so,

$$n_p = n_{po} \, e^{(qU/kT)} \qquad \text{-10}$$

$$p_p = p_{po} \, e^{(-qU/kT)} \qquad \text{-11}$$

Thus, at the surface the densities are given by

$$n_s = n_i \, e^{q(U_S - U_B)/kT} \qquad \text{-12}$$

$$p_s = n_i \, e^{q(U_B - U_S)/kT} \qquad \text{-13}$$

and, at equilibrium , when $U_B=0$

$$n_s = n_{po} \, e^{(qU_S/kT)} \qquad \text{-14}$$

$$p_s = p_{po} \, e^{(-qU_S/kT)} \qquad \text{-15}$$

From Equations **12** and **13** the following regions of surface potential can be distinguished:

$U_S < 0$	Accumulation of holes, bands bend upward.
$U_S = 0$	Flatband condition.
$U_B > U_S > 0$	Depletion of holes, bands bend downward.
$U_S = U_B$	Midgap condition with $n_s = n_p = n_i$ (the intrinsic semiconductor concentration).
$U_S > U_B$	Inversion, electron enhancement at semiconductor surface causes bands to bend further downward.

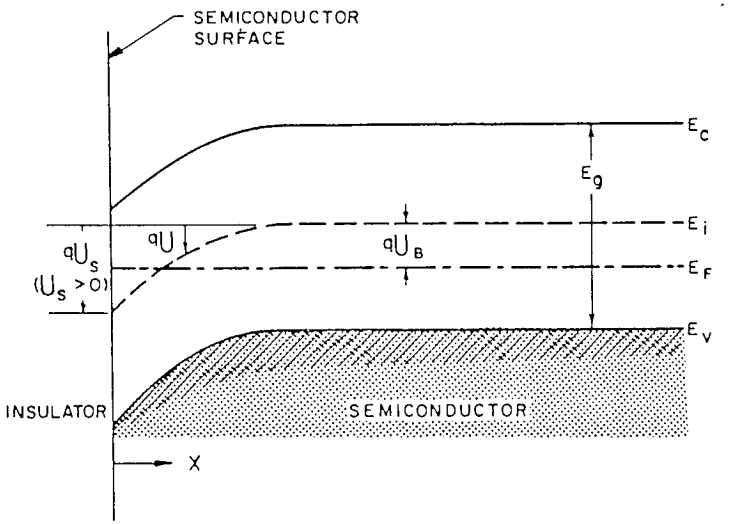

Figure 4: An energy band diagram showing the surface of a p-type semiconductor. The potential U, defined as zero in the bulk semiconductor, is measured with respect to the intrinsic semiconductor Fermi level E_i. The surface potential is positive, as shown. Three main cases can exist:

(a) Accumulation of majority carriers occurs when $U_S<0$

(b) Depletion of majority carriers occurs when $U_B>U_S>0$

(c) Inversion of majority carriers occurs when $U_S>U_B$

Since the ideal MOSC is a planar structure it may be assumed to behave one-dimensionally and so Poisson's equation may be used to find the potential, U , as a function of distance in the semiconductor. The assumptions made of the devices, in order to apply Poisson's equation, are that the semiconductor:

(1) is non-degenerate

(2) has a constant doping profile

and (3) is of a sufficient thickness that E -> 0 as x -> back contact

Thus,

$$\frac{d^2U}{dx^2} = -\frac{P(x)}{\epsilon_S} \qquad -16$$

where ϵ_S is the permittivity of the semiconductor and P(x) is the total space charge density given by

$$P(x) = q\,(N_D^+ - N_A^- + p_p - n_p) \qquad -17$$

where N_D^+ and N_A^- are the densities of ionized donors, respectively.

Considering the bulk of the semiconductor, far from the surface, by the conditions set for an ideal MOSC, charge neutrality must exist. Therefore P(x) = 0 and U = 0 and so

$$N_D^+ - N_A^- = n_{po} - p_{po} \qquad -18$$

Thus, in general for any value of U, from Equations **12** and **13**

$$p_p - n_p = p_{po}\, e^{-\beta U} - n_{po}\, e^{\beta U} \qquad -19$$

where $\beta = q/kT$.

The resultant Poisson's equation to be solved is, therefore

$$\frac{\partial^2 U}{\partial x^2} = \frac{-q}{\epsilon_S}\left[p_{po}\,(e^{-\beta U} - 1) - n_{po}\, e^{\beta U} - 1)\right] \qquad -20$$

Integrating Equation **20**, from the bulk towards the surface [14], thus

$$\int_0^{\frac{\partial U}{\partial x}} \frac{\partial U}{\partial x}\, d\left(\frac{\partial U}{\partial x}\right) = \frac{-q}{\epsilon_s}\int_0^U p_{po}(e^{-\beta U} - 1) - n_{po}(e^{\beta U} - 1)\, dU \qquad -21$$

gives the relation between the electric field ($E = -dU/dx$) and the potential, U:

$$E^2 = \frac{(2kT)^2}{2\epsilon_s} p_{po} \beta \left[\left(e^{-\beta U} + \beta U - 1 \right) + n_{po} \left(e^{\beta U} - \beta U - 1 \right) \right] \qquad -22$$

Let $$\lambda_D = \sqrt{\frac{kT\epsilon_s}{p_{po} q^2}} = \sqrt{\frac{\epsilon_s}{q p_{po} \beta}} \qquad -23$$

where λ_D is the extrinsic Debye length for holes. Physically, this quantity λ_D is the maximum distance that the charge field around a hole, in the extrinsic p-type semiconductor under analysis, can interact.

Also, let f be a function such that

$$f\left\{ \beta U, \frac{n_{po}}{p_{po}} \right\} = \left[\left(e^{-\beta U} + \beta U - 1 \right) + n_{po} \left(e^{\beta U} - \beta U - 1 \right) \right]^{1/2} \geq 0 \qquad -24$$

Then, the electric field becomes

$$E = -\frac{\partial U}{\partial x} = \pm \frac{\sqrt{2kT}}{q\lambda_D} f\left\{ \beta U \frac{n_{po}}{p_{po}} \right\} \qquad -25$$

with positive sign for $U > 0$ and negative sign for $U < 0$.

To determine the electric field at the surface when $U = U_S$ using Equation 25, gives

$$E_S = \pm \frac{\sqrt{2kT}}{q\lambda_D} f\left\{ \beta U_S, \frac{n_{po}}{p_{po}} \right\} \qquad -26$$

Similarly, by Gauss's law, the space charge per unit area required to produce this field is

$$Q_S = -\epsilon_S E_S = \pm \frac{\sqrt{2\epsilon_S kT}}{q\lambda_D} f\left\{ \beta U, \frac{n_{po}}{p_{po}} \right\} \qquad -27$$

A typical variation of the space charge density, Q_S, as a function of the surface potential, U_S, is shown in Figure 5 for p-type Si, with $N_A = 4 * 10^{15}$ cm^{-3}, at room temperature.

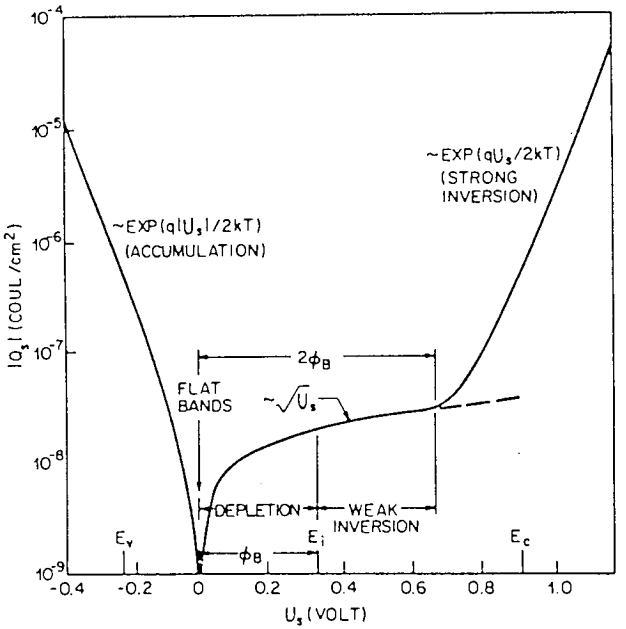

Figure 5: The variation of space-charge density in the semiconductor, $|Q_S|$, of a p-type MOSC as a function of surface potential, U_S, for a p-type substrate device with $N_A=4*10^{15}$ cm^{-3} at room temperature; U_B is the potential difference between the Fermi level and the intrinsic level of the bulk semiconductor.
(After GARRETT and BRATTAIN, Reference 18)

It can be seen that for negative U_S, Q_S is positive and corresponds to the accumulation region ; the function f is dominated by the first term in Equation **24**, and

$$Q_S \approx e^{(q|U_S|/2kT)} \quad , \; U_S<0 \qquad \textbf{-27a}$$

For $U_S = 0$; flatband conditions exist and $Q_S = 0$

For $U_B > U_S > 0$; depletion conditions exist and $Q_S<0$

When $U_S > U_B$ the function f is dominated by the second term in Equation **24** and

$$Q_S \approx \sqrt{U_S} \quad , \; U_S > U_B \qquad \textbf{-27b}$$

For $U_S \gg U_B$, the inversion case is evident from the dominance of the fourth term over the function f, that is

$$Q_S \approx -e^{(q|U_S|/2kT)} \quad , \; U_S \gg U_B \qquad \textbf{-27c}$$

Also, this strong inversion is seen to begin at a surface potential $U_{S(inv)}$ where

$$U_{S(inv)} \approx 2U_B = \frac{2kT}{q} \ln\left(N_A / n_i\right) \qquad \textbf{-28}$$

and is thus dependent solely upon the number of acceptors in the extrinsic semiconductor.

The differential capacitance of the semiconductor depletion layer , c_D, is given by

$$c_D = \frac{\partial Q_S}{\partial U_S} = \frac{c_S}{\sqrt{2}\lambda_D} \left[\frac{1 - e^{-\beta U_S} + (n_{po}/p_{po})(e^{\beta U_S} - 1)}{f\left\{\beta U_S, \frac{n_{po}}{p_{po}}\right\}}\right] \quad F\,cm^{-2} \qquad \textbf{-29}$$

Thus, at flatbands where, $U_S=0$, the differential capacitance can be obtained from expansion of the exponential terms in Equation **29** into series to obtain

$$c_{D(flatbands)} = c_S/\lambda_D \quad F\,cm^{-2} \qquad \textbf{-30}$$

It can therefore be seen that the charge associated with (majority carrier) accumulation and (minority

carrier) inversion must reside in an extremely narrow portion of the semiconductor immediately adjacent to the oxide-semiconductor interface.

By comparison , the depleted portion of the semiconductor under moderate depletion biasing extends much further into the semiconductor; in fact, the depletion region width increases only slightly once the semiconductor inverts. This occurs because the highly-peaked inversion charge near the semiconductor-insulator interface is nearly sufficient, in itself, to shield the interior of the semiconductor from any additional charge placed on the MOSC gate electrode.

2.2.2 Gate Voltage Relationship

Throughout the previous subsection, the discussion of semiconductor electrostatics was described with the biasing state expressed in terms of the semiconductor surface potential, U_S. However, the theory formulated in this manner is dependent only on the properties of the semiconductor; U_S is an internal system constraint or boundary condition.

It is the externally applied gate potential, V, which is subject to direct control in the MOSC structure. Thus, if the results of the previous subsection are to be of any practical use , an expression relating V and U_S must be established; this section is devoted to deriving such a relationship.

The applied gate potential, V, in the ideal MOSC structure, is dropped partly across the oxide, ΔV_{OX} , and partly across the semiconductor, ΔV_{SC} , thus

$$V = \Delta V_{OX} + \Delta V_{SC} \qquad -31$$

Because V=0 in the semiconductor bulk (by definition of an ideal MOSC) the voltage drop across the semiconductor is simply

$$\Delta V_{SC} = V|_{x=0} = \frac{kT}{q} U_S \qquad -32$$

Developing a relationship between V and U_S is reduced to expressing ΔV_{OX} in terms of U_S.

By the definition of an ideal MOSC, in the ideal insulator with no charge carriers or charge centres

$$\frac{dE_{ox}}{dT'} = 0 \qquad -33$$

and

$$E_{ox} = -\frac{dV_{ox}}{dT} = \text{constant} \qquad -34$$

Therefore

$$\Delta V_{ox} = \int_{-T'}^{0} E_{ox}\, dT = T' E_{ox} \qquad -35$$

where T' is the oxide (insulator) thickness.

The boundary conditions on the fields normal to an interface between two dissimilar materials requires

$$(D_S - D_{ox})\big|_{ox\text{-}sc\ interface} = Q_{ox\text{-}sc\ interface} \qquad -36$$

where D = CE is the dielectric displacement and $Q_{ox\text{-}sc}$ is the surface centre charge per unit area located at the interface.

Since $Q_{ox\text{-}sc\ interface} = 0$ in the idealised structure

$$D_{ox} = D_{sc}\big|_{x=0} \qquad -37$$

$$E_{ox} = (K_S / K_O)\, E_S \qquad -38$$

and

$$\Delta V_{ox} = (K_S / K_O)\ T'\ E_S = T'^{1} E_S \qquad -39$$

where $T'^{1} = (K_S / K_O)\ T'$; K_S is the semiconductor dielectric constant; K_O, the oxide dielectric constant; and E_S is the electric field in the semiconductor at the oxide-semiconductor interface.

Substituting Equations 32 and 39 into Equation 31 gives

$$V = \frac{kT}{q} U_S \pm T'^{1} E_S \qquad -40$$

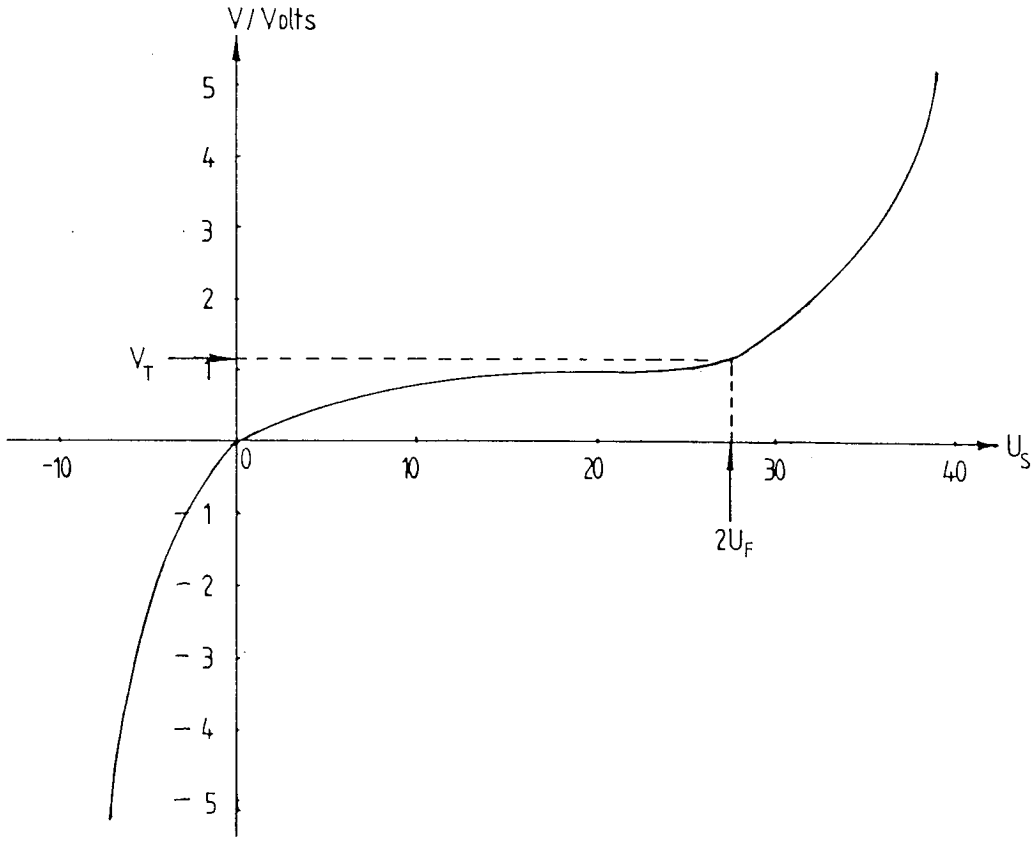

Figure 6: Typical interrelationship betwen the applied gate voltage,V, and the semiconductor surface potential, U_S, for a device with the parameters: device oxide thickness, T'=100nm; Fermi potential, U_F=12 at a temperature of 300°K.
(After PIERRET, Reference 19)

Substituting for V in Equation **25** gives

$$V = \frac{kT}{q}\left[U_S \pm T^1 \left(\sqrt{}^2 / kT\right) f\left\{ \beta U_S, \frac{n_{po}}{p_{po}} \right\}\right] \qquad \text{- 41}$$

The V - U_S dependence calculated from Equation **41** employing a typical set of device parameters (T'=100nm, U_F =12, T=300° k) is displayed[15] in Figure 6, which illustrates certain important features of the gate voltage relationship: U_S is a rapidly varying function of V when the device is depletion biased. However, when the device is accumulated ($U_S < 0$) or inverted ($U_S > 2\ U_F$), a large change in gate voltage is necessary in order to produce a small change in U_S. This implies that the gate voltage divides between the oxide and the semiconductor when the device is under depletion biasing. Under inversion and accumulation biasing, changes in the applied potential are almost totally across the oxide. The depletion bias region extends from only V=0 to V≈1.1Volts which demonstrates that, since the character of the semiconductor changes dramatically in progressing from one side of the depletion region to the other, a significant variation in the electrical characteristics over a narrow range of voltages is expected.

2.3 Ideal MOSC C-V Characteristics

In MOS device analysis the C-V characteristic can be used to reveal the internal nature of the device under test; for example, the C-V characteristic provides a means of determining at a glance what band bending is occurring inside the semiconductor for a given applied gate voltage. The C-V characteristic also serves as a powerful diagnostic tool for identifying deviations from the ideal in both the oxide and semiconductor. In fact, a large percentage of the available knowledge about the MOS system was assembled by analysing the differences between the observed capacitance-voltage characteristics and the MOS C-V characteristics predicted on a theoretical basis assuming an ideal structure.

This section is devoted primarily to examining the arguments which lead to the expected C-V characteristics of the ideal MOSC structure. The majority of the development assumes a static state, as described in the previous sections, and is concerned with two limiting cases: the low-frequency

and high-frequency limits. (These limiting cases designations refer to the frequency of the a.c. signal used in the capacitance measurements).

Figure 7(a) shows the band diagram of an ideal MIS structure with the appropriate band bending for an identical semiconductor to that shown in Figure 4. The charge distribution is shown in Figure 7(b); for the condition of charge neutrality in the system, it is required that

$$Q_M = Q_n + q N_A W = Q_S \qquad -42$$

where Q_M is the charge per unit area on the metal gate electrode; Q_n is the electron charge per unit area in the inversion region; and $q N_A W$ is the ionised acceptors per unit area in the space-charge region of with W. Q_S is the total charge per unit area in the semiconductor.

The electric field and potential distributions are obtained by first and second order integrations of the one-dimensional form of Poisson's equation; these are shown schematically in Figures 7(c) and 7(d) respectively.

Since the structure is considered to be ideal, the assumption that there is no difference between the work functions of the metal and the semiconductor may be made, and so the applied voltage will appear partly across the oxide, V_{ox} , and partly across the semiconductor, V_{sc}. Thus, Equation **31** holds and

$$V = V_{ox} + V_{sc} = V_{ox} + U_S \qquad -43$$

where V_{ox} is the potential drop across the oxide, given by

$$V_{ox} = E_{ox}\, T' = \frac{|Q_S|\, T'}{\varepsilon_{ox}} = \frac{Q_S}{C_{ox}} \qquad -44$$

The total capacitance, c, of the system is a series combination of the oxide capacitance, c_{ox} , (=C_{ox} /T') and the semiconductor depletion-layer capacitance, c_d :

$$c = \frac{c_{ox}\, c_d}{c_{ox} + c_d} \qquad F\,cm^{-2} \qquad -45$$

For a given oxide thickness, T', the value of c_{ox} is constant and corresponds to the maximum capacitance of the system. The capacitance, c_d, as given by Equation **29** ,depends on the applied

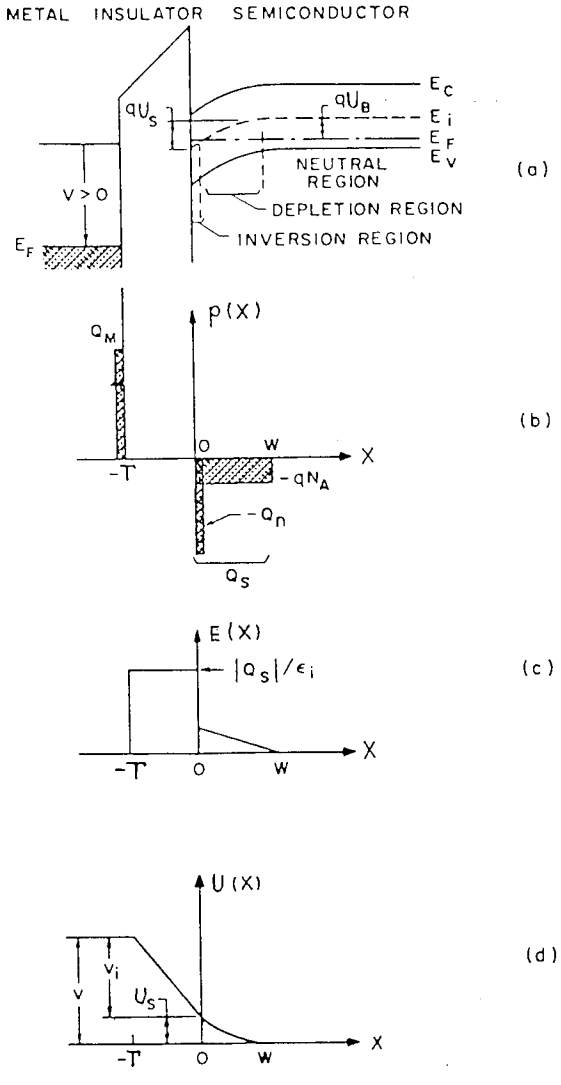

Figure 7: (a) The band diagram of an ideal MOSC with a p-type semiconductor substrate when under the inversion condition.
(b) The charge distribution in the device
(c) The electric field distribution in the device
(d) The potential distribution in the device

voltage. The total capacitance at the flatband (that is, $U_S=0$) condition, c_{fb}, is obtained from Equations 30 and 45, thus

$$c_{fb} = \frac{\epsilon_{ox}}{T + \frac{\epsilon_{ox}}{\epsilon_S}\lambda_D} = \frac{\epsilon_{ox}}{T + \frac{\epsilon_{ox}}{\epsilon_S}\sqrt{\frac{kT\epsilon_S}{p_{po}q^2}}} \quad -46$$

where ϵ_{ox} and ϵ_S are the permittivities of the oxide and semiconductor, respectively, and λ_D the Debye length given by Equation 23. The combination of Equations 29,43,44,45 and 46 gives the complete description of the C-V curve of an ideal MOS system, as shown in Figure 8.

In describing Figure 8; it can be seen that at negative gate voltages (accumulation of holes) there is a high differential capacitance of the semiconductor, and as a result the total capacitance of the structure is close to that of the oxide capacitance. As the negative voltage is reduced sufficiently a depletion region, which acts as a dielectric in series with the oxide, is formed near the semiconductor surface; the total capacitance therefore decreases. The minimum capacitance and the corresponding minimum voltage are designated c_{min} and V_{min}, respectively (see Figure 8).

The increase of the capacitance depends on the ability of the electron concentration to follow the superimposed a.c. signal; this only happens at low frequencies (of the order of tens to hundreds of Hz) where the recombination-generation rates of minority carriers (electrons in this p-type device) can keep-up with the small-signal variation and lead to charge exchange with the inversion layer in step with the measurement signal. (Experimentally[20-21], it is found that, for the Al-SiO_2-Si system, this frequency is between 5 and 100Hz). As a consequence, MOS C-V curves measured at high (KHz) frequencies do not display the increase of capacitance , as shown in Figure 8,curve(b).

Figure 8,curve(c) shows the capacitance curve expected under deep-depletion (pulse) conditions, which is directly related to breakdown phenomena described in Chapter 3 and 6; at even higher gate voltages, impact-ionization may occur at the semiconductor surface and the device may go through a transient "avalanche breakdown" stage which can be seen on both the C-V curve and the current-voltage curve for the device under test. This is also shown on curve (c) of Figure 8. (This process is discussed in detail in Chapter 3). A more in-depth treatment of the frequency dependence of the C-V characteristics of MOS systems, considered beyond the scope of this thesis, may be found in chapters 3 and 4 of the book by NICOLLIAN and BREWS[16].

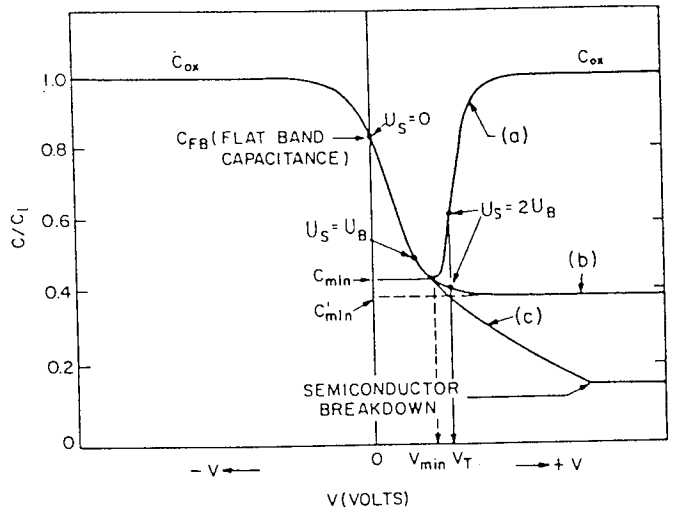

Figure 8: Capacitance-Voltage curves for a p-type MOSC:
(a) The low frequency (<10KHz) curve
(b) The high frequency (>100KHz) curve
and (c) The deep depletion condition.

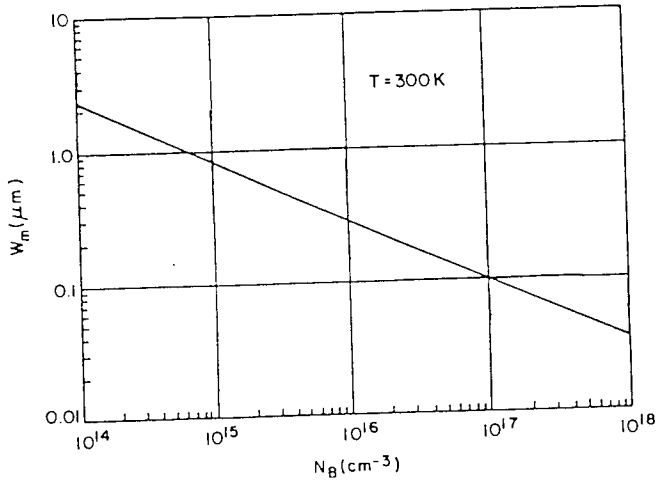

Figure 9: The relationship between the maximum depletion layer width of a semiconductor, W_m, under the strong inversion condition versus the semiconductor impurity concentration, N_B, for silicon at 300°K. [For p-type silicon $N_B=N_A$, and for n-type silicon $N_B=N_D$]

Figure 8 also shows the corresponding surface potentials of the p-type semiconductor MOSC under discussion. For an ideal MOSC: the flatband capacitance occurs at V=0, where U_S=0: the depletion region corresponds to a surface potential range from U_S=0 to U_S=U_B: weak inversion begins at U_S=U_B, which is slightly less than V_{min}: and the onset of strong inversion occurs at U_S=2U_B.

When the semiconductor surface is depleted, the ionized acceptor density in the depletion region is given by -q N_AW (Equation 10). Integrating Poisson's equation applied to this region yields the potential distribution in the depleted region, thus

$$U = U_S \left(1 - x / W\right)^2 \qquad -47$$

where U_S is given, in this instance, by

$$U_S = \frac{qN_AW^2}{2\epsilon_s} \qquad -48$$

Thus, when the applied gate voltage is increased U_S and W increase; eventually, strong inversion will occur (as shown in Figure 5). Strong inversion begins at $U_{S(inv)} \approx 2U_B$ and once it has occurred, the depletion-layer width reaches a maximum, W_m. When the bands are bent down far enough that U_S=2U_B, the semiconductor is effectively shielded from further penetration of the electric field by the inversion layer and even a very small increase in the band-bending (corresponding to a very small increase in the depletion-layer width) results in a very large increase in the charge density in the inversion layer.

The maximum width of the surface depletion region for the MOS system in strong inversion (under steady-state conditions) can be calculated from Equations 28 and 48 thus,

$$W_m \approx \sqrt{\frac{2\epsilon_S U_{S(inv)}}{qN_A}} = \sqrt{\frac{4\epsilon_S kT \ln\left(N_A / n_i\right)}{qN_A}} \qquad -49$$

The relationship between W_m and N_A is shown in Figure 9 for silicon (where N_A=N_B for p-type and N_A=N_D for n-type semiconductor).

Another quantity of interest is the so-called "turn-on" voltage (also called the threshold voltage) at

which strong inversion occurs. This is a useful quantity since it is this which gives a measure of the change of depletion-layer width under external influences (such as irradiation and high-field stressing).

From Equations **28** and **43** the threshold voltage for strong inversion, $V_{T(\text{strong inv.})}$, can be calculated

$$V_{T(\text{strong inv.})} = \frac{Q_S}{C_{ox}} + 2U_B \qquad -50$$

Because at the end of strong inversion $Q_S = q N_A W$, from Equation **10**, the threshold voltage is given by

$$V_{T(\text{onset})} \approx \frac{\sqrt{2\epsilon_S q N_A (2U_B)}}{C_{ox}} + 2U_B \qquad -51$$

The corresponding total capacitance is given by

$$C'_{min} \approx \frac{\epsilon_{ox}}{T' + (\epsilon_{ox}/\epsilon_S) W_m} \qquad -52$$

Figure 10 shows the high frequency capacitance curve for an ideal p-type MOSC; the dashed curves show the theoretically approximated segments of the C-V relationship.The approximated curve agrees remarkably well with those found experimentally.

The ideal MOS curves of the metal-SiO_2-Si system have been computed for various oxide thicknesses and semiconductor doping densities[22] using exact solutions to the theory presented in this section. Figure11 shows typical examples for p-type silicon: as the oxide becomes thinner the larger the variation of capacitance. Figure 12 shows the dependence of U_S on the applied voltage for the same system as in Figure 11. Figures 13 through to 16 show the normalised flatband capacitance, (C_{fb}/C_{ox}); the normalised minimum capacitances, (C_{min}/C_{ox}) and (C'_{min}/C_{ox}); and the threshold voltage (V_T) and minimum voltage (V_{min}) versus oxide thickness (with silicon doping concentration as the parameter) respectively.

The theory presented thus far has centered on MOS systems with p-type semiconductor (in particular, silicon) substrates. The conversion of this theory to that applicable to MOS systems with n-type substrates is achieved simply by changing the sign of the voltages applied to the device and

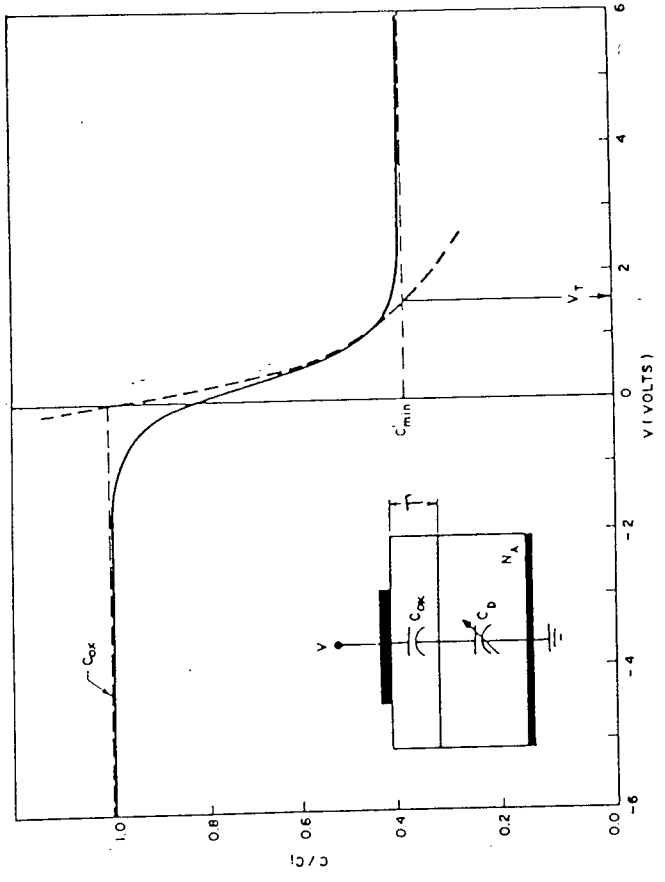

Figure 10: The high frequency C-V curve for an ideal p-type MOSC showing its approximated segments (dashed curves).

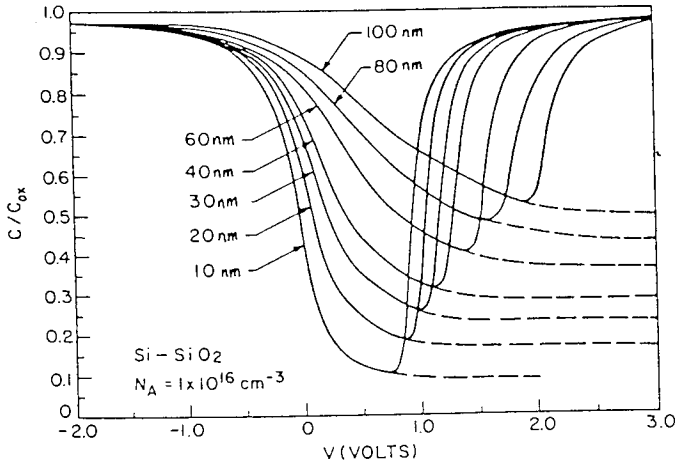

Figure 11: Low frequency (solid curves) and high frequency (dashed curves) C-V characteristics for ideal p-type MOSCs with various thicknesses of oxide. The structure is silicon-based with a semiconductor acceptor density, N_A, of $N_A=10^{16}$ cm^{-3}.
(After GOETZBERGER, Reference 22)

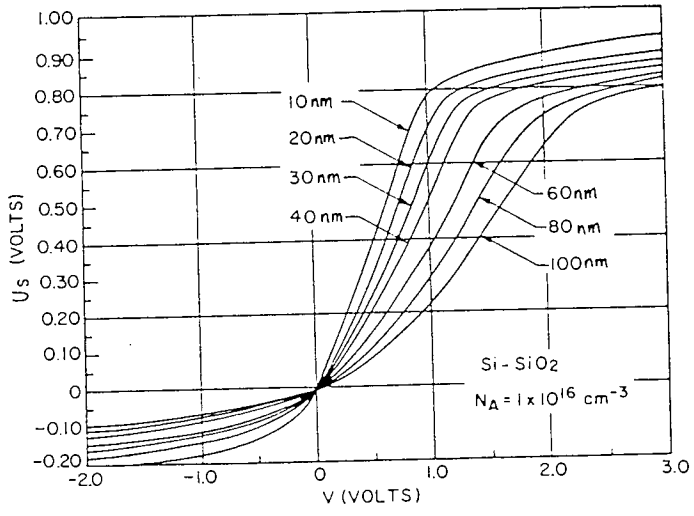

Figure 12: The surface potential, U_S, versus applied gate voltage for ideal p-type MOSCs with various thicknesses of oxide. The structure is silicon-based with a semiconductor acceptor density, N_A, of $N_A=10^{16}$ cm^{-3}.
(After GOETZBERGER, Reference 22)

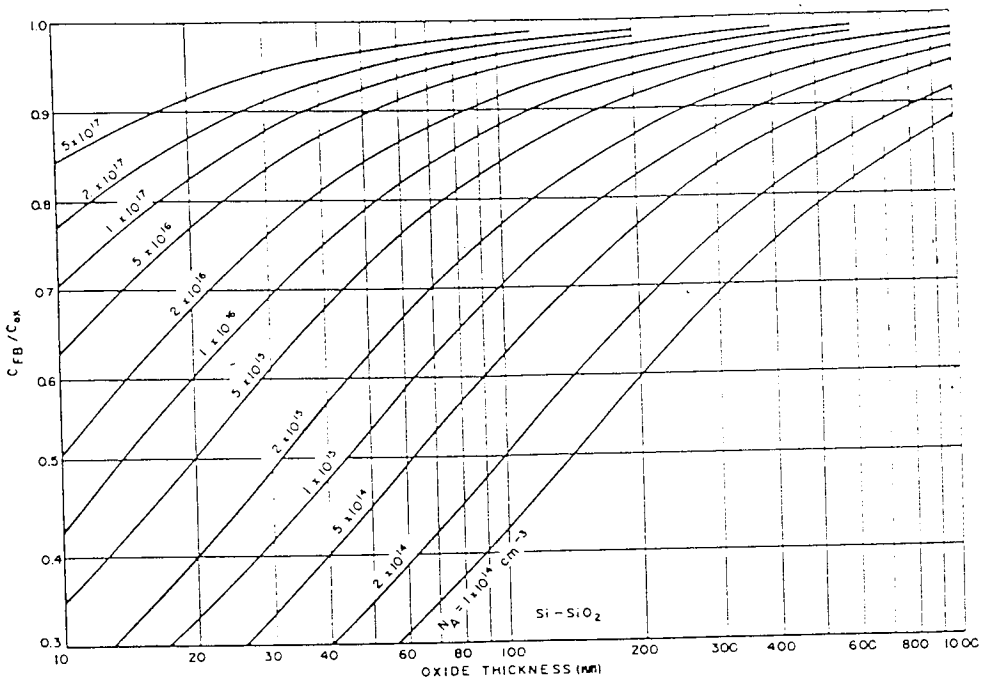

Figure 13: The normalised flatband capacitance versus oxide thickness with doping density as the parameter for an ideal p-type silicon-based MOSC.
(After GOETZBERGER, Reference 22)

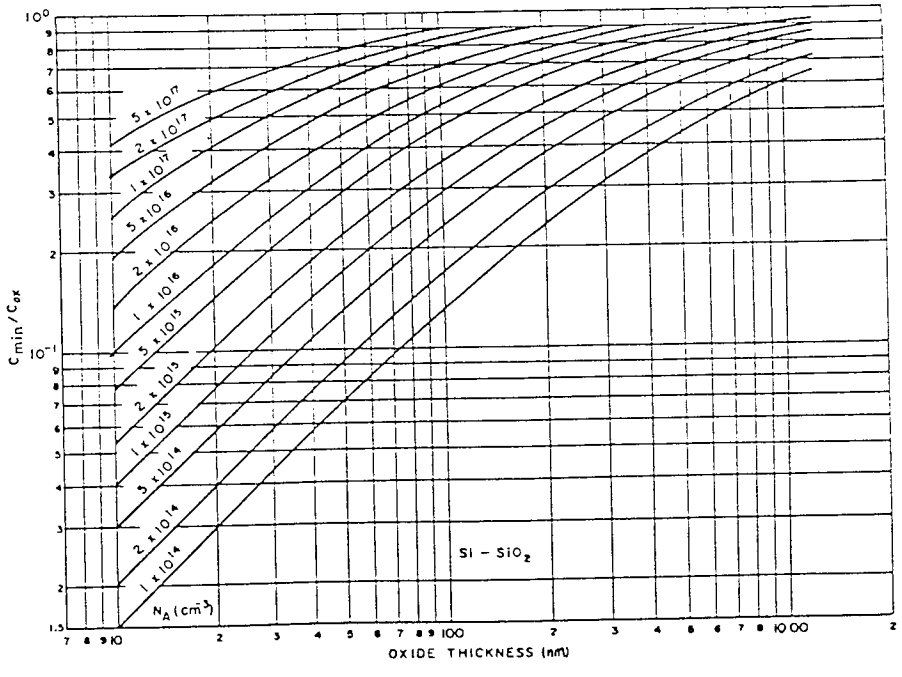

Figure 14: The normalised minimum capacitance versus oxide thickness with silicon doping as the parameter for an ideal p-type silicon-based MOSC under low frequency conditions.
(After GOETZBERGER, Reference 22)

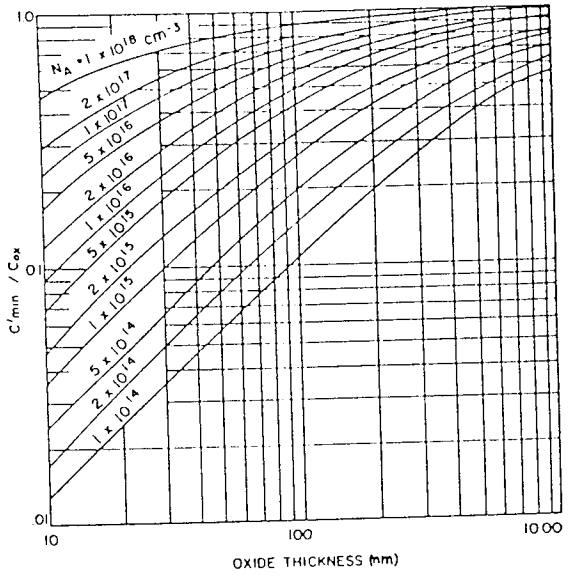

Figure 15: The normalised minimum capacitance versus oxide thickness with silicon doping as the parameter for an ideal p-type silicon-based MOSC under high frequency conditions.
(After GOETZBERGER, Reference 22)

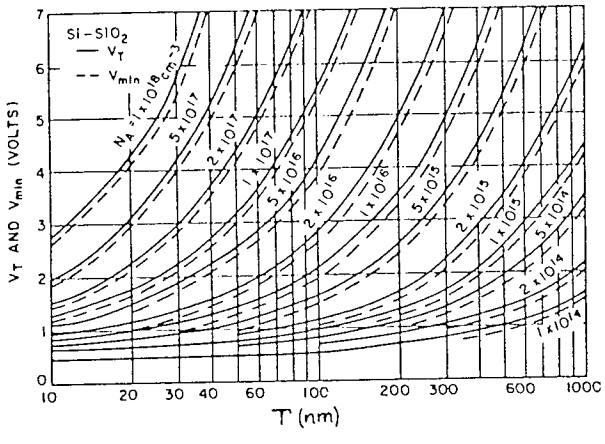

Figure 16: The threshold voltage and minimum voltage versus oxide thickness with silicon doping density as the parameter for ideal p-type silicon-based MOSCs.
(After GOETZBERGER, Reference 22)

appropriate symbols (for example, Q_p for Q_n). The C-V characteristics will have identical shapes, but be the mirror images of each other, and the threshold voltage is a negative quantity for an ideal MOSC on an n-type semiconductor substrate. For the sake of brevity, this is left to the reader and is not worked-through here.

The theory presented and the ideal MOS curves, shown in Figures 11 through to 15, will be used in subsequent sections to compare with experimental results and to understand practical MOS systems.

2.4 The Al-SiO_2-Si MOSC: A Theoretical Approach

Of all the possible MOSC structures, the Al-SiO_2-Si is the most extensively used and studied. The electrical characteristics of the SiO_2-Si system are approaching those of the ideal MOSC described in the previous sub-sections. However, for commonly used metal gate electrodes, the assumption (made in section **2.1**) that the work function difference between metal and semiconductor is zero is not valid: for example, aluminium has $q\Phi_m$ = 4.1 eV whereas the work function for, say, n-type silicon, may vary from 4.2 to 4.5 eV over the typical doping range of 10^{14} - 10^{18} cm^{-3}.

The effect of this work function difference on the characteristics of MOSCs is discussed in the next sub-section (**2.4.1**).

Also, there are various charges at the SiO_2-Si interface and in the bulk oxide which affect the device characteristics of real devices. These charges and their effect on ideal MOSC characteristics are discussed in section **2.4.2**.

Finally, the assumption that the insulator - SiO_2 in this case- is perfect and does not conduct (under normal temperature and bias conditions) is also not valid; the various mechanisms for carrier transport and resultant current flow in insulators are summarised and briefly, discussed with reference to the Al-SiO_2-Si MOSC structure, in section **2.4.3**.

2.4.1 The Work Function Difference

The work function of a semiconductor, $q\emptyset_s$, which is the energy difference between the vacuum level and the Fermi level (see Figure 2) varies with the doping concentration in the semiconductor. Thus, for a metal with a fixed work function, $q\emptyset_m$, the work function difference (given in Equations **1a** and **1b** for n-type and p-type semiconductor respectively) will vary depending on the doping of the semiconductor.

The gate electrode used in this study is aluminium; the work function difference, $q\emptyset_{ms}$, is shown in Figure 17 for aluminium gates and silicon substrates in both n- and p-type MOSCs with an ideal oxide layer for a large range of doping (impurity) concentrations of the semiconductor at room temperature.

Consider the isolated components of the MOSC system, as shown in Figure 18(a), joined together to form the non-ideal MOSC under zero bias (flatband condition in an ideal MOSC), as shown in Figure 18(b). It can be seen that $q\emptyset_m$ is smaller than $q\emptyset_s$, and their difference ,$q\emptyset_{ms}$, is negative and equal in magnitude to the voltage V_{fb}, the flatband voltage. At thermal equilibrium, the Fermi level must be constant and the vacuum level continuous; to accommodate the work function difference in real MOSCs, the semiconductor bands must, therefore, bend downwards, as shown in Figure 18(c). In order to obtain the ideal flatband condition, a voltage equal to the work function difference, $q(\emptyset_m - \emptyset_s)$, must be applied to the device; this corresponds to the situation shown in Figure 18(b), where a negative voltage, V_{fb}, must be applied to the metal gate electrode. Effectively, the surface is slightly depleted; the addition of the insulator has lowered the effective surface barriers and reduced the electric field in the insulator region. Figures 19(a) and (b) show the band diagrams of Al-SiO_2-Si MOSCs with an oxide thickness of 50nm grown on n-type Si, $10^{16}cm^{-3}$ doping density (Figure 19(a)[23]) and p-type Si, 10^{10} cm^{-3} doping density (Figure 19(b)[23]).

Thus, the work function difference (and any deviation from the ideal) modifies the relationship between the semiconductor surface potential and the applied gate voltage; a new V-U_s relationship is required to describe "real " MOSCs.

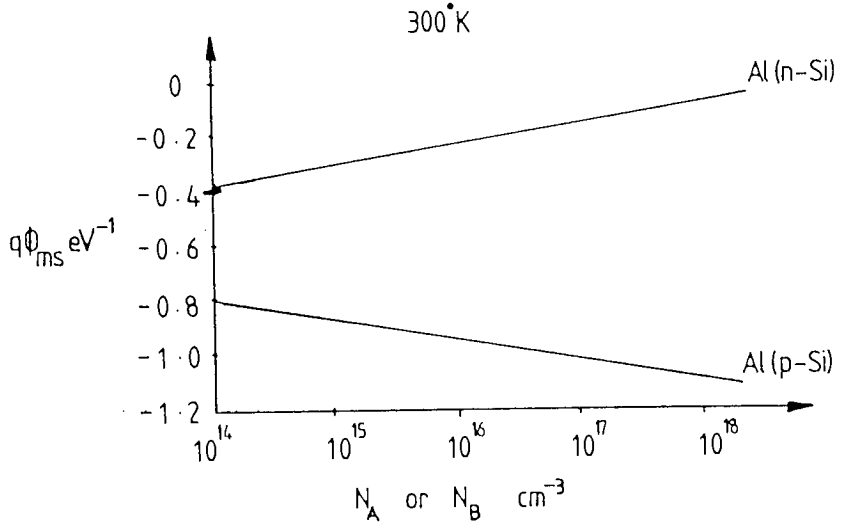

Figure 17: The work function difference as a function of background impurity concentration for n and p-type silicon-based MOSCs with aluminium gates and ideal oxide layers.

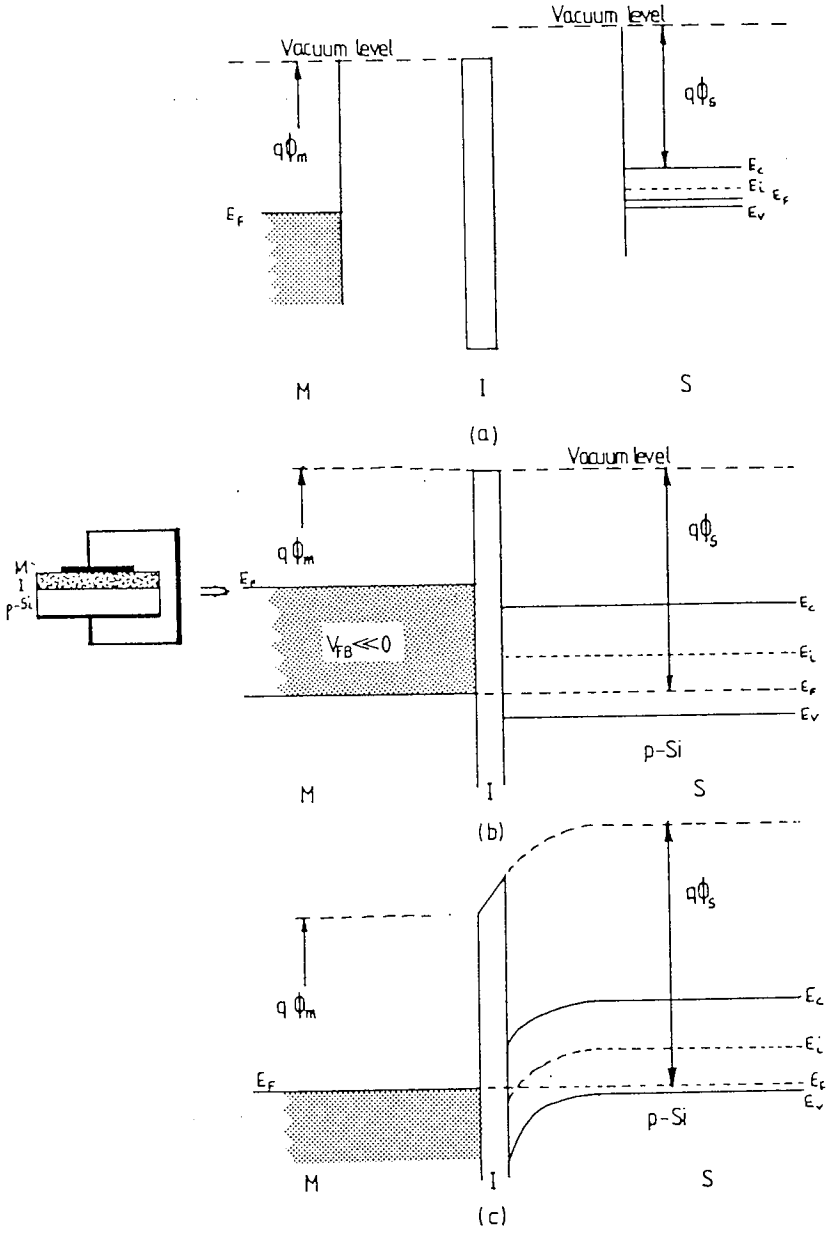

Figure 18: (a) The energy band diagram of the isolated components of an Al-SiO_2-Si MOSC under thermal equilibrium conditions.

(b) The energy band diagram of the resulting structure when the individual components of the MOSC, shown in Figure 18(a), are joined.

(c) The energy band diagram of the ideal p-type silicon-based MOSC shown in Figure 18(b) under thermal equilibrium conditions.

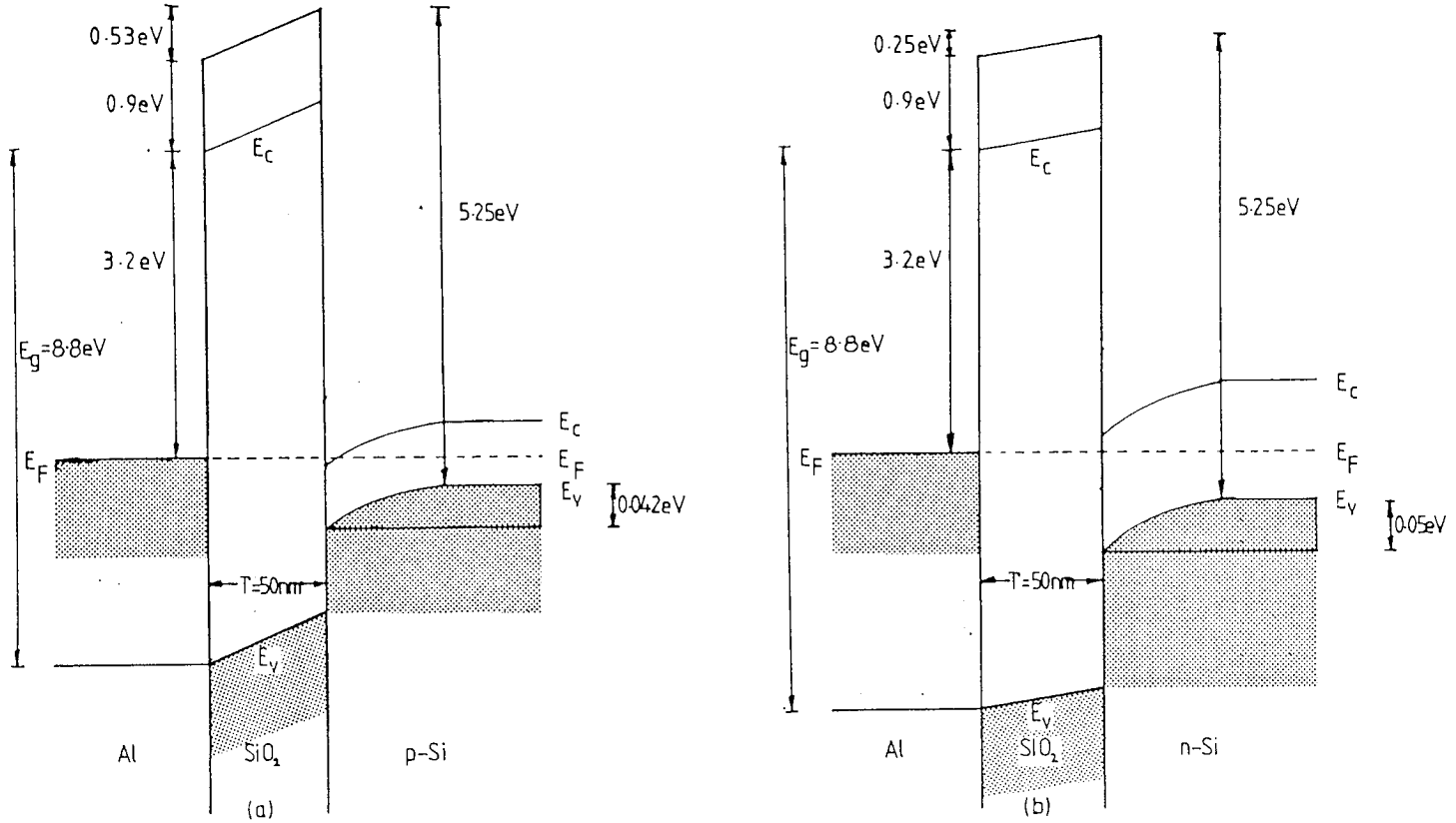

Figure 19: The energy band diagrams (drawn to scale) for n-type and p-type Al-SiO_2-Si MOSCs with oxide thicknesses of 50nm and silicon impurity concentrations of 10^{16} cm^{-3} and 10^{10} cm^{-3}, respectively.
(After DEAL, Reference 23)

If an arbitrary gate voltage, V_g , is applied to the MOSC structure whose band system is shown in Figure18(a) the situation shown in Figure 20 is seen; from Figure 20 it can be seen that

$$\underset{\text{metal side}}{\varnothing_m' - qV_g + q\Delta V_{ox}} = \underset{\text{semiconductor side}}{(E_c - E_F) - kTU_s + \varnothing_s'} \qquad -53$$

$$V_g - \left(\frac{kTU_s}{q} + \Delta V_{ox}\right) = \frac{1}{q}\left(\varnothing_m' - \varnothing_s' (E_c - E_F)\right) \qquad -54$$

Since $$\varnothing_{ms} = \frac{1}{q}\left\{\varnothing_m' - \varnothing_s' - (E_c - E_F)\right)$$

or $$\varnothing_{ms} = \frac{1}{q}\left\{\varnothing_m - \varnothing_s - (E_c - E_F)\right) \qquad -55$$

Recalling, from Equations **31** and **32**, that: $V = (kT / q)U_s + \Delta V_{ox}$, it can be seen that, for $V=V_g$

$$\Delta V_g = (V_g - V)\big|_{\text{same Us}} = \varnothing_{ms} \qquad -56$$

Equation **56** is interpreted as follows: to achieve a given U_s value inside a non-ideal MOSC structure , a voltage equal to $V + \varnothing_{ms}$ must be applied, where V is the gate voltage, in order to achieve the same U_s as if the structure were ideal.

Relative to the C-V characteristic for a given MOSC, since $\varnothing_{ms}$ is a voltage independent constant, a $\varnothing_{ms} \neq 0$ simply gives rise to a parallel translation of the entire C-V curve, as illustrated in Figure 21 for a high-frequency C-V measurement. Each capacitance value is totally determined by the U_s value inside the semiconductor and, therefore, occurs displaced by $\varnothing_{ms}$ volts relative to the ideal case ; this gives a new value of flatband voltage, V_{fb}' .

Thus, with no extraneous influences present (oxide charge, interface traps or interfacial charge) in the non-ideal MOSC a shift of the C-V characteristic is to be expected, the shift entirely dependent on the work function difference between the metal and the semiconductor's substrate.

In order to obtain an Al-SiO_2-Si MOSC with as near ideal characteristics as possible, the silicon doping density (at room temperature) is chosen such that $\varnothing_{ms}$ is as near to zero as is possible.

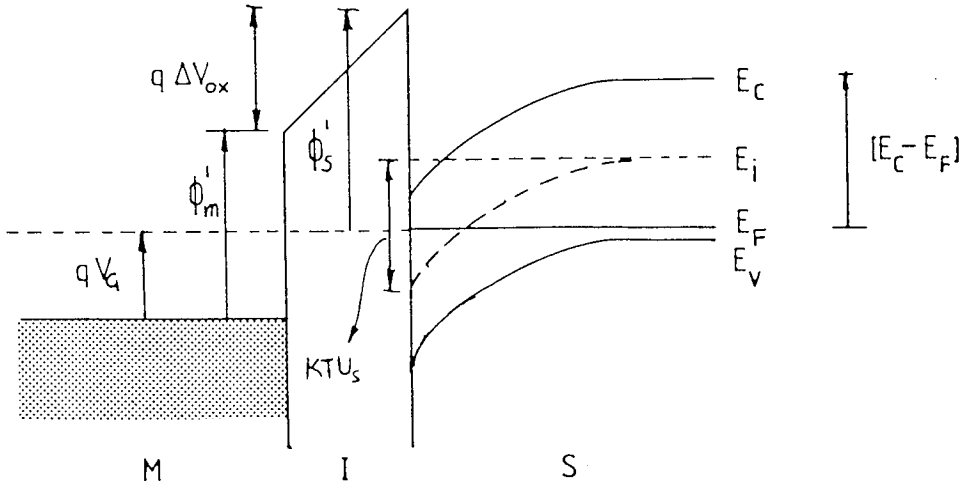

Figure 20: The band diagram and relevant energy differences for an arbitrarily-biased, non-ideal MOSC.

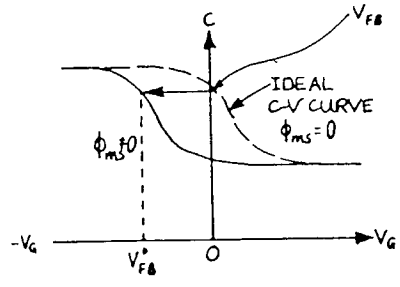

Figure 21: The effect of a non-zero work function difference on the ideal high frequency C-V characteristic of a p-type silicon based MOSC.

However, interface charge, oxide charge and traps exist in all real MOS devices and these too have a large effect on the MOSC characteristics, as discussed in the next sub-section.

2.4.2 Interface Trapped Charge and Oxide Charge

From the definition of an ideal MOSC[17] given in section **2.1** , the only charges that should exist in such an MOS structure, under any bias conditions, are those in the semiconductor and those with an equal, but opposite, sign on the metal surface adjacent to the insulator; this is not the case for Al-SiO_2-Si MOSCs, where the exact nature of the SiO_2-Si interface is not yet fully understood and the bulk oxide is by no means pure.

One thoroughly researched picture[17] of the interface is that the chemical composition of the interfacial region, as a consequence of thermal oxidation, is a single-crystal silicon layer followed by a monolayer of incompletely oxidised silicon, SiO_x, then a strained region of SiO_2 approximately 1nm to 4nm thick; the remainder of the layer is stoichiometric, strain-free, amorphous SiO_2. (The compound SiO_x is stoichiometric when x=2 and non-stoichiometric when 2>x>1). This is the generally agreed-upon view of the composition of thermally grown oxide layers on silicon.

Although models which detail the electrical behaviour of interfacial traps have been proposed, the physical nature of these traps has not yet been clarified. The weight of experimental evidence[24] supports the view that the interfacial traps arise, primarily, from unsatisfied chemical bonds (dangling bonds) at the semiconductor surface; when the Si lattice is abruptly terminated along a particular plane to form a surface, one of the four surface-atom bonds is left dangling, as shown schematically in Figure 22(a). Logically, the thermal formation of the SiO_2 layer ties-up some, but not all, of the Si-surface bonds. It is the remaining dangling bonds which become the interface traps shown in Figure 22(b). To add support to this simple physical model, consider a <100> surface of silicon where there are approximately $6.8 * 10^{14}$ atoms cm^{-2}; if one-thousandth of these formed interface traps, and one electronic charge is associated with each trap, the structure would contain $6.8 * 10^{11}$ traps cm^{-2}. This agrees very well with experimental evidence presented by DEAL[24-25].

Also, charges may exist in the oxide layer - oxide charges - which also affect MOS characteristics. The basic classifications[25] of these traps and charges are listed below and are shown schematically

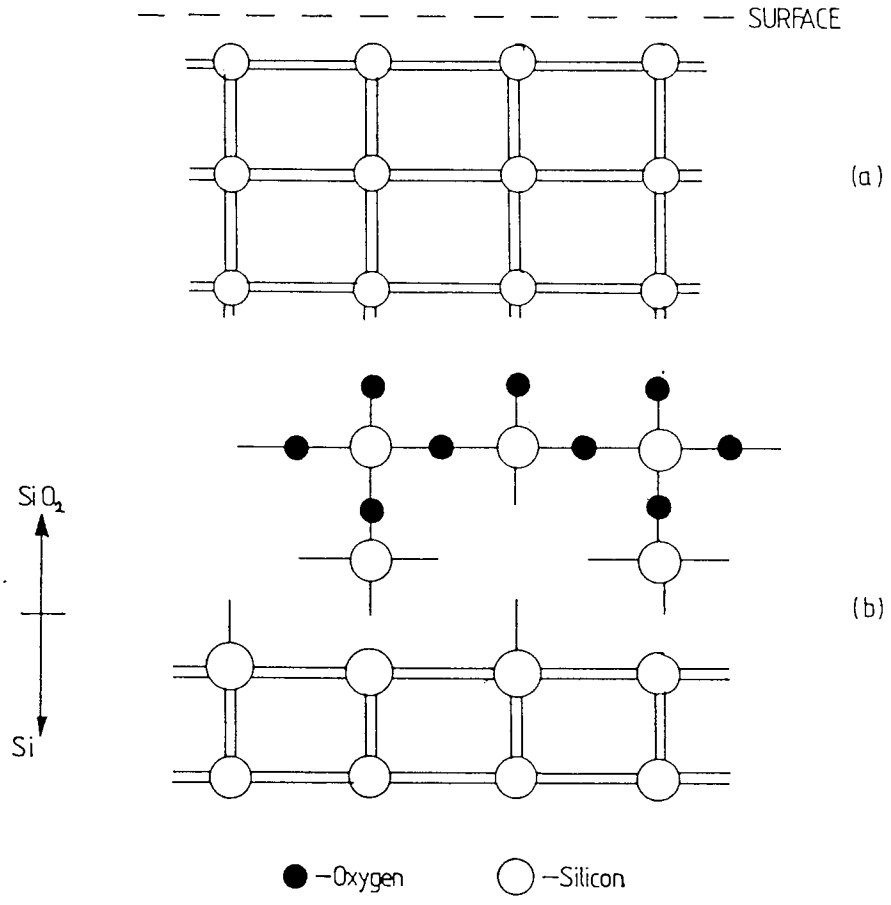

Figure 22: The physical model for interfacial traps:

(a) "Dangling bonds", which occur when the silicon lattice is abruptly terminated along a given plane to form a surface.

(b) post-oxidation dangling bonds (relative number greatly exaggerated) which become interfacial traps.

in Figure 23. Charges in a real MOSC consist of:

(1) Interface trapped charges, Q_{it}, which are charges located at the Si-SiO_2 interface with energy states in the silicon forbidden bandgap, which can exchange charges with the silicon very quickly (so-called "fast" states). Q_{it} can, possibly, be produced by excess silicon (trivalent Si), excess oxygen and impurities.

(2) Fixed oxide charges, Q_f, which are located at or near the interface and are immobile under an applied electric field.

(3) Oxide trapped charges, Q_{ot}, which can be created by, for example, hot-electron injection.These traps are distributed randomly in the oxide layer.

and (4) Mobile oxide charges, Q_m, such as sodium ions, which can move throughout the oxide layer under an applied bias or under variable temperature conditions.

The foregoing charges are the effective nett charge per unit area (that is, C cm^{-2}) which may be expressed as a number of unit charges cm^{-2}.

Because interface-trap levels are distributed across the silicon energy bandgap, the interface-trap density, D_{it}, is defined as

$$D_{it} = \frac{1}{q}\frac{dQ_{it}}{dE} \qquad \text{number of charges } cm^{-2}eV^{-1} \qquad -57$$

The magnitude of D_{it} is extremely dependent on even minor fabrication details (such as the cleaning materials used to clean the silicon wafers) and varies significantly from one batch of devices to another. Nevertheless, reproducible general trends have been reported[26]; the interfacial trap density has been found to be greatest on <111> silicon surfaces and least on <100> silicon surfaces, with the ratio of states on the two surfaces being approximately 3:1 ; after oxidation, in dry O_2 ambient, D_{it} is found to be of the order of 10^{11}-10^{12} states $cm^{-2}eV^{-1}$, with the density decreasing for increasing oxidation temperature[22]. This is why <100> silicon, oxidised at (optimum) high temperatures in dry oxygen, is most frequently chosen for high-quality MOS devices.

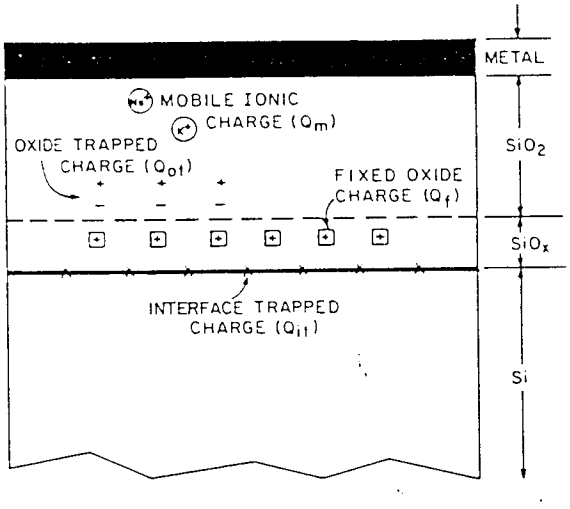

Figure 23: The terminology for charges associated with thermally oxidised silicon surfaces.
(After DEAL, Reference 25)

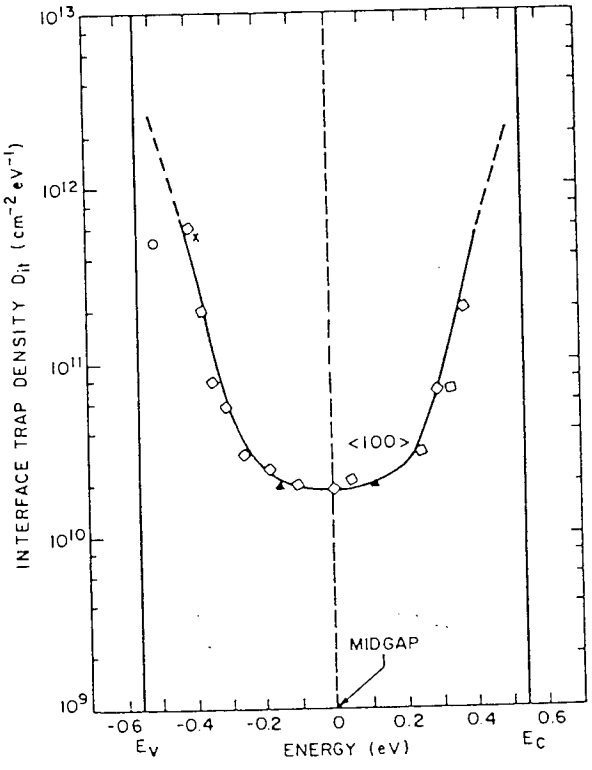

Figure 24: The density of interface traps, D_{it}, in thermally oxidised <100> silicon versus the trap energy in the forbidden gap.
(After WHITE and CRICCHI, Reference 29)

Annealing the oxidised silicon surfaces in dry H_2 at temperatures of ≤500°C has been shown to minimise D_{it}[27]. A mechanism underlying this has been proposed which adequately describes the annihilation of interface states by hydrogen migrating through the oxide layer and attaching itself to the Si dangling bonds; this makes the bond electrically inactive. Using hydrogen annealing , the value of D_{it} can be reduced to as low as 10^{10} $cm^{-2}eV^{-1}$, which is approximately one interface trapped charge per 10^5 surface atoms.

The interface-trap density in thermally oxidised <100> silicon versus trap energy for a typically fabricated MOSC is shown in Figure 24; near the midgap, D_{it} is approximately constant but increases toward the conduction and valence band edges. Figure 24 illustrates that the interface-trap density in the Si-SiO_2 system is composed of many levels, very closely spaced in energy and, in fact, appears as a continuum over the bandgap of the semiconductor.

Since interface-traps have several energy levels within the semiconductor bandgap they are able to exchange charge with the semiconductor; specifically, they can interact with the silicon conduction band by capturing electrons (an acceptor interface trap) or by emitting electrons (a donor interface trap) and, similarly, they can interact with the valence band by capturing or emitting holes. Capture or emission occurs when interface traps (also called interface states) change their occupancy level. Changes in occupancy can be produced by changes in the applied gate bias, as illustrated in Figure 25 for a p-type substrate MOSC. In Figure 25(a), no gate bias is applied to the MOSC and band-bending is caused by charged interface-traps (and the contribution to the flatband voltage due to $\emptyset_{ms} \neq 0$); the interface trap levels below the Fermi level are full and those below are empty.

In Figure 25(b), a negative gate bias is applied to the same MOSC, moving the valence band edge at the (silicon) surface toward the Fermi level; the interface-trap levels empty by capturing the majority carriers - holes in p-type semiconductor - until the equilibrium condition in Figure 25(b) is reached (if the negative gate bias is sufficient to invert the surface, equilibrium is reached involving both majority and minority carriers) .

In Figure 25(c), a positive gate bias is applied, moving the conduction band edge at the (silicon) surface toward the Fermi level and the interface-trap levels fill by emitting majority carriers until the equilibrium condition shown in Figure 25(c) is reached.

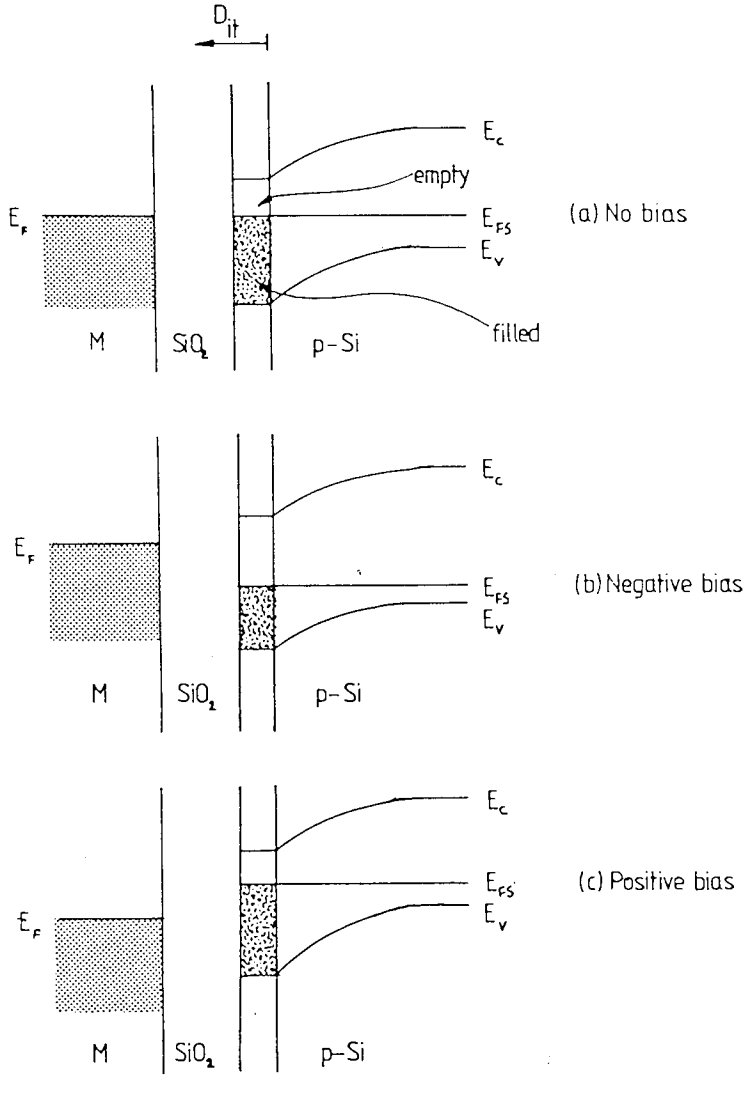

Figure 25: A band bending diagram to illustrate how interface traps change occupancy with applied gate bias in a p-type silicon-based MOSC. An arbitrary uniform distribution of trap levels is shown for illustration.

The change of charge of the interface traps when they cross the Fermi level contributes to the MOSC capacitance and alters the ideal MOSC C-V characteristics. The effects of interface traps on the MOSC C-V characteristic are described, with reference to recent experimental evidence, in section **2.5**.This alteration to the ideal characteristics can be a used as a measure of the interface-trap level density; in Chapter **5**, a novel technique for extracting D_{it} from high-frequency C-V curves is described.

Other charges which exist in the real MOSC, which have major effects on the ideal MOSC characteristics, are oxide charges: the fixed charge, Q_f, the oxide trapped charge, Q_{ot}, and the mobile ionic charge, Q_m, as shown in Figure 23 and described briefly above.

The fixed oxide charge has the following properties:

(a) It is fixed and cannot be charged or discharged over a wide variation of U_S.

(b) It is located within approximately 3nm of the Si-SiO_2 interface[16].

(c) It is generally positive and depends on the oxidation and annealing processes used during fabrication and on the silicon wafer crystal-orientation.

(d) Its density is not greatly affected by the oxide thickness or by the type or concentration of impurities in the silicon substrate.

In electrical measurements, Q_f can be regarded as a charge sheet located at the Si-SiO_2 interface. The origin of oxide fixed charge has not, as yet, been found; however, it has been suggested[16] that excess silicon (perhaps trivalent silicon) or the loss of an electron from excess oxygen carriers (non-bonding oxygen) near the Si-SiO_2 interface are possible causes.

Consider the case illustrated in Figure 26, which shows a cross-section through a MOSC having a positive Q_f and a negative gate bias: charge neutrality requires that every negative charge on the gate be compensated by an equal and opposite charge in the oxide and the silicon. For the ideal case, $Q_f = 0$, the entire compensation comes from the ionised donors; for a real MOSC with positive Q_f, part of the compensating charge must consist of Q_f, the rest of ionised donors.

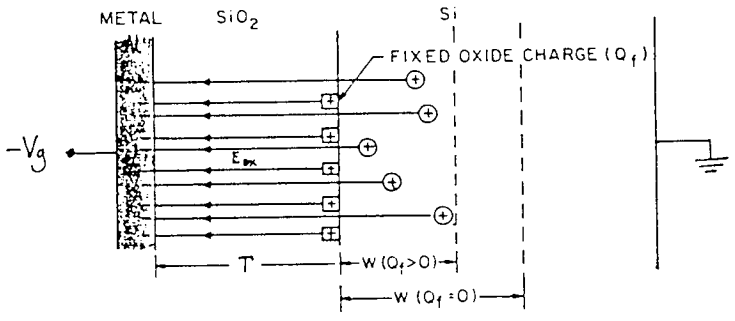

Figure 26: A schematic diagram showing the effect of a fixed oxide charge on an Al-SiO_2-Si MOSC.

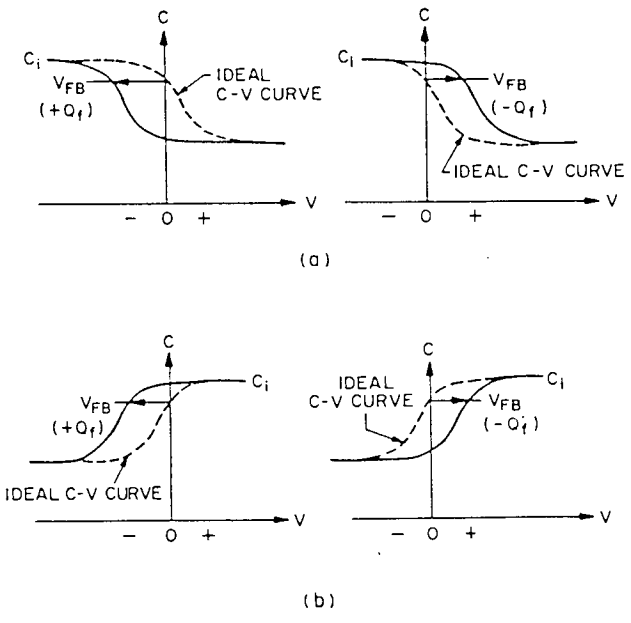

Figure 27: (a) The shift of the ideal C-V characteristic along the gate voltage axis due to positive and negative fixed oxide charge in a p-type MOSC.

(b) The shift of the ideal C-V characteristic along the gate voltage axis due to positive and negative fixed oxide charge in an n-type MOSC.

Figure 26 shows some field lines from Q_f terminating on negative charges on the aluminium gate and fewer field lines from ionised donors terminating on the gate than would exist if $Q_f = 0$. Because fewer ionised donors are required, the silicon depletion-layer width, W, will be smaller than $Q_f = 0$ at any given gate bias. Thus, using the results of section **2.3**, the capacitance will be higher than for the ideal case for all magnitudes of gate bias in the depletion and weak inversion regions; the result is a shift of the C-V curve toward more negative gate bias for positive Q_f and, by the same argument, a shift toward more positive gate bias for negative Q_f. This is illustrated for p-type and n-type semiconductors in Figures 27(a) and 27(b) respectively. The magnitude of the shift in the voltage due to the presence of fixed oxide charge in the MOSC is given by

$$\Delta V_f = \frac{Q_f}{C_{ox}} \quad \text{Volts} \qquad -58$$

Oxide trapped charge, Q_{ot}, can also cause a voltage shift of the ideal MOSC C-V curve. These oxide traps are associated with defects in the SiO_2 and usually occur during the MOSC fabrication process. The oxide traps are usually electronically neutral and are charged by introducing electrons (and holes) into the oxide. Figure 28 shows the band diagram, the charge distribution, the electric field and the potential for a p-type semiconductor MOSC with both fixed oxide charge and oxide trapped charge. On comparison with Figure 7, it can be seen that, for the same surface potential U_S, the effect of these charges is to shift the C-V curve toward negative voltage regimes. In this case, the magnitude of the voltage shift due to the oxide fixed charge is given, from Gauss's theorem, by

$$\Delta V_{ot} = \frac{Q_{ot}}{C_{ox}} = \frac{1}{C_{ox}} \left[\frac{1}{T'} \int_{T_o}^{T'} x\, \mu_{ot}(x)\, dx \right] \quad \text{Volts} \qquad -59$$

where Q_{ot} is the effective nett charge in bulk oxide traps per unit area of the Si-SiO_2 interface, and $\mu_{ot}(x)$ is the volume oxide trap density.

The charge due to mobile ions in the oxide layer was first demonstrated by SNOW et al[30] as being mainly responsible for the instability of the Si-SiO_2 system at high temperatures and high voltages.

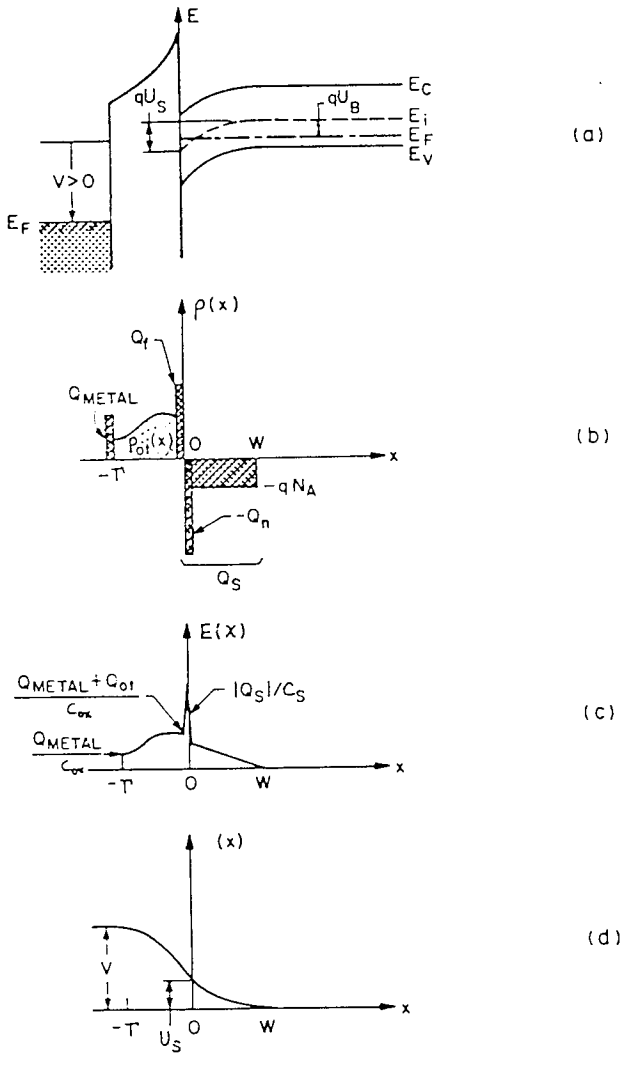

Figure 28: (a) The band diagram (b) The charge distribution
(c) The field distribution and (d) The potential diagram

for a p-type semiconductor based MOSC with a fixed oxide charge, Q_f, and oxide trapped charge, Q_{ot}.

Alkali metal ions, such as sodium and potassium (often encountered in MOSC fabrication proceses) can, depending on the biasing conditions, move back and forth through the oxide layer and thus give rise to voltage shifts in the C-V characteristics of the MOS system.

Figure 29 shows the sodium concentration in a silicon dioxide layer versus depth in the layer for a typically fabricated MOS device[31] (with T' = 540nm, $N_A = 5*10^{14}$ cm^{-3}); the large concentration of sodium ions ($3*10^{17}$ cm^{-3}) at the Si-SiO_2 interface cause a large flatband voltage shift and device instability. Such a flatband voltage shift caused by mobile ionic charge, ΔV_m, can , from Gauss's theorem, be expressed as

$$\Delta V_m = \frac{Q_m}{C_{ox}} = \frac{1}{C_{ox}} \left[\frac{1}{T'} \int_0^{T'} x\,\mu_m(x)\,dx \right] \quad \text{Volts} \qquad -60$$

where Q_m is the effective nett charge of mobile ions per unit area at the interface and $\mu_m(x)$ is the volume charge density of the mobile ions (that is, C cm^{-3}). The effects of this type of charge may be illustrated in an analogous fashion to Figure 28 by simply substituting for Q_m and $\mu_m(x)$.

Thus, the combined effect of the voltage shifts due to each type of oxide charge is

$$\Delta V = \Delta V_f + \Delta V_m + \Delta V_{ot} = \frac{Q_{ox}}{C_{ox}} \quad \text{Volts} \qquad -61$$

where Q_{ox} is the sum of the effective nett oxide charges per unit area (= $Q_f+Q_m+Q_{ot}$) at the Si-SiO_2 interface. Q_{ox} can, therefore be easily determined from the flatband voltage shift of the high-frequency C-V curve of an MOS device.

2.4.3 Carrier Transport in Insulating Films: Conduction in Non-Ideal MOSCs

In an ideal MOSC the conductance of the insulating layer is assumed to be zero. Real oxide layers, however, show carrier conduction when the electric field or temperature are sufficiently high.

Using Equations **27** and **44** to estimate the electric field in an insulating layer under biasing conditions, it can be seen that

$$E_{ox} = E_s\,(\epsilon_s / \epsilon_{ox}) \qquad -62$$

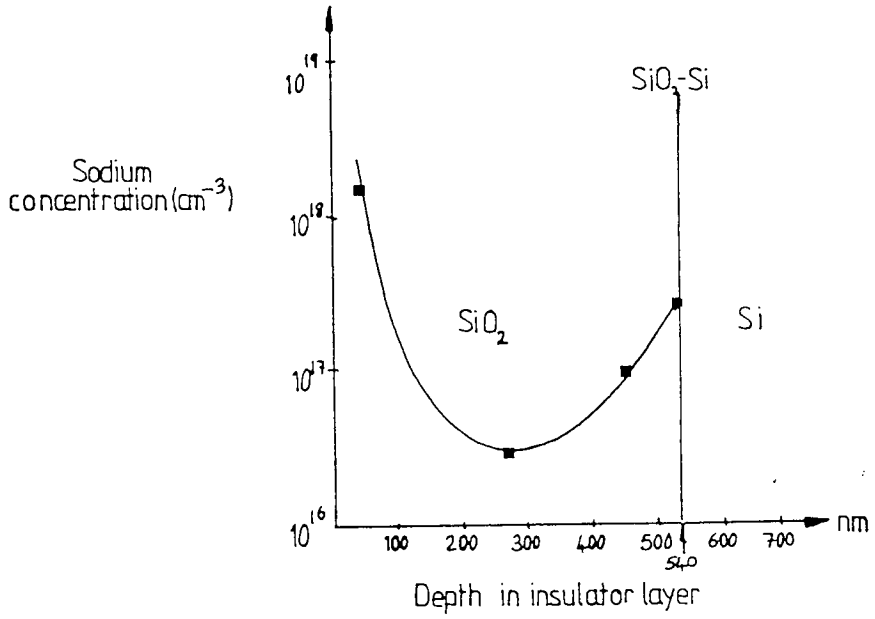

Figure 29: A plot of the sodium concentration found in a typical 540nm thick thermally grown SiO_2 layer of a MOS structure versus depth through the oxide.
(After YON, KO and KUPER, Reference 31)

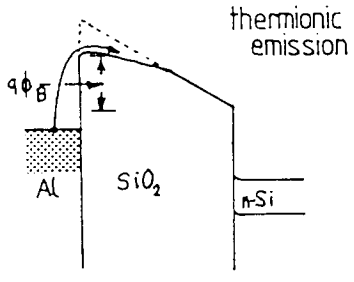

Figure 30: A band diagram illustrating Schottky emission from the metal-insulator interface in an Al-SiO_2-Si MOSC at room temperature.

where E_{ox} and E_s are the electric fields in the oxide and semiconductor respectively, and ϵ_s and ϵ_{ox} are the corresponding permittivities. The quantity $\epsilon_s / \epsilon_{ox}$ is approximately 3.0 for the Si-SiO_2 system; thus, the field in the oxide is approximately three times higher than in the semiconductor. At high fields (of the order of 10^6 V cm^{-1}) it can be shown that the hole and electron conduction in the SiO_2 are negligible, but mobile ions (such as sodium) can move through the oxide layer and give rise to an effective current flow. At even higher fields, but before insulator breakdown, when carrier conduction is greater, the MOSC may actually conduct. Table 1 summarises the basic conduction mechanisms in insulators and a brief resume´ of these processes is given below. More detailed discussion of the various conduction processes is beyond the scope of this thesis and the reader is, therefore, referred to the excellent texts by CHOPRA[32] and O'DWYER[33].

Schottky emission[33] of carriers through an MOSC is a process where thermionic emission across the metal-insulator interface or the insulator-semiconductor interface is responsible for carrier transport; this is illustrated on a band diagram in Figure 30. As can be seen from Table 1, a plot of $\ln(J / T^2)$ versus $1 / T$ would yield a straight line (with a slope determined by ϵ_{ox}) if the MOS structure were conducting by this mechanism.

The Poole-Frenkel process[34-35] is a field-enhanced thermal excitation of trapped electrons into the conduction band, as shown in Figure 31 for an Al-SiO_2-Si MOSC. For trap states with Coulomb potentials the expression is, virtually, identical to Schotty emission. The barrier height, however, is the depth of the trap potential well, and the quantity $\sqrt{q E / \pi \epsilon_{ox}}$ is larger than in the case of Schottky emission by a factor of two since the barrier lowering is twice as large due to the immobility of positive charge. Tunnel or field emission through the insulator region, shown in Figure 32 for an n-type substrate MOSC, is caused by high-field ionisation of trapped electrons being forced into the conduction band or by electrons quantum-mechanically tunnelling from the metal Fermi energy into the insulator conduction band. Tunnel emission has the strongest dependence on the applied voltage of all the conduction mechanisms, but is, essentially, independent of temperature; this is typical of so-called "hot-electron" injection processes.

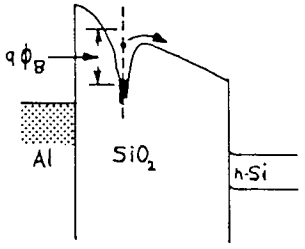

Figure 31: A band diagram illustrating Poole-Frenkel emission from trapped electrons in an n-type Al-SiO_2-Si MOSC at room temperature.

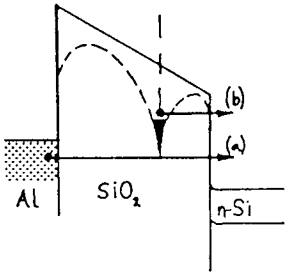

Figure 32: A band diagram illustrating tunnel or "hot" electron emission
(a) into the conduction band (only for oxides thinner than ≈10nm)
and (b) from traps in the insulator layer
in an n-type Al-SiO_2-Si MOSC at room temperature

PROCESS	EXPRESSION	VOLTAGE and TEMPERATURE DEPENDENCE
Schottky emission	$J = A^{\bullet} T^2 e \left[\frac{-q(\varnothing_b - \sqrt{qE/4\pi C_{ox}})}{kT}\right]$	$\approx T^2 e (a\sqrt{V}/T - q\varnothing_b / kT)$
Poole-Frenkel emission	$J \approx E e \left[\frac{-q(\varnothing_b - \sqrt{qE/\pi C_{ox}})}{kT}\right]$	$\approx V e (2a\sqrt{V}/T - q\varnothing_b / kT)$
Tunnel or field emission	$J \approx E^2 e \left[\frac{-4\sqrt{2m^{\bullet}}(q\varnothing_b)^{3/2}}{3qhE}\right]$	$\approx V^2 e (-a/V)$
Space-charge limited	$J \approx \frac{8C_{ox}\mu V^2}{9T'^3}$	$\approx V^2$
Ohmic conduction	$J \approx E e (-\Delta E_{ae}/kT)$	$\approx V e (-b/T)$
Ionic conduction	$J \approx E/T e (-\Delta E_{ai}/kT)$	$\approx V/T e (c/T)$

Table 1. Basic Conduction Processes in Insulators.

where

$A^{\bullet}$= effective Richardson constant; $\varnothing_b$= barrier height; E= electric field; C_{ox}= insulator dynamic permittivity; $m^{\bullet}$= effective mass; T'= insulator thickness; ΔE_{ae}= activation energy of electrons; ΔE_{ai}= activity energy of ions and $a = \sqrt{q/(4\pi C_{ox} T')}$; $V = E/T'$. Positive constants independent of V or T are *a*, *b*, and *c*.

Space-charge-limited conduction is the result of carrier injection into the insulator region when no compensating charge is present and is a bulk-limited conduction mechanism.

The current flow for the unipolar, trap-free MOSC case is proportional to the square of the applied voltage; at low voltages (and temperatures greater than room temperatures) the current flow is caused by thermally-excited electrons hopping from one isolated energy state to another. This mechanism yields an Ohmic characteristic which is exponentially dependent on temperature.

The ionic conduction process is similar to a diffusion process and, generally, d.c. ionic conductivity decreases during the time that the bias is applied, because ions cannot be readily injected into ,or extracted from, the insulator layer of the MOS structure; after an initial current flow, positive and negative space-charges build-up near the Al-SiO_2 and Si-SiO_2 interfaces causing a distortion of the potential distribution. When the field is removed, large internal fields remain which cause some, but not all, of the ions to flow back to their equilibrium position: as a result of this hysteresis effects in the I-V curves of MOS structures is seen.

For a given insulator, each conduction mechanism may dominate a particular applied voltage (and temperature) range. The processes are also not independent of one another; for example, in the case of large space-charge effects, the tunnelling characteristic is found to be very similar to Schottky emission.

More often than not, over the gate-voltage range used to investigate MOSCs, all the conduction processes come into effect and the conduction mechanism is a hybrid of all those mechanisms listed in Table 1.

An extermely important parameter of the MOS structure, in particular MOSCs, is the insulator maximum dielectric strength (also called the breakdown field). The essential breakdown processes in insulators are due to thermally and electrically initiated breakdown[36]. These are competing processes and the process with the lower field dominates, causing the breakdown. The mechanisms and models which describe dielectric breakdown processes and their initiation are discussed in detail in Chapter **3**, where a critical review of the available literature and experimental evidence is presented in order to consider the Al-SiO_2-Si MOSC under high-field stressing.

2.5 The Al-SiO_2-Si MOSC: Recent Experimental Findings

In this section some of the more important experimental findings that have emerged from studies of the Al-SiO_2-Si MOSC structure over the last decade are reviewed; more extensive details and references can be found in the book by NICOLLIAN and BREWS[16] and in the texts edited by SCHULZ and PENSL[37] and BARBE[38].

It must at this stage be emphasised that device characteristics are strongly dependent on the processing and fabrication techniques used in MOS technology; that is, MOSCs produced using the same process but, for example, having oxides thermally grown on substrates with differing doping densities and orientation, have markedly different characteristics (similarly, devices with the same substrate type but fabricated using differing processing techniques also have different characteristics).

The findings presented here are for MOSCs produced using very similar processes, fabrication techniques and silicon substrates to those used to make the MOSCs used in this study. The findings for virgin devices presented in this section show very similar characteristics to those used in this study (which are presented in Chapter 6).

2.5.1 Oxide Morphology and the Si-SiO_2 Interface

The basic structural unit of a thermally grown SiO_2 layer is a silicon ion surrounded tetrahedrally by four oxygen ions, as shown schematically in Figure 33. The silicon-to-oxygen internuclear distance is 0.16nm and the oxygen-to-oxygen proximity is 0.227nm. Several workers have found[39-41] that these tetrahedra are joined together in a variety of ways to form the various phases (or structures) of SiO_2; the basic crystalline structures of SiO_2 each have several modifications and, therefore, SiO_2 can exist in a large variety of crystalline forms. However, the amorphous structure grows when silicon is thermally oxidised and is by far the most important in MOSC applications.

The basic difference between a crystalline structure and the amorphous form is that the crystalline structure has long-range order, extending over many molecules, whereas the amorphous form is not ordered on a macroscopic scale (it has short-range order extending over just a few molecules). Recent investigations by YEH[42], KARUBE[43], DEAL[44] and EDAGAWA et al[45], agree with the

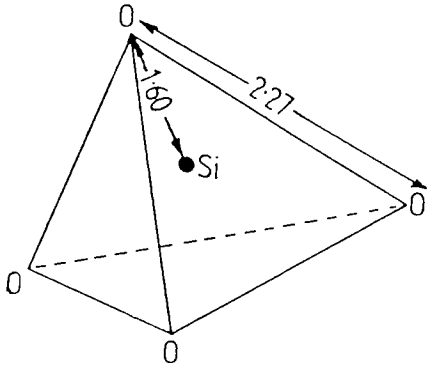

Figure 33: An illustration of the basic structural unit of SiO_2.

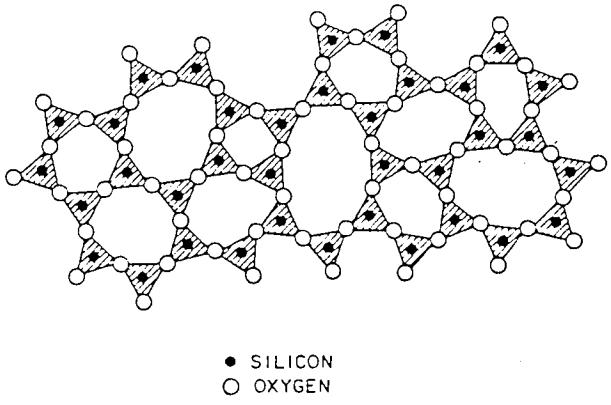

Figure 34: The amorphous structure of fused silica.
(After STEVELS, Reference 46)

earlier work of STEVELS[46] which show that, in amorphous SiO_2, there is a tendency for the formation of characteristic rings with six silicon atoms, as shown in Figure 34. Further work in this field by NAGASIMA[47] has revealed that such amorphous silica is, in fact, in a metastable state which tends toward a crystalline or devitrified state; this is especially facilitated by the presence of impurity ions (such as sodium) in the silica, which act as nucleation centres for the formation of crystallites. This crystallisation would produce severe mechanical strain and cracking of either the silica, the silicon substrate, or both. This, according to IRENE[48], may be the mechanism by which oxide traps are formed which, eventually, may lead to device breakdown under high-field stressing.

Compared with the crystalline structure of the most commonly found SiO_2 lattice - quartz - the amorphous state is very "open", with only 43% of the space in the amorphous form being occupied by SiO_2 molecules. KRIVANEK et al[49] suggest that this provides the means whereby a variety of electrically active impurities may enter and diffuse through the SiO_2 layer of a Si-SiO_2 based MOS structure. Such diffusion is unacceptable in MOS devices since the Si-SiO_2 interface is extremely sensitive to the smallest traces of electrically active impurities, and in some cases may dominate the electrical properties of the device; WOODS and WILLIAMS [50] have shown that sodium ion concentrations in the low 10^9 cm^{-2} range (measured at room temperature) can, in a p-type silicon Al- SiO_2-Si capacitor (T'=100nm), produce a flatband voltage shift of up to 0.3V.

This emphasises the importance of the Si-SiO_2 interface within the thermally grown amorphous Silicon dioxide layers used in MOS technology; the oxidation of a silicon surface produces a layer whose atomic arrangement is not well understood but dominates MOSC characteristics.

Many authors[51-59] have proposed that there is a non-stoichiometric transition layer, often described as SiO_x, separating the silicon substrate from the stoichiometric SiO_2 (where x lies between 1 and 2).The detailed atomic structure of the transition layer, including its uniformity and width, its structural disorder and affinity for impurity atoms, continues to be a subject of debate. One popular model for non-crystalline SiO_2 and the Si-SiO_2 interface is the cluster Bethe lattice model, described by LAUGHLIN et al[60] and SAKURI and SUGANO[61], which takes the topological aspects of structural disorder into account.

This model is simple in form and can be easily given parameters which suit SiO_2; HERMANN[62]

used the Bethe model to study the electronic and lattice- vibrational spectral properties associated with ideal and real interfaces in Al-Si-SiO_2 MOSCs with, assumed, perfectly flat interfaces and concluded that the oxide within 1-3nm of the silicon surface is, in fact, strained SiO_2 which, although stoichiometric, is chemically different from the bulk SiO_2 because of an excess of silicon atoms. Considerable evidence is given in support of such a region by GRUNTHANER et al[63] who used XPS to determine the concentration of silicon atoms at the interface; similar work by FELDMAN et al[64] shows that an excess of approximately $2*10^{15}$ cm^{-2} silicon atoms is typical in Al-SiO_2-Si MOSCs produced using various fabrication techniques, giving further credence to the existence of a silicon-rich layer at the interface.

Another popular model of non-crystalline SiO_2 grown on silicon is the continuous random network model[65-69] which proposes that the grown layer is composed of a variety of randomly oriented SiO_4 tetrahedra which are linked to form a continous network of Si-O-Si bonds. Models of this type have recently been employed to describe the electrical properties of the Si-SiO_2 interface in MOSCs produced on a variety of n-type and p-type <100> silicon [70]; DOHLER and co-workers[71] concluded from this work, in conjunction with their own studies on Al-SiO_2-Si MOSCs (T_{ox}≈ 100-400nm), that it is the effects of such a continuous random network which increases the dominance of interface traps over the bulk oxide traps; this dominance was seen to such an extent that the breakdown voltage was decreased for p-type devices (and increased for n-type devices) and the threshold voltage was similarly affected, in a fashion seen only in very-thin-oxide devices by other workers[72].

Most of the descriptions of the Si-SiO_2 interface in MOS devices assume that the interface is perfectly flat; however, recently, evidence has been presented[73-74] to show that the Si-SiO_2 is, in fact, quite rough by MOS technology standards. BLANC et al[75] and KRIVANEK et al[73-74], using electron microscopy with a resolution of approximately 1nm (the resolution in the SiO_2 is not known), have shown that a typically-grown SiO_2-on-Si structure has peaks and troughs ranging from 2nm to 4nm above (or below) the mean position of the interface. CHEN and SUGANO[76] have extended this work and found particles at the interface,which varied from 2nm to 5nm in size, which

were identified to be crystalline silicon clusters; the typical cluster density was $6*10^{11}$ cm^{-2} of interface. CHEN and SUGANO also found that the density of these crystallites correlates well with an increase in the SiO_2 dielectric breakdown defect-density, as reported by OSBURN and ORMOND[77].

It has been concluded that such crystalline silicon clusters at the interface could be responsible for both the increased surface roughness reported by KRIVANEK[73-74] and the increased density of silicon atoms at the Si-SiO_2 interface, which, combined with a random network of SiO_4 molecules in the bulk oxide, produce the anomalously large defect-densities and trap densities seen in even high-quality Al-SiO2-Si MOSCs fabricated by the most modern techniques.

Few workers report any anomalies in the structure and surface roughness at the Al-SiO_2 interface; the interface is still assumed to be perfectly flat (and smooth) with a total atomic mis-match of the two layers.

The implications of these results on the idealised picture of the real Al-SiO_2-Si MOSC are, therefore:

(a) No longer can the Si-SiO_2 interface be thought of as being composed of crystalline SiO_2 overlaying crystalline Si with ideal bonding between the two.

(b) The SiO_2 layer may not be stoichiometric throughout the interface, which may be the explanation for the observation of silicon-rich layers in the oxide.

(c) There are electrically active ion impurities in the oxide which contribute to anomalous behaviour of MOSCs.

and (d) the Si-SiO_2 interface is not perfectly flat, as assumed in the idealised model, causing deviations in the band bending approximations and decreased breakdown potentials for devices.

2.5.2 Interface Traps, Oxide Charge and Trapping Characteristics

In section 2.4.2 the theoretical characteristics for Al-SiO_2-Si MOSCs with interface traps and oxide charge are presented; in this section, experimental evidence is presented to show the effects of such traps and charge on the electrical characteristics of real MOSCs.

Many workers have striven to explain the presence of interface traps and oxide charge, and to determine their individual effect on Al-SiO_2-Si MOSCs (for examples, see references 78-85). As a consequence, a variety of techniques have been devised to study these, including: photo-ionization methods[86], avalanche techniques[87] and, by far the most versatile, the C-V technique[88].

Over the last two decades this technique has revealed substantial information on the nature of interface traps and oxide charge: DEAL[89] has reviewed seventeen different types of defects proposed by other workers which could cause interface states and affect the ideal C-V characteristic for an Al-SiO_2-Si MOSC. By far the most important of these are: the inclusion of impurity defects (Na^+ ions, excess silicon ions and water molecules, for examples) in the device at the time of fabrication and lattice mis-match at the interface.

According to LENAHAN and DRESSENDORFER[90], these defects cause hole traps in the oxide which affect the C-V curve by shifting the mid-gap voltage of the curve by an amount ΔV_{mg}, such that

$$\Delta V_{mg} = D_{ht} \frac{q}{C_{ox}} \qquad -64$$

where D_{ht} is the density of hole traps in the oxide layer. This agrees well with the work of FISCHETTI and RICCO[91] who have shown that positive charge (hole traps) generated at the interface is related to slow states (traps deep in the oxide) caused by unidentified ionic species and that there is a strong correlation between slow states and hole traps, and fast states (traps close to the interface) and electron traps: the effect on the C-V curve for MOSCs is demonstrated admirably by the work of ZAININGER and HEIMAN[92] who showed that, assuming very little trapped charge in the oxide layer

at the outset of testing a virgin MOSC, four main results are possible:

(1) Positive bias shifts the C-V curve to the left, due to injection of positive charge from the metal gate electrode (polarisation has occured).

(2) Positive bias shifts the C-V curve to the right due, to injection of negative charge from the silicon (electron trapping).

(3) Negative bias shifts the C-V curve to the left, due to injection of positive charge from the silicon (hole trapping).

and (4) negative bias shifts the C-V curve to the right, due to charge injection of negative charge from the metal (polarisation has occured).

The assumption that there is very little trapped charge in the virgin MOSC structure at the outset of testing is fallacious; the best Al-SiO_2-Si MOSCs, fabricated with the most modern techniques , may have as few as 10^{10} q $cm^{-2}eV^{-1}$ at flatband conditions. This, according to YOUNG[93] (who assumes that a lattice mis-match between the silicon and the oxide layer is the only defect in the device) is near the theoretically-attainable minimum number for silicon devices. The results presented by SCHULZ[80] for a <100> n-type silicon Al-SiO_2-Si MOSC with a 64nm oxide layer (reproduced in Figure 35) show a D_{it} at flatband conditions of approaching $10^{10}cm^{-2}$ eV^{-1}, which produced a flatband-voltage voltage shift of -0.65V; this is a near-ideal MOSC .

YOUNG[82] attributes this voltage shift, ΔV_{fb} at flatband conditions, to a filling of traps in the oxide and throughout the interface by charge-carriers with a charge centroid which covers the entire oxide thickness, such that

$$\Delta V_{fb} = q \frac{(N\bar{x})}{\epsilon_{ox}} \qquad -65$$

where N is the total number of filled traps in the oxide cm^{-2} and $\bar{x}$ is the centroid of the charge measured with respect to the Al gate electrode.

Photo-injection I-V techniques, performed by SAH et al[94], have shown that this charge centroid

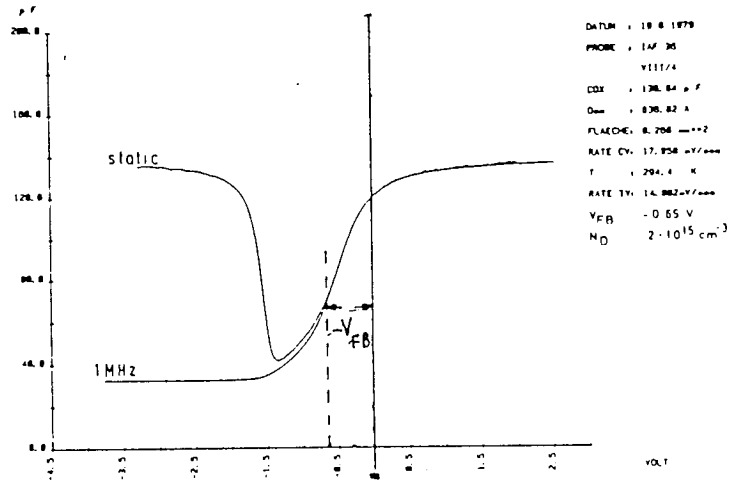

Figure 35:The C-V characteristic for a typical MOSC fabricated on n-type silicon with a doping density of $N_D=2*10^{15}$ cm^{-3} and oxide thickness of 63.7nm. $D_{it} \approx 10^{10}$ eV^{-1} cm^{-2} at the flatbands condition.
(After SCHULTZ, Reference 80)

occupies almost the whole of the oxide thickness, and that

$$\Delta V_{fb} = c\ (T' - 9*10^{-9}) \quad , \ c \text{ is some constant} \qquad -66$$

Thus , SAH et al[94]believe that there is a strong relationship between the flatband voltage shift and the device thickness minus the width of the region not occupied by the charge centroid; this implies that, in real MOSCs, one should see an increase in ΔV_{fb} with incresing device oxide thickness, T', tending to a limit dependent on the proportion of the oxide layer consumed by the charge centroid.This is corroborated by the work of NICOLLIAN and BREWS[16].

One therefore expects any virgin Al-SiO_2-Si based device (with either n-type or p-type silicon substrate) to have an intrinsic ΔV_{fb} due to trapped charge (at the interface and/or throughout the oxide layer) directly proportional to the total number of traps and charges.

Most workers amalgamate the effects due to oxide charge and interface traps under the general term for the density of interface traps, D_{it}, since using C-V techniques it is not possible to distinguish between the effect of each trap type or charge carrier present, just the overall effect. (However, a novel technique to calculate the D_{it} and Q_{ox} values from the high-frequency C-V characteristics for an MOS device is presented in Chapter 5).

The trapping characteristics of devices cannot, unfortunately, be studied using the C-V technique and only the effects of the traps present may be evaluated. Avalanche charge-injection techniques, such as those presented by WOLTERS and VERWEY[95], however, can reveal aspects of the trapping process; in particular, the probability of varying trapping efficiency (or a capture cross-section for trapping) has been proposed and investigated. This concept, of a capture cross-section for trapping can be used to explain the recent results of DIMARIA[96] and YOUNG[97] who, by ion implantation and irradiation techniques, are able to introduce a known number of traps to Al-SiO_2-Si MOS devices and investigate their effect. WOLTERS and VERWEY[95]suggest that traps are generated at specific trapping sites throughout the interface such that a number of hole and electron traps may be introduced to a previously "clean" device when under various conditions of bias or avalanche injection; these traps may then be filled by positive or negative charge injection

or by "hot" electron injection while the device is under high-field stressing. (Concurrently proposed is the application of the Zeldovitsj equation[98], used in chemisorption kinetics, to give the required trapping characteristics shown by most Al-SiO_2-Si type devices; further description of their work in this field is inappropriate here, and beyond the scope of this study).

The work of DIMARIA[96] and YOUNG[97] and the proposals of WOLTERS and VERWEY[95] can be used to perhaps explain why results presented by early workers in the field[78-82]show anomalous trap densities under high field stressingor irradiation conditions, which is discussed in Chapter **4**.

The implications of these recent findings are that:

(1) Typical C-V curves for real Al-SiO_2-Si MOSCs are similar to those of SUZUKI et al[99] presented in Figure 36 and 37.

(2) Flatband-voltage voltage-shifts, V_{fb}, are to be expected in real, virgin devices, which are proportional to the thickness of the oxide and density of traps within the device.

(3) Typical virgin device trap densities (equivalent to D_{it} for C-V measurements) are of the order of 10^{10} cm^{-2} eV^{-1} at flatband conditions for clean devices.

(4) Traps occur at various trapping sites which are mainly at intrinsic defect or impurity defect centres in the SiO_2 (or at the Si-SiO_2 interface) and have various capture cross-sections dependent upon the trap energy and position in the oxide.

and (5) trap occupation may be effected by several mechanisms for a device under bias, with different types of trap for different of charge carriers; there are, essentially, hole traps (acceptor traps) and electron traps (donor traps) which may be occupied by injected charge, injected from the metal (Al) gate or semiconductor (Si) substrate depending on the device bias polarity.

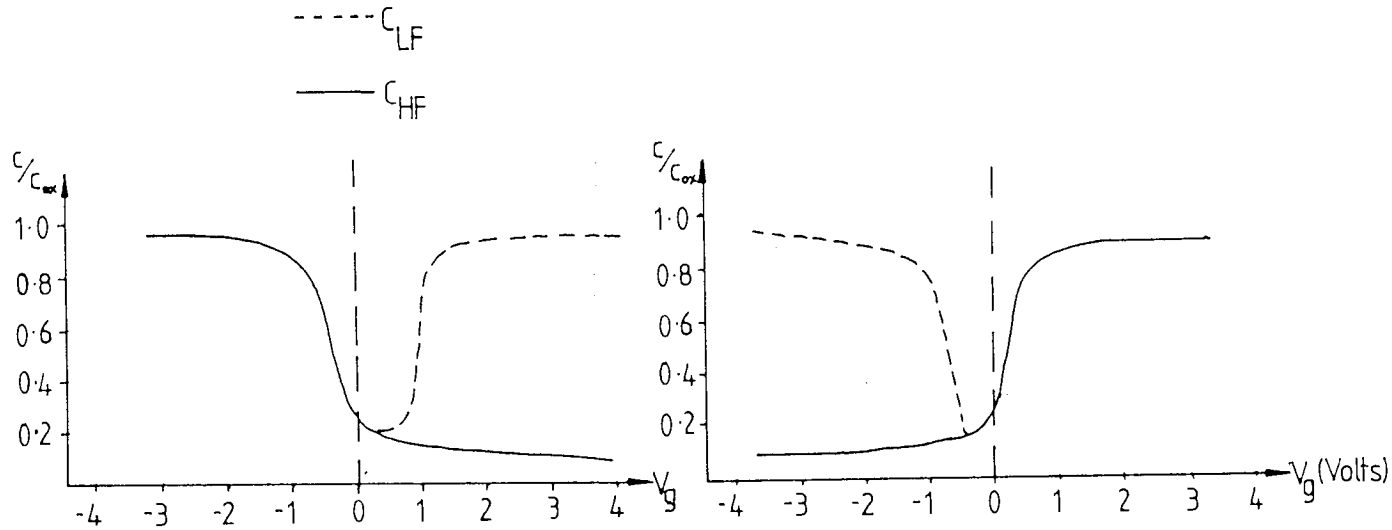

Figure 36: 23Ωcm [100] p-Type Si, Al-SiO_2-Si MOSC. T=140nm.

Figure 37: 5·5Ωcm [100] n-Type Si, Al-SiO_2- Si MOSC. T = 161nm.

Figure 36: Experimentally determined high (C_{HF}) and low (C_{LF}) frequency C-V curves for a <100>p-type silicon-based Al-SiO_2-Si MOSC.
(After SUZUKI, Reference 99)

Figure 37: Experimentally determined high (C_{HF}) and low (C_{LF}) frequency C-V curves for a <100> n-type silicon-based Al-SiO_2-Si MOSC.
(After SUZUKI, Reference 99)

2.5.3 Charge Injection and D.C. Characteristics

Experimental evidence that positive charge is induced in thin films of thermally grown SiO_2 under high-field stressing has been reported by several investigators[100-102]. In the MOSCs used in their research, the current in the device is limited by the electrode barrier. At a moderate applied field, according to LENZLIGER and SNOW[103], the current reproduces a Fowler-Nordheim characteristic for electron tunneling into the $SiO_2$from the cathode[100,103]; when the current is increased sufficiently, the current deviates from the Fowler-Nordheim characteristic , becoming larger[101], as shown in Figure 38. This effect is interpreted by GOODMAN [104] as being due to a positive charge generated by ionizing collisions of injected electrons with bound electrons. The electrons, being mobile[105], are quickly swept-out by the applied field, while the relatively immobile holes[106-107] are left, giving rise to a nett positive charge (as described in section **2.5.2**) .

Further evidence for electron (and hole) injection is given by many workers , but there is still considerable controversy over what mechanism is responsible for this in MOSC oxides under high-field stressing[108-111]. According to SHIRLEY[112] the most likely mechanism is impact-ionization by electrons at the Si-SiO_2 or Al-SiO_2 interfaces, depending on the polarity of the applied field, producing immobile holes in the oxide; further interfacial trap formation and filling of traps leads to a buildup of positive in the oxide. As is shown in section **2.5.2**, this positive charge produces a shift of the C-V curve for the device to a negative regime. SOLOMON[115] proposes that hole injection follows a similar mechanism.

An explanation as to why impact-ionization should occur initially is perhaps given in the work of DIMARIA et al[114] who suggest that impact-ionization is the result of hot-electron injection from very shallow interface traps (fast surface states); such injection could occur due to surface roughness of the substrate and defects in lattice matching at the interface.

NICOLLIAN and GOETZBERGER[115] have determined that, generally, electron injection occurs when the substrate is p-type and hole injection occurs when the substrate is n-type semiconductor. Such injection from electrodes into the SiO_2 layer governs the flow of current through an MOS device, as briefly described in section **2.4.3**. ZAZOUK et al[116] have demonstrated that the current flow (d.c. characteristics) in Al-SiO_2-Si <100> n-type and <100> p-type substrate MOSCs is

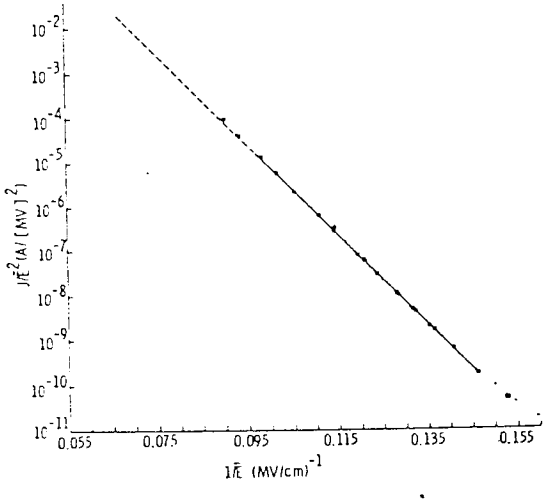

Figure 38: A Fowler-Nordheim plot for a SiO_2 layer, thickness 49.4nm; deviations from the linear relationship at high fields are due to positive charge in the film induced by electron injection from the cathode.
(After SHATZKES and AV-RON, Reference 102)

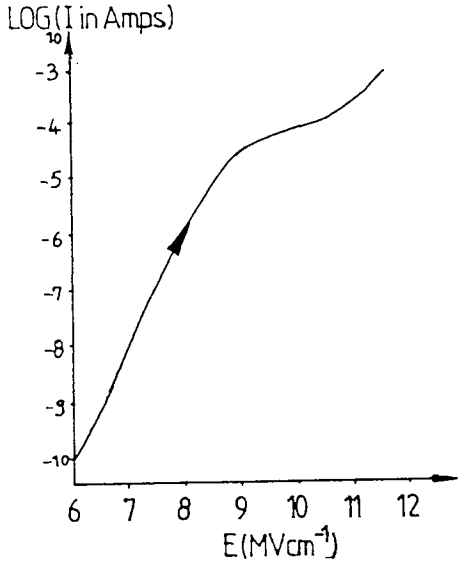

Figure 39: Experimentally determined I-V characteristic for a <100> n-type 2Ωcm silicon based Al-SiO_2-Si MOSC with an oxide layer of 150nm.
The "ledge" is due to quasi-saturation of the current as traps fill; conduction then follows a displaced Fowler-Nordheim conduction process.
(After SOLOMON, Reference 113)

dependent on:

(1) the total time of application of the field; carrier trapping has been shown[11] to be strongly time dependent

(2) the polarity of the applied voltage; a greater current flow is seen with the silicon biased negatively with respect to the Al gate electrode rather than positively, for both n-type and p-type silicon substrate devices

(3) the applied field strength

and (4) the oxide film thickness; the thicker the film, the greater the current flow. For very thin films (<20nm) the converse is true.

Further investigation of these dependencies by SOLOMON[113] and HARTMANN[117] using ramped current I-V techniques reveal I-V characteristics typical of those shown in Figures 39 and 40. The "ledge" in the I-V curve shown in Figure 39 is very important; KLEIN and SOLOMON[118] explain this in terms of a quasi-saturation of current whilst traps are filling and producing an internal field build-up which opposes injection.

When the traps are completely filled the current increase follows a displaced Fowler-Nordheim characteristic, where the field appears displaced by an amount ΔF_L, such that

$$\Delta F_L = \frac{q N_t}{C C_{ox}} \left(1 - \bar{x}/T\right) \qquad -67$$

Thus, the trapping parameters of the oxide in the device under test may be simply evaluated from the width of the ledge in the I-V curve.

Figure 40 shows the work of HARTMANN[117] where the characteristic ledge, ΔF_L, is not seen ; according to SOLOMON[113], this is because the ramp-rate of the applied field used in HARTMANN'S experiments was so slow that there could be no build-up of internal field to oppose carrier injection and the device could, therefore, follow normal Fowler-Nordheim injection

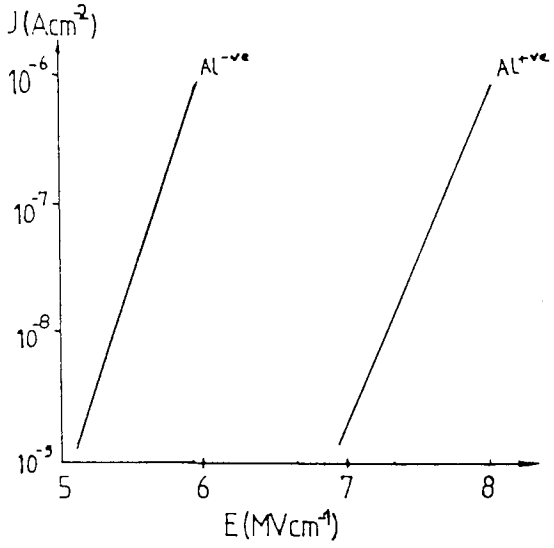

Figure 40: Experimentally determined I-V characteristic for a <100> p-type 7Ωcm silicon based Al-SiO_2-Si MOSC with an oxide layer of 127nm.
The quasi-saturation of current is not seen here since the device follows Fowler-Nordheim characteristics due to the low sweep-rate of the applied field.
(After HARTMANN, Reference 117)

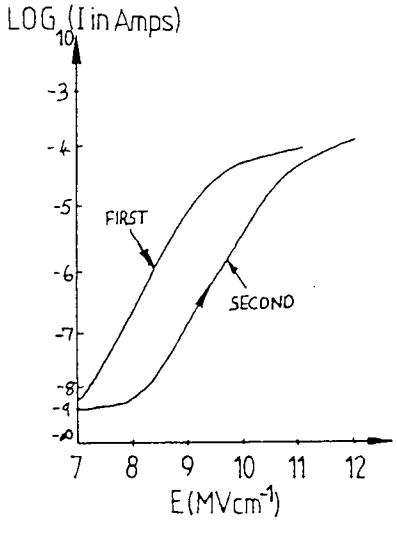

Figure 41: Sequentially ramped gate voltage I-V characteristics for a <100> n-type Al-SiO_2-Si MOSC with a 150nm oxide layer; the first curve was recorded with a slow ramp rate, the second curve was recorded immediately after the first the same voltage-ramp rate. The device broke down at the end of the second voltage ramp.
(After SOLOMON, Reference 113)

processes. On removal of the current ramp and subsequent, rapidly followed, ramping it is seen that the I-V characteristic is further shifted to higher applied field regimes, until the device breaks down, as shown in Figure 41. If, however, the current ramp is reversed in polarity on the subsequent sweep considerable hysteresis in the I-V characteristic is seen; this is due to the partial filling of traps which cannot empty (or take a much longer time than the current sweep to do so), as shown in Figure 42.

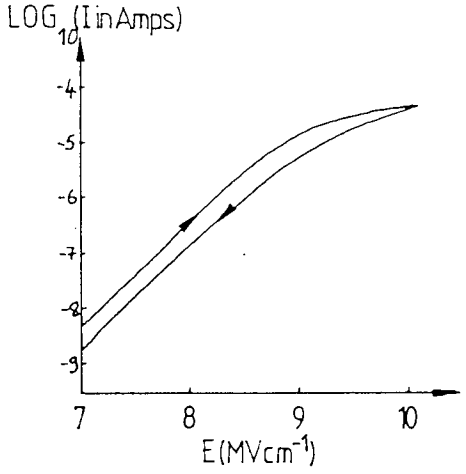

Figure 42: Ramped gate voltage I-V characteristics for a <100> n-type Al-SiO_2-Si MOSC with a 150nm oxide layer; hysteresis of the I-V curve due to some traps remaining filled when the field strength is decreased can be clearly seen.
(After SOLOMON, Reference 113)

The implications of these findings in the idealised description of the Al-SiO_2-Si MOSC are that:

(1) Real Al-SiO_2-Si MOSCs display carrier injection phenomena characterised by a build-up of positive charge in the oxide; this is seen as a displacement of the C-V curve towards negative voltage regimes.

(2) Real devices are able to conduct under high applied field conditions, with the conduction mainly dominated by a Fowler-Nordheim mechanism which is dependent on the length of time of application of the gatebias, the applied field strength and the oxide thickness.

and (3) typical I-V curves for real Al-SiO_2-Si MOSCs are similar to those of SOLOMON[113] presented in Figure 39; there is a characteristic shift in this (Fowler-Nordheim) curve which is due to a quasi-saturation of current during trap population by carrier injection.

CHAPTER THREE.

MOSCs UNDER EXTERNAL INFLUENCES 1: DIELECTRIC BREAKDOWN CONDITIONS

The electric fields applied across MOSCs are generally quite large (of the order of MV cm^{-1}, equivalent to 10V across an oxide layer of 100nm thick) and approach the breakdown strengths for typical bulk dielectrics (for examples: silica, 6-9MVcm^{-1}; alumina, 4-8MVcm^{-1}).

The poorly understood phenomena of electrical breakdown of bulk insulators has been the subject of numerous experimental and theoretical treatments which have been thoroughly reviewed by many workers: for examples, the reader is referred to the comprehensive works of O'DWYER[119], SIMMONS[120], and WOLTERS and VERWEY[121] . These concentrate on various forms of excess current mechanisms for breakdown, mainly those caused by thermal instabilities (Joule heating leading to cumulative thermal ionization of the insulator), defects (induced by ionization of impurities or structural defects) or avalanche breakdowns (in which avalanche multiplication of carriers takes place because of ionization of the lattice by collision with energetic electrons).

Although these treatments may be applied to breakdown in thin film dielectrics, it is those breakdown processes which take place in Al-SiO_2-Si MOSCs which are not caused by defects (weak spots) or high temperatures, but due to an intrinsic breakdown mechanism specific to the nature of the MOS system, which are of most interest to the MOS technologist; considerable controversy has arisen in the last decade about the nature and cause of these intrinsic breakdowns. In this chapter a brief survey of the novel techniques used to study the high-field and breakdown properties of Al-SiO_2-Si MOSCs in particular is presented, including a review of the more recent experimental result involving both shorting and non-shorting dielectric breakdowns. Non-thermal breakdown theories are presented for models of breakdown induced by various electronic processes; these are critically reviewed in the light of the experimental evidence available, and their relevance to the Si-SiO_2 system is discussed.

For more general information on breakdown in MOSC insulators the reader is referred to the recent review article by KLEIN[122], while a bibliography of early work in the field is given in the survey by AGARWAL[123].

3.1 Breakdown Testing: Novel Techniques

Many testing methods have been used to obtain data on breakdown, and other related topics, in SiO_2; techniques used to pinpoint and characterise defects, such as scanning and transmission electron microscopies, thermal decoration of defects and liquid crystal methods, are dealt with in an excellent review article by KERN[124], and will not be dealt with here. By far the bulk of breakdown work involves standard electrical testing procedures; that is, application of a ramp or step voltage to MOSCs and monitoring voltage, current and 'breakdown' as functions of time and temperature, and using statistical analysis to characterise the device and oxide. In addition to these methods (to be discussed in section **3.3**) mention will now be made of other novel techniques which are used to study high-field and breakdown properties of MOSCs, the results from which are used in this chapter and have been used in forming a physical and electronic model for the MOS system to aid the understanding of breakdown in devices such as the MOSC.

Since breakdown is a property of both the insulator and the electrodes in the MOS system, testing methods involving electrodeless or special electrode configurations are of particular interest. Laser induced breakdown in insulators has been reported [126-127], with breakdown field in fused silica on silicon of 11.7 $MVcm^{-1}$. Corona discharges have been used by WILLIAMS and WOODS[128] and by WEMBERG[129], where the corona serves as a counter electrode instead of the conventional aluminium layer; fields in the oxide as high as 14 $MVcm^{-1}$ have been obtained using a negative corona polarity, where electron injection into the oxide is inhibited.

According to BUDENSTEIN[130], who, like WILLIAMS and WOODS, used a Kelvin probe[128] to measure the oxide surface potential, such techniques eliminate the charge collection at the Al-SiO_2 interface and so give a true measure of the oxide breakdown field. This implies that the metal electrode reduces the breakdown strength of SiO_2 in the metal-SiO_2-Si system, since an accepted value for the breakdown potential strength of SiO_2-on-Si is in the 6-9 $MVcm^{-1}$ range[131].

Internal photoemission, used first on MOSCs by WILLIAMS[132], whereby the thickness and spectral dependence of stimulated photoemission from the oxide layer of an MOSC structure with an ultra-thin (<20nm) top metal electrode are investigated, has been used extensively [132-133] to study MOS properties such as the electrodes barrier height and electron trapping, while the use of ionizing radiation in MOSCs has given valuable information on electron[134] and hole[135-136]

transport properties and the SiO_2 bandgap[136] and valence band structure[137].

Fission-fragments can also be used as a tool to study breakdown, as is demonstrated by the work of TOMMASINO et al[139] who used a Cf^{252} source to irradiate MOSCs under bias and obtained a correlation between the incidence of fission-fragments and the number of breakdowns occurring in the MOSCs which were not due to defects, but appear to be intrinsic breakdowns (this is discussed in great detail in Chapter **4,** which deals with radiation effects in MOSCs). Fission-fragments are seen to induce breakdown, the study of which may add another facet to the complex process of intrinsic dielectric breakdown.

3.2 The Breakdown Event

The most recent, and generally accepted, description of the breakdown event is that proposed by KLEIN[139], who describes breakdown in MOSCs as a multistage event, consisting of:

(1) an initiating stage, followed by

(2) instability and current runaway

(3) the voltage collapse and discharge of the electrostatic energy stored in the specimen

and (4) the establishment of a new low-voltage state.

The discharge usually occurs in a filament of oxide and, for MOSCs with thin (<100nm) counter electrodes, non-shorting breakdowns, where the high localised currents and temperatures evaporate the electrode material around the breakdown channel, may occur[140], isolating the damaged area.

For the non-shorting event, two additional steps are required in Klein's description:

(5) quenching of the hot breakdown channel

and (6) recovery of the circuit via series-resistance sample-capacitance time constant.

Klein postulates the existence of a short gaseous arc during the destructive stage of the breakdown, with a voltage of approximately 10V needed to sustain it. Arc temperatures of over 4000°k have been measured spectroscopically by OSBURN and ORMOND[141] who correlated the energy for destruction of the oxide with the electrostatic energy stored in the MOSC.

In the case for shorting breakdowns, where the top gate electrode is comparatively thick (>100nm), the top metal electrode is melted but does not evaporate; the molten metal replaces the filament of oxide, which has evaporated to leave a small channel or crater, and creates a conducting path from the metal gate electrode to very near (or even into) the silicon substrate. If, after breakdown, this conducting channel only reaches part-way into the oxide the likelyhood that a further breakdown will occur at this (defect) site due to field-enhancement is very great, and subsequent breakdowns at this site will, eventually, produce a shorting breakdown.

The non-shorting form of breakdown has been studied in depth by YANG et al[142] who present evidence of interesting star-shaped patterns of destruction in their <100> silicon-based MOSCs after breakdown testing which is attributed to asymmetry in the <100> silicon substrate properties. The usual form of the non-shorting breakdown "pit" is a volcano-like crater, often from 2nm to 8nm across, and nearly the depth of the oxide layer[139].

SHATZKES et al[143], using nanosecond pulsed-voltage techniques, claim a true switching behaviour in their MOSCs which is phenomenologically similar to non-shorting breakdowns; however, they maintain that their low-voltage state was a true high-voltage conductivity state of SiO_2, sustained by impact ionization and injection, rather than by a gaseous arc, even with thick top gate electrodes.

3.3 Breakdown Testing: Electrical Techniques

Breakdown data for SiO_2-on-Si based MOSCs has been reported for a variety of devices fabricated using a variety of processes; both shorting and non-shorting breakdown data is available. For non-shorting breakdowns, many breakdown tests may be carried out on a single MOSC whereas in contrast many MOSCs are needed to investigate shorting breakdowns.

Breakdown detection is usually performed by sensing the associated voltage drop across a sample series resistor (often between1 and10MΩ, dependent on the device under test) which is included in the circuit to limit the current flow through the MOSC at the time of breakdown. For MOSCs under bias such that they are in an "accumulation" state (as described in section **2.2.1**), pulses of several volts amplitude and of microseconds duration are possible on non-shorting breakdown[140,142].

Several workers[130,144-145] have used oxide leakage current levels to define breakdown;

however, this author believes that care must be exercised when interpreting data using this definition because high currents can flow through the oxide without breakdown due to the Fowler-Nordheim conduction mechanism, particularly in thin oxides (where breakdown fields are higher[146]).

Figure 43 shows a typical circuit for measuring breakdown voltages and currents; the inclusion of a timer circuit permits breakdown versus time experiments to be carried out. OSBURN[141], in his timer-testing technique, distinguishes between the first (non-shorting) and final (shorting) breakdown, although it is not clear to what extent the final shorting breakdown is a fundamental property of the insulator. Using either shorting or non-shorting breakdowns, breakdown testing is performed using a ramped or stepped applied field in which either the applied voltage causing breakdown or the times to (and between) breakdowns are measured; these are further divided into short-time tests (usually ramped-voltage tests) and longtime tests (usually stepped-voltage tests), often at elevated MOSC temperatures. Long-time elevated-temperature tests are known as "lifetime" tests and are widely used by industry to assess the reliability of their final product; breakdown in this mode of testing is called "wearout" by OSBURN et al[147], who use the results of wearout tests to determine the activation energy for breakdown.

The most common forms of electrical breakdown testing have been used in this study ; these are described in Chapter 5 (Experimental Techniques) and, for the sake of brevity, will not be discussed here also.

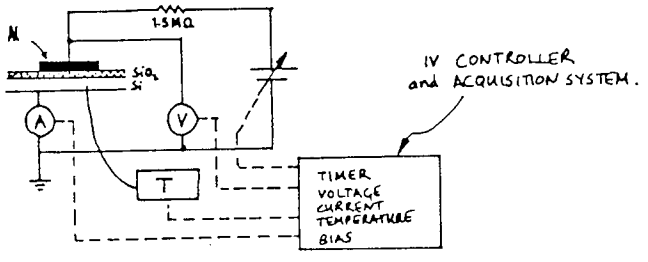

Figure 43: A typical breakdown voltage and timer system for the acquisition of breakdown statistics.

3.4 Breakdown Statistics

Using the fast-ramped-voltage technique, histograms of breakdown voltages in SiO_2 have been presented by many workers.A typical histogram, obtained by OSBURN and ORMOND[141] is presented in Figure 44; FRITSCHE[144] separated his data into histograms with primary, secondary and tertiary peaks, the primary peak being in the field range 6-10 $MVcm^{-1}$, and related the primary peak to the intrinsic breakdown mechanism and the secondary and tertiary peaks due to defect-related breakdowns. OSBURN and ORMOND identify the primary peak with their final breakdown histogram, but attribute details of the secondary and tertiary peaks to FRITSCHE'S testing method. Histograms are particularly useful in identifying trends in breakdown voltages, and

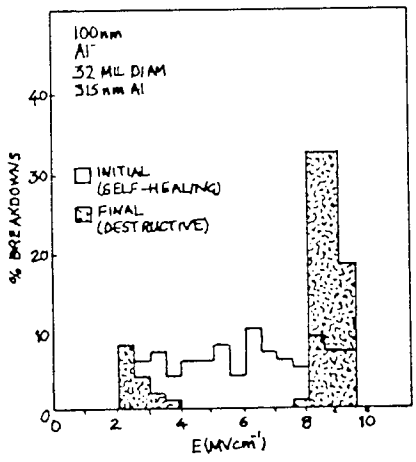

Figure 44: An initial and final breakdown histogram for a <100> p-type 2-4Ωcm silicon based Al-SiO_2-Si MOSC with a 100nm oxide layer and 31.5nm Al gate electrode (32 mil diameter); the gate was negatively biased with respect to the silicon substrate. (After OSBURN and ORMOND, Reference 141)

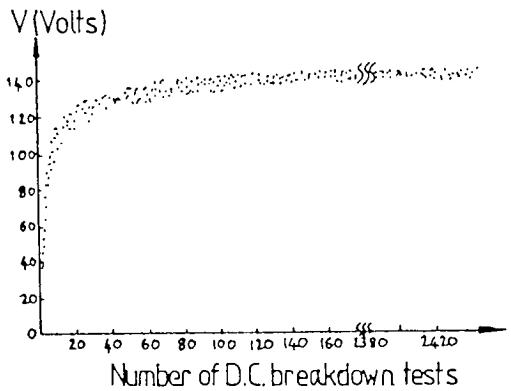

Figure 45: A plot showing the non-shorting breakdown response of a <100> n-type 14-21Ωcm silicon based Al-SiO_2-Si MOSC with a 200nm oxide layer and 27nm Al gate electrode (1mm diameter) with the number of tests performed; the gate was positively biased with respect to the silicon substrate.
(After KLEIN, Reference 139)

especially in determining the breakdown strength of a particular batch of devices.

Both intrinsic breakdown and defect-related breakdown have been shown to be both oxide field and length-of time-of-application-of-field dependent[139-148]; defect-related breakdown has also been shown to be area dependent, although this is to be expected since, although the defects over a particularly small area may be considered randomly sited, over the much larger area of oxide covered by the gate electrode they might appear more evenly distributed.

3.4.1 Intrinsic Breakdown Time and Field Dependence

The results presented by KLEIN[139] for a series of consecutive breakdown tests, using non-shorting breakdowns in Al-SiO_2-Si MOSCs, are shown in Figure 45; the process of weak spot elimination is clearly depicted. However, even after reaching a statistically stationary state, the breakdown voltage is seen to continue to fluctuate about a mean value.KLEIN believes that this fluctuation results from an inherent randomness associated with an intrinsic breakdown mechanism. On applying stepped voltages and monitoring breakdown times, using a non-shorting-breakdown detection circuit, times to breakdown[148]in SiO_2-on-Si based MOSCs have been found to follow a Poisson distribution, which is the necessary requirement for the breakdown events to display randomness.The field dependence of the mean time to breakdown for SiO_2 in similar MOSCs is shown in Figure 46, reproduced from KLEIN[139], and it can be seen that the times to breakdown decreases quasi-exponentially with the applied field. For SiO_2 the curve is very steep and this, together with the Poisson-like distribution has led many workers to believe[144-145] that intrinsic breakdown in SiO_2 is time independent. SOLOMON[148]has demonstrated that this, however, is not the case and intrinsic breakdown is indeed time dependent; the model SOLOMON has proposed to correlate the statistics of ramped and stepped breakdown events in the intrinsic breakdown regime gives excellent agreement with later work shown, as a ramped-voltage breakdown-voltage versus probability of breakdown histogram, in Figure 47.

Very little evidence exists to suggest that Al-SiO_2-Si MOSCs under breakdown conditions (after defect related breakdowns have been eliminated by weak spot elimination) do not demonstrate a field and time dependence for intrinsic breakdown; this is a major factor in the most recent models

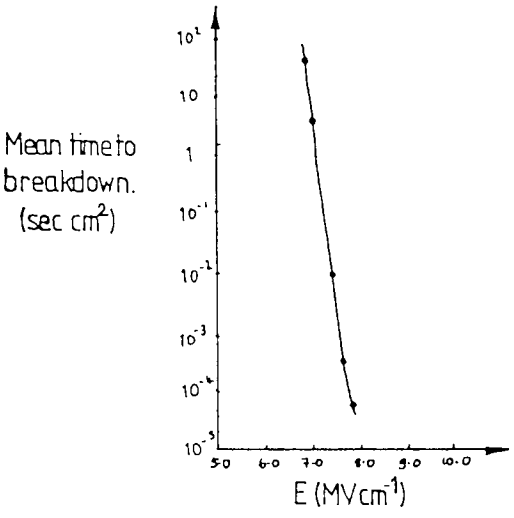

Figure 46: A plot showing the increase in breakdown rate versus the electric field applied to a <100> n-type 0.01Ωcm silicon based Al-SiO_2-Si MOSC with a 150nm oxide layer and 36nm Al gate electrode (1mmdiameter); the gate was positively biased with respect to the silicon substrate.
(After KLEIN, Reference 139)

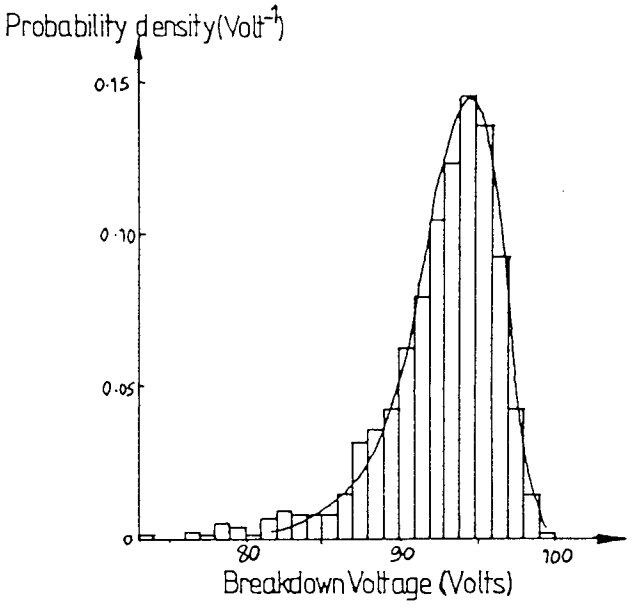

Figure 47: The probability density function and histogram of breakdown voltages of a <100> p-type silicon-based Al-SiO_2-Si MOSC with a 97.2nm oxide layer and 27nm Al gate electrode (1mmdiameter); the gate was positively biased with respect to the silicon substrate.
(After SOLOMON et al, Reference 148)

based on impact-ionization discussed in section **3.6**.

3.4.2 Defect-Related Breakdowns: Area Dependence

Defects in SiO_2 are generally quantised by a defect density, D, which, although not always recognised as such, is a function of both oxide field and time-of-field-application[147]. Thus

$$D = D(F,t) \qquad \textbf{-68}$$

where $D(F,t)$ is the (infinitessimal) probability cm^{-2} for a defect-related breakdown to occur in the time, t, of application of the field ,F. The yield, Y(F , t), for a MOSC to survive the breakdown testing is given by OSBURN and CHOU[147] in a form equivalent to

$$Y = e^{-AD} \qquad \textbf{-69}$$

where A is the MOSC gate electrode area in cm^{-2}. However, MEEK and BRAUN[149] and LI and MASERJIAN[150], following PRICE[151], suggest that the yield is more likely expressed as

$$Y = \frac{1}{(1+AD)} \qquad \textbf{-70}$$

The latter formulation is based on Bose-Einstein statistics, where the defects are assumed to be indistinguishable; however

(1) there is no physical reason to believe that defects are indistinguishable.

and (2) according to BUDENSTEIN[130], Equation **70** violates the principle of statistical independence for parallel-connected capacitors.

Thus, one expects an exponential dependence of defect-related breakdowns on the area of the gate electrode covering the oxide in the MOSC.

A quasi-exponential dependence of defect-related breakdowns on field has been found by OSBURN[141]; however, in the high field region the defect related breakdowns become

indistinguishable from those due to intrinsic breakdown mechanisms and Equation **30** is a better description of the breakdown dependence on A and D.

Since for different substrate materials and fabrication processes different dependencies of the defect density, field and length-of- time-of-application of field on breakdown may be expected, the results presented by workers may not always be compared on any quantifiable basis.

3.5 Breakdown Process and Materials Dependence

The effects of processing and of materials' dependence on breakdown in Al-SiO_2-Si MOSCs has been extensively studied and, in itself, represents a large proportion of the published material concerning breakdown in MOSCs; a summary of the conclusions drawn from the most recent, available data is given in Tables 2 and 3 which consider the effects of MOSC parameters (such as oxide thickness, temperature, polarity of applied field and silicon substrate doping density) and of processing parameters (such as oxidation temperature, oxidation ambient and so on), respectively.

In compiling the tables, data was drawn from:

References 121,122,130 and 152. -Table 2

and References 121,122,131 and 135. -Table 3

Table 2 is divided into three columns considering the effect of: maximum breakdown field, defect density and the time-to-wearout on the breakdown characteristics of similarly fabricated Si-SiO_2 based MOSCs since the effect of processing on these parameters is found to be considerably different according to which type of breakdown (intrinsic or defect-related) is considered. The post-metallisation annealing (PMA) factor is the difference in the various parameters between the device being given PMA (in a dry N_2 / H_2 mixture, 15% H_2 at 450°C) and not being annealed; the electrode material factor is for those gate electrodes chosen different from aluminium (considered as the electrode producing the highest dielectric breakdown strength and lowest number of defects in the MOSC).

Here "defects" refers to low-field breakdowns obtained during relatively short timescale room-temperature measurements while wear-out refers to results from extended high-field stressing.

Table 3 shows the effect of processing on the two main parameters of breakdown dependence considered by workers: the maximum breakdown field and the defect density dependencies. These are shown with respect to the effect of increasing the processing parameters (oxidation temperature, oxidation ambient and so on) from the process which produced the best quality MOSCs with the highest breakdown field strength and the minimum number of defects.The presence of a thin (≈10nm) phosphosilicate glass overlay remaining on the surface of the silicon substrate after cleaning, and just pre-processing, has also been considered; the usual effect of such a layer is to passivate the surface states in existence on the "clean" silicon substrate.

Parameter increased	*Effect on Maximum Breakdown Field*	*Effect on Defect Density*	*Effect on Wearout Time*
Oxide Thickness	Decreases (121)	Increases (121) Constant (130) Decreases (152)	Increases (152)
MOSC Temperature	Increases (152)	Constant (152)	Decreases (152)
Post-metallisation Anneal	Constant (130)	Increases (130)	Decreases (130)
Electrode material	Constant (121,122)	Constant (121)	Increases (121)
Polarity of Gate Electrode	Constant (121,122)	Constant (121)	Decreases (121) (Al+ ve)
Silicon Substrate Doping Density	Decreases (122)	Constant (122)	Increases (122)

Table 2. Parameter Effects and Materials Dependence of Breakdown of Si-SiO_2 Based MOSCs

(The figures in brackets refer to the source Reference number)

Parameter increased	*Effect on Maximum Breakdown Field*	*Effect on Defect Density*
Oxidation Temperature	X	Increases (122)
Oxidation Ambient (Wet to Dry)	Constant (121,122)	Increases (121)
Extended Mid-Oxidation N_2 Anneal	X	Increases (130)
Presence of HCl	Decreases (131)	Decreases (131)
Phosphosilicate Glass Layer (≈10nm) on Substrate	Increases (135)	Decreases (135)

Table 3. Effects of processing on Breakdown in SiO_2-Si based MOSCs

An "X" in any position means that the dependence has not been satisfactorily established.

(The figures in brackets refer to the source Reference number).

3.5.1 Intrinsic Breakdown

The dependencies of the maximum breakdown field on the parameters in Table 2 can be seen to be is slight, except for the thickness dependence for oxide films thinner than 50nm, as determined by DISTEFANO and SHATZKES[153] and illustrated in Figure 48.

The temperature dependence, as shown in Figure 49 for an Al-SiO_2-Si MOSC with the aluminium negatively biased, is, according to OSBURN and ORMOND[141], although slight, highly significant to the intrinsic breakdown mechanism.

The relative independence of breakdown parameters on the gate electrode material, as demonstrated by WOLTERS and VERWEY[121] and KLEIN[122] is remarkable considering that current flow in the MOSC is limited by Fowler-Nordheim tunnelling, and even for the gate biased negative varies very little, especially for devices with aluminium electrodes.

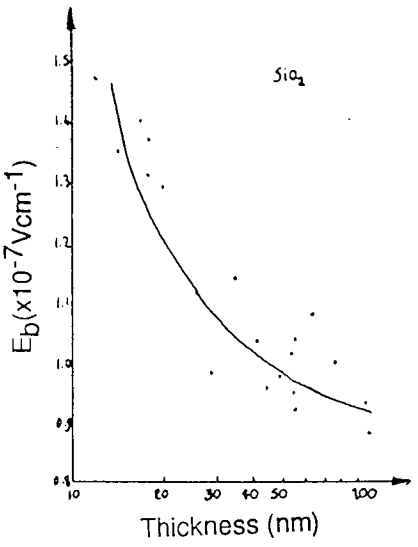

Figure 48: The dielectric strength experimentally determined as a function of the thickness of SiO_2 layer in a p-type silicon-based Al-SiO_2-Si MOSC.
(After DiSTEFANO and SHATZKES, Reference153)

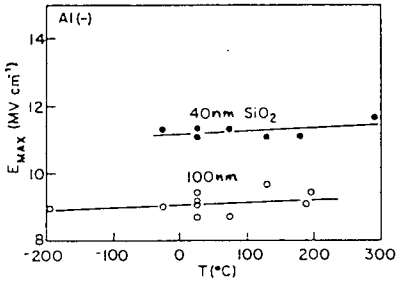

Figure 49: The effect of measurement temperature on the breakdown field strength of <100> p-type silicon-based Al-SiO_2-Si MOSCs; the gate was negatively biased with respect to the silicon substrate.
(After OSBURN and ORMOND, Reference 141)

3.5.2 Defects

The density of defect-related breakdowns in SiO_2 based MOSCs is found to be affected by the quality of the semiconductor wafer (substrate) and wafer cleaning procedures[124,154] before fabrication of each batch of MOSCs, and also by the cleanliness of the oxidation furnace and metallisation chamber. It is an extremely complex procedure to include all the possible variables of the fabrication process which affect the generation of defects in the fabricated MOSC in one function determining the outcome of a particular set of fabrication conditions. Absolute values of the defect density are dependent on the defining threshold for defects (see section **3.4**) and the method of detection. It is not surprising, therefore, that few clear trends are observed in Tables 2 and 3; indeed, the thickness dependence is still unclear, with the defect density increasing with increasing thickness[121], remaining constant[130] or decreasing[152].

The effect of PMA on the density of defects is clearer; Budenstein has found the defect density to dramatically increase after extended PMAs (of approximately 80minutes at 500°C) for aluminium gate electrodes. Optical and metallographic examinations have shown that aluminium reacts with the underlying SiO_2 at these temperatures, causing short-circuit paths through the oxide to the substrate by aluminium diffusion; some correlation of the number of defect-related breakdowns with dry-processing (at approximately 1500°C) is shown in Table 3. Both HCl and a thin layer of phosphosilicate glass, both used to stabilise MOSFETs against threshold voltage instabilities, also reduce defect densities[131,135], whereas high oxidation temperatures [122] and nitrogen anneals of the just-grown oxide layer (at approximately 800°C in dry N_2) increase defects[121].

3.5.3 Wearout

Most of the published data presented for wearout of MOSCs is due to OSBURN and co-workers[146,147,154]. Times to breakdown are exponentially field and temperature activated and show strong polarity and electrode material dependencies.

Figures 50 shows the maximum time to failure for MOSCs, with aluminium gate electrodes, at 300°C, for the Al gate both negatively and positively biased. Figure 51 shows the temperature dependence of wearout for similar devices with the Al gate electrode positively biased. It can be

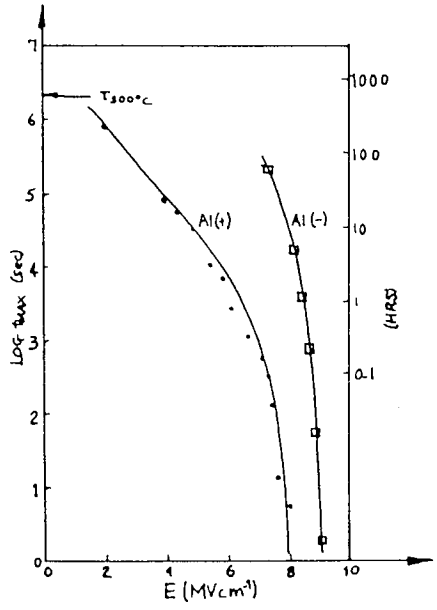

Figure 50: The maximum time-to-failure as a function of applied field and Al gate electrode polarity for a <100> p-type silicon-based Al-SiO_2-Si MOSC with a 35nm oxide layer ; measurements were made at 300°C.
(After OSBURN and BASSOUS, Reference 154)

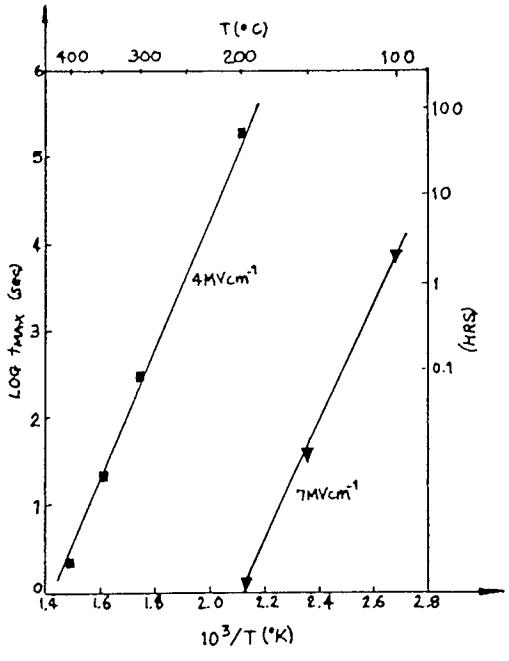

Figure 51: The temperature dependence of wearout for a <100> p-type silicon-based Al-SiO_2-Si MOSC with a 35nm oxide layer ; the gate was positively biased with respect to the silicon substrate.
(After OSBURN and BASSOUS, Reference 154)

concluded from these Figures that the electrode material and polarity dependence of wearout depends primarily on the anode material and the temperature, to the exclusion of most of the other effects.

It can be concluded from section **3.5** to **3.5.3** that comparing Al-SiO_2-Si MOSCs on any quantitative basis requires a thorough knowledge of the processes by which the devices have been fabricated. It also enables the choice of the process conditions in order to fabricate MOSCs which have high dielectric breakdown strengths and low defect densities to be made. From Tables 2 and 3 and the brief summary of process dependencies found by other workers given above, perhaps the ideal MOSC fabrication process, to produce low defect-density and high breakdown strength devices, might include

(1) Low doping-density <100> silicon substrates, with a thin (≈10nm) phosphosilicate glass passivating layer overlaying the surface after cleaning.

(2) a thermally grown oxide layer grown at minimal (≈ 1100°C) temperatures in wet or dry conditions

(3) an aluminium gate electrode

and (4) a post-metallisation anneal at low (≈400°C) temperatures.

3.6 Intrinsic Breakdown Mechanisms

Breakdown mechanisms have been identified for breakdowns where current runaway is caused by electromechanical[155] or by thermal instabilities[156] in MOSCs. The former is frequently observed in silicon based MOSCs, the thermal nature of the process clearly recognisable and the breakdown voltages found by a.c, d.c, and pulse experiments agree well with the theoretically calculated values for a wide range of temperatures and oxide fields; breakdown due to thermal instabilities alone have been observed in Al-SiO2-Si MOSCs[157] for oxide field as high as 9.5 $MVcm^{-1}$.

For applied gate voltages in the breakdown voltage regime for MOSCs, minute leakage currents

through the insulator layer produce a negligible temperature rise; breakdown in such cases cannot, therefore, be ascribed to thermal instabilities. From the work of VON HIPPEL[158], a mechanism for such breakdowns, based on an electronic impact-ionization process within the insulating layer, has been suggested as the cause for such non-thermal breakdowns[9]. The aim of this section is to review the main non-thermal breakdown theories and to discuss these with respect to recent experimental evidence.

3.6.1 Ion-induced and Other Non-Thermal Breakdown Models

A purely ion-induced mechanism has been proposed by GUNDLAPP and SCHNUPP[159] to explain breakdown in very thin (<10nm thick) SiO_2 films in Si-based MOSCs. In this model ionic transport of the anode to the cathode and the formation of metallic protrusions as a result is postulated. The increasing field-enhancement at a protrusion accelerates it's growth and this positive feedback effect leads to runaway in growth and to a local breakdown at the protrusion; the time to breakdown is found, by calculation, to be inversly proportional to an exponential function of the field. Experimental evidence has not, as yet, been found for this mechanism in ultra-thin films but there is no reason why this simple model should be thickness limited; it is probably an example of much more complex electromechanical processes that lead to breakdown by the formation of a metallic or semiconducting bridge across the insulator in MOS devices. CHOU and ELDRIDGE[160]have found that, in SiO_2 at elevated temperatures, the development of breakdowns is promoted by the electrode metal-oxide reaction, which may lead to the growth of conducting bridges. OSBURN and CHOU[147]have proposed that the high temperature breakdowns (which occur at far lower fields than room temperature breakdowns) arise because of localised thermal runaway due to a localised barrier height lowering at the electrode-oxide interface and not as that CHOU and EILDRIDGE had previously proposed. However, extrapolation of OSBURN'S and CHOU'S data indicates that the high temperature breakdowns are, fortunately, not operative at MOS device working temperatures.

An ionic theory, based on the assumption that breakdowns in SiO_2 are initiated at isolated (1-10nm in diameter) protrusions that exist naturally on the surface of the cathode, has been developed by RIDLEY[161]. Field enhancements at such a protrusion by a factor of ten would produce current

densities of approximately 10^5-10^8 Acm^{-2}, raising the temperature locally by hundreds of degrees Celsius. Such a temperature rise would generate ions by dissociation of contaminant particles and the positive ions produced could move toward the protrusion and enhance the field and cuurent injection locally; this positive feedback effect could cause current runaway for oxide fields above a certain critical field, F_r. Although no explicit relationships have been derived for the critical field, it appears that in this model F_r decreases with increasing (ambient) temperature and is strongly dependent om the electrode metal. These phenomena are not confirmed in SiO_2 since, according to OSBURN et al[141,146]experimentally, F_r does not depend on the electrode metal and only a very slight increase in F_r with temperature is found. It therefore seems unlikely that the model proposed by Ridley is a good, whole description of intrinsic breakdown in MOS devices.

BUDENSTEIN[130] proposes that the mechanism of dielectric breakdown in solids involves the formation of a gaseous channel through the dielectric. The high conductance on breakdown is associated with this channel and not with conduction through the solid itself. The formation of a gaseous channel before a marked change in conductance is ascribed to energy supply from the external source and its storage in the solid by polarisation, collision ionization, trapping and atomic displacement resulting in a change in the local charge balance and in broken molecular bonds. This author believes, however, that the formation of such a gaseous channel at even low voltages would be detectable as a marked change in conductance due to the agglomeration of contaminant particles around the channel, forming a conductive path from near the oxide-semiconductor interface to the gate electrode; this is, in fact, typical of the effects of the passage of ionizing radiation through an insulating layer with detectable contamination levels of Na^+ ions[232] (see Chapter 4, section 4.4).

JONSCHER and LACOSTE[162] propose a similar breakdown model to that of RIDLEY[161], whereby point defects exist in the insulator region. On application of a high field, charge carriers are assumed to generate additional defects preferentially at existing defects. A cumulative process sets in, with the formation of defect clusters by carriers; it is proposed that these clusters could grow by further defect generation into a highly conducting channel connecting the gate electrode to the semiconductor substrate and producing destructive breakdown. This has not in practice, however, been seen to be the case.

Degradation processes have been invoked to interpret certain breakdown observations in thermally grown SiO_2 in Al-SiO_2-Si MOSCs: Positive sodium ion drift toward the cathode has been found to decrease the breakdown voltage considerably. Bias temperature-stressing of the MOSCs for C-V calculations has shown that such Na^+drift can produce increasing field enhancement at the cathode which OSBURN and RAIDER[163] have shown to cause breakdown by basic electronic conduction processes at a critical field. Negative charge accumulation has been observed by HARARI[164] prior to breakdown in SiO_2-based MOSCs with thin (<30nm thick) oxides as a result of electron trapping enhanced by trap generation; a field distortion is assumed to be created and breakdown is again interpreted to arise when a field, in this case at the anode, becomes critically high and causes breakdown by basic electronic conduction processes.

Other breakdown mechanisms of interest are due to electromechanical and double-injection processes, which have both been treated analytically: the electromechanical mechanism proposed by GARTON and STARK[155]succesfully explains the breakdown of "soft" SiO_2, while the double-injection process proposed by BARNETT and MILNES[165] has been applied, in the main, to semiconductors. According to SCHMIDLIN[166], double-injection can cause current runaway in insulators when positive carriers are trapped at the cathode and negative carriers at the anode; instability of such a nature has not, as yet, been found to be the case for SiO_2.

3.6.2 Electronic Impact-Ionization Models

In semiconductors such as silicon, breakdown by impact-ionization is described by a two-carrier ionization model. The positive feedback effect, which causes instability and current runaway in this model, is the mutual enhancement of carrier multiplication by holes and electrons, both of which produce electron-hole pairs on impact ionization.

In wide bandgap insulators such as silicon dioxide, impact-ionization is believed to be feasible by one type of carrier only, owing to deep trapping of the second carrier type[167]. Under such circumstances, different instability mechanisms, such as those proposed by O'DWYER[9], are thought to apply. Assuming that the ionizing carriers are electrons, the mechanism proposed may be seen in a simple form which has the following features: electrons injected from the cathode

traverse the insulator (SiO_2) layer rapidly; these electrons can produce electron-hole pairs by impact-ionization, and the holes generated become deeply trapped. The effective mobility of the holes is very small and so a positive charge arises which enhances the cathode field and hence enhances the current injection and impact ionization. The effect of this regenerative process is successfully opposed for fields below the current runaway field, F_r, by hole removal, by drift or electron-hole recombination. For fields larger than F_r, however, instabilities arise and it is proposed that the time to current runaway, t_r, decreases quasi-exponentially with increasing field[139].

The first theoretical analysis of this model was presented by O'DWYER[9] for the case when impact-ionization is opposed by drift (the ID model). This theoretical form of the model can only be obtained by numerical methods; KASHAT and KLEIN[168] have developed an approximate treatment of the model which results in closed expressions for F_r and t_r. The F_r values calculated from the approximate form are only a few percent less than those obtained using O'DWYER'S rigorous treatment.

The theory for the case where the effect of impact-ionization is opposed by recombination (the IR model) has been analysed by DISTEFANO and SHATZKES[169] and by KLEIN and SOLOMON[170]. F_r and t_r can be calculated by determining the condition for current runaway from the set of conduction equations for an insulator. To illustrate this approach the set of equations for the IR model is given with the assumptions that the insulator is planar and current injection from the cathode occurs by tunnelling[170]:

$$j = AF_C\, e^{(-B/F_C)^2} \qquad -71$$

$$\frac{\partial F}{\partial x} = \frac{qp}{\epsilon_0 \epsilon} \qquad -72$$

$$\frac{\partial p}{\partial t} = j/q\ (a - sp) \qquad -73$$

and

$$a = a_0\, e^{(-H/F)} \qquad -74$$

Equation **71** is the Fowler-Nordheim equation for current density j. Equation **72** is Poisson's

equation. Equation **73** is the rate equation for holes, where a is the ionization coefficient, s is the recombination cross-section and p is the hole density. Equation **74** gives a simple form of the field dependence of a. F is the field, F_c the cathode field, q the electronic charge and C_o and C the absolute and relative permittivities of free space and the insulator, respectively.

The remaining symbols represent constants; according to O'DWYER[9], the constant H in Equation **74**, for the ionization coefficient a , depends on the energy of impact-ionization, E_i, and the mean free path for a phonon collision in the direction of the field, l_p , such that

$$H = E_i / (q\ l_p) \qquad \textbf{-75}$$

The solutions to Equations **70-72** give expressions for F_r and t_r for the IR model. Expressions for F_r and t_r have also been derived for two cases of the ID model: in the first, for small ionization, the product aT'<1, and in the second, for large ionization, aT'>1 (where T' is the oxide thickness). These relationships are given in Table 4 for comparison with the IR model. Table 4 also gives expressions for a simple two-carrier ionization model if equality of hole and electron ionization coefficients and a uniform field in the insulator are assumed.

For the ID models it is assumed that holes are released by tunnelling from traps and the hole mobility, μ_p, is given by

$$\mu_p = CF\ e^{(-D/F)} \qquad \textbf{-76}$$

where C and D are constants[167].

The problem as to which of these models applies to the Al-SiO_2-Si MOSC under various conditions this author approaches from a qualitative standpoint: current runaway by one-carrier ionization is dependent on positive feedback to establish a positive space-charge region in the SiO_2. For this reason, the faster the holes are removed from the oxide, the larger the rate of hole generation by impact-ionization must be for current runaway and the larger the breakdown field. The model is strongly dependent on the magnitude of the effective hole mobility, and this may have values that

vary over many orders of magnitude.

For extremely low effective mobilities, say 10^{-13} $cm^2V^{-1}s^{-1}$, hole removal takes place mainly by recombination and for breakdown the IR model applies. With increasing mobility, hole removal can become more effective by drift than by recombination; in this case the small ionization ID model (for which the product $aT'<1$) can become operative. A further increase in μ_p leads to the case of the large ionization ID model with $aT'>1$ for runaway to occur. A qualitative change in the breakdown process must then arise in the breakdown process since for $aT'>1$, injected electrons produce small avalanches and breakdown may then also occur by consecutive avalanches at one spot[171]. For a further increase in the effective hole mobility, high mobility holes appear in the valence band of the oxide; if these holes cannot establish the positive charge needed for current runaway, but can generate sufficient electron-hole pairs by impact-ionization, the two-carrier model would be the accurate description of the breakdown mechanism in operation.

3.6.3 Discussion of the Impact Ionization Models

The results summarised in Table 4 show clearly defined runaway conditions, but they relate to idealised models. Models which are descriptions of real MOSCs are certainly far more complex: the physical processes which determine j, a , s and μ_p can be very different from those presented in Table 4; for example, a model has been proposed by O'DWYER[119] which includes a derivation of the current runaway for the ID model when current injection into the insulator is thermionic. Other variations arise in the calculations when the trapping of positive charge is restricted to a thin layer at the cathode. Trapping of electrons is known to strongly influence the breakdown process and has been found [168] to increase F_r; in contrast, field ionization of states below the Fermi level and positive ion motion toward the cathode decreases Fr[168] .

The results shown in Table 4 were obtained on the assumption that the effective ionization coefficient, a, is position independent in the insulator (oxide) layer; in fact, electrons from the cathode have to fall through a potentialdrop of at least E_i/q before they can ionize by impact, and no impact ionization takes place at a narrow band at the cathode. Also, the mean electronic temperature increases toward the anode, as does the ionization rate[172]. The IR model proposed

	Model	F_r	t_r for $F > F_r$	Whether electrode dependent	
				F_r	Transient
Increasing hole mobility ↓	IR	$\frac{\exp(H/F_{ar})}{(H/F_{ar})^2} = \frac{qa_0T}{HS\epsilon_0\epsilon}$ with $F_r = F_{ar}(1 + F_{ar}\ H)$	$\frac{2\epsilon_0\epsilon}{ABa_0T}\exp\left(\frac{B+H}{F}\right)$	No	Yes
	ID small ionization	$\frac{\exp\{(B+H-D)/F_r\}}{\{(B+H-D)/F_r\}^2} = \frac{e\,a_0AB\,T^2}{2\epsilon_0\epsilon C(B+H-D)^2}$	$\frac{2\epsilon_0\epsilon}{ABaT}\exp\left(\frac{B+H}{F}\right)$	Yes	No
	ID large ionization	$\frac{F_r^2\exp\{(B-D)/F_r\}}{\exp\{a_0T\ \exp(-H/F_r)\}-1} = \frac{eABT}{2\epsilon_0\epsilon C}$	$\frac{2\epsilon_0\epsilon\exp(B\ F)}{AB[\exp\{a_0T\ \exp(-H\cdot F)\}-1]}$	Slightly	
	Two-carrier ionization	$\exp(H/F) = a_0T$ when $a_h = a_e$			

Table 4: A Summary of the Models of Dielectric Breakdown by Impact - Ionization.

by DISTEFANO and SHATZKES[169] takes these effects into account and numerical calculations for oxide layers thinner than 100nm (wherein the effects above would be most prevalent) result in F_r values higher than those obtained with the IR model shown in Table 4.

The expressions for F_r and t_r in Table 4 are deterministic solutions to sets of conduction equations; they do not take into account the finite properties of the electronic carrier and the important influence of fluctuations of these on breakdown. Fluctuations diminish breakdown fields to below their deterministic value and restrict breakdown events in MOSCs to small volumes. The latter effect is widely observed[139] and the stochastic nature of breakdown events has been proved for SiO_2[148].

No calculations are available for the effect of fluctuations on F_r and t_r, except for the large ionization ID model; this case has been treated by KLEIN[171] in an approximated theory based on the "succession of avalanches" model (presented earlier in this chapter). In this hybrid model, most of the avalanches produced by electrons injected into the insulator are ineffectual in causing breakdown. Breakdown can only arise in the stochastic event when a sufficiently rapid succession of avalanches occurs at one place in the insulator.

3.6.4 Comparison With Observations

Both direct and indirect breakdown data are measured to establish the breakdown propertiesof MOSCs: direct data give the thickness, temperature, electrode material and time dependencies of the breakdown field; indirect data are obtained by measuring charges in the insulator[121], by studying electroluminescence[173] or by determining the influence of ionizing radiations[10], ion implantation[174], fission fragments[138] and other variables on breakdown.

Many workers have presented data which is in agreement with one of the models presented in Table 4 and, for instance, the exponential nature of the field dependence of t_r is widely observed[171]. Such a functional dependence, however, is predicted also by models which are not based on impact-ionization. Ambiguities arise, therefore, and these are found even within the framework of the impact-ionization models.

This can be well illustrated with the example of the dependence of the breakdown field on oxide thickness; many attempts to establish this property can be found in the literature[119]. An inspection of the relationships for F_r in Table 4 shows that the functional dependence of F_r on T' can hardly reveal which of the four models is pertinent in a given case. The electrode dependence and the current transients are much stronger indicators of the breakdown mechanism.

The identification of the breakdown mechanism is usually a difficult task and the question arises as to which experimental evidence supports the impact-ionization breakdown process?. This is illustrated with several interesting results: assuming that impact ionization occurs in thermally grown SiO_2 at the breakdown fields expected and not before, SOLOMON and KLEIN[175] have determined the field dependence for a from current transients: $a = 6.5*10^{11} e^{(-180 / F)}$ cm^{-1}, where F is the field expressed in $MVcm^{-1}$. This is in agreement with the functional dependence of Equation **75** which is based on a simple impact-ionisation theory. Since F_r has been observed to be rather electrode independent[141] an IR model is thought to explain breakdown in thermally grown SiO_2 in Al-SiO_2-Si MOSCs[169]. Generally the application of the IR model to breakdown in SiO_2 films thicker than 15nm has been fairly well supported by observations[169] on the thickness, temperature and electrode dependencies of breakdown on current and voltage transients[175] and on positive charge generation[176] (which produces the feedback effect for current instability).

The origin of positive charge generation by band-to-band impact-ionization is, however, a subject of serious dispute since alternative sources of positive generation are known[177]. This has been strikingly illustrated by SOLOMON and AITKEN[178] who performed experiments on Al-SiO_2-Si MOSCs at fields approaching $9MVcm^{-1}$ with negative gate metal polarity; rapid positive charge generation was found near the metal electrode at a rate decreasing with increasing temperature and this charge generation can be ascribed to impact-ionization and subsequent hole trapping. Positive charge generation, however, was found near the positively biased silicon substrate electrode too. The charge grew at a slow rate which was temperature independent; this charge could only slightly influence breakdown. SOLOMON and PANTELIDES[70] have also investigated the energy distribution of electrons emitted from Al-SiO_2-Si MOSCs, with oxide thicknesses of 30nm and aluminium gate electrodes 12nm thick, under bias to fields of between 6.7 and $10MVcm^{-1}$.

Electrons with energies gerater than the bandgap of SiO_2 (≈8.8eV) were observed although the number of such electrons was greatly decreased by attenuation in the aluminium gate electrode. This result offers further evidence to support the interpretation of breakdown by impact-ionization in SiO_2 layers and calls for additional experiments to assess the attenuation by the thin Al gate electrode and to assess the numbers of above-bandgap electrons.

The conclusions which may be drawn from the data presented above from recent studies of the breakdown process in Al-SiO_2-Si MOSCs may be summarised, thus:

(1) When breakdown processes are described by the IR model the critical field, F_r, and the time-to-breakdown, t_r, increase with increasing trapped electron charge.

(2) In processes described by the ID breakdown model, F_r and t_r can be strongly affected by the magnitude of the trapped electron charge. The effect of the electron charge is much more pronounced in the small ionization ID model than in thel arge ionization ID model. Experimental data available shows the increase in F_r and t_r with the increase in electron charge, exhibiting a protective effect from breakdown.

(3) The time-to-breakdown on slow ramped- voltage tests is proportional to t_r on stepped-voltage tests. This proportionality does not hold true in fast ramp-voltage tests and the ramp breakdown characteristic is anomalous in a range in which t_r and field decrease together. An anomalous characteristic is an indication of electron trapping prior to the development of the breakdown process and a protective effect from breakdown by the electron charge. The protective effect decreases in the anomalous range of the characteristics.

(4) Relations for the calculation of F_r and t_r are assembled in Table 4. These relations are simple and offer good insight into the effect of processes producing breakdown.

(5) The breakdown properties of an insulator are strongly dependent on the properties of electron and hole traps. Since trap states can be subject to large variations, dependent on the fabrication processes used, significant differences can be expected from independent breakdown observations on different batches of devices.

and (6) Breakdown observations on SiO_2 can be well interpreted by the theories developed in this chapter, as demonstrated by the recent work of ALBERT and KLEIN[179] and KLEIN[152].

CHAPTER FOUR .

MOSCs UNDER EXTERNAL INFLUENCES 2: IRRADIATION

In this chapter radiation damage and radiation effects in SiO_2 and how these affect Al-SiO_2-Si MOSC characteristics are discussed. Radiation induced effects, such as oxide charge buildup, interface trap generation and radiation induced dielectric breakdown, are treated individually; experimental evidence for these effects is presented in summary form and the mechanisms and models which appear to describe and account for these are reviewed.

4.1 Radiation Effects in SiO_2 and Si-Based MOSCs

The importance of radiation arises mainly from interest in operating semiconductor devices in industrial, space and military applications in a radiation environment and device fabrication processes (such as electron beam deposition, sputtering, ion etching and ion implantation) which expose the device to radiation field far in excess of those encountered naturally. Such radiation consists mainly of high energy particles such as electrons, neutrons and protons, and energetic X-ray and gamma-ray photons. In many situation devices may be exposed to other radiation field, such as alpha-particles and fission-fragments, particularly in the nuclear power industry.

The principal cause of radiation damage varies with the application. For industrial applications associated with instrumentation in nuclear reactors and high energy X-ray machines, as well as military applications where the device must survive exposure to nuclear weapons, energetic neutrons and photons are of primary importance. In processing, such as electron-beam deposition and sputtering, photons and ions are of primary importance. For space applications, electrons and protons produce most of the damage in semiconductor devices.

In silicon-based MOSCs, radiation damage in either the silicon or the SiO_2 will affect device characteristics. In either material, radiation effects can be placed in two broad classes:

(1) Effects arising from electron-hole pair production in the material by ionizing radiation -or ionization damage

and (2) effects resulting from defects in the silicon lattice and the oxide produced by energy particles -or displacement damage.

The two phenomena often occur together but result from quite different interactions of the radiation; they have different consequences in the semiconductor and in the insulator of MOSCs.

4.1.1 Ionization and Displacement Damage

Ionization, or the creation of electron-hole pairs or ions in a solid, can be directly produced by either charged particles or photons. Figure 52 illustrates electron-hole pair production in any crystalline solid[180]. Any charged particle passing through the crystal produces ionization by collisions with electrons bound to lattice atoms. In insulators and semiconductors, these collisions excite electrons into the conduction band leaving holes in the valence band; thus, electron-hole pairs are produced as the incident

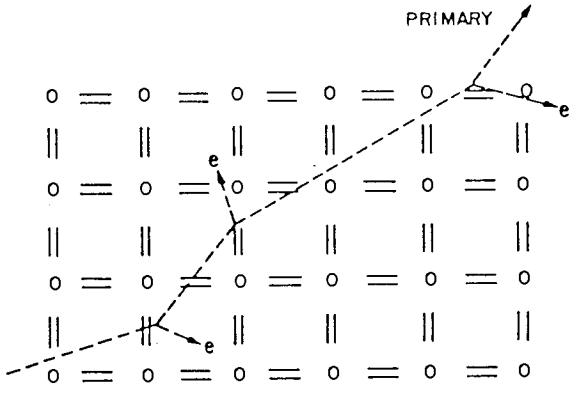

Figure 52: A schematic diagram showing the production of electron-hole pairs by the collision of a charged particle with the valence electrons in silicon.
(After PECK et al, Reference 180)

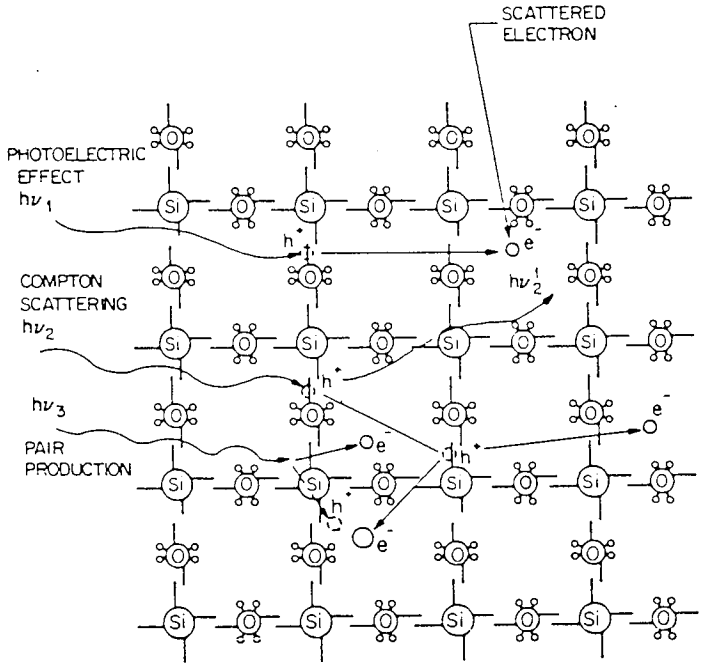

Figure 53: A schematic representation of the ionization processes which can occur in SiO_2.

charged particle loses energy to electrons bound to the molecules bound to the lattice (or, in the case of amorphous materials, by interaction with the electrons bound in the short-range order clusters of molecules), in exact analogy with the production of electron-hole pairs by photons. Neutrons and gamma-rays also cause ionization of the material through which they pass by intermediate reactions which produce charged particles that go on to ionize the material. As far as the effects that depend on ionization or electron-hole pair production are concerned, the originating particles identity is incidental. All that matters is how much energy is lost in the solid by the particle; the number of electron-hole pairs produced is then proportional to this energy loss.

Figure 53 illustrates the ionization process in crystalline SiO_2. In order of increasing energy, these ionization processes include:

(1) the photoelectric effect

(2) Compton scattering

and (3) electron-hole pair production.

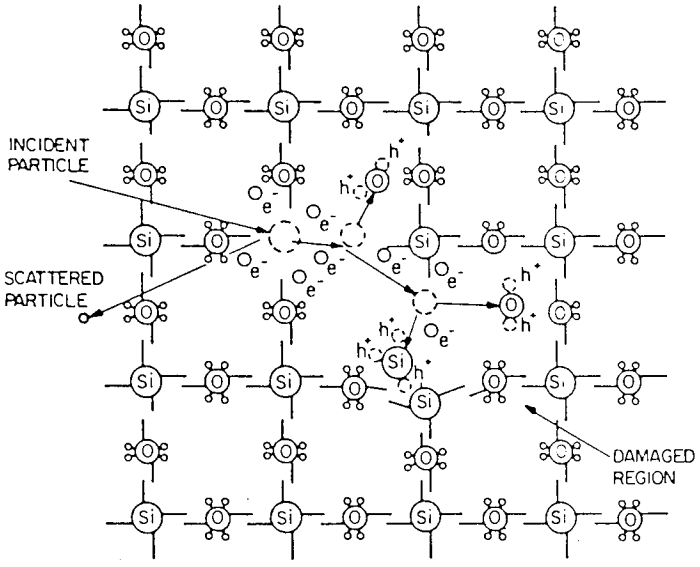

Figure 54: A schematic representation of the displacement processes which can occur in SiO_2.

At photon energies less than the bandgap of SiO_2 (≈8.8eV), no electron-hole pairs can be generated. However, if the photon energy is greater than the barrier energy at either the metal-oxide or the oxide-semiconductor interfaces of an MOS device, a photocurrent will occur by carrier injection from one of the electrodes; which electrode depends on the polarity of the bias applied across the structure. Such currents due to electron emission by UV light have been studied in detail by NING, who gives a review of recent work in this field[181]. In general, the injected photocurrent saturates at a relatively low bias, which indicates that virtually all of the injected electrons reach the opposite electrode.

otons with energy greater than the bandgap of silicon or SiO_2 can cause photoconductivity by
e generation of electron-hole pairs; in SiO_2, this would require 8-9eV photons, whereas 3-5eV
iotons cause only photoemission of electrons from the electrodes. The energy of the incident
ioton is completely absorbed, and the valence electron injected into the conduction band has an
iergy which is equal to that of the initial photon energy minus the binding energy of the electron
i the lattice atom. This energy is dissipated as kinetic energy by the electron injected into the
onduction band. If the injected electron has sufficient kinetic energy it can produce secondary
lectrons as it moves through the material. For even greater energy photons, electrons can be
ijected from the K and L shells of the atoms in the material. The subsequent transition of electrons
rom the outer shells to the K or L shell is accomplished by the emission of additional X-ray photons,
which in turn can produce further ionization of the SiO_2.

In a Compton-scattering collision (which occurs for still higher energy photons) an incident photon creates an electron-hole pair. The photon energy is large compared with the binding energy of an electron to a lattice atom. Only some of the energy of the incident photon is transferred to the electron, in contrast to the photoelectric effect, where all of the photon energy is absorbed. The scattered photon in the Compton effect can continue to produce more electron-hole pairs until it is completely absorbed. The KE of the scattered electron can be a significant fraction (>0.5) of the incident photon energy so a large amount of secondary ionization can be produced as the electron is decelerated by the material. If the scattered electron energy is of the order of several hundred KeV, displacement damage can also be produced.

When the incident photon energy exceeds 1.02MeV, the interaction of the photon with the Coulomb field of the nuclei of the lattice atoms may result in the creation of an electron-positron pair. The photon is completely annihilated and the energy in excess that is required to produce the electron-positron pair is approximately evenly distributed between the two particles as KE. Photon energies high enough to produce electron-positron pairs are not usually encountered in radiation

environments in most applications (but are most frequently found in the nuclear power industry) and electron-hole pair production is the usual form of radiation effect encountered.

In silicon, electron-hole pairs tend to recombine with a time constant that is the conventional lifetime. Therefore, all effects in this class in silicon are transient and persist for the order of a lifetime after the excitation is removed. The electron-hole pairs produced in the silicon alter its conductivity and also contribute to anomalous currents in MOSCs.

Pulsed ionizing radiation can alter the conductivities of MOSCs by many orders of magnitude. On the other hand, in response to a single energetic particle, these effects can be extremely small.

Figure 54 illustrates the second principal type of radiation damage, displacement damage, which can occur in a solid as a result of collisions of energetic particles, such as neutrons, with the nuclei of atoms in the lattice or clusters in the material. If such a collision transfers sufficient energy to the struck atom, this atom can be dislodged from its normal site and subsequently strike and dislodge other atoms from their sites before coming to rest in an interstitial site. The cascade of displaced atoms form disordered regions or damage clusters containing interstitial atoms, lattice vacancies and more complex defects. In addition to the displacement damage, a large amount of ionization can also be produced as valence electron bonds are broken in the displacement process.

Displacement damage is rare compared to the ionization events produced by charged particles and photons discussed previously, but displacement damage creates permanent (or at least semi-permanent) defects in the amorphous material or lattice structure. Defects and defect clusters can act as recombination-generation centres in silicon and amorphous SiO_2. These centres reduce minority carrier lifetime in silicon and increase the conductivity of amorphous SiO_2. In silicon-based MOSCs, increasing the density of generation-recombination centres in the silicon by displacement damage can increase reverse currents due to increased carrier generation.

In contrast to electron-hole pair production by ionizing radiation, which depends only on the energy but not the type of incident particle, radiation damage that produces displacements of lattice atoms is extremely dependent on the particular particle. Energetic proton, for example, are far more effective in producing lattice damage than energetic electrons. BRUCKER et al[182] and STAPOR et al[183] have investigated the damage equivalence of electrons, protons, gamma-rays and heavy ions in silicon-based MOS devices: they conclude that the damage sensitivity for low energy protons is reduced compared that of electrons and heavy ions because the highly ionizing particles produce

initial recombination of the electron-hole pairs, reducing the number of holes reaching the Si-SiO_2 interface where trapping occurs. The proton dependence is a function of oxide electric field, incident particle

angle and particle stopping power. For heavy-ion irradiation of devices under bias, charge recombination is reported as being so pronounced that flatband voltage shifts in the C-V curves of the device (compared with the virgin device characteristics) were only a few percent of those measured for proton exposures.

Work by BRUCKER[184] and SROUR, OTHMER and CHEN[185] on neutron effects in Si-based MOSTs has revealed that reactor neutrons produce heavy displacement damage in the oxide layer with the associated increase in base-emitter current. It has not, however, been shown that the base-emitter current increase is wholly due to to the neutron because of the (unavoidable) gamma background radiation producing surface damage by means of secondary Compton electrons. As far as MOSCs are concerned, in a reactor neutron field the effects predicted are: an increase in bulk recombination current in the silicon[184] and fluence-related changes in the dark current at room temperature (seen as a near-linear shift in the I-V curve with increasing neutron fluence).

Since much of the information concerning neutron irradiations is military oriented, little work pertinent to this study is available; most of the more recent laboratory and industrial results published concern reactor neutron irradiation of instruments and LSI devices (such as CCDs).

4.1.2 Radiation Induced Effects

SZEDON and SANDOR[186] are among the first workers to recognise that the change in MOS device characteristics during (and after) irradiation is caused by the formation of positive charge in the oxide layer of the device. This has led to an intensive study of radiation effects in SiO_2. In many cases the radiation damage in the SiO_2 is the dominant effect: it has been shown by SROUR, CURTIS and CHOU[187] that, radiation damage in the semiconductor due to low energy particles is less important than that in the oxide since the incident radiation may lose so much energy in creating damage in the oxide that it has insufficient energy to create noticeable damage in the semiconductor. For higher energy radiations the three main degradation mechanisms in

semiconductors (lifetime degradation, carrier removal and trapping and mobility degradation) arise due mainly to displacement-type damage resulting from exposure to neutrons and all occur in the substrate. However, the primary failure mode for MOSCs in a radiation environment is that due to a buildup of oxide charge and surface-effects at the metal-oxide and oxide-semiconductor interfaces. These are termed "radiation induced effects" and are discussed in detail in section **4.2** and **4.3**.

TOMMASINO, KLEIN and SOLOMON[13] have shown that fission-fragments can cause another form of damage in MOSCs; for MOSCs under bias and fission-fragment irradiation this results in dielectric breakdown occurring at far lower fields than those due to the field alone. Testing MOSCs in various radiation fields other workers have demonstrated[188] pulsed and continuous-radiation induced breakdown in MOSCs. This has become a topic of great importance since it has been suggested [14] that such devices might prove invaluable as dosimeters and as a research tool to investigate neutron (or electron) induced fission in the nuclear power industry . Radiation induced dielectric breakdown is discussed in section **4.4**, where mechanisms and models are presented and compared with recent experimental results.

4.2 Radiation Induced Oxide Charge (RIOC)

The MOSC is widely used in the study of radiation effects in SiO_2. Figure 55 shows the work of SNOW et al[190] and illustrates the effect of ionizing radiation on the C-V characteristics of an n-type <100> Si-based Al-SiO_2-Si MOSC; it shows a set of high (1MHz) frequency C-V curves before device irradiation and after exposure to a total dose of 60KRads(SiO_2) and 2MRads(SiO_2) Co^{60} gamma-radiation with the device biased (+2.5V on the gate aluminium electrode), respectively. The C-V curves can be seen to have shifted along the voltage axis to higher negative voltages, thus indicating (from the results of Chapter **2**) that positive charge has been induced in the oxide by exposure to ionizing radiation whilst under bias conditions; also, the induced positive oxide charge-density can be seen to increases with increasing total absorbed radiation dose. In addition to the shift of the C-V curve along the voltage axis, the shape of the curve has been distorted. After exposure to ionizing radiation the C-V curves are "stretched-out" along the voltage axis; this is

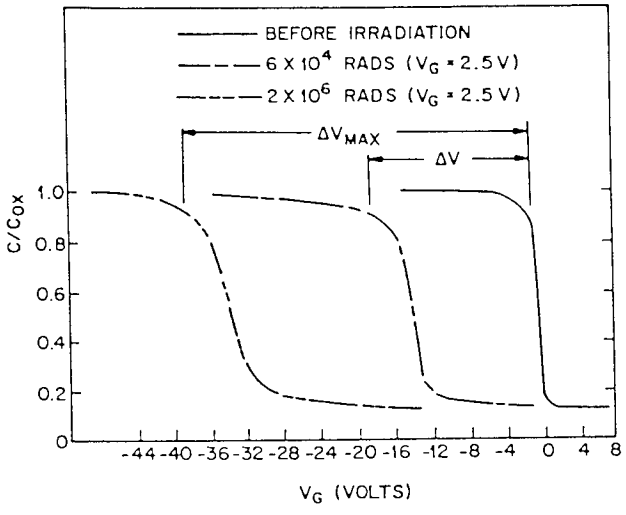

Figure 55:The shift along the voltage axis, ΔV, in the MOSC C-V characteristic as a result of irradiation of the MOSC by Co^{60} gamma-radiation to two different dose levels whilst under the same positive gate biasV_G=2.5V; the MOSC was a <100> n-type silicon-based Al-SiO_2-Si MOSC with a 120nm oxide layer and 1μm Al gate electrode; the gate was positively biased with respect to the silicon substrate.
(After GWYN, Reference 189)

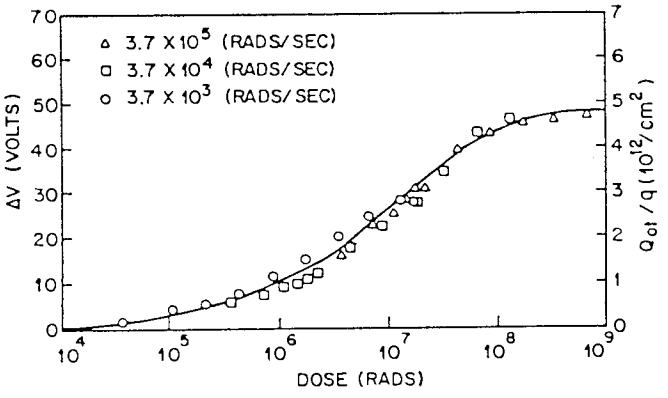

Figure 56: The shift along the voltage axis, ΔV, and the corresponding charge, $Q_{ot}=\Delta V c_{ox}$, in the MOSC C-V characteristic as a result of irradiation of the MOSC by Co^{60} gamma-radiation whilst under the same positive gate biasV_G=2.0V, shown as a function of radiation dose; the MOSC was a <100> n-type silicon-based Al-SiO_2-Si MOSC with a 200nm oxide layer and thick Al gate electrode; the gate was positively biased with respect to the silicon substrate.
(After SNOW et al, Reference 190)

caused by either an increase in the number of gross charge non-uniformities or by an increase in the interface trap level density (which will be discussed in section 4.3).

4.2.1 Electrical Properties of RIOC

Figure 56 shows the voltage shift, ΔV, of the C-V characteristics of an Al-SiO_2-Si MOSC as a function of radiation dose in SiO_2 at various cumulative doses (for various dose rates). The flatband-voltage voltage-shift, ΔV, is taken as the shift from the flatband voltage for the same device when unirradiated. A different MOSC was used from the same batch for each indicated dose rate. A noticeable voltage shift begins to appear at approximately 1KRad(SiO_2) and ΔV saturates above a dose of 100MRad(SiO_2). Two important factors in the effects of ionizing radiation on the flatband voltage shift are evident from Figure 56:

(1) the saturation of ΔV with dose

and (2) the dependence of ΔV not on dose rate but only on the total absorbed dose D = Rt, where t is time and R the rate.

Since all the charge for positive gate bias is known to reside at or very near to the Si-SiO_2 interface, the charge density per unit area, Q_{ot}, of the radiation induced charge is given approximately by

$$Q_{ot} = c_{ox} \Delta V \qquad -77$$

A scale for Q_{ot} is also shown on Figure 56.

Figure 57(a) shows[191] ΔV as a function of dose with positive gate bias applied during irradiation wit Co^{60} gamma-radiation as the parameter and Figure 57(b) shows[191] ΔV as a function of dose of the same radiation source as for Figure 57(a) but with negative bias applied to the device during irradiation; it can be seen that at high doses, ΔV saturates and ΔV at saturation is dependent on the

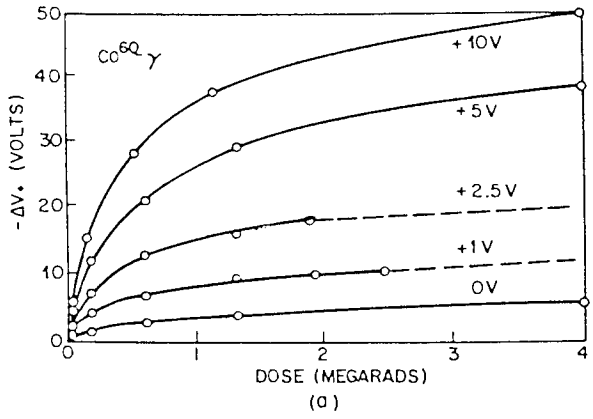

Figure 57: (a) The shift along the voltage axis, $-\Delta V_+$, the MOSC C-V characteristic as a result of irradiation of the MOSC by Co^{60} gamma-radiation whilst under various positive gate biases, shown as a function of radiation dose; the MOSC was a <100> n-type silicon-based Al-SiO_2-Si MOSC with a 160nm dry thermally grown oxide layer and thick Al gate electrode.
(After MITCHELL, Reference 191)

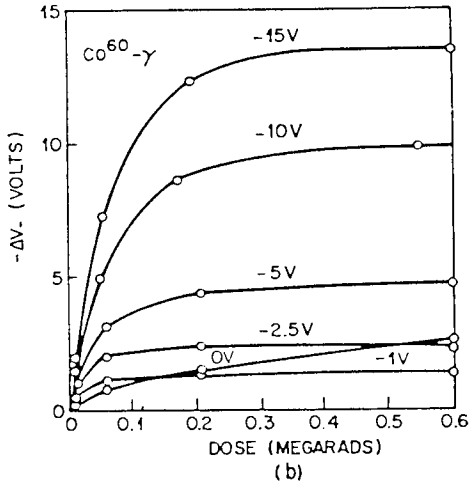

Figure 57: (b) As for Figure 57(a), the shift along the voltage axis, $-\Delta V_-$, the MOSC C-V characteristic as a result of irradiation of the MOSC by Co^{60} gamma-radiation whilst under various negative gate biases, shown as a function of radiation dose; the MOSC was a <100> n-type silicon-based Al-SiO_2-Si MOSC with a 160nm dry thermally grown oxide layer and thick Al gate electrode.
(After MITCHELL, Reference 191)

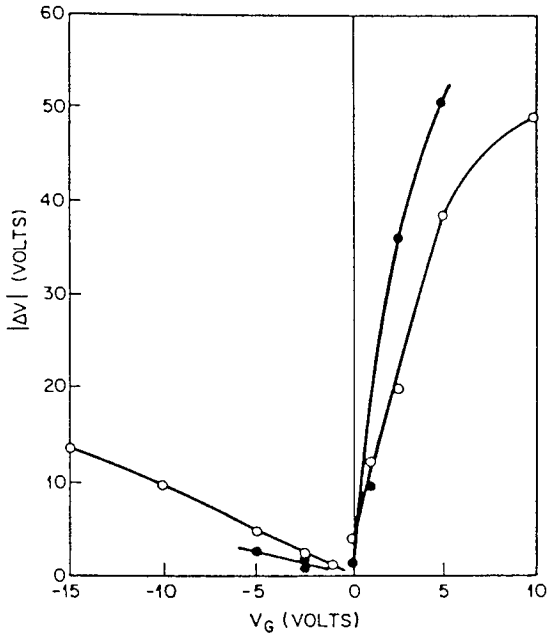

Figure 58: The change in the threshold voltage of a <100> n-type Al-SiO_2-Si MOSC as a function of gate bias applied during irradiation, after a dose of 4MRad(SiO_2) of Co^{60} gamma radiation. Results for two different thickness oxide MOSCs are shown: open circles denote a 160nm thick sputtered oxide; Filled circles denote a 120nm dry thermal oxide device.
(After MITCHELL, Reference 191)

polarity and magnitude of the applied gate voltage during irradiation.

The values of ΔV at a dose of 4MRads(SiO_2), denoted as $|\Delta V|$, from curves such as those shown in Figures 57(a) and (b), are plotted in Figure 58 as a function of gate bias applied during irradiation for both polarities[191]. For negative bias bias, $|\Delta V|$ is the saturated value of ΔV, whereas for positive bia it is approximately two-thirds of ΔV; thus, although $|\Delta V|$ at a given gate bias is dependent on the fabrication processes used to construct the device, the saturation voltage shift due to induced positive oxide charge is far greater for positive bias than for negative bias applied to the MOSC throughout irradiation.

A model which qualitatively explains this behaviour is described in section **4.2.4.**

4.2.2 Location in the Oxide Layer

Etching experiments on MOSCs which have been irradiated with positive gate bias applied during X-ray, gamma-ray or high energy electron irradiation have shown that the RIOC and charged interface traps are located within tens of nanometres of the Si-SiO_2 interface[192]. No charge has been found to be distributed through the bulk of the oxide. Etch-off experiments and barrier-height-reduction mechanisms by internal photoemission of electrons from the Al gate electrode have shown[192] that, after irradiation with negative gate bias applied during irradiation, some of the positive oxide charge produced by radiation is localised at the Al-SiO_2 interface (the density of hole traps at the Al-SiO_2 interface may, however, well depend on contaminants introduced during processing[193]). Barrier-height lowering by internal photoemission of electrons from the Al gate is, however, conclusive evidence that charge of some kind is located at the Al-SiO_2 interface; a lowering of the Al-SiO_2 barrier height of 0.65eV for a dose of 1MRad(SiO_2) and 0.9eV for 10MRad(SiO_2) has been observed in Al-SiO_2-Si MOSCs[192]. Because the image potential at the interface, which accounts for barrier-height-lowering, is prominent in approximately the first 2nm from the interface a portion of the charge must be located very near the interface, otherwise barrier lowering of the magnitude reported by workers would not be feasible. According to the most recent investigations by SHANFIELD and MORIWAKI[194] however, the charge may extend beyond this depth.

4.2.3 Annealing Effects

Figure 59 illustrates how oxide charge can be thermally annealed from an MOS structure and Figure 59(a) shows the annealing of RIOC by illumination with UV light[190]. To investigate this effect quantitatively, SNOW et al[190]have investigated MOSCs (with ultrathin Al gate electrodes, semi-transparent to UV light) which have been irradiated with Co^{60} gamma-radiation to a total dose of 3MRad(SiO_2) whilst biased at +2V on the Al gate, and then annealed using a UV source and monochromator. The MOSCs were exposed to equal numbers of UV photons; the percentage annealing is shown in Figure 59(a) where it can be seen that there is a sharp threshold for annealing to be initiated which is consistent with the Si-SiO_2barrier energy of 4.25eV. Thus, when an irradiated MOSC is annealed it can be assumed that electrons are injected from the silicon into the oxide conduction band which subsequently neutralise the RIOC. According to KNOLL, BRAUNIG and FAHRNER[193] this is the mechanism underlying the near-complete recovery of MOSCs from RIOC upon UV annealing and this mechanism is also applicable to the early work on thermal annealing by SNOW et al[190]; however, a single activation energy characteristic of the annealing process has not, as yet, been reported.

Figure 59(b) shows the thermal annealing of RIOC as a function of time and temperature for Al-SiO_2-Si MOSCs which had been irradiated with Co^{60} gamma-radiation to a total dose of 3MRad(SiO_2). It can be seen that high (≈500°C) temperature annealing can very nearly return the flatband-voltage for the irradiated device to that of the virgin device.

Thus, thermal and UV annealing have been shown to reduce RIOC in MOSCs to near-zero charge densities regardless of the total radiation dose and gate magnitude and polarity during irradiation. Room temperature annealing is assumed to occur,but workers have reported that this annealing is extremely small and near-undetectable changes in the RIOC charge density have been reported[190-191,193].

4.2.4 Models for RIOC

Two decades ago ZAININGER[195], followed independently by GROVE and SNOW[196] soon after, proposed the following simple model for RIOC which quantitatively explains most of the observed

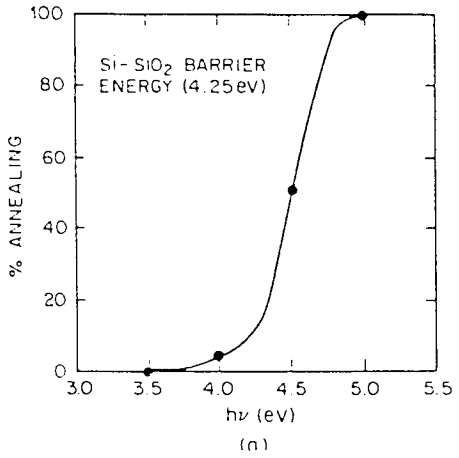

Figure 59: (a) The percentage annealing of radiation induced oxide charge shown as a function of photon energy; the data points correspond to an Al-SiO_2-Si MOSC exposed to equal numbers of photons (of the indicated energy) after irradiation with Co^{60} gamma radiation to a total dose of 3MRad(SiO_2) whilst under constant gate bias of +2v relative to the silicon substrate. The device was a <100> p-type silicon based MOSC with a120 nm oxide layer.
(After SNOW et al, Reference 190)

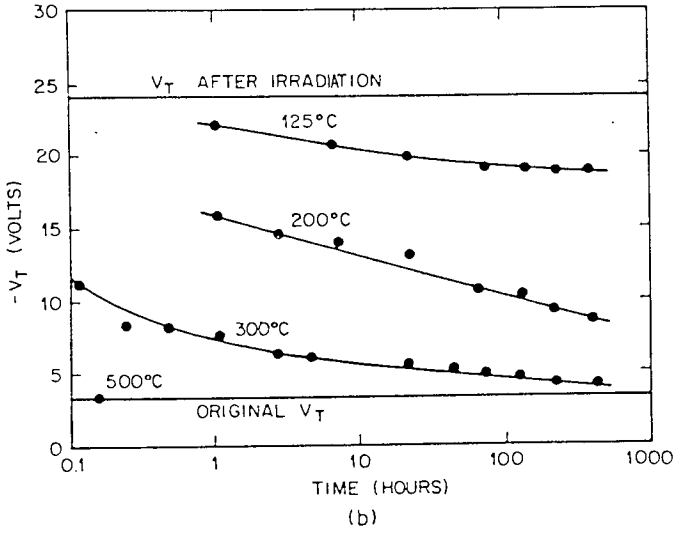

Figure 59: (b) Thermal annealing of the radiation induced oxide charge shown as a function of time and of temperature. A gate bias of +2V with respect to the silicon substrate was applied during irradiation with Co^{60} gamma radiation to a total dose of 3MRad(SiO_2). The device was of the same type and from the same batch as that in Figure 59(a).
(After SNOW et al, Reference 190)

features of oxide positive charge buildup in MOS devices, which has not, as yet, been superceded by a model which fits the experimental data available as simply and more precisely: Ionizing radiation, on passing through the oxide, creates electron-hole pairs in the oxide layer by breaking Si-O bonds, as illustrated in the band diagram Figure 60. Some of the generated carriers recombine, but most are driven toward the electrodes by the oxide field (created by the applied bias) during irradiation. Electrons rapidly drift toward the positive electrode, where most flow out into the external circuit, as shown in Figure 60. Very few electrons become trapped in the oxide. Once holes reach the Si-SiO_2 interface, a fraction become trapped (this fraction varies with the oxide growth technique used and may be as small as a few percent or less[197]) in this interfacial region (also shown in Figure 60).

It has been recently shown by SHANFIELD and MORIWAKI[194] that there is very little hole trapping anywhere in the oxide layer of MOSCs except at the Si-SiO_2 interface, and possibly the Al-SiO_2 interface, where hole traps are located. Trapped holes at the Si-SiO_2 interface constitute the radiation induced positive charge observed. These trapped holes may also be responsible for the increased interface trap level density usually associated with ionizing radiation effects at large doses, as described by KNOLL et al[193], but exactly how these interface traps are created is not known (this effect is described in detail in section **4.3**).

This model requires hole transport through the SiO_2 to occur; such hole transport in SiO_2 could be controlled by bulk oxide traps. (if such bulk hole traps exist they do not trap holes permanently and differ in this respect from hole traps at the Si-SiO_2 interface, which trap holes for a long time). If so, the times that holes spend in these traps are spread over a wide range and are comparable with the transit time of the holes across the oxide. As a result, the transit time, t_T, increases more rapidly than linearly with oxide thickness. The customary hole mobility, μ_p,

$$\mu_p = \frac{T}{t_T \, F_{ox}} \qquad \textbf{-78}$$

is then oxide thickness dependent, field dependent and time dependent. Hole transport cannot be described by drift alone and according to PFISTER and SCHER[198] must include capture and release of holes from bulk traps.

A number of models of this type have been proposed for such hole transport; the most successful

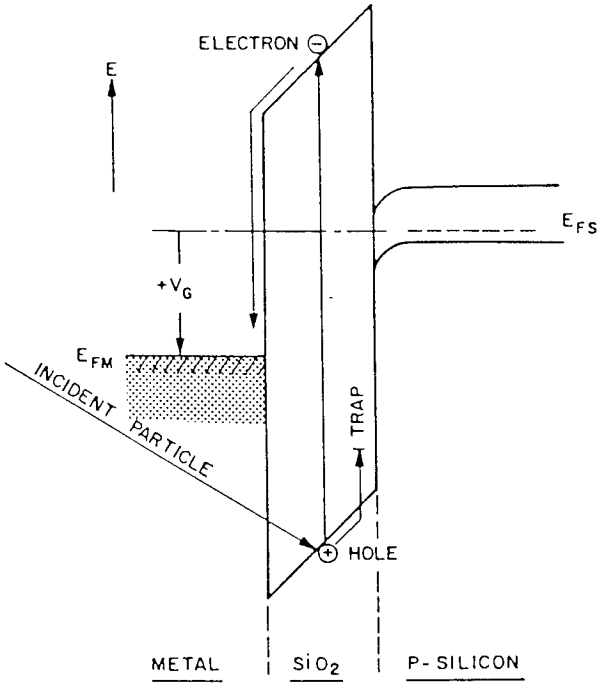

Figure 60: An energy band diagram for the Al-SiO_2-Si MOSC system illustrating the creation of an electron-hole pair in the SiO_2 by ionizing radiation and the subsequent drift of the hole (under the action of the positive gate bias) to the Si-SiO_2 interface where it is trapped to form positive oxide charge.

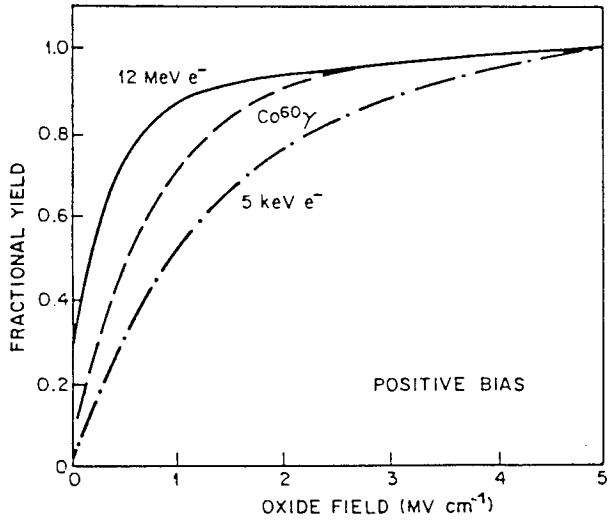

Figure 61: The fractional yield and energy dependence of fractional yield of generated electron-hole pairs which escape recombination under the action of a positive gate bias in <100> p-type Al-SiO_2-Si MOSCs with thermally grown oxides.
(After McGARRITY, Reference 202)

of these[197,199] describes hole transport as phonon assisted hopping between bulk oxide trap sites. However, theoretical objections[200] to this model have yet to be settled.

CURTIS and SROUR[201] have proposed another model, which describes hole transport as drift in the valence band interrupted by residence in bulk oxide traps. These two models are formally equivalent[198] , thus posing a problem in identifying the microscopic transport process.

The most recent model, proposed by KNOLL et al[193], and verified experimentally using tunnel injection techniques in sequence with ionizing irradiations, accounts for charge buildup considering hole trapping in neutral oxide states, the subsequent electron trapping (in now positively charged states) and detrapping of the captured electrons.

The fraction of electron-hole pairs which escape recombination is a function of the oxide field applied during irradiation and of the energy of the incident radiation. This fractional yield , based on the proposals made by MCGARRITY[202], is shown in Figure 61 for several types of radiation in Al-SiO_2-Si MOSCs. At low oxide fields, many electron-hole pairs recombine before the field sweeps the electrons away from the holes; the fractional yield increases almost linearly with field in the region below 0.5MVcm^{-1}. At fields above 2MVcm^{-1}, recombination is suppressed and nearly all the generated charge carriers are transported to the interfaces.

Using the Zaininger model and fractional yield dependence on field of Figure 61, the MOSC C-V curve voltage-shift versus gate bias during irradiation, shown in Figure 58, can be understood qualitatively: Firstly, for the low oxide fields shown in Figure 58, the fractional yield is proportional to the oxide field (from Figure 60) and hence to gate bias; thus, the linear dependence of voltage shift on gate bias is expected. Secondly, the steeper slope of voltage shift versus gate bias for positive gate bias compared with the slope for negative gate bias is explained by the different number of holes trapped near the Si-SiO_2 interface for these two polarities; thus, for a given oxide field applied during irradiation the same number of holes maybe generated regardless of bias polarity.

However, for positive gate bias, most holes drift toward the Si-SiO_2 interfaceand a fraction of those holes become trapped. For negative gate biases, most holes drift to the metal gate and only a fraction of those holes generated near the Si-SiO_2 interface become trapped there (a small number compared to the case for positive bias during irradiation).

Holes trapped near the Al-SiO_2 interface are not appropriate to this discussion because it is the

product of the trapped charge and its centroid with respect to the gate which determines the flatband voltage (see section 2.4.2) and the centroid of charge trapped near the gate is near zero.

4.2.5 Experimental Verification of the Model and Discussion

The early experiments of POWELL and DERBENWICK[203] support the ZAININGER[195] and GROVE[196] models, presented in the previous section, for the creation of RIOC. The main feature of their experimentation is the use of vacuum ultraviolet (VUV) photons as the ionizing radiation; the advantages of VUV being that the depth of light absorption in the SiO_2 can be controlled by varying the photon energy and that only electron-hole pairs are produced with no displacement damage or other effects (although lattice relaxation effects associated with electron-hole pair production may occur). The experiments were performed on MOSCs with semi-transparent Al gate electrodes (≈10nm thick) deposited on a 200nm thermally grown (in dry O_2) oxide layer on a 0.8 Ωcm <100>p-type silicon substrate. (The electrode configuration and optical apparatus are not described here); the pertinent results from their experiments are that:

(1) There is an energy threshold for the effect near the fundamental absorption edge of the SiO_2 (equivalent to the bandgap of 8.8eV).

(2) Light penetration was of the order of 10nm, thus localising electron-hole pair production to near the Al-SiO_2 interface.

and (3) The positive oxide charge induced was found to be localised at the Si-SiO_2 interface.

These results confirm experimentally the proposals set out in the two models described in the previous section.

Figure 62 shows the high (1MHz) frequency C-V curves for an MOSC irradiated at constant dose rate whilst under positive bias with photon energy as the parameter[203]: the C-V curves have been

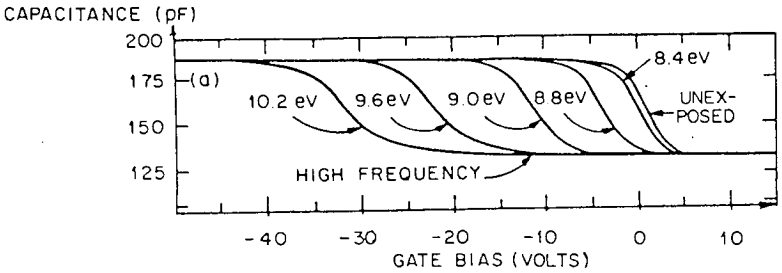

Figure 62: Hgh frequency MOSC C-V curves for irradiated <100> p-type Al-SiO_2-Si MOSCs, irradiated to a constant dose under positive gate bias with photon radiation energy as the parameter; the dose was $\approx 6.7 \cdot 10^{14}$ photons cm^{-2} which corresponds to approximately $2.4 \cdot 10^{8}$ Rad(SiO_2) at 10eV

[Since the magnitude of the positive charging varies directly with the number of electron-hole pairs produced, the photon dose is more meaningful than Rads as a measure of the incident radiation]
(After POWELL and DERBENWICK, Reference 203)

shifted to more negative gate bias regimes corresponding to the creation of positive charge in the oxide, as predicted in the model proposed by Zaininger. The shift is a strong function of photon energy, varying from essentially zero to 8.4eV to over 30V for a 10.2eV photon exposure. The charging threshold is approximately 8.8eV, very nearly the bandgap of SiO_2.

When negative gate biases were applied, it was found no nett charge was produced. This is interpreted as follows: consider first the application of positive gate bias and large (>10eV) photon energies; there are two processes which occur, electron-hole pair production in the oxide near the gate and hole injection from the Al gate into the oxide. Hole injection from the Al makes a minor contribution because no light reaches the silicon at the higher photon energies (however, according to OLDHAM[204], the accumulation of a large positive oxide charge could result in a sufficient field at the Si-SiO_2 interface to produce significant electron tunnelling from the Si into the SiO_2, which is one mechanism which may limit oxide charge accumulation at large doses and is believed to be responsible for at least part of some small relaxation effects observed following irradiation). The applied field rapidly sweeps electrons to the gate thereby avoiding significant recombination. There is neglible electron trapping in the oxide[204] because electron trapping is a very ineffecient process and most of the holes arriving at the Si-SiO_2 interface become trapped there. Thus, every photon which creates an electron-hole pair contributes a potential positive oxide charge.

For irradiation under negative gate bias, only pair production in the oxide near the gate and electron injection fom the gate can occur. There can be very little (or no) oxide charging because holes will move toward the Al gate and, if trapped, can be annihilated by electrons injected from the gate. (At lower photon energies, some positive oxide charging might occur because electron-hole pairs are created near the Si-SiO_2 interface and hole injection from the Si may become significant as more photons reach the silicon).

Many workers have investigated RIOC effects due to other radiations such as alpha-particles and protons and found that similar mechanisms to that described above for photons occur for each radiation field investigated: BOESCH and TAYLOR[205] have recently reported that high energy ionizing radiations (Co^{60} gamma-rays and LINAC electron beams) used to irradiate a variety of MOSCs produced positive charge in the oxide such that one electron-hole pair is produced for

each 18eV absorbed in the oxide. This yield has been found to be dependent on the internal electric field in the oxide, which corroborates the work of AUSMAN and MCLEAN[206].

For high linear energy transfer (LET) radiations, such as alpha-particles, the Al gate electrodes used by OLDHAM and MCGARRITY[207] were thin enough (105nm) that the energy lost by the charged particles will be almost neglible (a 2MeV alpha-particle passing through the 105nm of Al would lose slightly less than 0.04MeV[208] and for 700KeV protons, the energy lost in this thickness gate electrode is even less, 0.005 MeV) and so all radiation effects are, approximately, due to the oxide only. The RIOC produced by 2MeV particles has been found to produce a flatband voltage shift of approximately -6mVper 3.8K Rad(SiO_2) at an applied field of +1MVcm^{-1} applied to the gate in 35nm thick oxide Al-SiO_2-Si MOSCs with thin (105nm) gate electrodes; the voltage shift increasing linearly with dose and oxide thickness.

For proton irradiations on similar devices under the same electrical conditions the voltage shift was seen to be much smaller, approximately +3mVper 0.54 KRad(SiO_2). OLDHAM and MCGARRITY[207] ascribe this voltage shift as purely radiation induced positive oxide charge by the mechanism described for photons and not due to interface state generation. KNOLL, BRAUNIG and FAHRNER[193] have produced similar results, conluding that any injected electrons produced in the oxide layer by irradiation of the silicon substrate (whilst the device is under positive bias) need to gain sufficient KE in the high field across the insulator to generate electron-hole pairs by impact-ionization; thus, high-energy high-LET particles produce a smaller RIOC than do low-energy high-LET particles because of recombination effects in the oxide near the Si-SiO_2 interface where interface traps may be generated by the radiation.

Very little work has been reported for RIOC by neutrons via displacement damage and intermediate ionizations in the oxide layer. The majority of the work published is based on interface state generation and neutron effects in the silicon substate producing oxide charge rather than induced oxide charge by effects in the oxide. However, SROUR et al[209] have produced a further model for radiation interaction with MOSCs; it is an analysis of the radiation effects of neutrons on the depletion region in MOSCs producing a build-up of positive charge. The model is based upon data from an investigation of the degradation of the generation lifetime (a characteristic time associated with the thermal generation of carriers in the depletion region of MOSCs) due to the introduction of

jeneration centres in the depletion region bulk by neutron irradiation. MCLEAN[210] has noted, lowever, that this model is based upon results of a study which used a radiation source with a :oncomitant gamma-radiation incident on the MOSCs under test, which could be the primary effect producing the observed positive oxide charge build-up, rather than the neutron irradiation on which the model is based.

There is little evidence to suggest that neutrons produce an intrinsic build-up of positive oxide charge and the evidence produced in favour of this is, in this authors opinion, more likely due to effects in the silicon substrate than in the oxide layer.

4.3 Radiation Induced Interface States (RIIS)

Although ionizing radiation does not create energy levels (traps) in the oxide, it does generate interface trap levels within the silicon bandgap of MOS devices; such traps are similar to the intrinsic hole traps which occur at the Si-SiO_2 interface, as discussed in section **2.5.2.**

Much experimentation has been carried out in order to identify the nature of radiation induced interface traps and, despite a wealth of evidence to suggest mechanisms for RIIS generation, no firm conclusions have yet been reached or may be drawn from the data.

4.3.1 Evidence for RIIS Generation

The principal evidence for the generation of interface trap levels is the radiation-induced distortion of C-V and I-V curves of MOSCs (and other MOS devices) as shown in Figure 63 for a typical silicon-based MOSC after Co^{60} irradiation. However, as discussed in section **2.5.2**, gross charge non-uniformities and intrinsic interface traps can produce similar distortions in the C-V and I-V curves of MOSCs. To distinguish between these two sources of distortion, one procedure is to measure (indirectly) the surface recombination-velocity in the device.

If interface traps are produced uniformly across the interface, then, according to WINOKUR et al[211], the surface recombination velocity is proportional to the interface trap level density and the square root of the product of the hole and electron capture cross sections. These parameters can be measured independently using the conductance method (described in detail in the text by

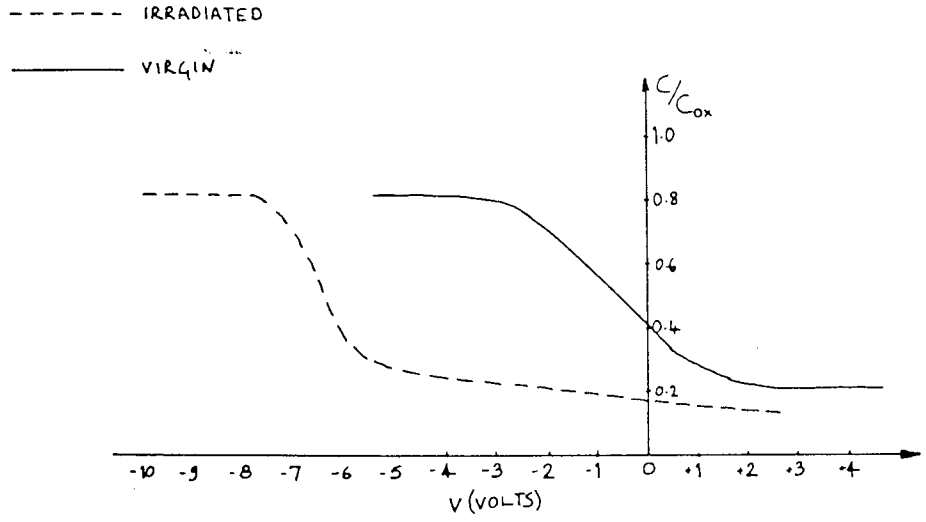

Figure 63: (a) Distortion of the C-V curve for a <100> p-type Al-SiO_2-Si MOSC with a thermally grown 91nm oxide layer after irradiation under positive gate bias of 5V to a total Co^{60} gamma radiation dose of 2.5MRad(SiO_2).
(After WINOKUR et al, Reference 211)

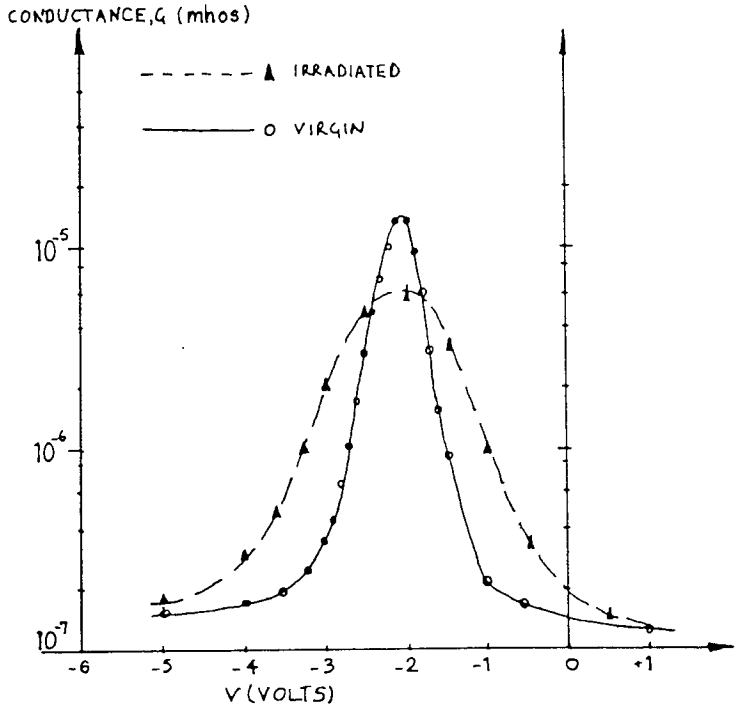

Figure 63: (b) Distortion of the G-V curve for the same device and radiation, bias parameters as in Figure 63(a).
(After WINOKUR et al, Reference 211)

NICOLLIAN and BREWS[16]) to ensure that the interface traps are produced by the radiation. To measure surface recombination velocity, S_0, a small reverse bias, V_r, is applied (V_r =0.3V is not atypical) to the gate electrode of the MOSC and the reverse current is measured as a function of the gate bias; a peak occurs in the I-V characteristic when the silicon surface under the oxide is depleted because depletion allows current to be generated through interface trap levels near midgap. The current peak is due to the surface component of the generation current, $I_{gen\ s}$, and is related to S_0 by

$$I_{gen\ s} = q\, n_i\, S_0\, A_g \qquad -79$$

where A_g is the gate area[211].

Figure 64 shows S_0 as a function of Co^{60} gamma-radiation dose for an MOSC exposed with V_g=0. The value of S_0 prior to irradiation was 5 cm sec^{-1}; this illustrates that S_0 increases with dose and finally saturates for doses above 100MRads(SiO_2). The increases in S_0 takes place over the same dose range as the distortion of the C-V and I-V curves, and this suggests that S_0 increases because of radiation induced interface states (traps) increasing D_{it}.

WINOKUR et al[211] have concluded that, for such Co^{60} irradiations, D_{it} is uniformly distributed in energy near the centre of the bandgap and, therefore, S_0 and D_{it} are related thus

$$S_0 = {}^1/_2\, \bar{v}\, \pi\, kT\, Dit\ \sqrt{(s_n\, s_p)} \qquad -80$$

where s_n and s_p are the electron and hole capture cross-sections, respectively; v is the thermal velocity, assumed to be the same for electrons and holes; and T is the absolute temperature.

An order of magnitude estimate for the product $s_n\, s_p$ for RIIS can be found from Equation **80** using measurements obtained from the MOSC and D_{it} from conductance measurements; this leads to $\sqrt{s_n\, s_p}$ of the order of 10^{-16} to10^{-15} cm^2, which is in good agreement with the data obtained directly from conductance measurements of interface traps on the same dry thermal oxide after irradiation[211]. Conductance measurements can also be used to demonstrate that s_n and s_p are

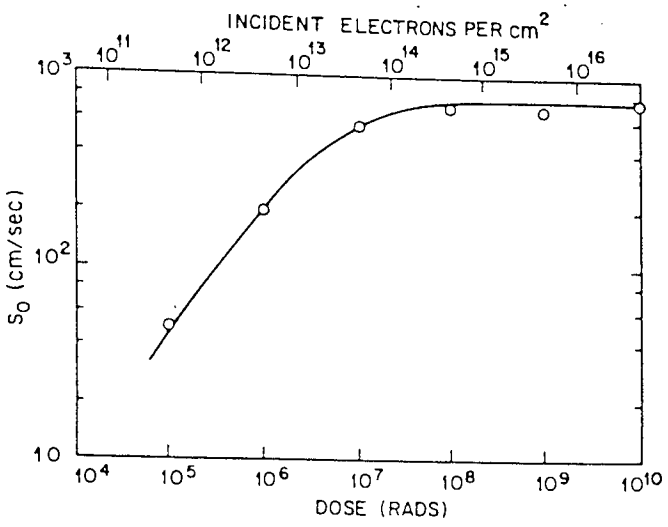

Figure 64: The surface recombination velocity, S_0, of a depleted silicon surface as a function of radiation dose for a (100) p-type Al-SiO_2-Si MOSC with a thermally grown 91nm oxide layer; the pre-irradiation value for S_0 was ≈5cm s^{-1}.
(After WINOKUR et al, Reference 211)

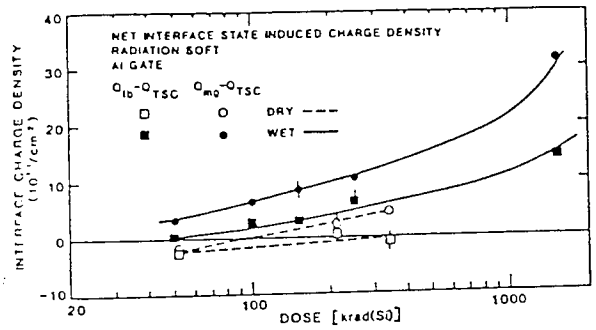

Figure 65: A plot of the interface charge densityversus total Co^{60} gamma irradiation dose for a <100> p-type 0.8-1.2 Ωcm silicon-based Al-SiO_2-Si MOSC with a 115nm oxide layer; the dashed curves refer to dry thermally grown oxide devices, the full curves refer to wet thermally grown oxide devices.
(After SHANFIELD, Reference 220)

invariant with irradiation and consequently the increase in S_0 with dose shown in Figure 64 is, according to Equation **80**, due to an increase in D_{it} with dose. Thus, ionizing radiation generates interface traps (states), and increases D_{it} with increasing dose, in MOSCs.

Many workers have reported the buildup of interface states in MOSCs due to ionizing radiation effects; in general, the data published provides near-conclusive evidence for ionizing radiation induced interface trap generation such that the increase in D_{it} with dose is near-linear for negatively biased devices under irradiation (see, for examples, the recent experimental data in References 212-219). SHANFIELD[220], however, reports that gamma-radiation generates interface states which trap holes and produce results, similar to those presented in Figure 65 where a definite increase in interface states can be seen over a large dose range, with a $(dose)^{2/3}$ dependence on production of interface states. KNOLL et al[219] have produced data which affirms this for Al-SiO_2-Si MOSCs, and is reproduced in Figure 66 where the growth of D_{it} can be seen to be linear in only the dose in low KRad(SiO_2) dose range; there is no evidence to suggest that different ionizing radiations should produce anything other than a linear dependence of D_{it} with low dose, although the relative effectiveness of generation of interface states is in agreement with the correlation between radiation damage in MOSCs discussed in section **4.2.5**. The more heavily-ionizing radiations (for example, alpha-particles) produce more interface states with the same dose than less-ionizing radiations (for example, gamma-radiation)[214-215].

This dose dependence of interface trap buildup is well-recognised and, in recent years, a great deal of empirical information concerning this dependence has been obtained; also the dependence of this buildup with time, oxide field and bias polarity has been reported[211-212,223]. It has been shown that interface trap buildup can occur in MOSCs only if a positive bias is maintained on the gate during the entire buildup process during and after irradiation[224]; thus, the buildup has been shown to be strongly time dependent. Interface trap buildup has also been shown to be temperature dependent[212,215]; D_{it} decreasing with increasing temperature during (or after) irradiation due to an annealing effect.

Evidence exists to suggest that the buildup of interface states is a two-stage process dependent on field-induced ion release in the bulk oxide of MOSCs under bias and irradiation[223]. This forms

the basis of an empirical model which has been proposed by MCLEAN[223], discussed in section 2.2.3 and will not be dwelled upon here.

Evidence that non-directly ionizing radiation, such as neutron radiation, produces interface states has been produced by SROUR et al[209]; however, this evidence is based on purely the changes in the surface-recombination velocity of silicon-based MOSCs when exposed to reactor neutrons. In this authors view, no firm conclusion can be drawn from these data since, almost certainly, there would have been concomitant gamma-radiation with the reactor neutrons and also no evidence has been produced to show the (expected) C-V and I-V curve distortion for the devices; a variety of extraneous effects may, therefore, be responsible. WINOKUR and BOESCH[212] have performed experiments using similar MOSCs to those of SROUR et al[209]and found no shift or increase in distortion of the C-V curves for the devices after reactor neutron irradiation, as may be expected if these neutrons were producing large numbers of interface states; the increase in surface recombination velocity with neutron irradiation has been ascribed to neutron induced damage in the silicon depletion region and not due to an increase in interface states at the Si-SiO_2 interface.

4.3.2 Annealing Effects

The increase in surface recombination velocity and density of interface traps in MOSCs exposed to ionizing radiation can be thermally annealed in the same temperature range as discussed previously for oxide charge[212,215]. Annealing curves for Al-SiO_2-Si MOSCs are presented[215] in Figure 67; the devices were irradiated at zero gate bias to a total absorbed dose of approximately 10^9Rad(SiO2) of 20KeV electrons; the devices were heated from room temperature in 25°C steps to the final testing temperature for 5 minutes at each temperature increment. Figure 67 shows that some annealing took place over the entire temperature range and that the MOSCs were completely annealed at 300°C. Because S_0 is proportional to D_{it} one can see that Figure 67 indicates an annealing (reduction) of radiation induced interface states in the device.

Several other workers have demonstrated similar annealing effects in Al-SiO_2-Si MOSCs (for examples, see References 216-222) and report that, in a similar fashion to that for RIOC, radiation induced interface states produced by ionizing radiation can be annealed[216] from such a device at

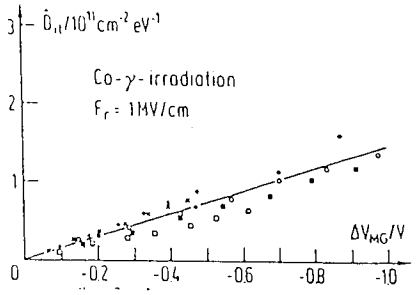

Figure 66: A plot of the generation of interface state density, D_{it}, versus Co^{60} gamma irradiation dose for several <111> n-type 4.1-7 Ωcm silicon-based Al-SiO_2-Si MOSCs with 115nm oxide layers; the devices were biased such that the oxide field was $1MVcm^{-1}$.
(After KNOLL et al, Reference 219)

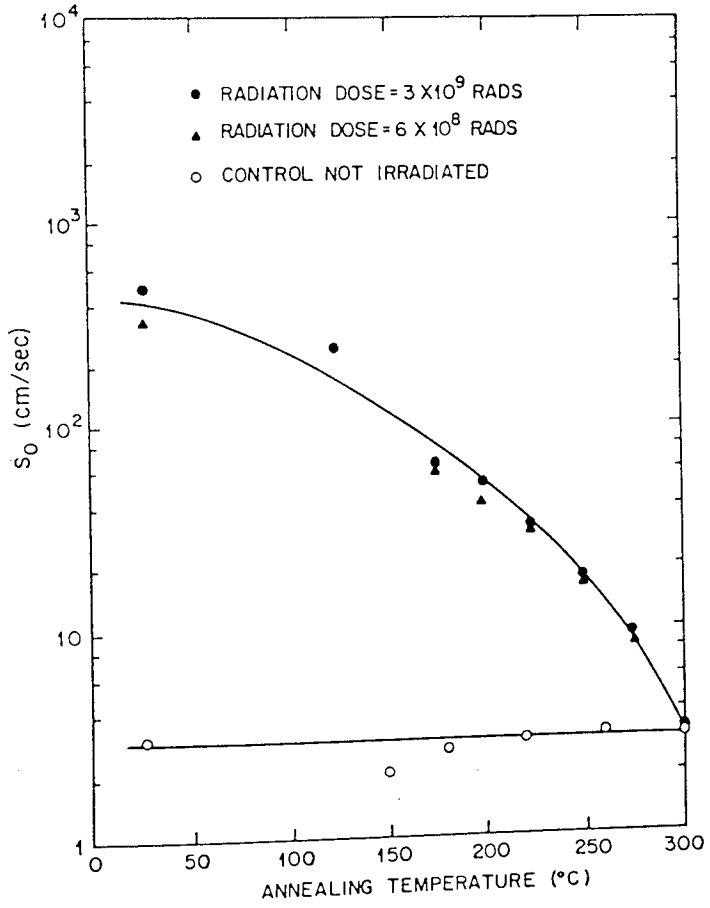

Figure 67: The surface recombination velocity, S_0, of an electron irradiated oxide as a function of the post-irradiation annealing temperature; the devices were <100> n-type silicon-based Al-SiO_2-Si MOSCs with 200nm dry thermally grown oxide layers. The irradiated MOSCs were annealed for 5min at each temperature, with the temperature increased in 25°C increments. The doses shown on the diagram, and a control (unirradiated) device curve is shown for comparison.
(After WINOKUR, Reference 215)

temperatures above 290°C. These workers show that there is some evidence to suggest that room temperature annealing over long (hundreds of hours) time periods is the case for the observed gradual relaxation of RIIS in MOSCs, as reported by STASSINOPOULOS[222] and shown in Figure 68 for post-irradiation room (20°C) temperature annealing of MOSCs exposed to a mixed electron, proton and gamma-radiation radiation field.

4.3.3 Empirical Models for RIIS Generation

Evidence that the buildup of interface states in irradiated MOSCs is a complex time-dependent two-stage process has been presented by many workers[220-224]: the first stage, which occurs during the time («1s) required for radiation-generated holes to travel to the Si-SiO_2 interface under positive bias, determines the final (or saturation) value of D_{it} and has been found to be field dependent and temperature independent; this stage depends critically on some interaction of the holes as they traverse the oxide layer: the second stage, which begins after the holes have reached the interface and, at room temperature, continues for thousands (or even tens of thousands) of seconds, determines the time scale for the buildup and has found to be both field and temperature dependent. According to WINOKUR[225], the buildup is observed only if a positive (or zero) bias is maintained on the gate during the entire buildup process. Switching to negative bias after the first (transport) stage inhibits further interface state generation, and if the bias is switched negative for some period of time and then back to positive, D_{it} is reduced to below the value obtained if a positive bias is maintained throughout the buildup process.

The bulk of the evidence presented by workers has been summarised by WINOKUR[225]and has lead to the proposal that two key factors in RIIS generation are:

(1) the existence of the interaction between radiation-generated holes in the bulk oxide layer

and (2) the role of water-related species and defects in the oxide.

Two models have been propósed which include these proposed factors: SAH[226] has proposed

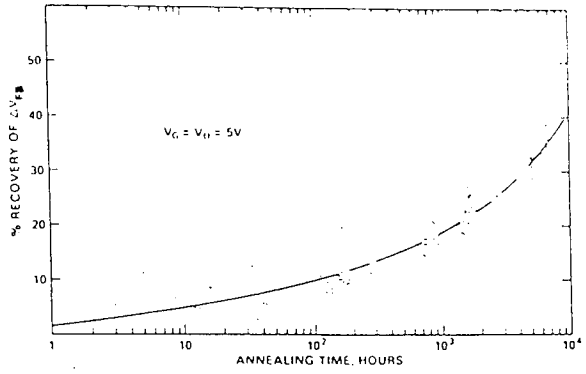

Figure 68: A plot of the percentage recovery of <100> n-type silicon-based Al-SiO_2-Si MOSCs with 162nm oxide layers after combinations of electron, proton and gamma irradiation; the gate electrode was biased to +5V with respect to the silicon substrate. The percentage recovery is measured as a function of percentage recovery of flatband voltage measured from the change in distortion of the C-V curve for the irradiated devices compared with the annealed devices.
(After STASSINOPOLOUS, Reference 222)

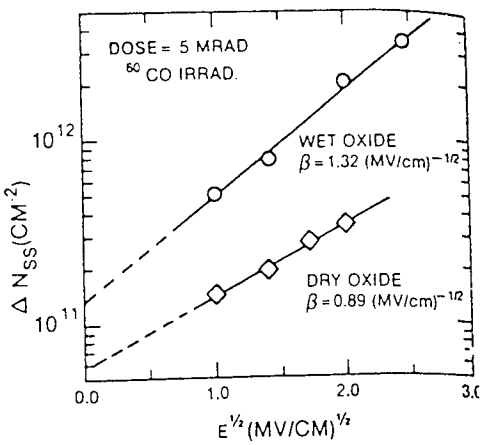

Figure 69: The field dependence of the final interface state density, N_{SS}, for two oxides, one wet the other dry grown, after a total dose of 5MRad(SiO_2) Co^{60} gamma radiation. In both cases, the data has been adjusted to account for the field dependent yield of holes.
(After McLEAN, Reference 223)

that the holes when under a positive gate bias interact in the interface region to break weak Si-OH bonds, freeing OH^- radicals to drift toward the gate, leaving dangling Si bonds which result in interface states. However, the two-stage nature of the buildup cannot be understood with this model, especially the long-term generation process continuing long after the hole transport is complete. SVENSSON[227] has postulated a possible two-stage process, based on the previous work of REVESZ[228], in which transporting holes break Si- H bonds in the bulk of the oxide layer, leading to positively charged trivalent-Si centres in the bulk and neutral interstitial hydrogen atoms which are free to diffuse throughout the oxide; the atomic hydrogen which diffuses to the interface reacts with Si- H bonds in the interfacial region to form molecular hydrogen and to leave dangling silicon bonds, which, as in the SAH model, results in the creation of interface states.This model involves a two-stage process as required by the experimental evidence but, however, fails to explain the field and polarity dependencies of the second stage. In particular, it fails to explain how the field during the second stage affects the timescale for buildup and how reversing the bias polarity inhibits interface generation. SHINO et al[229] have recently suggested that, since interface traps appear to be generated under a positive oxide field, breaking the Si-OH bonds at the Si-SiO_2 interface, enhanced by hole capturing, is the dominant generation mechanism.

MCLEAN[223] has compiled the experimental evidence supporting a two-stage process, together with the proposed mechanisms for RIIS generation, into an empirical model of the two-stage process which gives the mathematical dependencies on time, field, temperature and radiation dose. It is, by far, the most succinct model which exists to date which explains RIIS generation.

The two-stage character of the buildup process can, according to MCLEAN[223], be expressed as

$$\Delta N_{SS}(t) = N_{SS}^{\infty}[E_1,D]\, f\{t/T\} \qquad -81$$

where the change of interface state density as a function of time, $\Delta N_{SS}(t)$, is written as the product of two expressions: the saturated values of D_{it} at long time, N_{SS}^{∞}: and a time dependent function, $f\{t/T\}$, which approaches unity at very long times. The densities $\Delta N_{SS}(t)$ and N_{SS}^{∞} in Equation **81** represent integrated values of the interface state distributions over a selected energy interval in the Si bandgap. The saturation value, N_{SS}^{∞} is determined soley by the first stage of the process, during

the time that the holes move through the oxide film, and is a function of irradiation dose, D, and field applied during the first stage, E1, but is independent of temperature. The time dependence of the buildup is the timescale T $[T,E_2]$, which depends on the temperature, T, and the field applied during the second (long-term buildup) stage, E_2, and not on the field or temperature during the first stage.

The explicit dose and field dependence of the "first stage function", N_{SS}^{∞}, is given by

$$N_{SS}^{\infty}[E_1,D] = A_g D^{2/3} e^{(\beta \sqrt{E_1})} \qquad -82$$

The functional dependencies are the same in wet and dry grown oxides, although the numerical constants vary between the oxides[225].The rather unexpected two-thirds power law dependence on dose has been observed to apply to a number of aluminium-gated silicon-based MOSCs with different oxides over a range of doses with no apparent saturation[225].

This dependence has not been fully verified and its origins are uncertain, but MCLEAN includes it in his empirical model[223]. The exponential dependence of N_{SS}^{∞} on $\sqrt{E}$ is evident from the semilog plot of N_{SS}^{∞} versus $\sqrt{E}$ shown in Figure 69 for wet and dry grown SiO_2-on-Si after total dose exposure of 5MRad(SiO_2) Co^{60} irradiations.

Although for a fixed dose N_{SS}^{∞} is determined by the field during the first stage, $N_{SS}(t)$ does not achieve the saturation value until very long times after irradiation. At room temperature and for positive bias, the interface states begin to manifest typically in the range from 0.1 to 1.0s after the initiation of irradiation and continue increasing in approximately a logarithmic fashion until saturation occurs at thousands to tens-of-thousands of seconds. Hence, according to Mclean, for positive bias the second stage time-dependent function can be expressed as

$$f\{t/T\} = b \ln(1 + t/T) \qquad (V_g>0) \qquad -83$$

fot t less than a time t_s at which saturation occurs. The factor b is chosen such that $f\{t/T\}$ ->unity

as t -> t_s, that is, $b = [\ln(1 + t/T)]^{-1}$.

For negative bias

$$f\{t/T\} = 0 \qquad (V_g<0) \qquad -84$$

The important quantity associated with the second stage appears to be the timescale T for the buildup which has been found to be both temperature and field activated. McLEAN describes this by

the expression

$$T = T_0 \, e^{[(\Delta / kT) - aE_2)]} \qquad -85$$

where Δ is an activation energy and a and T_0 are constants. This has been found to be the case by WINOKUR et al[211].

Consider an analysis of the time dependent data as a function of temperature and field in the oxide; McLEAN takes the time at which half of the final (saturated) interface state density is reached, $T_{0.5}$. In Figure 70 a plot of $\log T_{0.5}$ versus reciprocal temperature (an Arrhenius plot) over the temperature range 273 to 324°K for an Al-SiO_2-Si MOSC at a constant applied field is shown. From the gradient of the straight line estimate to fit the data the activation energy for trap generation is 0.82eV. In Figure 71, $\log T_{0.5}$ is plotted versus applied field (of 2 to 6 $MVcm^{-1}$) at room (20°C) temperature; the exponential dependence of $T_{0.5}$ is evident, and a value of the constant a in Equation 76 of a = 0.51$MVcm^{-1}$is easily obtained. Finally, using the room temperature value of $T_{0.5}$ together with the estimated value of the activation energy the pre-exponential factor T_0 associated with the half-buildup time can be seen to be $T_0 \approx 2*10^{-13}$ seconds. This is well in agreement with the experimental data presented by WINOKUR et al[211]and gives great credence to the empirical model.

It is evident from the empirical model of the interface state buildup that extremely complex microscopic mechanisms must be involved in the process; these are considered beyond the scope of this thesis and the reader is refferred to the work of MCLEAN[223] for further discussion of these.

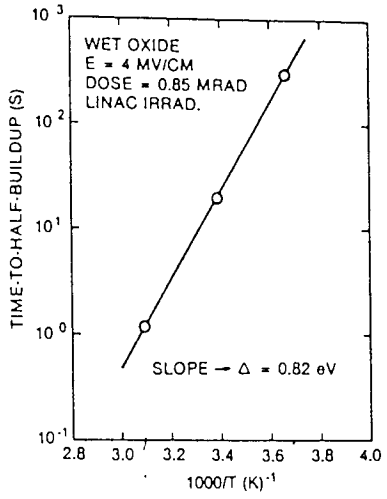

Figure 70: A second-stage activation energy analysis for a wet grown oxide in an Al-SiO_2-Si MOSC after a total dose of 0.8MRad(SiO_2) from a LINAC; the plot shows the $\log_{10}$time at which half the saturated interface state density is achieved versus the reciprocal temperature.
(After McLEAN, Reference 223)

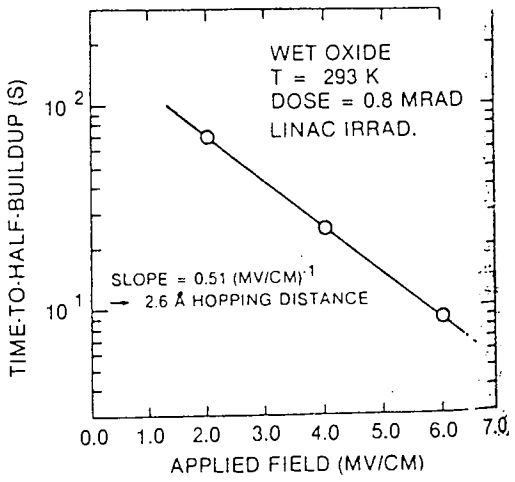

Figure 71: A plot showing the effect of field on the buildup time of surface states; the data is plotted to show the $\log_{10}$time at which half the saturated interface state density is achieved versus the applied field for a wet grown oxide in an Al-SiO_2-Si MOSC.
(After McLEAN, Reference 223)

4.3.4 Implications of the Empirical Model

Considering the field dependence of the first stage, that is, of the saturated interface density shown in Figures 69 and 70: the exponential dependence on the square root of the field is the fingerprint of charge ejection over a field-reduced Coulombic barrier ($^1/_r$ potential) or Schottky effect. This would suggest some interaction of the radiation generated holes in which an ionic charge is released. The fact that the first stage is temperature independent suggests that the thermal energy is not significant to the process and that, essentially, all the energy for any bond-breaking and ion release is derived from the transporting holes.

One possibility for this process is a mechanism in which a hole makes a transition to a localised trap site adjacent to (or involving) a weakly bound ion impurity where the initial overall charge state of the impurity is neutral. Considering the work of MCLEAN et al[197], HUGHES[230], CURTIS et al[201] and BOESCH et al[205] on hole transport in SiO_2, a broad distribution of energies in the range 0.5 to 1.0eV is expected to be deposited locally whenever a hole undergoes a trapping event (or , according to TZOU et al[213], a polaron hopping transition); the ion is then liberated by a sudden localised energy excitation. If the released ion has positive charge then the interaction probably involves a charge transfer process in which the hole is annihilated by an electron initially involved in bonding the ion, and the positive charge is carried by the ion. The defect remains in a neutral charge state.

Based on the observation that positive bias must be applied to the oxide in order for interface state buildup to occur[224] , one might associate the first stage with an interaction of the hole-flux at the Si-SiO_2 interface rather than in the SiO_2 bulk. However, field switching experiments performed by BOESCH et al[205] indicate that this is not the case.

Table 5 summarises the reported effects of gate bias polarities during the first and second stages of interface trap buildup for Al-SiO_2-Si MOSCs during and after Co^{60} gamma-irradiation. For the case where a negative gate bias was applied to the gate during the hole transport (first) stage, but then the polarity was switched positive at approximately 1 second and maintained until approximately 10^4 seconds after irradiation, the observed result has been shown to be a buildup of N_{ss} comparable to that for the case where the gate bias is maintained positive throughout. Since in the case of negative polarity during the hole transport phase,essentially, all the holes are removed at the gate,

these reults imply that the first stage interaction occurs in the bulk of the oxide layer.

Gate Polarities		
1st Stage 0 -1 seconds	2nd Stage 10-10^4 seconds	N_{SS} Buildup
POSITIVE	POSITIVE	YES
NEGATIVE	NEGATIVE	NO
POSITIVE	NEGATIVE	NO
NEGATIVE	POSITIVE	YES

Table 5. The Effect of Gate Bias on N_{SS} in Al-SiO_2-Si MOSCs during and after Co^{60} Irradiation (After BOESCH et al[205]).

For the case where a negative gate bias was applied to the gate during the hole transport (first) stage, but then the polarity was switched positive at approximately 1 second and maintained until approximately 10^4 seconds after irradiation, the observed result has been shown to be a buildup of N_{SS} comparable to that for the case where the gate bias is maintained positive throughout. Since in the case of negative polarity during the hole transport phase,essentially, all the holes are removed at the gate, these reults imply that the first stage interaction occurs in the bulk of the oxide layer. Also, the final number of interface states is directly related to the number of ions released during the first stage, and this number is determined by the magnitude of the applied field, but not its polarity, during the hole transport process.

With the first stage process apparently that of ion release in the bulk oxide, the interpretation of the second stage (long-time) buildup could be that of a field-assisted ionic transport to the Si-SiO_2 interface, with a subsequent interaction of ions at the interface producing the observed interface states.

From Table 5 it can be seen that the important polarity condition for N_{SS} buildup is positive gate bias during the second, long-term, buildup stage. This then implies a positively charged ion species

which would drift toward th Si-SiO_2 interface under positive bias; it is reasonable to assume that the ion is H^+, since hydrogen is expected to be relatively mobile in SiO_2 at room temperature and since, according to WINOKUR and BOESCH[225], the difference between the buildup of N_{ss} in wet and dry grown oxides appears to be only one of magnitude.

To summarise, a great deal of the empirical information obtained from the electrical measurements of RIIS can be understood simply on the basis of a positive ion release in the bulk SiO_2 layer by hole transport and the subsequent field induced drift of the ions to the Si-SiO_2 interface, as described by MCLEAN'S two-stage empirical model of interface state buildup[223]. This agrees well with the essenceof the model proposed by SVENSSON[227]with the modification that, perhaps, hydrogen ions instead of neutral atomic hydrogen are released and diffuse in the bulk SiO_2 layer.

4.4 Radiation Induced Dielectric Breakdown (RIDB)

Radiation induced dielectric breakdown (RIDB) in MOSCs was first reported by TOMMASINO, KLEIN and SOLOMON[13] in 1974; in their studies of fission-fragment induced breakdown in Al-SiO_2-Si MOSCs the possibility of using this style of device as a research tool was mooted. Since then, several workers have verified the initial findings and used MOSCs for fission-fragment dosimetry. However, investigations of the breakdown response of MOSCs to other radiations has been limited to alpha-particles, heavy ions and LINAC pulsed radiations; little, if any, work has been reported on the breakdown response of MOSCs under neutron, proton, gamma and electron irradiation.

RIDB differs from intrinsic breakdowns and defect-related breakdowns both in the posiible mechanisms causing the breakdowns and the field at which it occurs. The breakdown field of devices under fission-fragment irradiation has been found to be markedly lower than that for intrinsic or defect-related breakdown.

In this section, evidence of RIDB is presented; various models (and mechanisms) proposed to describe the RIDB process are reviewed and compared with recent experimental observations made on Al-SiO_2-Si MOSCs in various radiation fields.

4.4.1 Evidence for RIDB

In a series of papers[13,231-234], KLEIN, TOMMASINO and SOLOMON have presented evidence to show that, when exposed to Cf^{252} fission-fragments, Al-SiO_2-Si MOSCs with thin gate electrodes exhibit dielectric breakdown at a lower applied voltage than the intrinsic breakdown (or defect-related breakdown) voltage for the same device. The breakdowns have been shown to be non-shorting if a thin (<50nm) Al gate electrode is used and the number of breakdowns correlate with the approximate number of fission-fragment incident on the MOSC gate electrode. Figure 72 shows typical breakdown data for the rate of breakdowns in an Al-SiO_2-Si MOSC with 115nm dry-grown SiO_2 on a <100> p-type Si substrate; the Al gate electrode is 30nm thick and negatively biased with respect to an Ohmic contact on the underside of the silicon substrate.

As can be seen from Figure 72, the breakdown voltage for the device when exposed in vacuum to a Cf^{252} source is markedly lower than that due to the applied field only. In this instance, no investigation was made as to whether this was due to the fission-fragment inducing breakdown, or the concomitant alpha-particles and neutrons from the Cf^{252} source used. In a later work[233] the relationship between the number of fission-fragment crossing the gate electrode and the number of breakdowns has been investigated; this data is represented in Figure73. As can be clearly seen there is a very strong correlation between breakdown counts and number of incident fission-fragments.

TOMMASINO et al[233] have also investigated the effect of alpha-particles (from an Am^{241} source) on similar Al-SiO_2-Si MOSCs and found no evidence of induced breakdown. From these results it has been concluded that alpha-particles could not induce breakdown.

The size and shape of the breakdown pits in many devices have been analysed and found to be indistinguishable from those due to intrinsic and defect-related breakdowns; typically the breakdown spots are of the order of 4 to 6μm across and approximately circular, as shown in Figure 74.

Initial proposals of mechanisms for such radiation-induced breakdown are based on evidence of current pulse production in the devices tested when irradiated with a fission-fragment or alpha-particle source. Charge pulses of approximately 10^{-15}C have been associated with the passage of a fission-fragment through the oxide layer, the mean pulse size increasing with

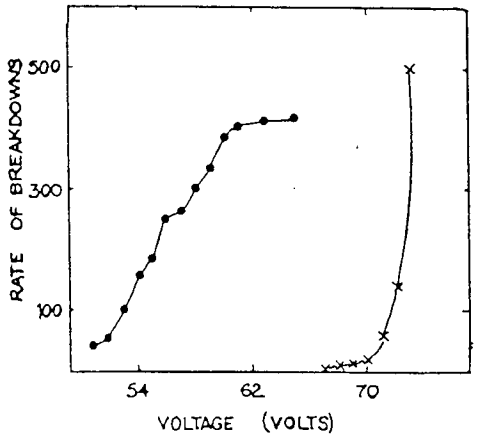

Figure 72: A plot showing the rate of breakdowns per 100s versus the applied gate voltage to a <100> p-type Al-SiO_2-Si MOSC with a 115nm oxide layer. The Al gate was 30nm thick and negatively biased with respect to the silicon substrate; the device area was $8.2*10^{-2}$ cm^{-2}.
Crosses indicate intrinsic (or defect-related) breakdowns due to the applied field only.
Circles indicate breakdowns initiated at a lower field due to fission-fragment irradiation of the device.
(After TOMMASINO et al, Reference 13)

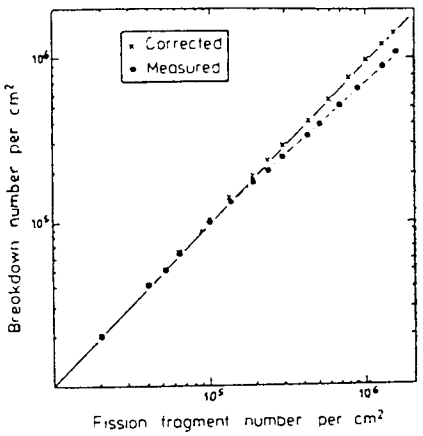

Figure 73: The relationship between the number of breakdown counts and the number of fission-fragments impinging on a <100> p-type Al-SiO_2-Si MOSC with a 38nm dry thermally grown oxide layer. The Al gate was 15nm thick and negatively biased with respect to the silicon substrate.
(After TOMMASINO, Reference 233)

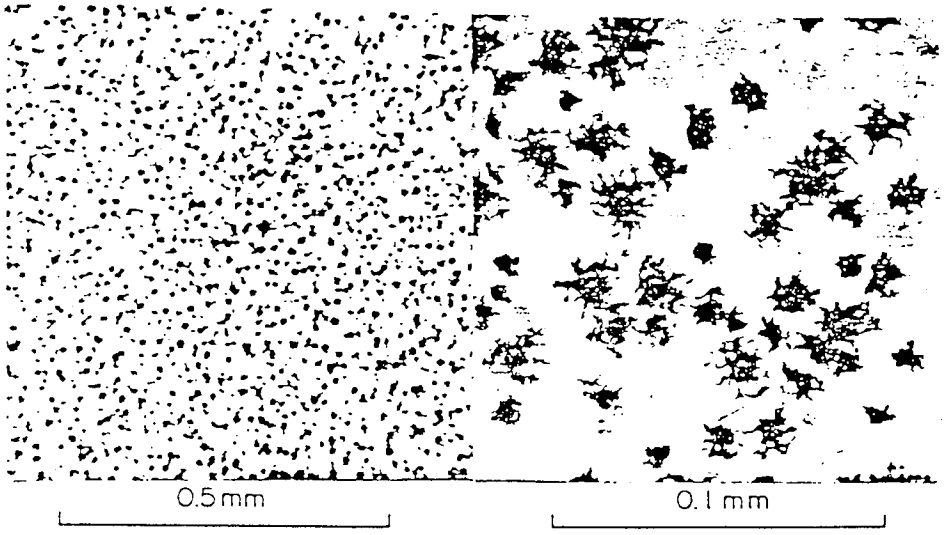

Figure 74: An optical micrograph of sites of fission-fragment induced breakdowns in a <100> p-type Al-SiO_2-Si MOSC shown at two magnifications: the left-hand photograph is taken at a magnification of x140, the right-hand photograph is taken at a magnification of x700.
(After TOMMASINO, Reference 233)

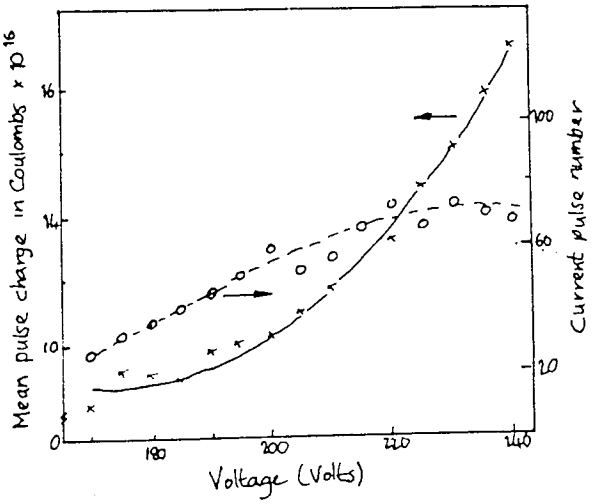

Figure 75: (a) A plot of the mean pulse charge (crosses) and number of current pulses (circles) as a function of the bias voltage applied to a <100> p-type Al-SiO_2-Si MOSC with a 380nm oxide layer and 20nm Al gate electrode; the gate electrode was biased negatively with respect to the silicon substrate.
(After KLEIN, Reference 234)

increasing bias across the MOSC. Figure 75(a) shows a plot of the mean pulse charge (and number of pulses per 100s) as a function of the bias applied across an Al-SiO_2-Si MOSC; a typical pulse from the MOSC under irradiation is shown, together with the pulse detection circuit used, in Figure 75(b). KLEIN, SOLOMON and TOMMASINO[234] have used pulse-height analysis to investigate the distribution of current pulses with channel number using a multichannel analyser connected to the detector circuit shown in Figure 75(b); the spectrum obtained is shown in Figure 76 and consists of two partially overlapping peaks due to light and heavy fission-fragments, respectively[232,234], similar to that obtained with a silicon surface-barrier detector, but with low resolution. KLEIN et al[234] have concluded that breakdown counting and current pulse counting of fission-fragment induced phenomena are valuable techniques but, the signal-to-noise ratio for current pulse counting is too low, the large pulses at high field being most easily detected but often swamped in noise.

SMIRNOV and EISMONT[235] have investigated the effects of heavy ions and alpha-particles on MOSCs with <100> n-type silicon substrates. They have reported similar results to those of TOMMASINO et al for <100> p-type silicon substrate MOSCs. The "counting characteristics" for such an n-type MOSC are shown in Figure 77 and can be seen to be similar to those shown in Figure 72 for p-type MOSC. SMIRNOV and EISMONT report a threshold minimum energy of ion for detection as (18±2)MeV for a mean light ion (or fission-fragment) at a plateau operating voltage of 85V for the device. (This was later modified to a registration ability of the devices to heavy-ions with a stopping power in SiO_2 greater than ((22±2) $MeVmg^{-1}cm^{-2}$). This implies that such devices will not respond by RIDB to alpha-particle or any other radiation which cannot deposit enough (at least (22±2) MeV mg^{-1} cm^{-2}) energy in the oxide layer.

DONICHKIN, SMIRNOV and EISMONT[236] have reported that the energy threshold for registration is larger than ≈15 $MeVmg^{-1}cm^{-2}$ and the registration capacity (that is, the number of radiation induced non-shorting breakdowns the device can sustain before failure) for n-type devices of $\approx 3*10^6$ cm^{-2} and for p-type devices $\approx 10^4$ cm^{-2} is typical; DONICHKIN et al have concluded from their investigations that the breakdown pulse-height distribution is not dependent on the energy and ionizing power of the charged particles incident on MOSCs since these devices, when used in conjunction with a multichannel analyser in a similar fashion to a silicon surface-barrier detector, do not give the energy spectrum of the irradiating source; a later study by GANGRSKII, MILLER and UTENOV[237] has verified these results and draws similar conclusions, with the proposal that

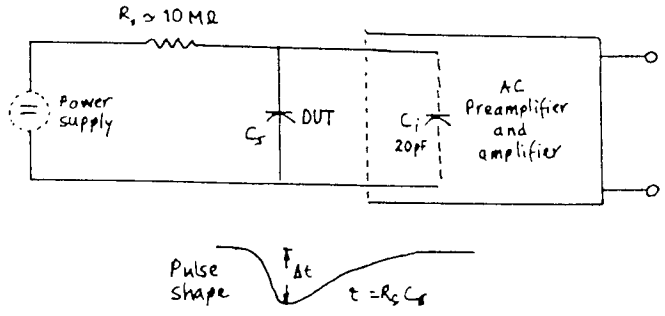

Figure 75:(b) A typical pulse detector circuit used to detect the passage of fission-fragments through the oxide layer of an MOSC; inset is shown a typical output pulse from a MOSC under fission-fragment irradiation using such a circuit.
(After KLEIN, Reference 234)

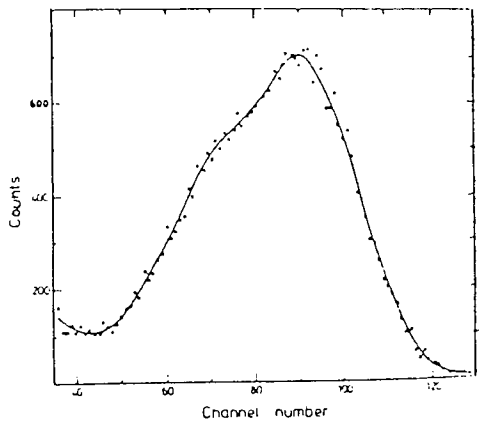

Figure 76: Spectrum of pulse-height distribution versus channel number of a multichannel analyser for amplified current pulses due to fission-fragment radiation effects on the oxide of a <100> p-type Al-SiO_2-Si MOSC with a 380nm oxide layer and 20nm Al gate electrode.
(After KLEIN, Reference 234)

MOSCs be used for detectors in investigations where high time-resolution and high selectivity of recording of fission-fragment is required. GANGRSKII et al report that the time resolution of Al-SiO_2-Si n and p-type MOSCs is not less than 10 $nsecV^{-1}$ for devices working in the plateau operating region for fission-fragment detection described by KLEIN et al[234].They too report no evidence for RIDB by other radiation, only weak current pulses being detected.

SMIRNOV, EISMONT, NOGA and RANJUK[238] report no response of Al-SiO_2-Si n-type MOSCs to pulsed gamma or pulsed electron irradiations. The possibility of application of these MOSCs to the study of electro and photo-fission of heavy nuclides has been proposed, based on SMIRNOVet al's studies of U^{238}, Bi^{209} and Ta^{181} 1.2GeV electron induced fission-fragment irradiation, where from the available data the devices appear transparent to the fission-fragment initiating radiation; this is similar to the proposal of DORSCHEL et al[239] who have investigated the feasibility of using MOSCs combined with a fissile radiator (for example, U^{235}) as neutron detectors , as shown schematically in Figure 78. In the investigations by SMIRNOV et al, no effects were seen when the devices were irradiated (with and without constant gate bias) with the electron beam alone and it has been concluded that even high energy electrons do not induce breakdown in Al-SiO_2-Si MOSCs. (Electrons do, however, induce large (10^{-12}C) current pulses [238]which can be easily detected with the method used by KLEIN et al[234]).

The voltage characteristics of the neutron / fissile-radiator-induced breakdowns are shown in Figure 79 (reproduced from Reference 239) for an Al-SiO_2-Si MOSC with <100> n-type silicon substrate; reactor neutrons were the fission-initiating radiation with flux densities of:$1.6*10^7$ $cm^{-2}s^{-1}$ with energy lower than 0.4eV; $1.5*10^7$ $cm^{-2}s^{-1}$ with energy between 0.4eV and 1MeV; and $2.8*10^6$ $cm^{-2}s^{-1}$ with energy above 1MeV (calibrated using gold activation detectors) to produce threshold-induced fission-fragment which irradiated the device. There is no evidence to suggest that neutrons alone induce breakdowns when the fissile-radiator is removed and this has been confirmed by work presented in the recent review article by SMIRNOV and EISMONT[240].

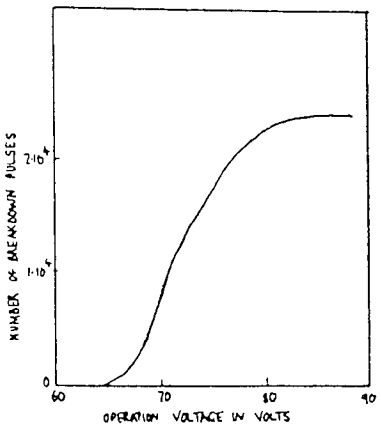

Figure 77: The counting characteristics of a <100> n-type Al-SiO_2-Si MOSC with a dry thermally grown 140nm oxide layer. The Al gate electrode was 50nm thick and biased negatively with respect to the Ohmic contact on the underside of the silicon substrate.
(After SMIRNOV and EISMONT, Reference 235)

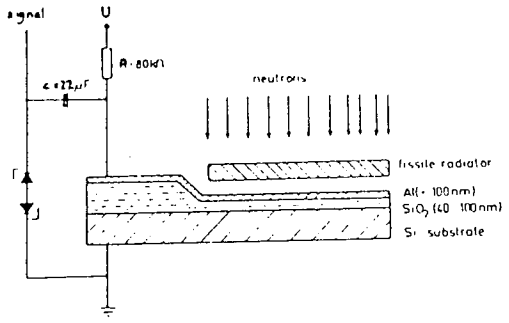

Figure 78: Scheme of the MOSC fission-fragment detector and associated circuitry to detect neutrons via an (n,f) reaction in a fissile radiator placed close to the detector Al gate electrode.
(After DORSCHEL et al, Reference 239)

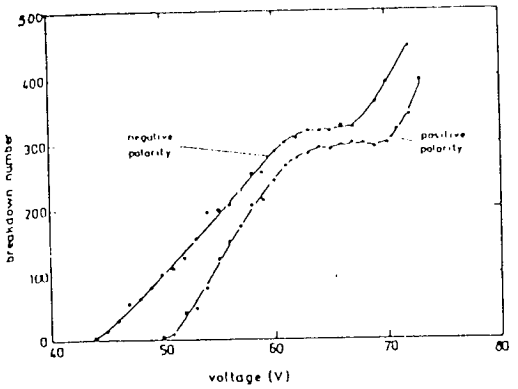

Figure 79: The voltage characteristics of a neutron detector (as shown in Figure 78) using fission-fragments from a fissile radiator to induce non-shorting breakdowns in a <100> n-type Al-SiO_2-Si MOSC with a dry thermally grown 80nm oxide layer; the Al gate electrode was 10nm thick.
The two curves show the breakdown characteristics for negatively and positively biased devices.
(After DORSCHEL et al, Reference 239)

4.4.2 Mechanisms and Models

Breakdown due only to the applied field has been discused in Chapter 3; it has been shown that breakdowns are not thermal in SiO_2 because the leakage currents prior to breakdown are very small and no observable temperature rises occur. The breakdowns appear to be electronic, initiated by a small rate of impact-ionization. The rate of this impact-ionization decreases approximately exponentially with decreasing field, so that no impact ionization is expected to occur below the field range of the breakdown characteristic.

TOMMASINO,KLEIN and SOLOMON[232] have proposed a series of mechanisms which give a simple model of fission-fragment effects in MOSCs under bias: a fission-fragment crossing the oxide layer of the MOSC produces large changes along its track including a thermal spike, large ionization, atomic dislacement damage, possibly nuclear reactions and melting. These are very complex and transient processes which may lower the breakdown voltage in a number of ways. The effect of the thermal pulse (or spike) on breakdown has been treated by KLEIN[167] who has shown that such a pulse can theoretically initiate breakdown; accordingly, a thermal spike initiates breakdown when it increases the local conductivity sufficiently to cause a significant further temperature rise by Joule heating. The field at which thermal breakdown occurs due to a thermal spike can be calculated by stipulating that local current runaway arises before the local temperature spike dissipates by heat transfer. Such a calculation is illustrated for a much-simplified model; the fission-fragment, characterised by a stopping power W in the insulator, is assumed to produce, in the insulator, instantaneously a temperature rise $T_f - T_0$ above the ambient temperature T_0 uniformly in a cylindrical track of cross section A along the track, as illustrated in Figure 80, and is given by

$$T_f - T_0 = W / cA \qquad -86$$

where c is the specific heat per volume of the insulator layer. The temperature rise initiates a significant current in the insulator, the density of which is j_0 at temperature T_f and $j_0 e^{[a(T-T_f)]}$ at higher temperatures T, 'a' being a constant.

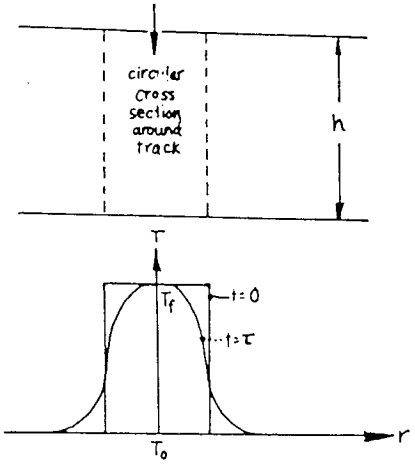

Figure 80: Sketches of the heated cylindrical volume around a fission-fragment track and the temperature distributions at t=o and t=*t*.
(After TOMMASINO et al, Reference 234)

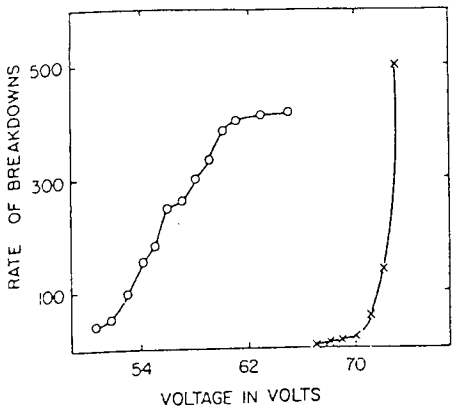

Figure 81: The rate of breakdowns per 100s versus voltage applied to a SiO_2 detector.
Crosses indicate breakdowns due to the applied field.
Circles indicate breakdowns due to the incidence of fission-fragments at a lower field.
(After TOMMASINO et al, Reference 234)

Heat conduction can be neglected when the rate of temperature rise in the small cylinder of insulator is related to the Joule heating by

$$T' c A \frac{dT}{dt} = j_0 e^{[a(T-T_f)]} A F T' \qquad -87$$

where t is the time , F the field in the insulator and T' the insulator thickness.

Integration of Equation **86** shows that the current and temperature runaway, $j \to \infty$ and $T \to \infty$ occur after a time t such that

$$t = c / a F j_0 \qquad -88$$

The current runaway can occur only if t is short enough so that heat transfer from the cylinder during t is negligible. The limit of t has been estimated by KLEIN[122], from data on the heat conduction in cylindrical bodies, to be

$$t \leq A / 60K \qquad -89$$

where K is the thermal diffusivity around the track of the fission-fragment.

Replacing t in Equation **89**; the smallest current density at t=0 required for thermal runaway is

$$j_0 \geq 60cK / a A F \qquad -90$$

Applying these results to an Al-SiO_2-Si MOSC with a 115nm thich oxide layer, using Equations **86** and **89** (and using the general information concerning properties of light and heavy fission-fragments given in Table 6) replacing $W = 10600 eV nm^{-1}$ for a light fission-fragment, $c \approx 25°K^{-1}cm^{-3}$ and $K = 7*10^{-3}\ cm^2 s^{-1}$ one can calculate $T_f - T_0$ and t , given a value for A. The thermal spike affects the track and the surrounding volume where ionization takes place, and there is uncertainty regarding the magnitude of the cross section of the track, A. Estimating a range for A of $3*10^{-13} < A < 3*10^{-11}$ gives $6*10^{-13} < t < 6*10^{-11}$ second and $28300 > (T_f - T_0) > 283°K$.

Fragment Type	*Light*	*Heavy*
Mean energy, Mev	103.8	79.4
Mean mass number	106.0	141.9
Mean charge number	42.5	55.5
Stopping power in Al, $eVnm^{-1}$	11200	11400
Stopping power W in SiO_2, $eVnm^{-1}$	10600	12000

Table 6. Relevant properties of light and heavy fission fragments

To assess the possibility of thermal runaway, the required current density j_0 as a function of A must be compared with the current density arising due to the thermal spike. Little is known about the electrical conduction properties of thermally grown highest-purity silicon dioxide films at high temperatures and high fields. Low field measurements by MILLS and KROGER[241] at 600°C have shown SiO_2 conductivities of up to $10^{-6}\Omega^{-1}cm^{-1}$, indicating both ionic and electronic conduction with an ionic transference number of 0.4. CHOU[242] has observed, at 340°C, electronic currents with an activation energy of 2.5eV, due to thermionic injection from Al gate electrodes. TOMMASINO et al[232] assume that such thermionic injection arises also at high temperatures and have calculated the current density, j_f, due to the thermal spike with

$$j_f = AT_f^2 \, e \, \frac{\{-[E - \sqrt{F}\sqrt{(e^{3/2}/4\pi C_o C)}]\}}{kT_f}$$

$$= AT^2 \, e^{(-B/T_f)} \qquad -91$$

Here A = 120 $A/cm^{-2}\,°K^{-2}$ and E, the activation energy is 2.5eV, $C_o = 8.85 * 10^{-12}$ Farad m^{-1}, and the dielectric constant of SiO_2 is taken to be C=3.8. F has been chosen to be 5.4 $MVcm^{-1}$, since above this field all the fission-fragments in KLEIN'S experiments caused breakdowns, as shown in Figure 81.

In Figure 82, j_f as a function of instantaneous temperature rise $T_f - T_o$ is plotted; $T_f - T_o$ is given by

the upper horizontal scale while the lower scale gives the corresponding cross sections, A, calculated with Equation 75 for mean light fission-fragment. Figure 82 also presents j_o, the current density for thermal runaway, calculated using 89. To find values of the constant a in Equation 89 account is taken of the differences in the conduction relation, given in Equation 86, used in the derivation of Equation 86 and in the relation for thermionic injection. Stipulating that for both relations at the temperature T_f, current densities and their derivatives with respect to temperature are equal, $a = B / T_f^2$ is obtained.

Figure 82 shows that the current densities j_o required for thermal runaway are very high, much larger than the thermionic current densities in SiO_2 over a wide range of values for A. Thermal breakdown is therefore rather unlikely by this conduction mechanism.

Curve (c) in Figure 82 indicates that, to some extent, this may be the case even if the activation energy of the thermionic injection would only be 1.5eV.

These findings on thermal breakdown have, of course, restricted validity, owing to the great simplifications in the model and owing to the fact that the dominant conduction mechanism above 1000°C, or even lower, may be very different from thermionic injection.

An alternative electronic breakdown mechanism may be operative due to the ionization produced by ∂-rays around the track. Calculations by KATZ and KOBETICH[243] show that the ionization spike produces temporarily very large positive charges and fields around the track. These fields cause electron injection from the electrodes and in the insulator recombination takes place. When an external field is applied the field is enhanced at the cathode and diminished at the anode, and most of the injection occurs at the cathode. For sufficiently large external fields the injected electrons cause impact-ionization and breakdown becomes possible.

Whilst a simple relation can be derived to illustrate conditions for thermal breakdown by fission-fragment, conditions for electronic breakdown are more complex, as shown in Chapter 3. It is necessary in order to discuss the lowering of the breakdown field for RIDB to develop a new interpretation of the impact-ionization mechanism: for this reason a different interpretation of electronic breakdown in silicon dioxide due only to the applied field from that presented in Chapter 3 will be discussed.

TOMMASINO et al's breakdown observations indicate that in the range of fields where breakdown

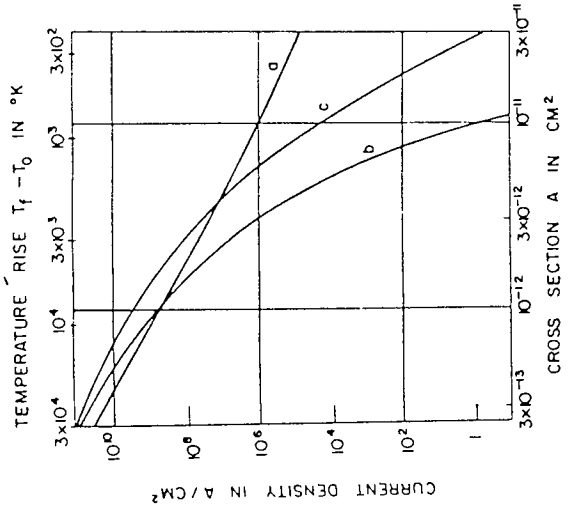

Figure 82: Current densities versus thermal spike cross-section:
(a) Current density j_0 required for thermal runaway.
(b) Current density j_f required of thermionic injection, E=2.5eV.
and (c) Current density j_f required of thermionic injection, E=1.5eV.
(After TOMMASINO et al, Reference 234)

takes place impact ionization occurs by electrons injected at the cathode. The ionization coefficient,a , has been determined experimentally [232] as a function of field for oxides on n-type silicon substrates and

$$a = B\,e^{(-C/F)} \qquad -92$$

where $B=6.5*10^{11}$ cm^{-1} and $C = 180 MVcm^{-1}$.

The injected electrons traverse the insulator layer and leave behind positive charges due to ionization events, and, according to SWAN[244] and O"DWYER[9] a regenerative process takes place. The positive space charge increases the cathode field and the electron injection rate, which further increases the ionization rate. This effect is opposed by recombination of injected electrons with positive charge centres. For the influence of these processes on the positive charge particle density, N^+, a simplified rate equation for a unit-area T'- thick oxide layer is

$$\frac{dN^+}{dt} = j/q\,[a - s\,N^+] \qquad -93$$

where t is the time, j is the current density crossing the insulator, and s is the electron-positive-charge recombination cross section. The first term in Equation 93 is the ionization and the second term is the recombination rate.

When ionization is balanced by recombinations,

$$N^+ = a/s \qquad -94$$

Owing to the presence of positive charge the field is distorted in the insulator, being largest at the cathode. As a is an exponential function of the field, field distortions enhance its effectivemagnitude as if an average field $F+g\,N^+$ would act, where g is a coefficient. Using the field $F+g\,N^+$ for the evaluation of the ionization coefficient and replacing a in Equations 85 and 87

$$N^+ = (B/s)\,e^{[-C/(F+g\,N+)]}$$

$$\approx (B/s)\,e^{[-C/F]}\,e^{[g\,C\,N^+/F_C 2]} \qquad -95$$

This equation has solutions only below a limit for which $N^+ < N_C^+$ and $F < F_C$, the subscript referring

to critical magnitudes which are related by

$$N_c^+ = F_c^2 / g\,B \qquad -96$$

For fields greater than F_c recombinations cannot balance impact ionizations and positive space charge, and current runaway and breakdown arise.

The field F_c corresponds to the idealised condition of uniform current runaway of the entire sample. Owing to local fluctuations in positive space charges, breakdowns occur locally at fields lower than F_c. Indeed, breakdowns due only to the field are observed in 100nm thick SiO_2 films approximately from 8 to 10 $MVcm^{-1}$ (see Figure 81). In this range the ionization coefficient increases from 10^2 to 10^4 cm^{-1} and is very small at lower fields.

The interesting point for the instability, expressed by Equation **95** , is that when breakdown is due only to an applied field, the corresponding field distortions are small and the cathode field may only be a few percent higher than the applied field. The nature of the field variation is illustrated as a function of X perpendicular to the electrodes by the solid line in Figure 83(a), while the dotted line indicates the applied field.

The field distortion is markedly different when electronic breakdown arises due to the passage of a fission-fragment. Before the passage of the fragment, the relatively low applied field is illustrated in Figure 83(b) by the dotted line. The passage of a fission-fragment causes a positive charge around the track which produces a large instantaneous field distortion. An indication of this field distortion is shown by the solid line in Figure 83(b). The field is very small at the anode, but large enough at the cathode to cause impact ionization to occur (shown in Figure 83(b) by the shaded portion). This impact ionization induces breakdown by fragments, when in the total insulator thickness the ionization rate is larger than the recombination rate, leading to current runaway. As the possibility of impact ionization is dependent on the mass and energy of the fission-fragment, the magnitude of the breakdown fields depends on the properties of the fission fragment.

The ionization produced by fission-fragment can be calculated using the method of KATZ et al[243]and, as the ionization coefficients and recombination cross section have been determined experimentally by KLEIN et al[234], it appears to be feasible, though complex, to calculate the breakdown voltages as a function of fragment mass and energy.

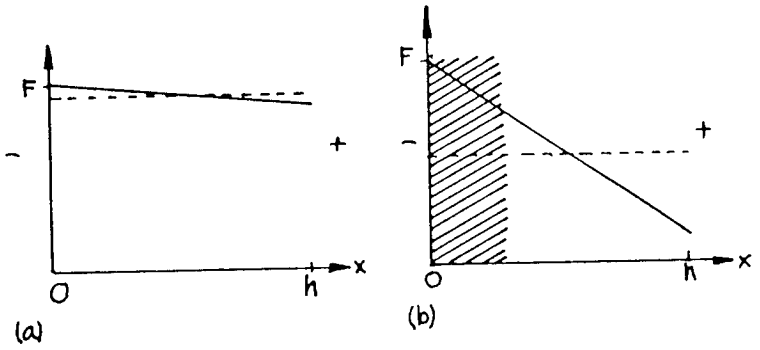

Figure 83: The field distribution in the insulator as a function of the coordinate x on breakdown:
(a) Due to the field only.
and (b) Due to a fission-fragment and the field.

The least amenable to assessment is the influence of material changes along the track of the fission-fragment. A displacement spike is found and instantaneous local melting may occur in the electrodes but the effect of these changes on the breakdown field is unclear.

The experimental evidence found by TOMMASINO et al[234] is in itself insufficient to identify the mechanism causing lowering of the breakdown field in SiO_2; any of the discussed effects may be operative separately or act together.

However, KLEIN[245] has recently proposed a model, based on the IR model discussed in Chapter 3, which deals with the passage of a fission-fragment through the oxide layer producing a large positive charge around its track by ionization and its effect on the breakdown field. The IR model presented in Chapter 3 assumes no charges are trapped in the insulator prior to application of a bias voltage to the MOSC and that the initial field is uniform. KLEIN considers the passage of a fission-fragment through the oxide of an MOSC at time t=0 producing a large positive charge around its track by ionization. Data on the ionization energy deposited will indicate vast initial excess charge densities and electric fields around the fission-fragment track, rapidly decreasing radially and with time. Calculation of the breakdown voltage would be prohibitively complex in this case. The KLEIN model is simple and very useful since comparison of its calculations with the experimental data available indicate its validity and results in a more detailed understanding of the proceses during the breakdown event.

The model is one-dimensional with the X-direction perpendicular to the electrodes. The trajectory of the fission-fragment is in the X-direction (KLEIN disregards the dispersion in the angle of trajectories to the X-direction and the material inhomogeneity caused by the displacement spike is also disregarded). The fission-fragment is assumed to produce a uniform hole density p°_{o} at t=0, implying that radial hole density decreases are neglected.

The field as a function of X in the MOSC at t=0 is shown in Figure 84 for the case when a steady external field F` is applied. F` is smaller than ${}_{o}F_{r}$` the mean critical field for $p^{\circ}_{o}=0$, and the application of F` by itself causes no breakdown. The passage of a fission-fragment, however, enhances the cathode field by ΔF_c due to the positive charge produced. Impact ionization can then take place in the vicinity of the cathode; KLEIN [234] has determined the conditions for breakdown in this case.

The assumptions that electron-hole recombination is the main process opposing the effect of

impact ionization, that ΔF_c is not much larger than F` and current injection remains negligible at the anode, as indicated in Figure 84, are also made. Calculation of the critical field F_r for current runaway by the IR model involves solving a set of conduction equations[13] as was performed in Chapter **3**, namely the equation for the current density, j, which in the case of current injection by Fowler-Nordheim tunneling is

$$j = A F_c^2 \, e^{(-B/F_c)} \qquad -97$$

with F_c the cathode field, *A* and *B* constants; the rate equation for hole density, p, accounting for impact ionization and recombination

$$\frac{\partial p}{\partial t} = \frac{j}{q}(a - sp) \qquad -98$$

where t is time, *a* the coefficient of impact- ionization , and *s* the electron-hole recombination cross-section; the field dependence of *a*

$$a = a_0 \, e^{(-H/F)} \qquad -99$$

with F the field, a_0 and *H* constants; and Poisson's equation

$$\frac{\partial E}{\partial X} = \frac{qp}{\epsilon_0 \epsilon} \qquad -100$$

with ϵ_0 and ϵ the absolute and relative permittivities of free space and the oxide, respectively. The initial condition resulting from the passage of the fission-fragment is $p = p^\circ_0$ at t=0.

A time-dependent analytical solution of the set of equations could not be found for the present case and an approximate calculation of the critical breakdown voltage is discussed.

KLEIN assumes that current runaway arises after the passage of a fission-fragment, when at t=0 the effect of impact ionization on the current is larger than that of recombination and by stipulating that the time derivative of the current density j'>0, implying with Equation **97** that F_c', the time derivative of the catode field is also greater than zero at t=0.

In contrast, when $F_c'<0$ KLEIN assumes that a rapid decreases in hole and current density follows.

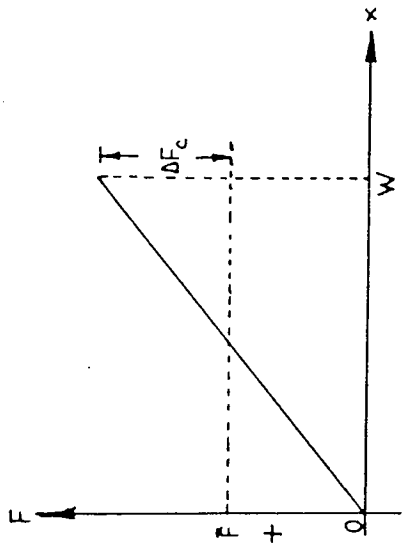

Figure 84: The electric field as a function of x in the MOSC in the presence of a uniform hole density.

These assumptions for an appropriate treatment can be seen to be suported by the results of the following calculations.

KLEIN has derived a relation for F_C' and found first the expression for the cathode field F_C:

$$F_C = F` + {}^1/_{T'} \int_0^{T'} \frac{qp}{\epsilon_o \epsilon} X dX \qquad \text{-101}$$

Here F` is the mean field applied to the MOSC. The time derivative F_C'

$$Fc' = {}^1/_{T'} \left({}^\partial/_{\partial t}\right) \int_0^{T'} \frac{qp}{\epsilon_o \epsilon} X dX \qquad \text{-102}$$

and replacment for $({}^{\partial p}/_{\partial t})$ from Equation 98 gives

$$F_C' = \frac{j}{\epsilon_o \epsilon T'} \int_0^{T'} (a - ap) X dX \qquad \text{-103}$$

The condition $F_C' = 0$ at t=o determines the lower bound, that is the critical cathode field F_{Cr} for current runaway and the relation for the calculation is, with Equation **103**

$$\int_0^{T'} a\, X\, dX = \int_0^{T'} s\, p_o\, X dX \qquad \text{-104}$$

where p has been replaced by p_o.

Equation 99 can be replaced for a in Equation **104**. an approximate form for a is

$$a = a\, e^{bF} \qquad \text{-105}$$

with $$a = e^{(-2H/F_C)} \quad \text{and} \quad b = H / F_C^2 \qquad \text{-106}$$

The relations for the constants a and b have been obtained by equating a and (da/dF) at $F=F_c$ in Equations **99** and **105**.

The X dependence of a is obtained by replacing for F the field distribution which, as shown in Figure 84 is at t=0 given by

$$F = F` + \frac{qp_o}{\epsilon_o \epsilon}\left(X - T'/_2\right) = F` - \Delta F_c + 2\Delta F_c (X/T') \qquad \textbf{-107}$$

ΔF_c is the initial field enhancement at the cathode and

$$\Delta F_c = q p_o T' / 2\epsilon_o \epsilon \qquad \textbf{-108}$$

Integration of Equation **104** results in

$$\frac{a_o T'^2 F_{cr}^4 e^{(-H/F_{cr})}}{4(\Delta F_c H)^2}\left[\frac{2H\Delta F_c}{F_{cr}^2} + e\left\{\frac{-2\Delta F_c H}{F_{cr}^2}\right\} - 1\right]$$

$$= \frac{\epsilon_o \epsilon_s T \Delta F_c}{q} \qquad \textbf{-109}$$

The left-hand side of Equation **109** times $j/\epsilon_o \epsilon T'$ represents the effect of impact ionization increasing F_c', while $j/\epsilon_o \epsilon T'$ times the right-hand side is the opposing effect of recombination.

Equation **109** can be solved by numerical methods to evaluate the critical field F_{cr}, such that

$$e^{\frac{H}{F_{cr}}} = \frac{a_o q T}{\epsilon_o \epsilon_s H}\frac{F_{cr}^4}{4H(\Delta F_c)^3}\frac{2\Delta F_c H}{F_{cr}^2} + e^{\left(\frac{2\Delta F_c H}{F_{cr}^2}\right)} - 1 \qquad \textbf{-110}$$

The mean critical field F_r' is obtained immediately from Equations **108** and **110**, since with Equation **107**

$$F_r' = F_{cr} - \Delta F_c \qquad \text{-111}$$

To compare the breakdown field on the passage of a fission-fragment, $T'F_r'$, with the breakdown field of the oxide due to the application of the field only, $T'_o F_r'$. ${}_oF_r'$ denotes the mean critical field for current runaway in the latter case, when no charges are present in the insulator at t=0.

KLEIN, in an earlier publication[13], derived relations for the evaluation of ${}_oF_r'$ and ${}_oF_{ar}$, the critical anode field and are expressed as

$$e\frac{(H/{}_oF_{ar})}{(H/{}_oF_{ar})^2} = \frac{a_o q T}{C_o Cs\ H} = M \qquad \text{-112}$$

and

$$\frac{{}_oF_r'}{{}_oF_{ar}} = 1 + \frac{{}_oF_{ar}}{H} \qquad \text{-113}$$

Here M denotes a material constant.

By replacing the left-hand side of Equation **112** with $(a_o q T'/ C_o Cs\ H)$ in Equation **110** and by assuming that $(2\Delta F_c H / F_{cr}^2) \gg 1$, a relation for ${}^{F_r'}/_{oF_r'}$ can be derived. Using Equations **110** to **113** one obtains, after algebraic manipulations,

$$\frac{F_r'}{{}_oF_r'} = \frac{\left\{1 - \frac{{}_oF_{ar}}{H}\ ln\ \frac{H\Delta F_c{}^2}{2\,{}_oF_{ar}F_{cr}}\right\}^{-1} - \frac{\Delta F_c}{{}_oF_{ar}}}{1+{}_oF_{ar}\ /\ H} \qquad \text{-114}$$

Equation **114** represents the ratio of the mean fields for current runaway for the two cases with initial and with no initial positive charge in the insulator. ${}^{F_r'}/_{oF_r'}$ in Equation **114** is essentially a function of two ratios $({}_oF_{ar} / H)$ and $(\Delta F_c / {}_oF_{ar})$. The ratio $({}_oF_{ar} / H)$ is a normalised anode breakdown field when an electric field only is applied to the MOSC, and $(\Delta F_c / {}_oF_{ar})$ gives the effect of the positive charge produced by the fission-fragment. The effect of the ratio $(\Delta F_c / F_{cr})$ in the logarithmic term of Equation **114** can be closely approximated by $(\Delta F_c / {}_oF_{ar})$, as shown by numerical computations[245].

KLEIN has evaluated $(F_r`/{}_oF_r`)$ as a function of $(\Delta F_c / {}_oF_{ar})$ and has plotted the results with $({}_oF_{ar}/H)$ as the parameter; this is reproduced in Figure 85. The Figure shows that the mean breakdown field on the passage of a fission-fragment is lower than on the application of the field only. The lowering of the breakdown field is the larger, the larger $(\Delta F_c / {}_oF_{ar})$ and the smaller $({}_oF_{ar} / H)$.

Figure 86 presents the ratio $(F_{cr} / {}_oF_r`)$ as a function of $(\Delta F_c / {}_oF_{ar})$, with $({}_oF_{ar} / H)$ as the parameter;the figure shows that the cathode field at t=0 on breakdown due to the passage of a fission-fragment is larger than the mean breakdown field on the application of an electric field only. The increase in the cathode breakdown field is the larger, the larger both $({}_oF_{ar} / H)$ and $(\Delta F_c / {}_oF_{ar})$.

Equation **110** for the current runaway field F_{cr} ca in approximation be written in a much simpler form, when

$$2\Delta F_c H / F_{cr}^2 \gg | e^{(-2\Delta F_c H / F_{cr}^2)} - 1 |$$

and

$$e^{\frac{H}{F_{cr}}} \approx \frac{MF_{cr}^2}{2\ \Delta F_{cr}} = \frac{a_o q T'}{2\epsilon_o \epsilon_s H} \frac{F_{cr}}{\Delta F_c} \qquad \textbf{-115}$$

An alternative form of the runaway condition is then easily obtained by writing $a_{cr} = a_o e^{(-H / F_{cr})}$ and by replacing ΔF_c in Equation **108** with $qp_oT' / 2C_oC$ thus

$$a_{cr} \approx s\, p_o\, (H\Delta F_c / F^2_{cr}) \qquad \textbf{-116}$$

where a_c is the coefficient of impact ionization at the cathode and $a_c = a_{cr}$, when $F_c = F_{cr}$.

A simple physical meaning is contained in this relation: Equation 98 shows that when $a_c = s\, p_o$, the rate of ionization equals the rate of recombination at the cathode. Such a rate of ionization is insufficient for current runaway, and for instability a_{cr} is at least $(H\Delta F_c / F^2_{cr})$ times larger than the rate of recombination at the cathode at t=0. According to SOLOMON and KLEIN[246] the ratio $(H\Delta F_c / F^2_{cr})$ is approximately 9 in thermally grown SiO_2 when ΔF_c=4, H=180 and F_{cr}=8.9MVcm^{-1}.

A short summary of the KLEIN model and analysis presented above is: relations have been derived for breakdown fields of fission-fragment induced breakdown events. An approximate form of these

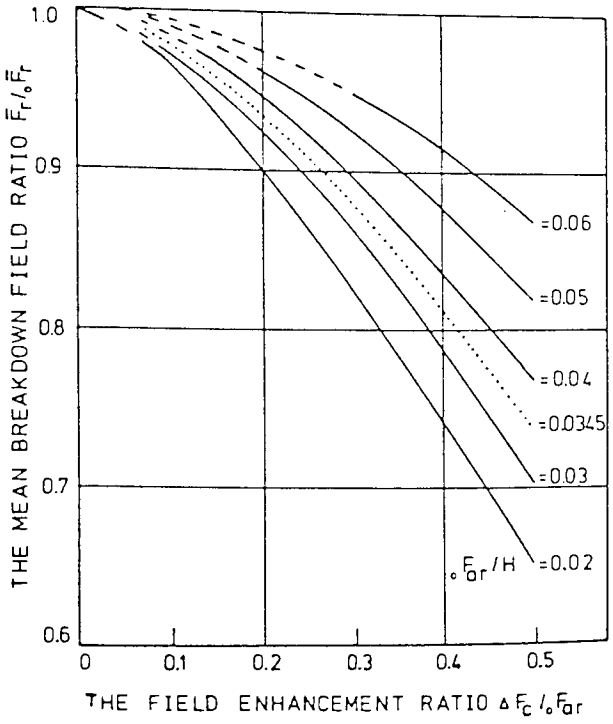

Figure 85: The ratio of the mean critical (breakdown) field by a fission-fragment and by the electric field only, $F_r/{}_oF_r$, as a function of $\Delta F_c/{}_oF_{ar}$, with ${}_oF_{ar}/H$ as the parameter. ΔF_c is the cathode field increase due to the passage of the fission-fragment and ${}_oF_{ar}$ is the normalised critical anode field on the application of an electric field. (After KLEIN, Reference 245)

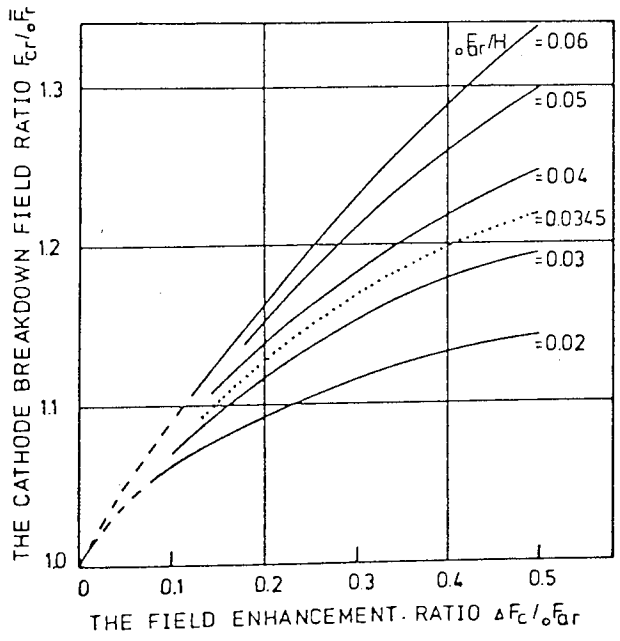

Figure 86: The ratio of the critical cathode (breakdown) field F_{cr} by a fission-fragment and the mean critical (breakdown) field ${}_oF_r$, with $F_{cr}/{}_oF_r$ as the parameter. ΔF_c is the cathode field increase due to the passage of the fission-fragment and ${}_oF_{ar}$ is the normalised critical anode field on the application of an electric field. (After KLEIN, Reference 245)

relations is simple. These relations show that on breakdown induced by a fission-fragment the mean applied field is smaller, but the cathode field is larger, than the mean applied field on breakdown due to the application of an electric field only.

4.4.3 Discussion of the Models

The relation derived for the critical field, F_r`, in the KLEIN analysis is approximate, based on the assumption of Equation **104** that F_c' is zero at the cathode at t=0. The results of Equation **109** permit assessment of the appropriateness of this assumption.

The effect of impact ionization on F_c', ($j / C_o CT'$ times the left-hand side of Equation **109**) can be seen to vary as some exponential function of the cathode field F_c. In contrast, the opposing effect of recombination, $j / C_o CT'$ times the right-hand side of Equation **109** is constant. F_{cr} is therefore sharply defined at t=0.

Equations **103**,**104** and **109** indicate the nature of the current transients after the passage of the fission-fragment:

(1) A small increase in F_c above F_{cr} enhances considerably the effect of impact ionization against that of recombination, leading to a continued increase in F_c to current runaway and breakdown.

(2) However, when F_c is slightly smaller than F_{cr} the effect of impact ionization decreases sharply below that of recombination and rapid disappearance of the hole charge and of current is expected at the track of the fission-fragment. Thus, the functional dependence of the effects suggests that the approximate model for current runaway offers a reasonable basis for the calculation of F_r`.

KLEIN has not accounted for the secondary effects in the calculations owing to their approximate

nature; according to SHATZKES[247], such an effect, decreasing $F_r`$, is the reduction of the width of the energy barrier at the cathode due to the distributed hole charge.

Another effect, increasing $F_r`$, is that of dead-space for impact ionization at the cathode, as discussed in the early work of KLEIN and TOMMASINO[13].

Equations **110** and **114** are not valid when the magnitude of the ratio ($F_r` / {}_oF_r`$) is close to unity. In this case $F_r`$ depends on the hole density produced by the action of the electric field only. The curves shown in Figures 85 and 86 are, therefore, plotted as dotted lines when ($F_r` / {}_oF_r`$) values are close to unity.

Considering the properties of fission-fragment from a Cf^{252} source presented in Table 6, and comparing the breakdown counts produced by Cf^{252} fission-fragments in Figure 81 with the results of calculations from the KLEIN analysis gives an interesting insight into RIDB by fission-fragment: the critical breakdown voltage ${}_oV_r = {}_oF_r`T'$ due to the application of the field only can be seen to be approximately 74V, using the right-hand curve of Figure 81. An accurate determination of ${}_oV_r$ is not possible because fluctuations and low field breakdown processes also cause breakdown at voltages below ${}_oV_r$. The rapid rise in the breakdown rate indicates that the error in the assessment of the breakdown voltage is probably small.

The determination of the representative, critical voltage $V_r = F_r`T'$ for fission-fragment with the left-hand curve of Figure 81 is also subject to some uncertainty owing to spread in the mass number and in the angle of incidence of the fission-fragment. V_r can be seen to be approximately 54V for the heavy fragments and 58.5V for the light fragments, and the rise of the breakdown rate curve shows that the error is again relatively small.

Using these experimental results on $V_r / {}_oV_r = F_r / {}_oF_r`$ and Equations **114** and **111**, the magnitudes of ΔF_c and F_{cr} can be evaluated for the fission-fragment induced breakdowns. For this purpose the magnitude of ${}_oF_{ar}$ has been determined using Equation **113** for ${}_oV_r$ = 74V, T'=115nm and H=180 $MVcm^{-1}$. KLEIN has obtained an unusually low value for ${}_oF_{ar} = 6.22MVcm^{-1}$ and found ${}_oF_{ar}/H=0.0345$. Curves for the parameter ${}_oF_{ar}/H$ are plotted as dotted lines in Figures

85 and 86. Results of the calculations are tabulated in Table 7 for the two kinds of fission-fragment, presenting F_r` /$_oF_r$`, $\Delta F_c/_oF_{ar}$, ΔF_c, ΔF_r`, F_{cr}, and p_o. The magnitude of p_o has been obtained using Equation **108** with the value for ΔF_c calculated. The results of Table 7 show that the lowering of the breakdown voltage by the passage of a fission-fragment can be well explained by cathode field enhancements of a few $MVcm^{-1}$ in magnitude.

The physical meaning of the result estimating the ionization energy required for the creation of the positive charge about the track of the fission-fragment is perhapsgiven in an assessment of the positive charge at t=0 combined with calculations of the spatial distribution of ionization. Calculations performed by KATZ and SOLOMON[243] for quartz have shown that the ionization energy and the positive charge decrease rapidly about the fission-fragment track. A cylinder of uniform charge density and equal charge would, for Cf^{252} fission-fragment, very approximately have a diameter of 40nm and a volume $v_b \approx 1.5*10^{-16}cm^3$. This cylinder can be considered the initial breakdown channel. Assuming that the hole density in the cylinder is P_o, the number of holes, P, in the breakdown channel is $p_o v_b$, and P derived from breakdown calculations is also tabulated in Table 7.

The ionization energy spent in the generation of the P holes is not known. Since much of the ionization is due to energetic secondary electrons, KLEIN assumes as a first approach that the mean ionization energy is that of energetic electrons, approximately three times the band gap energy, that is , $3E_g \approx 30eV$ for SiO_2 and the ionization energy for P holes deposited around the track is given in the last row of Table 7.

When the ionization energy derived from the breakdown results is compared with the ionization energy determined from the stopping power data presented in the last row of Table 6, a vast discrepancy can be seen, even if the mean ionization energy or P are incresed several times. Thus, while the simple breakdown model satisfactorarily fits breakdown observations, the energy deposited and hence approximately the values of p_o calculated with the breakdown data are two orders of magnitude smaller than those determined from the stopping power data.

The p_o values estimated with the stopping power data indicate vast initial electric fields around the track, very much larger than the field applied to theMOSC. The question arises as to why the vast

fields do not cause breakdown by themselves, or at least at applied voltages very much lower than observed ?.

TOMMASINO et al[13] have shown that such a breakdown could not be thermal, since the energy deposited was likely to dissipate from the microscopic breakdown channel by thermal conduction before current runaway could take place.

Fragment Type		*Light Fragment*	*Heavy Fragment*
The ratio $F_r` / {}_oF_r`$		0.79	0.73
The ratio $\Delta F_c / {}_oF_{ar}$		0.43	0.51
The field enhancement, ΔF_c	in $MVcm^{-1}$	2.7	3.2
The critical applied field, $F_r`$	in $MVcm^{-1}$	5.1	4.7
The critical cathode field, F_{cr}	in $MVcm^{-1}$	8.8	8.9
The hole density, p_o	cm^{-3}	10^{18}	$1.2*10^{18}$
Number of holes in the breakdown channel, P		145	173
Approximate ionization energy for P holes in the breakdown channel,	in eV	4300	5200
Ionization energy deposited around fission-fragment track,	in eV	$1.2*10^6$	$1.4*10^6$

Table 7. Data of breakdown events produced by fission-fragments (After KLEIN, Reference 245)

A simple analytical development of the KLEIN model which also regards the feasibility of breakdown by impact ionization when fields are vast is easily described: the breakdown results of the analysis given by Equations **111** and **114** are not applicable when p_o is very large. One reason is that an electron current is in this case injected along the fission-fragment track from both electrodes. The principal reason, however, is that extremely complex processes of conduction, recombination and ionization take place immediately after the passage of the fission-fragment, not accounted for by the

simple KLEIN breakdown model.

In conclusion, experimental data of fission-fragment induced breakdown in MOSCs can be well calculated with a simple breakdown model presented by KLEIN[234]. However, contradictions in the magnitudes of F_r` and p_o remain to be explained satisfactorily.

CHAPTER FIVE .

EXPERIMENTAL TECHNIQUES

As stated and illustrated in previous chapters, the materials and fabrication process dependencies of MOS structures is a key factor in the quality, stability and electrical response of MOSCs. In order that the results of this study be compared on a quantitative (as well as qualitative) basis with those of other workers, a detailed description of the materials, processes and apparatus used to construct the MOScs used in this study is given in the first section of this chapter.

There are numerous techniques for the evaluation of MOS devices; those chosen for this study are considered by the author to be the methods which provide the most easily obtained and comprehensive data in order to evaluate and analyse the electrical and physical characteristics of the MOSCs before, during and after irradiation with various radiation sources. These methods are discussed with particular emphasis on their application to the detection and understanding of radiation effects on the microscopic-physical and, in particular, the gross-electrical characteristics of silicon-based MOSCs.

In order that the radiation response of the devices be compared with the data and models presented by other workers, the various radiation sources, their spectra and the irradiation geometries used are summarised.

5.1 MOSC Fabrication

The MOS capacitor consists of a semiconductor wafer substrate, an Ohmic back contact to the semiconductor wafer, a thin (either grown or deposited) insulator layer overlaying the front of the wafer, and a metal gate electrode overlaying the insulator, as illustrated in Figure 1(a). The device structure chosen for this study is the silicon-based MOSC with a thermally grown oxide layer, an aluminium ohmic contact and a thin aluminium gate electrode; the general device structure is shown in Figure 1(b) and a whole wafer of completed, unmounted devices is shown in Figure 87.

The MOSCs were fabricated by Plessey Semiconductors (UK) Limited at their Plymouth (CMOS) and Swindon fabrication centres, who also provided the silicon substrates and pure Al contact/electrode metal. The characteristics of the silicon substrates, the nature of the oxide layer and the aluminium contacts and electrodes are briefly described in section **5.1.1**, together with detailed tabulated descriptions of the fabrication processes and parameters, electrode mask designs and configurations used , in section **5.1.2** .

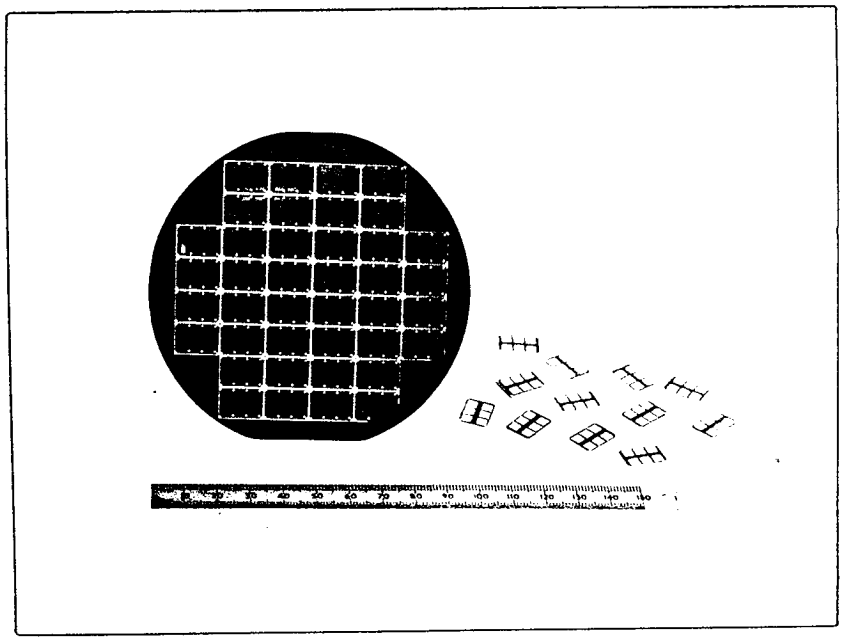

Figure 87: A photograph of a 100mm wafer of completed Al-SiO_2-Si MOSCs; several diced chips of MOSCs are also shown.

For the majority of the irradiations, a large number of devices with different oxide thicknesses and substrate types needed to be irradiated together in order to ensure the parameters of radiation dose rate, total dose and bias were identical for each device in a similar substrate type/oxide thickness category; to this end a novel but simple mounting technique and biasing system has been devised and this is described and illustrated in section **5.1.3**.

5.1.1 Materials

The MOSCs were fabricated using Wacker Corporation four-inch diameter silicon wafers; these were from Czochralski-grown n and p-type silicon ingots which had been sliced into <100> crystal orientation wafers, polished one side and abraded on the back face using standard polishing and abrading techniques[250]. The characteristics of the wafers used are listed in Table 8.

Property †		*Characteristic*
Resistivity (phosphorus)n-type	(Ωcm)	2 - 4
Resistivity (boron)p-type	(Ωcm)	14 - 21 and 2 1- 25
Minority carrier lifetime	(μs)	30 - 300
Oxygen	(ppma)	8 - 19
Carbon	(ppma)	2 - 5
Dislocations(before processing)	(cm^{-2})	<400
Diameter	(mm)	100 - 102
Thickness	(mm)	0.48 - 0.50
Slice bow	(μm)	< 25
Slice taper	(μm)	<15
Surface flatness	(μm)	< 5
Heavy-metal impurities	(ppba)	<1

Table 8. Silicon wafer pre-processing characteristics.

(† ppma = parts per 10^6atoms; ppba = parts per 10^9atoms)

Thirty-six wafers were used in all, eighteen wafers of each type, three for each proposed thickness

of oxide; these were taken from a single batch of each silicon resistivity and type which had been previously inspected for microscopic surface aberrations and defects. The type, resistivity, proposed oxide thickness and identification code was carefully scribed on the back face of the wafers prior to cleaning for identification after whole-wafer processing.

The aluminium used for the Ohmic contact and electrode depositions was in the form of a Perkin Elmer 4410 sputtering target of assured 99.99% purity held under vacuum of 10^{-7}mbar in the Perkin Elmer 4410 magnetron sputterer deposition chamber.

5.1.2 Processing: Oxide growth, Metallization and Annealing

Since thermally grown oxide layers on silicon are of a far higher quality than most of the commonly deposited insulator layers (which tend to have large interface state densities, large fixed oxide charge and enormous mobile ionic oxide charge densities), this was the form of insulator layer chosen for the MOSCs fabricated for the study. The process and growth kinetics of such silicon dioxide layers has been very well investigated and documented and, therefore, the reader is referred to the recent and comprehensive works of GHANDI[251] and KATZ[252].

The silicon wafers described above were prepared for the oxidation furnace in ultraclean conditions using the RCA cleaning procedure[16,251] and inserted into the furnace in batches of six (three each of n and p-type wafer) on standard quartz four-inch wafer carriers. Since the Plessey oxidation furnaces are fully automated the furnace process parameters (withdrawal rates, ramp rates, gas flow and temperature) were pre-programmed via microprocessor control programs for each proposed oxide thickness according to the standard Plessey CMOS gate-oxide growth procedure[253]; these parameters are listed, along with the wafer identification, type, proposed oxide thickness, oxidation times, oxidation ambient (wet /dry, with or without HCl) and actual oxide thickness in Table 9.

The oxide thicknesses proposed to be grown were 40nm, 70nm, 100nm, 270nm, 500nm and 1.2µm; the actual, post-oxidation oxide thicknesses are taken as the average of five measurements over the oxidised surface using a pre-calibrated NanoSpec refractive index film thickness monitor[252].

After oxidation all the wafers were annealed in a N_2 ambient at 1000°C in a similarly automated Plessey annealing furnace to reduce the fixed oxide charge to the order of $10^{11}cm^{-3}$, as described

Wafer Identification	Substrate Type	Resistivity Ohm-cm	Proposed Oxide Thickness nm	Actual Oxide Thickness nm	Oxidation Type (Ambient)	Oxidation Temperature °C	Oxidation Times min
N2-4 40A	N	2-4	40	42.6	* #	950	52
N2-4 40B	N	2-4	40	42.7	Dry Oxidation with HCl		
N2-4 40C	N	2-4	40	42.5			
P21-25 40A	P	21-25	40	39.3			
P21-25 40B	P	21-25	40	39.4			
P21-25 40C	P	21-25	40	39.3			
N2-4 70A	N	2-4	70	84.3	#	900	8-45-5
N2-4 70B	N	2-4	70	84.2	Dry-Wet-Dry ($2H_2O$)		
N2-4 70C	N	2-4	70	84.3			
P21-25 70A	P	21-25	70	83.3			
P21-25 70B	P	21-25	70	83.3			
P21-25 70C	P	21-25	70	83.2			
N2-4 100A	N	2-4	100	107.7	#	900	8-45-5
N2-4 100B	N	2-4	100	107.8	Dry-Wet-Dry ($2H_2O$)		
N2-4 100C	N	2-4	100	107.7			
P14-21 100A	P	14-21	100	107.7			
P14-21 100B	P	14-21	100	107.8			
P14-21 100C	P	14-21	100	107.7			

Anneal ed after oxide growth in dry nitrogen at 100°C for 150 mins.

* A high-temperature (1100°C) drive-in occurred after oxidation.

Table 9: Silicon Wafer and Oxide Growth Parameters.

Wafer Identification	Substrate Type	Resistivity Ohm-cm	Proposed Oxide Thickness nm	Actual Oxide Thickness nm	Oxidation Type (Ambient)	Oxidation Temperature °C	Oxidation Times min
N2-4 270A	N	2-4	270	247.7	* # Dry-Wet-Dry HCl ($2H_2O$)	1000	92-31-17
N2-4 270B	N	2-4	270	246.6			
N2-4 270C	N	2-4	270	246.9			
P14-21 270A	P	14-21	270	237.7			
P14-21 270B	P	14-21	270	236.9			
P14-21 270C	P	14-21	270	237.5			
N2-4 500A	N	2-4	500	588.4	# Dry-Wet-Dry ($2H_2O$)	900	10-375-5
N2-4 500B	N	2-4	500	588.3			
N2-4 500C	N	2-4	500	588.3			
P21-25 500A	P	21-25	500	566.8			
P21-25 500B	P	21-25	500	566.7			
P21-25 500C	P	21-25	500	566.8			
N2-4 1200A	N	2-4	1200	1287.7	# Dry-Wet-Dry (N_2/O_2)	900	10-1130-20
N2-4 1200B	N	2-4	1200	1285.6			
N2-4 1200C	N	2-4	1200	1289.5			
P14-21 1200A	P	14-21	1200	1264.7			
P14-21 1200B	P	14-21	1200	1265.6			
P14-21 1200C	P	14-21	1200	1267.1			

Anneal ed after oxide growth in dry nitrogen at 100°C for 150 mins.

* A high-temperature (1100°C) drive-in occurred after oxidation.

Table 9: Silicon Wafer and Oxide Growth Parameters.

in Chapter 2. Before metallization at Plessey, Swindon (UK), the devices were stored and transported in airtight and UV light-proof static-free carrying cases to prevent the unwanted buildup of oxide charge and surface imperfections due to atmospheric particles.

Because of the necessity to use thin gate electrodes (for the study of RIDB using non-shorting breakdowns and to minimise energy losses in the gate rather than the oxide layer) a 1μm-thick probing pad was considered essential so that during testing no contact was directly made with the electrode by the probe tip and therefore the electrode was not damaged in any way prior to testing (which in itself could cause breakdown) and so that the entire gate area could be irradiated with no (unquantifiable) shielding by the probe. The electrode and probing pad configuration were designed by the author using a PRIME computer and the GAELIC program language CAD system via the Rutherford Appleton Laboratory, Oxford (UK) and these are shown schematically in Figure88; as can be seen there are six individual MOSCs on each chip, placed far enough apart to enable individual device irradiations and to bias devices on the same chip with different magnitude and polarity gate voltages (whilst the ohmic contact is kept at zero volts with respect to the gate electrode) with no possibility if interaction between devices by fringing fields or ion impurity diffusion. These designs (coded for a David Mann 3600 mask fabricating machine) were used by Plessey, Swindon to fabricate two six-inch photolithography masks, one for the 2.5mm^2 50nm Al gate electrodes and the other for the 0.5mm^2 1μm thick probing pads. Both masks have 2μm alignment marks and identification windows which are reproduced on each electrode chip during metallization.

Because thin (50nm) aluminium gate electrodes were required a specially designed metallization process was developed at Plessey, Swindon (UK) to deposit the 50nm Al layer over the1μm Al probing pads with a perfect metallic contact. The custom-designed process is detailed below in Table 10; all the thirty-six oxidised wafers were metallized on the front face in the same process run to ensure the same processing conditions and Al thickness for each wafer. Metallization of the back face was performed at the end of the process run.

After metallization all the wafers were annealed in nitrogen to anneal the fast surface states caused by dangling bonds, as described in Chapter 2. It is not found to be neccessary to use a hydrogen / nitrogen anneal when using thin Al electrodes since sufficient hydrogen is released by the layer to produce the same annealing[253] as with a nitrogen ambient. (For further, more detailed, information

Stage	*Process*	*Comments*
1.	Sputter pre-clean	(1) 10 mins in H_2SO_4/H_2O_2 at 135°C (2) Quench / rinse in deionized H_2O (3) 15 secs in 40:1 BOE at 25°C (4) Quench / rinse in deionized H_2O
2.	Sputter deposition	1µm Al in Perkin Elmer 4410 Magnetron Sputterer at 10^{-8}mbar.
3.	Resist coat / softbake	GCA 9000 track coater Hoeschst Chemicals AZ1350J at 6000rpm to give 1.5µm resist coat. Track in-line bake at 95°C for 5mins.
4.	Align / expose Probe area mask	Canon PLA501FA proximity aligner ≈50mW exposure (as measured at 365nm). Printed at 20µm gap.
5.	Develop	60 secs in 0.22 normality developer at 20°C. Quench / rinse in deionized water.
6.	Hardbake	100°C for 30 mins in free standing oven.
7.	Etch	Etch to clear (in MIT† Al etch at 40°C) + 10% overetch for ≈ 3-4 mins. Quench / rinse in deionized water.
8.	Resist strip	GCA 9000 strip track. 20secs n-butyl acetate spray.
9.	Sputter deposition	50nm in Perkin Elmer 4410 sputterer at 10^{-8}mbar.
10.	Resist coat / softbake	As step 3.
11.	Align /Expose Electrode mask	As step 4.
12.	Develop	As step 5.
13.	Hardbake	As step 6.
14.	Etch	As step 7, but total etch time ≈ 30 secs.
15.	Resist strip	As step 8.
16.	Sputter deposition	As step 2, but with Al deposited on wafer backs.
17.	Stray particulate removal	As step 8.
18.	Sinter / anneal	500°C in N_2 bubbled through water (wet ambient) for 15 mins.

Table 10. Wafer Metallization Process Parameters.

(† refer to Reference 251 for information concerning the MIT etch process).

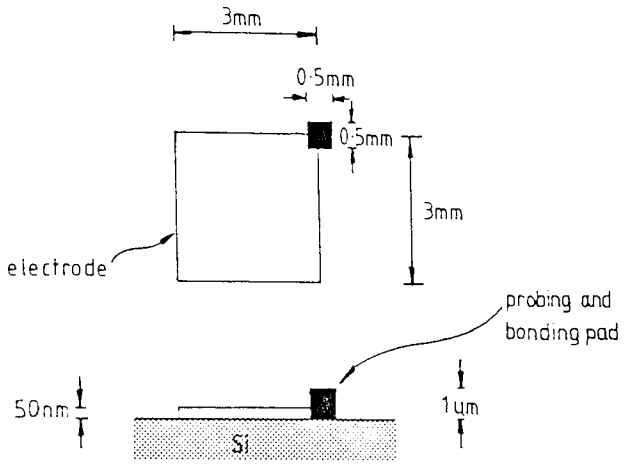

Figure 88: The electrode and probing pad configuration for the completed MOSC chips .

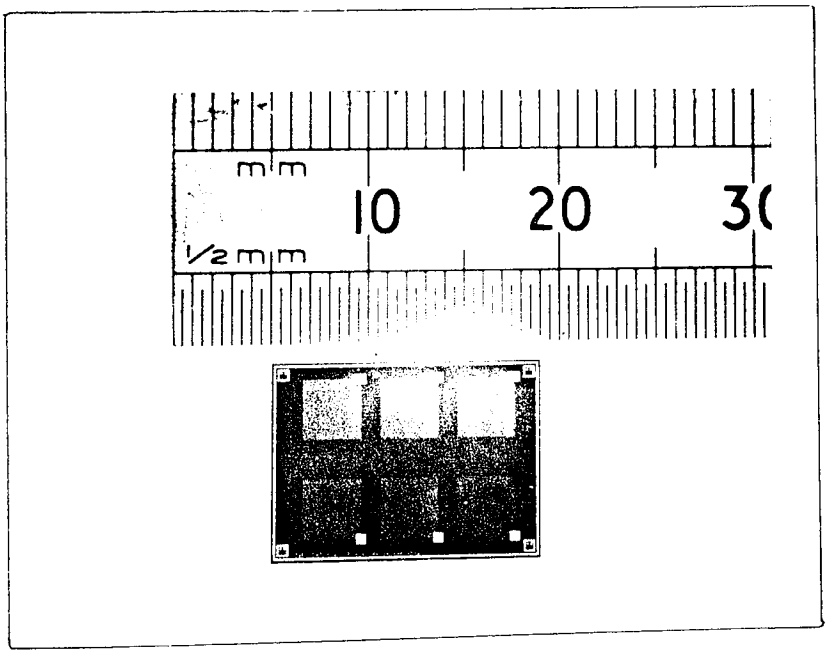

Figure 89: A photograph of a completed single chip of six Al-SiO_2-Si MOSCs.

on the subtleties of the metallization process the reader is referred to the recent overview of FRASER[254]).

In Figure 87 a whole wafer of completed Al-SiO_2-Si MOSCs can be seen; each wafer carried forty chips with six MOSCs per chip (8640 MOSCs on all thirty-six wafers). At Plessey, Swindon each wafer was diced to 50% through the wafer along scribe lines (which were included in the mask designs) using an ultra high-speed diamond-tipped cutting wheel; the semi-diced wafers were transported in shock-proof, airtight and UV lightproof containers. Figure 89 shows a completed chip of six MOSCs ready for mounting / testing which has been manually cleaved from the others on the wafer .

5.1.3 Mounting

In order to irradiate an entire selection of different substrate type and oxide thickness devices under the same radiation type, dose rate, total dose and bias conditions it was necessary to mount the devices in a novel way; Figure 90 shows the layout of a 40 line copper-clad Veroboard sheet where each board had mounted upon it twenty-four chips, two of each thickness and type of device . Various combinations of bias could be applied to each chip by using the lines of copper cladding on the reverse of the sheet of Veroboard to which the devices were attatched, each line being at a different voltage for each particular device on the chip; it is a simple task to connect each MOSC probing pad to the required voltage supply line by using upright pins connected to the copper cladding on the board underside and fine copper wire connected to the pins and probing pads by silver paste, as shown schematically in Figure 91.

The bias voltages chosen were 0V (device top electrode shorted to the ohmic contact), device not connected to any bias, +1.5V,-1.5V,+9V and -9V since these are all well below the device breakdown voltages for the devices and are in the range suggested by other workers to produce the largest magnitude effects (for details, see Chapters 3 and 4); these were all supplied by battery sources connected to the copper cladding strips of the Veroboard by a 40-way edge connector. The Ohmic contact covering the underside of each chip was connected to a horizontally placed clean copper strip, glued to the unclad side of the board, by using silver paste, and this was in turn connected to the appropriate (negative or positive pole) bias of the batteries in the voltage source

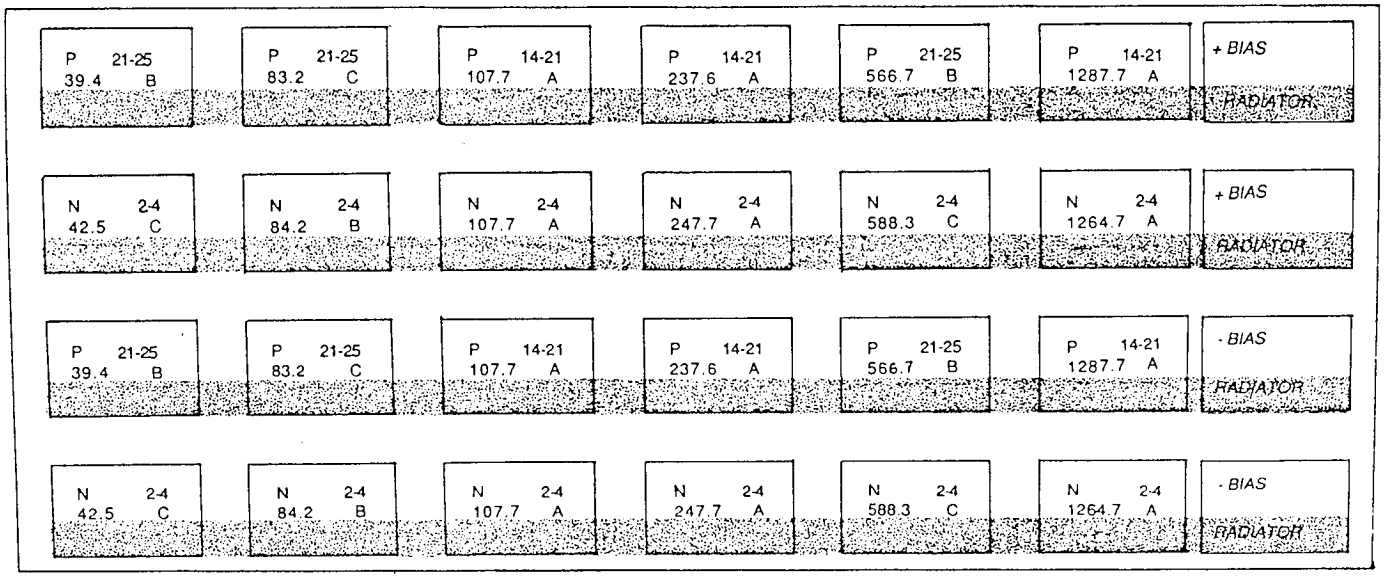

KEY: *Type Resistivity (Ωcm)*

Thickness(nm) Wafer ID

Figure 90: The layout and device parameters for chips of Al-SiO_2-Si MOSCs on the Veroboard multi-bias arrangement described in the text and illustrated in Figures 91(b) and 92.

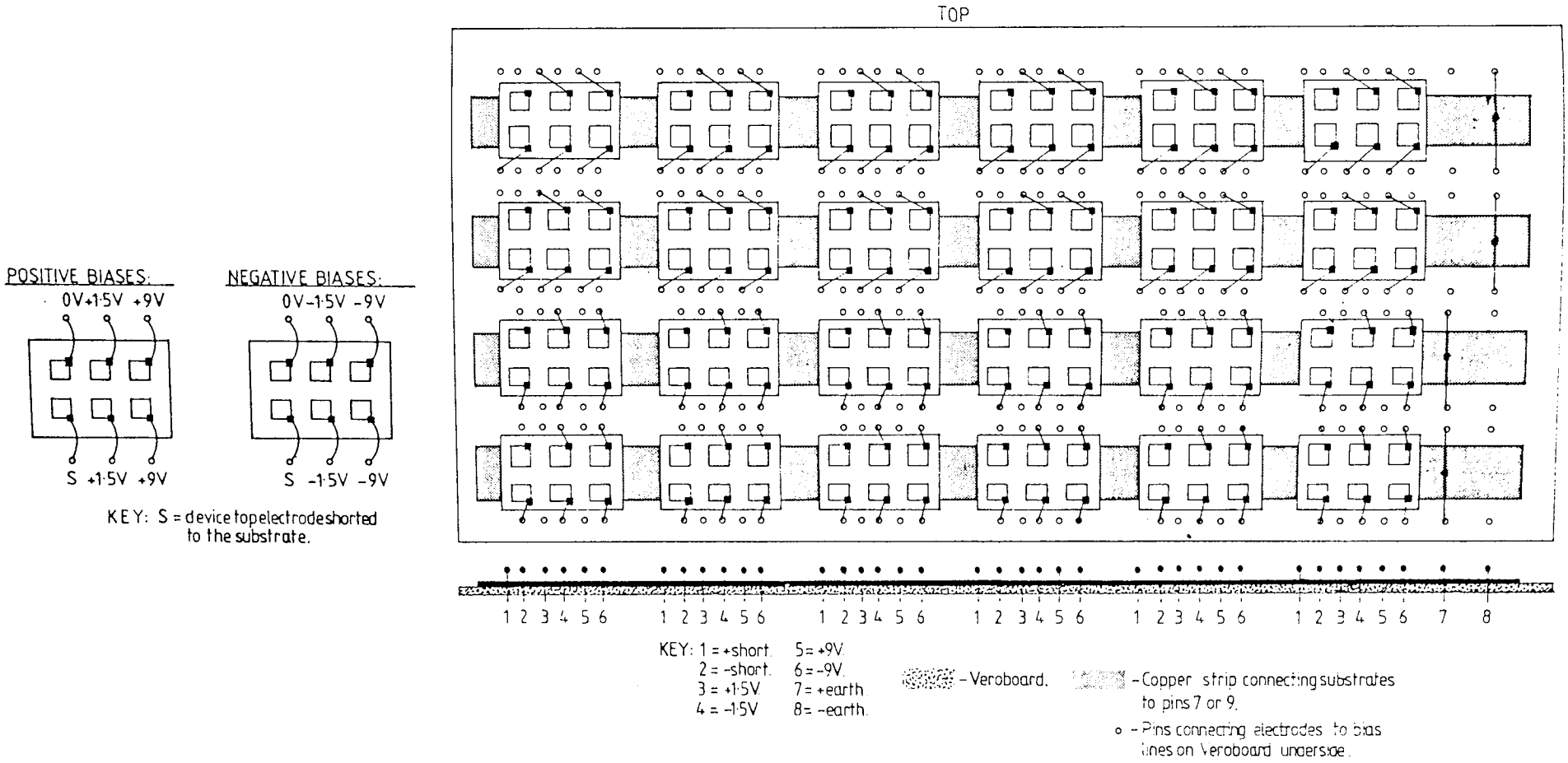

Figure 91: (a) The bias supply to individual devices on each chip.

Figure 91: (b) The complete biasing arrangement for each board of 24 chips.

via a spare pin of the 40-way edge connector.

Four rows of chips were used to include the possibility of irradiating a similar number and type of devices with recoil-protons from a hydrogenous radiator placed in contact with the lower three devices of each chip so that comparison between purely neutron-irradiated and neutron/recoil-proton irradiated devices could be made (described in section **5.4**).

A photograph of a board and the voltage supply box, both of which had to be small and portable in order to irradiate the board with the devices under bias in the small irradiation chambers available, is shown in Figure 92.

The remainder of the devices which were not mounted in this fashion were used for physical examinations, and breakdown testing and individual irradiations using the probing system described in the next section.

5.2 Device Evaluation: Electrical Properties

Three approaches to the problem of evaluation of the electrical properties of the MOSCs were decided upon: a study of dielectric breakdown before and during irradiation with various sources using known breakown evaluation techniques; I-V curve plotting and analysis before and after irradiation; and C-V curve plotting and analysis to determine the various MOSC parameters before, during and after irradiation. These are believed to provide most easily the data necessary to understand the RIDB phenomenon and other radiation effects in MOSCs in order to supplement the body of knowledge already available in this field.

5.2.1 Breakdown Testing

The techniques used for breakdown testing follow those of other workers in the field (as discussed in Chapter **3**) and concentrate on two main features of the breakdown phenomenon: the magnitude and dependencies of the breakdown field and anomalous device breakdown behaviour when irradiated with fission-fragments; and the pulse output characteristics from the devices on breakdown and under irradiation.

A simple probe station was constructed in order to apply a bias voltage to the MOSCs without any

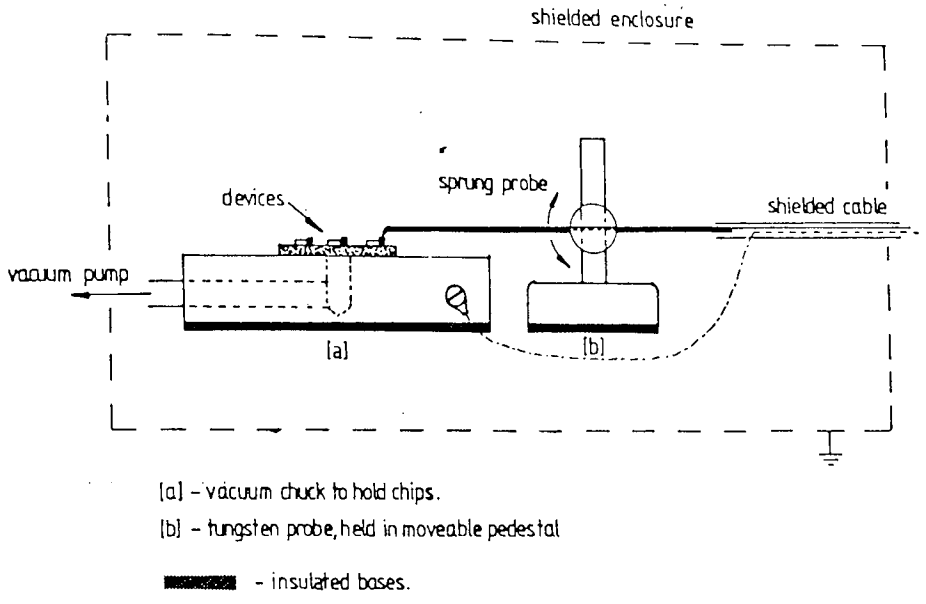

Figure 93: A schematic diagram of the MOSC voltage probe assembly used for breakdown testing.

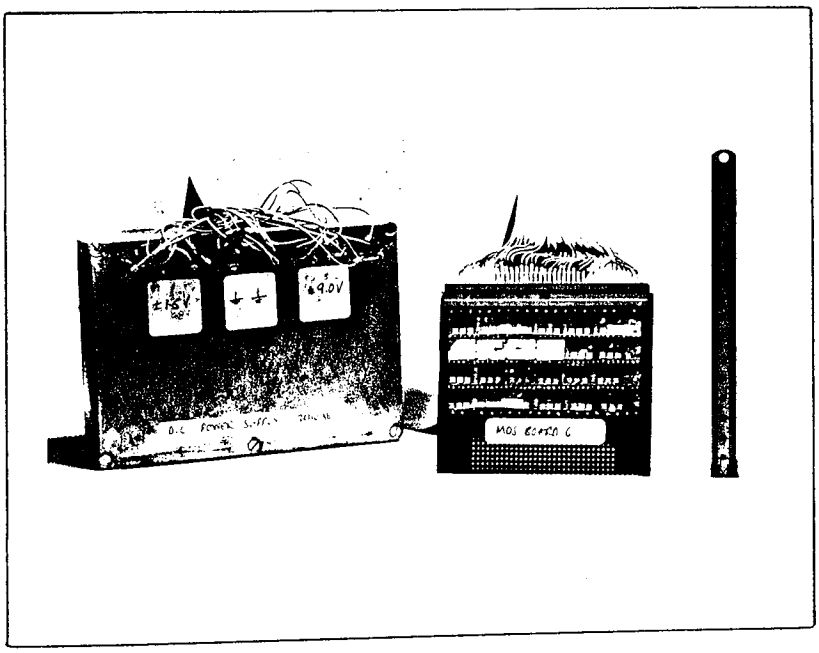

Figure 92: A photograph of a bias-board and the bias supply; d.c. biases of 0V, ±1.5V, ±9V and device-shorted could be supplied with this arrangement.

complicated mounting procedure and for fast turn-around time of sample testing; the probe assembly and test stage were encased in a large, lightproof, dry, earthed aluminium surround in order to prevent detection of extraneous electromagnetic radiation by the MOSC whilst under test and kept in a dry ambient to prevent leakage currents between the terminals on the probe box and ground. The probe itself was a 30mm long, 0.2 mm diameter tungsten wire (in order to prevent high contact resistance to the Al gates) which had been sharpened electrolytically and attached to the manipulator stage. A schematic diagram of the probe assembly and stage is shown in Figure 93.

Four simple arrangements of apparatus have been used to investigate the main features of breakdown and these are shown in Figures 94 to 97. Figure 94 shows the experimental arrangement to determine the non-shorting breakdown field for the MOSCs; the bias supply was a vernier calibrated J&P ±0-3kV regulated EHT source supplied via a 1MΩ series resistor as a current limiter to prevent propagation of breakdowns and shorting of the device (this limiting resistor was removed to determine the shorting or final breakdown strength of the device under investigation). The bias supply to the devices was step-wise increased in magnitude by increments dependent on the estimated breakdown voltage of the device. The device current was measured using a Keithley Model 614 picoammeter ($5*10^{15}\Omega$ input impedance, 10^{-14} ±1% sensitivity) and the voltage drop across the device by a Gould Advance DMM Model 7A voltmeter ($2*10^{10}\Omega$ input impedance, 10^{-5}±1% sensitivity). The times to breakdown were measured using an Ortec Scaler-Timer module connected to the amplifier output of the picoammeter in order to sense an increase in current flow through the device at breakdown. This system enabled the breakdown voltage (and I-V curves) to be measured before, during and after breakdown caused by irradiation.

Figure 95 shows the apparatus used to count the number of non-shorting breakdowns and RIDBs in any given time period (the bias supply, limiting resistance, scaler-timer and voltage / current measuring instruments are the same as those described above); the output pulse from the MOSC on breakdown was pre-amplified using an Ortec Model115 pre-amp and amplified using an Ortec Model 4185 amplifier to provide saturation pulses of approximately +9V which were fed via an Ortec Model 350 single channel analyser with a very wide energy-window into the scaler-timer; one pulse per radiation interaction was assumed. All of these modules were powered by a J&P NIM bin. Using this system the breakdown statistics for the MOSCs under investigation were determined for devices when virgin and when irradiated.

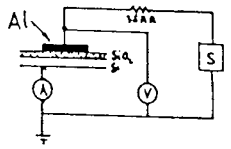

A - picoammeter
V - digital voltmeter
S - d.c. stepped-bias, switchable polarity voltage supply.

Figure 94: A schematic diagram of the apparatus used to determine the breakdown strength of the Al-SiO_2-Si MOSCs with and without radiation fields.

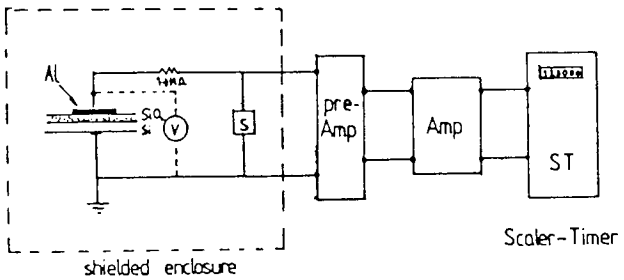

Figure 95: A schematic diagram of the apparatus used to determine the breakdown statistics for the Al-SiO_2-Si MOSCs within and without radiation fields.

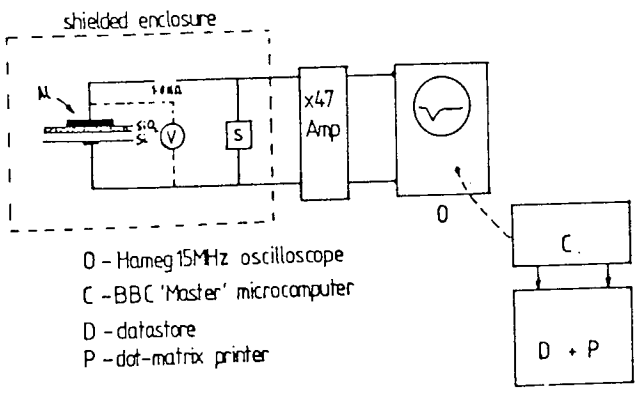

Figure 96: A schematic diagram of the apparatus used to investigate the pulse output from the Al-SiO_2-Si MOSCs before and during irradiation.

Figure 96 shows the apparatus used to investigate the (current transient) pulse characteristics during breakdown, during irradiation without breakdown and during irradiation with breakdown. In this case a simple home-built non-shaping, calibrated gain *47 amplifier (circuit diagram shown in Figure 96(a)) was used in conjunction with a Hameg HM208 15MHz storage oscilloscope controlled by a BBC Model 'B' microcomputer which was used to store pulse data on floppy-disc and to analyse the various parameters of the pulse shape, (also connected to an Epson FX81 dot-matrix printer to provide a trace of the pulse shape); the bias supply to the MOSCs was the same as those described above. The computer program used to acquire and analyse data from the Hameg oscilloscope is given in Appendix 1. With this system the pulse time constant, pulse voltage and corresponding mean pulse charge were determined in order to estimate the charge injection to the insulator layer by the radiation field under investigation and it's subsequent effect on the breakdown voltage and I-V and C-V characteristics for the device.

Figure 97 shows the experimental arrangement used to investigate the pulse-heights of corresponding pulses from MOSCs with and without a gate bias and under irradiation from a variety of sources. This was performed using the calibrated gain x47 amplifier (with a decoupling resistance of 1MΩ) in conjunction with a Canberra Series 35 V-1.2 multichannel analyser to analyse the distribution of pulse sizes from irradiated MOSCs under various bias conditions, which provided information as to the detection abilities of, and radiation interaction mechanism with, the MOSCs.

The above techniques have been used to determine the breakdown parameters for devices under irradiation and stepped bias voltage application.

For ramped bias application the J&P regulated EHT 0-3kV bias supply was replaced with a Hewlett-packard HP6827A voltage source with an incorporated high-speed amplifier. This has enabled an investigation into propagating breakdowns to be made and, when used in conjunction with the circuit shown in Figure 98, the fast-ramped-voltage MOSC breakdown characterstics of the devices were tested (in a similar fashion to that of BUDENSTEIN[130], discussed in Chapter 3). The SCR circuit in Figure 98 is a semiconductor controlled rectifier which, in conjunction with the limiter circuit, enables the voltage at which a pre-breakdown current increase occurs by displaying a single pulse (triggered from the Hewlett-Packard HP 6827A pulser by the sudden current increase) on the Hameg HM208 storage oscilloscope (set to store a single sweep triggered by a pulse input) and prevents any more than one breakdown occurring before a manual resetting of the ramp voltage;

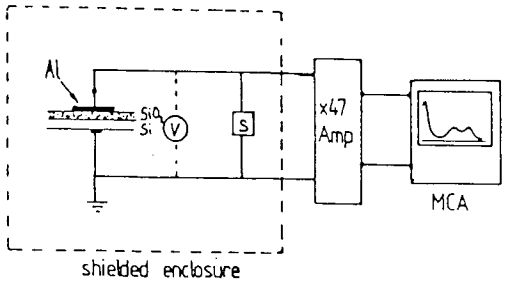

Figure 97: A schematic diagram of the apparatus used to investigate the pulse height from the Al-SiO_2-Si MOSCs during irradiation.

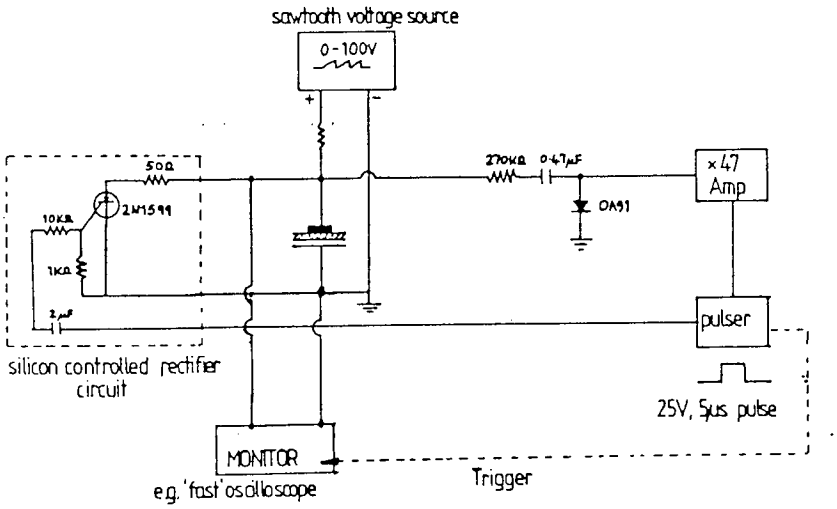

Figure 98: A schematic diagram of the apparatus used to determine the breakdown strength and times to breakdown of the Al-SiO_2-Si MOSCs under high-field stressing, as used by BUDENSTEIN and HAYES (Reference 130).

this has enabled a quantitative analysis of the onset of breakdown during RIDB and a qualitative analysis of the pre-breakdown processes involved.

The results of these investigations on the Al-SiO_2-Si MOSCs fabricated and described in section **5.1** are presented in Chapter **6** and discussed with relevance to the known properties of such devices in Chapter **7**.

5.2.2 Current-Voltage (I-V) Techniques

Two arrangements to investigate the I-V characteristics of devices were used in the study: the first was the simple arrangement shown in Figure 94, where the I-V characteristics of MOSCs approaching breakdown and during breakdown (either intrinsic or radiation-induced breakdown) were investigated. These were used to analyse the high-field conduction properties of MOSCs, when biased with stepped and ramped voltages applied to the Al gate electrodes, in order to determine the mechanism for breakdown (as discussed in Chapter **3**) in these applied field ranges. The second, and far more sensitive, technique was the computer controlled I-V data acquisition arrangement shown in Figure 99. The sample stage was a hot-probe assembly with a heated stage and tungsten probe, enclosed in a dry, earthed, lightproof aluminium enclosure. The computer was a Hewlett-Packard 9836 microcomputer used to control a Hewlett-Packard HP4140B programmable combined voltage source and picoammeter. The computer control program, originally designed to acquire MOSFET and CCD I-V data , is given in Appendix **2**. The gate bias was applied in a ramped and stepped fashion for each data acquisition run with a constant ramp rate of $1Vs^{-1}$ and step rate of 1V every second with the same data acquisition time of 0.2s between steps.

For several devices the sample stage was heated using a built-in 10W wirewound resistance heater and the I-V data for the heated samples at temperatures above room temperature and up to 376°K, as measured with a calibrated chrome-alumel thermocouple in the heater base, was acquired. The stage temperature was regulated using a calibrated thermostat; thermal equilibrium is thought to have been attained between the sample and the heated stage after a few minutes of the stage reaching and stabilising at the measurement temperature; this arrangement has enabled the determination (using the results of Chapter 3) of the low-field (dark) conduction mechanisms taking place in the MOSCs.

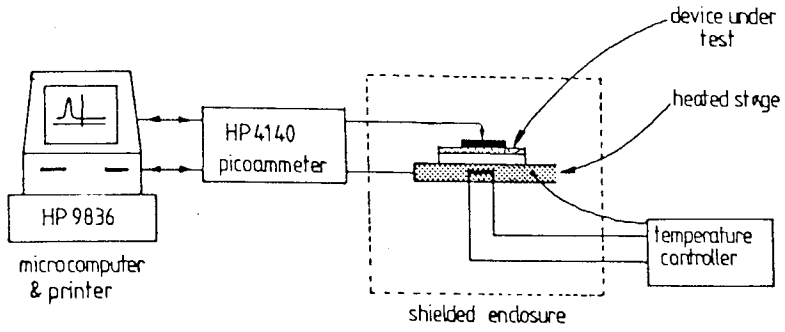

Figure 99: A schematic diagram of the computer-controlled apparatus used to determine the Current-Voltage characteristics for the Al-SiO_2-Si MOSCs.

From the combined data from the two techniques, a complete description of the conduction of the MOSCs before and after irradiation and breakdown for the whole gate voltage range is possible. This has been used to extend the KLEIN[234] model for the observed lowering of the breakdown voltage for MOS devices under RIDB.

The results of these investigations on the Al-SiO_2-Si MOSCs fabricated and described in section **5.1** are presented in Chapter **6** and discussed with relevance to the known properties of such devices in Chapter **7**.

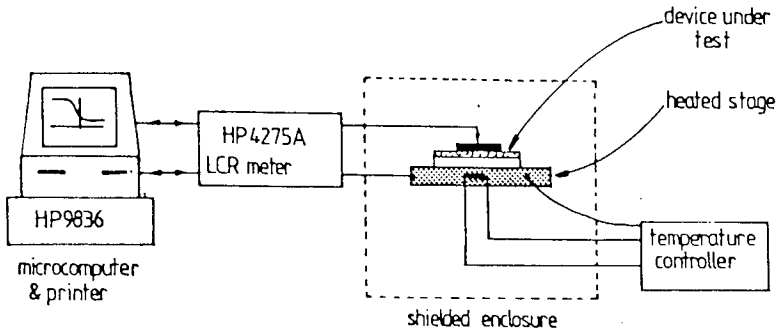

Figure 100: A schematic diagram of the computer-controlled apparatus used to determine the Capacitance-Voltage characteristics for the Al-SiO_2-Si MOSCs.

5.2.3 Capacitance-Voltage (C-V) Techniques and Analysis

The results of Chapter 2 show the dependence of the capacitance of the ideal MOS structure on the applied gate voltage. This property in MOSCs can be used to identify the various characteristics of real (non-ideal) devices and is an extremely versatile technique in the sense that, from a relatively simple analysis of one capacitance versus applied gate voltage curve, many complex generic characteristics can be obtained.

In the MIS capacitance method, a dc electric field is applied between the gate electrode and the ohmic contact on the underside of the silicon substrate. For a given value of this field a definite charge distribution in the MIS system will arise. The differential capacitance of the silicon space-charge region is then measured by superimposing a small (mV) a.c. voltage on the d.c. bias. The differential capacitance as a function of the applied bias can then be determined to obtain a capacitance-voltage relationship for the device under test. The relevant theory supporting this technique has been described in Chapter 2.

The arrangement used to obtain C-V curves for the MOSCs studied are shown in Figure 100. The probe assembly and stage were the same as those for the computer controlled I-V technique described above. This C-V system was a Hewlett-Packard HP 4275A multifrequency LCR meter and combined ramped voltage supply which was controlled using a Hewlett-Packard HP 9836 microcomputer. The data acquisition program is shown in Appendix 3. Typical bias voltage ranges were from -35V to +35V (maximum possible magnitudes of gate voltage from the voltage source used) with the capacitance measured at 0.25V increments and from -10V to +10V, in 0.1V increments. Although the style (square wave, sine wave or sawtooth wave), frequency and

magnitude of the superimposed a.c. signal could be varied, measurements were made for a 1MHz sinusoidally varying 0.05V rms a.c. superimposed signal because these are the ideal high-frequency parameters for the C-V curve analysis used. The gate voltage ramp rate was kept constant for all the measurements at $0.25Vs^{-1}$ in order to eliminate high ramp rate anomalies in the C-V curve and to prevent a near static-state capacitance effect which occurs with lower ramp rates[16].

Each MOSC investigated was tested before and after irradiation with various radiation fields and before and after breakdown as soon as was possible in order to minimise room temperature annealing and other effects; the C-V data was stored on floppy-disc and plotted using a Hewlett-Packard flatbed plotter with a standard axis, information and data plotting program.

The above system could also be used to investigate the conductance versus voltage (G-V) characteristics of the MIS system since the series conductance of the device was measured concurrently with the differential capacitance by the HP4275A LCR meter; the same procedure was followed as for C-V data acquisition since the data acquisition program written for the system (shown in Appendix 3) also enabled the microcomputer to store and print the G-V data in the same fashion as for C-V curve plotting. The G-V characteristic has not, however, been used extensively because of ambiguity in the interpretation of the data acquired and served mainly as a check of the position of the flatband voltage characteristic.

A simple analysis to determine the average interface trap density, D_{it}, from the 1MHz C-V curves obtained for the MOSCs has been developed. The procedure requires the measurement of the C-V characteristic in only four points and, although an approximate method, is sensitive to interface trap levels of a minimum of $\approx 2*10^{10} cm^{-2} eV^{-1}$ with an error of, at worst for the greatest substrate doping (where the error would be greatest), of $\approx$ 10% . Although this analysis is based on that of TERMAN[255], it does not require numerical computation nor graphical differentiation of the experimental results. This method and the associated error analysis is presented in Appendix **4**.

Using the results of Chapter **2** and the analysis of JAKUBOWSKI and INIEWSKI[256], a simple series of formulae have been developed to approximately determine the normalised Fermi potential, $|U_F|$, the Fermi potential, U_F, the impurity concentration, N_A (or N_B), and the total oxide charge density from the high-frequency C-V curves of virgin and irradiated MOSCs. These formulae are derived

and presented in Appendix **5**.

A short program to calculate all of these values by using the combined derived formulae for the various characteristics of the 1MHz curves obtained by the C-V technique described above has been written for the BBC 'B' microcomputer and used to analyse quickly the effects of a number of parameters imposed on the MOSCs investigated; this program is presented in Appendix **6**.

The C-V technique and the analysis described above (and in Appendices **4** to **6**) have been used to investigate the nature and characteristics of the MOSCs before and after irradiation and dielectric breakdown given a number of boundary conditions imposed during the investigations; the results of these investigations on Al-SiO_2-Si MOSCs are presented in Chapter **6** and discussed with relevance to the known properties of such devices in Chapter **7**.

5.3 Device Evaluation: Physical Properties

The techniques chosen to investigate virgin and irradiated MOSCs and MOSCs which had undergone dielectric breakdown of some kind all focus on microscopic evaluation of the sufaces and interfaces of the devices; generally the information sought was of a structural rather than chemical basis, although some investigation has been made into the chemical nature of the interfaces and the effects of various radiations on the chemical structure at the Si-SiO_2 interface.

Depth profiling of the various MOSCs under investigation was performed using ion-etching combined with Auger electron spectroscopy (AES) and electron spectroscopy for chemical analysis (ESCA), to provide a qualitative and (approximate) quantitative analysis of various regions in the structures.

Three-dimensional interferometry has been used to examine the surfaces of silicon wafers, before processing, SiO_2 layers (pre-metallization), Al gate electrodes and breakdown pits to determine the physical nature of the various layers, interfaces and breakdown-damaged regions of the Al-SiO_2-Si structure.

Optical and scanning electron microscopy (SEM) have been used to record the surface defects and breakdown pits observed in MOSCs before and after intrinsic and radiation induced dielectric breakdown; SEM combined with fine-beam ESCA apparatus has been used to identify the

elemental composition of breakdown pits in order to clarify the noumena (presented in Chapter **3**) surrounding the description of the pits and their composition.

5.3.1 AES and ESCA Techniques

When an inner-shell vacancy (K, L or M) is created in an atom by electron bombardment in the 1-10KeV range, an outer-shell electron decays into this vacancy; the excess energy associated with this event can be dissipated as either a photon (X-ray emission) or by another electron (Auger emission). The initial energy of the ejected Auger electron is determined by the energy levels involved and is therefore characteristic of the emitting atom. In some cases, the energy of the Auger electron can also reflect the chemical state of the emitting atom. If the emission process occurs sufficiently close to the sample surface (0.3-2nm for 0.05-2KeV electrons), there is a high probability that the Auger electron will escape the sample with its initial characteristic energy. If the Auger electron undergoes an inelastic collision, as will most electrons emitted from deeper than a few atomic layers, it will lose part of its original energy and therefore lose its identity. These inelastically scattered Auger electrons and the various other electron emission processes produce a large "continuum" background in the electron energy spectrum; the discrete Auger peaks are small compared to this large background and require special techniques (spectrum differentiation, for example) to enhance peak-to-background signals.

Auger electron spectroscopy is characterised by the use of a very narrow (0.1-500μm diameter) electron beam (often a 3KeV fine-focussed X-ray gun) used to bombard selected areas of a surface and the subsequent detection and characterisation of the Auger electrons emitted from the bombarded region using complex detection, spectrum differentiation and analysis techniques. Energy and intensity analyses of the Auger electrons permit qualitative and quantitative analyses to be performed on the small volume of material bounded by the diameter of the primary electron beam and the Auger electron escape depth (0.3-2nm, depending on the energy of the Auger transition); the resulting spectrum can show the relative proportions of the elemental composition of the surface in the bombarded region and the energy window for more detailed chemical investigation by ESCA. Review articles by CHANG[257] and SHIRLEY[258] provide very detailed discussion of AES, and the reader is referred to these in particular for further information.

The interaction of X-rays with a sample produces photoionization with the ejection of an inner- or outer-shell electron. The ESCA technique is characterised by the use of a specific photon energy (AlK_a or MgK_a, for examples) for bombardment which, with electron energy analysis permits the determination of the binding energy of the electron from the relationship

$$E_{photoelectron} = E_{photon} - E_{binding} + \Delta E \qquad -117$$

where ΔE is a correction factor for the work function difference between the sample and the electron spectrometer. Since the photon energy (E_{photon}) is fixed, the binding energy ($E_{binding}$) is characteristic of the emitting atom. A surface analysis can be obtained from the electron energy spectrum because the escape depth of the (0.02-1.5KeV) photoelectrons is of the order of 0.3-2nm. The binding energy will invariably be influenced by the surrounding of the emitting atom and thus, photoelectron energy can be used to determine the bonding characteristics of (or the elements bonded to) the emitting atom. When irradiated samples and virgin samples are compared (over the same energy window) using ESCA , the bonds broken by the radiation (if any) can be clearly seen as a small shift in the spectrum due to a change in the bonding characteristics of the atoms in the area under examination; this shift cannot be seen for any other effect than bond damage. Again, for further, more detailed description of the technique and analysis the reader is referred to SHIRLEY[258] and McHUGH[259].

When both AES and ESCA are used in conjunction with ion-beam etching (a technique whereby a finely focussed ($\approx \mu m$) argon or other ion beam is used to sputter a small portion of the surface away to reveal a new area for examination directly ($\approx$ nm) below the previous site) it is possible, by alternate etches and ESCA /AES investigations to examine a long thin cylinder of the sample which enters into the depth of the sample by some distance, depending on the etch-depth between investigations and the number of etches. This can be used to characterise the chemical nature of, for example, the interfaces of Al-SiO_2-Si MOSCs, where the bonding and chemical composition are least well understood and to investigate the effects of irradiation on the chemical nature of the interfaces. For more detailed discussion of ion-beam etching, and its use in conjunction with AES and ESCA, the reader is referred to the review article by MAYER and ZIEGLER[260].

Both AES and ESCA combined with ion-beam etching have been used to characterise the nature of the Si-SiO_2 interface before and after irradiation with various ionizing and non-directly ionizing sources. This was carried out under ultra-high vacuum (10^{-9}mbar) conditions in standard surface analysis apparatus; the system used was a computer controlled Kratos Instruments XSAM 800 combined surface analysis and ion-beam etching system, with a built-in computer analysis and data plotting system (for technical details of this machine the reader is referred to the manufacturers specifications, since further discussion of the machine itself is considered beyond the scope of this thesis).

The question as to whether what is observed using these techniques is due to the externally imposed conditions (bias, breakdown or irradiation) or due to the effects of the X-ray source or ion-beam etching and investigation conditions is one of constant debate among many workers; since, in this study, very great care was taken to reproduce the same testing conditions for each device, this author assumes that the effect of the bombarding X-rays and ion-beam are the same for each device and investigation and, therefore, that a qualitative (and quantitative) analysis between results is valid, the effects of the experimental process being a constant of the same magnitude in each investigation.

The results of these investigations on a variety of Al-SiO_2-Si MOSCs is presented in Chapter 6 and discussed in Chapter7, with relevance to the previously presented models of the Si-SiO_2 interface, the expected effects of radiation upon it and possible influence by the testing techniques.

5.3.2 Three-dimensional Interferometry

The TOLANSKY[261] technique of using the interference fringes produced by the highly reflecting surface of a uniformly flat thin film and a second highly reflective plane sheet or mirror in close proximity with the film to determine the film thickness is a very accurate and widely used method. With the advent of extreme-precision computer-controlled interferometers, and the recent development of computational methods for ellipsometric parameters in non-uniform films on solid substrates[262], a similar technique can be used to determine the microtopography of non-uniform,

"rough" (but still highly reflective) films.

The technique developed by JINSHEN and MINGQI[262] for analysis of the interference patterns produced by interferometry with a non-uniform, rough film has been used by 3M, Swansea (UK), to develop a computer-controlled interferometer to study small areas of such films on a microtopographic basis[263] and to provide a three-dimensional image of the area under examination with various statistical analyses to determine the surface roughness and mean surface defect height (or depth). Typical areas of examination were of the order of $\approx 100\mu m^2$. This apparatus and technique has been used in this study to examine the surface of the Al gate electrodes, thermally grown layers of SiO_2-on-Si and Si substrates of the MOSCs before and after irradiation, and intrinsic and radiation induced dielectric breakdown; the very complex description of the interferometer and mathematical analysis are thought to be beyond the scope of this thesis and the reader is referred to 3M, Swansea for further information [263].

The results of these investigations, presented in Chapter **6**, have been used to describe the nature of the Si surface and Si-SiO_2 interface before and after irradiation and breakdown and in Chapter **7** the conclusions drawn from these findings have been used to dispute the proposed nature of these regions (as discussed in Chapter **2**).

5.3.3 Microscopy

Simple microscopy techniques have been used to examine the surfaces of MOSCs before and after irradiation and breakdown to determine the size and shape of the breakdown pits.

Optical microscopy was performed using Riechert and Olympus microscopes to magnifications of up to *2k and images recorded with non-distorting (35mm and Polaroid) cameras. These were used to count breakdowns and to measure the diameter of breakdown holes (using standard metric graticules) to determine the (approximate) size of the breakdown pits for various intrinsic and radiation-induced breakdowns.

More detailed examination of the electrode surface and breakdown pits was carried out using a Cambridge Stereoscan scanning electron microscope with integral Kevex detector and LINK system for electron spectroscopy of the area of the sample (typically $1\mu m^2$) under investigation.

Magnifications of up to *20k have been used to study the nature and elemental composition of the various breakdown pits and to determine the various parameters for breakdown. (The reader is referred to the many texts available on this microscopy technique for information concerning the modes of operation and the instrumentation required for such a microscope, and to Cambridge Instruments for technical specifications of this particular instrument).

The results of these investigations on Al-SiO_2-Si MOSCs are presented in Chapter **6** and discussed in Chapter **7** with relevance to the proposed nature of such breakdown pits and surface physical characteristics (as presented in Chapter **3**).

5.4 Irradiations: Sources and Techniques

Irradiations of the Al-SiO_2-Si MOSCs described in section **5.1** under various bias conditions have been performed using Am^{241}-alpha and Co^{60}-gamma radiations, accelerator neutrons, Am^{241}/Be neutrons, mixed neutron/recoil-proton fields (neutron-induced from a hydrogenous layer), and Cf^{252} fission-fragments (with concomitant alpha and neutron fields). These were performed on all the oxide thickness and types of devices concurrently using the novel bias arrangement described in section **5.1.3** and on a series of individual devices using the voltage probe assembly described in section **5.2.1**, (except for the accelerator-neutron irradiations which were only on board-mounted devices).

The sources, their characteristics and theexperimental arrangement for each type of irradiation are described in the proceeding sections; theparameters for each bias-board irradiation are tabulated in Tables13. The calibration and dosimetry calculations for each radiation source used are presented in Appendices **7** to **12**.

5.4.1 Alpha-particle Irradiations

The alpha-particle irradiations were performed with a 0.108mCi $_{95}Am^{241}$ source provided by Berkeley Nuclear Laboratories, Gloucestershire. This was in the form of a 10mm diameter disc of the isotope mounted on an 11mm diameter stud (with 5BA, 7mm long screw fitting on the backside).

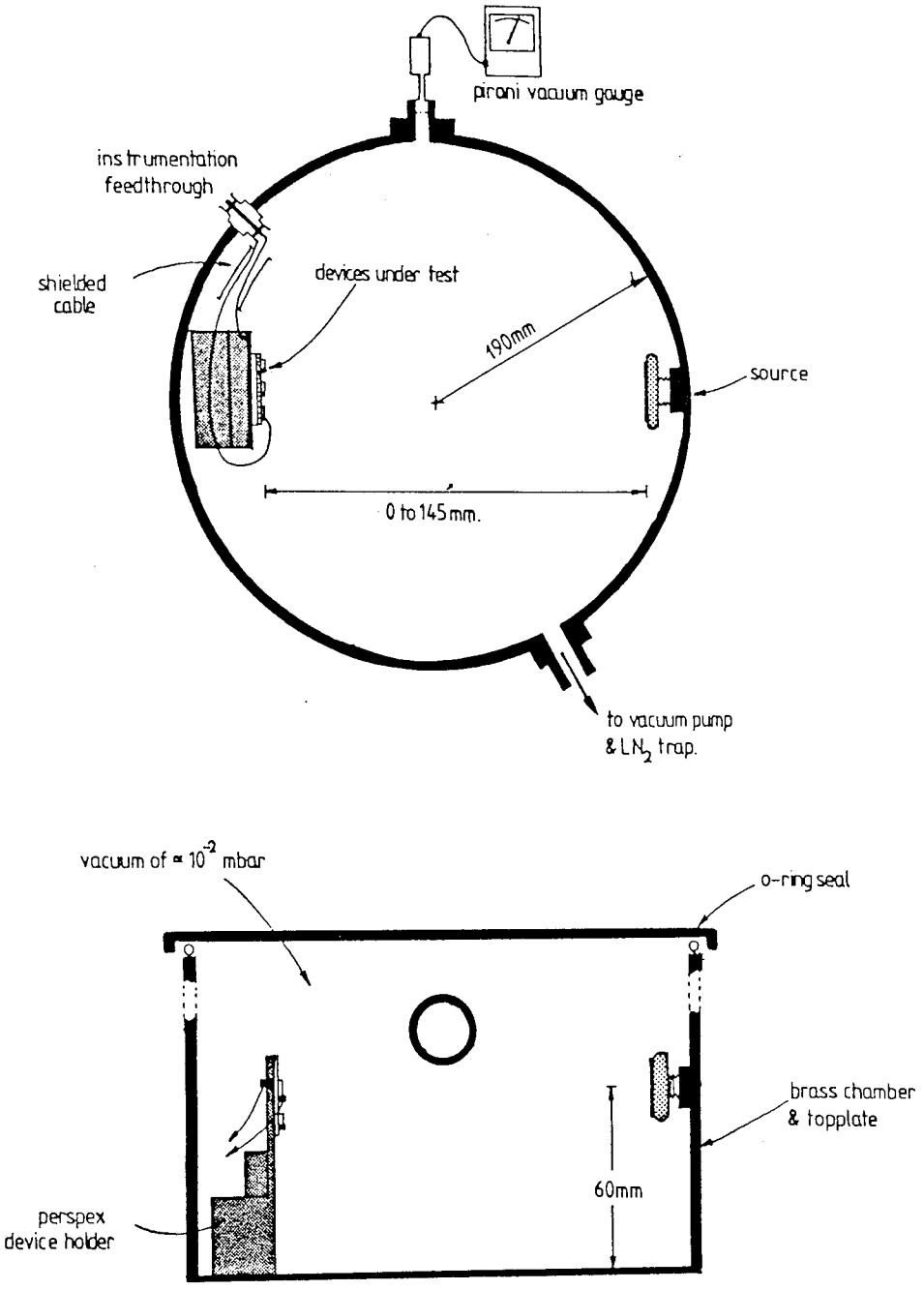

Figure 101: A schematic diagram of the vacuum irradiation chamber.

The source characteristics are given below in Table 11.

Nuclide and half-life	*Decay type*	*Particle energies and transition probabilities* MeV		*Electromagnetic transitions* MeV	
$_{95}Am^{241}$	Alpha	5.387	1.6%	0.026	2.5%
		5.442	12.5%	0.033	0.1%
433 years		5.484	85.2%	0.043	0.1%
		5.511	0.20%	0.0595	35.3%
		5.543	0.34%	0.099	0.02%
		others	low	0.103	0.02%
				0.125	0.004%
				others	low

Table 11. Am^{241} alpha-particle source characterstics.

(After Reference 264).

All the irradiations were carried out in a vacuum of approximately $3*10^{-2}$mbar in the vacuum chamber shown (schematically) in Figure 101; the chamber was easily evacuated to this pressure with a standard Genevac single-stage rotary vacuum pump and liquid nitrogen trapping. The source calibration details and calculations of the absorbed doses in SiO_2, and so on, are presented in Appendix **7**. The total absorbed dose, dose rate and other parameters for the bias-board alpha-irradiations are presented in Table 13.

These irradiations have been used to study the effects of alpha-irradiation on the various electrical parameters of the Al-SiO_2-Si MOSCs (determined from the C-V and I-V techniques) and also to investigate the pulses produced in MOSCs as a result of irradiation combined with a study of the possibility of RIDB by alpha-irradiation. The results of these investigations is presented in Chapter **6** and these are discussed in Chapter **7** with respect to the results of other workers (as presented in Chapters **3** and **4**).

5.4.2 Gamma Irradiations

The gamma-irradiations were performed using two sources: the majority of the irradiations were performed on bias-board mounted devices using the Precisa 217 (Pantatron Ltd) gamma-irradiation

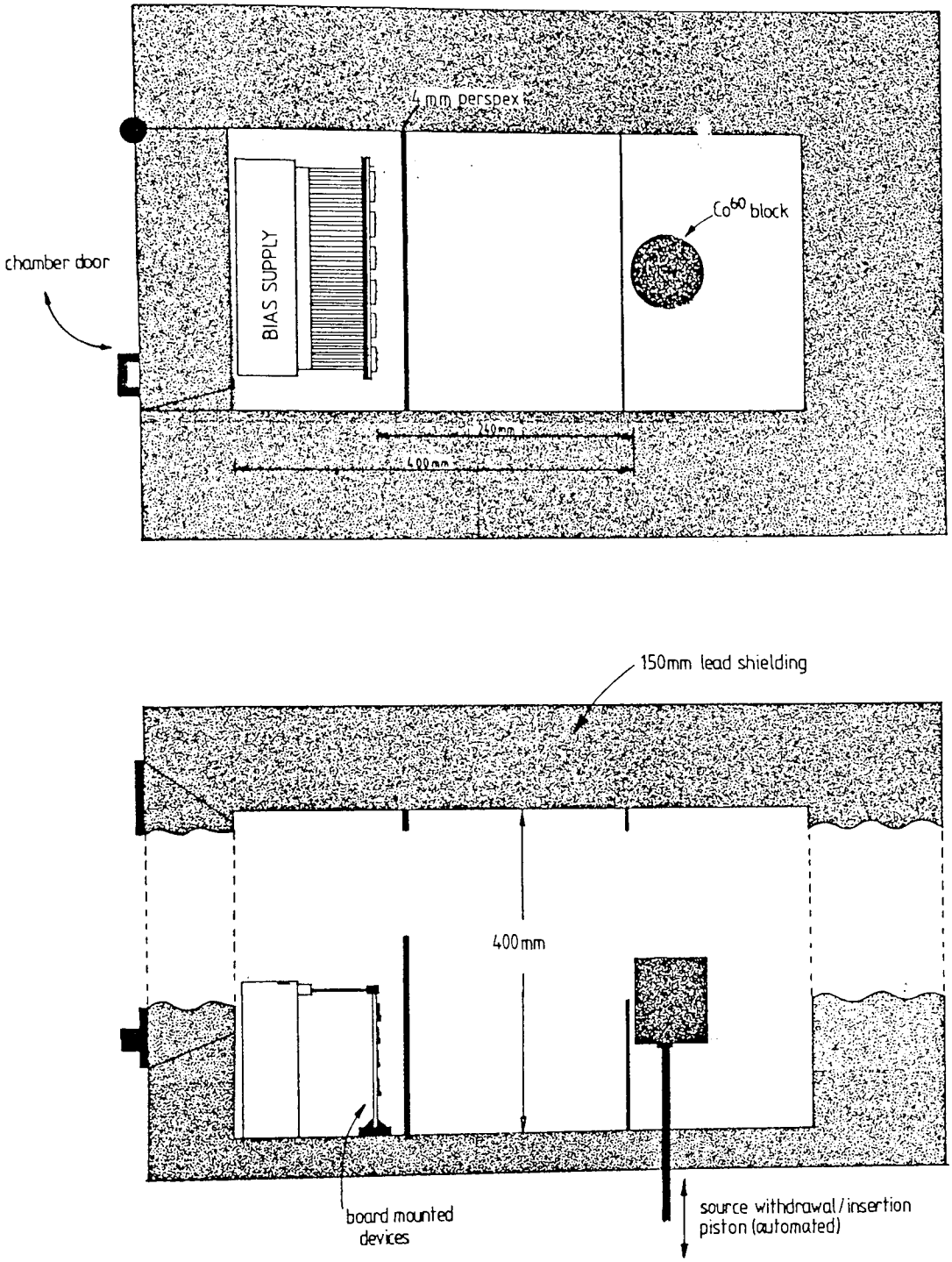

Figure102: The experimental arrangement of the high dose-rate Co^{60} gamma irradiation facility.

facility at Birmingham University (UK); the source was a 950Ci $_{27}Co^{60}$ source arranged in the configuration shown (schematically) in Figure 102. Other gamma irradiations were performed in-house on single devices with an approximately 2mCi $_{27}Co^{60}$ source in the evacuable chamber shown in Figure 101. Both sources have the same characteristics, given below in Table 12. The calibration calculations and absorbed dose in SiO_2 calculations are presented in Appendix **8.** The total absorbed dose, dose rate and other parameters for the bias-board gamma-irradiations are presented in Table 13.

Nuclide and half-life	*Decay type*	*Particle energies and transition probabilities* MeV		*Electromagnetic transitions* MeV	
$_{27}Co^{60}$	β^-	0.318	99.9%	1.173	99.86%
		1.491	0.1%	1.333	99.98%
5.27years				others	<0.01%

Table 12. Co^{60}gamma-irradiation source characterstics.

(After Reference 264).

These irradiations have been used to study the effects of gamma-irradiation on the various electrical parameters of the Al-SiO_2-Si MOSCs (determined from the C-V and I-V techniques) and also to investigate the pulses produced in MOSCs as a result of irradiation combined with a study of the possibility of RIDB by continuous gamma-irradiation (no investigation of pulsed gamma-irradiation was possible). The results of these investigations is presented in Chapter **6** and these are discussed in Chapter **7** with respect to the results of other workers (as presented in Chapters **3** and **4**).

Board number:	*Radiation type*	*Dose rate* $KRad(SiO_2)hr^{-1}$	*Integrated dose* $KRad(SiO_2)$
13	alpha	$(4.89\pm0.02)*10^{-2}$	10.00±0.75
14	alpha	$(4.89\pm0.02)*10^{-2}$	5.00±0.38
15	alpha	$(4.89\pm0.02)*10^{-2}$	1.00±0.075
16	alpha	$(4.89\pm0.02)*10^{-2}$	0.5±0.038
17	gamma	(1.359±0.001)	10.01±0.68
18	gamma	(1.359±0.001)	5.01±0.34
19	gamma	(1.359±0.001)	1.01±0.068
20	gamma	(1.359±0.001)	0.51±0.035

Table 13. Alpha and gamma irradiation parameters.

5.4.3 Neutron Irradiations

Two neutron sources were used: a series of irradiations were performed using the low-scatter facility associated with a 3MV Van de Graaff at the National Physical Laboratories, Teddington (UK). A series of irradiations to integrated flux densities of (approximately) 10^5, 10^6, 10^7, and 10^8 neutrons cm^{-2} using 0.5MeV, 1MeV, and 2.5MeV neutrons were made on a number of bias-board mounted devices. Twelve boards were used in all. The neutron energies used and neutron fluence for the bias-board neutron irradiations are presented in Table 14. The reactions used, particle beam parameters, target properties and resulting neutron energies are presented in Appendix **9**, together with details of the calibration of the neutron fluences and energies used for the irradiations.

A 3Ci $_{95}Am^{241}$/Be source was used to irradiate a number of devices with gate biases applied using the voltage probe assembly described in section **5.2.1**; these were performed in-house under standard neutron-irradiation conditions with the source (a cylindrical block of Am^{241} and powdered Be, ≈22mm in diameter and ≈60mm long, encased in a thin lead container and connected to a 1m long handling rod) positioned at such a distance from the device under irradiation to permit uniform

irradiation, typically 15cm. Concomitant gamma-radiation from the Am^{241}/Be source were shielded from the device by 3.5mm of lead placed around the source.The source calibration details, source neutron energy spectrum, and calculations of the absorbed doses in SiO_2, displacement damage caused by the neutrons and other details are presented in Appendix **10**.

These irradiations have been used to study the effects of neutron-irradiation on the various electrical parameters of the Al-SiO_2-Si MOSCs (determined from the C-V and I-V techniques) and also to investigate any pulses produced in MOSCs as a result of irradiation combined with a study of the possibility of RIDB by neutron-irradiation. The results of these investigations is presented in Chapter **6** and these are discussed in Chapter **7** with respect to the results of other workers (as presented in Chapters **3** and **4**).

5.4.4 Recoil-proton Irradiations

For neutron energies less than approximately 290MeV, when a neutron collides with a nucleon it undergoes mainly elastic scattering; for neutron energies less than approximately 8MeV, neutrons which impinge on an absorber containing hydrogen may undergo a variety of nuclear reactions, one of which is the (n,p) reaction whereby a recoil-proton is produced in the interaction. A typical absorber might be a thin (≈mm thick) hydrogenous radiator such as a plastic. Other reactions might include elastic (n,alpha), (n,gamma) and inelastic (n,n) reactions, but the cross-section for these are small compared with that for the elastic (n,p) reaction, which is between approximately 8 and 1 barns for incident neutron energy of 0.4 to 10MeV (the approximate energy range of neutrons available for the investigations in this project).

A thin (0.13mm thick) hydrogenous sheet (plastic, ≈11mgcm^{-2}) in contact with the Al gate electrode was used as the recoil-proton radiator for this study, used with the two neutron sources described above; a strip of this material was positioned over a strip of various MOSCs on each bias board as shown in Figures 91(a) and 91(b). The various details of cross-sections for interactions, recoil-proton/neutron ratios for each neutron energy and dose, and other calculations and details of these irradiations are presented in Appendix **11**. The recoil-proton fluence and initiating neutron energy for the bias-board recoil-proton irradiations is presented in Table 14.

These irradiations have been used to study the effects of mixed neutron/recoil-proton radiation fields on the various electrical parameters of the Al-SiO_2-Si MOSCs (determined from the C-V and I-V techniques) and also to investigate any pulses produced in MOSCs as a result of this radiation combined with a study of the possibility of RIDB by recoil-protons. It has been suggested[14] that if recoil-protons produced by neutrons in the energy range 0.1-10MeV induce breakdowns in Al-SiO_2-Si MOSCs, this may be a valuable neutron personal-dosimetry technique; the feasibility of this proposal and the results of the various investigations described above are presented in Chapter **6** and discussed in Chapter **7** with respect to the results of other workers (as presented in Chapters **3** and **4**).

Board number:	*Neutron energy* MeV	*Neutron fluence* n cm^{-2}	*Recoil-proton fluence* p cm^{-2}
1	1.056 ± 0.024	$(1.00\pm0.030)*10^8$	$(4.34\pm0.17)*10^4$
2	1.056 ± 0.024	$(1.89\pm0.033)*10^7$	$(8.47\pm0.34)*10^3$
3	1.056 ± 0.024	$(1.12\pm0.034)*10^6$	$(5.02\pm0.21)*10^2$
4	1.056 ± 0.024	$(9.60\pm0.077)*10^4$	$(3.53\pm0.10)*10^1$
5	0.496 ± 0.005	$(1.02\pm0.031)*10^8$	$(6.38\pm0.32)*10^4$
6	0.496 ± 0.005	$(1.05\pm0.032)*10^7$	$(6.40\pm0.32)*10^3$
7	0.496 ± 0.005	$(1.09\pm0.033)*10^6$	$(6.43\pm0.33)*10^2$
8	0.496 ± 0.005	$(1.11\pm0.089)*10^5$	$(6.45\pm0.34)*10^1$
9	2.499 ± 0.016	$(9.99\pm0.030)*10^7$	$(2.53\pm0.76)*10^4$
10	2.499 ± 0.016	$(9.96\pm0.030)*10^6$	$(2.51\pm0.75)*10^3$
11	2.499 ± 0.016	$(1.00\pm0.030)*10^6$	$(2.53\pm0.76)*10^2$
12	2.499 ± 0.016	$(1.15\pm0.921)*10^5$	$(2.64\pm0.79)*10^1$

Table 14. Neutron and recoil-proton irradiation parameters.

5.4.5 Fission-fragment Irradiations

Fission-fragment irradiations of individual devices were performed using an ≈0.7μCi planar $_{98}Cf^{252}$ source. The source was in the form of a thin disc (25mm in diameter, 0.5mm thick) with an active area of ≈6mm diameter at the centre of the disc; this was held in a simple jig such that the source could be positioned above a device at a known distance from the deviceby using shims of an accurately known thickness, as shown scematically in Figure 103. Irradiations were performed in the vacuum chamber,shown in Figure 101, in order to irradiate the devices with the full spectrum of fission-fragments (so as to irradiate with the most energetic fission-fragments) and in dry air at various known source-to-device separations in order to irradiate with (heavy and light) fission-fragments of lower, calculated energies.

Nuclide and half-life	*Decay type*	*Particle energies and transition probabilities* MeV		*Electromagnetic transitions* MeV
$_{98}Cf^{252}$	alpha	5.974	0.3%	up to ≈9MeV†
		6.075	15%	
2.65years		6.118	81.6%	
		others	low	
	spontaneous fission		3.1%	
	gamma	associated with the alpha-transitions, of low intensity		

Table 15. Cf^{252}fission-fragment irradiation source characterstics.

† The spontaneous fission events and the subsequent decay of fission products produce approximately 20 gamma-rays per fission. This gamma-radiation covers an energy range to ≈9MeV.
Each fission also produces on average ≈4 fast neutrons.

(After Reference 264)

The source characteristics are given above in Table15 and calculations of the fission-fragment intensity, ratios of fission-fragments to alpha and neutron intensities, stopping powers of light and heavy fission-fragments in air(their range), Al and in SiO_2, its spectrum and other characteristics are

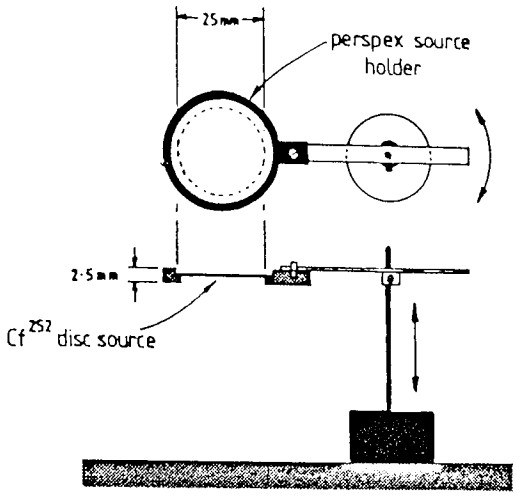

Figure 103: The experimental arrangement of the Cf^{252} source.

presented in Appendix **12**.

Irradiations have been performed to study the effects of fission-fragment irradiation (with concomitant alpha and neutron radiations) on the various electrical parameters of the Al-SiO_2-Si MOSCs (determined from the C-V and I-V techniques) and also to investigate the pulses produced in MOSCs as a result of this radiation. A thorough study of RIDB by the fission-fragments versus fission-fragment residual energy (range in air) and gate voltage, and an investigation into the detection properties of the MOSCs (for examples, the average size of breakdown pits and the maximum numberof RIDBs each type of MOSC could sustain before failure) has revealed a deal of new information on RIDB in Al-SiO_2-Si MOSCs. The results of the various investigations described above are presented in Chapter **6** and discussed in Chapter **7** with respect to the results of other workers (as presented in Chapter **4**). The new findings have been used to dispute previously proposed mechanisms and models of breakdown and to extend the generally accepted KLEIN[234] model for RIDB (presented in Chapter **4**).

In this chapter, the processes and techniques used to fabricate and mount a large number of Al-SiO_2-Si MOSCs and the techniques, experimental arrangements and apparatus used to investigate their electrical and physical characteristics have been described. Various sources of radiations used in this study of radiation effects on Al-SiO_2-Si MOSCs have been briefly described in terms of their physical and nuclear characteristics; for more detailed descriptions of the physical and nuclear nature of these sources, their radiations and their detection and associated dosimetry, the reader is referred to the technical data available[264] and the various texts available on the subject.

CHAPTER SIX.

EXPERIMENTAL FINDINGS

In this chapter the results of a series of detailed investigations into the physical and electrical nature of the Al-SiO_2-Si MOSCs described in Chapter 5 under various conditions are presented. These investigations were motivated by the need to understand the effects of several radiations on the dielectric breakdown process in such devices in order to evaluate the feasibility of the devices as "breakdown detectors" of radiations by RIDB, in particular as neutron detectors via the (n,p) reaction in a hydrogenous layer placed in close contact with an MOSC.

Firstly, results are presented for investigations of the unirradiated Al-SiO_2-Si MOSCs showing their innate electrical and physical characteristics under various bias conditions, including intrinsic and defect-related dielectric breakdown. Results are then presented for these (Al-SiO_2-Si MOSC) devices under various conditions of bias and irradiation, with the effects of each radiation field on the physical and, particularly, the electrical nature of the devices being evaluated using the criteria and techniques presented in previous chapters.

These results are discussed in detail in Chapter 7, which considers the effects of each radiation field individually, and radiation en masse, on the Al-SiO_2-Si MOSCs tested, with a particular emphasis on intrinsic dielectric breakdown and the various changes in the breakdown characteristics, and other electrical properties, of such devices as a result of exposure to the various radiations.

6.1 The Virgin Al-SiO_2-Si MOSCs

In order to determine the innate characteristics of each batch of devices, two chips of each device type and oxide thickness were investigated prior to any form of mounting, biasing or irradiation. To ensure valid comparisons of devices under different conditions can be made, these were taken from the same batch of devices as those used in all the investigations.

Physical investigation of a selection of the devices (using scanning electron microscopy and 3-d interferometry) has revealed that the surface of the silicon wafer at the pre-processing stage is not perfectly flat and smooth, as can be seen on the typical interferogram in Figure 104 for a standard Czochralski-grown <100> silicon wafer; the approximate surface roughness is 4.6nm RMS which would suggest a field enhancement of at worst +13% in a 40nm thick device which, according to

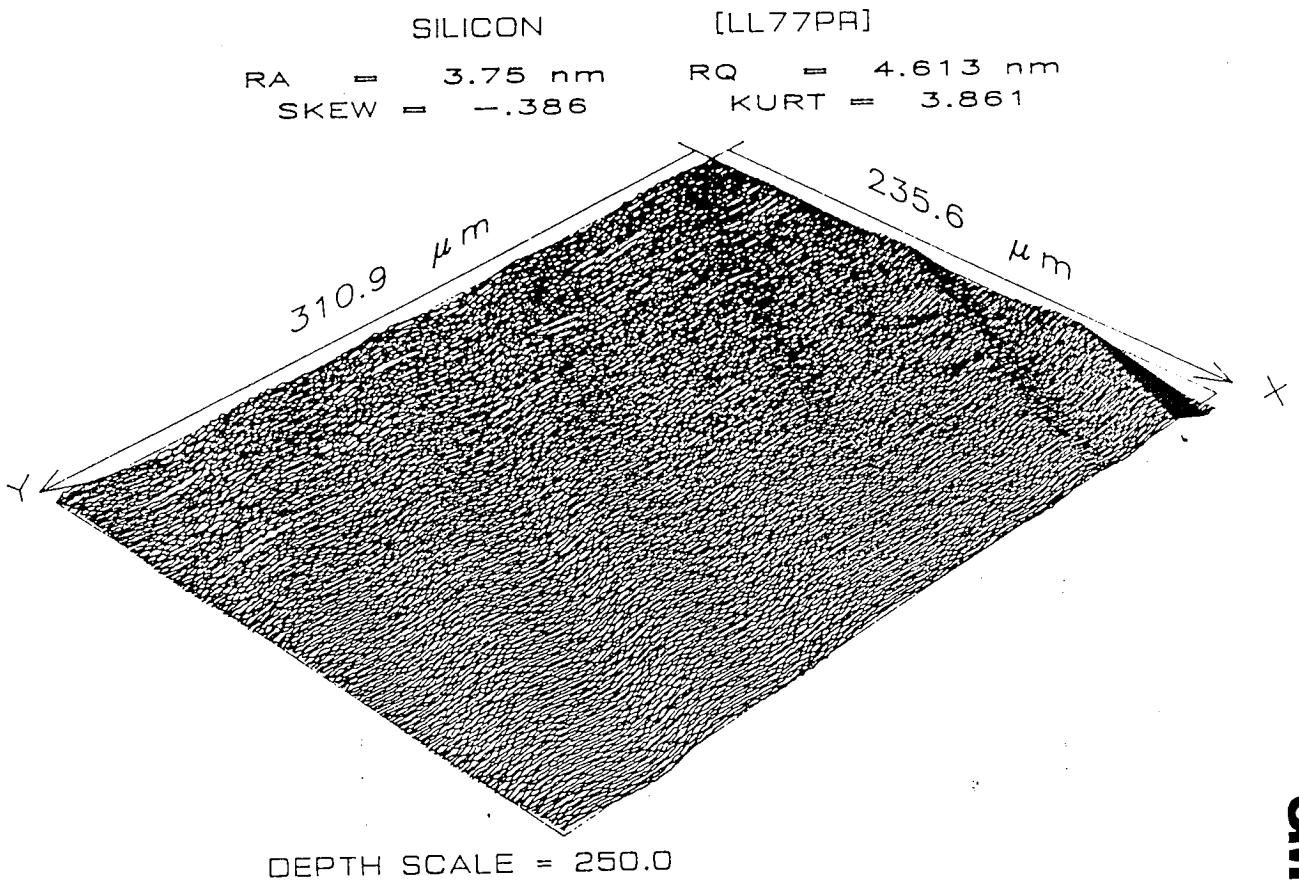

Figure 104: An interferogram of a Czochralski-grown silicon wafer before processing. RA is the centre line average roughness; RQ is the root mean square roughness; SKEW is the degree of asymmetry or departure from symmetry of the aperity distribution; KURT is the degree of peakedness of a distribution, relative to a normal distribution.

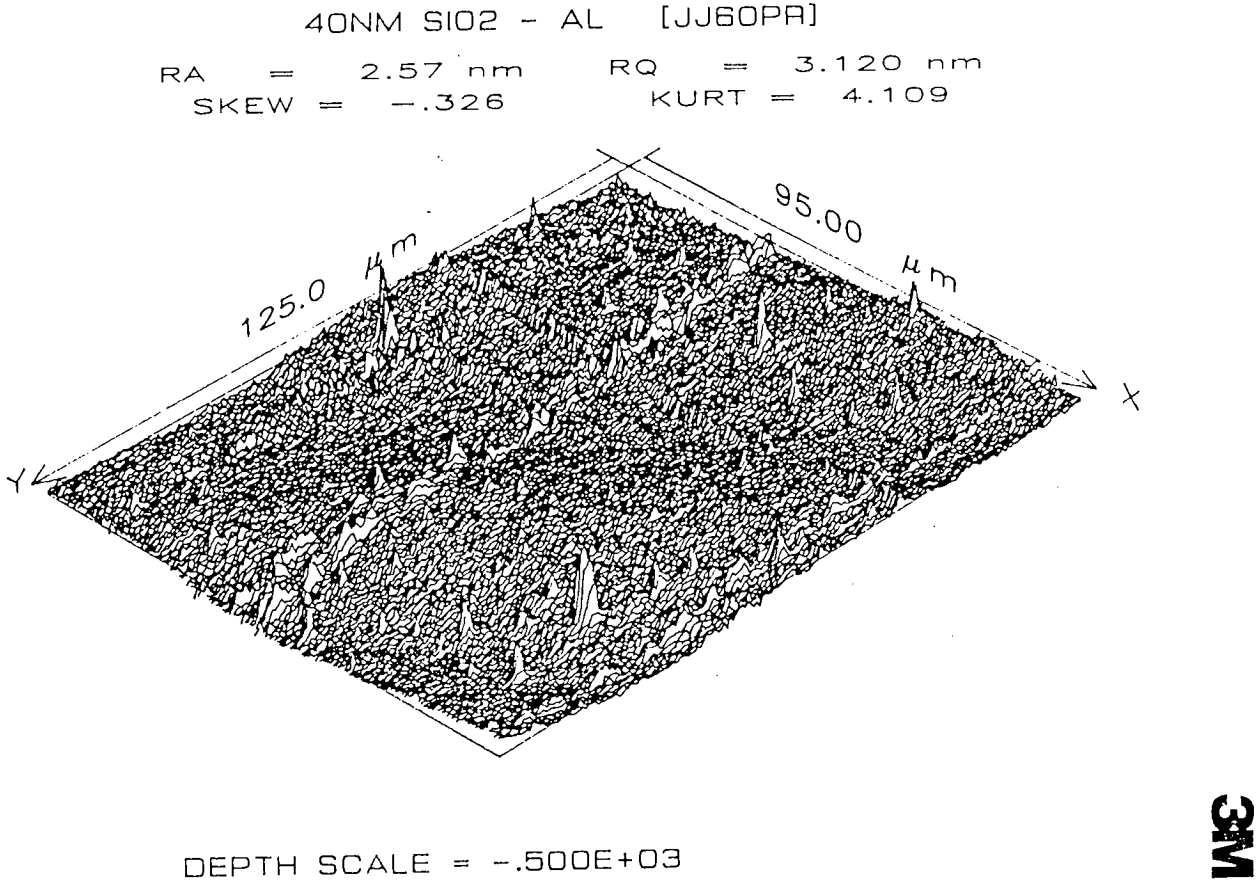

Figure105: An interferogram of the Al-SiO_2 interface of a 40nm oxide MOSC after Al etch-off using 60% NaOH solution.
The interferogram shows an inverted view of the surface in order to aid measurement of surface imperfections.

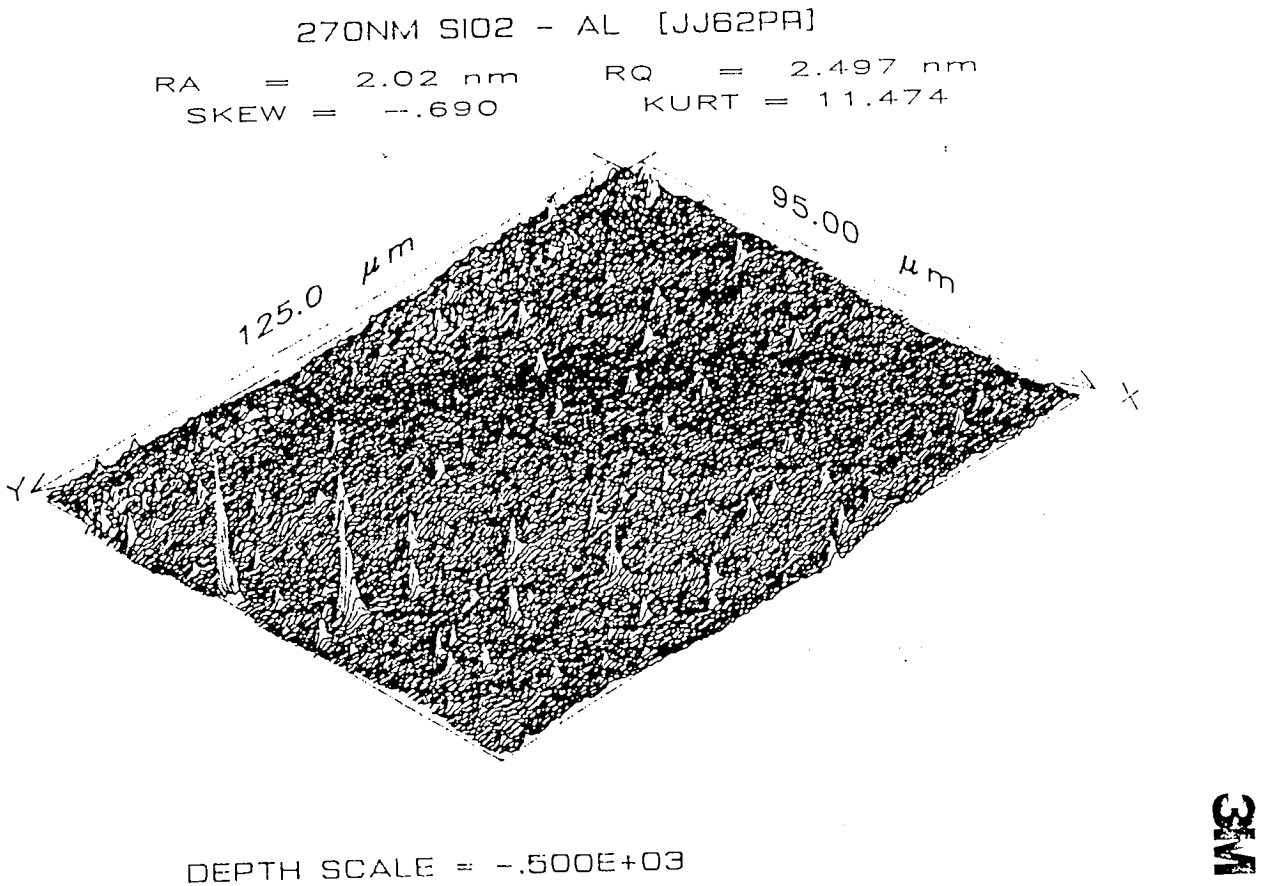

Figure106: An interferogram of the Al-SiO_2 interface of a 270nm oxide MOSC after Al etch-off using 60% NaOH solution.
The interferogram shows an inverted view of the surface in order to aid measurement of surface imperfections.

the KLEIN model[234], is large enough to initiate defect-related breakdown; this, however, would not produce a large enough field enhancement to initiate breakdown in a much thicker device, the enhancement being only ≈2% in a 270nm thick oxide device, far smaller (according to KLEIN[152,234]) than the critical field enhancement factor necessary for defect-related breakdown in even the thinnest of devices.

A post-metallization etch-off experiment (using a 20 second immersion in 50% NaOH solution at room temperature to remove the Al electrodes, rinse in deionized water followed by hot-air drying) on a variety of devices has revealed that the surface of the SiO_2-Al interface is also not flat and smooth as assumed. Figures 105 and 106 show inverted-field interferograms of two such etched devices, typical of the large sample tested; clearly visible are a number of dimples as large as ≈30nm into the SiO_2 and scratches across the oxide surface of the order of 10nm, which were at first thought to be replicas of the defects on the silicon substrate after oxide growth. However, from comparison with a similar interferogram of an unmetallized wafer after oxide growth, shown in Figure 107, again typical of the batch tested, it is clear that these are due either to the etch process or due to damage before or during metallization. Figure 108 shows a sample which was not metallized but was etched in a similar way to the metallized chips and shows no sign of such surface defects; it has been concluded that the metallization process is the cause of such surface defects, possibly due to back-sputtering of the oxide surface at already weak spots during Al deposition using the magnetron sputterer. Such large defects could cause field enhancements of the order of +12% in the 270nm devices (and +75% in the 40nm devices) which, combined with the enhancement due to the surface roughness of the underlying substrate provide large enough field enhancement factors for defect-related breakdown to occur at below the expected field range, as noted by several workers[149-151] (and is described in Chapter 2).

The Si-SiO_2 interface of several processed silicon wafers was examined using AES and ESCA combined with ion beam etching. Figures 109(a) - (c) show a typical series of AES spectra for the SiO_2 layer, the Si-SiO_2 interface, and the Si substrate, respectively for successive ion-beam etches on a 40nm thick oxide device, etching through the oxide to the silicon substrate. The etch-rate was determined to be similar to that of silicon nitride (which was used as a guide rate) at approximately 1.5nm min^{-1}. From a detailed ESCA analysis of the region determined by AES to be the interface,

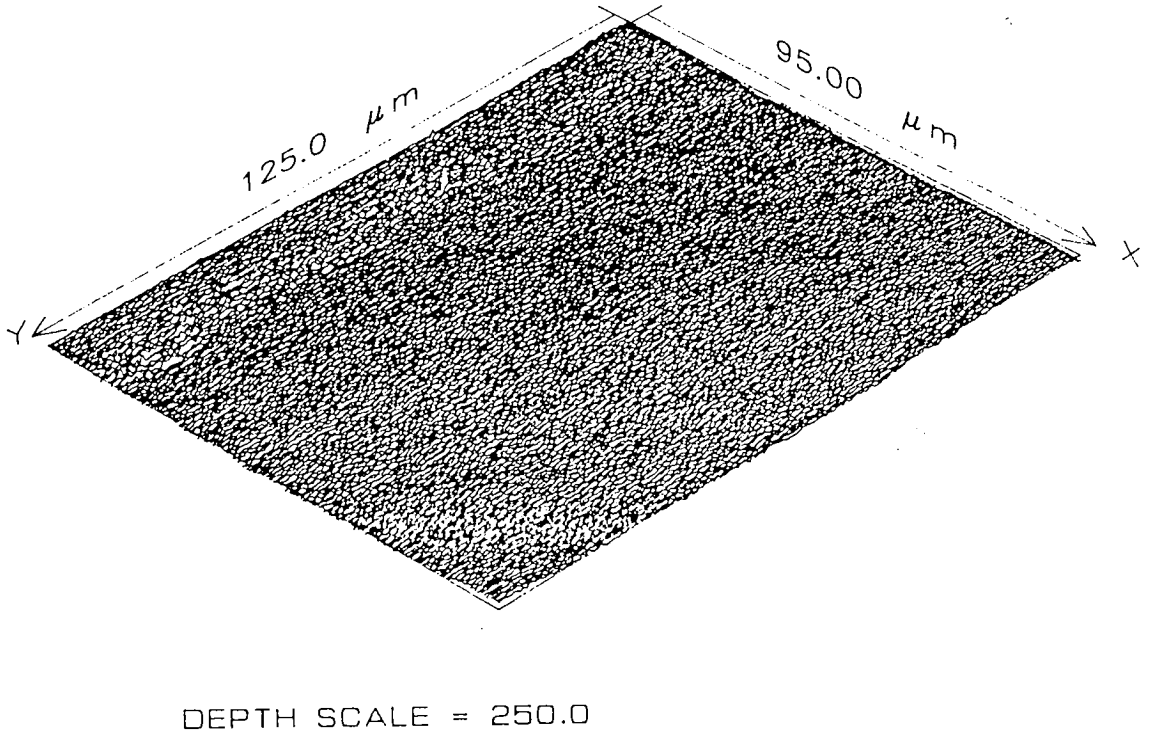

Figure107: An interferogram of the surface of a 1200nm thick SiO_2 layer at the pre-metallization stage.
[The surface wave pattern seen is not due to the sample surface but the interferometer and is corrected for in the analysis for the surface characteristics].

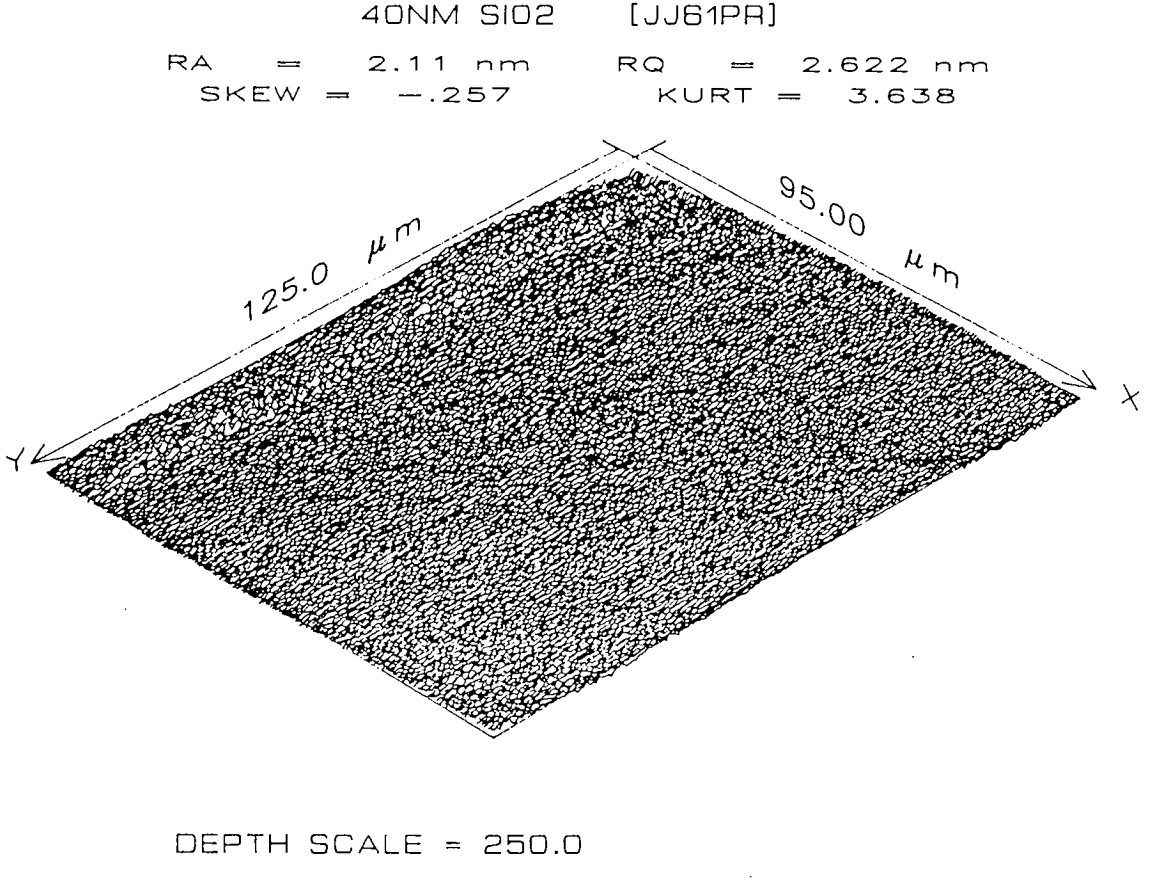

Figure108: An interferogram of the surface of a 40nm thick SiO_2 layer at the pre-metallization stage after 60% NaOH etch process.

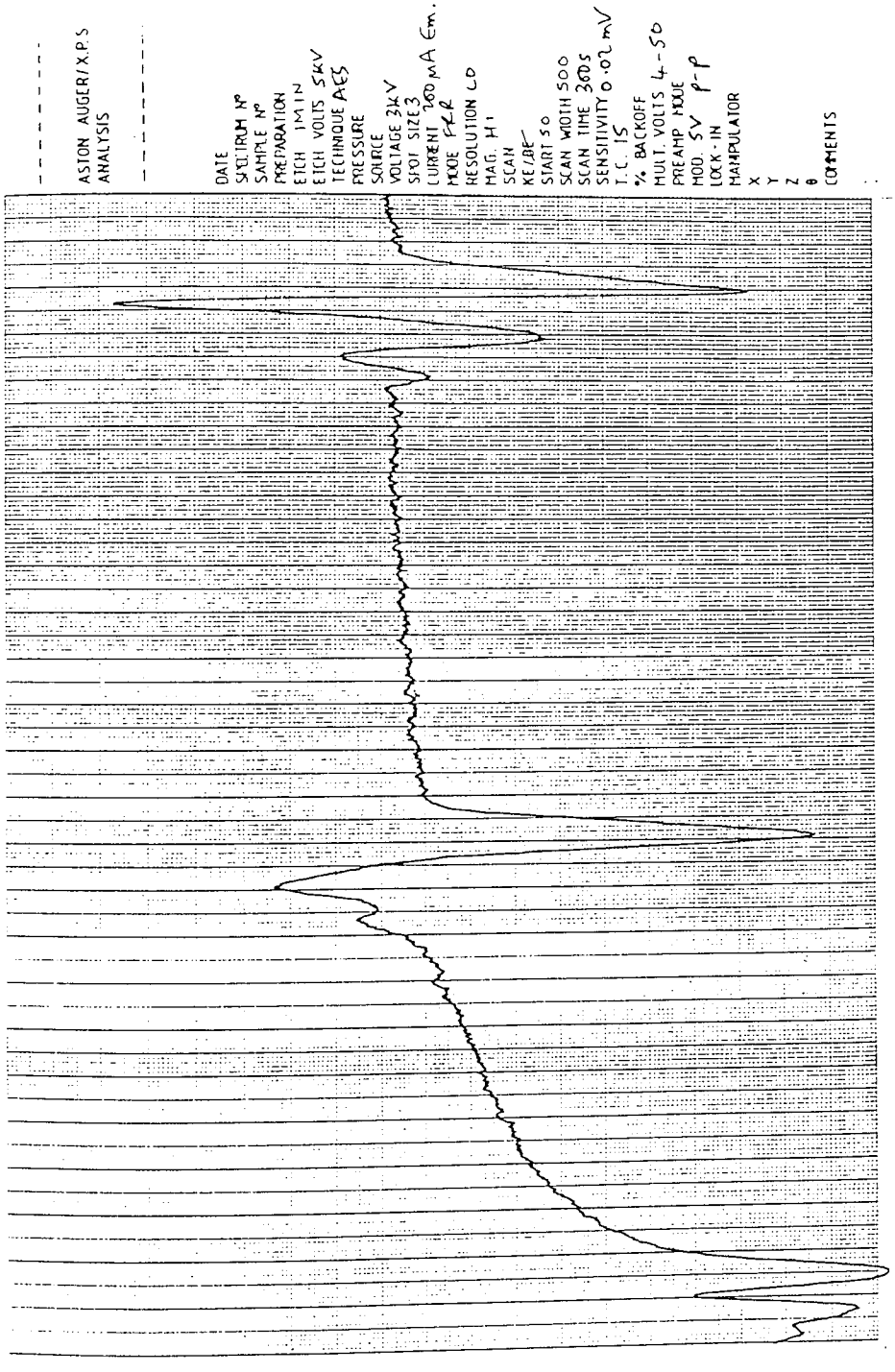

Figure109: (a) An AES spectrum of a virgin, thermally grown SiO_2-on-Si layer. The oxide layer was 60nm thick, and grown on p-type silicon substrate using the fabrication processes described in the text.

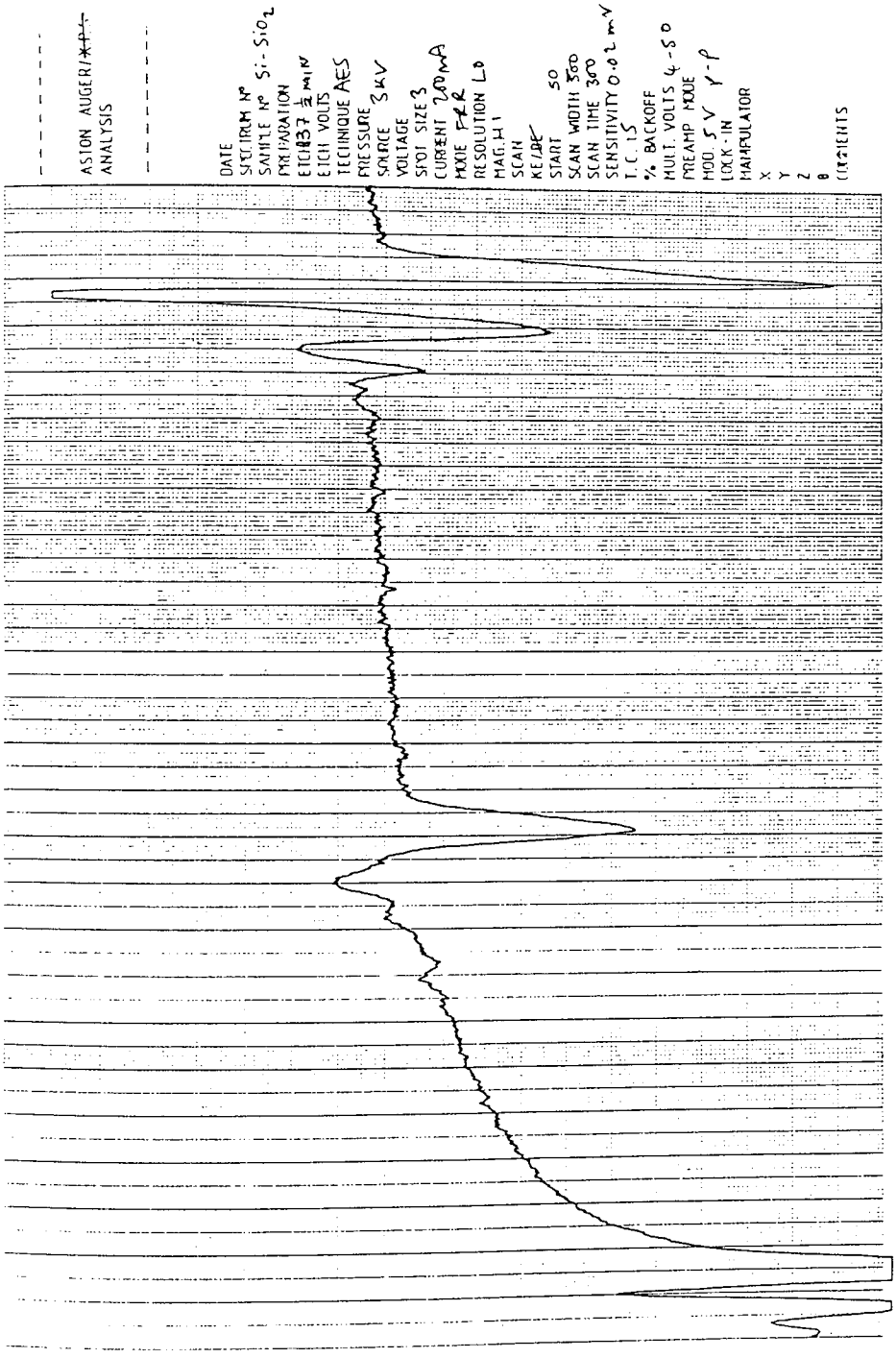

Figure109: (b) An AES spectrum of a virgin, thermally grown SiO_2-Si interface. The oxide layer was 60nm thick, and grown on p-type silicon substrate using the fabrication processes described in the text.

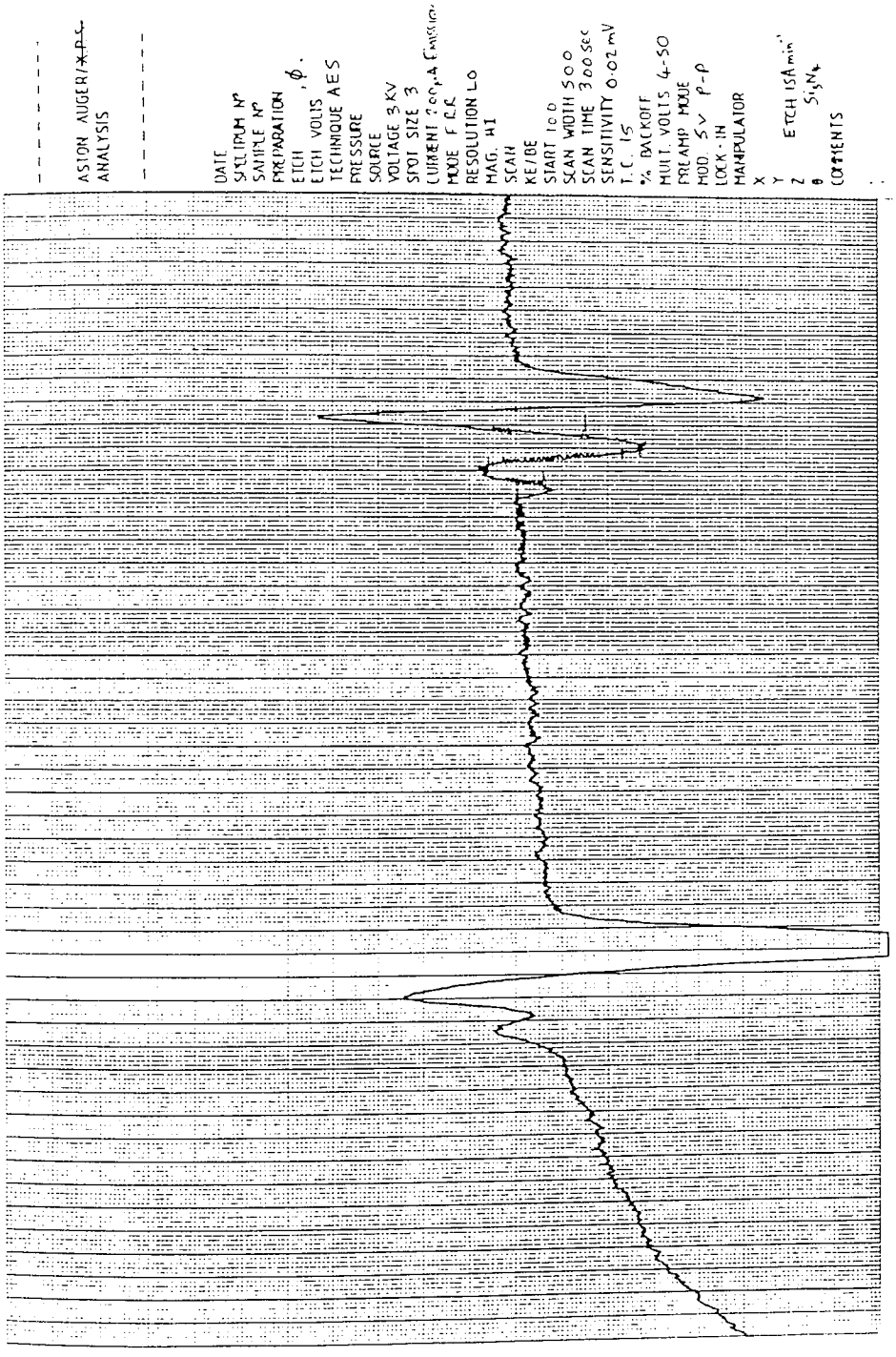

Figure 109: (c) An AES spectrum of a virgin Si wafer.

shown in Figure 110, it is perhaps evident that the interface is composed of SiO_2 with a slight excess of silicon (perhaps 3%) compared with the spectrum for the SiO_2 layer for the same sample. However, because of the unquantified effects of the ion-beam, the possibility of the etch-pit reaching into the silicon substrate at its apex when data recorded is from all around the pit, and the low resolution of the apparatus (and technique) used, no firm conclusion as to the nature of the interface should be inferred from these results. However, it may be conjectured that this excess of silicon is evidence of a silicon-rich layer adjacent to the interface as proposed by GRUNTHANER et al[63] and HERMANN et al[64] (as described in section **2.5.1**). No evidence of large concentrations of any ionic species was found either in the bulk oxide layer or at the Si-SiO_2 interface, although the poor sensitivity of the techniques used (at best, a less than 3% concentration of any species in the $100\mu m^2$ area investigated is undetectable) which may not detect such species does not preclude their existence.

The devices were typical of high-quality industrially fabricated MOS structures, as is clearly seen by their 1MHz C-V characteristics shown in Figures 111 and 112 for typical n-type and p-type devices of various thicknesses, respectively; their electrical parameters (calculated using the approximate calculations and computer program given in Appendices 4-6) are tabulated in Table 16 which, for comparison with results shown later for other investigations, shows the average values for the density of interface states, oxide charge density, flatband voltage shift, and normalised Fermi potential for each type and thickness of oxide device investigated.

The similarity between these curves and the ideal MOSC curves shown in Chapter **2** clearly demonstrates their nearness to ideal device parameters, with flatband voltage shifts of the order of -1.5V showing a trapped positive oxide charge of approximately 10^{11} q cm^{-2} eV^{-1}. However, on Figure 111 for the 1MHz C-V characteristics of the n-type devices, a slight distortion or flattening in the C-V curves at numerically large negative voltages (less than ≈ -3V) can be seen; this is possibly due to the high doping density of the silicon substrate and an insufficient post-metallization anneal to remove fast-surface states from the interface (the effects of which have been discussed in section **2.5.2**). At more negative voltages (less than ≈ -12V) a decrease in the expected capacitance can be seen; this may be attributed to deep depletion effects due to deeply-trapped ionic species (perhaps sodium?) which have been incorporated at some time during oxide growth.

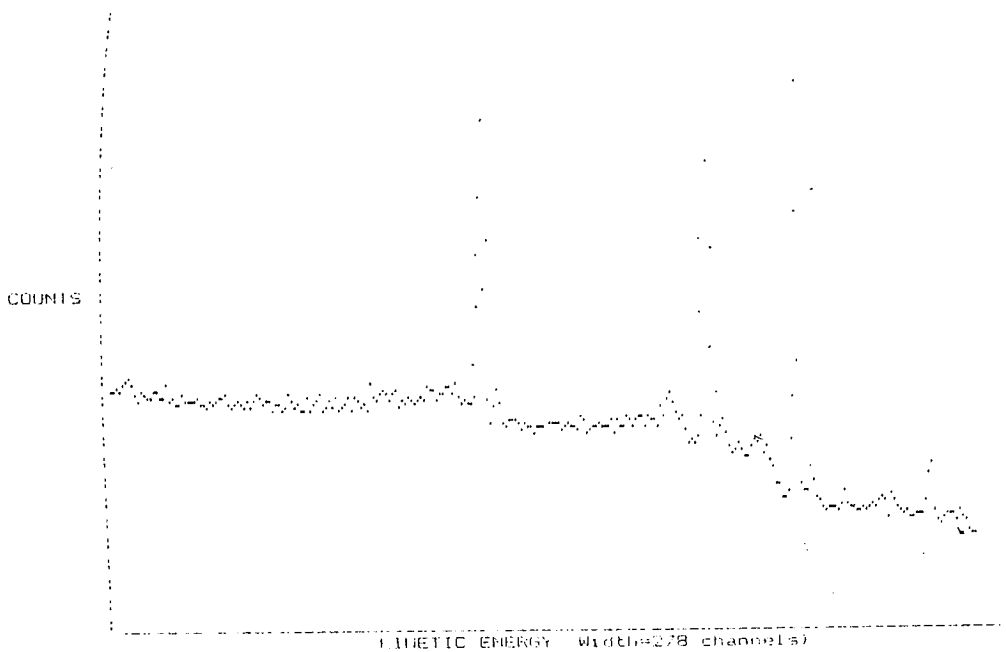

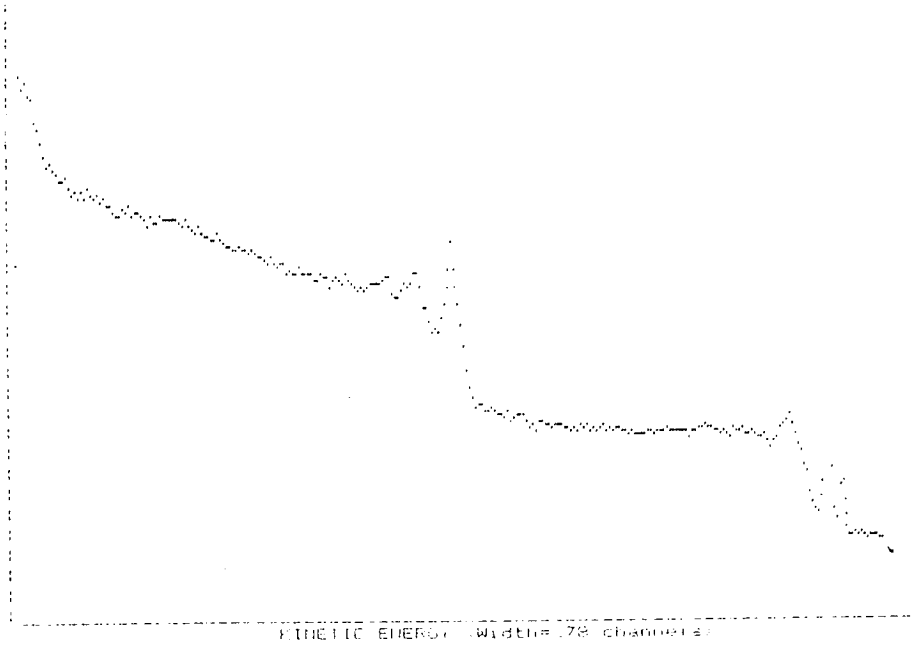

**********Spectral Information**********
Spectrum Number=5
Sample:- P21-25-s00C Region:-WIDE
Magnesium X-ray Radiation Source
Gun Voltage=15 kV Gun Current=15 milliamps
Fat-Constant Analyser Energy, Energy=50
Source Slit=3 Analyser Slit=3
Counting Period= 1.00 seconds

Number of Scans	1
Step size in electron volts	1.00000
Number of channels	900
Maximum number of counts in spectrum	9296
Scale factor(multiply counts by this factor)	1
Scan width(e.v)	500.0
Start kinetic energy(e.v)	251.0

**********Spectral Information**********
Spectrum Number=5
Sample:- P21-25-s00C Region:-WIDE
Magnesium X-ray Radiation Source
Gun Voltage=15 kV Gun Current=15 milliamps
Fat-Constant Analyser Energy, Energy=50
Source Slit=3 Analyser Slit=3
Counting Period= 1.00 seconds

Number of Scans	1
Step size in electron volts	1.00000
Number of channels	901
Maximum number of counts in spectrum	3296
Scale factor(multiply counts by this factor)	1
Scan width(e.v)	501.0
Start kinetic energy(e.v)	250.0

Figure 110: An ESCA spectrum of the Si-SiO_2 interface.

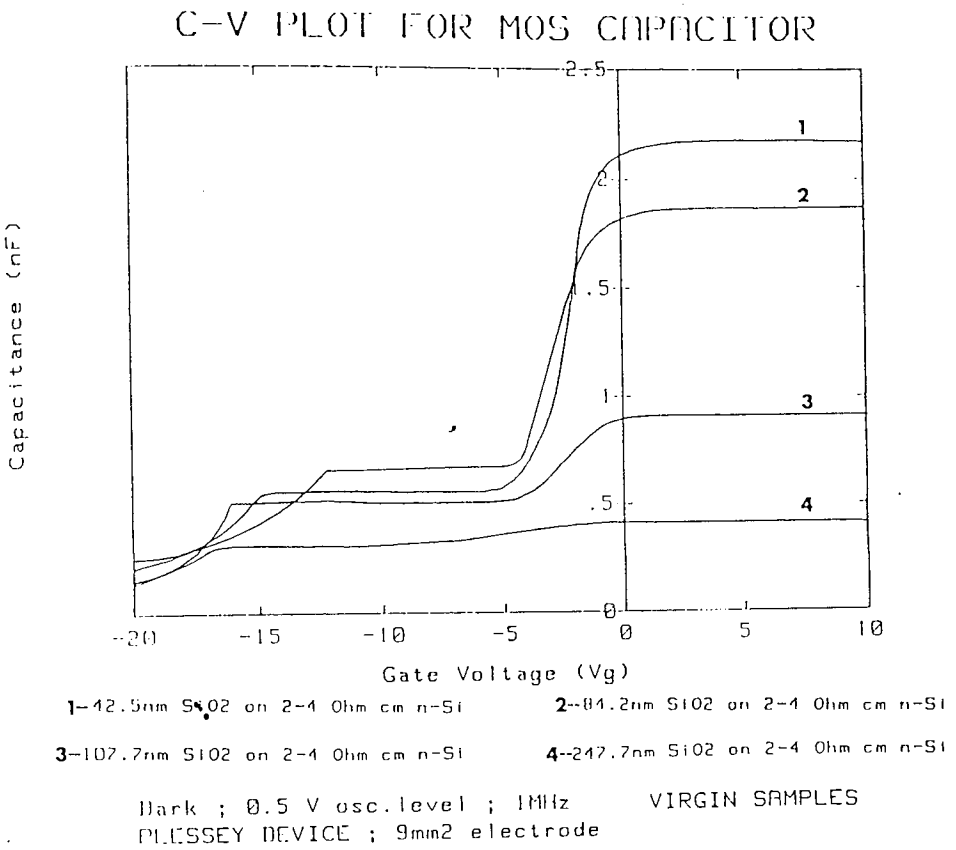

Figure 111: The 1MHz C-V characteristics for virgin n-type Al-SiO_2-Si MOSCs with various oxide thicknesses.

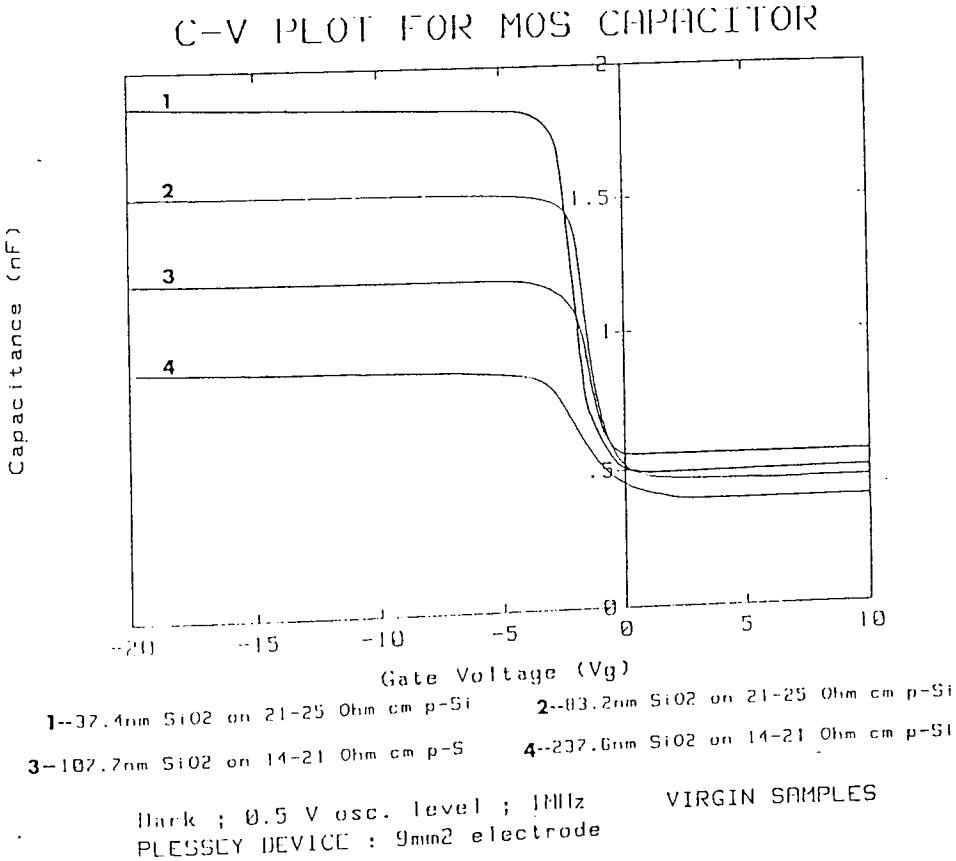

Figure 112: The 1MHz C-V characteristics for virgin p-type Al-SiO_2-Si MOSCs with various oxide thicknesses.

Why, since both n and p-type devices were fabricated during each process run, this has not affected the p-type devices in a similar fashion is not yet known.

Device Identification [Type, Resistivity / Wafer, (Ωcm)			T] (nm)	D_{it} q eV^{-1} cm^{-2}	Q_{ot} qcm^{-2}	Vf_b Volts	$\|U_f\|$ mVolts
n	2-4	C	42.5	$1.17*10^{11}$	$2.92*10^{12}$	-1.23	2.59
n	2-4	B	84.2	$1.28*10^{11}$	$5.71*10^{12}$	-1.11	2.67
n	2-4	A	107.7	$1.41*10^{11}$	$6.32*10^{12}$	-1.32	2.71
n	2-4	A	247.7	$2.23*10^{11}$	$1.19*10^{13}$	-2.06	2.83
n	2-4	C	588.3	$3.11*10^{11}$	$5.93*10^{13}$	-1.62	2.89
n	2-4	A	1264.7	$3.89*10^{11}$	$9.97*10^{13}$	-2.11	2.96
p	21-25	B	39.4	$1.19*10^{11}$	$1.17*10^{12}$	-1.52	2.69
p	21-25	C	83.2	$1.24*10^{11}$	$4.51*10^{12}$	-1.12	2.76
p	14-21	A	107.7	$1.36*10^{11}$	$4.92*10^{12}$	-3.21	2.82
p	14-21	A	237.6	$2.03*10^{11}$	$1.23*10^{13}$	-1.41	2.91
p	21-25	B	566.7	$2.99*10^{11}$	$5.00*10^{13}$	-1.09	2.98
p	14-21	A	1287.7	$3.62*10^{11}$	$8.27*10^{13}$	-1.13	3.07

Table 16. Electrical parameters of Virgin n and p-type MOSCS.

The breakdown and I-V characteristics of the various devices were determined using the techniques described in Chapter **5**. Breakdown testing was performed at room temperature using the voltage probe assembly and breakdown apparatus with the shielded enclosure arrangement shown in Figures 93 and 95, and stepped gate-voltage application.

The breakdown characteristics for both n and p-type devices are very similar, as can be seen in Figures 113(a) and (b), which show the number of non-shorting breakdowns (defect-related and intrinsic) versus applied gate voltage and respective field. An exponential rise in the number of

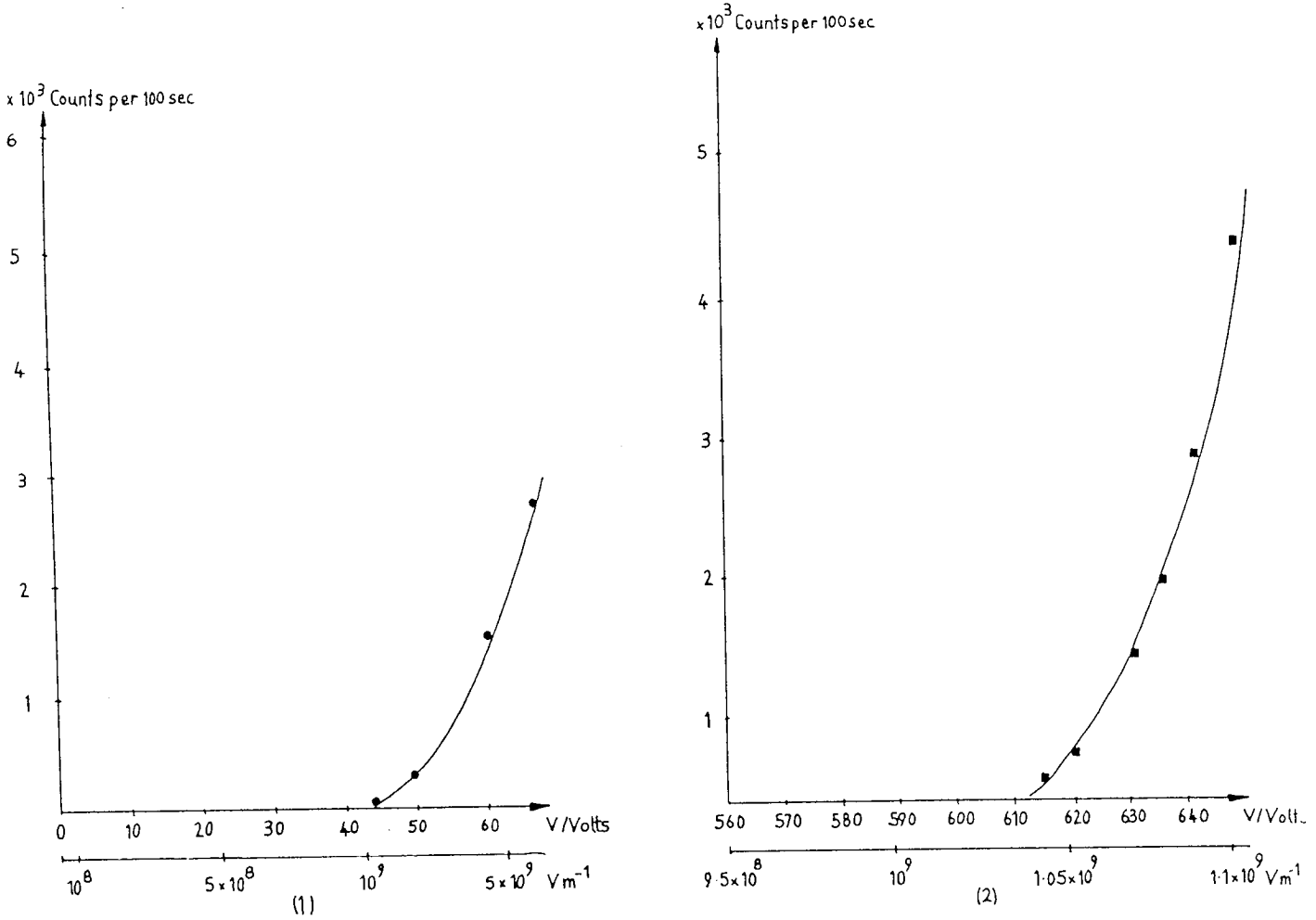

Figure 113: (a) A plot of the number of breakdown pulses versus the applied gate voltage and corresponding oxide field for an n-type Al-SiO_2-Si MOSC with (1) a 42.5nm oxide layer; (2) a 588.3nm oxide layer.

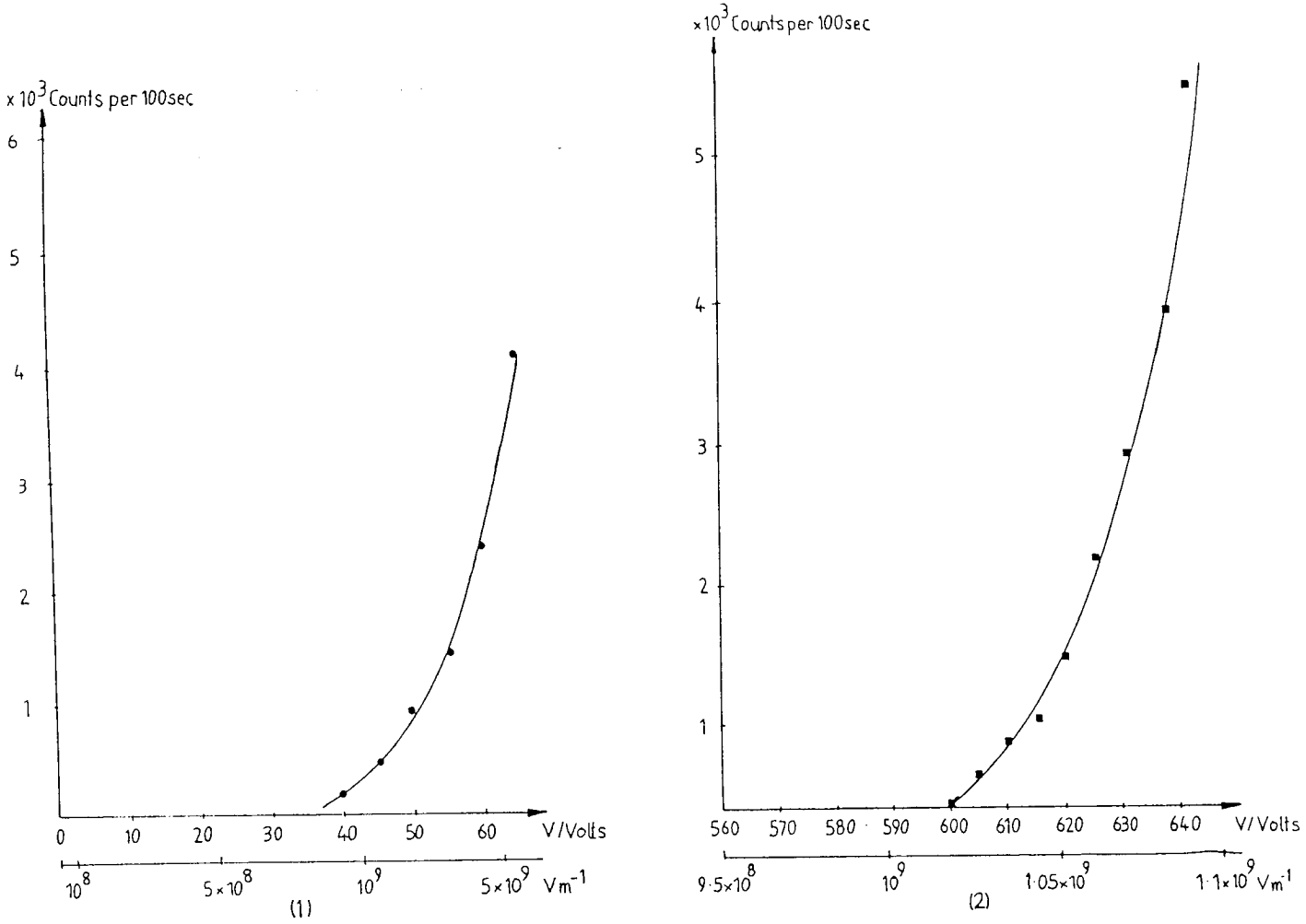

Figure 113: (b) A plot of the number of breakdown pulses versus the applied gate voltage and corresponding oxide field for a p-type Al-SiO_2-Si MOSC with.
(1) a 37.4nm oxide layer; (2) a 566.7nm oxide layer.

breakdowns can be seen with increasing applied gate voltage, with device destruction occurring within an ≈50% increase in applied gate voltage over the onset of breakdown voltage.

Physical examination of the effects of breakdown on the device revealed breakdown pits with two types of breakdown damage: both forms of breakdown pit are craters of between 10 and 50μm in diameter for n-type devices and between 2 and 6μm for p-type devices, independent of the magnitude and polarity of the applied field.

The pits were frequently surrounded by surface damage of the Al gate electrode, possibly due to multiple breakdown at the same breakdown site, and were typical of those shown in the photographs in Figures 114(a) and (b); often this damage covered a large area (≈0.1mm^2 per breakdown) of the device, as shown in the photographs in Figure 115(a) and (b). Inverted-field interferograms of the breakdown sites, typical of those shown in Figures 116(a) and (b), reveal the two forms of breakdown pit and show that one form, for non-shorting breakdowns, the crater depths were approximately 50% of the thickness of the oxide layer, and the other form, those due to shorting breakdowns, reached the entire thickness of the oxide. Shorting breakdowns were those in which a small trace of Al could be found (using the SEM with Kevex detector and LINK ESCA system) at the base of the deeper craters, indicating a possibly conducting channel between the semiconductor substrate (or very near to it) and the top Al electrode. From these results a proposal as to which mechanisms form the possible physical basis of defect-related and intrinsic breakdown has been made.

The approximate number of breakdowns the device can sustain before failure has been estimated (by counting the number of breakdown pits over a large area of the device and extrapolating the data obtained) as typically being ≈10^3 per device for an n-type device and ≈10^4per device for a p-type device; these values, however, are very much smaller than the total (measured) number of breakdown pulses from each type of device recorded before device failure, typically between 10^6 and10^8 per device, for n and p-type devices respectively. The conclusion drawn from this is that several breakdown pulses occur due to breakdown at each site, and the previously held proposal that each breakdown site produces a single breakdown pulse is not a valid description of the breakdown processes occurring.

A study of the breakdown field versus device (oxide layer) thickness has revealed characteristics typical of those shown in Figures 117and 118, which are in contradiction with the results of other

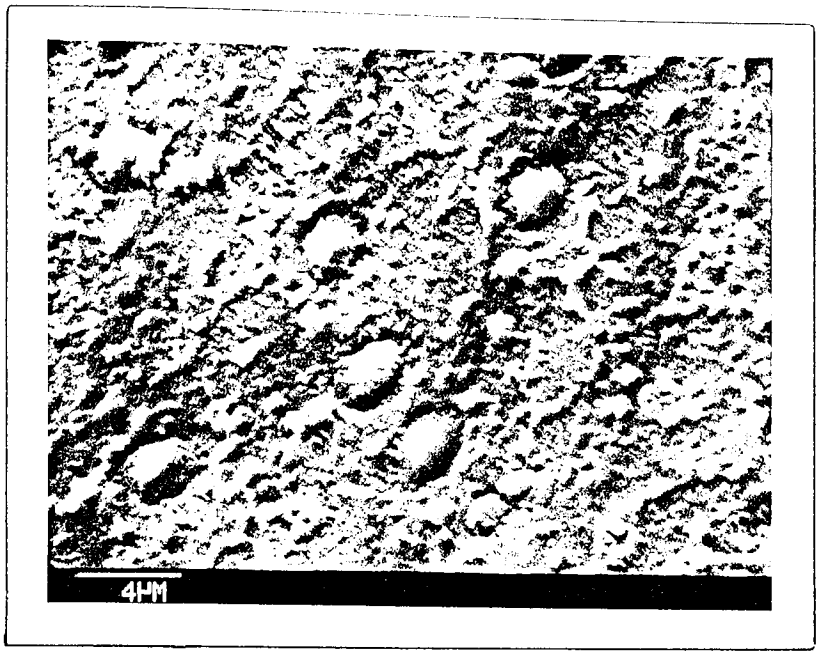

Figure 114: (a) SEM micrographs of various breakdown pits and damage to the Al gate electrode. Magnification x $3.75*10^3$

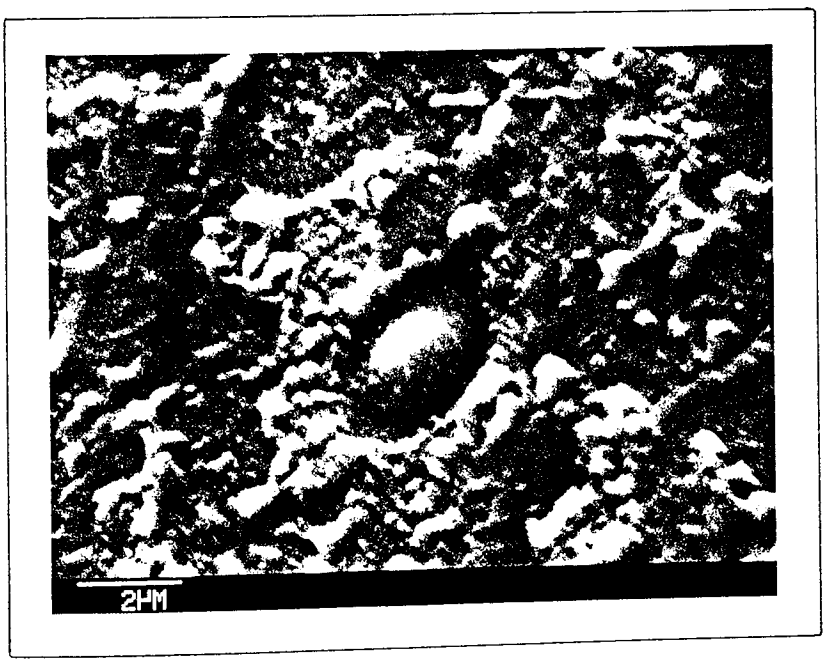

Figure 114: (b) SEM micrographs of various breakdown pits and damage to the Al gate electrode. Magnification x $7.5*10^3$

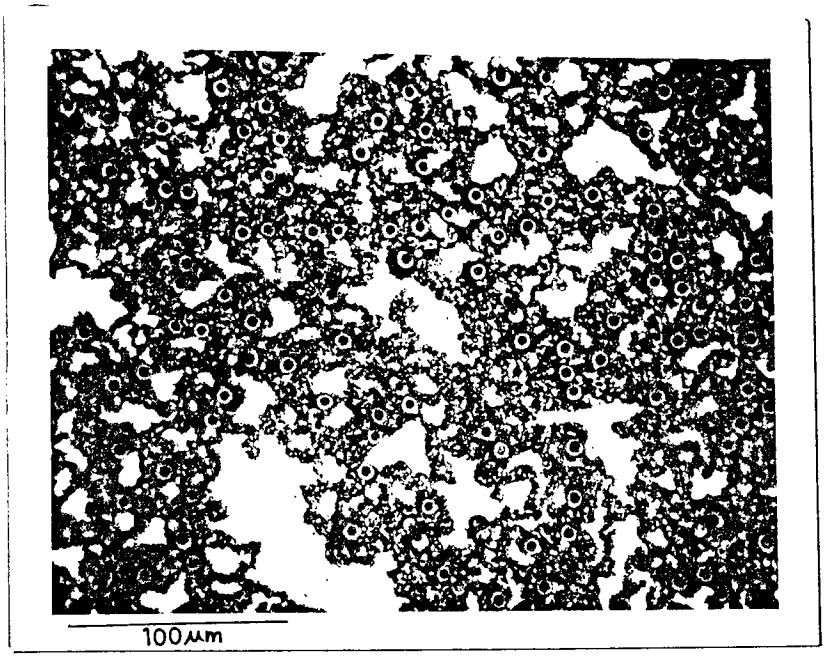

Figure 115: (a) Optical photographs of various breakdown sites; Magnification x370

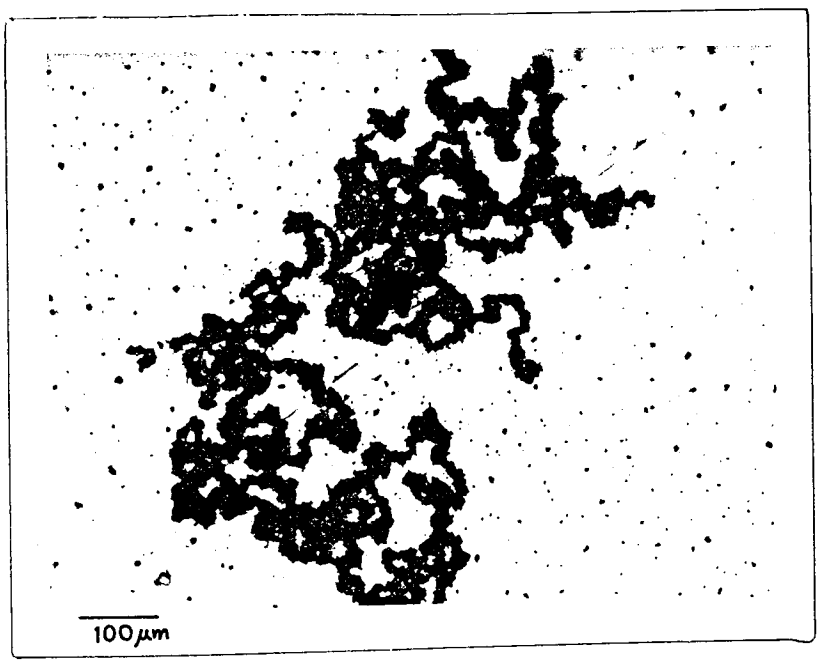

Figure 115: (b) Optical photographs of a single breakdown site and the associated electrode damage; Magnification x970

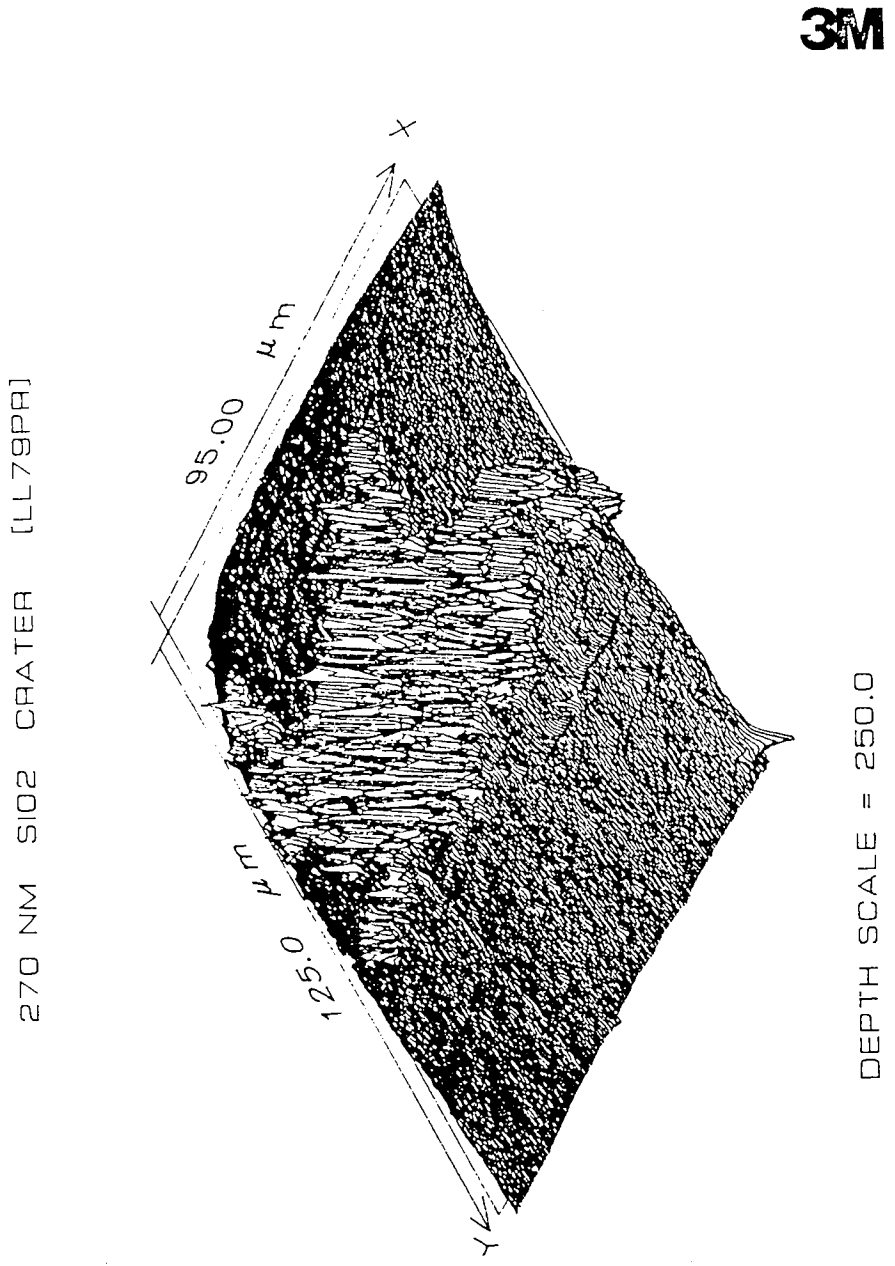

Figure 116: (a) Interferograms of various breakdown craters and damage to the Al gate electrode of an Al-SiO_2-Si MOSC with a 270nm oxide layer.

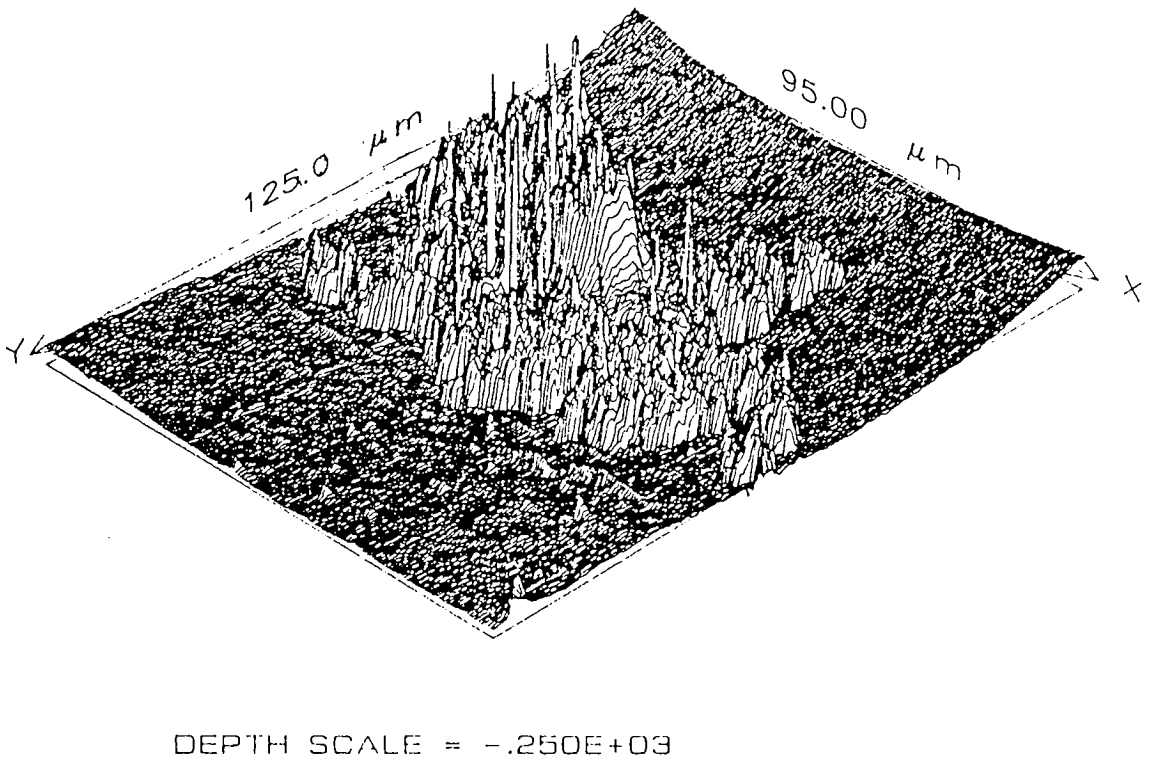

Figure 116: (b) Interferograms of various breakdown craters and damage to the Al gate electrode of an Al-SiO_2-Si MOSC with a 270nm oxide layer .

The interferogram shows an inverted view of the surface in order to aid measurement of surface imperfections.

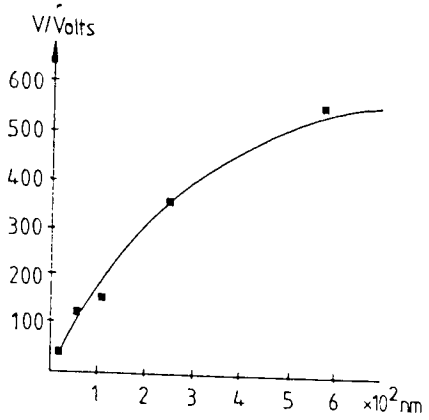

Figure 117: Breakdown voltage versus thickness dependence for various oxide thickness n-type Al-SiO_2-Si MOSCs.

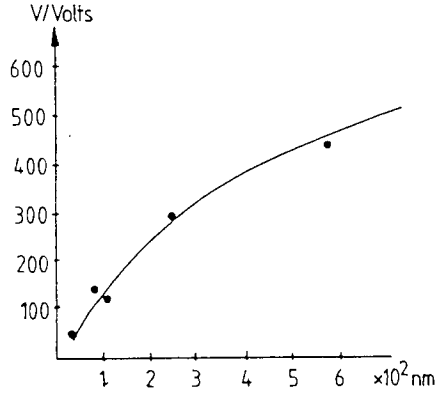

Figure 118: Breakdown voltage versus thickness dependence for various oxide thickness p-type Al-SiO_2-Si MOSCs.

workers who have observed a decrease in breakdown field with increasing oxide thickness (as noted in the discussion in Chapter **3**); since the Al gate area was kept constant, the observed near-linear relationship between the breakdown field and the oxide thickness can be ascribed to the possibility that the majority of the breakdowns are due to defects at both the Si-SiO_2 and the Al-SiO_2 interfaces and throughout the oxide layer. Although no physical evidence for this has been found it seemed the likely explanation since one might propose that the density of defects in the device increases with increasing oxide thickness (as demonstrated by WOLTERS and VERWEY[121]), and thus the density of defect-related breakdowns increases likewise. However, these results imply that very few (if any) intrinsic breakdowns are occurring in the applied gate voltage ranges tested, and that defects were not eliminated by high-field stressing before the failure of the devices, as has been seen by other workers in the field[142,148].

To examine this further, a study of the number of breakdowns at the (approximately pre-determined) field for the onset of breakdown versus the oxide thickness was performed. Typical results are shown in Figure 119 and 120 for n and p-type devices, repectively, where it may clearly be seen that there is no significant variation in the number of breakdowns at the breakdown field with the device oxide thickness; this precludes the proposal made previously that the majority of the breakdowns are defect-related and suggests that the majority of the breakdowns are instead of a thermal or intrinsic nature, with the defect-related breakdowns being eliminated at comparatively low fields. Thermal processes seem unlikely, since an examination of the I-V curves presented in Figures 121 and 122 show that, typically, the current flow in the devices prior to breakdown is too small to generate the temperatures required to initiate thermal breakdown. This is discussed more fully in Chapter **7**, where application of the models proposed for have been used to determine the breakdown process occurring and conclusions as to the innate nature of the Al-SiO_2-Si MOSCs tested are made.

Histograms showing the maximum (shorting) breakdown field distributions for both n and p-type devices of all thicknesses have been made and are shown in Figures 123(a) and (b). It can clearly be seen that the modal breakdown field strength of the n-type devices was between 10.75 and 11$MVcm^{-1}$ and between 9 and 9.25$MVcm^{-1}$ for the p-type devices. These are very high values compared with those of other workers[141,144], who have found the average value for the

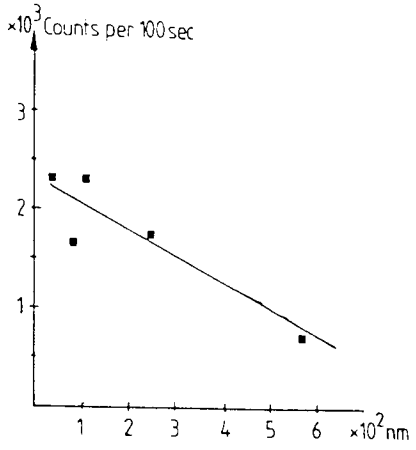

Figure 119: A plot of the number of device breakdown counts versus the device oxide thickness measured at a pre-determined breakdown field for various n-type Al-SiO_2-Si MOSCs.

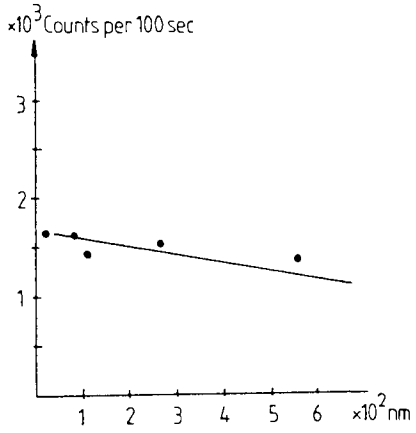

Figure 120: A plot of the number of device breakdown counts versus the device oxide thickness measured at a pre-determined breakdown field for various p-type Al-SiO_2-Si MOSCs.

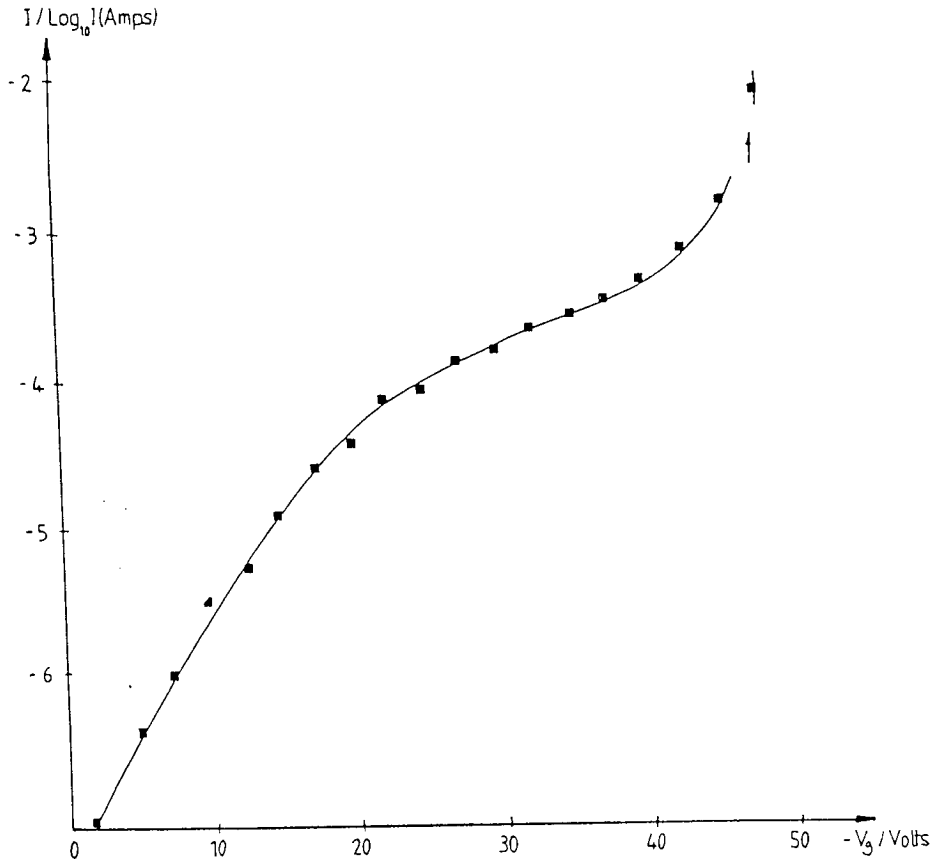

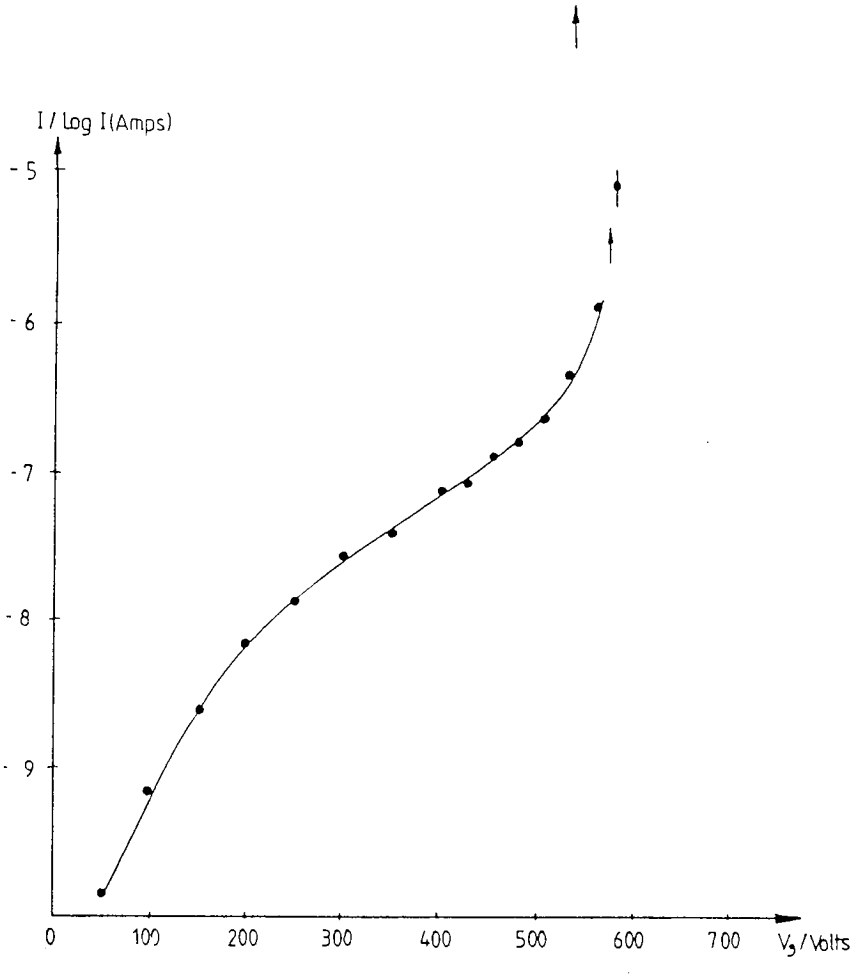

Figure 121: Typical I-V curves for the virgin n-type Al-SiO_2-Si MOSCs tested. The device oxide thicknesses shown are 42.5nm and 588.3nm.

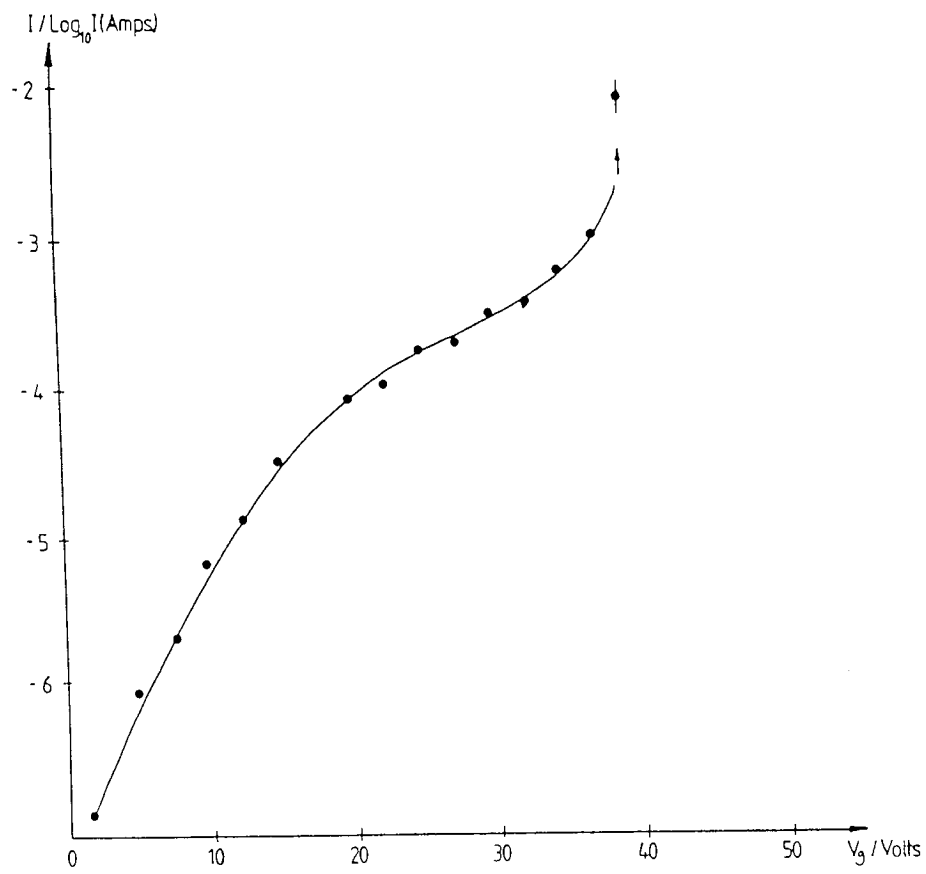

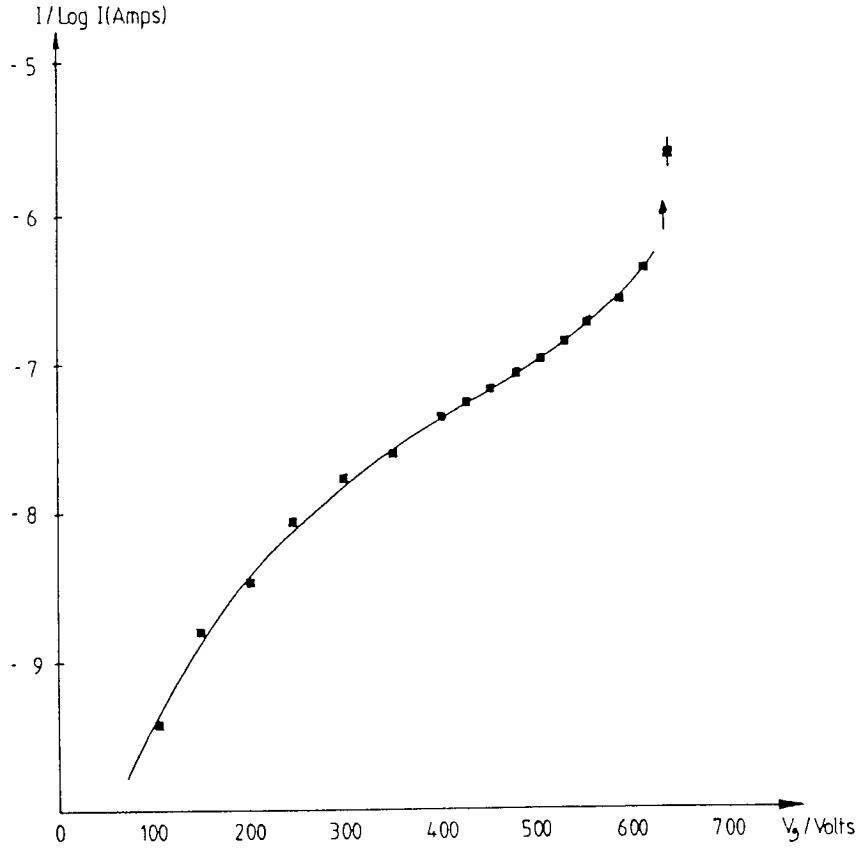

Figure 122: Typical I-V curves for the virgin p-type Al-SiO_2-Si MOSCs tested. The device oxide thicknesses shown are 37.4nm and 566.7nm..

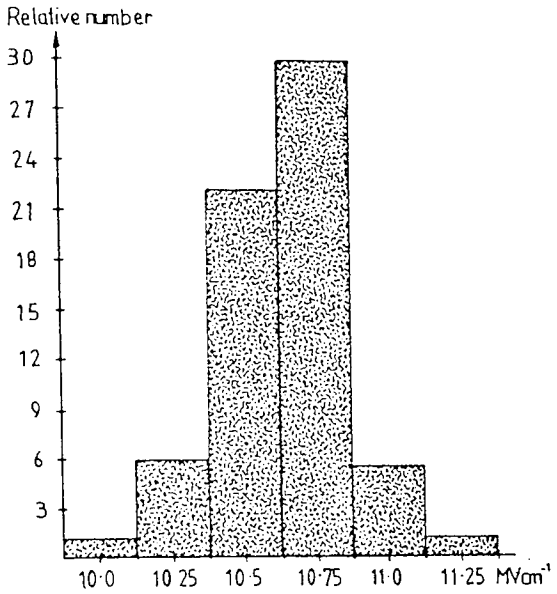

Figure 123: (a) Histogram to show the breakdown field distribution determined from a large number of virgin n-type Al-SiO_2-Si MOSCs.

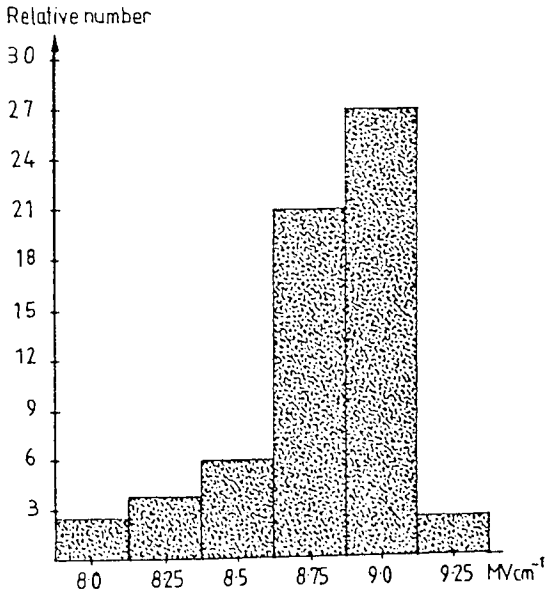

Figure 123 (b) Histogram to show the breakdown field distribution determined from a large number of virgin p-type Al-SiO_2-Si MOSCs.

breakdown field strength (of similar oxide thickness n and p-type MOSCs fabricated in a similar fashion to those used in this study) to be approximately 9.5MVcm^{-1}; this demonstrates the very high quality of the devices.

Further results which incorporate data on the innate characteristics of the devices tested are presented for comparison in each of the following sections, alongside the physical and electrical response of the MOSCs to the various radiation fields used.

6.2 Alpha Irradiations

In order to investigate the effects of alpha-particle irradiation on the breakdown characteristics and physical properties of the Al-SiO_2-Si MOSCs, a large number of individual devices were irradiated; to determine the effects of total dose, bias magnitude and bias polarity, four sets of board-mounted devices (boards 13 to 16 inclusive) were also irradiated under the same conditions as the individual devices and tested using the various techniques available. The device mounting, probing and examination techniques, together with the electrical techniques which were used have been described in Chapter 5.

To briefly summarise the experimental conditions: all the irradiations were performed under vacuum at a pressure of approximately $3*10^{-2}$mbar in the vacuum chamber illustrated in Figure 101 using a 0.108mCi $_{95}Am^{241}$ alpha-particle source, the details of which may be found in Appendix 7. For uniformity of total dose over the entire area of the board-mounted samples, the source was placed at the maximum distance (0.2m) from the boards which led to a maximum possible error in the dose calculations of +7.5% for devices at the centre of the board compared with those at the edge of the board; the dose rate , total dose and error details for these irradiations are presented in Table 13. The voltage range of the biases used for board mounted devices was from -9V to +9V, and included zero bias and the top-gate electrode connected to the Ohmic contact for the open-circuit condition; the biasing arrangement is shown in Figures 91(a) and 91(b). For individual device irradiations a 1MΩ limiting resistor, in series with the EHT bias supply and top gate electrode, was used to prevent avalanche breakdowns; this was removed for I-V characteristic determinations for the devices so that current runaway and the onset of breakdown could be studied. The limiting resistor was not necessary for the board irradiations because of the low bias voltages used, well

below the breakdown fields for even the thinnest oxide devices under investigation.

The salient results from these investigations are presented in the proceeding paragraphs, with the conclusions drawn from them discussed in Chapters 7 and 8.

Several MOSCs of each types and oxide thickness were investigated whilst under irradiation with applied fields ranging between $-10MVcm^{-1}$ and $+10MVcm^{-1}$ across the devices (the negative sign indicating that the top electrode was at a negative potential with respect to the Ohmic contact). There was no evidence to suggest that the alpha irradiation in any way affected the breakdown characteristics of the devices, which followed breakdown characteristics nearly identical to those shown in Figures113 to 116.

Physical examination of the devices after irradiation, but before any defect-related or intrinsic breakdown had occurred, showed no evidence of any effects on the structure, and examination of breakdown pits which occurred in the expected (defect-related and intrinsic breakdown) field range showed no observable differences from those for virgin devices, as typified in Figures 112 to 114. It has been concluded that alpha-particles from the Am^{241} source used do not induce dielectric breakdown.

However, for devices under zero bias conditions, current pulse output from the devices was easily detectable and the number of pulses per second correlated (approximately) with the expected number of alpha particles crossing the MOSC per second, and was initially believed to be independent of device oxide thickness.

When bias was applied across the devices, a decrease in the number and magnitude of the pulses was seen, regardless of the polarity of the bias, the pulse number decreasing with increasing magnitude of bias; this effect was found to be more apparent in n-type devices than in p-type devices with no obvious dependence on the device oxide thickness. Figures 124 and 125 show the number of pulses per100s versus channel number of a multichannel analyser from an n-type (42.5nm oxide layer) MOSC and a p-type (39.4nm oxide thickness) MOSC under alpha-particle irradiation, respectively; the output from an Ortec silicon surface-barrier (SSB) detector (with a similarly sized active area) under the same irradiation geometry and conditions is presented for comparison. The similarity between the output from the p-type MOSC and the SSB detector is quite evident, the resolution of the SSB being slightly better than that of the MOSC for the thin-oxide device shown; the thicker the oxide layer of the MOSC under test, the worse the resolution of the

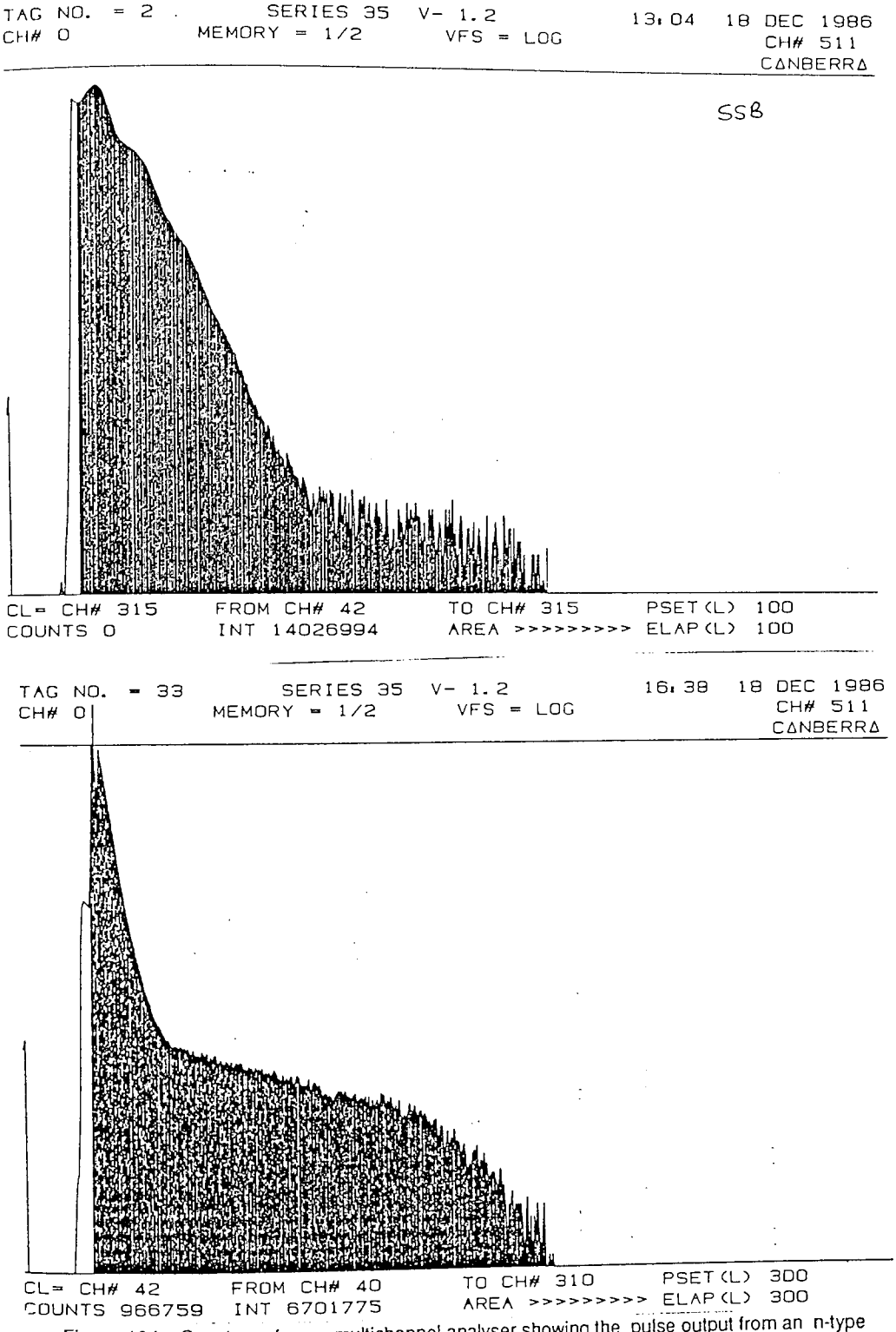

Figure 124: Spectrum from a multichannel analyser showing the pulse output from an n-type Al-Si-SiO_2 MOSC with a 70nm thick oxide layer under alpha-particle irradiation from an Am^{241} source.
The output spectrum from a SSB detector is shown for comparison.

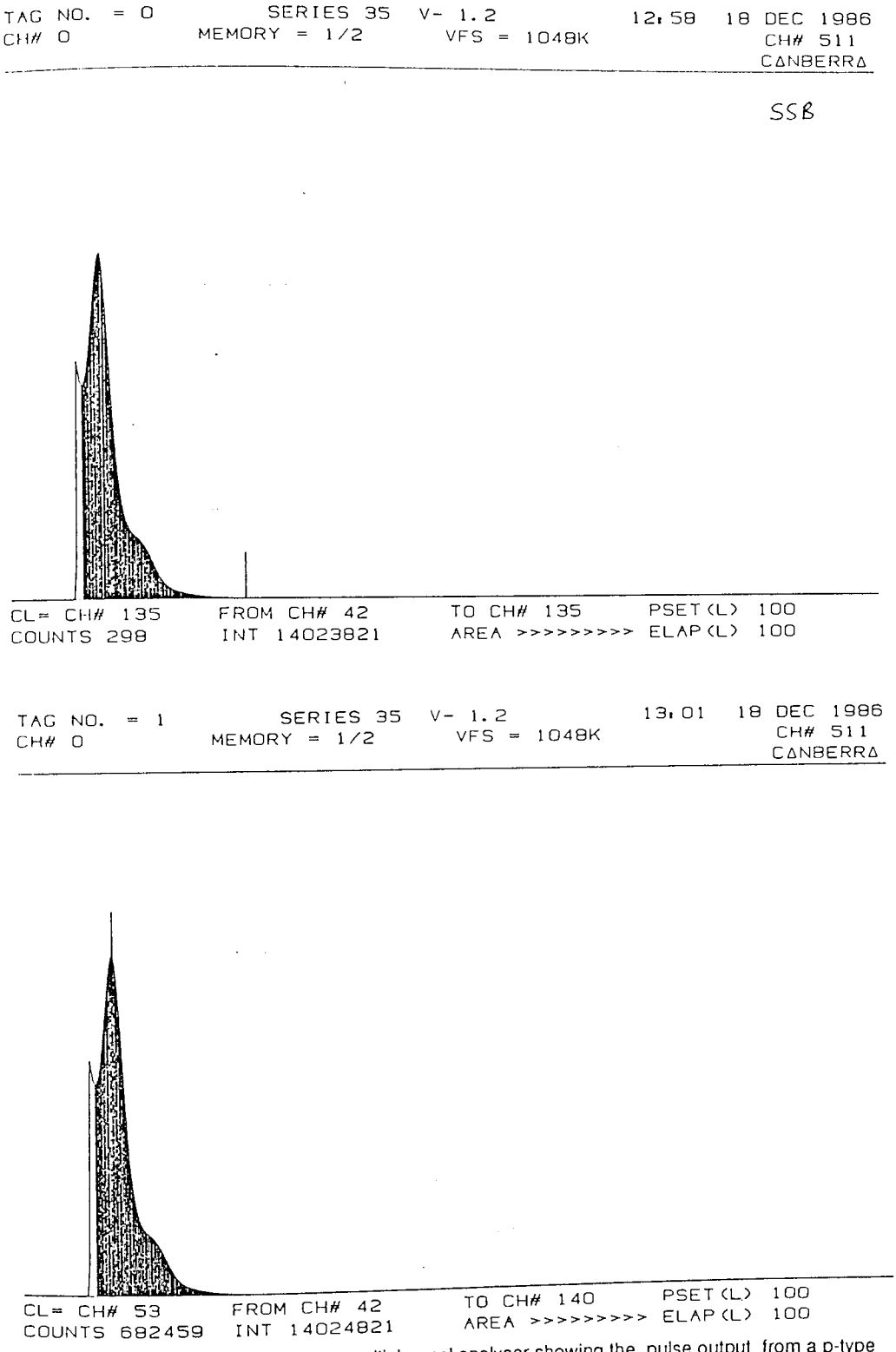

Figure 125: Spectrum from a multichannel analyser showing the pulse output from a p-type Al-Si-SiO_2 MOSC with a 70nm thick oxide layer under alpha-particle irradiation from an Am^{241} source.
The output spectrum from a SSB detector is shown for comparison.

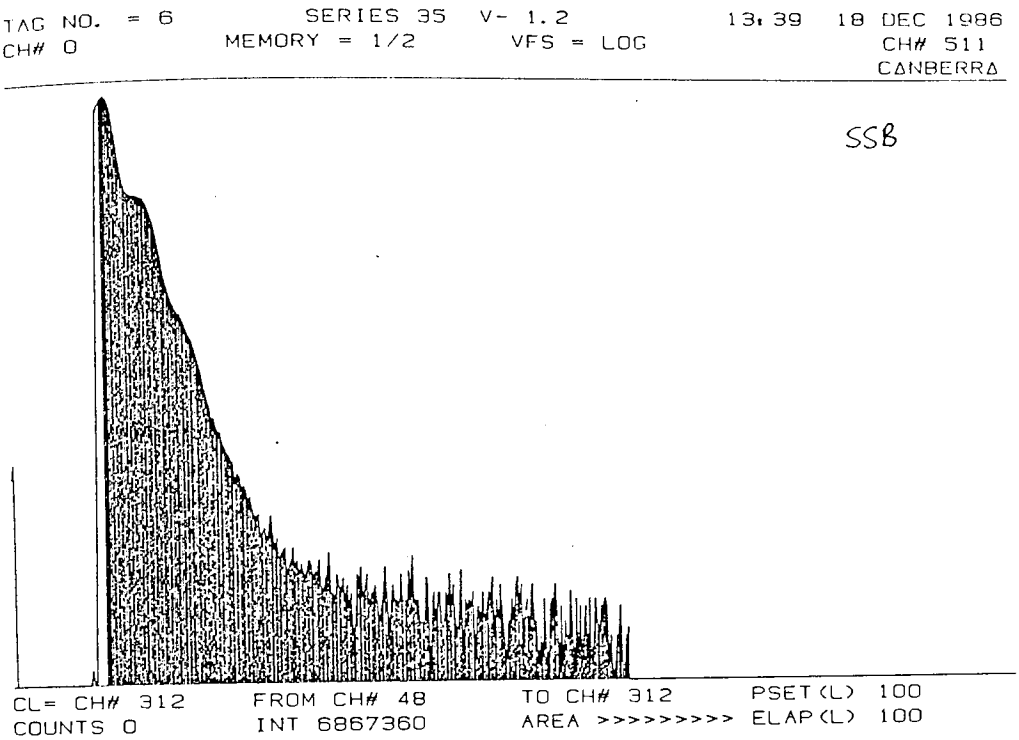

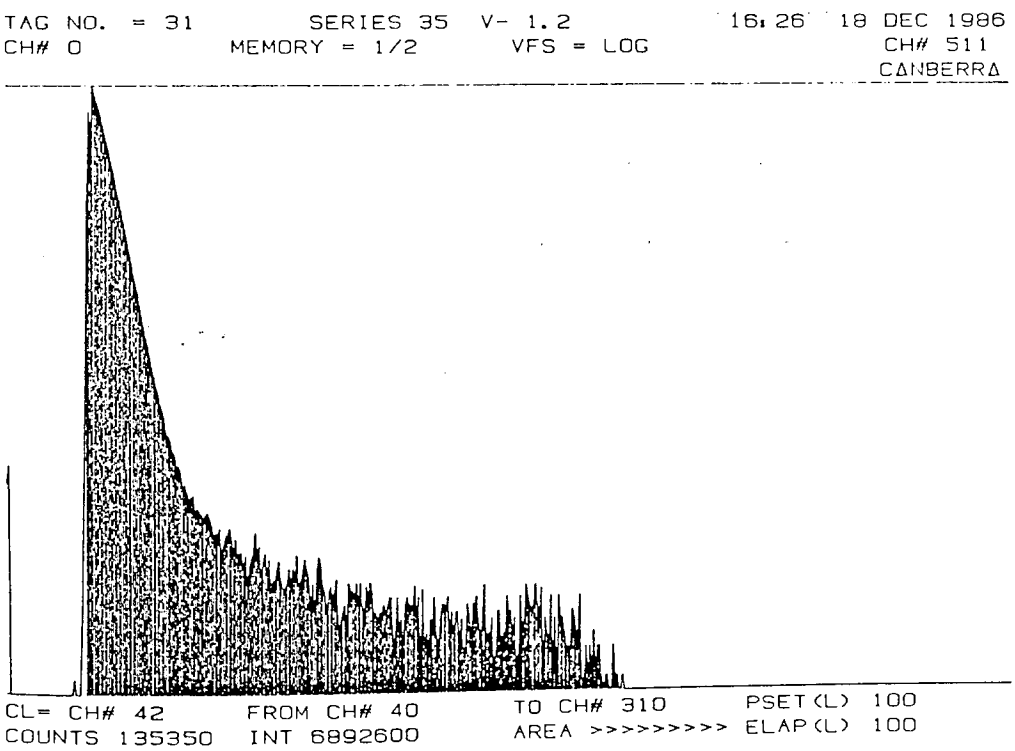

Figure 126: Spectrum from a multichannel analyser showing the pulse output from a p-type Al-Si-SiO_2 MOSC with a 1200nm thick oxide layer under alpha-particle irradiation from an Am^{241} source.
The output spectrum from a SSB detector is shown for comparison.

device to the incident alpha-irradiation, as can be seen in Figures126.

Application of bias to the devices was seen to diminish the output pulse number and increase the noise seen at low channel numbers, regardless of the polarity or magnitude of the bias, but not to decrease the size of the pulses. An investigation of the magnitude of the pulses induced in the devices has revealed an equivalent voltage-pulse shape typical of that shown in Figure 127. The size of the pulses varied in the μA range, with no apparent dependence on the device thickness.

The C-V characteristics of the devices were noticeably altered by the alpha-irradiation, as can be seen in Figures 128 to 135. The effect of the polarity and magnitude of the bias applied during irradiation is clearly seen on the C-V characteristics shown in Figures 128 to 131, for n-type and p-type MOSCs with thick and thin oxides, respectively, irradiated to a total dose of 10KRad(SiO_2).

The irradiation can be seen to have shifted the C-V curves to more negative gate voltage regimes, this being typical of positive charge injection in the oxide layer of the device, the shift being greatest for positively biased devices, and least for negatively biased devices.

The oxide positive charge buildup can also be seen for devices irradiated with no applied gate bias, the magnitude of the C-V characteristic shift being greater than that for negative biases but smaller than that for positive biases; this is indicative of charge injection from the silicon substrate being the dominant mechanism for the characteristic shift, rather than a deposited charge from the irradiation.

Figures 132 to 135 show the effects of radiation dose on n-type and p-type MOSCs with thick and thin oxides, respectively, all under zero gate bias during irradiation. As can clearly be seen, the greater the dose, the greater the shift in C-V curve to more negative regimes. This indicates a correlation between total dose and the magnitude of the curve shift.

Figures 136, 137 and 138 show plots, for both n and p-type MOSCs, of the flatband voltage shift versus alpha-radiation dose in SiO_2, density of interface state generation versus dose and oxide charge density versus dose, respectively, for various device oxide thicknesses and applied bias magnitudes. From these it is evident that a near linear relationship exists between the effects of the radiation and the total radiation dose and applied bias magnitude for the dose range investigated.

The effect of irradiation on the I-V characteristics for the devices were barely detectable with the apparatus used, possibly because of the transience of the current pulses producing too small a change in the current flow in the device; it is uncertain whether the effects seen are due to a slight hysteresis in the I-V curves due to the time-dependence of the current flow through the devices or

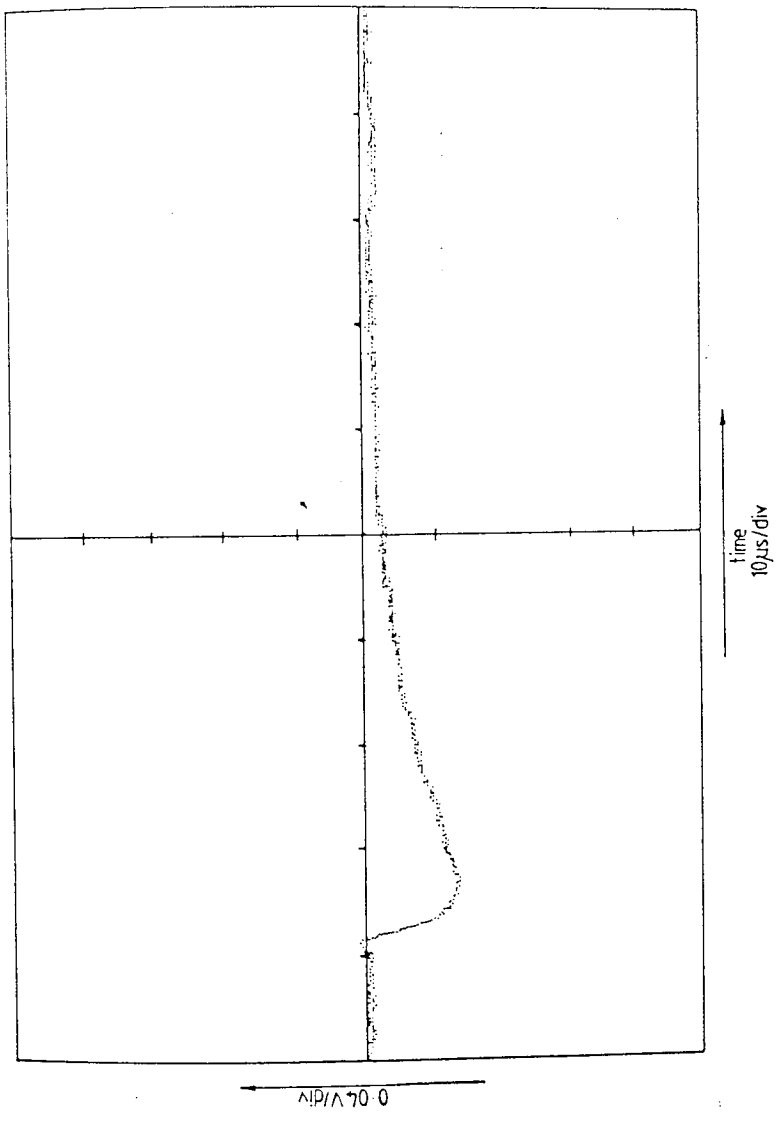

Figure 127: Oscilloscope trace of a typical (voltage equivalent) current pulse induced in a p-type Al-Si-SiO_2 MOSC with a 70nm thick oxide layer under alpha-particle irradiation from an Am^{241} source .

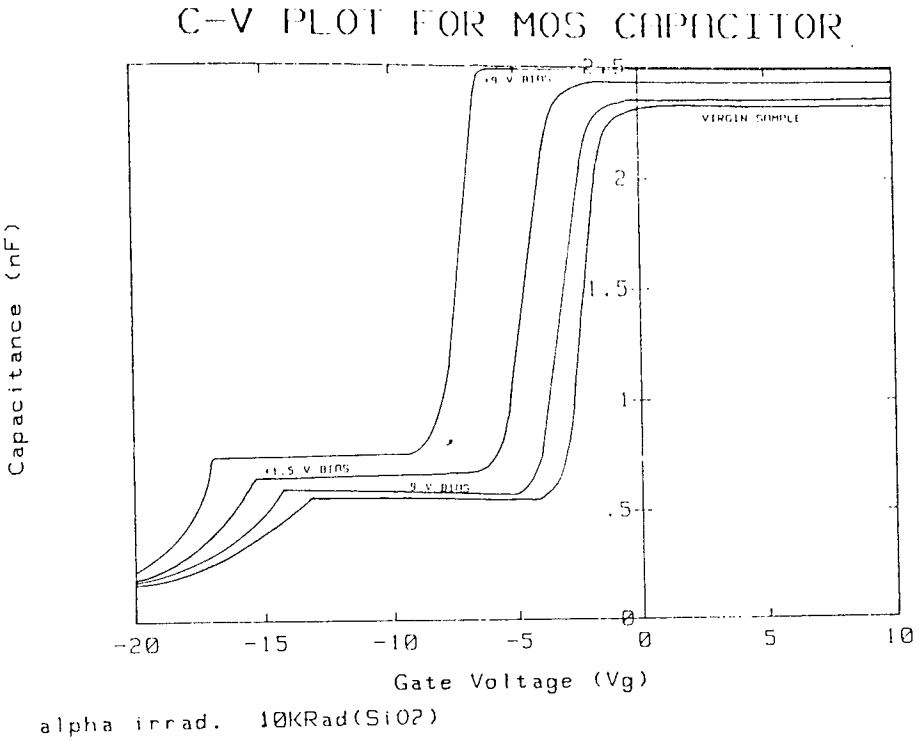

Figure 128: Effect of magnitude of the bias applied during alpha-particle irradiation from an Am^{241} source on the 1MHz C-V characteristics of an n-type Al-SiO_2-Si MOSC with 42.5nm thick oxide layer.
Total dose 10KRad(SiO_2).

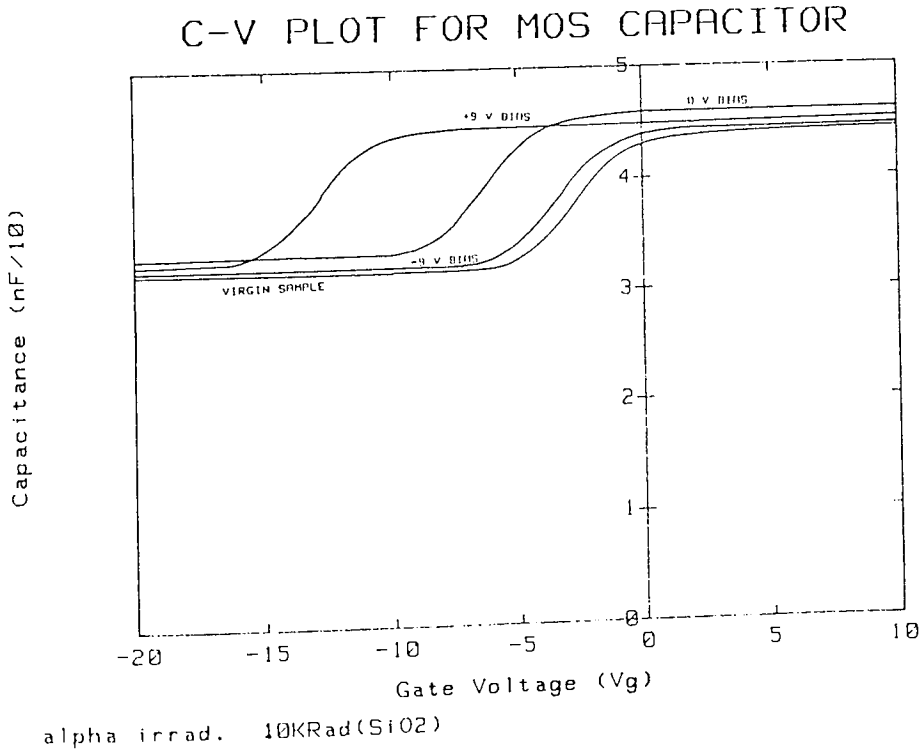

Figure 129: Effect of magnitude of the bias applied during alpha-particle irradiation from an Am^{241} source on the 1MHz C-V characteristics of an n-type Al-SiO_2-Si MOSC with 588.3nm thick oxide layer.
Total dose 10KRad(SiO_2).

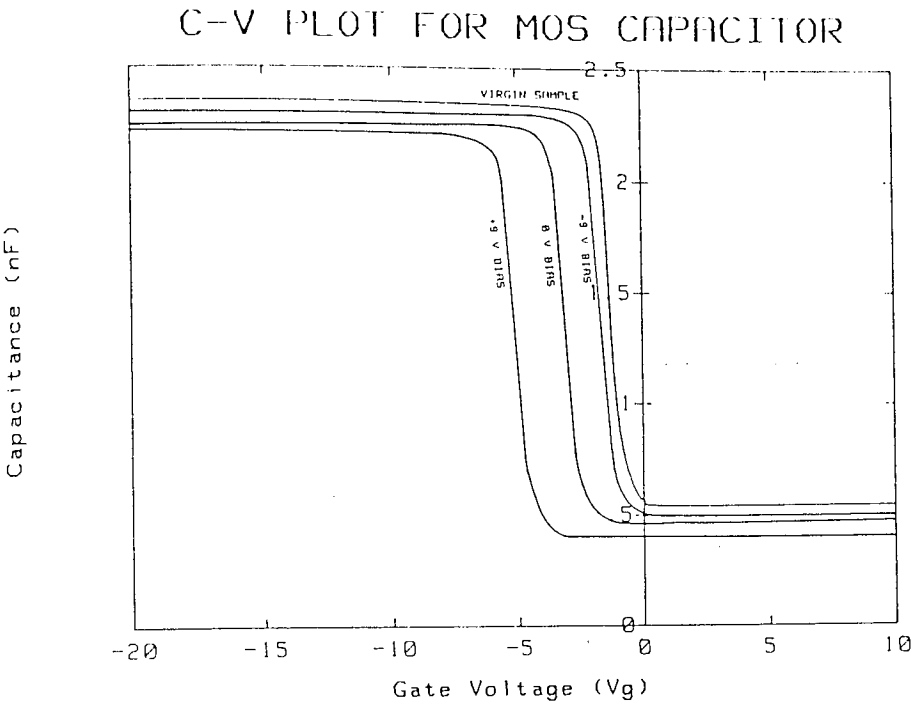

Figure 130: Effect of magnitude of the bias applied during alpha-particle irradiation from an Am^{241} source on the 1MHz C-V characteristics of a p-type Al-SiO_2-Si MOSC with 37.4nm thick oxide layer.
Total dose 10KRad(SiO_2).

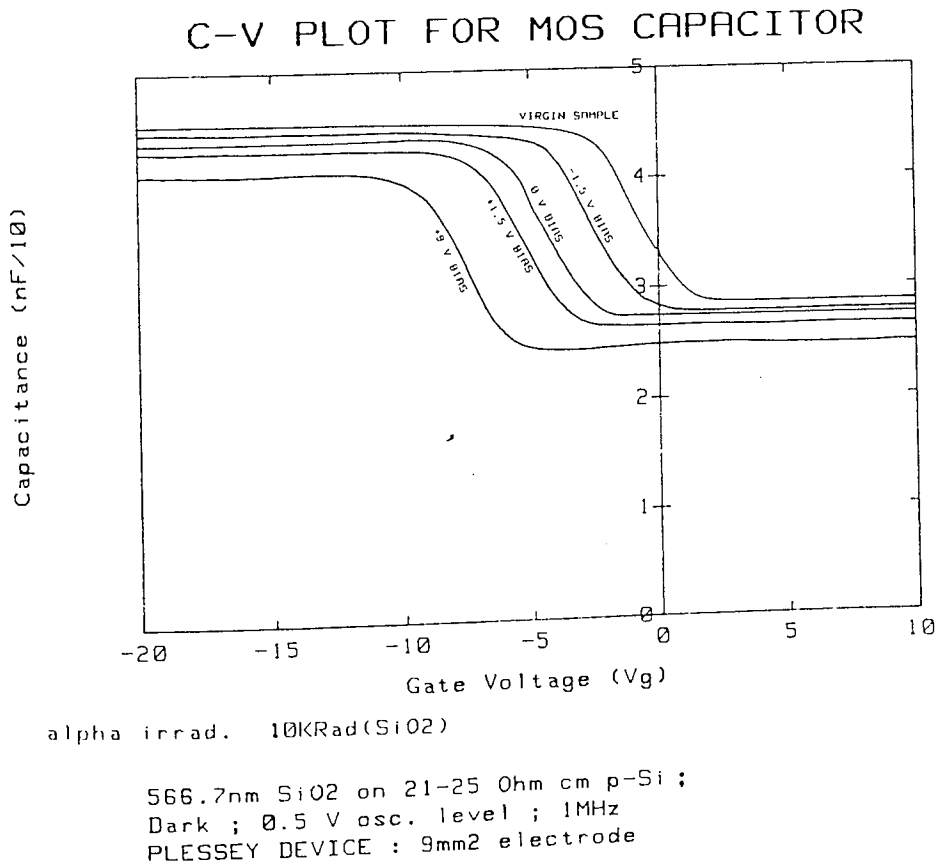

Figure 131: Effect of magnitude of the bias applied during alpha-particle irradiation from an Am^{241} source on the 1MHz C-V characteristics of a p-type Al-SiO_2-Si MOSC with 566.7nm thick oxide layer.
Total dose 10KRad(SiO_2).

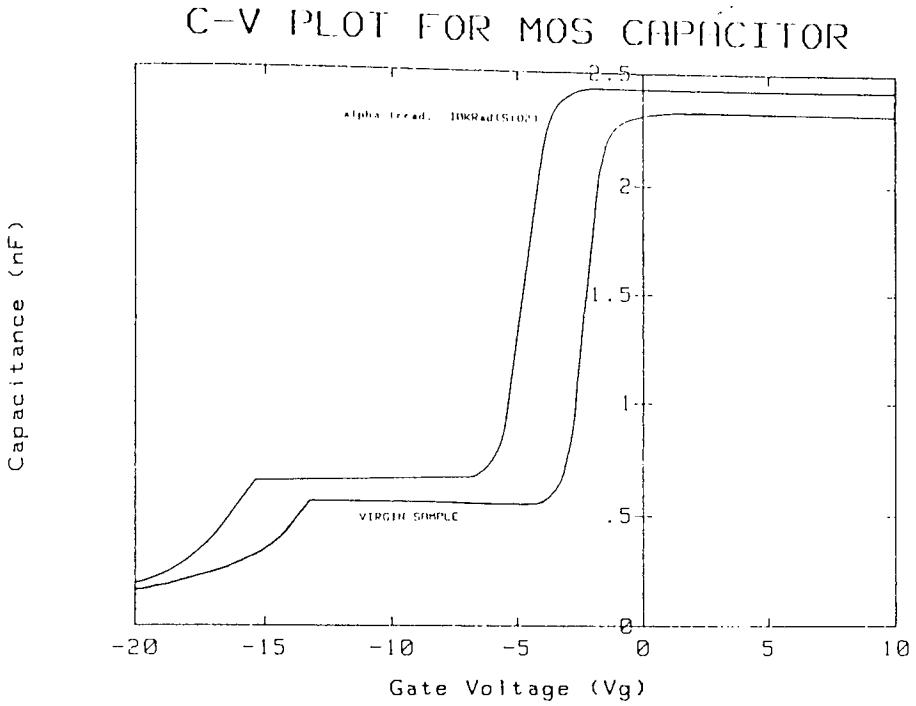

alpha irrad. 10KRad(SiO2)

42.5nm SiO2 on 2-4 Ohm cm n-Si ; 0 V BIAS
Dark ; 0.5 V osc.level ; 1MHz
PLESSEY DEVICE ; 9mm2 electrode

Figure 132: Effect of magnitude of a total dose of 10KRad(SiO_2) alpha-particle irradiation from an Am^{241} source on the 1MHz C-V characteristics of an n-type Al-SiO_2-Si MOSC with 42.5nm thick oxide layer.
0V bias applied during irradiation.

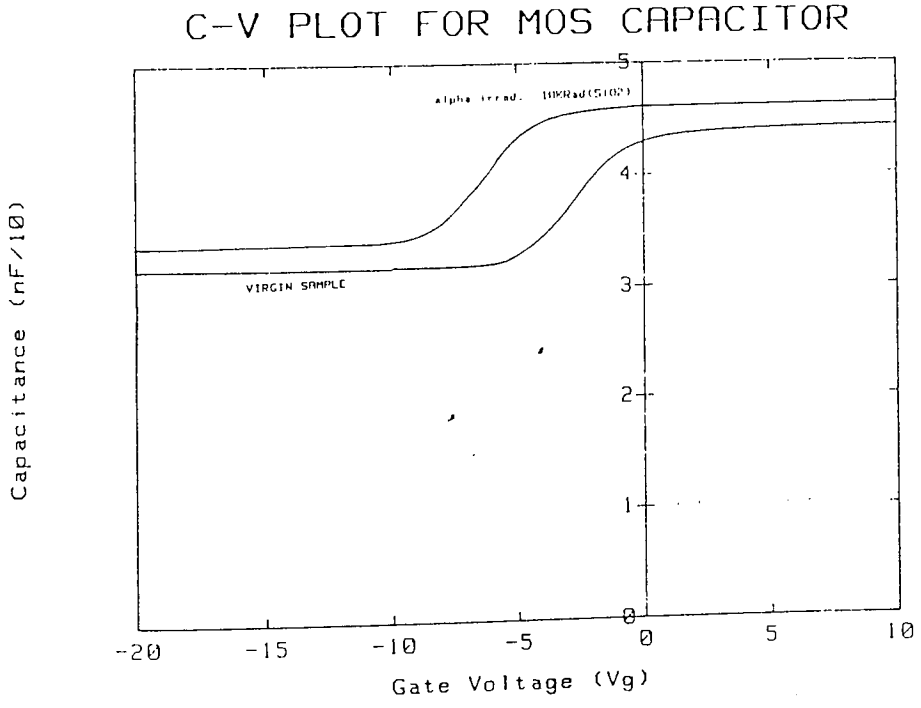

alpha irrad. 10KRad(SiO2)

588.3nm SiO2 on 2-4 Ohm cm n-Si ; 0 V BIAS
Dark ; 0.5 V osc. level ; 1MHz
PLESSEY DEVICE : 9mm2 electrode

Figure 133: Effect of magnitude of a total dose of 10KRad(SiO_2)alpha-particle irradiation from an Am^{241} source on the 1MHz C-V characteristics of an n-type Al-SiO_2-Si MOSC with 588.3nm thick oxide layer.
0V bias applied during irradiation.

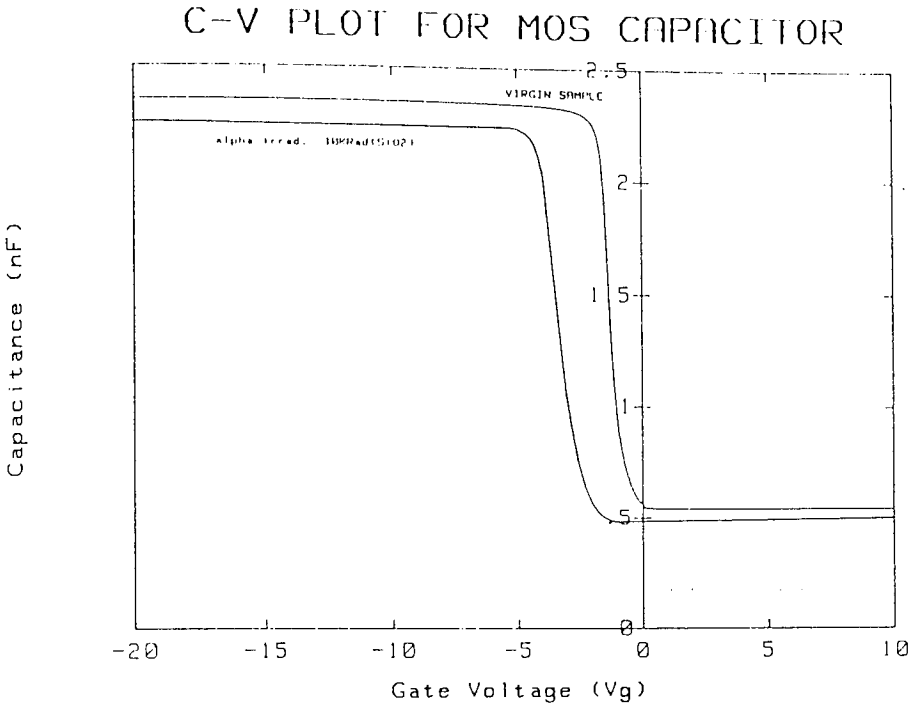

alpha irrad. 10KRad(SiO2)

37.4nm SiO2 on 21-25 Ohm cm p-Si ; 0 V BIAS
Dark ; 0.5 V osc. level ; 1MHz
PLESSEY DEVICE : 9mm2 ELECTRODE

Figure 134: Effect of magnitude of a total dose of 10KRad(SiO_2) alpha-particle irradiation from an Am^{241} source on the 1MHz C-V characteristics of a p-type Al-SiO_2-Si MOSC with 37.4nm thick oxide layer.
0V bias applied during irradiation.

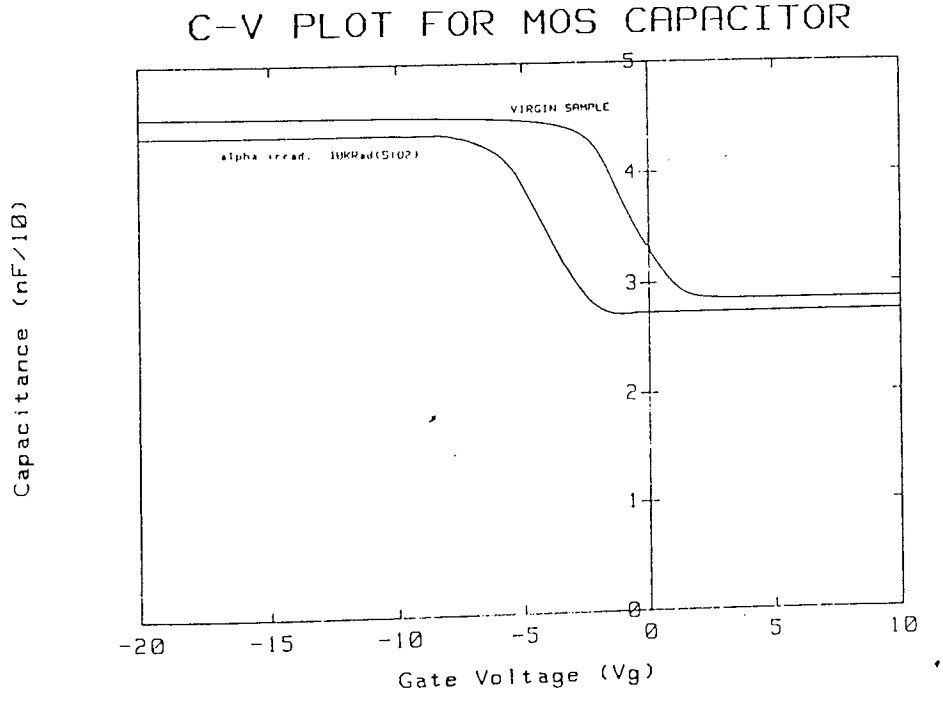

alpha irrad. 10KRad(SiO2)

566.7nm SiO2 on 21-25 Ohm cm p-Si ; 0 V BIAS
Dark ; 0.5 V osc. level ; 1MHz
PLESSEY DEVICE : 9mm2 electrode

Figure 135: Effect of magnitude of a total dose of 10KRad(SiO_2) alpha-particle irradiation from an Am^{241} source on the 1MHz C-V characteristics of a p-type Al-SiO_2-Si MOSC with 566.7nm thick oxide layer.
0V bias applied during irradiation.

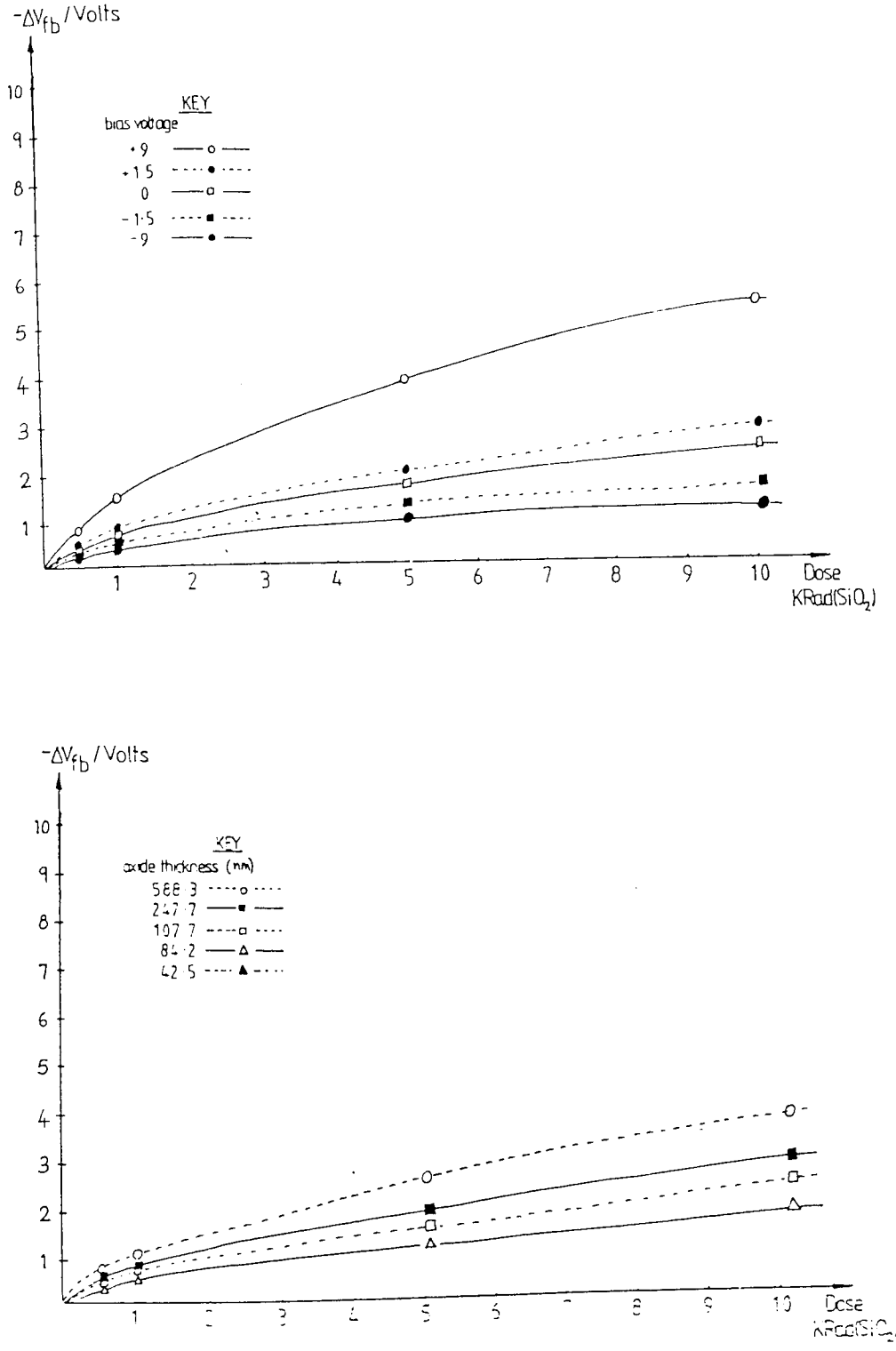

Figure 136: A plot of the shift in flatband voltage (ΔV_{fb}) versus alpha-particle irradiation dose from an Am^{241} source for various oxide thicknessdevices with the MOSC device type and bias polarity as parameters.

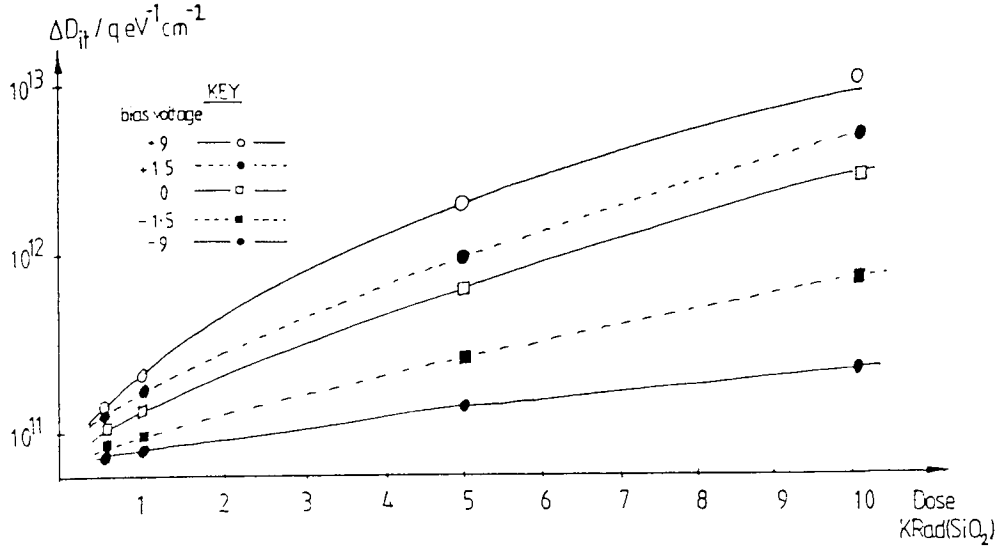

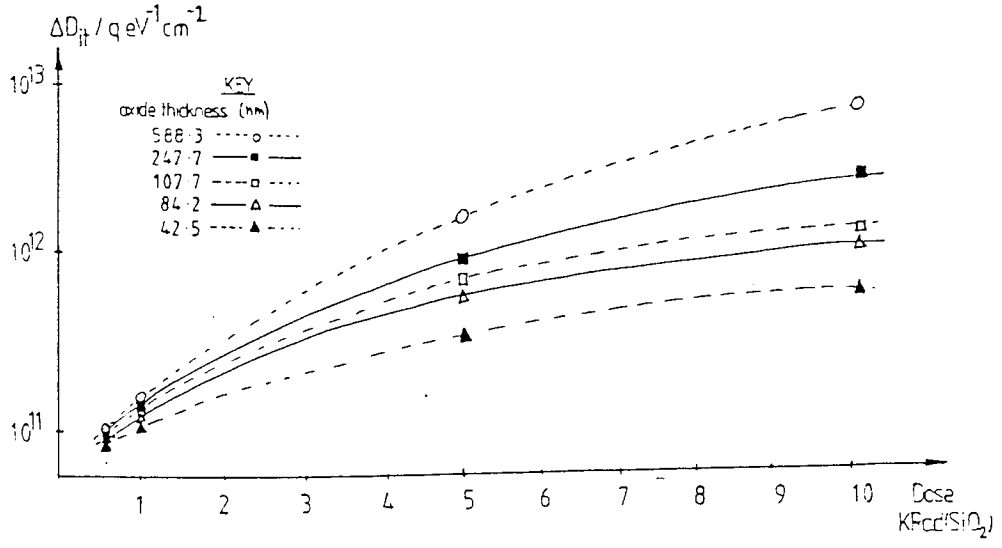

Figure 137: A plot of the density of interface states (D_{it}) versus alpha-particle irradiation dose from an Am^{241} source for various oxide thicknessdevices with the MOSC device type and bias polarity as parameters.

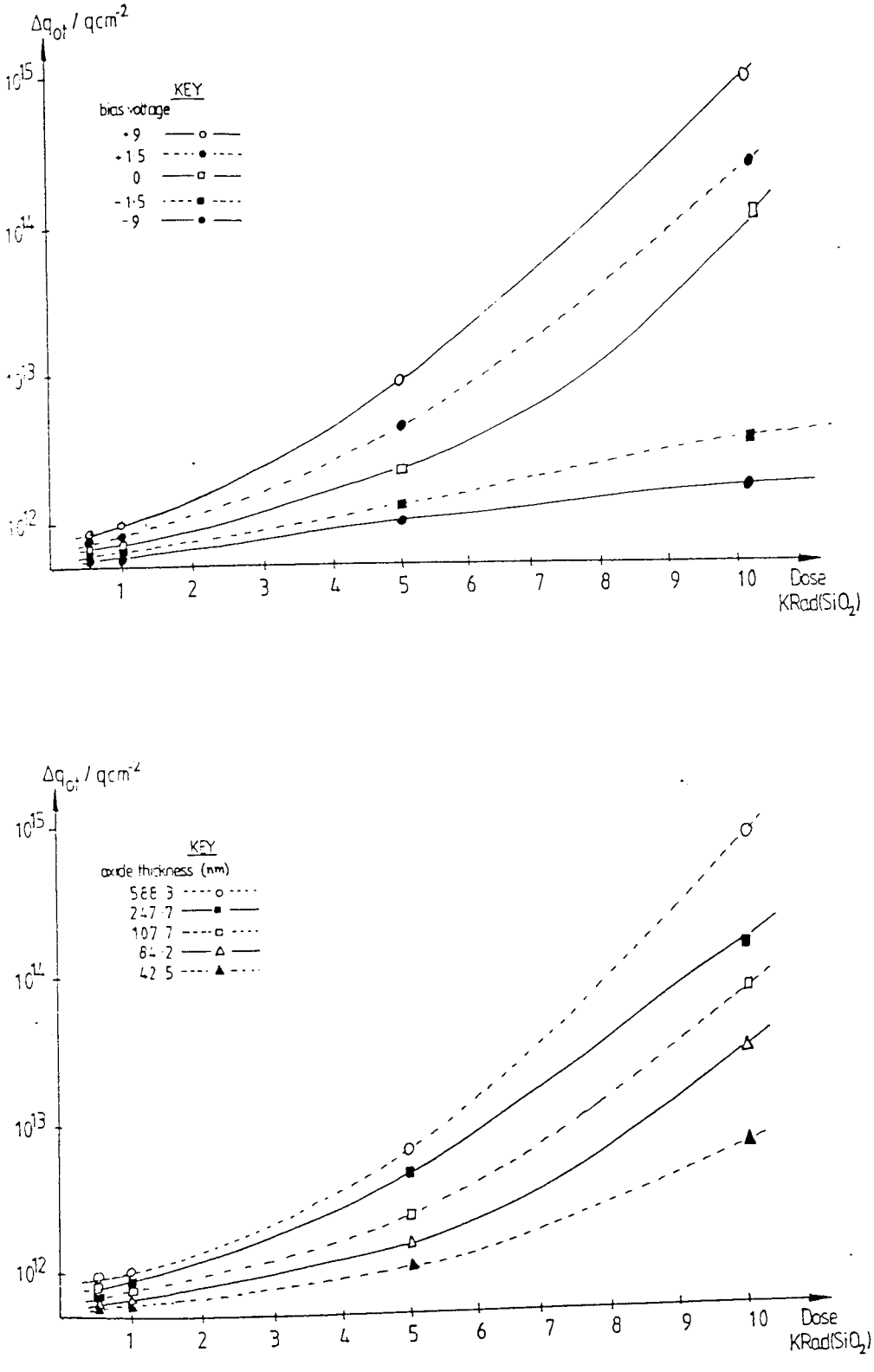

Figure 138: A plot of the oxide charge density (q_{ot}) versus alpha-particle irradiation dose from an Am^{241} source for various oxide thickness devices with the MOSC device type and bias polarity as parameters.

due to some effect of the current pulses produced by the passage of the alpha- radiation through the oxide layer. It is felt that this data, because of its possible misinterpretation, is not worthy of presentation until further evidence can be obtained.

Comparisons with the data presented by other workers in the field and the conclusions which have been drawn from these results are presented in Chapters7 and 8.

6.3 Gamma Irradiations

In order to investigate the effects of gamma irradiation on the breakdown characteristics and physical properties of the Al-SiO_2-Si MOSCs, a large number of individual devices were irradiated; to determine the effects of total dose, bias magnitude and bias polarity, four sets of board-mounted devices (boards 17 to 20 inclusive) were also irradiated using the gamma-irradiation facility at Birmingham University (UK). The device mounting, probing and examination techniques, together with the electrical techniques which were used have been described in Chapter **5**.

To briefly summarise the experimental conditions: individual device irradiations were performed under vacuum at a pressure of approximately $3*10^{-2}$mbar in the vacuum chamber illustrated in Figure 101 using a 1.86mCi $_{27}Co^{60}$ source, the characteristics of which are presented in Table 12 and the calibration details may be found in Appendix **8.** The irradiation geometry is presented in Figure 102.

The majority of the gamma irradiations were performed on board mounted MOSCS using the 950Ci Precisa 217 $_{27}Co^{60}$ source at Birmingham University (UK), the details of which may be found in Appendix **8**, its characteristics in Table 12 and the irradiation geometry in Figure 102. For uniformity of total dose over the entire area of the board-mounted samples, the source was placed at the maximum distance (0.24m) from the boards which led to a maximum possible error in the dose calculations of +6.8% for devices at the centre of the board compared with those at the edge of the board; the dose rate, total dose and error details for these irradiations are presented in Table 13. The voltage range of the biases used for board mounted devices was from -9V to +9V, and included zero bias and the top-gate electrode connected to the Ohmic contact for the open-circuit condition; the biasing arrangement is shown in Figures 91(a) and 91(b). For individual device

irradiations a 1MΩ limiting resistor, in series with the EHT bias supply and top gate electrode, was used to prevent avalanche breakdowns; this was removed for I-V characteristic determinations for the devices so that current runaway and the onset of breakdown could be studied. The limiting resistor was not necessary for the board irradiations because of the low bias voltages used, well below the breakdown fields for even the thinnest oxide devices under investigation.

The salient results from these investigations are presented in the proceeding paragraphs, with the conclusions drawn from them discussed in Chapters **7** and **8**.

Several MOSCs of each types and oxide thickness were investigated whilst under irradiation with applied fields ranging between $-10MVcm^{-1}$ and $+10MVcm^{-1}$ across the devices (the negative sign indicating that the top electrode was at a negative potential with respect to the Ohmic contact). There was no evidence to suggest that the gamma irradiation in any way affected the breakdown characteristics of the devices, which followed breakdown characteristics nearly identical to those shown in Figures113 to 116.

Physical examination of the devices after irradiation, but before any defect-related or intrinsic breakdown had occurred, showed no evidence of any effects on the structure, and examination of breakdown pits which occurred in the expected (defect-related and intrinsic breakdown) field range showed no observable differences from those for virgin devices, as typified in Figures 112 to 114. It has been concluded that gamma radiation from the weak Co^{60} source used do not induce dielectric breakdown.

Investigation of the chemical nature of the Si-SiO_2interface and bulk SiO_2 using AES and ESCA showed spectra with no apparent differences from those for virgin devices, as typified by Figures 109(a) to (c) and Figure110; this, however, does not preclude the existence of radiation damage in the structure, since the techniques used are insensitive to chemical shifts expected from ionizing-radiation damage caused by these (comparitively) low doses.

No pulse output was seen from the devices under irradiation for both devices with and without various combinations of magnitudes and polarities of applied bias; the devices appeared invisible to gamma radiation. This is believed to be a strong argument in favour of the devices as novel detectors for dosimetry techniques in situations where alpha and gamma radiations are concomitant.

However, the C-V characteristics of the devices were noticeably altered by the gamma-irradiation, as

can be seen in Figures 139 to 146. The effect of the polarity and magnitude of the bias applied during irradiation is clearly seen on the C-V characteristics shown in Figures 139 to 142, for n-type and p-type MOSCs with thick and thin oxides, respectively, irradiated to a total dose of 10KRad(SiO_2). The irradiation can be seen to have shifted the C-V curves to more negative gate voltage regimes, this being typical of positive charge injection in the oxide layer of the device, the shift being greatest for positively biased devices, and least for negatively biased devices.

The oxide positive charge buildup can also be seen for devices irradiated with no applied gate bias, the magnitude of the C-V characteristic shift being greater than that for negative biases but smaller than that for positive biases; this is indicative of charge injection from the silicon substrate being the dominant mechanism for the characteristic shift, rather than a deposited charge from the irradiation.

Figures 143to 146 show the effects of radiation dose on n-type and p-type MOSCs with thick and thin oxides, respectively, all under zero gate bias during irradiation. As can clearly be seen, the greater the dose, the greater the shift in C-V curve to more negative gate-bias regimes. This indicates a correlation between total dose and the magnitude of the curve shift. The shift can be seen to marginally increase the effective capacitance of the n-type MOSCs and to similarly decrease the effective capacitance of the p-type MOSCS; the converse of the effect seen for similar devices when irradiated under bias with alpha-radiation. This effect is possibly due to the alteration in the C-V characteristic by the introduction of fast-surface states, as described in Chapter **4**, although its origins are, at present, uncertain.

Figures 147, 148 and 149 show plots, for both n and p-type MOSCs, of the flatband voltage shift versus gamma radiation dose in SiO_2, density of interface state generation versus dose and oxide charge density versus dose, respectively, for various device oxide thicknesses and applied bias magnitudes. From these it is evident that an approximately linear relationship exists between the effects of the radiation and the total radiation dose and applied bias magnitude for the dose range investigated.

An investigation into the effects of gamma-irradiation on the I-V characteristics of the devices revealed that, (in a similar fashion to those curves for alpha irradiation) the effect of irradiation on the devices were barely detectable with the apparatus used, and again it is uncertain whether the extremely small effect seen was due to a slight hysteresis in the I-V curves due to the time-dependence of the current flow through the devices or due to some effect produced by the

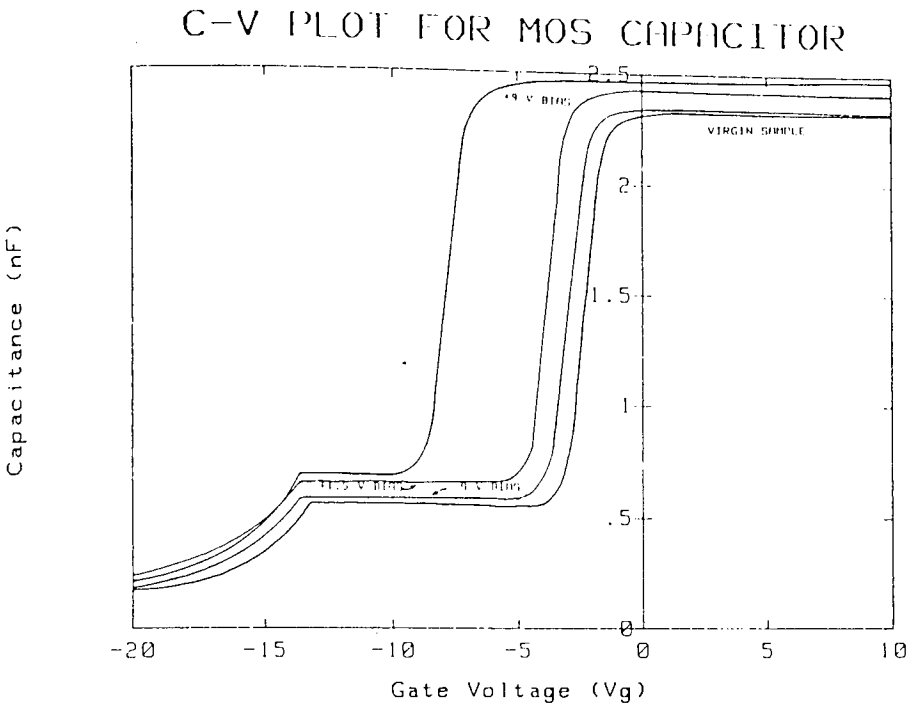

Figure 139: Effect of magnitude of the bias applied during gamma irradiation from a Co^{60} source on the 1MHz C-V characteristics of an n-type Al-SiO_2-Si MOSC with 42.5nm thick oxide layer.
Total dose 10KRad(SiO_2).

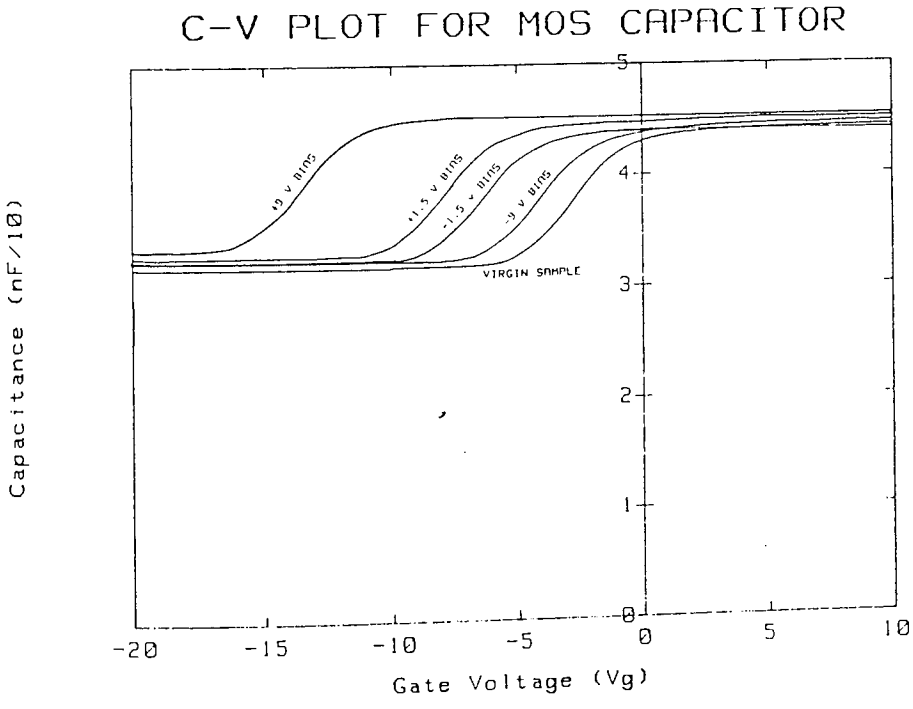

Figure 140: Effect of magnitude of the bias applied during gamma irradiation from a Co^{60} source on the 1MHz C-V characteristics of an n-type Al-SiO_2-Si MOSC with 588.3nm thick oxide layer.
Total dose 10KRad(SiO_2).

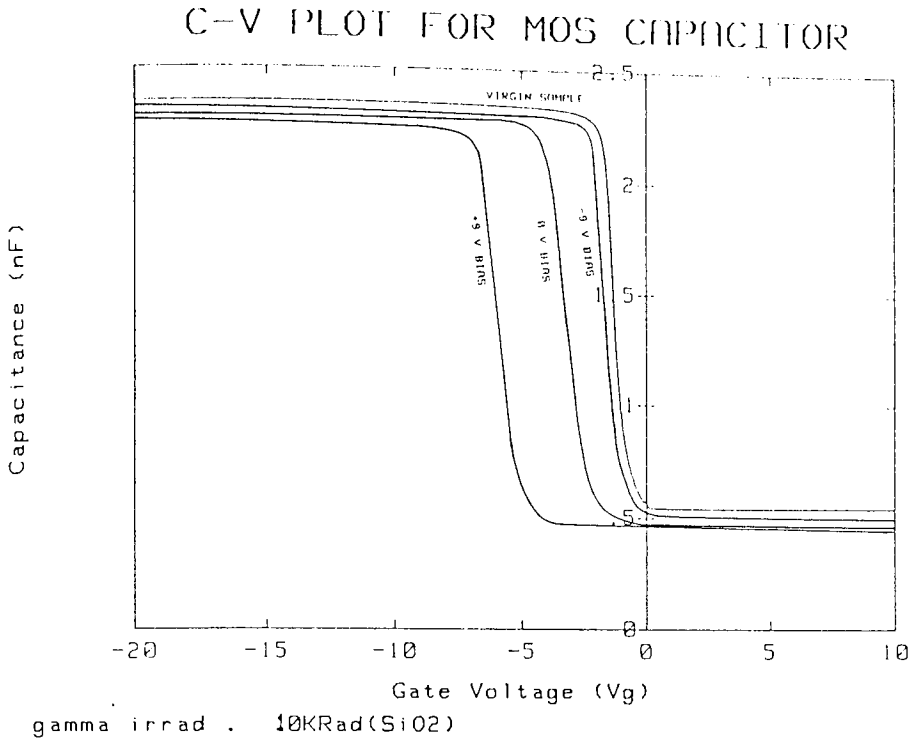

Figure 141: Effect of magnitude of the bias applied during gamma irradiation from a Co^{60} source on the 1MHz C-V characteristics of a p-type Al-SiO_2-Si MOSC with 37.4nm thick oxide layer.
Total dose 10KRad(SiO_2).

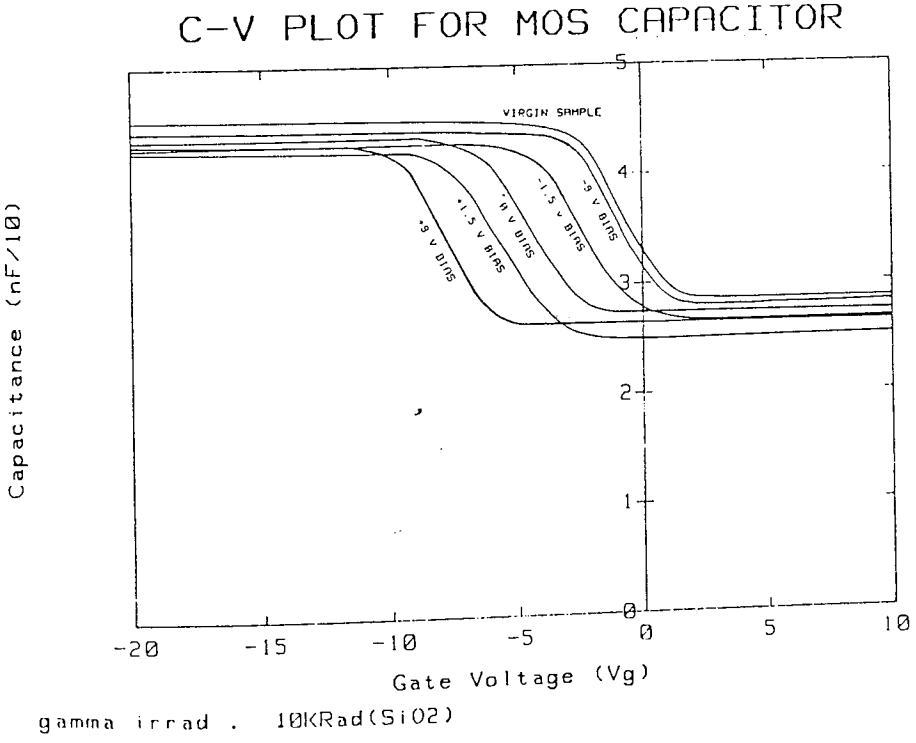

Figure 142: Effect of magnitude of the bias applied during gamma irradiation from a Co^{60} source on the 1MHz C-V characteristics of a p-type Al-SiO_2-Si MOSC with 566.7nm thick oxide layer.
Total dose 10KRad(SiO_2).

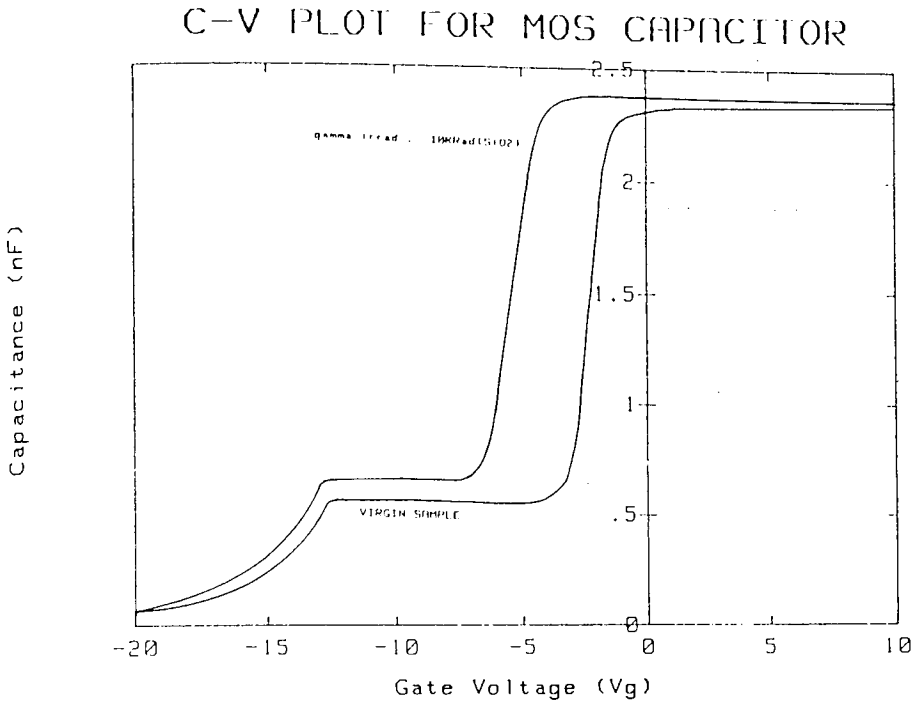

gamma irrad . 10KRad(SiO2)

42.5nm SiO2 on 2-4 Ohm cm n-Si ; 0 V BIAS
Dark ; 0.5 V osc.level ; 1MHz
PLESSEY DEVICE ; 9mm2 electrode

Figure 143: Effect of magnitude of a total dose of 10KRad(SiO_2) gamma- irradiation from a Co^{60} source on the 1MHz C-V characteristics of an n-type Al-SiO_2-Si MOSC with 42.5nm thick oxide layer.
0V bias applied during irradiation.

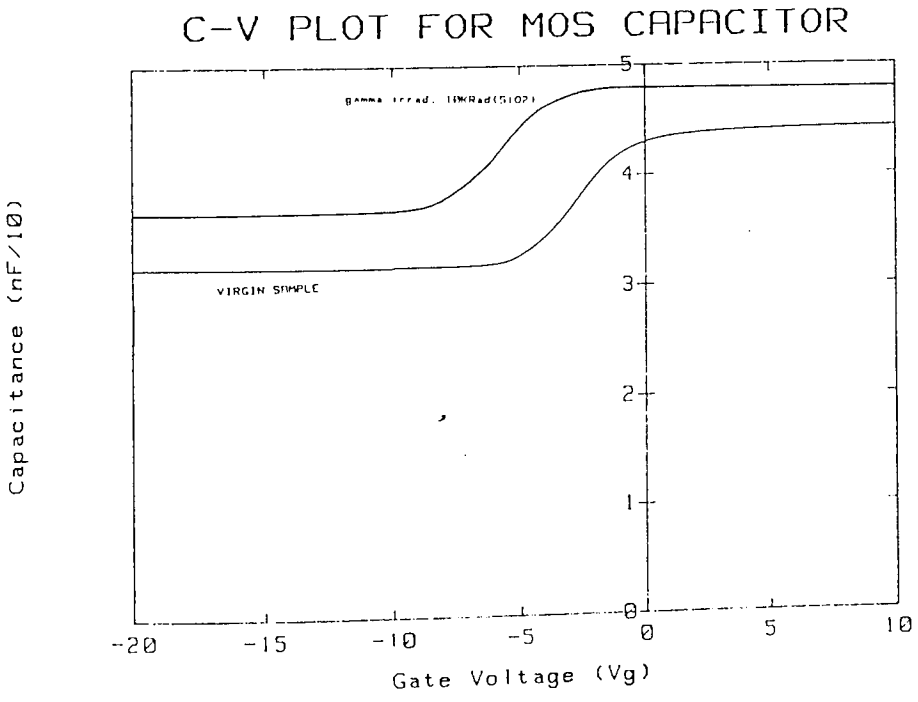

gamma irrad. 10KRad(SiO2)

588.3nm SiO2 on 2-4 Ohm cm n-Si ; 0 V BIAS
Dark ; 0.5 V osc. level ; 1MHz
PLESSEY DEVICE : 9mm2 electrode

Figure 144: Effect of magnitude of a total dose of 10KRad(SiO_2) gamma- irradiation from a Co^{60} source on the 1MHz C-V characteristics of an n-type Al-SiO_2-Si MOSC with 588.3nm thick oxide layer.
0V bias applied during irradiation.

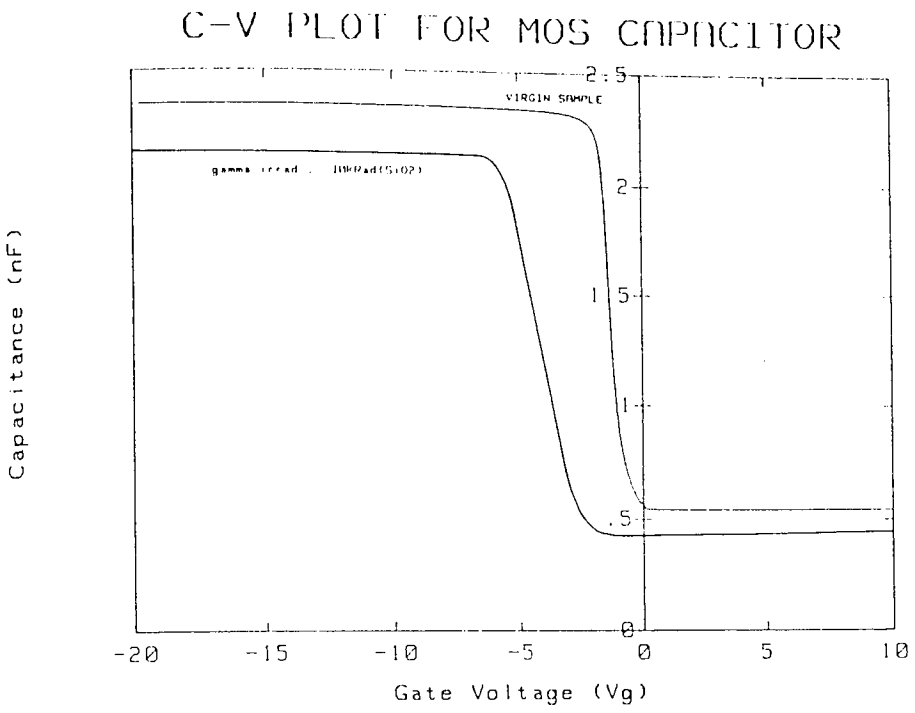

gamma irrad. 10KRad(SiO2)

37.4nm SiO2 on 21-25 Ohm cm p-Si ; 0 V BIAS
Dark ; 0.5 V osc. level ; 1MHz
PLESSEY DEVICE : 9mm2 ELECTRODE

Figure 145: Effect of magnitude of a total dose of 10KRad(SiO_2) gamma-irradiation from a Co^{60} source on the 1MHz C-V characteristics of a p-type Al-SiO_2-Si MOSC with 37.4nm thick oxide layer.
0V bias applied during irradiation.

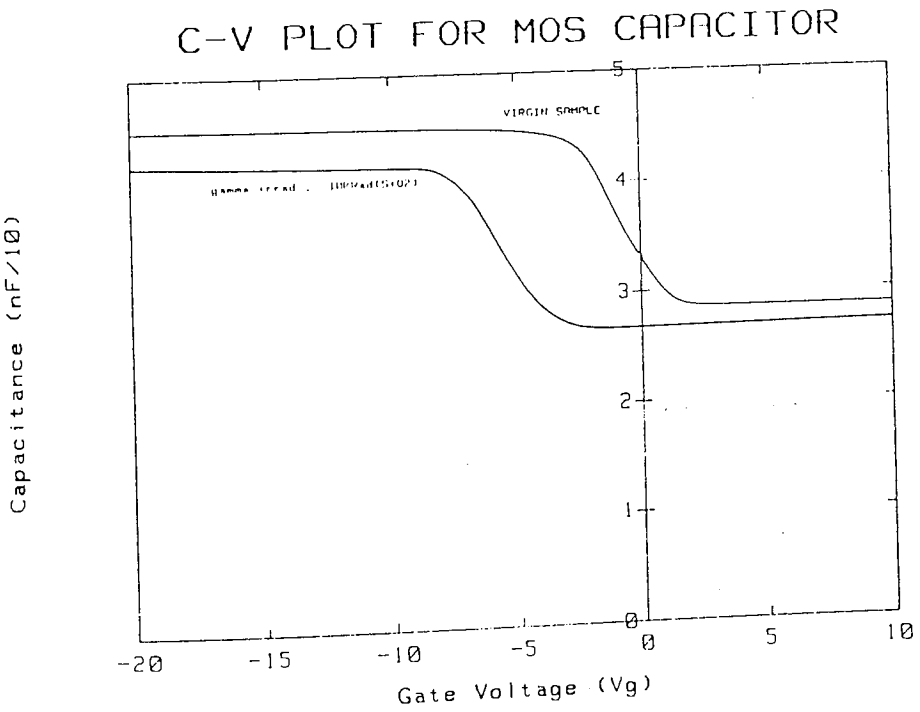

gamma irrad . 10KRad(SiO2)

566.7nm SiO2 on 21-25 Ohm cm p-Si ; 0 V BIAS
Dark ; 0.5 V osc. level ; 1MHz
PLESSEY DEVICE : 9mm2 electrode

Figure 146: Effect of magnitude of a total dose of 10KRad(SiO_2) gamma-irradiation from a Co^{60} source on the 1MHz C-V characteristics of a p-type Al-SiO_2-Si MOSC with 566.7nm thick oxide layer.
0V bias applied during irradiation.

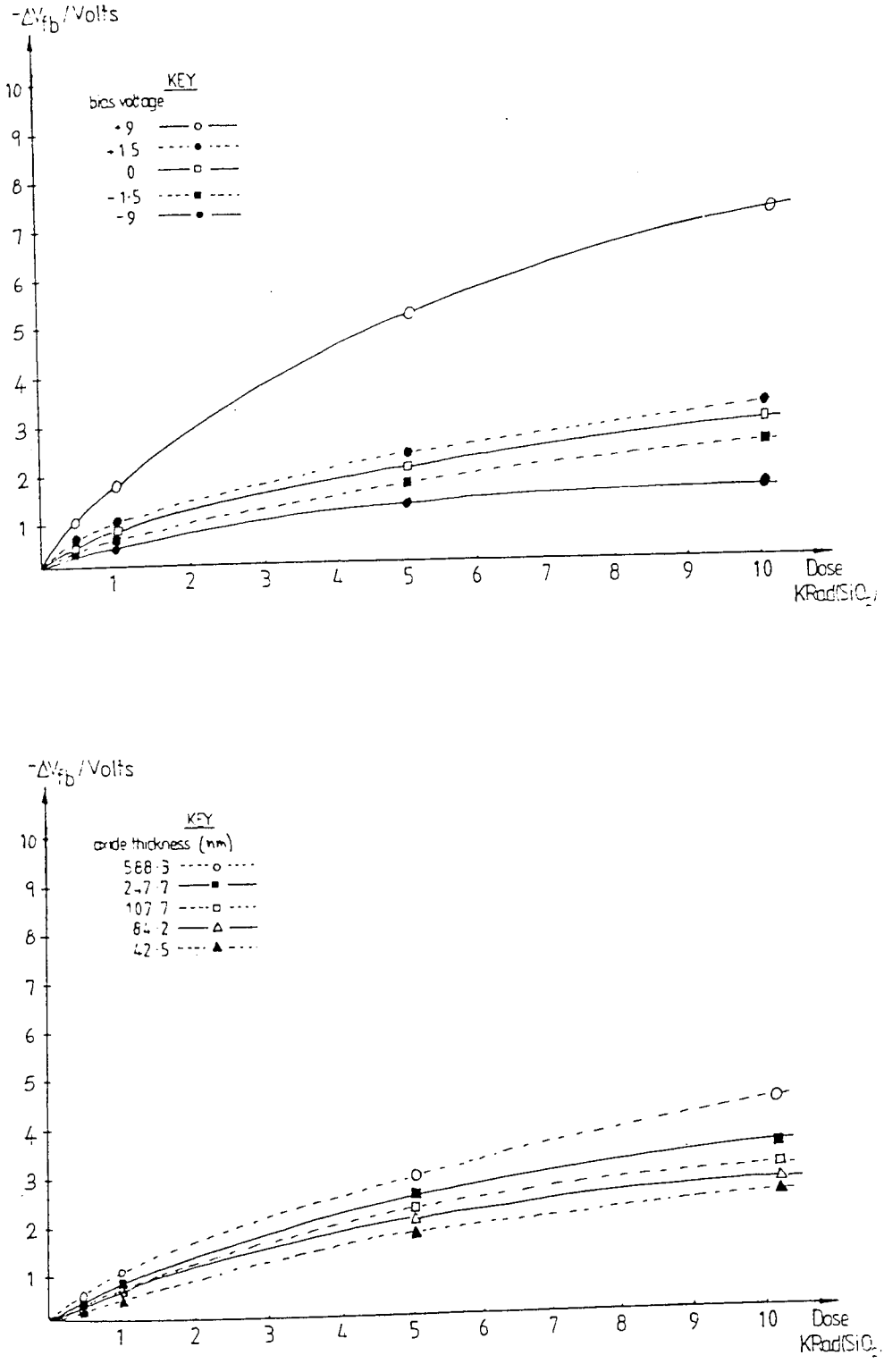

Figure 147: A plot of the shift in flatband voltage (ΔV_{fb}) versusgamma-irradiation dose from a Co^{60} source for various oxide thickness devices with the MOSC device type and bias polarity parameters.

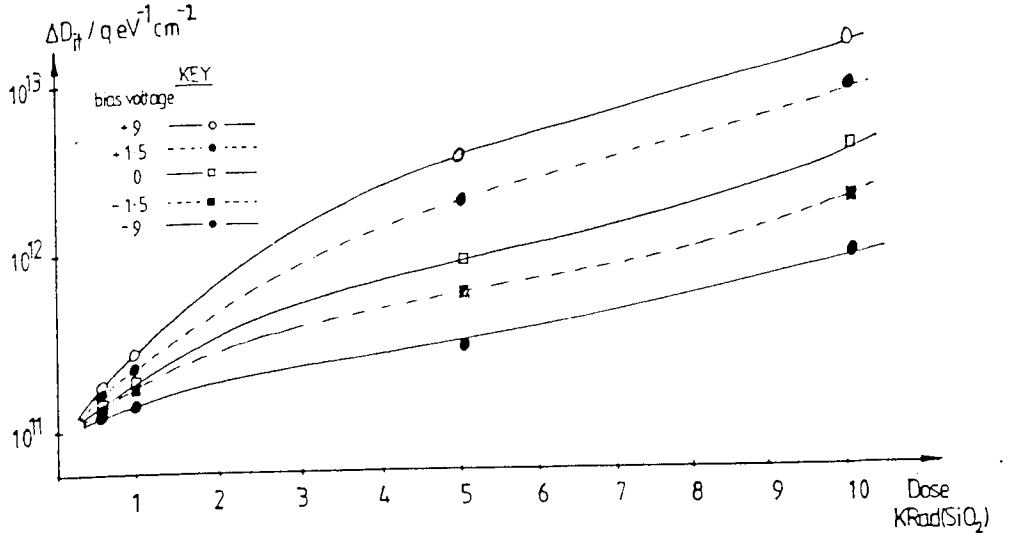

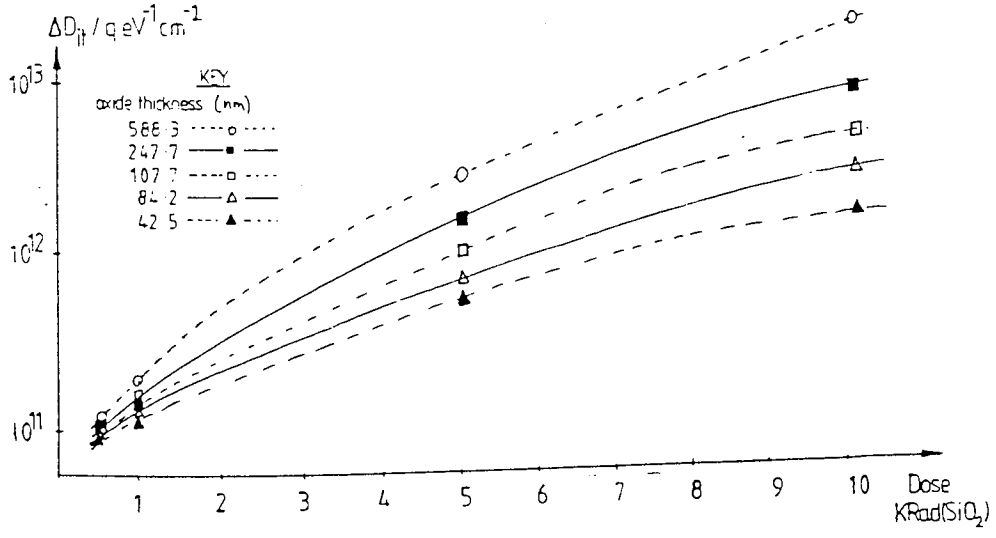

Figure 148: A plot of the density of interface states (D_{it}) versus gamma- irradiation dose from a Co^{60} source for various oxide thicknessdevices with the MOSC device type and bias polarity as parameters.

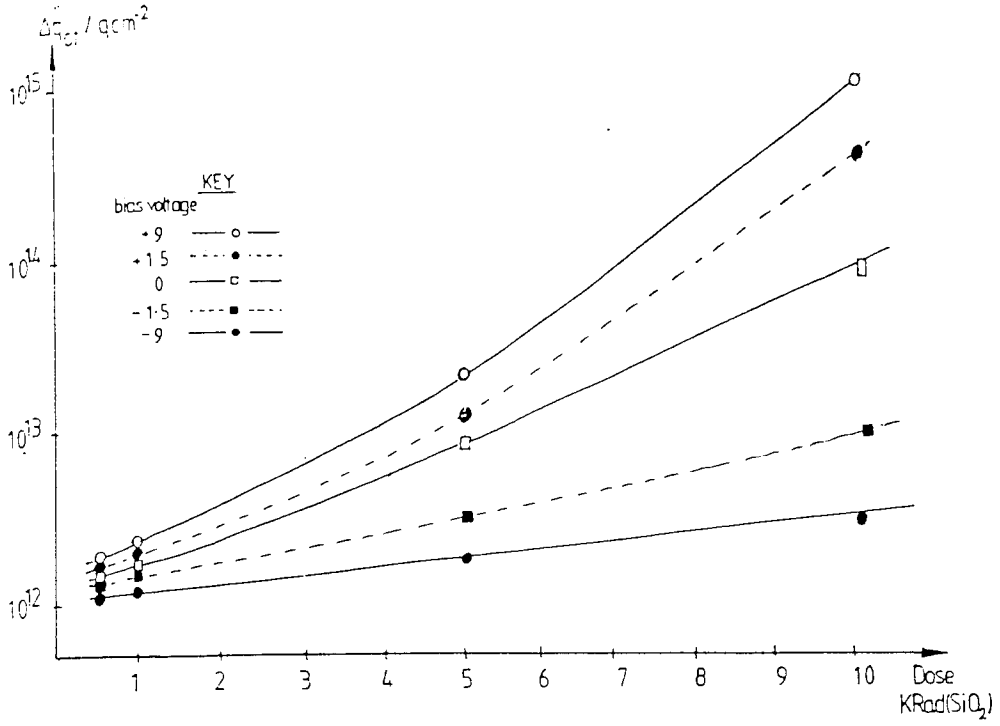

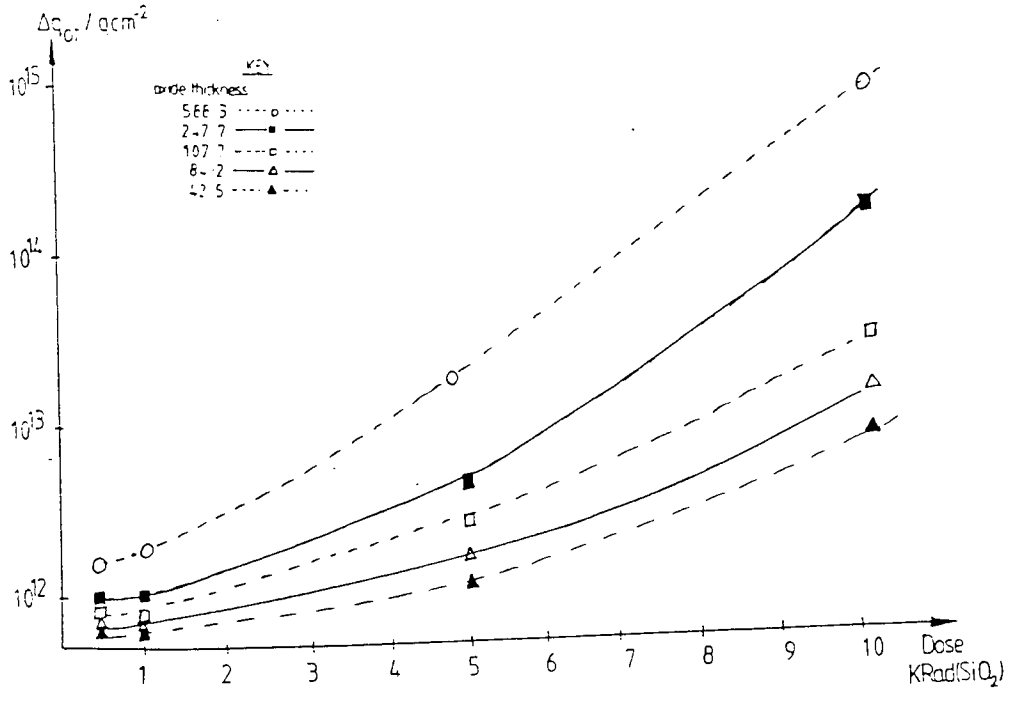

Figure 149: A plot of the oxide charge density (q_{ot}) versusgamma- irradiation dose from a Co^{60} source for various oxide thickness devices with the MOSC device type and bias polarity as parameters.

passage of the gamma- radiation through the oxide layer. It is felt that this data, because of its possible misinterpretation, is not worthy of presentation until further evidence can be obtained. Comparisons with the data presented by other workers in the field and the conclusions which have been drawn from these results are presented in Chapters7 and 8.

6.4 Neutron and Recoil-Proton Irradiations

In order to investigate the effects of neutron and recoil-proton irradiation on the breakdown characteristics and physical properties of the Al-SiO_2-Si MOSCs, a large number of individual devices were irradiated using an $_{95}Am^{241}$/Be neutron source; to determine the effects of total dose, bias magnitude and bias polarity, twelve sets of board-mounted devices (boards1 to12 inclusive) were also neutron-irradiated using the 3MV Van der Graff accelerator associated with the low-scatter facility at the National Physical Laboratories (NPL), Teddington (UK). The device mounting, probing and examination techniques, together with the electrical techniques which were used have been described in Chapter 5.

To briefly summarise the experimental conditions: individual device irradiations were performed using a 3Ci $_{95}Am^{241}$/Be source, the characteristics and calibration details of which may be found in Appendix **10.** The source was held at (0.15±0.001)m from the devices and was shielded from concomitant gamma-radiation by 3.5mm of lead sheet, as described in section **5.4.3**. Recoil-proton irradiations used the same source and irradiation geometry with a hydrogenous radiator placed directly in front of the MOSC under test; details of the radiator can be found in section **5.4.4** and the calibration of the source and other details of the recoil-proton irradiations may be found in Appendix **11**.

The majority of the neutron irradiations were performed on board mounted MOSCS using the neutron irradiation facility at the NPL(UK), the details of which may be found in Appendix **9**, and its characteristics in Table 14. For uniformity of total dose over the entire area of the board-mounted samples, the source was placed at the maximum distance (0.20m) from the boards which led to a maximum possible error in the dose calculations of ±3% for the majority of the irradiations. and ±8% for the very short time irradiations, with a dose variation of approximately -5% from the centre to the

edge of the boards; the dose rate, total dose and error details for these irradiations are presented in Table 14, with further details in Appendix 9.

The voltage range of the biases used for board mounted devices was from -9V to +9V, and included zero bias and the top-gate electrode connected to the Ohmic contact for the open-circuit condition (these were kept as similar in magnitude to those used in the other investigations as was possible); the biasing arrangement is, again, shown in Figures 91(a) and 91(b).

For individual device irradiations a 1MΩ limiting resistor, in series with the EHT bias supply and top gate electrode, was used to prevent avalanche breakdowns; this was removed for I-V characteristic determinations for the devices so that current runaway and the onset of breakdown could be studied. The limiting resistor was not necessary for the board irradiations because of the low bias voltages used, well below the breakdown fields for even the thinnest oxide devices under investigation.

The results from these investigations are presented in the proceeding paragraphs, with the conclusions drawn from them discussed in Chapters 7 and 8.

Several MOSCs of each types and oxide thickness were investigated whilst under irradiation with neutrons from the Am^{241}/Be source and with applied fields ranging between $-10MVcm^{-1}$ and $+10MVcm^{-1}$ across the devices (the negative sign indicating that the top electrode was at a negative potential with respect to the Ohmic contact). There was no evidence to suggest that the neutron or concomitant recoil-proton irradiation in any way affected the breakdown characteristics of the devices, which followed breakdown characteristics nearly identical to those shown in Figures113 to 116.

Physical examination of the devices after irradiation, but before any defect-related or intrinsic breakdown had occurred showed no evidence of any effects on the structure, and examination of breakdown pits which occurred in the expected (defect-related and intrinsic breakdown) field range showed no observable differences from those for virgin devices, as typified in Figures 112 to 114. It has been concluded that neutron radiation in the 0.4-10MeV range from the Am^{241}/Be source used and the recoil-protons from the hydrogenous radiator (induced by the (n,p) reaction by neutrons from the same source) do not induce dielectric breakdown.

Investigation of the chemical nature of the Si-SiO_2 interface and bulk SiO_2 using AES and ESCA showed spectra with no apparent differences from those for virgin devices, as typified by Figures

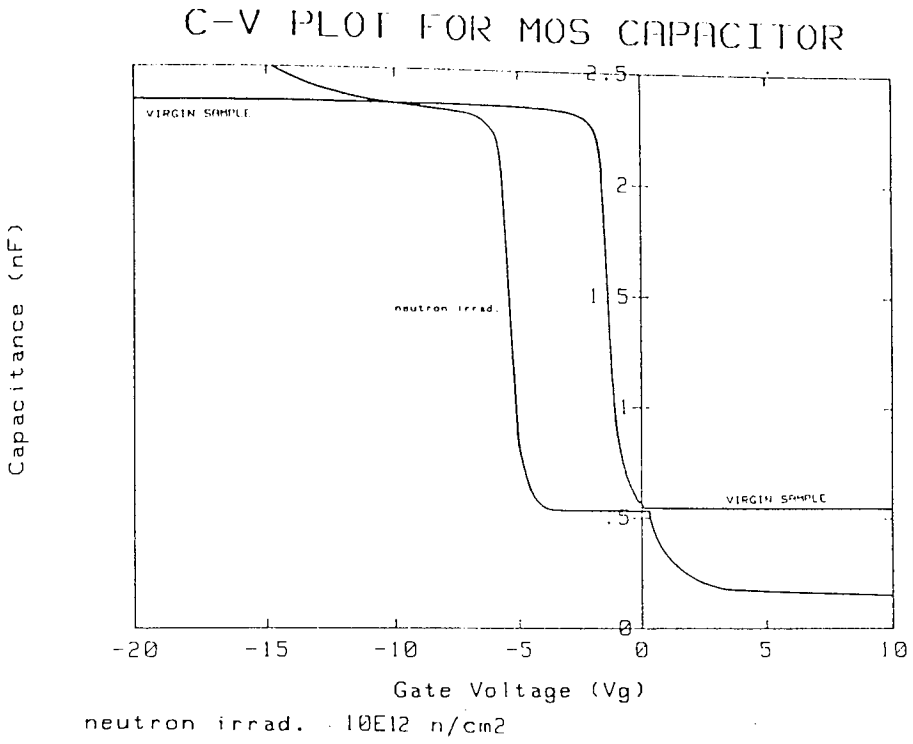

Figure 150: Effect of magnitude of a total dose of 10^{12} n cm^{-2} and associated recoil-proton irradiation on the 1MHz C-V characteristics of a p-type Al-SiO_2-Si MOSC with 37.4nm thick oxide layer.
0V bias applied during irradiation.

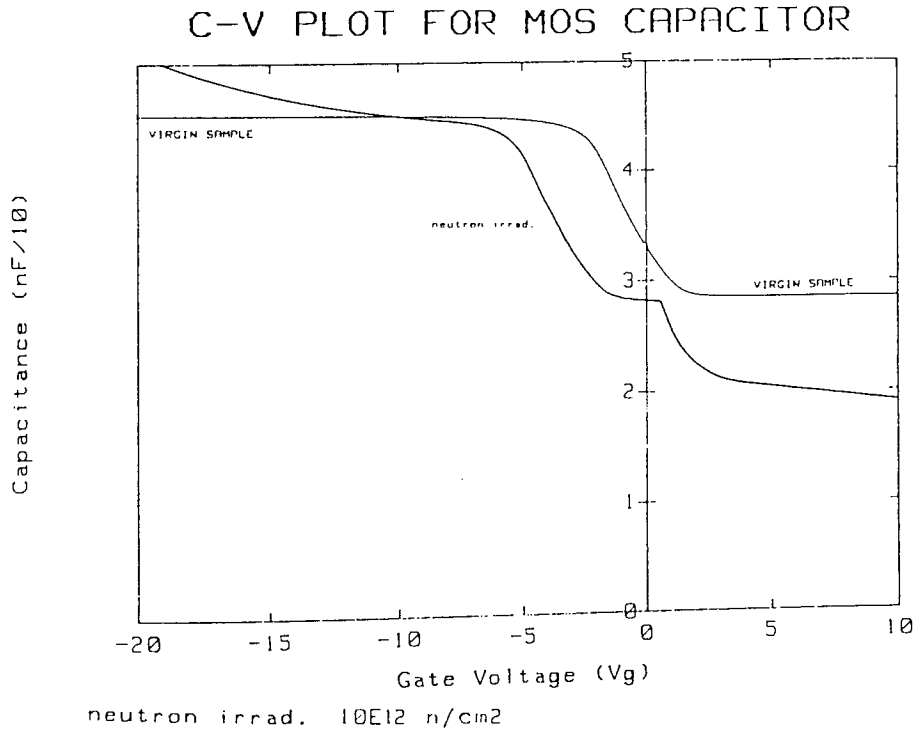

Figure 151: Effect of magnitude of a total dose of 10^{12} n cm^{-2} and associated recoil-proton irradiation on the 1MHz C-V characteristics of a p-type Al-SiO_2-Si MOSC with 566.7nmthick oxide layer.
0V bias applied during irradiation.

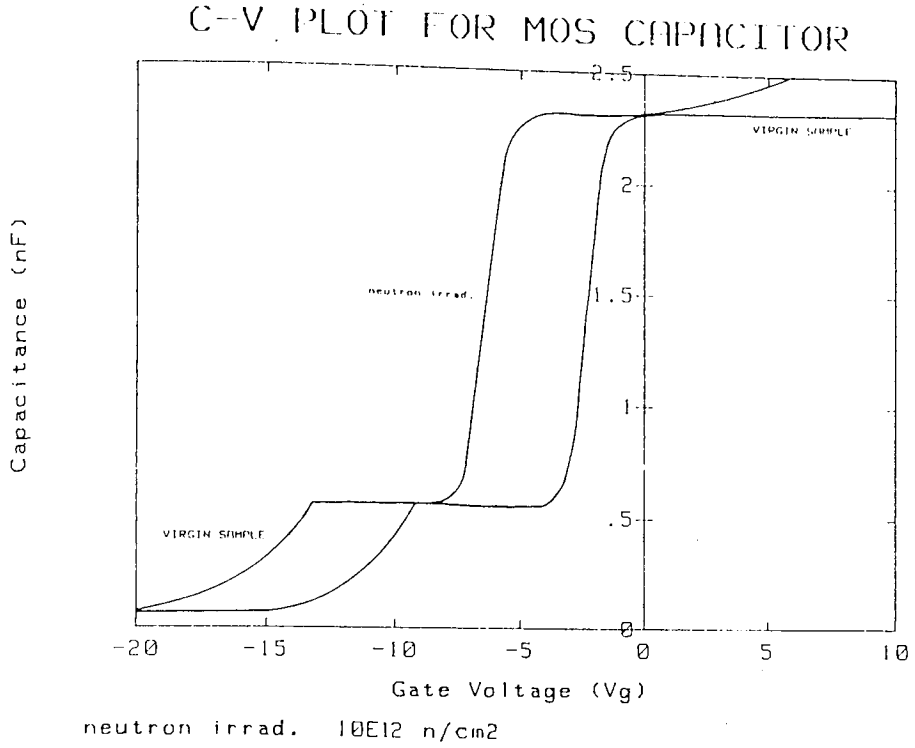

Figure 152: Effect of magnitude of a total dose of 10^{12} n cm^{-2} and associated recoil-proton irradiation on the 1MHz C-V characteristics of an n-type Al-SiO_2-Si MOSC with 42.5nm thick oxide layer.
0V bias applied during irradiation.

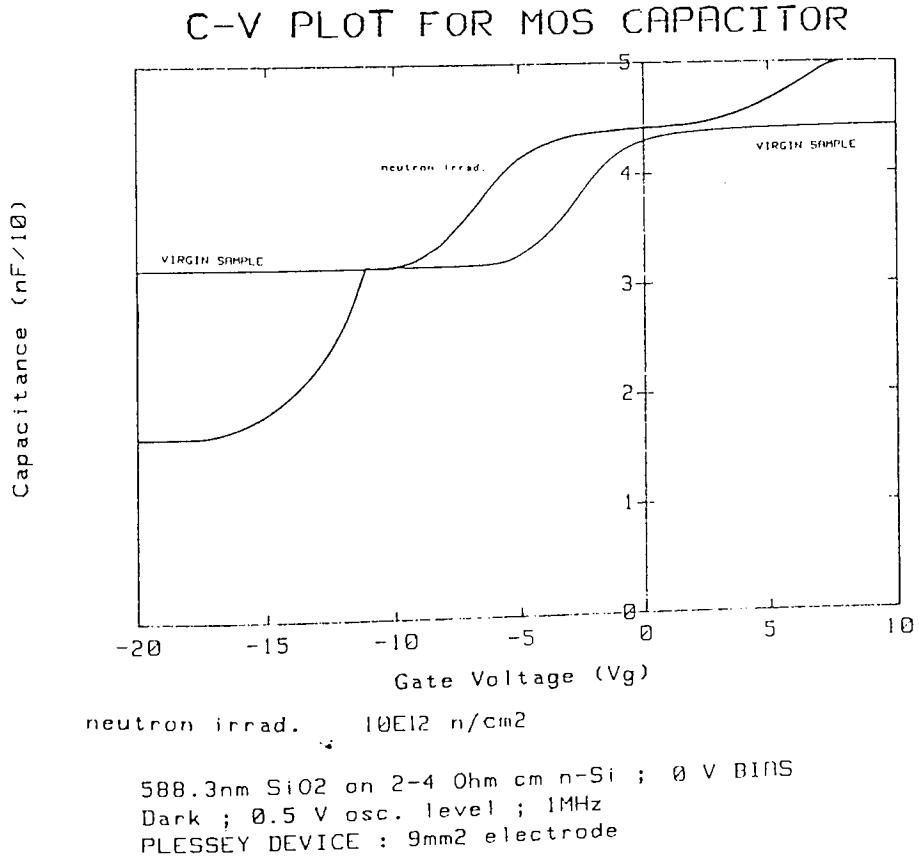

Figure 153: Effect of magnitude of a total dose of 10^{12} n cm^{-2} and associated recoil-proton irradiation on the 1MHz C-V characteristics of an n-type Al-SiO_2-Si MOSC with 588.3nm thick oxide layer.
0V bias applied during irradiation.

109(a) to (c) and Figure110; this, however, does not preclude the existence of radiation damage in the structure, since the techniques used are insensitive to chemical shifts expected from the displacement damage caused by the relatively few neutron interactions, and insensitive to the even fewer recoil-proton interactions with their associated ionization damage. Calculations of the approximate number of displacements caused in the SiO_2 layers by the incident neutrons, based on tabulated data of interaction cross-sections for neutrons with silicon and oxygen, are presented in Appendix 13.

No pulse output was seen from the devices under irradiation for both devices with and without various combinations of magnitudes and polarities of applied bias; the devices appeared invisible to neutron and recoil-proton radiations.

The appearance that the MOSCs are invisible to the neutron and recoil-proton radiations in this energy range precludes the feasibility of the devices as novel neutron or recoil-proton detectors for personal dosimetry, as proposed in sections 1.4 and 5.4.4.

However, the C-V characteristics of the devices were minimally altered by the combined neutron and recoil-proton radiation field, as can be seen in Figures 150 to 153 for n-type and p-type MOSCs with thick and thin oxides, respectively, irradiated to a total dose of 10^{12} n cm^{-2}, but were not altered by the neutron field alone. This implies that the low number of recoil-protons which irradiated the devices caused the noticeable shift in the C-V curves to more negative gate voltage regimes, this being typical of positive charge injection in the oxide layer of the device. The oxide positive charge buildup can be seen for devices irradiated with no applied gate bias, the application of bias having no effect on the magnitude of the C-V curve shift. Also evident from the C-V curves for the irradiated devices is the introduction (or generation) of slow states causing the onset of deep-depletion and the introduction (or generation) of fast surface states causing the anomalous behaviour at high device capacitances; these effects are described and explained in sections 2.4.2 and 2.5.2. Such effects were also seen for devices irradiated with only neutrons and are therefore believed to be due to the neutrons alone, possibly from displacment damage in the oxide and at the interface.

Figures 154, 155 and 156 show plots, for both n and p-type MOSCs, of the flatband voltage shift versus neutron and recoil-proton radiation dose (expressed as the numbers of neutrons and recoil protons incident cm^{-2} on the devices), density of interface state generation versus dose and oxide

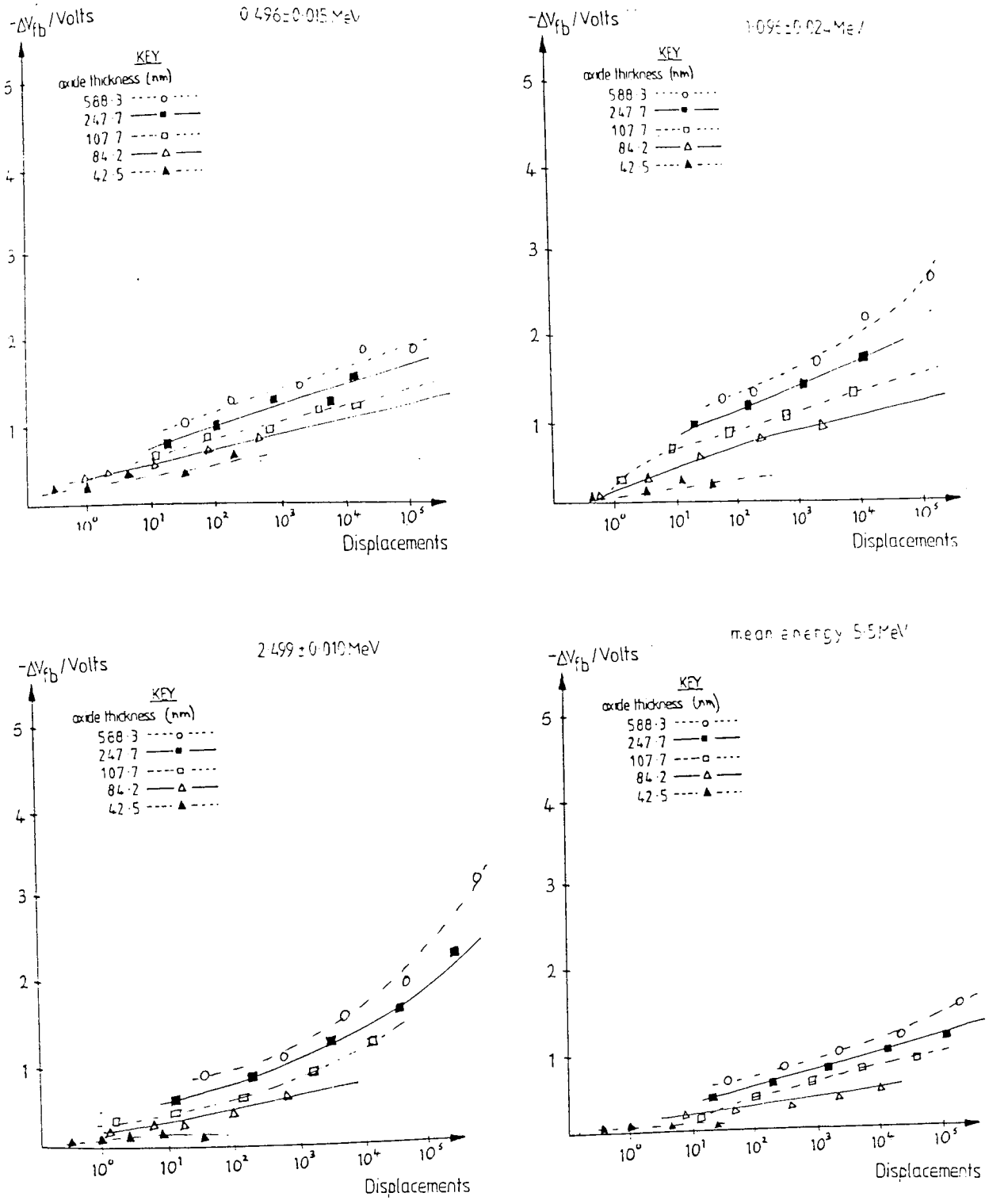

Figure 154: A plot of the shift in flatband voltage (ΔV_{fb}) versus neutron and associated recoil-proton irradiation for various oxide thickness devices with the MOSC device type, bias polarity and neutron energy as parameters.

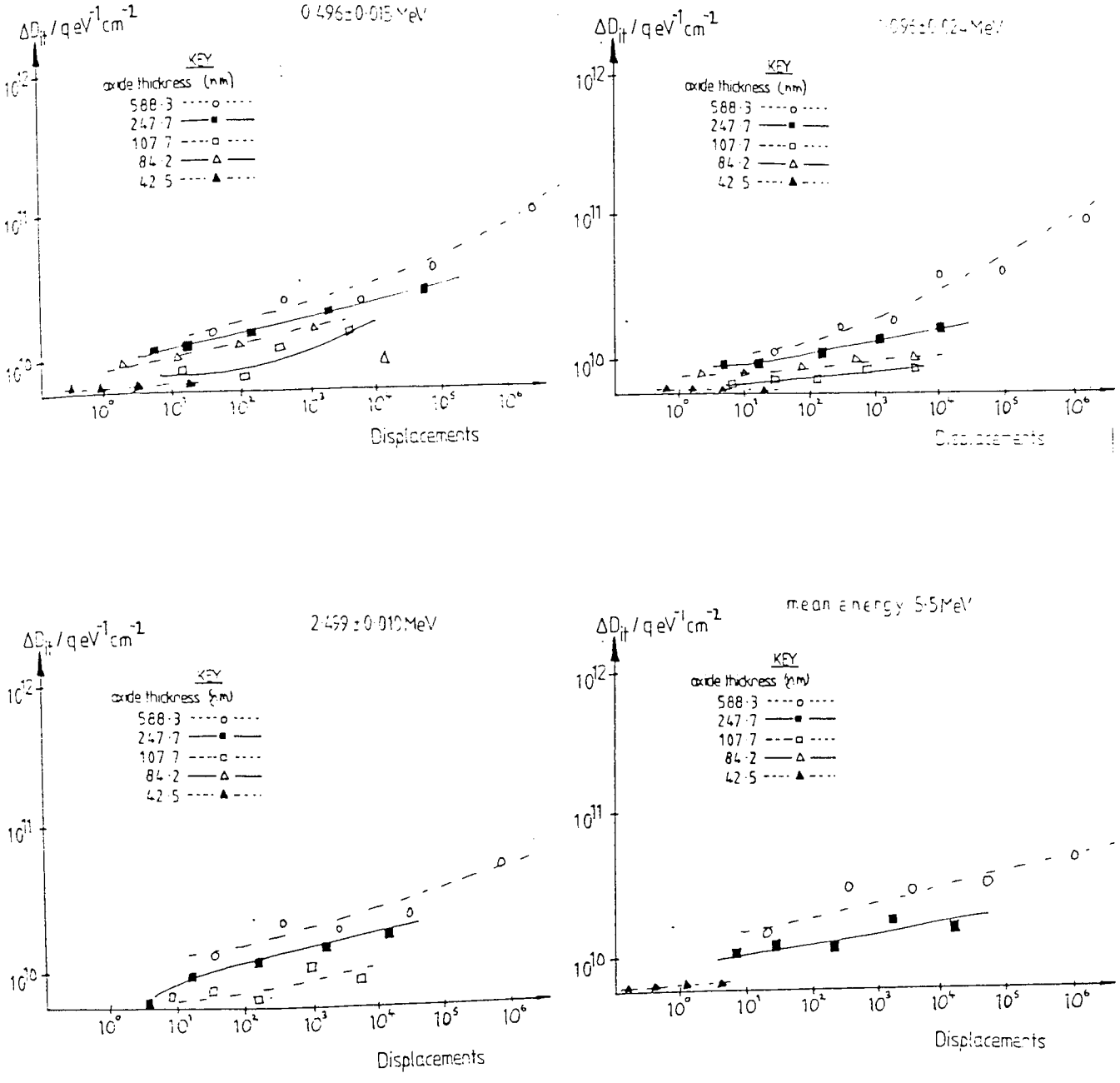

Figure 155: A plot of the density of interface states (D_{it}) versus neutron and associated recoil-proton irradiation for various oxide thickness devices with the MOSC device type and bias polarity and neutron energy as parameters.

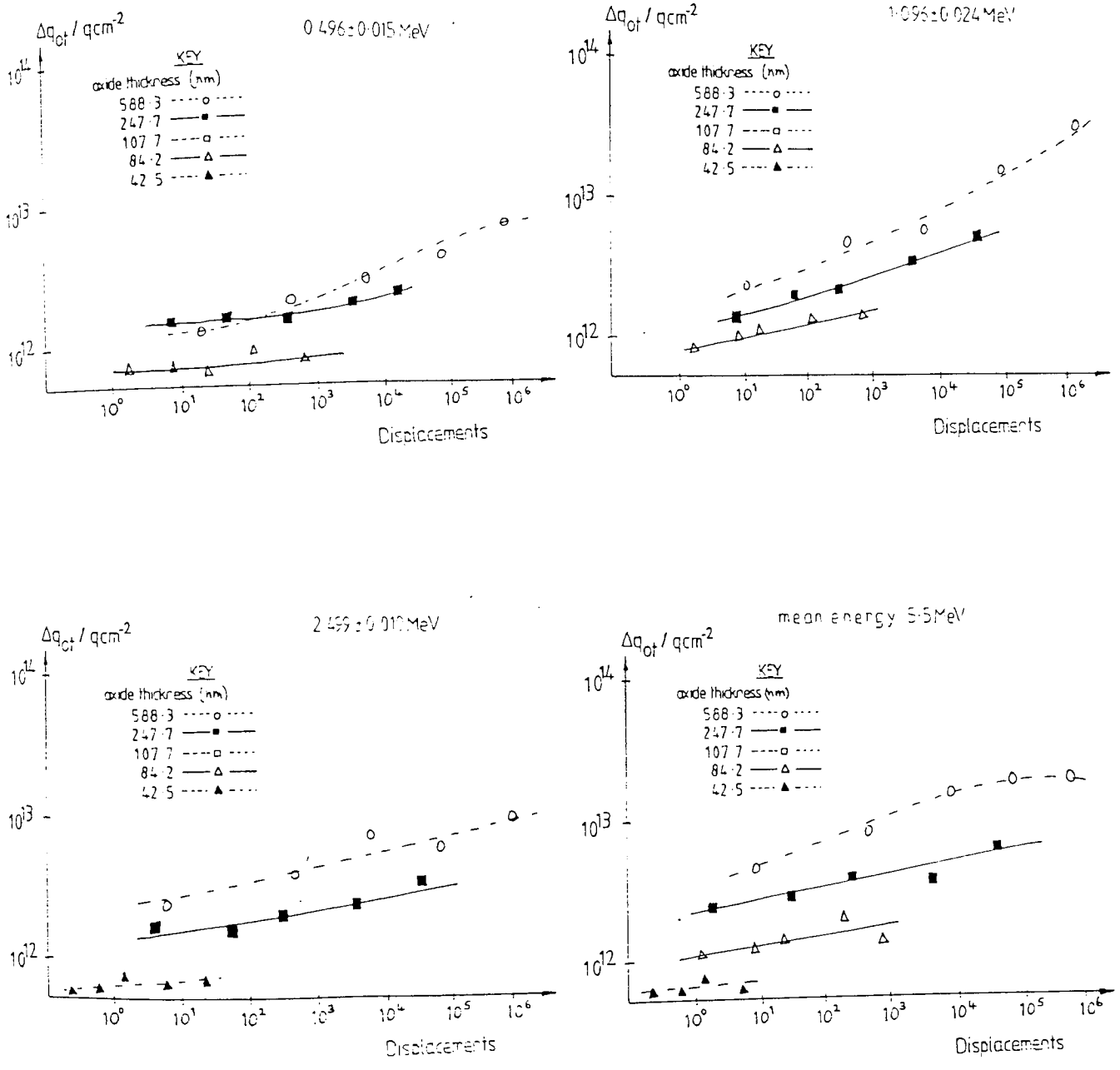

Figure 156: A plot of the oxide charge density (q_{ot}) versus neutron and associated recoil-proton irradiation for various oxide thickness devices with the MOSC device type and bias polarity and neutron energy as parameters.

charge density versus dose, respectively, for various device oxide thicknesses and neutron irradiation energies. From these it is evident that a near-linear relationship exists between the effects of the radiations and the total radiation dose which is energy dependent, as would be expected if the shift of the C-V curve seen is due entirely to the recoil-protons (whose generation in the hydrogenous layer is a function of incident neutron energy).

The effect of irradiation on the I-V characteristics for the devices was undetectable with the apparatus used. It is believed that any effects on the I-V characteristics of the MOSCs due to the neutrons or recoil-protons would have been clearly evident if the effects were to affect device parameters in any detrimental way.

Comparisons with the data presented by other workers in the field and the conclusions which have been drawn from these results are presented in Chapters7 and 8.

6.5 Fission-Fragment Irradiations

In order to investigate the effects of fission-fragment irradiation on the breakdown characteristics and physical properties of the Al-SiO_2-Si MOSCs, a large number of individual devices were irradiated; the device mounting, probing and examination techniques, together with the electrical techniques which were used have been described in Chapter 5.

To briefly summarise the experimental conditions: individual device irradiations were performed under vacuum at a pressure of approximately $3*10^{-2}$mbar in the vacuum chamber illustrated in Figure 101 and in the shielded enclosure shown in Figure 93 using a $0.7\mu Ci_{98}Cf^{2522}$ source, the characteristics of which and the calibration details are presented in Table 15 and Appendix 12, respectively. The irradiation geometries used are presented in Figure 103, which shows the source arrangement for vacuum irradiations and for irradiations where the the source-to-device distance was varied between 2.51±0.05mm and 13.84±0.06mm to provide different residual energy fission-fragments (after slowing in air). The range in air versus residual energy and stopping power in SiO_2 for light and heavy fission-fragments is presented in Appendix 14.

For most device irradiations a 1MΩ limiting resistor, in series with the EHT bias supply and top ga electrode, was used to prevent avalanche breakdowns; this was removed for I-V characteristic

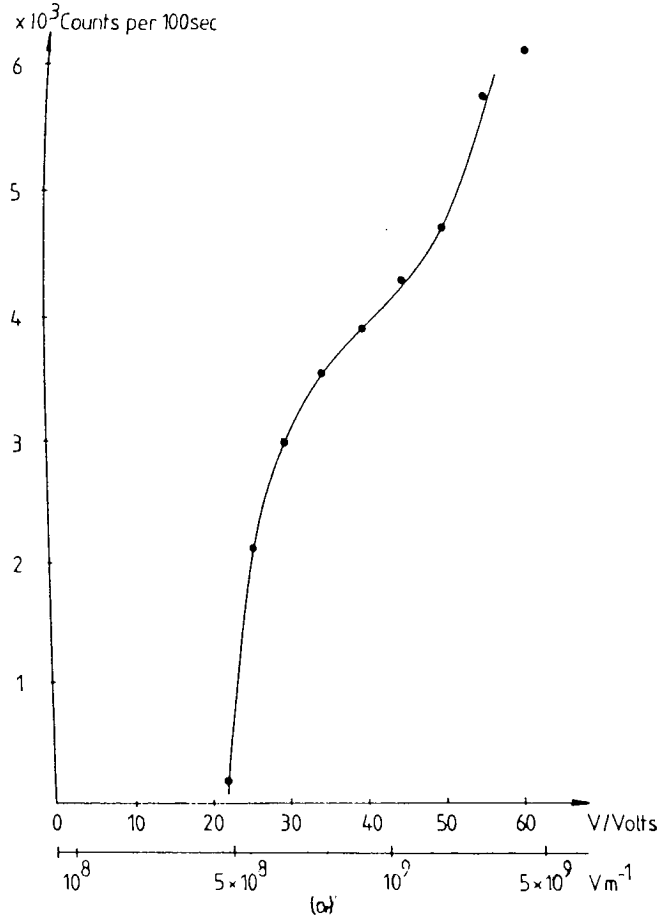

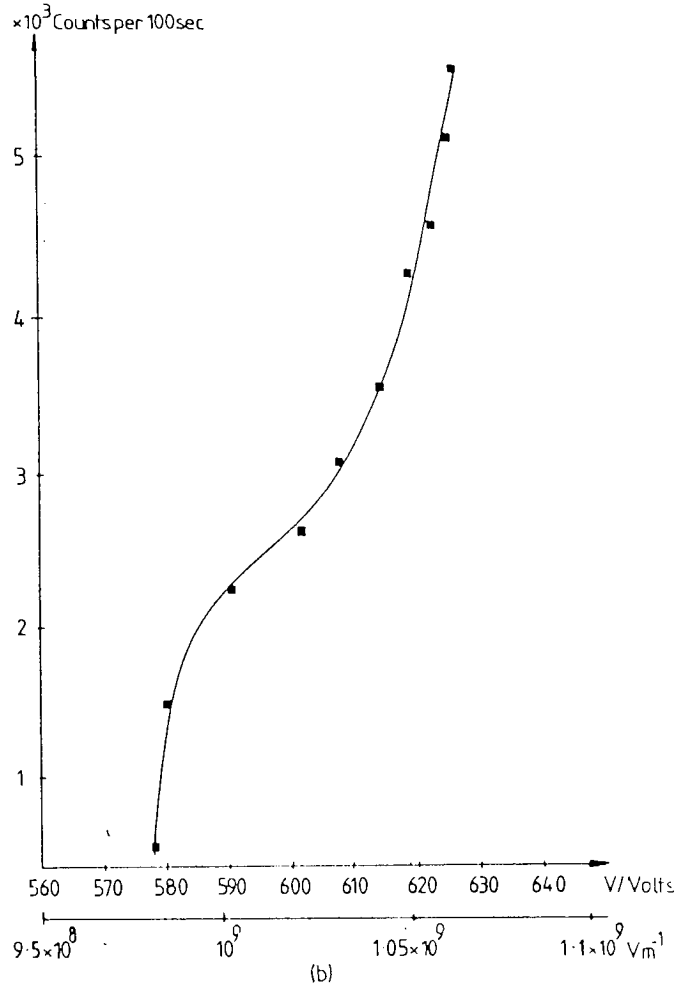

Figure 157: (a) A plot of the number of the number of breakdown pulses versus the applied gate voltage and corresponding oxide field for an n-type Al-SiO_2-Si MOSC with a 42.5nm thick oxide layer under fission-fragment irradiation from a Cf^{252} source.

Figure 157: (b) A plot of the number of the number of breakdown pulses versus the applied gate voltage and corresponding oxide field for an n-type Al-SiO_2-Si MOSC with a 588.3nm thick oxide layer under fission-fragment irradiation from a Cf^{252} source.

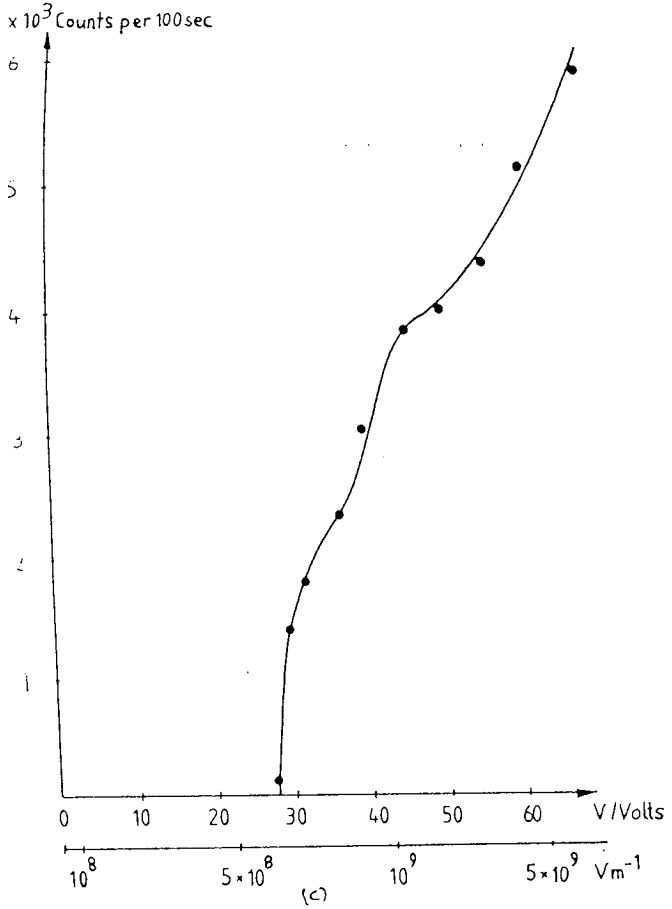

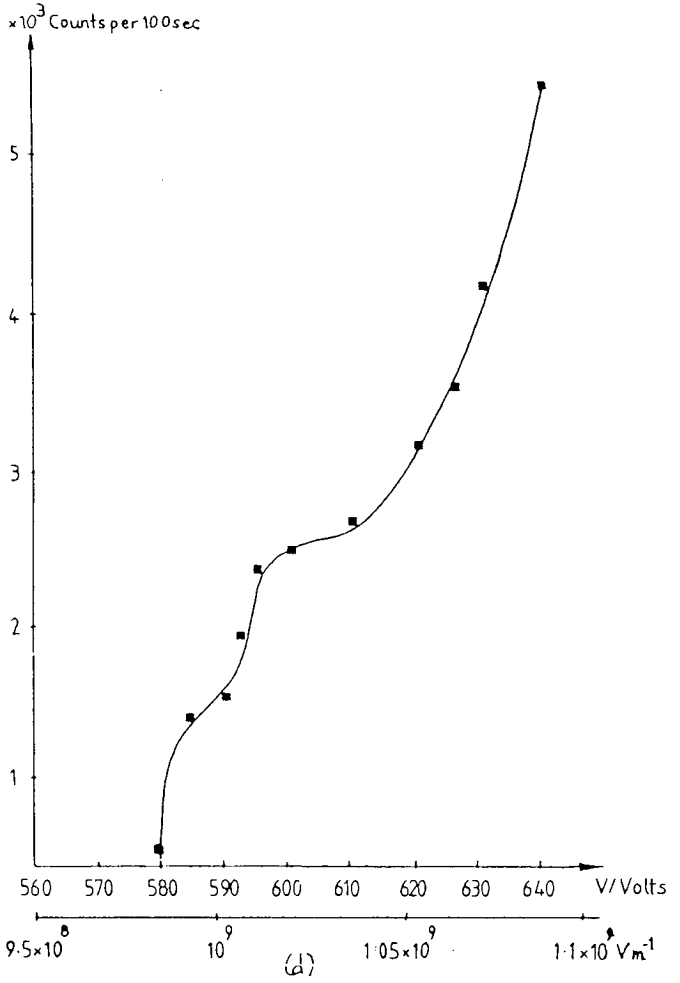

Figure 157: (c) A plot of the number of the number of breakdown pulses versus the applied gate voltage and corresponding oxide field for a p-type Al-SiO_2-Si MOSC with a 37.4nm thick oxide layer under fission-fragment irradiation from a Cf^{252} source.

Figure 157: (d) A plot of the number of the number of breakdown pulses versus the applied gate voltage and corresponding oxide field for a p-type Al-SiO_2-Si MOSC with a 566.7nm thick oxide layer under fission-fragment irradiation from a Cf^{252} source.

determinations for the devices so that current runaway and the onset of breakdown could be studied.

(Since the effects of the radiations concomitant with the fission-fragments from the Cf^{252} source used - alpha and neutron radiations - have been shown to produce no effect on the breakdown characteristics for the devices, these radiation fields have been ignored in discussion of the fission-fragment induced breakdown process caused by fission-fragments from this source).

The salient results from these investigations are presented in the proceeding paragraphs, with the conclusions drawn from them discussed in Chapters **7** and **8**.

The breakdown and I-V characteristics of the various devices under irradiation from the Cf^{252} source whilst under vacuum of $\approx 3*10^{-2}$mbar were determined using the techniques described in Chapter **5**. Breakdown testing was performed at room temperature using the voltage probe assembly and breakdown apparatus with the shielded enclosure arrangement shown in Figures 93 and 95, and stepped gate-voltage application, using oxide fields between $-11MVcm^{-1}$ and $+11MVcm^{-1}$, dependent on the device intrinsic (and defect-related) breakdown strength.

The breakdown characteristics for n and p-type devices whilst under irradiation are presented in Figures 157(a) to (d), which show typical curves for thick and thin-oxide MOSCs with the number of radiation-induced non-shorting breakdowns versus applied gate voltage and respective field as parameters alongside the breakdown characteristics for the devices when no radiation was present. An exponential rise in the number of breakdowns can be seen with increasing applied gate voltage, occurring at fields well below those for intrinsic or defect-related breakdown, with a characteristic knee in the curve for the n-type devices, not present in the curves for p-type devices.

Device destruction occurred within an ≈90% increase in applied gate voltage over the onset of radiation-induced-breakdown voltage for the thinnest oxide devices, falling to ≈15% for the thickest oxide devices, implying that the thinner devices have an operating plateau (that is, a voltage range for detection of fission-fragments by radiation-induced breakdown) which is far more extensive than that for thicker devices; this would suggest that thinner oxide devices are more feasible as fission-fragment detectors than thicker oxide devices since the operating region occurs for much lower oxide fields than the intrinsic or defect-related breakdown fields.

Physical examination of the effects of radiation-induced breakdowns on the device revealed breakdown pits with two types of breakdown damage: both forms of breakdown pit are craters of

between 10 and 50μm in diameter for n-type devices and between 2 and 6μm for p-type devices, independent of the magnitude and polarity of the applied field with the same shape and characteristics as those due to intrinsic (or defect-related)breakdowns presented in Section **6.1** for virgin devices.

The pits were rarely surrounded by surface damage of the Al gate electrode, unlike those due to intrinsic or defect-related breakdowns, and were typical of those shown in the photographs in Figures 158(a) to (c), which implies a single non-shorting breakdown had occurred at the breakdown site; inverted-field interferograms of the breakdown sites, typical of those shown for virgin devices in Figures 114(a) and (b), have revealed that the two forms of radiation-induced breakdown pits are almost identical to those for virgin devices; for the most common form of crater found on the devices, the crater depths were approximately 50% of the thickness of the oxide layer and were typical in dimensions of those shown in Figures 158(a) and (b). The other form, shown in Figure 158(c) reached the entire thickness of the oxide and produced star-shaped breakdown patterns in the Al metal surrounding the breakdown site, similar to those reported by YANG et al[142]. In a similar fashion to intrinsic and defect-related shorting breakdowns, for several devices tested a small trace of Al could be found (using the SEM with Kevex detector and LINK ESCA system) at the base of the deeper craters, indicating a possibly conducting channel between the semiconductor substrate (or very near to it) and the top Al electrode, perhaps indicating that the fission-fragments had initiated a breakdown process similar to that for intrinsic (or defect-related) breakdown at a far lower field than expected.From these results a proposal as to which mechanisms form the possible physical basis of radiation-induced breakdown has been made.

The approximate number of radiation-induced breakdowns the device can sustain before failure has been estimated (by counting the number of breakdown pits over a large area of the device and extrapolating the data obtained) as typically being $\approx 10^4$ per device for an n-type device and $\approx 10^5$per device for a p-type device; these values are of the same order as the total (measured) number of breakdown pulses from each type of device recorded before device failure, typically between 10^4 and10^6 per device, for n and p-type devices respectively. The conclusion drawn from this is that each pulse occurs due to a breakdown at each site and, therefore, unlike defect related and intrinsic breakdown results presented in section **6.1** for virgin devices, in the case of fission-fragment induced breakdowns at oxide fields far lower than the (expected) oxide breakdown

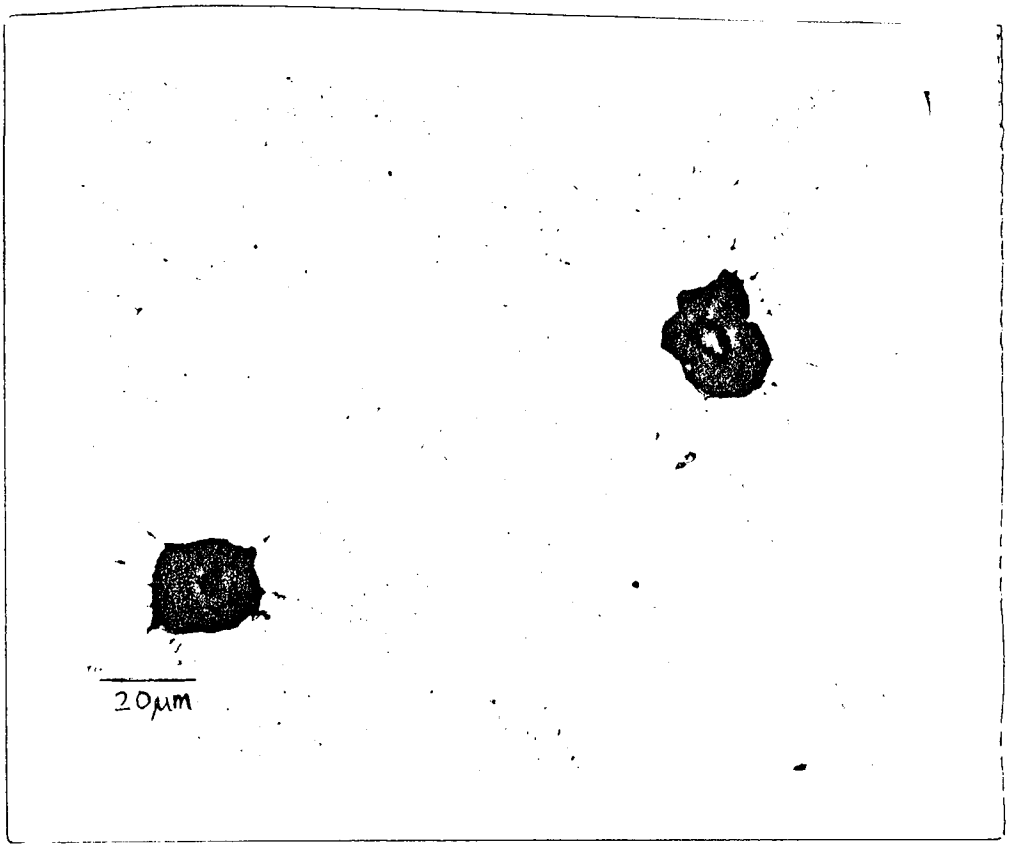

Figure 158: (a) Optical micrograph of two fission-fragment-induced breakdown pits. Magnification x160

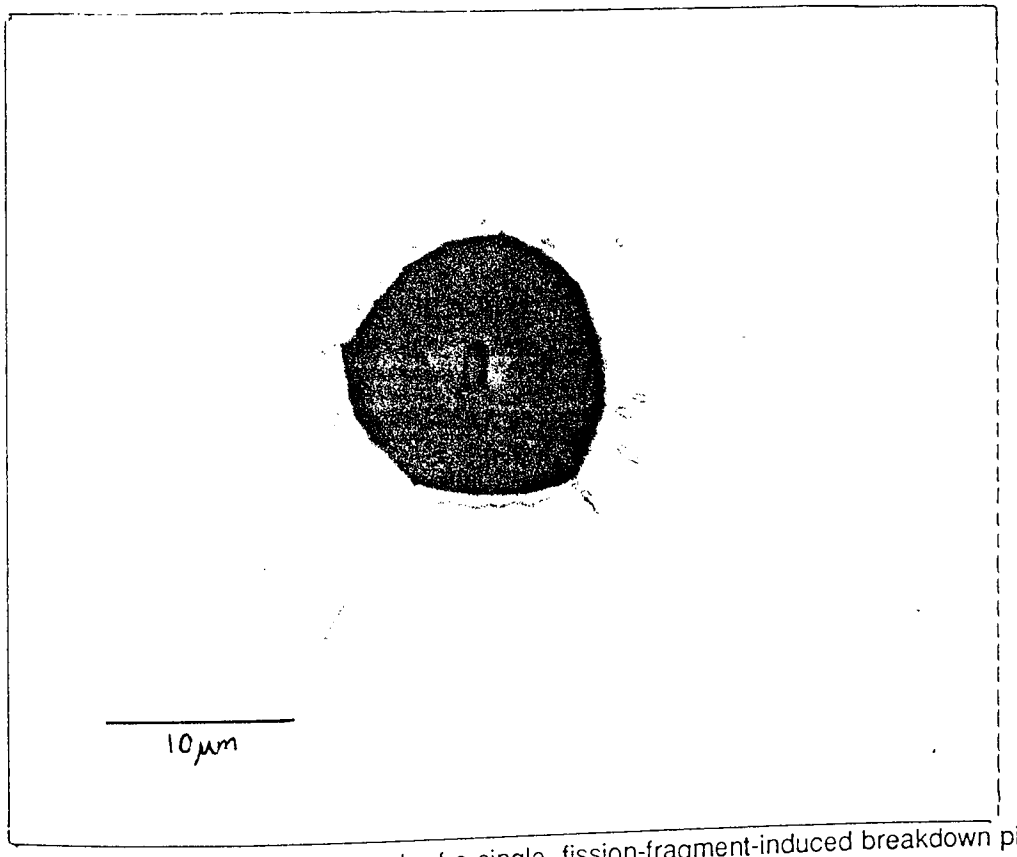

Figure 158: (b) Optical micrograph of a single fission-fragment-induced breakdown pit; note the dark central area of the pit which is the base of the crater, and surrounding the electrode hole there are splashes of electrode material. Magnification x370

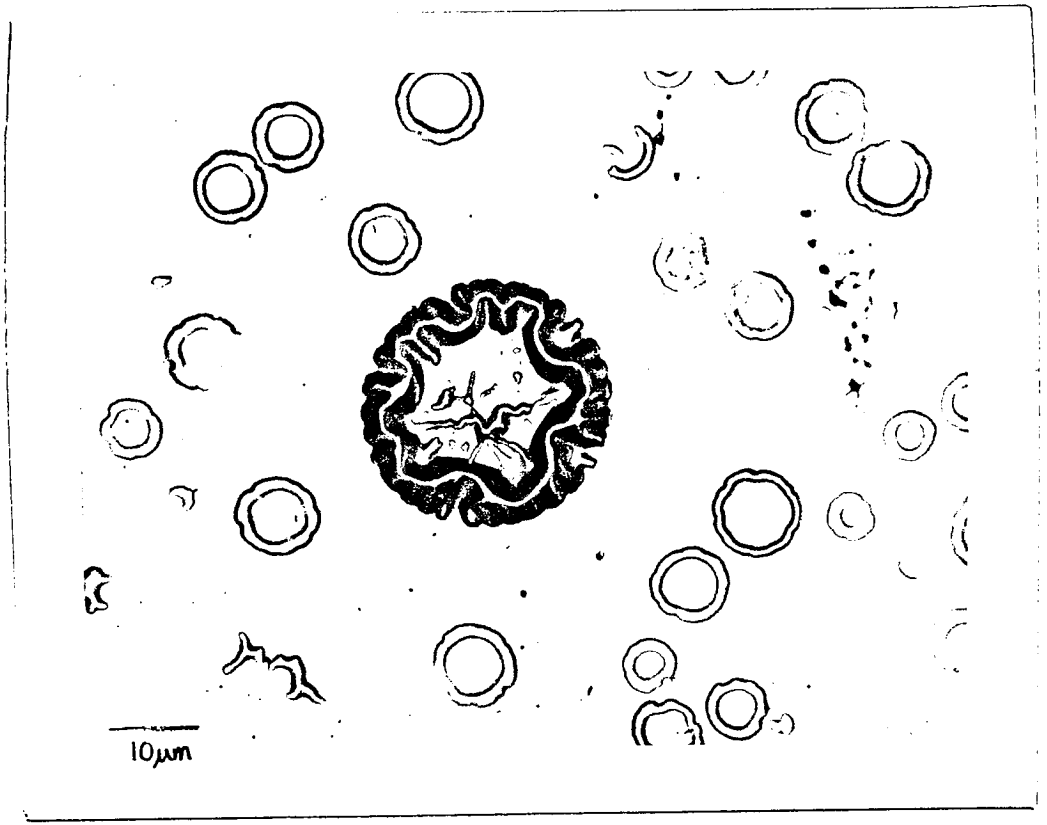

Figure 158: (c) Optical micrograph of a fission-fragment-induced breakdown pit; this shows a shorting-breakdown in which the top gate electrode has partially melted and dropped into the crater formed by the vaporisation of the oxide below, electrically joining the silicon substrate to the top gate electrode.
Magnification x820

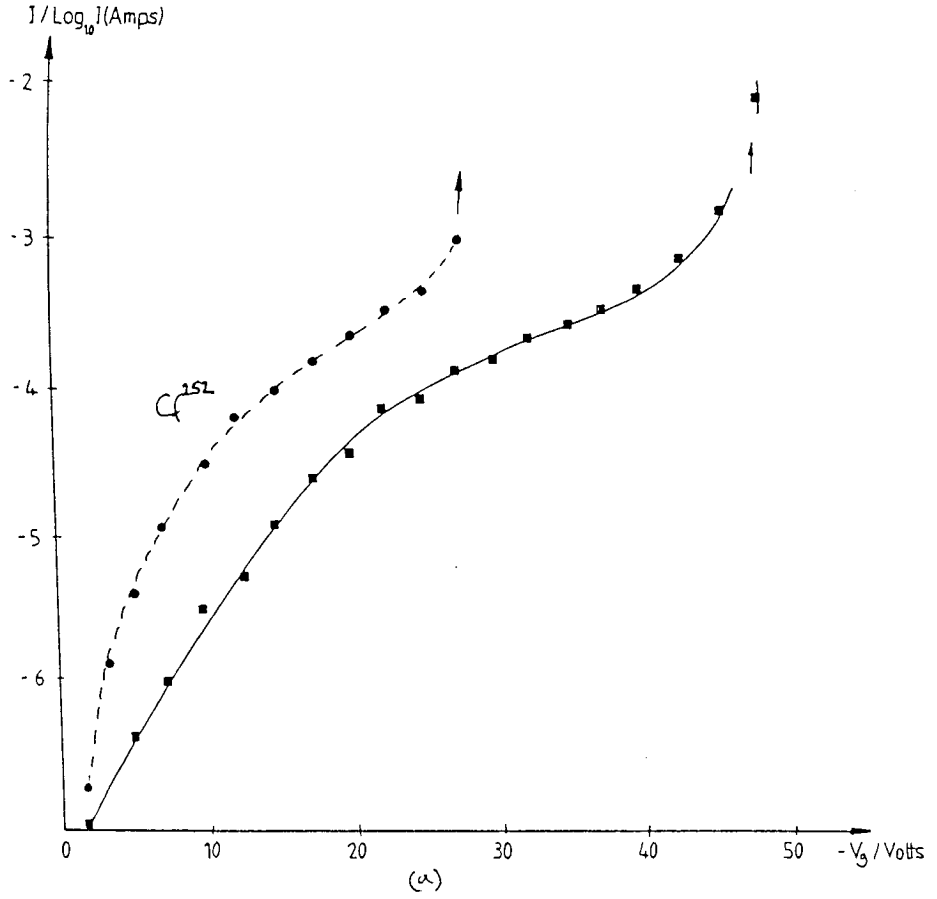

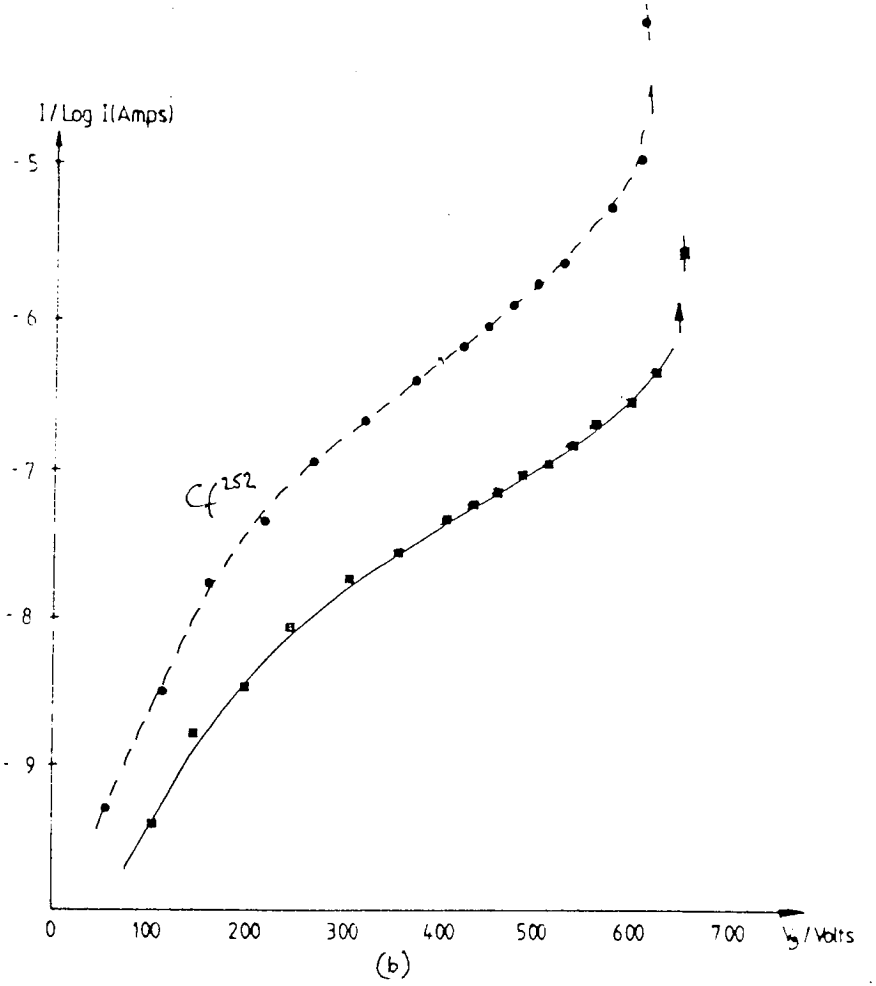

Figure 159: (a) I-V curves for a typical n-type Al-SiO_2-Si MOSC with 42.5nm thick oxide within and without a Cf^{252} fission-fragment irradiation field.

Figure 159: (b) I-V curves for a typical n-type Al-SiO_2-Si MOSC with 588.3nmthick oxide within and without a Cf^{252} fission-fragment irradiation field.

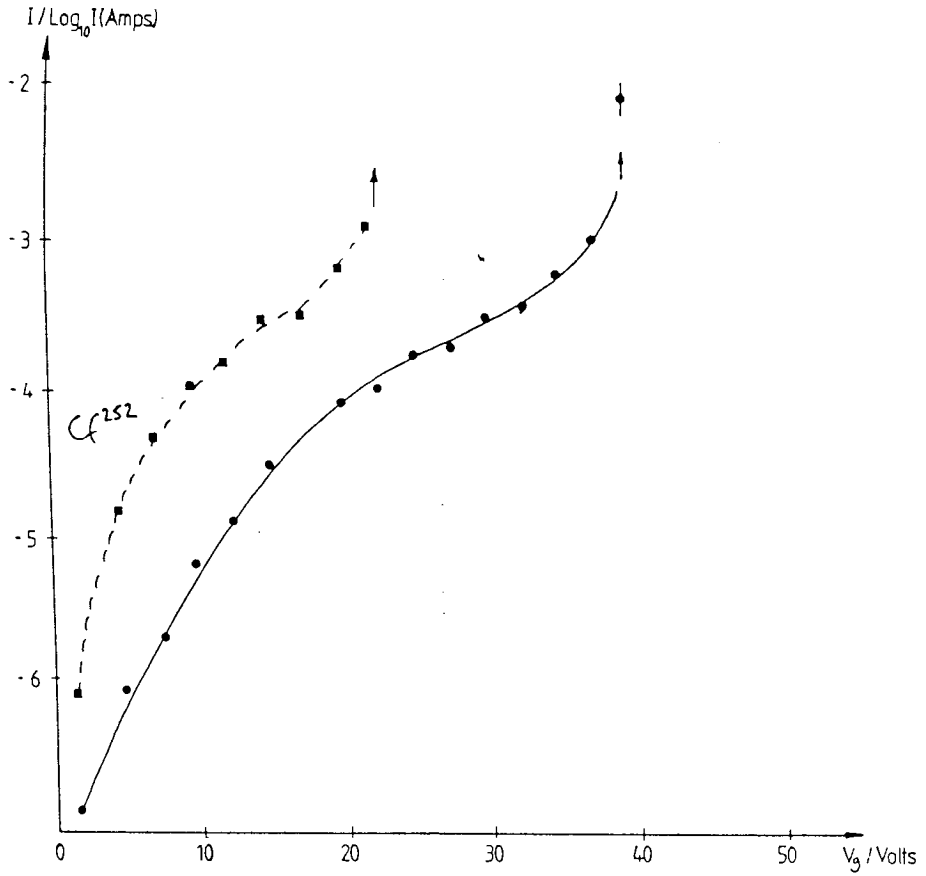

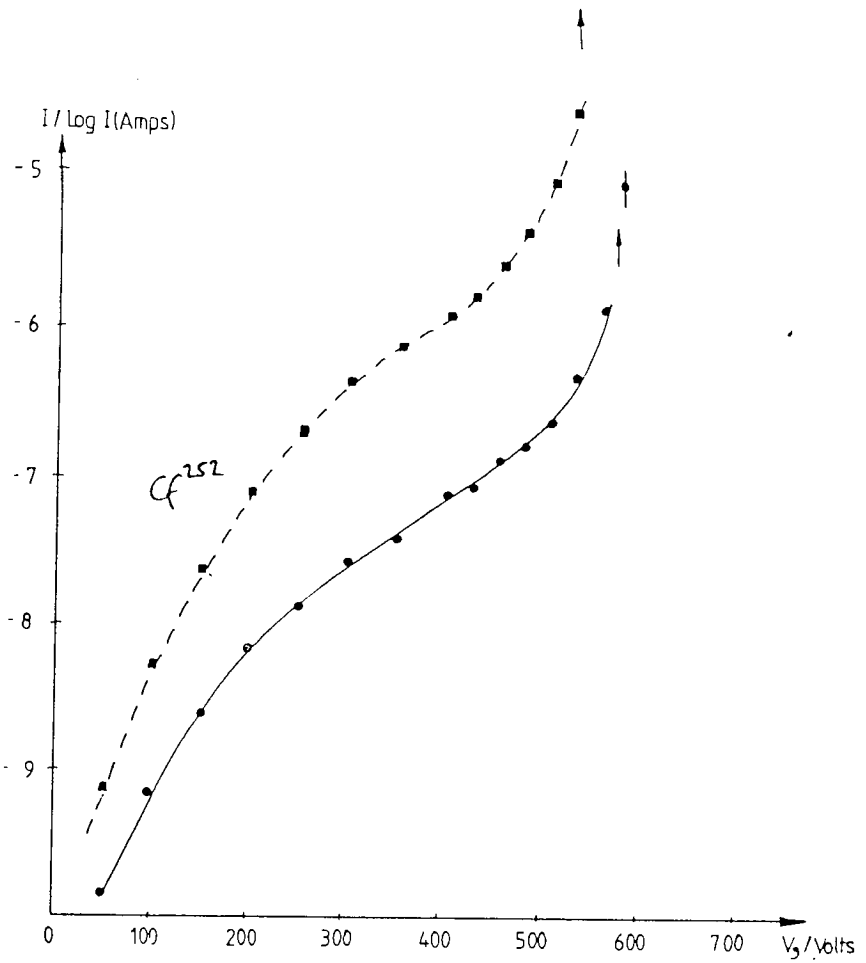

Figure 160: (a) I-V curves for a typical p-type Al-SiO_2-Si MOSC with 37.4nmthick oxide within and without a Cf^{252} fission-fragment irradiation field.

Figure 160: (b) I-V curves for a typical p-type Al-SiO_2-Si MOSC with 566.7nmthick oxide within and without a Cf^{252} fission-fragment irradiation field.

field strength, the proposal that each breakdown site is the product of a single breakdown pulse due to the passage of a single or several fission-fragments at that point appears to be a valid description of the breakdown processes occurring.

A study of the breakdown field versus device (oxide layer) thickness for devices under fission-fragment irradiation has revealed characteristics typical of those shown in Figures 161 and 162 ; since the Al gate area was kept constant, the observed near-linear relationship between the breakdown field and the oxide thickness for the pre-intrinsic breakdown field range can be ascribed to the possibility that the breakdown mechanism for fission-fragment induced breakdowns is linearly thickness dependent; however, the plot of the number of fission-fragment induced breakdowns versus oxide thickness, shown in Figure 163 and 164, indicating a decrease in the number of breakdowns with increasing oxide thickness appears to contradict this proposal.

Histograms showing the maximum breakdown field distributions for both n and p-type devices of all thicknesses for devices whilst under fission-fragment irradiation have been made and are shown in Figures 165 and 166. It can clearly be seen that the modal breakdown field strength of the n-type devices was reduced from the virgin device value of between 10.75 and 11MVcm^{-1} to between 8.5 and 8.75Mvcm^{-1} and similarly for the p-type devices from between 9 and 9.25MVcm^{-1} to between 10 and 10.25MVcm^{-1}. This demonstrates the reduction in oxide breakdown field strength for devices which breakdown whilst under fission-fragment irradiation.

An investigation of the breakdown characteristics of the various oxide thickness and types of MOSC when irradiated with different residual energy fission-fragments (the characteristics of which are shown in Appendix **14**) has revealed curves typical of those shown in Figures 167(a) and (b) for n-type devices and in Figures 168(a) and (b) for p-type devices. The fission-fragments were energy-selected by placing the Cf^{252} source at known distances from the MOSC under test and calibrating the source-to-device distance with the known properties of light (A≈106, Z≈43) and heavy (A≈142, Z≈55) fission-fragments from tabulated data[265]; this has been used to find the threshold for detection of fission-fragments in terms of the stopping power in SiO_2. Figure 169 shows the threshold voltage for detection of both light and heavy fission-fragments versus the stopping power of the fission-fragments in the various devices; the effect of the thin Al layer has been taken into account in the calculation of the stopping powers in the devices. From extrapolation of the stopping power versus threshold voltage for detection (fission-fragment

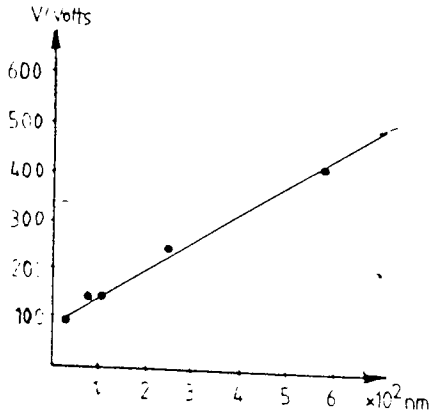

Figure 161: A plot of breakdown voltage versus device oxide thickness for n-type Al-SiO_2-Si MOSCs under fission-fragment irradiation.

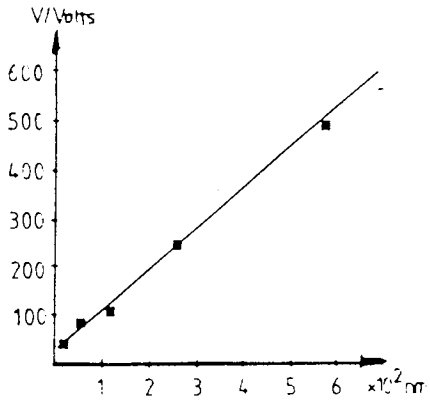

Figure 162: A plot of breakdown voltage versus device oxide thickness for p-type Al-SiO_2-Si MOSCs under fission-fragment irradiation.

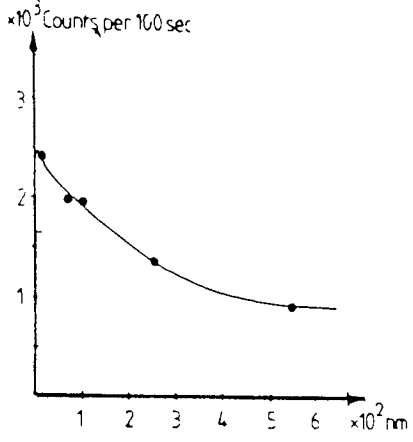

Figure 163: A plot of the number of breakdowns occuring at the breakdown "plateau voltage" versus device oxidethickness for n-type Al-SiO_2-Si MOSCs under fission-fragment irradiation from a Cf^{252} source.

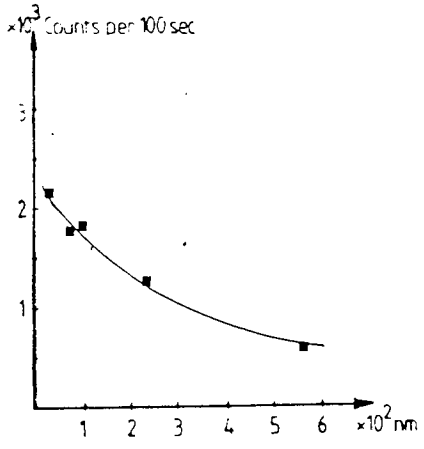

Figure 164: A plot of the number of breakdowns occuring at the breakdown "plateau voltage" versus device oxide thickness for p-type Al-SiO_2-Si MOSCs under fission-fragment irradiation from a Cf^{252} source.

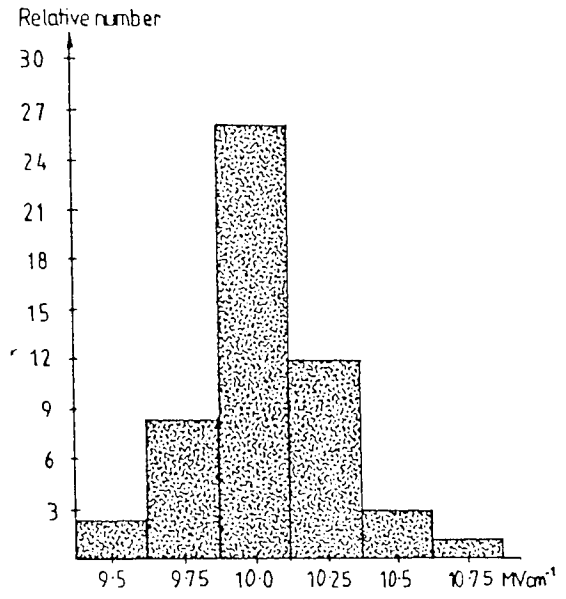

Figure 165: Histogram to show the breakdown field distribution determined from a large number of n-type Al-SiO_2-Si MOSCs under fission-fragment (from a Cf^{252} source) induced breakdown.

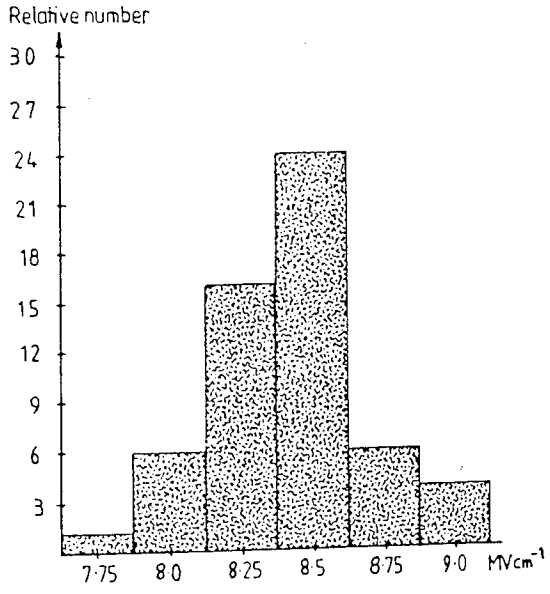

Figure 166: Histogram to show the breakdown field distribution determined from a large number of p-type Al-SiO_2-Si MOSCs under fission-fragment (from a Cf^{252} source) induced breakdown.

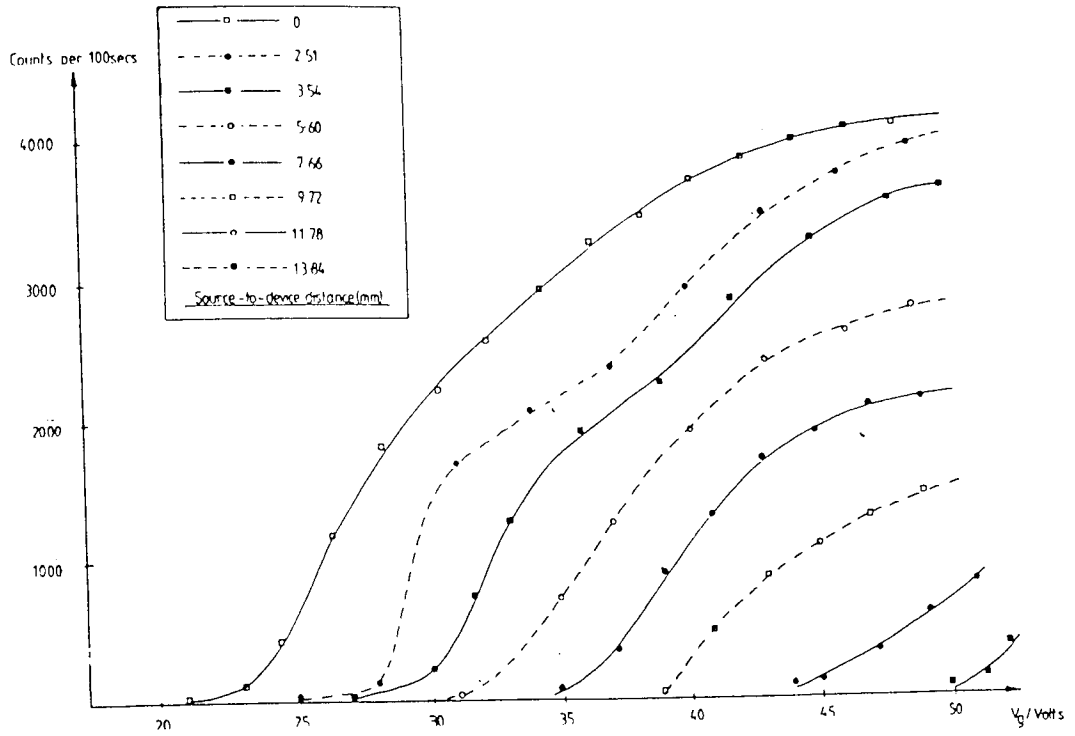

Figure 167: (a) A plot of the number of breakdown pulses versus the applied gate voltage and corresponding oxide field for an n-type Al-SiO_2-Si MOSC with a 42.5nm thick oxide layer under fission-fragment irradiation from a Cf^{252} source with source-to-device distance (and corresponding fragment residual energy) as the parameter.

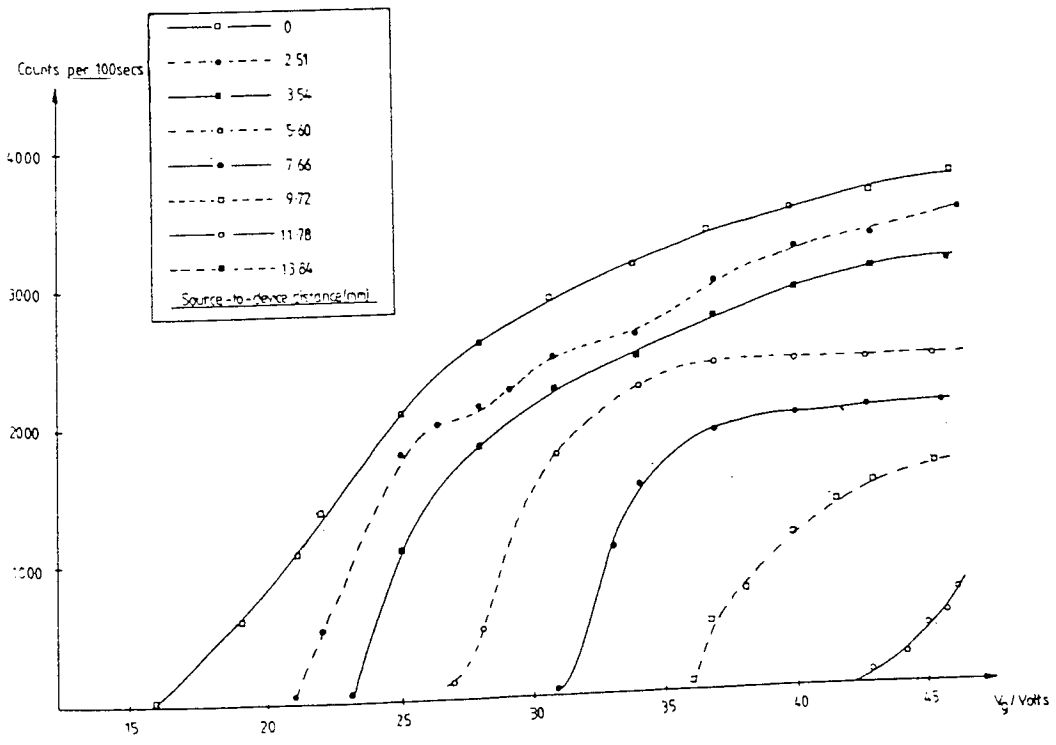

Figure 167: (b) A plot of the number of breakdown pulses versus the applied gate voltage and corresponding oxide field for an n-type Al-SiO_2-Si MOSC with a 588.3nm thick oxide layer under fission-fragment irradiation from a Cf^{252} source with source-to-device distance (and corresponding fragment residual energy) as the parameter.

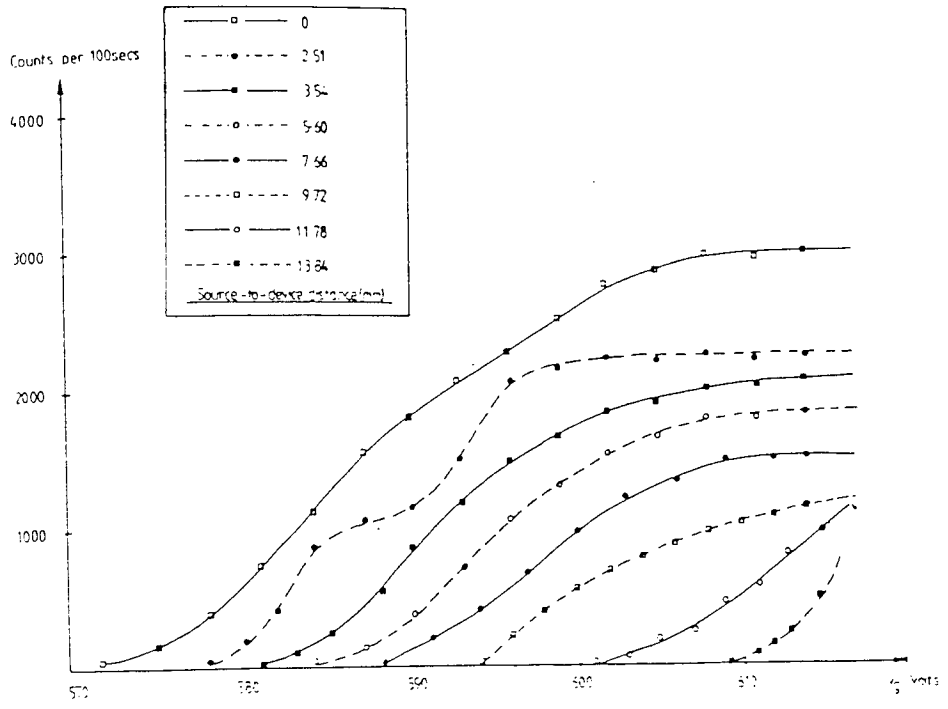

Figure 168: (a) A plot of the number of breakdown pulses versus the applied gate voltage and corresponding oxide field for a p-type Al-SiO_2-Si MOSC with a 37.4nm thick oxide layer underfission-fragment irradiation from a Cf^{252} source with source-to-device distance (and corresponding fragment residual energy) as the parameter.

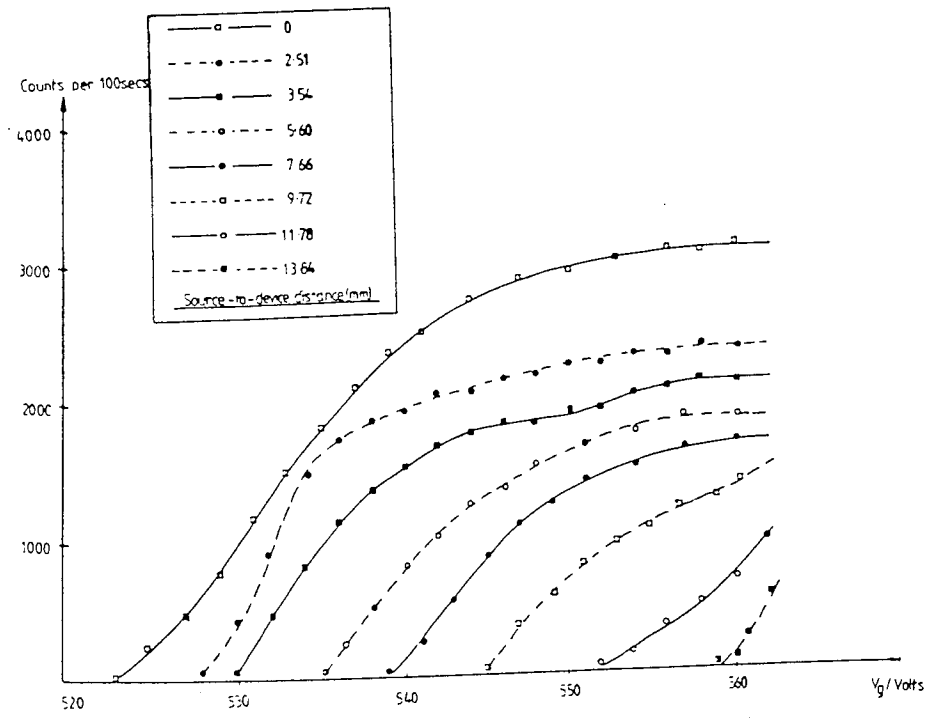

Figure 168: (b) A plot of the number of breakdown pulses versus the applied gate voltage and corresponding oxide field for a p-type Al-SiO_2-Si MOSC with a 566.7nm thick oxide layer under fission-fragment irradiation from a Cf^{252} source with source-to-device distance (and corresponding fragment residual energy) as the parameter.

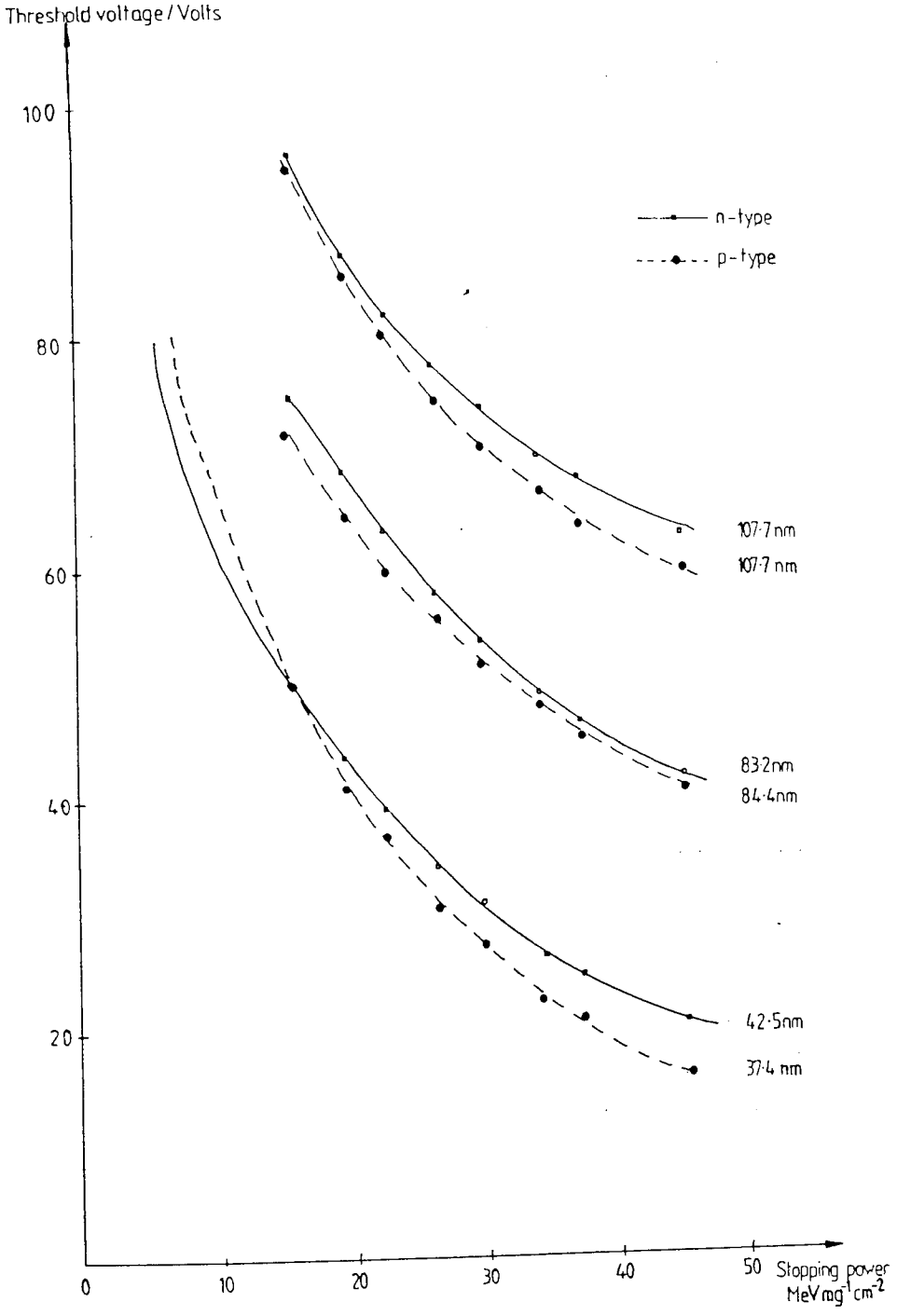

Figure 169: A plot of the breakdown threshold voltage for typical n and p-type Al-SiO_2-Si MOSCs versus stopping power of the fission-fragments in SiO_2.

induced breakdown), it can be seen that the n-type MOSCs have a registration ability of heavy ions with a stopping power in SiO_2 of greater than 6 $MeVmg^{-1}cm^2$ and p-type devices have a registration ability of heavy ions with a stopping power in SiO_2 of greater than 9 $MeVmg^{-1}cm^2$. Thus, the n-type MOSCs were more sensitive to the breakdown effects produced by the passage of fission-fragments than were the p-type devices. These figures are approximately 50% lower than those reported by DONICHKIN et al[236], who report a mean minimum threshold energy for registration of fission-fragments of $\approx 15 MeVmg^{-1}cm^2$. A proposal for why these MOSCs show such ability to detect (respond) to fission-fragments is discussed in terms of the KLEIN[245] model for RIDB in Chapter 7.

The I-V characteristics for the MOSCs under fission-fragment irradiation revealed curves typical of those shown in Figures 159(a) and (b) and 160(a) and (b) for n and p-type devices, respectively; the I-V curves of the same devices before irradiation are given for comparison. The curves both MOSCs within and without the fission-fragment radiation field are similar to those for MIS devices operating by a space charge limited conduction mechanism with a constant electron mobility; at high applied fields this dependence can be seen to move to a Schottky or thermionic based conduction mechanism. It can also be seen that the devices appear to conduct to a greater extent when under fission-fragment irradiation than when not, implying a charge injection or charge deposit in the device under these conditions. Hysteresis of the I-V curves was seen to be minimal for downward-stepped applied voltages from the breakdown condition in both irradiated and virgin device circumstances. The curves were quite repeatable with very similar characteristics until the devices experienced shorting breakdowns, when the I-V curves became nearly horizontal at high (mA) current values, suggesting device failure.

A series of detailed investigations into the effects of the radiation from the Cf^{252} source on the bulk electrical characteristics of the devices when not high-field stressed has revealed current pulses produced in the devices typical of that shown in Figure 170. These are similar in shape to that for alpha-irradiation, presented in section 6.2, but of a far greater current magnitude. When bias was applied across the devices, a decrease in the number and magnitude of the pulses was seen, regardless of the polarity of the bias, the pulse number decreasing with increasing magnitude of bias; this effect was found to be more apparent in n-type devices than in p-type devices with no obvious dependence on the device oxide thickness. Figures 171 and 172 show the number of

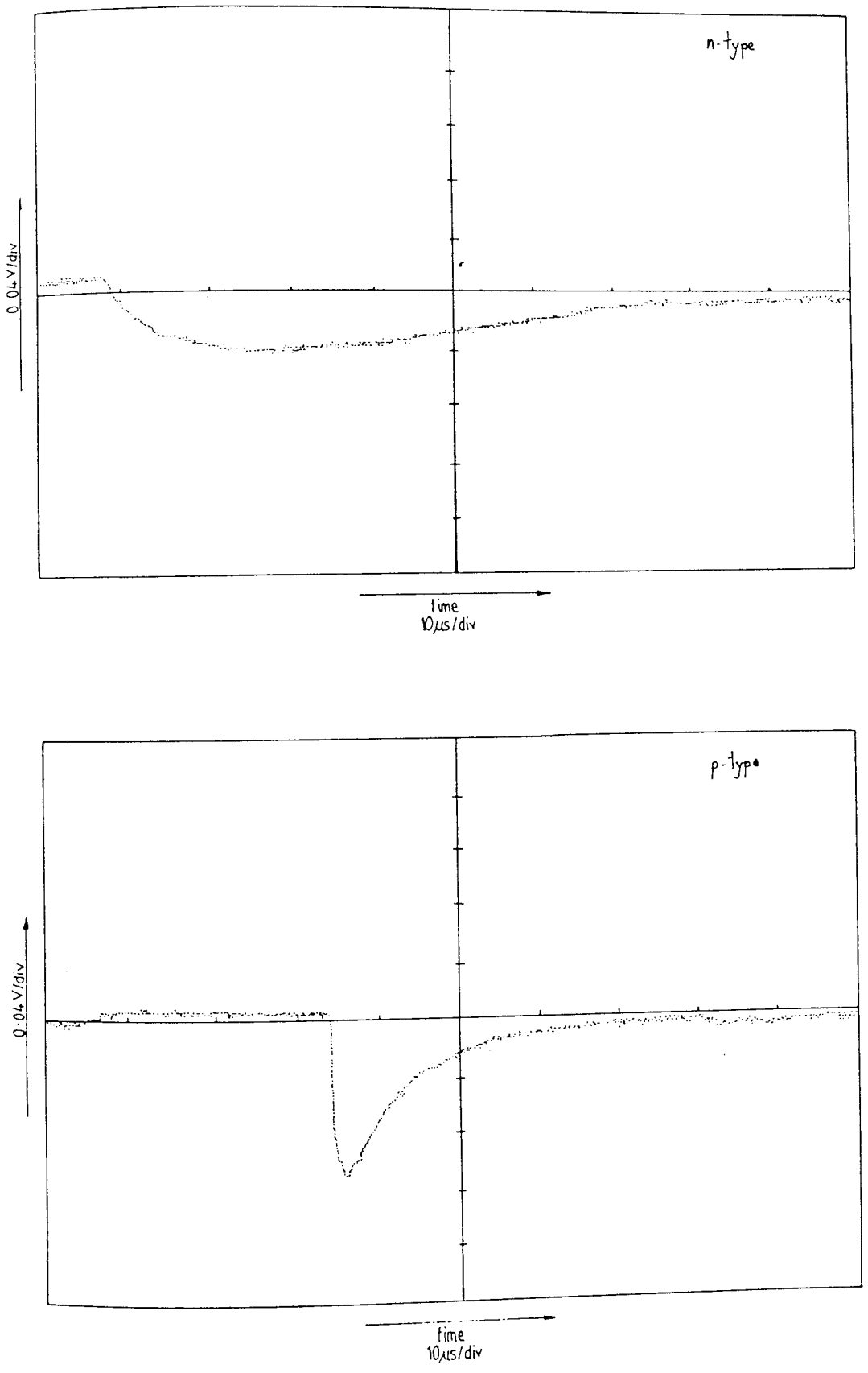

Figure 170: Oscilloscope traces of typical fission-fragment-induced current pulses in n and p-type Al-SiO_2-Si MOSCs.

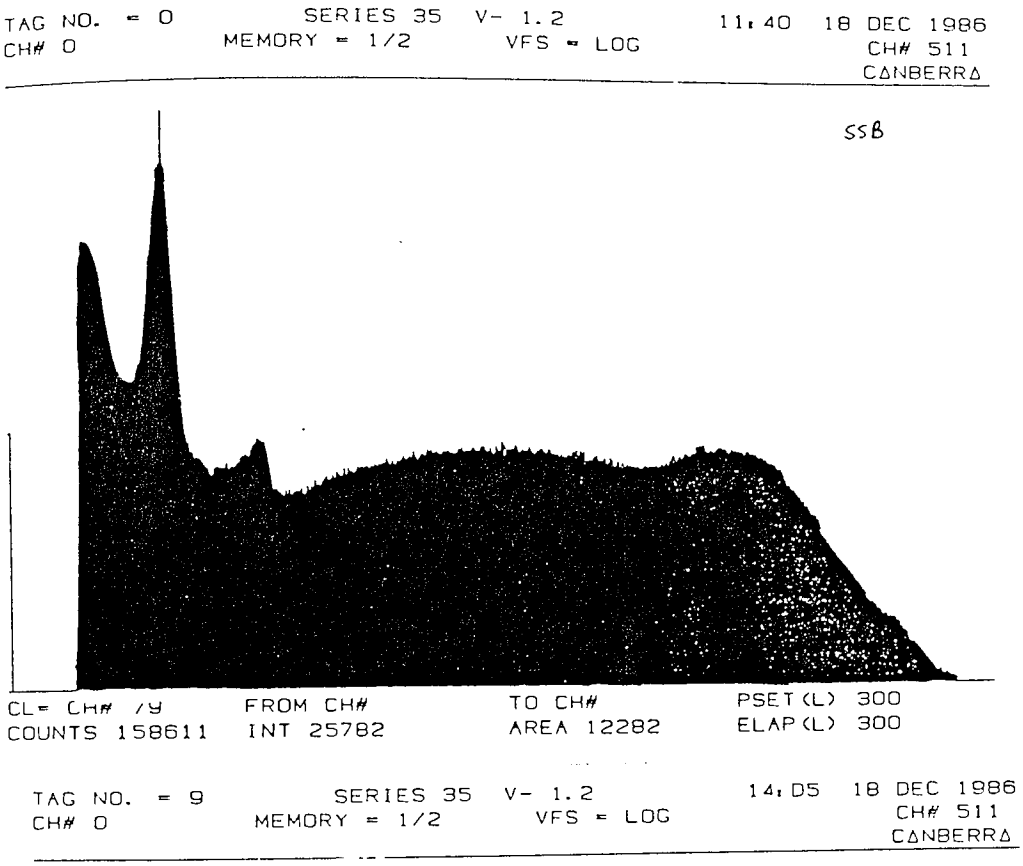

Figure 171: Spectrum from a multichannel analyser showing the pulse output from an n-type Al-Si-SiO_2 MOSC with a 70nm thick oxide layer under fission-fragment irradiation from a Cf^{252} source. The output spectrum from a SSB detector is shown for comparison.

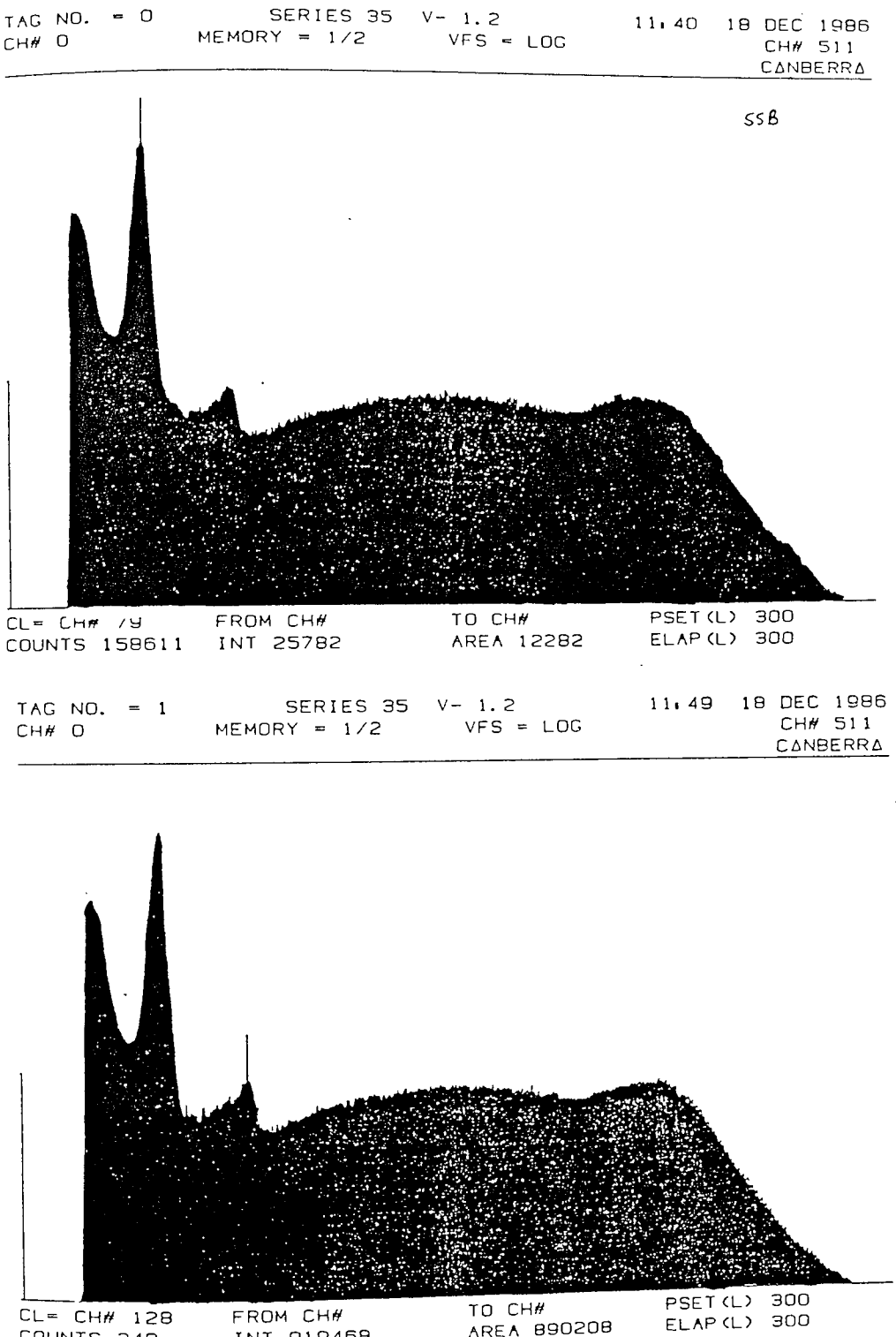

Figure 172: Spectrum from a multichannel analyser showing the pulse output from a p-type Al-Si-SiO_2 MOSC with a 70nm thick oxide layer under fission-fragment irradiation from a Cf^{252} source. The output spectrum from a SSB detector is shown for comparison.

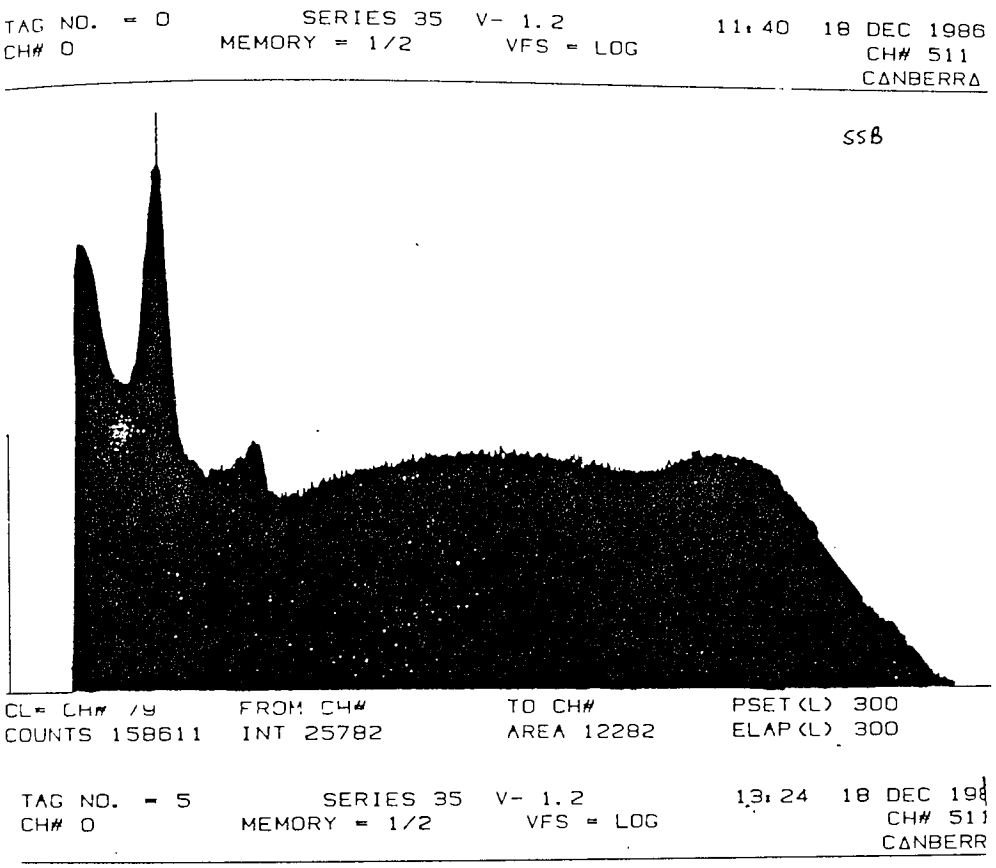

Figure 173: Spectrum from a multichannel analyser showing the pulse output from a p-type Al-Si-SiO_2 MOSC with a 500nm thick oxide layer under fission-fragment irradiation from a Cf^{252} source. The output spectrum from a SSB detector is shown for comparison.

pulses per100s versus channel number of a multichannel analyser from an n-type (42.5nm oxide layer) MOSC and a p-type (39.4nm oxide thickness) MOSC, respectively, when under vacuum and irradiation from the Cf^{252} source; the output from an Ortec silicon surface-barrier (SSB) detector (with a similarly sized active area) under the same irradiation geometry and conditions is presented for comparison. The similarity between the output from the p-type MOSC and the SSB detector is quite evident, the resolution of the SSB being slightly better than that of the MOSC for the thin-oxide device shown; the thicker the oxide layer of the MOSC under test, the worse the resolution of the device to the incident alpha and fission-fragment radiations, as can be seen in Figure173. As with the detection of alpha-particles shown in section **6.1**, the n-type devices showed poor detection properties.

Application of bias to the devices was seen to diminish the output pulse number and increase the noise seen at low channel numbers, regardless of the polarity or magnitude of the bias, but not to decrease the size of the pulses. An investigation of the magnitude of the pulses induced in the devices has revealed an equivalent voltage-pulse shape typical of that shown in Figure 170. The size of the pulses varied in the 10^{-5} to 10^{-4}A range, with no apparent dependence on the device thickness.

The C-V characteristics of the devices were noticeably altered by the Cf^{252} radiation field, as can be seen in Figures 174 ,175 and 176 which show the flatband voltage shift versus estimated Cf^{252} radiation dose, density of interface state generation versus dose and oxide charge density versus dose, respectively, for various device oxide thicknesses irradiated to a total dose of 10^4 fission-fragments cm^{-2} and the associated alpha-particle and neutron radiations from the Cf^{252} source; it was not possible to test the effects of fission-fragments independently of the other radiations concomitant from the Cf^{252} source.

Oxide positive charge buildup can be seen for devices irradiated with no applied gate bias and for devices which have experienced breakdown whilst under irradiation; this is perhaps indicative of deposited charge from the irradiation rather than due to charge injection from the silicon substrate since the plots also show that devices which experienced intrinsic or defect-related breakdown (and not radiation induced breakdown) exhibit characteristics of negative charge injection from either the silicon substrate or the Al gate electrode.

This is more clearly seen in Figures 177 and 178 which show the C-V curves for typical n and p-type

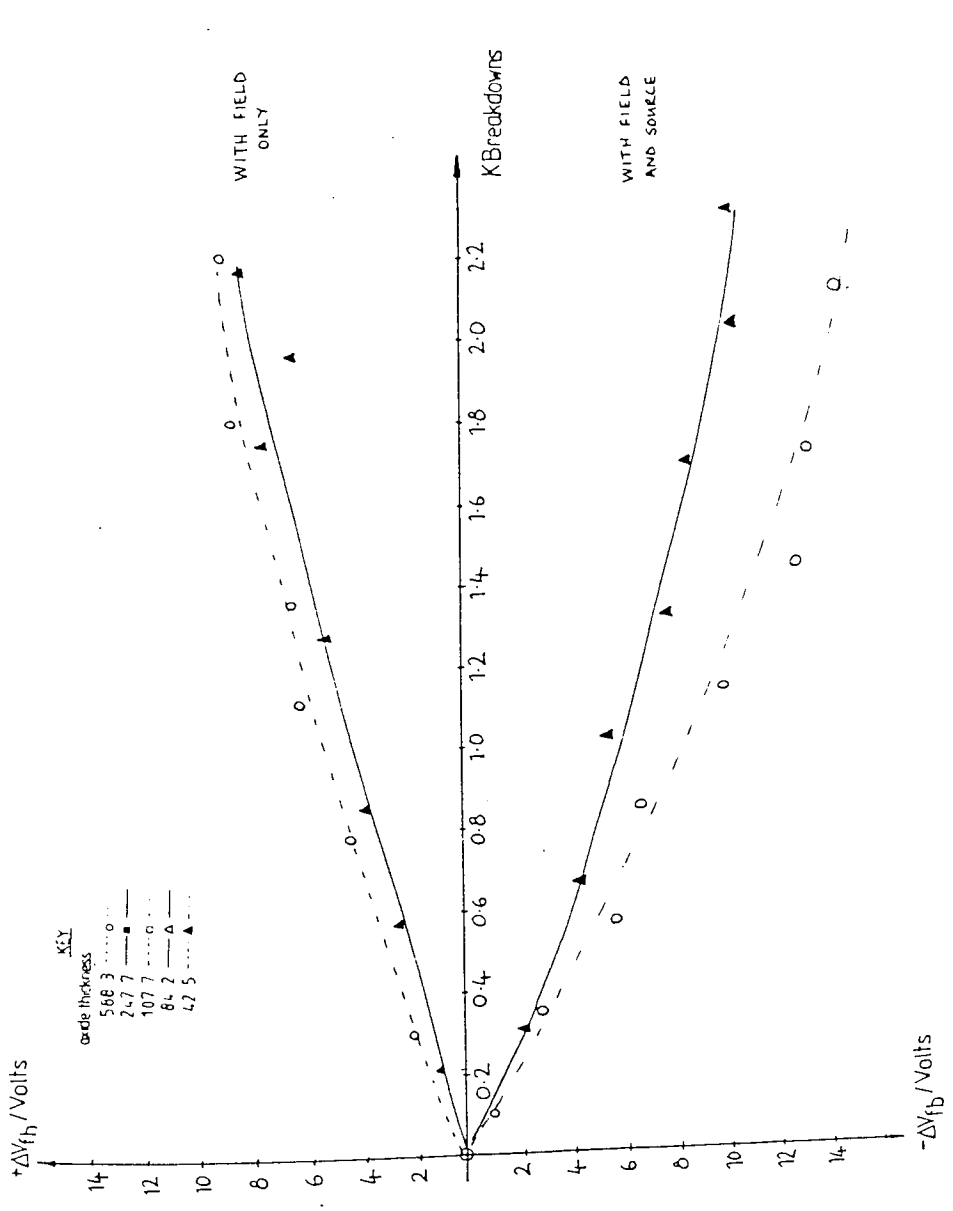

Figure 174: A plot of the shift in flatband voltage (ΔV_{fb}) versus total number of fission-fragments crossing the deviceand number of fission-fragment induced breakdowns for various oxide thickness devices with the MOSC device type and bias polarity as parameters.

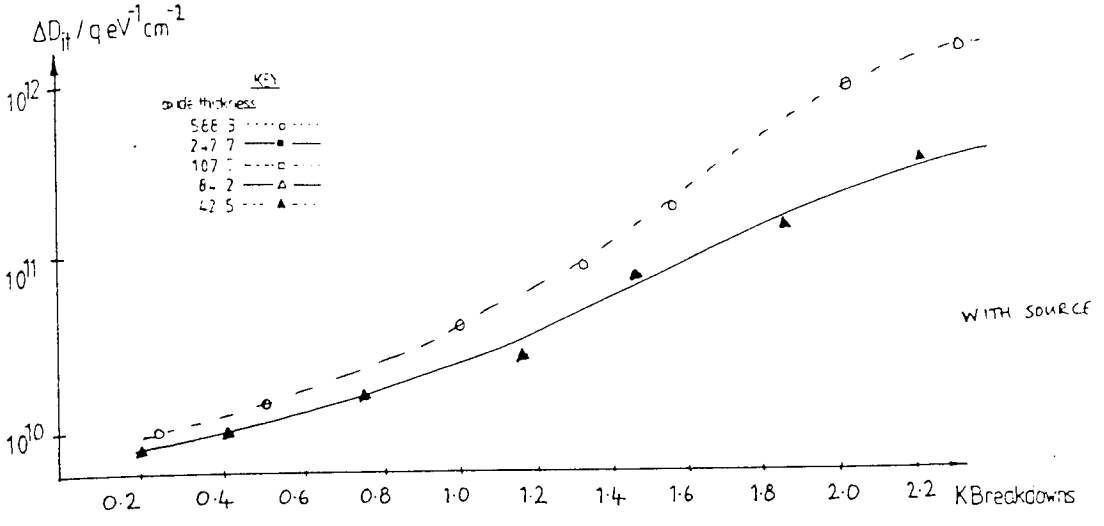

Figure 175: A plot of the density of interface states (D_{it}) versus total number of fission-fragments crossing the device and number of fission-fragment induced breakdowns for various oxide thickness devices with the MOSC device type as the parameter.

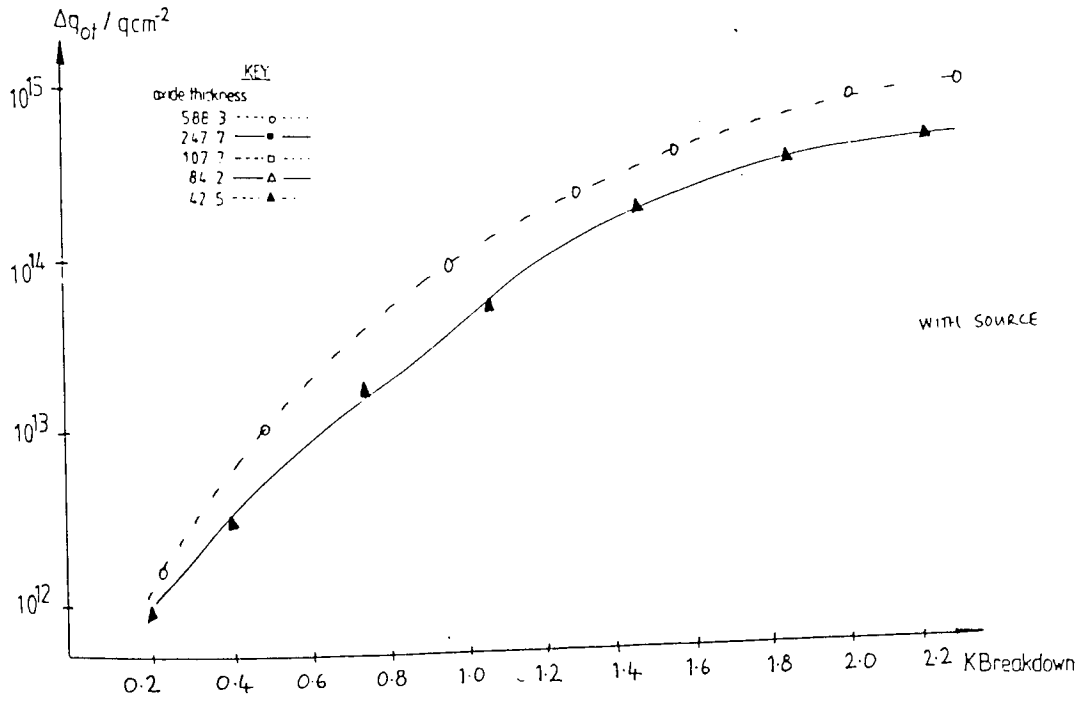

Figure 176: A plot of the oxide charge density (q_{ot}) versus total number of fission-fragments crossing the device and number of fission-fragment induced breakdowns for various oxide thickness devices with the MOSC device type as the parameter.

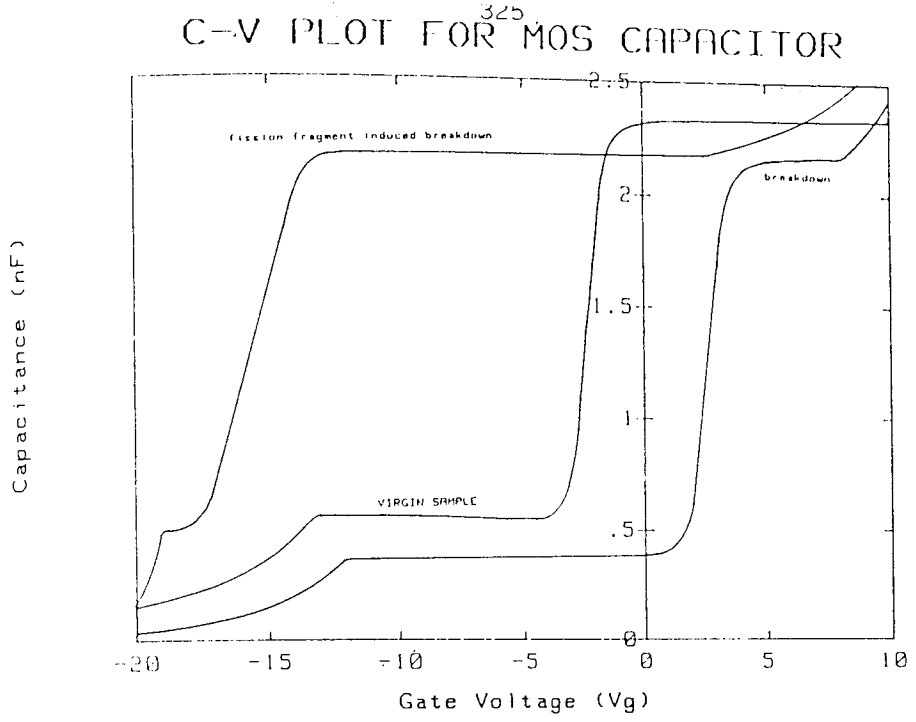

Cf252 fission-fragment induced breakdown & breakdown

42.5nm SiO2 on 2-4 Ohm cm n-Si
Dark ; 0.5 V osc.level ; 1MHz
PLESSEY DEVICE ; 9mm2 electrode

Figure 177: 1MHz C-V plots for a typical n-type Al-SiO_2-Si MOSC with a 42.5nm thick oxide layer which have experienced fission-fragment-induced and intrinsic (or defect-related) breakdown.

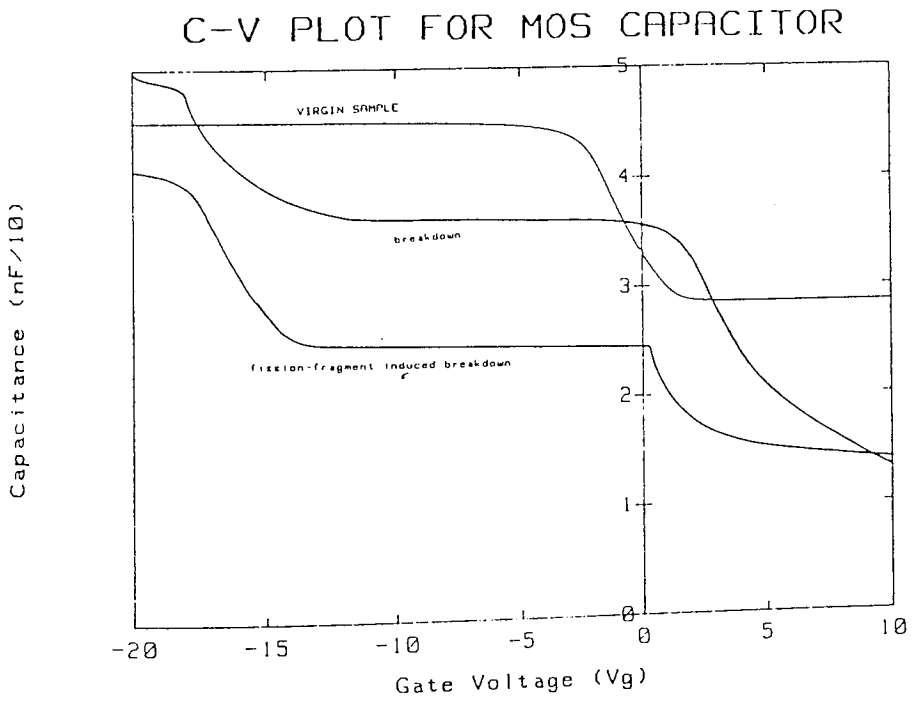

Cf252 fission-fragment induced breakdown & breakdown

566.7nm SiO2 on 21-25 Ohm cm p-Si
Dark ; 0.5 V osc. level ; 1MHz
PLESSEY DEVICE : 9mm2 electrode

Figure 178: 1MHz C-V plots for a typical p-type Al-SiO_2-Si MOSC with a 566.7nm thick oxide layer which have experienced fission-fragment-induced and intrinsic (or defect-related) breakdown.

devices before and after RIDB and intrinsic (or defect-related) breakdown; the direction and magnitudes of the shift in the curves can clearly be seen, along with the characteristic distortion of the C-V curve due to the introduction (or generation) of fast and slow surface states. The slow surface states, which are found deep in the oxide, force the device into the deep-depletion mode of operation and can be seen to be more pronounced for devices which have experienced radiation induced breakdown than those which broke down due to an intrinsic or defect-related mechanism, whereas the fast surface states, found close to the interface, are more evident for devices which broke down due to intrinsic (or defect-related) breakdown mechanisms; these effects are described and explained in sections **2.4.2** and **2.5.2**. This observation of the generation (or introduction) of such energy states has provided evidence which has been used to propose an extension to the KLEIN model[245] which is presented in Chapter **7**.

CHAPTER SEVEN.

DISCUSSION

In previous chapters a wide range of evidence has been presented, both theoretical and experimental, which forms the basis of a framework for understanding the principal effects of nuclear radiation on Al-SiO_2-Si MOSCs.

For the purpose of the following discussion, and because of the necessity to distinguish between the effects of the various radiations used in this study, a brief summary of the important experimental findings that have emerged from this investigation is presented in two forms: the first presents a tabulated summary of the principal effects of the individual radiations on the MOSCs in terms of their effects on the various parameters evaluated (for examples: breakdown strength, flatband voltage shift, density of interface states, and oxide charge density), with a brief explanation of the data presented; the second presents a brief summary of the effects of nuclear radiation en masse on the Al-SiO_2-Si MOSCs in terms of general effects on the overall electrical behaviour of the devices and changes in the physical characteristics (associated with virgin MOSC structures) due to irradiation.

These observations on the principal experimental findings have been used to propose an improved framework for understanding intrinsic (and defect-related) breakdown in Al-SiO_2-Si MOSCs and the effects of radiation on these phenomena, and to extend the knowledge of the general effects of radiation on the physical characteristics and electrical behaviour of such structures. The discussion which envelops these is presented in the following sections, with qualitative and quantitative extensions to the relevant models for device behaviour where possible.

The characteristics of the virgin devices are not presented here other than for comparison with devices post-irradiation, and the reader is referred to section **6.1** of the previous chapter for a relevant summary of device parameters and other data.

7.1 Summary: The Principal Effects of Various Radiations on Al-SiO_2-Si MOSCs

In Tables 17 to 21, summaries of the principal effects of alpha, gamma, neutron and recoil-proton, neutron, and fission-fragment irradiation, respectively, on the electrical and physical characteristics of thin (≈100nm) and thick-oxide (≈600nm) Al-SiO_2-Si MOSCs are presented; these represent typical findings from the various investigations, as reported in sections **6.2** to **6.5** of the previous

EFFECT / RADIATION	BIAS	Magnitude of the Generation of Oxide Charge[2].		Magnitude of the Generation of Interface States[3].		Occurrence of Radiation Induced Dielectric Breakdown. $MVcm^{-1}$		ΔV_{fb} (Volts)^t		ΔQ_t (qcm^{-2})^t		ΔD_{it} ($qcm^{-2}eV^{-1}$)^t		Effect of Radiation on the I-V Curve.		Current Pulses detectable in the Devices?		Changes in the AES/ESCA Spectrums? 1) at interface 2) in bulk oxide	
TYPE		n	p	n	p	n	p	n	p	n	p	n	p	n	p	n	p	n	p
Am^{241} Alpha	+	L +Ve	L +Ve	L	L	N	N	-5.53	-4.39	2.84×10^{13}	1.77×10^{13}	6.4×10^{11}	4.86×10^{11}	N	N	S	M	N N	N N
	0	M +Ve	M +Ve	M	M	-	-	-2.41	-2.34	1.24×10^{13}	9.43×10^{12}	2.78×10^{11}	2.59×10^{11}	N	N	M	L	N N	N N
	−	S +Ve	S +Ve	S	S	N	N	-1.14	-0.96	5.86×10^{12}	3.87×10^{11}	1.32×10^{11}	4.86×10^{11}	N	N	S	M	N N	N N

Table 17(a): The Effects of Am^{241} Alpha-radiation on Al-SiO_2-Si MOSCs Thin (≃100nm) Oxides.

KEY: 2 - determined from the shift of C-V curves.
3 - determined from the distortion in C-V curves.
t - for 10KRad(SiO_2) total dose in the cases for alpha and gamma irradiations.
- for 10^8 neutrons cm^{-2}, 0.5 & 2.5MeV Neutrons and associated Recoil-Protons.
- for approximately 10^4 breakdowns cm^{-2} for Fission-fragment irradiations.

L - Large effect
M - Intermediate effect
S - Small effect
N - No effect detectable.
- No observable difference from zero bias conditions

EFFECT / RADIATION	BIAS	Magnitude of the Generation of Oxide Charge[2].		Magnitude of the Generation of Interface States[3].		Occurrence of Radiation Induced Dielectric Breakdown. $MVcm^{-1}$		ΔV_{fb} (Volts)^t		ΔQ_t $(qcm^{-2})^t$		ΔD_{it} $(qcm^{-2}eV)^t$		Effect of Radiation on the I-V Curve.		Current Pulses detectable in the Devices?		Changes in the AES/ESCA Spectrums? 1) at interface 2) in bulk oxide	
TYPE		n	p	n	p	n	p	n	p	n	p	n	p	n	p	n	p	n	p
Am^{241} Alpha	+	L +Ve	L +Ve	L	L	N	N	-8.20	-7.14	2.99×10^{14}	3.28×10^{4}	1.57×10^{12}	1.96×10^{12}	N	N	S	S	N	N
																		N	N
	0	M +Ve	M +Ve	M	M	–	–	-3.48	-3.50	1.27×10^{14}	1.61×10^{14}	6.68×10^{11}	9.6×10^{11}	N	N	S	M	N	N
																		N	N
	–	S +Ve	S +Ve	S	S	N	N	-1.15	-1.44	6.02×10^{13}	6.61×10^{13}	3.17×10^{11}	3.95×10^{11}	N	N	S	S	N	N
																		N	N

Table 17(b): The Effects of Am^{241} Alpha-radiation on Al-SiO_2-Si MOSCs With Thick (≃600nm) Oxides.

KEY: 2 - determined from the shift of C-V curves.
3 - determined from the distortion in C-V curves.
t - for 10KRad(SiO_2) total dose in the cases for alpha and gamma irradiations.
- for 10^8neutrons cm^{-2}, 0.5 & 2.5MeV Neutrons and associated Recoil-Protons.
- for approximately 10^4 breakdowns cm^{-2} for Fission-fragment irradiations.

L - Large effect
M - Intermediate effect
S - Small effect
N - No effect detectable.
- No observable difference from zero bias conditions

EFFECT / RADIATION	BIAS	Magnitude of the Generation of Oxide Charge[2].		Magnitude of the Generation of Interface States[3].		Occurrence of Radiation Induced Dielectric Breakdown. $MVcm^{-1}$		ΔV_{fb} (Volts)^t		ΔQ_t $(qcm^{-2})^t$		ΔD_{it} $(qcm^{-2}eV)^t$		Effect of Radiation on the I-V Curve.		Current Pulses detectable in the Devices?		Changes in the AES/ESCA Spectrums? 1) at interface 2) in bulk oxide	
TYPE		n	p	n	p	n	p	n	p	n	p	n	p	n	p	n	p	n	p
Am^{241} Alpha	+	L +Ve	L +Ve	L	L	N	N	-8.20	-7.14	2.99×10^{14}	3.28×10^{4}	1.57×10^{12}	1.96×10^{12}	N	N	S	S	N	N
																		N	N
	0	M +Ve	M +Ve	M	M	–	–	-3.48	-3.50	1.27×10^{14}	1.61×10^{14}	6.68×10^{11}	9.6×10^{11}	N	N	S	M	N	N
																		N	N
	–	S +Ve	S +Ve	S	S	N	N	-1.15	-1.44	6.02×10^{13}	6.61×10^{13}	3.17×10^{11}	3.95×10^{11}	N	N	S	S	N	N
																		N	N

Table 17(b): The Effects of Am^{241} Alpha-radiation on Al-SiO_2-Si MOSCs With Thick (≃600nm) Oxides.

KEY: 2 – determined from the shift of C-V curves.
3 – determined from the distortion in C-V curves.
t – for 10KRad(SiO_2) total dose in the cases for alpha and gamma irradiations.
– for 10^8neutrons cm^{-2}, 0.5 & 2.5MeV Neutrons and associated Recoil-Protons.
– for approximately 10^4 breakdowns cm^{-2} for Fission-fragment irradiations.

L – Large effect
M – Intermediate effect
S – Small effect
N – No effect detectable.
– No observable difference from zero bias conditions

EFFECT / RADIATION	VBIAS	Magnitude of the Generation of Oxide Charge[2].		Magnitude of the Generation of Interface States[3].		Occurrence of Radiation Induced Dielectric Breakdown. $MVcm^{-1}$		ΔV_{fb} (Volts)^t		ΔQ_t $(qcm^{-2})^t$		ΔD_{it} $(qcm^{-2}eV)^t$		Effect of Radiation on the I-V Curve.		Current Pulses detectable in the Devices?		Changes in the AES/ESCA Spectrums? 1) at interface 2) in bulk oxide	
TYPE		n	p	n	p	n	p	n	p	n	p	n	p	n	p	n	p	n	p
Co^{60} Gamma	+	L +Ve	L +Ve	L	L	N	N	-6.83	-5.27	3.51×10^{13}	2.12×10^{13}	7.88×10^{11}	5.84×10^{11}	N	N	N	N	N	N
																		N	N
	0	L +Ve	L +Ve	M	M	–	–	-2.68	-2.60	1.38×10^{13}	1.05×10^{13}	3.09×10^{11}	2.88×10^{11}	–	–	N	N	N	N
																		N	N
	–	M +Ve	M +Ve	M	M	N	N	-1.16	-0.95	5.96×10^{12}	3.83×10^{12}	1.34×10^{11}	1.05×10^{11}	N	N	N	N	N	N
																		N	N

Table 18(a): The Effects of Co^{60} Gamma-radiation on Al-SiO_2-Si MOSCs With Thin (≅100nm) Oxides.

KEY: 2 - determined from the shift of C-V curves.
3 - determined from the distortion in C-V curves.
t - for 10KRad(SiO_2) total dose in the cases for alpha and gamma irradiations.
- for 10^8neutrons cm^{-2}, 0.5 & 2.5MeV Neutrons and associated Recoil-Protons.
- for approximately 10^4 breakdowns cm^{-2} for Fission-fragment irradiations.

L - Large effect
M - Intermediate effect
S - Small effect
N - No effect detectable.
- No observable difference from zero bias conditions

EFFECT / RADIATION	BIAS	Magnitude of the Generation of Oxide Charge[2].		Magnitude of the Generation of Interface States[3].		Occurrence of Radiation Induced Dielectric Breakdown. $MVcm^{-1}$		ΔV_{fb} (Volts)^t		ΔQ_t (qcm^{-2})^t		ΔD_{it} ($qcm^{-2}eV$)^t		Effect of Radiation on the I-V Curve.		Current Pulses detectable in the Devices?		Changes in the AES/ESCA Spectrums? 1) at interface 2) in bulk oxide	
TYPE	..	n	p	n	p	n	p	n	p	n	p	n	p	n	p	n	p	n	p
Co^{60} Gamma	+	L +Ve	L +Ve	L	L	N	N	-10.63	-9.10	3.88×10^{14}	4.18×10^{14}	2.05×10^{12}	2.50×10^{12}	N	N	N	N	N	N
																		N	N
	0	L +Ve	L +Ve	M	M	-	-	-4.06	-4.08	1.48×10^{14}	1.87×10^{14}	7.79×10^{11}	1.12×10^{12}	-	-	N	N	N	N
																		N	N
	-	M +Ve	M +Ve	M	M	N	N	-1.76	-1.50	6.42×10^{13}	6.89×10^{13}	3.38×10^{11}	4.11×10^{11}	N	N			N	N
																		N	N

Table 18(b): The Effects of Co^{60} Gamma-radiation on Al-SiO_2-Si MOSCs With Thick (≈600nm) Oxides.

KEY: 2 - determined from the shift of C-V curves.
3 - determined from the distortion in C-V curves.
t - for 10KRad(SiO_2) total dose in the cases for alpha and gamma irradiations.
- for 10^8neutrons cm^{-2}, 0.5 & 2.5MeV Neutrons and associated Recoil-Protons.
- for approximately 10^4 breakdowns cm^{-2} for Fission-fragment irradiations.

L - Large effect
M - Intermediate effect
S - Small effect
N - No effect detectable.
- No observable difference from zero bias conditions

EFFECT / RADIATION	BIAS	Magnitude of the Generation of Oxide Charge[2].		Magnitude of the Generation of Interface States[3].		Occurrence of Radiation Induced Dielectric Breakdown. $MVcm^{-1}$		ΔV_{fb} (Volts)^t		ΔQ_t (qcm^{-2})^t		ΔD_{it} ($qcm^{-2}eV$)^t		Effect of Radiation on the I-V Curve.		Current Pulses detectable in the Devices?		Changes in the AES/ESCA Spectrums? 1) at interface 2) in bulk oxide	
TYPE		n	p	n	p	n	p	n	p	n	p	n	p	n	p	n	p	n	p
Neutrons & Recoil-Protons	+	S/M	S/M	S/M	S/M	N	N	#	#	#	#	#	#	N	N	N	N	N N	N N
	0	S/M	S/M	S/M	S/M	—	—	-0.54 -0.38	-0.52 -0.37	2.78×10^{12} 1.95×10^{12}	7.09×10^{12} 1.49×10^{12}	6.78×10^{10} 4.38×10^{10}	5.98×10^{10} 4.10×10^{10}	—	—	N	N	N N	N N
	−	S/M	S/M	S/M	S/M	N	N	#	#	#	#	#	#	N	N	N	N	N N	N N

Table 19(a): The Effects of Neutron and Recoil-Proton Radiations on Al-SiO_2-Si MOSCS With Thin (≃100nm) Oxides.

KEY: 2 - determined from the shift of C-V curves.
3 - determined from the distortion in C-V curves.
t - for 10KRad(SiO_2) total dose in the cases for alpha and gamma irradiations.
- for 10^8neutrons cm^{-2}, 0.5 & 2.5MeV Neutrons and associated Recoil-Protons.
- for approximately 10^4 breakdowns cm^{-2} for Fission-fragment irradiations.

L - Large effect
M - Intermediate effect
S - Small effect
N - No effect detectable.
- No observable difference from zero bias conditions

EFFECT / RADIATION	BIAS	Magnitude of the Generation of Oxide Charge[2].		Magnitude of the Generation of Interface States[3].		Occurrence of Radiation Induced Dielectric Breakdown. $MVcm^{-1}$		ΔV_{fb} (Volts)^t		ΔQ_t $(qcm^{-2})^t$		ΔD_{it} $(qcm^{-2}eV)^t$		Effect of Radiation on the I-V Curve.		Current Pulses detectable in the Devices?		Changes in the AES/ESCA Spectrums? 1) at interface 2) in bulk oxide	
TYPE		n	p	n	p	n	p	n	p	n	p	n	p	n	p	n	p	n	p
Neutrons & Recoil-Protons	+	S/M	S/M	S/M	S/M	N	N	#	#	#	#	#	#	N	N	N	N	N N	N N
	0	S/M	S/M	S/M	S/M	–	–	-0.66 -0.47	-0.67 -0.47	2.41×10^{13} 1.72×10^{13}	3.08×10^{13} 2.16×10^{13}	1.27×10^{11} 9.03×10^{10}	1.83×10^{11} 1.29×10^{11}	–	–	N	N	N N	N N
	–	S/M	S/M	S/M	S/M	N	N	#	#	#	#	#	#	N	N	N	N	N N	N N

Table 19(b): The Effects of Neutron and Recoil-Proton Radiations on Al-SiO_2-Si MOSCS With Thick (≃600nm) Oxides.

KEY: 2 - determined from the shift of C-V curves.
3 - determined from the distortion in C-V curves.
t - for 10KRad(SiO_2) total dose in the cases for alpha and gamma irradiations.
- for 10^8neutrons cm^{-2}, 0.5 & 2.5MeV Neutrons and associated Recoil-Protons.
- for approximately 10^4 breakdowns cm^{-2} for Fission-fragment irradiations.

L - Large effect
M - Intermediate effect
S - Small effect
N - No effect detectable.
- No observable difference from zero bias conditions

EFFECT / RADIATION	BIAS	Magnitude of the Generation of Oxide Charge[2].		Magnitude of the Generation of Interfac States[3].		Occurrence of Radiatio Induced Dielectric Breakdown. $MVcm^{-1}$		ΔV_{fb} (Volts)^t		ΔQ_t $(qcm^{-2})^t$		ΔD_{it} $(qcm^{-2}eV)^t$		Effect of Radiation on the I-V Curve.		Current Pulses detectable in the Devices?		Changes in the AES/ESCA Spectrums? 1) at interface 2) in bulk oxide	
TYPE		n	p	n	p	n	p	n	p	n	p	n	p	n	p	n	p	n	p
Neutrons (0.5MeV & 2.5MeV)	+	S	S	S	S	N	N	#	#	#	#	#	#	N	N	N	N	N N	N N
	0	S	S	S	S	N	N	−0.21 −0.13	−0.20 −0.12	1.08×10^{12} 6.68×10^{11}	8.06×10^{11} 4.84×10^{11}	2.42×10^{10} 1.50×10^{10}	2.21×10^{10} 1.33×10^{10}	—	—	N	N	N N	N N
	−	S	S	S	S	N	N	#	#	#	#	#	#	N	N	N	N	N N	N N

Table 20(a): The Effects of Neutron Radiation on Al-SiO_2-Si MOSCs With Thin (≃100nm) Oxides.

KEY: 2 - determined from the shift of C-V curves.
3 - determined from the distortion in C-V curves.
t - for 10KRad(SiO_2) total dose in the cases for alpha and gamma irradiations.
- for 10^8neutrons cm^{-2}, 0.5 & 2.5MeV Neutrons and associated Recoil-Protons.
- for approximately 10^4 breakdowns cm^{-2} for Fission-fragment irradiations.

L - Large effect
M - Intermediate effect
S - Small effect
N - No effect detectable.
- No observable difference from zero bias conditions

EFFECT / RADIATION	BIAS	Magnitude of the Generation of Oxide Charge[2].		Magnitude of the Generation of Interface States[3].		Occurrence of Radiation Induced Dielectric Breakdown. $MVcm^{-1}$		ΔV_{fb} (Volts)^t		ΔQ_t $(qcm^{-2})^t$		ΔD_{it} $(qcm^{-2}eV)^t$		Effect of Radiation on the I-V Curve.		Current Pulses detectable in the Devices?		Changes in the AES/ESCA Spectrums? 1) at interface 2) in bulk oxide	
TYPE		n	p	n	p	n	p	n	p	n	p	n	p	n	p	n	p	n	p
Neutrons (0.5MeV & 2.5MeV)	+	S	S	S	S	N	N	#	#	#	#	#	#	N	N	N	N	N	N
																		N	N
	0	S	S	S	S	N	N	-0.20	-0.16	7.3×10^{12}	8.27×10^{12}	3.86×10^{10}	4.94×10^{10}	-	-	N	N	N	N
								-0.18	-0.12	5.86×10^{12}	5.51×10^{12}	3.07×10^{10}	3.29×10^{10}					N	N
	-	S	S	S	S	N	N	#	#	#	#	#	#	N	N	N	N	N	N
																		N	N

Table 20(b): The Effects of Neutron Radiation on Al-SiO_2-Si MOSCS With Thick (≃600nm) Oxides.

KEY: 2 - determined from the shift of C-V curves.
3 - determined from the distortion in C-V curves.
t - for 10KRad(SiO_2) total dose in the cases for alpha and gamma irradiations.
- for 10^8neutrons cm^{-2}, 0.5 & 2.5MeV Neutrons and associated Recoil-Protons.
- for approximately 10^4 breakdowns cm^{-2} for Fission-fragment irradiations.

L - Large effect
M - Intermediate effect
S - Small effect
N - No effect detectable.
- No observable difference from zero bias conditions

EFFECT / RADIATION	BIAS	Magnitude of the Generation of Oxide Charge[2].		Magnitude of the Generation of Interface States[3].		Occurrence of Radiation Induced Dielectric Breakdown. $MVcm^{-1}$		ΔV_{fb} (Volts)^t		ΔQ_t (qcm^{-2})^t		ΔD_{it} ($qcm^{-2}eV^{-1}$)^t		Effect of Radiation on the I-V Curve.		Current Pulses detectable in the Devices?		Changes in the AES/ESCA Spectrums? 1) at interface 2) in bulk oxide	
TYPE		n	p	n	p	n	p	n	p	n	p	n	p	n	p	n	p	n	p
Cf^{252} Fission Fragments	+	L +Ve	L +Ve	M	M	9.75 -10.0	9.0 -8.25	-15.62	-15.79	7.22×10^{13}	6.36×10^{13}	1.73×10^{12}	1.75×10^{12}	M	M	M	L	L	L
																		L	L
	0	L +Ve	L +Ve	M	M	—	—	-12.02	-12.41	5.47×10^{13}	4.98×10^{13}	4.77×10^{12}	1.37×10^{12}	S	S	S	L	S	S
																		S	S
	−	M +Ve	M +Ve	M	S	10.0 -10.25	8.5 -8.75	-3.16	-4.03	1.47×10^{13}	1.31×10^{13}	1.31×10^{13}	4.69×10^{11}	M	M	M	L	M	M
																		M	M

Table 21(a): The Effects of Cf^{252} Fission-Fragments on Al-SiO_2-Si MOSCs With Thin (≈100nm) Oxides.

KEY: 2 - determined from the shift of C-V curves.
3 - determined from the distortion in C-V curves.
t - for 10KRad(SiO_2) total dose in the cases for alpha and gamma irradiations.
- for 10^8neutrons cm^{-2}, 0.5 & 2.5MeV Neutrons and associated Recoil-Protons.
- for approximately 10^4 breakdowns cm^{-2} for Fission-fragment irradiations.

L - Large effect
M - Intermediate effect
S - Small effect
N - No effect detectable.
- No observable difference from zero bias conditions

EFFECT / RADIATION	BIAS	Magnitude of the Generation of Oxide Charge[2].		Magnitude of the Generation of Interface States[3].		Occurrence of Radiation Induced Dielectric Breakdown. $MVcm^{-1}$		ΔV_{fb} (Volts)^t		ΔQ_t $(qcm^{-2})^t$		ΔD_{it} $(qcm^{-2}eV)^t$		Effect of Radiation on the I-V Curve.		Current Pulses detectable in the Devices?		Changes in the AES/ESCA Spectrums? 1) at interface 2) in bulk oxide	
TYPE		n	p	n	p	n	p	n	p	n	p	n	p	n	p	n	p	n	p
Cf^{252} Fission Fragments	+	L +Ve	L +Ve	M	M	9.25 - 9.5	7.25 - 8.0	-14.23	-16.81	5.19×10^{14}	7.32×10^{14}	2.73×10^{12}	4.61×10^{12}	L	L	S	M	L	L
																		L	L
	0	L +Ve	L +Ve	M	M	—	—	-10.89	-11.98	3.68×10^{14}	5.50×10^{14}	2.12×10^{12}	3.11×10^{12}	S	S	S	L	S	S
																		S	S
	−	M +Ve	M +Ve	M	S	9.5 - 9.75	8.25 - 8.5	-1.10	-3.61	3.92×10^{13}	1.82×10^{14}	1.44×10^{12}	2.97×10^{12}	L	L	S	M	M	M
																		M	M

Table 21(b): The Effects of Cf^{252} Fission-Fragments on Al-SiO_2-Si MOSCs Thick (≅600nm) Oxides.

KEY: 2 - determined from the shift of C-V curves.
3 - determined from the distortion in C-V curves.
t - for 10KRad(SiO_2) total dose in the cases for alpha and gamma irradiations.
- for 10^8neutrons cm^{-2}, 0.5 & 2.5MeV Neutrons and associated Recoil-Protons.
- for approximately 10^4 breakdowns cm^{-2} for Fission-fragment irradiations.

L - Large effect
M - Intermediate effect
S - Small effect
N - No effect detectable.
- No observable difference from zero bias conditions

EFFECT / RADIATION	BIAS	Magnitude of the Generation of Oxide Charge[2].		Magnitude of the Generation of Interface States[3].		Dielectric Breakdown Strength $MVcm^{-1}$		ΔV_{fb} (Volts)^t		ΔQ_t $(qcm^{-2})^t$		ΔD_{it} $(qcm^{-2}eV)^t$		Effect on the I-V Curve.		Current Pulses detectable in the Devices?		Changes in the AES/ESCA Spectrums? 1) at interface 2) in bulk oxide	
TYPE		n	p	n	p	n	p	n	p	n	p	n	p	n	p	n	p	n	p
Intrinsic & Defect - Related Breakdown	+	L -Ve	L -Ve	S	S	10·25 -10·5	8·5 -8·75	+3·83	+5·09	$1·97\times10^{13}$	$2·05\times10^{13}$	$4·42\times10^{11}$	$5·64\times10^{11}$	L	L	L	L	L L	L L
	0	—	—	—	—	—	—	—	—	—	—	—	—	—	—	—	—	— —	— —
	−	M -Ve	M -Ve	M	M	10·25 -11·0	9·0 -9·75	+1·14	+2·09	$6·12\times10^{12}$	$7·14\times10^{11}$	$1·47\times10^{11}$	$2·61\times10^{11}$	M	M	L	L	M M	M M

Table 22(a): The Effects of Dielectric Breakdown on Al-SiO_2-Si MOSCS With Thin (≃100nm) Oxides.

KEY: 2 - determined from the shift of C-V curves.
3 - determined from the distortion in C-V curves.
t - for 10KRad(SiO_2) total dose in the cases for alpha and gamma irradiations.
- for 10^8neutrons cm^{-2}, 0.5 & 2.5MeV Neutrons and associated Recoil-Protons.
- for approximately 10^4 breakdowns cm^{-2} for Fission-fragment irradiations.

L - Large effect
M - Intermediate effect
S - Small effect
N - No effect detectable.
- No observable difference from zero bias conditions

EFFECT / RADIATION	BIAS	Magnitude of the Generation of Oxide Charge[2].		Magnitude of the Generation of Interface States[3].		Dielectric Breakdown Strength $MVcm^{-1}$		ΔV_{fb} (Volts)^t		ΔQ_t $(qcm^{-2})^t$		ΔD_{it} $(qcm^{-2}eV)^t$		Effect on the I-V Curve.		Current Pulses detectable in the Devices?		Changes in the AES/ESCA Spectrums? 1) at interface 2) in bulk oxide	
TYPE		n	p	n	p	n	p	n	p	n	p	n	p	n	p	n	p	n	p
Intrinsic & Defect - Related Breakdown	+	L -Ve	L -Ve	S	S	9.75 -10.0	8.0 -8.75	+3.61	+5.63	1.31×10^{14}	2.58×10^{14}	6.93×10^{11}	1.54×10^{12}	L	L	L	L	L	L
																		L	L
	0	—	—	—	—	—	—	—	—	—	—	—	—	—	—	—	—	—	—
																		—	—
	-	M -Ve	M -Ve	M	M	10.25 -10.5	8.75 -9.25	+0.86	+1.12	4.16×10^{13}	4.98×10^{13}	1.69×10^{11}	2.87×10^{8}	M	M	L	L	M	M
																		M	M

Table 22(b): The Effects of Dielectric Breakdown on Al-SiO_2-Si MOSCS With Thick (≈600nm) Oxides.

KEY: 2 - determined from the shift of C-V curves.
3 - determined from the distortion in C-V curves.
t - for 10KRad(SiO_2)' total dose in the cases for alpha and gamma irradiations.
- for 10^8neutrons cm^{-2}, 0.5 & 2.5MeV Neutrons and associated Recoil-Protons.
- for approximately 10^4 breakdowns cm^{-2} for Fission-fragment irradiations.

L - Large effect
M - Intermediate effect
S - Small effect
N - No effect detectable.
- No observable difference from zero bias conditions

chapter.

Table 22 is a similarly tabulated summary of the effects of intrinsic and defect-related dielectric breakdown on such Al-SiO_2-Si MOSCs, as reported in section **6.1** of the previous chapter.

The magnitude of each effect is expressed qualitatively in terms of the effect on the various parameters as compared with the same parameter for the virgin device: thus, a large effect is one considered to alter the device characteristic beyond recovery, whereas a small effect is one which, although valid within the limits of experimental error, maybe removed by device annealing or by some other technique. Thus, the generation of interface states and oxide charge, changes in the ESCA and AES spectra, variation in the I-V characteristic, evidence of pulse generation and dielectric breakdown in the devices due to the various radiations and due to intrinsic (or defect-related) effects have been considered qualitatively; these effects have also, where possible, been presented quantitatively in order to present the reader with data easily compared with that for virgin devices, as reported in Table 16.

It is evident from the summary tables that each radiation produces markedly different magnitudes of effects for a similar total radiation dose in the SiO_2 layer: the generation of a positive oxide charge in the devices, for example, appears at first sight to correlate with the magnitude of linear energy transfer, LET, of each radiation (linear attenuation in the case of gamma radiation), such that the greater the LET of the radiation, the greater the generation of positive oxide charge in the device, the effect being greatest for devices biased positively, and least for devices biased negatively with respect to Ohmic contact on the underside of the silicon substrate; the effect is more noticeable in n-type devices than in p-type devices. An order of magnitude for the degree of generation of positive oxide charge in the worst case is $\approx 1*10^{11}$ charges $Rad(SiO_2)^{-1}cm^{-2}$ for fission-fragment irradiation, equivalent to a charge generation of approximately $2*10^{-8}C$. The radiation which generates the least positive charge in the devices can be seen to be fast-neutron (2.5MeV) radiation, which generates approximately $\approx 6*10^{8}$ charges$Rad(SiO_2)^{-1}cm^{-2}$, equivalent to approximately $1*10^{-10}C$, in the MOSCs. These are clearly seen from the magnitudes of the shifts in the flatband voltage after irradiation with the various radiations, the effect being generally greatest for fission-fragment irradiation and ranging from approximately -17V for the worst case to only (approximately) -0.1V for neutron irradiation.

The magnitude of the generation of interface states also appears to similarly correlate with the magnitude of the LET of the radiation; fission-fragment irradiation appears to produce by far the most interface states in both thin and thick devices, again the effect being greatest for devices biased positively, and least for devices biased negatively, with respect to the Ohmic contact on the underside of the silicon substrate and, again, the effect more noticeable in n-type devices than in p-type devices. Typical values for the increase in the density of interface states generated in Al-SiO_2-Si MOSCs by fission-fragment irradiation are of the order of 10^{12} $qcm^{-2}eV^{-1}$ for an irradiation of 10^4 fission-fragments cm^{-2} for p-type devices with (small) positive bias applied to the top Al gate electrode, and of the order of $10^{11}qcm^{-2}eV^{-1}$ for an irradiation of 10^4 fission-fragments cm^{-2} for n-type devices with (small) negative bias applied to the top Al gate electrode. Typical values for the density of interface states generated in alpha and gamma-irradiated MOSCs are similar in magnitude to those for fission-fragment irradiated devices, varying between 10^{12} $qcm^{-2}eV^{-1}$ and 10^{10} $qcm^{-2}eV^{-1}$.

An interesting result is that generation of interface states by neutron irradiation of the devices is evident from the slight distortion of the flatbands region of the C-V characteristic, an effect which is disputed by several workers[209,212]; simple estimations of the surface recombination velocity (approximately 5.7cm s^{-1} for the virgin devices tested) from the I-V characteristics of virgin and irradiated devices, and using Equations 79 and 80, reveal that the surface recombination velocity has, as a result of an increase in the number of interface states, increased by approximately 3.2cms^{-1} to 8.9cms^{-1}. Similar estimations for fission-fragment irradiated devices indicate that, for the thickest devices which received a total dose of $4*10^4$ fission-fragments cm^{-2}, the surface recombination velocity increased to approximately 17.3cms^{-1} from the virgin device value of approximately 5.7cms^{-1}. These indicate that, since after neutron (or other) irradiation the surface recombination velocity of the devices has increased, and there is evidence of distortion in the C-V curve in the flatband voltage region, neutron irradiation does generate interface states in the devices, albeit a small-magnitude affect. A typical order of magnitude increase in the number of interface states generated by a fluence of 10^8 neutrons cm^{-2} (0.5MeV) is $2*10^{10}$ $qcm^{-2}eV^{-1}$ for a thin (≈100nm) p-type device under zero bias, and similarly for a thick (≈600nm) n-type device, an increase in the density of interface states of $\approx 3*10^{10}$ $qcm^{-2}eV^{-1}$ is typical. No variation in the magnitudes of the generation of interface states were seen for devices under different conditions

of bias and bias polarity, all data being identical to that for the zero bias condition.

An anomaly in the correspondence between the LET of the radiation and the increase in the various electrical and physical parameters discussed can be seen; gamma-irradiation of the devices appears to generate a greater oxide charge (and corresponding flatband-voltage voltage-shift) and a greater number of interface states than does an equivalent dose of alpha-radiation; although the effects of the two radiations are of the same order of magnitude in both thick and thin devices, this cannot be discounted as simply experimental error variation in the results since the magnitudes of the effects are statistically significant compared with the margin for error (as discussed in Appendix 4).

Evidence has been presented to demonstrate that a combined field of neutron and recoil-proton radiation effects a greater magnitude of positive charge generation (by an approximate factor of three increase) and interface state generation (by an approximate factor of four increase) than the same neutron-only irradiation; this would suggest that recoil-protons also generate such charge and interface states, though once again the effect is comparatively weak.

The ability of each radiation to generate oxide charge (and corresponding flatband-voltage voltage-shift) and to generate interface states in the MOSCs appears to follow the scheme:

fission-fragments > gamma > alpha > neutrons/recoil-protons > neutrons

with the order of magnitude of ratios for the generation of interface states for equivalent p-type devices being:

1 : 0.54 : 0.43 : 0.03(7) : 0.01(4)

and for equivalent n-type devices being:

1 : 0.75 : 0.56 : 0.03(6) : 0.01(4)

The order of magnitude of ratios for the oxide charge generation follows a very similar pattern (which is not unexpected because of the intimacy of the two effects) being, for equivalent p-type devices:

1 : 0.54 : 0.42 : 0.03(6) : 0.01(4)

and for equivalent n-type devices :

1 : 0.75 : 0.58 : 0.03(9) : 0.01(5)

The similarity between these "damage equivalence" ratios for the generation of interface states and for generation of positive oxide charge is , in the case of neutron irradiations, further clear evidence

of the generation of interface states by the neutron irradiation and not due to neutron damage in the silicon substrate alone. In the cases for alpha, gamma, and fission-fragment irradiations of Al-SiO_2-Si MOSCs, these results shed new light on the work of BRUCKER et al[182] and STAPOR et al[183].

Changes in the I-V characteristics of the MOSCs during and after irradiation were only detected for devices exposed to fission-fragments. The magnitude of the shift in current at any given gate bias can be seen to vary exponentially with the applied bias for devices exposed whilst under bias, and was only slight for devices exposed without bias; a typical estimation of the size of current increase for thin-oxide (≈40nm) n and p-type devices when under irradiation conditions at pre-breakdown fields ranges between $2*10^{-8}$A and $1*10^{-4}$A for fields between 2.5MVcm^{-1} and 10MVcm^{-1}, and between $2*10^{-10}$A and$5*10^{-7}$A for fields between 0.1MVcm^{-1} and 10MVcm^{-1}for thick-oxide (≈500nm) n and p-type devices. The upper limit of these are comparable with data from injection experiments (to determine the mechanism inducing breakdown in such MOSCs) as reported by other workers [70,121,178] and discussed in Chapter **3**. This shift in the I-V characteristic can be seen to be also dependent on the flux of fission fragments crossing the MOSC, the greater the fission-fragment flux the greater the current flow in the device; no saturation of this effect was seen.

For both types of Al-SiO_2-Si MOSC, current pulses were detectable for alpha and fission-fragment irradiation; however, no pulses were detected in the devices for gamma, neutron/recoil-proton, and neutron irradiations. The pulses were negative and exponential in character, ranging between 35μs and 70μs for either alpha or fission-fragment irradiation, and ranged between 10^{-6}A and 10^{-4}A for alpha and fission-fragment irradiation, respectively. A strong correlation between the number of particles crossing the devices and the number of pulses detected for both types of device was observed, although p-type devices acted as more efficient detectors than n-type devices, which appeared to have a lower signal-to-noise ratio.

A pulse-height analysis of the distribution of the pulses (using a multichannel analyser) showed that both device types detected alpha and fission-fragment radiation in a similar fashion to a silicon surface-barrier detector (SSB) and were invisible to the other radiation fields used in the study. The p-type devices were far more effective detectors than the n-type devices, which barely responded to either radiation field. The thin-oxide p-type devices approached the resolution of the SSB; the thick-oxide p-type devices detected the radiations with a far lower resolution, the thickest oxide

(≈1.2μm) p-type device barely responding to the passage of either radiation.

Typical virgin device breakdown fields ranged between 11MVcm^{-1} for the thinnest n-type devices to 8.25MVcm^{-1} for the thickest p-type devices, the n-type devices typically displaying breakdown strengths approximately 17% greater than equivalent oxide thickness p-type devices. Typically the breakdown strength for devices were greatest for the devices when under reverse-bias conditions.

Radiation induced dielectric breakdown occurred only for fission-fragment irradiation; there was no evidence to suggest that any of the other radiations had any effect on the breakdown characteristics of the devices. Typical device breakdown fields for MOSCs under fission-fragment irradiation ranged between 10.25MVcm^{-1} for the thinnest n-type devices to 8MVcm^{-1} for the thickest p-type devices, the n-type devices typically displaying breakdown strengths approximately 15% greater than equivalent oxide thickness p-type devices. Typically the breakdown strengths for devices, were again, greatest for the devices when under reverse-bias conditions. The threshold for detection of light and heavy fission fragments has been determined, and n-type devices have a registration ability of only those heavy ions with a stopping power in SiO_2 of greater than 6MeVmg^{-1}cm^{-2}, and p-type devices have, at best, a registration ability of only those heavy ions with a stopping power in SiO_2 of greater than 9MeVmg^{-1}cm^{-2}; these are far lower than those reported by other workers[236]. Typically, the n-type devices could detect (by radiation induced breakdown) ≈10^4 fission-fragments cm^{-2} and p-type devices ≈10^{5}cm^{-2} before device failure due to shorting breakdown or insufficient gate electrode unaffected to enable device operation.

Breakdown craters in the devices which suffered radiation induced breakdown were similar to those for intrinsic (or other) breakdown in virgin devices and, typically, 10μm to 50μm in diameter for n-type devices and 2μm to 6μm diameter for p-type devices, independent of the magnitude and polarity of the applied field. The crater depth varied between ≈50% of the oxide thickness and the entire oxide thickness depending on the form of breakdown (that is, whether non-shorting or shorting in nature).

Again, only the devices irradiated with fission-fragments showed any alteration to the AES and ESCA spectra of the interfaces and bulk oxide. No effect was detectable for the other radiation fields tested. The largest effects were seen for devices irradiated with fission-fragments whilst under reverse-bias conditions (although these results show only minor variations in the chemical structure of the oxide and the interface, which may be due to extraneous conditions in the test

chamber).

A summary of the effects of the individual radiation fields on the Al-SiO_2-Si MOSCs tested has been presented in tabular form with a brief explanation of each principal effect and its affect on the device characteristics. These results are used in proceeding sections to propose an improved framework for understanding intrinsic (and defect-related) breakdown in Al-SiO_2-Si MOSCs and the effects of radiation on these phenomena, and to extend the knowledge of the general effects of radiation on the physical characteristics and electrical behaviour of such structures.

7.2 Summary: The General Effects of Radiation En Masse on Al-SiO_2-Si MOSCs

In this section a brief summary of the effects of nuclear radiation en masse on the Al-SiO_2-Si MOSCs, in terms of general effects on the overall electrical behaviour of the devices and changes in the physical characteristics (associated with virgin MOSC structures), is presented;

(1). All the radiations tested generate positive charge in Al-SiO_2-Si MOSCs, characterised by a shift of the entire C-V characteristic for the devices to (more) negative bias voltage regimes.

The magnitude of the shift is dependent on: the LET of the radiation; the total radiation dose (or fluence); the bias magnitude; and the bias polarity.

Shifts are greatest for: thick-oxide p-type devices; reverse bias conditions; high-LET radiations; and large doses, and are least for: thin-oxide n-type devices; forward bias conditions; low-LET radiations; and low doses.

The zero bias condition produces charge generation in the MOSCs which is intermediate between that for forward and reverse bias conditions.

(2). All the radiations tested generate interface states in Al-SiO_2-Si MOSCs, characterised by a distortion of the C-V characteristic for the devices in the flatband-voltage region of the curve.

The magnitude of the distortion is dependent on: the LET of the radiation; the total radiation dose (or fluence); the bias magnitude; and the bias polarity.

The distortion is greatest for: thick-oxide p-type devices; forward bias conditions; high-LET radiations; and large doses, and are least for: thin-oxide n-type devices; reverse bias conditions; low-LET radiations; and low doses.

The zero bias condition produces interface state generation in the MOSCs which is intermediate between that for forward and reverse bias conditions.

(3). In general, the radiations tested did not appear to affect the I-V characteristic of the Al-SiO_2-Si MOSCs for devices tested during irradiation, but all the radiation fields had an effect on the post-irradiation I-V characteristic; this post-irradiation effect was characterised by an increase in the surface recombination velocity for the devices, being greatest for the higher-LET radiations and for greater total radiation doses (or fluences).

For very-high-LET radiations, the I-V characteristic during irradiation was shifted to lower bias regimes, indicating a greater current flow through the device during irradiation; this was seen to be greatest for thick devices and least for thin devices, independent of device type and bias polarity in the pre-breakdown voltage region.

Some hysteresis of the I-V curves was seen with upward and downward bias, though this is attributable to charging effects in the devices due to mobile ionic charge carriers.

(4). Only high-LET radiation appeared to produce detectable current pulses in the devices during irradiation. The p-type devices were more sensitive to radiations than equivalent thickness n-type MOSCs, and the thick-oxide MOSCs less sensitive than thin-oxide devices. Pulses were negative and exponential in character of the order of μs to ms in duration.

Pulse-height analysis of the pulses with a multichannel analyser revealed that the thin-oxide p-type devices detect such radiations with a similar spectrum to that of a silicon surface barrier detector, the resolution approaching that of the SSB used and decreasing with increasing oxide thickness. The n-type devices were poor detectors when used in this fashion.

(5). The breakdown strength of virgin devices was lower for devices under forward bias conditions than under reverse bias, the lowering being of the order of 17% of the upper limit. The p-type devices typically had breakdown strengths in the region of $8MVcm^{-1}$ to $9MVcm^{-1}$, substantially lower than those of equivalent oxide thickness n-type devices, and was dependent on the device thickness; n-type devices, at best, displayed breakdown strengths in the region of $10.75MVcm^{-1}$ to $11MVcm^{-1}$, dependent on the device thickness.

Thinner oxide MOSCs generally displayed lower breakdown strengths than the thicker oxide devices.

The effect of (intrinsic or defect-related) breakdown on the C-V curve for devices which experienced only non-shorting breakdowns was to shift the C-V characteristic to more positive bias regimes, indicating the injection of negative charge to the device. This negative oxide charge was of the order of $\approx 10^{14}$ qcm^{-2} for 10^3 breakdowns cm^{-2}. Interface state generation by breakdown was comparatively small, of the order of 10^{11} q $cm^{-2}ev^{-1}$ to 10^{12} q $cm^{-2}eV^{-1}$, considering the charge injection and physical damage to the devices caused by breakdown.

(6). Radiation induced dielectric breakdown has been observed in all types and oxide thickness devices only for very-high-LET radiation (fission-fragments) and there was no evidence to suggest that any other radiation field tested affected the breakdown characteristics of the devices in any way.

The breakdown strength of devices whilst under fission-fragment irradiation was considerably lower than for virgin devices, being of the order of 16% lower overall. As for virgin devices under (intrinsic or defect-related) breakdown, the breakdown strength was lower for MOSCs under forward biasing than under reverse biasing, the difference being of the order of 16% of the upper limit. The p-type devices generally had breakdown strengths lower than those of equivalent oxide thickness n-type devices, typically of the region of $8MVcm^{-1}$ to $8.75MVcm^{-1}$, dependent on the device thickness; n-type devices, at best, displayed breakdown strengths in the region of $9.25MVcm^{-1}$ to $10.25MVcm^{-1}$.

Thinner oxide MOSCs when under irradiation and large gate bias conditions generally displayed lower breakdown strengths than the thicker oxide devices.

The effect of radiation induced breakdown on the C-V curve for devices (which experienced only non-shorting induced breakdowns) was to shift the C-V characteristic to more negative bias regimes, indicating the injection of positive charge (holes) to the device. This positive oxide charge was of the order of $\approx 10^{14}$ qcm^{-2} for 10^3 breakdowns cm^{-2}. Interface state generation by breakdown was comparatively small, of the order of 10^{12} q cm^{-2}eV^{-1}, considering the charge injection and physical damage to the devices caused by breakdown and the fission-fragments.

A typical characteristic of the devices is the correlation between the number of fission-fragment induced breakdowns and the fission-fragment dose, with each fission-fragment producing a single breakdown in the devices (when sufficiently biased), irrespective of device oxide thickness and type; p-type devices were generally more sensitive to fission-fragment radiation than equivalent oxide thickness n-type MOSCs.

The devices were only affected by fission-fragments if, for n-type MOSCs (irrespective of oxide thickness), the fragment had a stopping power in SiO_2 of at least ≈6 MeV mg^{-1}cm^{-2}, and in p-type devices (irrespective of oxide thickness) had a stopping power in SiO_2 of at least ≈ 9 MeV mg^{-1}cm^{-2}.

Typically the devices could detect 10^5 to 10^6 fission-fragments cm^{-2} before failure, and the breakdown craters were between 2μm and 55μm in diameter, dependent on the type of device, irrespective of breakdown field and bias polarity.

(7). No evidence of radiation induced changes in the structure of the interfaces (Al-SiO_2 and Si-SiO_2) was found for thin or thick-oxide devices of either type, except for fission fragment irradiation and breakdown where the effects were most pronounced for devices irradiated whilst under either bias condition. The effects were generally small, and in some cases could have been due to extraneous conditions in the investigation chamber.

Similarly, no evidence of radiation induced changes in the structure of the bulk oxide was found for thin or thick-oxide devices of either type, except for fission fragment irradiation and breakdown where, again, the effects were most pronounced for devices irradiated whilst under either bias condition. The effects were generally small and, again, in some cases could have been due to the test technique.

The evidence suggests that bond damage (breaking) is the most likely effect in both the case for the interfaces and for the bulk oxide; no evidence was found for the proposal of the possibility of the generation of a silicon-rich layer produced at the interface by irradiation, even in the case for dielectric breakdown or for radiation induced breakdown.

A summary of the effects of the radiation en masse on the Al-SiO_2-Si MOSCs tested has been presented. This is used in proceeding sections to propose an improved framework for understanding intrinsic (and defect-related) breakdown in Al-SiO_2-Si MOSCs and the effects of radiation on these phenomena, and to extend the knowledge of the general effects of radiation on the physical characteristics and electrical behaviour of such structures.

7.3 Intrinsic and Defect-related Dielectric Breakdown in Al-SiO_2-Si MOSCs

The similarity between the effects of intrinsic (or defect-related) breakdown and radiation induced breakdown on the Al-SiO_2-Si MOSCs tested suggests that the basic mechanism which describes the breakdown process is similar for both breakdown processes; the difference between the breakdown process in each case is the mechanism underlying the initiation of breakdown. It is therefore important to formulate a more detailed microscopic approach to understand the breakdown process overall. To this end, this section is devoted to discussion of the new data, accumulated from the investigations of the virgin Al-SiO_2-Si MOSCs under dielectric breakdown and high-field conditions, which, it is proposed, is applicable to devices which have undergone radiation induced dielectric breakdown.

From the theory presented in Chapters 2 and 3 it is clear that when a MOSC is stressed with a

constant voltage, a current is injected which decays with time. This decay is caused by space-charge evolution in the dielectric layer. After a certain duration of the injection suddenly breakdown takes place. The breakdown pits and associated channels which appear after breakdown are visible as one or more spots of similar size burnt in the electrode. The dimensions of the breakdown channel are known to depend on the dimensions of the MOSC[147,149]; typically, the dimensions of the breakdown channels formed by (intrinsic or defect-related) breakdown were between 2μm and 50μm in diameter. Probably the breakdown channel is generated by the discharge of the MOSC. The fact that the diameter of the breakdown channels appears to be independent of the gate voltage for breakdown (and thus injection current) indicates that the generation of these channels is mainly caused by the discharge energy.

It can therefore be assumed that a critical amount of charge is needed for breakdown. This can explain why some of the MOSCs displayed a delayed time-dependent breakdown with respect to the intrinsic time to breakdown mentioned in Chapter **3**. A proposed explanation for this is that these MOSCs are contaminated with ions or other species which form deep traps in the oxide. When the traps are filled during injection a space-charge develops which reduces further injection; the critical amount of charge needed for breakdown will be reached after a much larger injection period.

In general the current decay which occurs after breakdown (as shown in the oscilloscope trace in Figure 170) can be expressed as a power law of time $I \approx k\ t^{-a}$ where k is some constant and a is a real number. The amount of injected charge increases with the time integral of the current $Q \approx m\ t^{1-a}$ (m is some constant, $a \neq 1$). Q will increase indefinitely as long as $a \leq 1$ (when $a=1$, $Q \approx m \ln t$). When $a \geq 1$, Q will approach a finite size. Clearly, Q increases at a slower rate as a is smaller. Since a is a measure for the concentration of traps and their distance from the gate electrode[121], any increase (or differences between devices) in the time to breakdown can be explained by assuming that the local trap concentration is larger. This would explain the differences in the breakdown properties of the devices tested with a large initial interface trap density.

7.3.1 The pre-breakdown Stage

The onset of breakdown in an MOSC is first detected by a sudden increase of the current flow through the device (the injection current). When it exceeds a certain pre-selected value the device can be considered to have suffered a non-shorting breakdown; depending on the capacitance of the device, these currents must be fairly high to cause breakdown and the pulse output which can be easily detected from the transient increase (and following stabilisation) of the current flow. It is known that the field for current injection without dielectric breakdown in MOSCs decreases with increasing oxide thickness[121,130]; this was also seen to be the case for fields at which breakdown occurred in the devices and this suggests that current injection and dielectric breakdown in the devices are related. The field dependence of breakdown is very similar to that of injection[122] which adds further credence to the proposal that the two cases are related. The observation that the current density in the MOSCs decreased with (injection) time, caused by the evolution of the space charge in the dielectric, and continued up to the point of breakdown suggests that with increasing fields, higher currents are injected and the time to breakdown should decrease. This implies that the value of current at which breakdown occurred (as illustrated in Figures 121 and 122) was a minimum value rather than a critical value, and that a large degree of charge injection had to take place before the device could breakdown. It would seem likely, therefore, that the driving mechanism for intrinsic (or defect-related) breakdown is the amount of charge injected, corresponding to the amount of energy dissipated in the MOSC, and that the field strength is not the critical parameter.

Further corroboration for charge injection before breakdown is the evidence presented to illustrate the effects of breakdown on the C-V characteristics of the devices before and after breakdown (shift and distortion of the C-V curve) which demonstrates that lasting charge injection and the formation of interface states in the devices occurs for all devices in all situations of breakdown, which is not evident in low-voltage stressed devices.

Since it has been proposed that the breakdown of the MOSCs was due to the effects of charge injection in the pre-breakdown stage, discussion of the energy dissipation in the dielectric in this pre-breakdown stage is thought to be fruitful. Consider the energy dissipated during the pre-breakdown stage: any electron which has entered the dielectric at the negative electrode at $T'^{*}=T'_{0}$ and leaves the dielectric at the positive electrode at $T'^{*}=T'$ dissipates an amount of energy

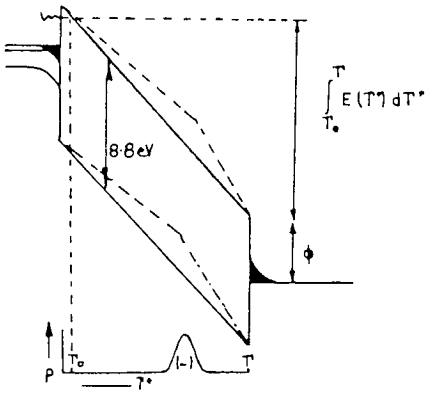

Figure 179: Energy-band diagram for electron injection by quantum mechanical tunnelling to a point in the dielectric of an Al-SiO_2-Si MOSC.

W, such that

$$W = q \int_{T'_o}^{T'} E(T'^*)\, dT'^* + q\emptyset \qquad -117$$

where E (T') is the local field strength at the point at which breakdown occurs, T'_o is the point in the oxide to which the electron can quantum-mechanically tunnel from the negative electrode, Ø is the work function difference when the electron is emitted from the dielectric to the positive electrode, and q the electronic charge. This is illustrated in Figure 179.

The energy dissipation in the dielectric must change with time and distance when a space charge evolves, but it seems practical to begin with the total charge, Q_{bd}, and the total potential drop between the electrodes. The total energy dissipation, W, is

$$W = Q_{bd}V = Q_{bd}\, E_{applied}\, T' \quad cm^{-2} \qquad -118$$

The rate of dissipation, P, is given by

$$P = J\, V = J\, E_{applied}\, T' \qquad -119$$

where J is the overall current density and T' is the oxide thickness.

An order of magnitude estimate for a typical thin-oxide (37.4nm) p-type MOSC can be made by taking the median values for J and $E_{applied}$ from Figures 121 and 122 and Figures 177 and 178: $J \approx 5*10^{-6}$ Acm^{-2}, $E_{applied} \approx 8 MVcm^{-1}$ (≈29V), and $Q_{bd} \approx 5*10^{-3}$ Ccm^{-2}. Values of $W \approx 0.15$ Jcm^{-2} and $P \approx 1.5*10^{-4}$ $Wattcm^{-2}$ are directly obtained.

Assuming that the electron flow is homogeneous over the whole electrode area, equating the heat production, P, to the heat loss by (homogeneous) thermal conduction yields the temperature gradient, $^{dt}/_{dT'}$. Since $J_{th} = g\ ^{dt}/_{dT'}$ and the specific heat capacity, g, is $g \approx 0.014 Jcm^{-1}s^{-1}K^{-1}$ for pure SiO_2, using the case for $P \approx 1.5*10^{-4}$ Wcm^{-2} yields a temperature gradient of $^{dt}/_{dT'} \approx$ $0.01 Kcm^{-1}$. This gradient is so small in the devices that temperature effects are negligible.

Assuming that the injection current is confined to some small volume (say,the breakdown channel) the heat production can still be seen to be of little importance to the onset of breakdown; assume that all the injected current is confined to a spherical volume with radius r in the middle of the SiO_2. The heat production must equal the loss of heat in a quasi-stationary case, therefore

$$2AJEr = -4\pi r^2 g \; dt/dr \qquad -120$$

where A is the gate electrode area, and E if the field strength (assumed to be constant over the sphere).

Thus

$$dt = -J \; A/2\pi \; E/g \; dr/r \qquad -121$$

Integrating over the surface of this sphere with $r=r_{min}$ to the electrode r=T'/2 where the temperature is assumed to be at room temperature, t_e, yields, for the surface of the sphere at $r=r_{min}$ a temperature t_s, thus

$$t_s - t_e = -J \; A/2\pi \; E/g \; \ln(2r_{min}/T') \qquad -122$$

Inserting the values of J and E as before, with $A=0.09cm^2$, T=37.4nm, and r_{min} =0.1μm (from Figures 114, 115 and 116) gives

$$t_s - t_e \approx 26\,K$$

The temperature of the sphere, t_s, is only 44 - 46K when the ambient is room temperature; the confinement of all the injected charge to this small region (considerably smaller than the very smallest effect seen in the MOSCs tested) has only raised the local temperature to a fraction of the of the estimated temperatures necessary to induce breakdown[156,157]. Thus, under these

conditions of J and E temperature effects are negligible; when J is of the order of three orders of magnitude higher the temperature effects become significant, provided the current injection is confined to such a small volume.

Having demonstrated that, in this case (which is typical of the MOSCs tested) under the specified conditions the Joule heating is insufficient to initiate breakdown, it is assumed that permanent, cumulative effects in the dielectric must take place. These probably occur in the form of imperfections (traps, interface states, atomic displacements and so on); it is proposed that such local increases in lattice energy are defects or damage which may be areas of further local charge injection and initiation sites for (future) breakdown. It is proposed that these areas are potential defect-related breakdown sites.

To test this further, consider the damage caused to the lattice as electrons are injected under high fields ("hot" electron injection) to various traps in the bulk oxide and at the interfaces: damaging the lattice must require at least the energy of formation of SiO_2, ΔH_{SiO2}, which is approximately $3.3^{*}10^{4} Jcm^{-3}$. The mean energy dissipated cm^{-3}, under the same conditions used in the previous argument, is

$$W_{/T'} = E\,Q_{bd} \approx 4^{*}10^{4}\ Jcm^{-3} \qquad -123$$

Apparently, this is just sufficient to disintegrate the lattice since $W_{/T'} > \Delta H_{SiO2}$. However, it is assumed that a large fraction of the energy dissipated in this volume will be lost by thermal conduction; most of this energy is lost by electron-phonon interaction in the conduction band. The interaction length would be so short that only a small fraction of the electrons will acquire sufficient energy to create a defect.

The quantity of energy gained when electrons leave the conduction band (for example, when they fall into a deep trap or to the Fermi level of the electrode) is much larger than that gained by drift in the field (unless "hot" electron effects occur). At the interface the energy gain, W_i, is given by

$$W_i = Q_{bd}\varnothing \approx 0.02\ Jcm^{-3} \qquad -124$$

where $\emptyset \approx 4V$ is taken for Al-SiO_2-Si MOSCs in this instance. In order to calculate the energy density, the assumption that the mean interaction length, L, is L=2nm, as according to NICOLLIAN and BREWS[16], is the case for 4eV electrons emitted into Al.

The mean energy density is then

$$W_i / L \approx 1 * 10^5 cm^{-3}$$

This density of energy is larger than that in Equation122 and hence in itself is sufficient to create damage at the interface, the difference now being that the individual electron energy is large enough to create defects. Thus, the injected current will damage especially the interface, as was seen in the ESCA and AES spectra of the devices tested. At the interface all the electrons will have sufficient energy to create damage, while in the conduction band only a small fraction will have sufficient energy.

Consider the same situation with the variation that the oxide or interface (or both) have become charged by, say, the passage of ionizing radiation (such as alpha, gamma or fission-fragment radiation) through the MOSC or by high-field injection to a defect; the charging that may occur could be the generation of interface states or the development of a fixed oxide charge.

Assuming that the subsequent dissipation of the conduction band energy of the electrons is confined to the same spot, it is proposed that, in the case for a defect present at the interface (such as a dimple or microprotrusion, as found on a number of virgin devices and shown in Figures 104 to 108), only a small part of the gate electrode has to be damaged and Q_{bd} is relatively small. The damage is now considered to be confined to the defect site at the interface. It is proposed that, even though comparable fields may be needed for injection, the damage is concentrated at the same spot and the damage, leading eventually to a short-circuiting path, takes much less charge.

When electrons fall into deep traps they are able to dissipate their energy into a relatively small volume; the overall energy dissipated at the traps is given by

-125

$$Q_S (d_T / L_T)$$

where L_T is the interaction length of the trap, d_T is the trap depth below the conduction band and

Q_S is the charge which is trapped during the high-field stressing.

Considering typical values[121] of $d_T \approx 2.4V$, $Q_S = 3*10^{-7}$ Ccm^{-2} (that is, the space charge needed for a flatband field shift of $1MVcm^{-1}$) and $L_T = \sqrt{s_c} = \sqrt{10^{-16}} = 10^{-8}cm$, where s_c is the capture cross section of neutral traps[121], gives

$$Q_S (d_T / L_T) \approx 72 Jcm^{-3}$$

This value is much smaller than the densities dissipated in the conduction band and at the interface. However, at traps that repeatedly capture and emit electrons, a multiple of this energy (dependent on the number of catches and emissions) must be dissipated during the high-field stress period. The individual electron energy is large, as in the case for dissipation at the interface.In contrast to the low overall energy density the local energy density dissipated by the electrons being trapped is very high, as can be seen from an estimation of the energy loss in a spherical volume $1/6(\pi L_T^3)$ bounded by the interaction length. Thus, the local energy density is found to be

$$d_T / 1/6(\pi L_T^3) \approx 7.4*10^5 \ Jcm^{-3} \qquad -126$$

This value is very high and is sufficient to heat the interaction volume to a 'temperature' of ≈1200°K. It is assumed that damage can also be generated at the injecting electrode, as has been shown by WOLTERS and VERWEY[121], although no evidence of this was found in the present study.
Thus, it has been shown that with oxide (or interface) charging, if electrons are injected to traps they might subsequently dissipate their conduction band energy which is sufficient to cause thermally initiated dielectric breakdown from defects or injection-current generated defects.

7.3.2 The Breakdown Stage

Consider the energy dissipated at the moment of breakdown: from the results presented in section 6.2, it is evident that the diameter of the breakdown crater (at the base of the breakdown pit and virtually identical in size for all the breakdown pits investigated) is dependent only on the type of device and not on the current with which the MOSC was stressed. It is therefore assumed that the stress current does not contribute very much to the energy needed to generate the breakdown pit.

The discharge current was far larger than the external current (for example, the external current was of the order of 100μA for most experiments), as it may be deduced from the fact that the voltage at breakdown was seen to drop sharply within a very short time span, Δt_{bd}, with $\Delta t_{bd}<10\mu s$. An estimate of the discharge current, I, from the displacement charge (given by ΣEA where Σ is the dielectric constant which is $\approx 3*10^{-13}$ for SiO_2) and Δt_{bd}, gives

$$I = (\Sigma EA) / (\Delta t_{bd}) \approx 2.4*10^{-2} A \qquad -127$$

where $A=0.09cm^{-2}$ is the MOSC top gate electrode area and the field just pre-breakdown was measured as $\approx 6MVcm^{-1}$.

Estimating the size of the channel generated at breakdown, A_c, to be for p-type devices approximately 4μm diameter or an area of $\approx 13\mu m^2$ (for n-type devices approximately 20μm in diameter, an area of $\approx 315\mu m^2$) it can be seen that the discharge current density is

$$J_{dis} = I / A_c \approx 1.8*10^5 \, Acm^{-2} \qquad -128$$

(This is very much smaller for n-type devices, with $J_{dis} \approx 7.5*10^3 \, Acm^{-2}$ and therefore its effects are negligible).

The total energy dissipated at breakdown, W_{bd}, for a MOSC with a unit area gate electrode and of unit oxide thickness is

$$W_{bd} = 0.5\Sigma E^2 + EJ\Delta t_{bd} \qquad -129$$

$$= 0.5(3.4*10^{-13})64*10^{12} + 6*10^6(5*10^{-6})10^{-5}$$

$$\approx 10.9 + 3*10^{-4} \, Jcm^{-3}$$

$$\approx 11 \, Jcm^{-3}$$

The second term, which represents the energy delivered by the external source during the interval Δt_{bd} of breakdown, is completely negligible except for when very large external current densities are applied (which is frequently the case when a voltage source such as the one used in this

investigation is used, where the current densities of $10^2 Acm^{-2}$ are common).

An estimate of the radius of the breakdown crater from the dissipated energy at the initiation site for breakdown can now be made: Since a voltage (rather than a current) source was used, at moderate injection currents the temperature at breakdown will be dependent on both terms of Equation **129**. The power dissipation is so large that a part of the Al electrode is melted and evaporated. It is proposed that this melted Al forms a ball of solid material which is responsible for the effects seen in various interferograms (Figures114(a) and (b)) and electron micrograph examinations (Figures 113(a) and(b))of the breakdown pits, where the silicon substrate has a breakdown crater embedded with Al which forms a shorting path between the top electrode and the silicon substrate.

Since the breakdown craters have very much larger dimensions than the oxide thickness the initiation site for breakdown is treated as a sphere evolving spherically to the larger dimensions. The melting of the relatively thin oxide layer can be neglected in this case. The thermal energy will be finally lost to the environment of the crater by thermal conduction.

Considering the observation that the silicon electrode was melted, an estimate of the radius of the molten sphere, R_m, can be made using the dimensions shown in Figures 113(a) and (b) and Figures114(a) and (b).

The heat generated by the discharge must be larger than (or equal to) that needed to melt the silicon over a radius R_m. Considering an external current density applied of $0.1 Acm^{-2}$, it is seen that

$$(0.5\Sigma E^2 + EJ\Delta t_{bd})\, AT' \geq 1.33\pi R_m^3 \left[H_{l,1700} - H_{c,298}\right] d_s / m \qquad \textbf{-130}$$

where $H_{l,1700}$ is the enthalpy at 1700K (just above the melting point) of the liquid silicon, and $H_{c,298}$ is the enthalpy at room temperature of crystalline silicon, both expressed in $Jmole^{-1}$. m is the molecular weight and d_s is the specific density (in gcm^{-3}). Since $\left[H_{1,1700} - H_{c,298}\right] \approx 205$ $KJmole^{-1}$ and $d_s \approx 2.66 gcm^{-3}$, using the data calculated in previous discussion and rearranging gives

$$R_m^3 \leq \frac{(0.5\Sigma E^2 + EJ\Delta t_{bd})\, AT'm}{1.33\pi \left[H_{1,1700} - H_{c,298}\right] d_s} \qquad \textbf{-131}$$

and thus

$$R_m \leq 1.6\mu m$$

The radius of the pit burnt in the silicon was observed to be of the order of 0.9μm in diameter and therefore this calculated value is of the same order of magnitude as the observed results.

From the fact that part of the electrode has erupted over the surface it can be concluded that the material has been evaporated under high pressure in the centre of the molten sphere. Performing the same calculation, but now with the enthalpy of Si just above the vaporization temperature (approximately 3600K) , it can be seen that with $[H_{g,3600} - H_{c,298}] = 525 KJmole^{-1}$, $R_g \leq 1.1\mu m$. This is the same order of magnitude as the radius of the base of the crater (as determined from the interferograms shown in Figures 114(a) and (b)). This is therefore probably where the breakdown was initiated, after which eruption took place. The experimental dimensions are in fairly good agreement with the calculated values, considering that part of the energy was lost when eruption took place. This makes it plausible, anyhow, that part of the breakdown channel has experienced temperatures above 3600°K; at this temperature the gas will be ionized and will be able to form a plasma of Si^+ and Al^+ ions, the corona of which is often visible.

Thus, it has been demonstrated that the thermal effects which take place at breakdown are large enough to cause the damage seen in Al-SiO_2-Si MOSCs and calculations made using simple approximations are in good agreement with the experimental data.

7.3.3 The Change in MOSC Characteristics due to Breakdown

The main characteristics of the C-V curves for the Al-SiO_2-Si MOSCs after breakdown is the evidence of generation of a large density of interface states (as would be expected considering the proposals of the last sections) and the generation of a very large negative oxide charge, which implies hole injection has taken place. This effect in the devices is unexpected considering the evidence reported by other workers[121,122,123] to show that electron injection is the typical effect detected. This build up in negative space charge may be explained using the arguments developed in the previous discussion which suggest that a buildup of electron trapping occurs at various generation sites, leading to breakdown. It is assumed that after breakdown all the electrons which have been trapped have, on the whole, left the traps and dissipated their conduction band

energy; the result is a large number of electron traps in the vicinity of the breakdown site which contribute to the large observed negative trapped charge, and the correspondingly large number of interface traps generated and abandoned in a similar fashion. This effect is characteristic of the high-field properties of fast surface (or interface) states[16,95,100-102].

7.3.4 The Model for Breakdown

In this section a qualitative model of what happens during carrier injection and breakdown is presented, which is different from the descriptions given by the ionization based models of Chapter 3. The most important conclusions and proposals from the experimental results presented in Chapter 6 and the discussion presented so far are:

(1). Breakdown appears to be the result of charge injection.
(2). The energy dissipated by the current is, in most cases, not sufficient to cause thermal runaway.
(3). The total amount of injected charge must be an important parameter.
(4). The charge needed for breakdown appears independent of the injection conditions.
(5). The changes induced by charge injection are permanent.
(6). A small injection may induce a positive space charge.
(7). A very large injection induces a negative space charge.
(8). Interface states are generated by this injection and breakdown.
(9). At the moment of breakdown the displacement charge provides the energy that causes the destruction of the MOSC.
(10). At breakdown, part of the MOSC oxide is gasified and a larger part is melted This results in a crater and pit in the silicon substrate and oxide layer, and the removal of the Al gate electrode in a small portion of the MOSC where breakdown has occurred.

Using these proposals and conclusions the driving force for the generation of damage, the possible growth of the discharge pattern, the nature of the negative charge and the final collapse of the high-field stressed Al-SiO_2-Si MOSC are briefly discussed.

As discussed above, the erosion of a conducting pathway through the oxide layer is proposed to be produced by the injection of charge. The simple assumption is that the injected electrons (or holes) gain enough kinetic energy to cause damage by interaction with the lattice. However, to

generate irreversible damage a considerable amount of energy is needed. Chemical changes and bond-breaking require energies of several eV. This is more than the average kinetic energy that electrons will gain in a wide-band gap insulator such as SiO_2. For instance, in SiO_2 the mean interaction length is only 0.3nm - 0.4nm, which implies that the electrons will only gain energies (on the average) of 0.3eV - 0.4eV in a field of $10MVcm^{-1}$. There may be a number of ' lucky ' electrons (those electrons which have, under unusual conditions, acquired a lucky drift and therefore are in an increased energy state[16]) that gain enough energy to produce damage; their number should increase exponentially with the field strength. It has, however, been proposed that the injection current needed for breakdown is not dependent on the field strength. The evidence for this phenomenon cannot be understood by the *lucky* electron model. This model also does not explain the evidence that other workers [103,161,162]who have found that breakdown can occur when a sufficient number of hot electrons are injected at very low fields.

If not the kinetic energy of the electrons, then it is probably the potential energy that indirectly causes the damage. The high potential energy of the electrons stems from the fact that SiO_2 is a wide-band energy gap insulator. Electrons injected over the high energy barrier in the conduction band would have a large potential energy of 4eV to 5eV above the Fermi level. This energy is probably lost when these electrons are captured in deep traps or emitted into one of the electrodes. Their potential energy has to be transferred to the atomic and electronic species of the trap and its environment or to those of the electrodes. Such energy (4eV - 5eV) is large enough to break bonds, ionize atoms and so on, and although the physical investigations (using ESCA and AES) of the MOSCs did not reveal these effects for any other than breakdown fields it does not preclude their existence for lower field effects.

Since several workers[130,139] have shown that occasionally electrons are emitted into the cathode of MOSCs under high-field stressing, and that this emission produces photons with energies up to 5eV, it can be conjectured that a mechanism for this energy transfer could be via the production of a photon. Photons of this energy are known to produce stable and interface states. A photon of 5eV would be hardly absorbed in SiO_2 and would have an interaction range stretching some way into the oxide layer, if not larger than the dielectrics thickness. States could thus be generated at some distance from the location of the energy production, for example, at the interface. The general

conclusion from this is that the charged particles, both electrons and holes, losing their high potential energy from the insulator conduction band or valence band , will cause a local disturbance of the dielectric and its interfaces; this may lead to bond breaking or displacements. The volume of disturbance could extend over a wider range than the specific spot at the interface.

The driving force for the breakdown is therefore the abrupt change in potential energy and the large associated discharge.

Such a discharge might follow the tree-shaped pattern shown in Figure 180. The channels are assumed to contain positive charges acting as local potential minima for injected electrons and negative charges acting similarly for injected holes. These positive charges would form deep traps for the electrons by their Coulomb attraction and have high local fields and capture cross sections. It is proposed that the growth of the channels is in the direction of maximum discharge of the injected electrons. This might be different from the direction of the applied field, and when injection and trapping is homogeneously distributed over a layer one might expect a tree-shaped pattern as shown in Figure 180(b) from the avalanche of injected electrons.

Above a certain current density (for example, at breakdown when the MOSC is discharged when the current density may be as high as $10^6 Acm^{-2}$) the channel would be heated due to the high current density and this would induce a higher trap level occupancy leading to an alteration of the space-charge during injection; thus, the space-charge might either inhibit or enhance injection, depending on its sign, and this would explain the different depths of breakdown crater observed (and shown in Figures 114(a) and (b)). This effect is a likely explanation for the damage which occurred for breakdowns previously classed as "shorting breakdowns" where injection appears to have been enhanced, causing a far greater degree of local damage and eventual device failure. In both inhibition and enhancement of injection, the electrons (or holes) would have to flow through a restricted area and the magnitude of the charge needed for breakdown should be seen to decrease for smaller injection currents.

The negatively charged states in the SiO_2 and at the interfaces, which were seen to occur for high field breakdown, are likely to be trapped electrons or interstitial sites where damage has occurred. Positive charged states in the SiO_2 and at the interfaces seen for low-field effects of breakdown are possibly trapped holes at Si and O atoms or Si^+, O^+ and Al^+ ions produced by the injection and subsequent damage.

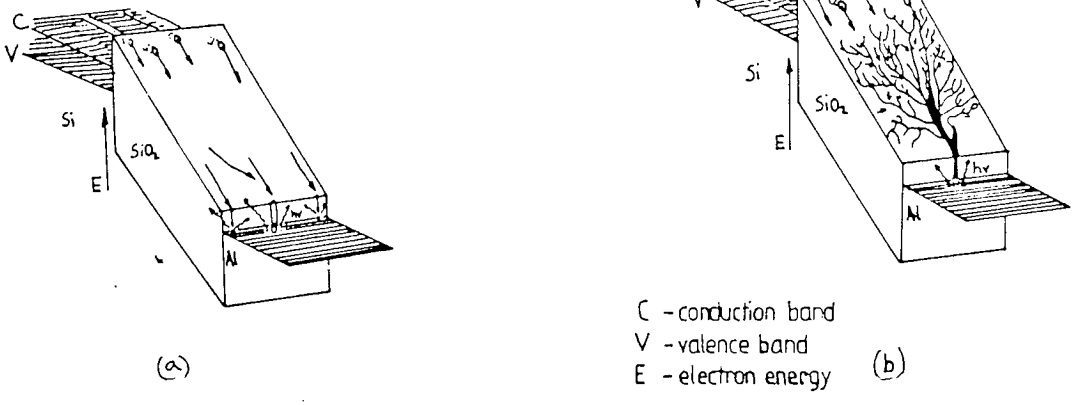

Figure 180: (a) Proposed initiation of a discharge pattern until dielectric breakdown in an Al-SiO_2-Si MOSC.

Figure 180: (b) Proposed growth of a discharge pattern until dielectric breakdown in an Al-SiO_2-Si MOSC.

It is proposed that the final collapse of one of the channels in the MOSC under high field stressing, causing a local breakdown, is the result of the channel reaching the vicinity of the opposite electrode where erosion of the oxide integrity would accelerate by high-field acceleration of the charge (producing hot electrons or hot holes, dependent on the polarity and type of injection occurring). The channel would subsequently be instantaneously heated (within nanoseconds, from the calculations of the previous discussion) when the energy of the charged MOSC is dissipated; temperatures can reach 300°K to 400°K and a hole is burnt in the top Al gate electrode (if it is thin enough, if not the oxide beneath it melts and causes a local damage site at which injection is enhanced). Depending on the energy released during the collapse (which may last for milliseconds before the MOSC recovers its pre-breakdown I-V characteristic) parts of the MOSC and substrate are evaporated leaving behind a crater. This process is repeated over the surface of the Al gate electrode until the device is destroyed through shorting breakdowns or insufficient remaining Al gate electrode to permit operation. These breakdowns occur primarily at physical defects in the oxide and at the silicon surface (such as those shown in Figures 104 to 106) at low fields and are quickly eliminated; at higher fields it is proposed that defects are created by electron or hole injection, depending on the device type, which, through an avalanche process breakdown with increasing injection which may be enhanced or inhibited by the field, depending on the device bias polarity.

Thus, intrinsic breakdown is a two-stage process: the first is the creation of structural changes in the dielectric layer which eventually leads to a low resistance path connecting the two electrodes; the second process is the instantaneous discharge of the MOSC via this low resistance path. The energy released at this discharge site leads to a permanent leaking of the dielectric (SiO_2) and a breakdown crater. Calculations have shown that at typical current densities electrons in the field do not have an energy density great enough to heat the dielectric substantially. This is even the case for when an electron is confined to a small filamentary path in the dielectric. However, when electrons loose their high potential energy, which they have in the conduction band of the insulator, over a short distance at the electrode or at a trap it has been shown that, theoretically, the energy density is sufficiently large to generate permanent damage. The importance of the potential energy for the generated damage, instead of the kinetic energy, would explain the observations made by other workers[121,130] that the charge necessary for breakdown, Q_{bd}, is largely

independent of the applied field (as was noted in section 5.2).

Structural changes in the dielectric also appear to depend on the injection mode and magnitude, and are characterised by traps and interface states. Positive space charge has been observed for very low injection, and negative space-charge for very high injection, with positive centres acting as deep traps for electrons and thus a site for dissipation of potential energy. This concentration of damage is proposed to cause tree-shaped patterns of discharge which would explain the conical craters observed to be formed in the dielectric layers during the breakdown process.

7.4 The Effects of Radiation on the Dielectric Breakdown of Al-SiO_2-Si MOSCs

The results of Chapter 6 clearly demonstrate that only those radiations with a stopping power of at least $\approx 6 MeVmg^{-1}cm$ in SiO_2 in n-type MOSCs and at least $\approx 9 MeVmg^{-1}cm$ in SiO_2 in p-type MOSCs will induce dielectric breakdown at lower fields than those for field-only breakdowns (as first reported by KLEIN[13]). Thus, radiation induced dielectric breakdown is limited to heavy ions and fission-fragments with such stopping powers, other radiations not appearing to have a sufficiently large linear energy transfer.

Considering the discussion for intrinsic and defect-related breakdown presented in the previous section, which proposes the breakdown process is a two-stage event dominated by the pre-breakdown increase in charge injection, would appear to remove the apparent contradictions in the KLEIN[245] model for RIDB; the discrepancies found in the magnitude of the positive charge and the breakdown voltages observed by KLEIN[245] and other workers[234,243] could be accounted for if one considers that the current runaway period (of duration $t_{r)}$ is only a second step, and a pre-runaway step based on impact-ionization takes place, as in the models proposed for intrinsic breakdown by DISTEFANO and SHATZKES[169] and KLEIN and SOLOMON[170].

It is proposed that the first step of the breakdown would be dominated by electron-hole pair recombination, owing to the extremely large number of charge carriers created (by ionization) in the oxide by the passage of a fission-fragment. In order to explain the observations made in this investigation it is necessary to assume that the hole density around the track formed by a fission-fragment decreases to some small fraction of its original magnitude by recombination in a

very short (perhaps picoseconds) time period. Current runaway could not take place in this time period due to this extremely short recombination time and thus large rate of decrease in the hole density.

The charges, however, could not completely vanish owing to the trapping properties of the insulator as is seen to occur from the shift in the flatband voltage in the C-V plots for devices post fission-fragment irradiation (and breakdown) shown in Figures 174 to 178. Some holes would remain trapped around the track of the fission-fragment and the associated electrons (by ionization) might lay further away from these holes than is expected with a simple ionization-recombination process. A nett rest hole density can be identified with that in the KLEIN[245] model, p_o, the densities of which have been presented in Table 6 and can be seen to have magnitudes which are expected (from density of interface states and trapped charge density calculations presented in Table 21) when high field trapping occurs in SiO_2.

As is evident from the shift in the flatband voltage of C-V characteristic for devices which have been irradiated without gate bias charges can remain trapped in the oxide layer for long times. Thus, when a field smaller than that needed for current runaway is applied (that is, $F<F_r$), the rest hole charge can be diminished or removed altogether by recombination with injected electrons (injected from either electrode) or by drift and subsequent recombination with electrons a (comparatively) large distance from the fission-fragment ionization track. On application of bias to the MOSC which which produces a field in the SiO_2 which is larger than the critical field for current runaway (that is , $F>F_r$), the hole density increases after a very brief initial recombination period and leads to the runaway described in section **7.3.1** and**7.3.2**. These processes are illustrated schematically in Figure 181, showing the proposed changes in the magnitudes of total hole density as a function of time, with the three cases of oxide field in the SiO_2 ($F<F_r$,$F=0$ and $F>F_r$) as the parameter.

This is an extended version of the KLEIN[245] model for dielectric breakdown in MOSCs induced by fission-fragments and can be summarised by: electron-hole recombination around the track of the fission-fragment is the dominant process immediately after the passage of the fragment. The hole density decreases around the track to a very small fraction of its original magnitude in a very short time but owing to the trapping properties of the insulator a nett rest hole density remains around the track. This hole density is associated with the large density of traps and interface states seen in

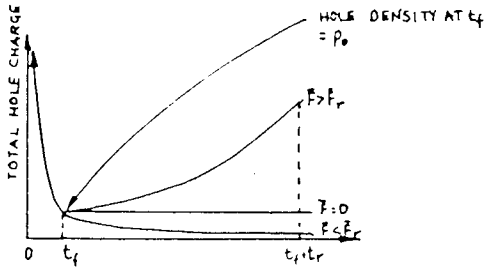

Figure 181: Qualitative based sketch of the total hole density as a function of time after the passage of a fission-fragment through an Al-SiO_2-Si MOSC.

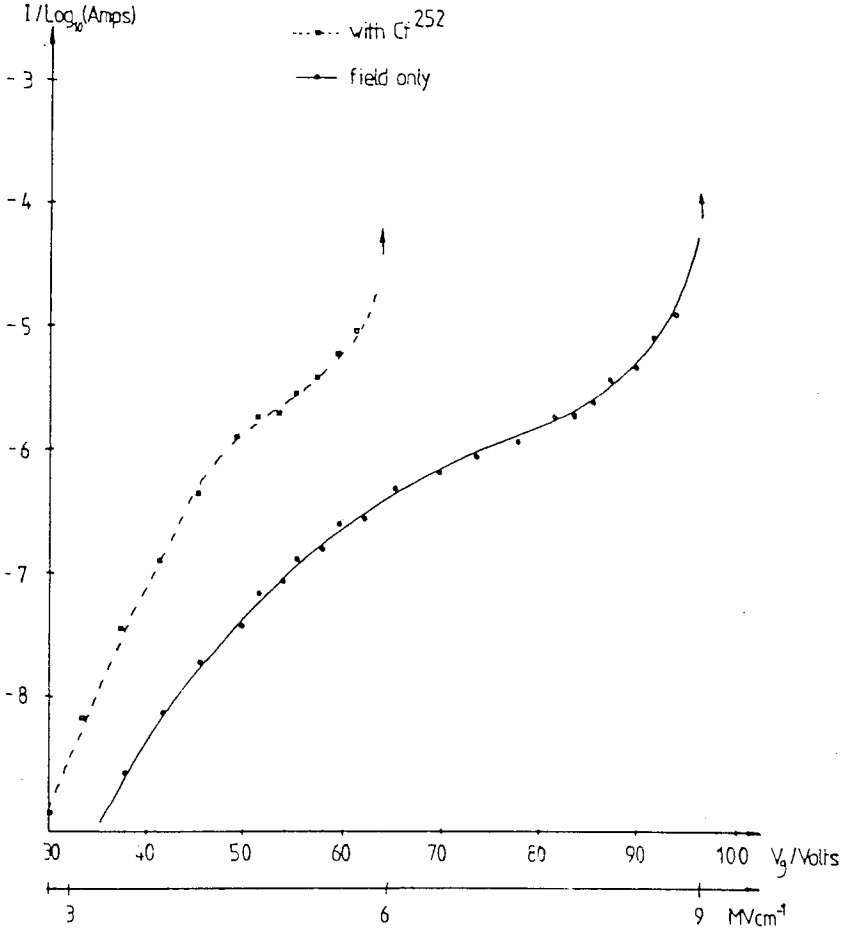

Figure 182: The typical I-V characteristic of an n-type Al-SiO_2-Si MOSC under fission-fragment irradiation.

fission-fragment irradiated MOSCs and is identified with p_0 in the simple model for RIDB proposed by KLEIN[245]. Breakdown is assumed to take place in a period much greater than the recombination period of the carriers.

The effect of fission-fragment irradiation on the I-V properties of the Al-SiO_2-Si MOSCs tested leads to a new proposal for injection effects which is directly linked with the arguments put forward in section **7.3.1**, and is relevant to the discussion of the proposed extension to the KLEIN[245] model.

Consider the effect of fission-fragment irradiation on the I-V characteristics of the Al-SiO_2-Si MOSCs, a typical example of which is shown in Figure 182; an anomalously high device current is seen for the device when under fission-fragment irradiation compared with the same device biased in a similar fashion before any irradiation. There have been two reasons proposed by other workers[178,179] to explain this and are applicable to the pre-breakdown current region (where it has been proposed injection takes place and forms defects or traps in the oxide at the interface and deep in the oxide): First is the possible lowering of the energy barrier at the interface by the charge created by the passage of the fission-fragments; the gate voltage is modified by the shift in flatband voltage due to injected charge (a result of the change in space-charge due to the continuous irradiation), and is associated with the generation of interface states and electron trapping effects seen in the corresponding C-V curve for the device (shown in Figure 177). However, it has already been shown (by KLEIN[245]) that the positive charge in the interfacial region or in the oxide weakens the oxide field in the neighborhood of the interface rather than strengthens it and, therefore, cannot lower the interface barrier. The second explanation, based on the work of SOLOMON and AITKEN[178], suggests that there is an increase in the number of electrons arriving at the interface, and proposes that the surface depletion region increases as a result of electron multiplication effects. However, the recent work of YAMABE and MIURA[266] has shown that this increase is insufficient to cause the anomalous device currents observed in this study.

A new mechanism is, therefore, proposed to explain the anomalous device current of devices under fission-fragment irradiation: the extent of damage in the devices due to (hot) electron injection is shown, effectively, by the change in the flatband voltage. This can be interpreted by considering the damage to the interface due to hot electron injection. According to LAUGHLIN et

al[60], SiH bonds are expected at the Si-SiO_2 interface; such a bond would be broken by hot electron injection resulting in a trivalent silicon atom and a hydrogen ion, the trivalent silicon atom at the silicon interface generally considered to form an interface state[78-85]. Theoretically[60], the trivalent silicon atom could bond with three oxygen atoms at the interface to give rise to a state which is between the Si and SiO_2 conduction band minimums. Electron injection, in particular hot electron injection, would permit electrons to tunnel into the conduction band of the SiO_2 through these intermediate levels as shown in Figure 183, which explains the anomalously high currents during irradiation. It would also explain why such evidence of anomalous injection is not evident in virgin MOSCs and devices post-irradiation since the existence of trivalent silicon atoms would in one case not exist and the other case have recombined with any available hydrogen atom as soon as the oxide field were decreased. The general effect of the radiation, therefore, is to increase the conductivity of the MOSCs whilst under fission-fragment irradiation; no evidence was found to suggest that any other of the radiation fields tested produced this effect and it has been concluded that these radiations are incapable of producing sufficient intermediary states to enable such increased (hot) electron injection.

One might expect that such intermediary states would not exist without their continuous generation by the effects of fission-fragment radiation on the MOSCs; no evidence of increased device current was seen for devices which had been fission-fragment irradiated and were subsequently examined. This expectation was borne out in the experimental evidence and suggests that the intermediate states are unstable and the trivalent silicon/oxygen bond dissolves when either the field is reduced sufficiently to allow trivalent silicon-hydrogen$^+$ recombination, or many more of these bonds are broken than are generated by the hot electron injection when the fission-fragment radiation field is removed.

An important finding of this investigation is, assuming the discussion presented in sections **7.3.1** to **7.3.4** is wholly applicable to radiation induced dielectric breakdown and the extension to the KLEIN[245] model is valid, that a new model is needed to explain several of the effects seen which are not described or explained by the KLEIN[245] model: KLEIN approaches the problem from the premise that high fields induce breakdown and the radiation affects the breakdown strength of the dielectric regardless of the changes in carrier injection and that therefore breakdown is primarily field

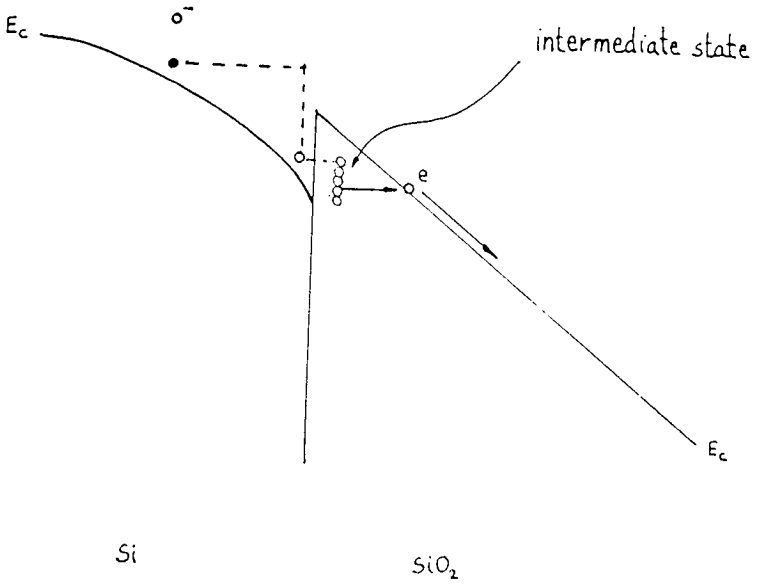

Figure 183: Electron tunnelling to a proposed intermediate state in the Si-SiO_2 band structure.

dependent. However, in the light of the new evidence it is proposed that radiation induced dielectric breakdown is the result of anomalous carrier injection from either electrode (specifically from surface asperities, inherent surface damage and carrier-generated damage) which is dramatically enhanced by very heavily ionizing radiation by electron-hole pair generation in the vicinity of these regions of (already) high carrier injection, leading to the generation of channels of defects (energy states and traps) around the path of the radiation and eventual breakdown of the channel. This would only require the minimum field for carrier injection (which may vary from device to device) to begin the avalanche process ; the breakdown process after initiation is believed to be identical to that for intrinsic (and defect-related) breakdown (discussed in section **7.3.1** to **7.3.4**). This would explain the observation that each fission-fragment, regardless of its stopping power in SiO_2, appears to induce a single breakdown.

It has already been shown that a minimum value of stopping power is required to induce breakdown; by the KLEIN[245] model all fission-fragments of this minimum energy induce breakdown if the field enhancement is great enough, the field enhancement being over the entire active area of the MOSC. Thus, by the KLEIN model, fission-fragments with a very large residual energy might be able to produce more than one breakdown per fragment by field enhancement at surface defects and sites in the neighborhood of the fission-fragment track through the SiO_2. This would contradict the experimental evidence presented, and seems unlikely considering the distribution of breakdown sites and energy distribution of the fission-fragment source used (where there are an approximately equal number of light and heavy fission-fragments).

Thus, radiation induced breakdown is a two-stage process: the first is the creation of structural changes in the dielectric layer due to anomalous charge injection which is locally greatly enhanced by the fission-fragment; this enhanced carrier-injection eventually leads to a low resistance path connecting the two electrodes. The second process is the instantaneous discharge of the MOSC via this low resistance path, as is the case for intrinsic dielectric breakdown. The energy released at this discharge site leads to a permanent leaking of the dielectric (SiO_2) and a breakdown crater, with an approximately one-to-one correspondence between the number of breakdowns and the number of fission-fragments crossing the MOSC in the same time period. There is a minimum residual energy of fission-fragment which can initiate breakdown. The energy and ionization

associated with the passage of a fission-fragment has been (previously) shown to be insufficient to initiate thermal breakdown.

A modification to the KLEIN[245] model has been made which eliminates previous contradictions in the various magnitudes of field and charge density necessary to initiate breakdown when radiation induced dielectric breakdown is described as being primarily field dependent; however, recent experimental evidence suggests that radiation induced dielectric breakdown is primarily dependent on the charge injection processes occurring in the MOSC under irradiation.

Therefore, it has been proposed that a new model to account for this primary dependence on injection current rather than field is needed; such a model would require further investigation and quantitative analysis of the charge injection properties of virgin Al-SiO_2-Si MOSCs and devices under irradiation.

7.5 General Observations on Radiation Effects in Al-SiO_2-Si MOSCs

The two primary effects of radiation on the Al-SiO_2-Si MOSCs tested in this investigation are positive oxide buildup and interface trap generation. A series of simple mechanisms for these effects are presented in this section of the discussion, which considers each of these effects in terms of the general effects of all the radiations tested.

The radiation sensitivity of the MOSCs has been assumed to be proportional to the magnitude of the residual trapped charge in the devices, since it is this effect which produced the greatest long term effect in irradiated MOSCs ; this concept, and that of a damage equivalence of various radiation fields, is discussed for radiation en masse and for the individual radiation fields.

7.5.1 Positive Oxide Charge Buildup

Radiation-induced positive oxide charge in Al-SiO_2-Si MOSCs is widely accepted to be caused by hole trapping in the oxide layer, where holes are generated by irradiation[186-189]. It is proposed that the flatband voltage shift following trapped holes can be written as a function of the oxide charge due to the generated hole density and the distance from the silicon substrate that these

holes are generated, thus

$$\Delta V_{fb} = q / C_{ox} \int_{0}^{T'} (T'-x)\, p(x)\, dx \qquad -132$$

where $$p(x) = N_T(x) [1-e^{(-s N_h(x))}] \qquad -133$$

where C_{ox} is the permittivity of the SiO_2, T' is the SiO_2 thickness, x is the distance from the silicon substrate, p(x) is the oxide charge density generated by the irradiation, $N_T(x)$ is the intrinsic hole trap distribution in the oxides, s is the hole capture cross-section, and $N_h(x)$ is the generated hole density, which is a function of the applied oxide field and total radiation dose.

High-energy radiation, such as gamma-rays, produces electron-hole pairs which are spread uniformly through the oxide layer. When the applied gate bias is near the initial value of the flatband voltage, V_{fb}, most of the electron hole pairs generated in the oxide would recombine, and a small fraction of the holes generated can be trapped at the same place without drifting away, because effectively no field is applied across the oxide. Therefore, the observed dependence of the shift in V_{fb} on the oxide thickness is the same as the dependence of the intrinsic hole trap density distribution in the oxide on the oxide thickness. If the hole trap distribution in the oxides is independent of the oxide thickness for a constant dose, the trapped hole distribution in the oxide generated by the irradiation is also independent of the oxide thickness for a constant radiation dose, which leads to a near linear dependence of the V_{fb} shift.

At a positive oxide field, the generated electrons drift more rapidly toward the gate electrode, whereas holes drift more slowly toward the silicon substrate[186]. Consequently, a large number of generated holes contribute to hole trapping in the oxides without recombination. The fraction of generated holes escaping recombination appears to be proportional to the field strength. At fields above $3MVcm^{-1}$, recombination appears to be suppressed and nearly all the generated holes are transported to the interface; therefore, the shift in V_{fb} is expected to increase with increasing field, as has been reported in the results from this investigation.

At very high fields (those approaching breakdown) of more than $8MVcm^{-1}$, negative charging in the

SiO_2 has been observed. This is attributed to the compensation of the positive oxide charge by electron trapping in sites with trapped holes, where electrons are injected from the silicon substrate by Fowler-Nordheim tunneling, which is enhanced by irradiation, because of electron-hole pair generation in the silicon substrate and at the Si-SiO_2 interface.

At a negative oxide field, most of the holes generated drift toward the gate electrode, and only a fraction of the holes generated near the Si-SiO_2 interface become trapped there, which leads to a smaller shift in V_{fb}, compared to that for a positive oxide field. Therefore the ratio of the shift in flatband voltage for negative and positive gate bias ($\Delta V_{fb-} / \Delta V_{fb+}$) depends on the hole trap density distribution in the oxides; the devices tested appear to have a density of hole traps with a large charge centroid, that is, hole traps extend deeply into the oxide from the Si-SiO_2 interface to the gate electrode. This may have arisen from nitrogen (or other impurity) incorporated in the oxides during growth, since hole traps are perhaps related to non-stoichiometry of the SiO_2.

This is the simple explanation derived to explain the results taken from the shift in C-V characteristic of the MOSCs due to irradiation, suggesting the generation of a positive oxide charge in the SiO_2, reported in Chapter 6.

7.5.2 Interface Trap Generation

In this discussion, the effect of interface trap generation in the oxide on the flatband voltage shift has been neglected. This effect can be estimated from the interface trap distribution and the assumption that the interface traps in the upper half of the SiO_2band gap are acceptor-type and those in the lower half are donor-type; the additional shift in V_{fb} caused by interface charging, ΔV_{it}, can be calculated thus

$$\Delta V_{it} = q/c_{ox} \int_{E_I}^{E_F} \Delta D_{it}\, dE \qquad -134$$

where c_{ox} is the oxide capacitance, ΔD_{it} is the change in the density of interface traps due to irradiation (determined from the change in slope of the C-V characteristic at the flatband condition), E_F is the Fermi level at the flatband condition, and E_i is the midgap energy. ΔV_{it} is estimated from the C-V characteristics presented in Chapter 6 to be at most approximately 12% of ΔV_{fb} for the greatest radiation dose and positive bias conditions; therefore, this interface charging is negligible,compared with the effect ΔV_{fb}, though not insignificant.

It has been proposed (in section7.3) that Si- H and Si- OH bond breaking at the Si-SiO_2 interface, which is known to occur in irradiated devices[227,228], is enhanced by electron or hole transfer to the interface. Such bond-breaking can produce trivalent silicon centres (≡Si·) at the interface, giving rise to a localised energy level in the forbidden gap (that is, the interface trap level). This reaction can be expressed as:

$$\equiv Si - H + \text{radiation} \rightarrow \equiv Si\cdot + H^+ \quad \text{(drift away)} \qquad -135$$

$$\equiv Si - OH + \text{radiation} \rightarrow \equiv Si\cdot + OH^- \quad \text{(drift away)} \qquad -136$$

Interface trap generation appeared to be larger for devices under positive gate bias than those under negative gate bias during irradiation, which would suggest that hole transport to the Si-SiO_2 interface is the most likely mechanism for the generation of interface traps. This in turn suggests that hole capturing at the interface is the dominant mechanism for breaking Si- OH bonds, rather than the electron impact process, and also that Si- OH bond breakage is the more probable reaction than Si- H bond breakage, since, according to SAH[226], OH^- ions easily drift away under a positive oxide field.

There is also, however, evidence to suggest that clustering of impurity ions (in particular Na^+ and Cl^-, introduced at the oxide growth stage) at the interface in irradiated MOSCs is responsible for the large interface trap density seen[89,90], and this would seem a more likely mechanism than that proposed above. This effect would explain the change in slope of the C-V curve observed in irradiated devices if one considers the effect of such clusters on the interfacial region: the surface potential is dependent on the bias voltage applied to the MOSC and on the fixed charge

distributions at the Si-SiO_2 and SiO_2-Al interfaces. If there is no trapped charge at the Si-SiO_2 interface and in the oxide, the oxide-semiconductor interface is an equipotential surface. A small, uniformly distributed density of charge due to trapped ions does not alter the equipotential surface other than to shift the C-V curve linearly along the voltage axis due to the small change in the surface potential of the device. If, however, the ions are not uniformly distributed but clustered, the interface is far from an equipotential surface, and regions of different surface potential would be seen. Such an effect would produce regions of varying equipotential in the device which would alter the C-V curve anomalously in the various bias regions (accumulation, depletion and so on) due to a change in the surface potentials, causing an anomalous change in the slope of the C-V curve over a large bias range. It is this effect, combined with the small linear shift in the C-V characteristic due to interface traps (described above) which has been used to calculate the density of interface states in the devices before and after irradiation (by the method described in Chapter **5** and Appendices **4** and **5**).

7.5.3 The Radiation Sensitivity of Al-SiO_2-Si MOSCs

The Al-SiO_2-Si MOSCs all responded to radiation by the shift of their C-V characteristic to more negative gate bias regimes due to the buildup of positive oxide charge in the devices, as discussed in section **7.5.1**. Since, unlike interface traps this effect on the devices did not appear to substantially decay over long time periods, such a shift may be used as a measure of the radiation sensitivity of the devices to various radiation fields. The shift, evaluated from the difference in the virgin device and irradiated device C-V characteristics, has been shown to be near-linear up to total fluences of 10KRad(SiO_2).

It is evident from the flatband-voltage voltage shifts that the radiation sensitivity of the devices follows the ratio

fission-fragments > gamma > alpha > neutrons/recoil-protons > neutrons

and the order of magnitude of these ratios for the oxide charge generation follows the ratio, for

equivalent p-type devices, :

1 : 0.54 : 0.42 : 0.03(6) : 0.01(4)

and for equivalent n-type devices :

1 : 0.75 : 0.58 : 0.03(9) : 0.01(5)

This may be equated to the damage equivalence of the radiations, such that fission-fragment irradiation of $4*10^3$ fission-fragments cm^{-2} produces an effect one hundred times larger than an irradiation of 5.5MeV neutrons to a fluence of 10^8 ncm^{-2}.

The anomalous result that a combined recoil-proton/neutron field should produce such a small change in the trapped charge in the devices may be explained by proposal that, since heavily ionizing particles appear to produce an initial recombination of the electron-hole pairs generated in the oxide and neutron irradiation appears to produce minimal oxide charge generation in the devices, a reduction in the number of holes reaching the SiO_2-Si interface where trapping occurs is expected due to the recoil-protons. The heavily ionizing radiation has reduced its own effect in the devices by enhancing recombination. This would suggest that the effect of the other heavily ionizing radiations has been diminished somewhat, and in fact the optimum sensitivity of the devices to such radiations is not seen.

This, however, is not evident from the devices ability to detect fission-fragment and alpha radiation in a similar fashion (and with similar resolution) to a silicon surface barrier detector; the feasibility of such devices as cheap, easily fabricated alternatives to such detectors is clear.

Since the MOSCs evaluated only displayed radiation induced dielectric breakdown phenomena for fission-fragment irradiation, the feasibility of such devices as radiation detectors using this mode of operation is limited to the detection of very heavily ionizing radiations. However, the invisibility of the devices operated in this mode to the other radiation fields is an advantage for experiments which require a high degree of sensitivity to fission-fragments in mixed fission-fragment / radiation fields.

The smallness of the effects of neutron irradiation on the MOSCs implies that the devices are not feasible as neutron detectors in the neutron energy range tested (0.5MeV to 10MeV), and the initial aim to develop such devices as neutron detectors could not, therefore, be fulfilled.

However, the results presented indicate that neutron irradiation with neutrons in the 0.5MeV to

10MeV energy range do produce a small number of interface states, which is more pronounced in thick devices than thin devices, an effect which may prove useful to workers investigating neutron irradiation effects in more complex MOS systems. The mechanism proposed for this interface state generation is that neutrons, by intermediate reactions with impurity ions at the interface, break Si-OH and Si- H bonds in the interfacial region, causing an excess of OH^- and H^+ ions which are free to drift under the action of the applied electric field. Since the effect was similar for positive, zero, and negative applied bias, the ions produced in this fashion must be produced both close to and throughout the oxide layer, where hole transport could produce such a small magnitude effect under natural drift of the ions to their respective electrodes.

CHAPTER EIGHT.

CONCLUSIONS AND SUGGESTIONS FOR FURTHER WORK

The theory underlying the electrical and physical properties of MOS systems has been presented. This has been applied to the Al-SiO_2-Si MOS capacitor structure, and the most recent experimental evidence giving insight into electrical and physical properties of such devices has been described and discussed with respect to their theorized properties.

In particular, the experimental evidence of the behaviour of Al-SiO_2-Si MOSCs under various conditions of high-field stressing, dielectric breakdown, irradiation and radiation induced dielectric breakdown has been described; the most recent, accepted mechanisms and models of device behaviour in these circumstances have been presented and discussed in the light of the experimental evidence available.

A wide range of experimental evidence has been presented, obtained using a variety of electrical and physical investigatory techniques, which shed new light on several properties of Al-SiO_2-Si MOSCs under the conditions mentioned above. In particular, new evidence of radiation effects in such devices has been presented, and new mechanisms and extensions to the available models for device behaviour under these conditions have been proposed which are consistent with the observations of other workers in the field.

Important modifications to the existing models for device behaviour under high-field stressing, and the effects of radiation on the properties of Al-SiO_2-Si MOSCs irradiated under high-field stressing, have been proposed; these indicate that a new model to describe device behaviour and, in particular, to describe radiation effects on the devices when under these conditions is required.

A brief summary of the conclusions drawn from the discussion of the principal experimental findings presented in the last chapter, and the theoretical considerations underlying these, are also briefly summarised.

Suggestions for a follow-up programme to the present investigation conclude this chapter; these broadly concentrate on the need to understand more fully the charge injection properties of virgin devices, and on the data necessary for the development of the new model to describe the effects of radiation on Al-SiO_2-Si MOSCs under high-field stressing.

8.1 The Principal Experimental Findings and Theoretical Considerations

The simple conclusions which can be drawn from the experimental evidence presented for intrinsic and defect-related dielectric breakdown in the Al-SiO_2-Si MOSCs tested may be summarised thus:

(1). Breakdown appears to be the result of charge injection.

(2). The energy dissipated by the current is, in most cases, not sufficient to cause thermal runaway.

(3). The total amount of injected charge must be an important parameter.

(4). The charge needed for breakdown appears independent of the injection conditions.

(5). The changes induced by charge injection are permanent.

(6). A small injection may induce a positive space charge.

(7). A very large injection induces a negative space charge.

(8). Interface states are generated by this injection and breakdown.

(9). At the moment of breakdown the displacement charge provides the energy that causes the destruction of the MOSC.

(10). At breakdown, part of the MOSC oxide is gasified and a larger part is melted. This results in a crater and pit in the silicon substrate and oxide layer, and the removal of the Al gate electrode in a small portion of the MOSC where breakdown has occurred.

These are wholly applicable to the study of radiation induced dielectric breakdown; it has also been concluded that the similarity between the effects of intrinsic (or defect-related) dielectric breakdown and radiation-induced dielectric breakdown shows that the same underlying mechanism for the breakdown process occurs in both cases, though the breakdown initiation process is different.

Only very high LET radiation (for example, fission-fragment radiation) is capable of inducing breakdown; charge injection from the silicon substrate is enhanced by radiation induced trapping close to the interface and throughout the oxide, which leads to conducting channels formed

through the oxide layer at substantially lower injection currents than those necessary for a similar effect in the intrinsic breakdown case. This qualitatively explains the effective lowering of the breakdown field observed for radiation induced breakdown, and is consistent with the observations reported by other workers in the field.

The accepted model for radiation induced breakdown has been extended by considering the effects of charge generation in the oxide; in the light of the new experimental evidence and this extension to the accepted model, it has been proposed that, in order to explain the results seen in this investigation, that radiation induced dielectric breakdown is primarily charge-injection dependent and not field dependent. Further data on the injection properties of the virgin device are needed, and data on the effects of radiation on the charge injection and physical properties of the devices are the necessary requirements to enable the derivation of the new model.

The effects of radiation en masse on the properties of Al-SiO_2-Si MOSCs are briefly summarised below:

(1). Radiation generates positive oxide charge in the oxide layer of MOSCs.

(2). The magnitude of the positive oxide charge is field, field polarity, radiation type, radiation dose and oxide thickness dependent; the larger the positive field, the thicker the oxide, the greater the dose, the greater the density of the trapped oxide charge.

(3). Radiation generates interface states and traps in MOSCs.

(4). The magnitude of the interface state density is field, radiation type, radiation dose and oxide thickness dependent; the larger the field, the thicker the oxide, the greater the dose, the greater the density of interface states and charge traps.

(5). The sensitivity of the MOSCs to radiation is governed by the radiation type and the thickness of the oxide; the thicker the oxide, the more ionizing the radiation, the more sensitive the MOSC.

Radiation generates positive oxide charge in biased and unbiased Al-SiO_2-Si MOSCs.The mechanism proposed to explain this effect offers a more qualitative description of the underlying processes than other mechanisms, and is more consistent with the data presented and the observations of other workers.

A mechanism proposed for the generation of interface traps by irradiation, based on bond-breaking at the Si-SiO_2 interface, is believed to be an adequate description of the underlying mechanism for the generation of radiation induced interface states and appears to be consistent with the results presented by other workers.

A description of the sensitivity of the devices to various radiations has led to the conclusion that the devices are debilitated by radiation to too great an extent and would not make good radiation detectors for dosimetry; however, because of the unusual properties exhibited by the MOSCs in their detection similarity to silicon surface barrier detectors, and their invisibility to any other than alpha and fission-fragment radiation fields, the devices are thought to have applications as fission-research tools.

8.2 Suggestions for Future Investigations

A follow-up programme to the present investigation would broadly concentrate on three main aspects: Firstly, it is necessary to investigate the charge injection characteristics of virgin Al-SiO_2-Si MOSCs. Immediate progress could be made by more information about the nature, magnitude, and mechanisms underlying such charge injection; here, the first interesting and very useful experiment would be to characterise the effects of a known injected charge on the C-V and I-V curves for various thickness and substrate type devices.

This would provide the basis for a second investigation into the nature of the charge injection occurring in the pre-breakdown stage of dielectric breakdown under high field stressing; it is envisaged that a study of charge injection with time, oxide thickness, gate electrode area, and breakdown field would be used to develop a new, quantitative model for intrinsic and defect-related

dielectric breakdown.

With new understanding of the effects of charge injection on the electrical characteristics of the MOSCs, an important objective would be a thorough study of the chemical and physical nature of the bulk oxide and the Si-SiO_2 interface using sensitive analysis techniques (such as secondary ion mass spectroscopy) to provide further (microscopic) evidence to develop a qualitative model of the effects of injection on the physical nature of the devices, and a mechanism describing the mode(s) of injection and locating sites where injection takes place.

A third investigation would be to study the effects of radiations of various energies, dose rates, and total doses on the injection characteristics already known for the MOSCs. The effect of known magnitudes of charge injection on the breakdown characteristics of devices under irradiation would provide useful data to compare with the effects of known magnitudes of charge injection on virgin, unirradiated devices. This would provide clear evidence to incorporate into the proposed new model for dielectric breakdown to formulate a theoretical approach to radiation induced dielectric breakdown, based upon charge injection rather than high field induced breakdown.

However, before embarking on these investigations, it would be highly desirable to develop the high-field breakdown apparatus to incorporate a microcomputer data aquisition system linked with sensitive I-V apparatus to measure the oxide field, magnitude of charge injection, time-to-breakdown, and number of breakdowns occurring in the device under test. One way to accomplish this would be to extend the apparatus used by WOLTERS and VERWEY[121] to incorporate a timing system and to add the Hewlett Packard I-V aquisition system used in this study; this would also provide the statistical information necessary to distinguish between the initial defect-related breakdowns and the intrinsic breakdowns.

To complement such a future experimental programme, some theoretical work would also be necessary. Here, a particularly valuable study would be of the interaction of charge carriers with the band structure of the SiO_2 and a simulation of the tunneling effects of (hot) electrons from the silicon substrate to traps of various energies in the silicon dioxide. Following this, a further simulation of the effect of a large deposition of charge into the oxide by irradiation, and the subsequent generation of traps which are filled and emptied by the effect of an applied field; the

principal value of this would be verification of the enhancement of charge injection at the Si-SiO_2 interface by the radiation, which it is proposed is seen in practice.

For these studies it would be assumed that the charge does not alter its characteristic when emitted to the oxide, electron-phonon interactions are negligible (thermal effects have already been shown to be minimal) and that the injected electrons surmount the surface barrier according to Fowler-Nordheim tunnelling theory.

Finally, it should be observed that this theoretical work would not only be meaningful to the present type of study, but also to those working on development of the microscopic theory of operation of all devices based on the Si-SiO_2 system.

APPENDICES.

1. Hameg Oscilloscope Data Acquisition Program for a BBC 'Master' Microcomputer.

```
 10HIMEM=&2500:K=1
 20 *LOAD BIN??%
 30 MODE0
 40 VDU24,0;100;1200;1000;
 50 VDU28,0,31,79,29
 60 CURR=0:CURY=0:FLAG=0:CHANNEL=1:TEM=0
 70 CLS:PRINT"T.O.F. SPECTROMETER DATA SYSTEM":FORZZ=1 TO3000:NEXT
 80 PRINT"N.B. ONLY FIRST 1024 POINTS AQUIRED"
 90 INPUT"FLASH FILTER SCOPE TIMEBASE SETTING (uS)";TB:TB=TB*10
100 P%=&A900
110 [OPT 3
120 .PROGbuf
130 base%=&FB00
140 init%=base%+0
150 write%=base%+3
160 datr%=base%+6
170 outm%=base%+9
180 .tmp% base%+11
190 sampel%=base%+15
200 ch cmd%=base%+16
210 am cmd%=base%+21
220
230 .g11%=&01
240 .k%=&04
250 .g21%=&08
260
270 .CH1:
280 dc1%=&14
```

```
300eoschr$=CHR$(13)
310PROCinitialise(0)
320CLS
330PROCpromt
340 PROCopt
350 GOTO340
360 INPUT"Filename for loading data from disc"F$
370 CURX=1:CURY=12:FLAG=0:PROCpromt
380PROCload(F$,"2500")
390 GOTO340
400 END
410END
420DEFPROCwritestring(primary%,secondary%,message$,termchr$)
430CALLwrstr%,primary%,secondary%,message$,termchr$
440ENDPROC
450
460DEFFNreadstring(primary%,secondary%,termchr$)
470LOCAL  message$
480message$=STRING$(255," ")
490CALLrdstr%,primary%,secondary%,message$,termchr$
500=message$
510
520DEFPROCoutputmemory(primary%,secondary%,start%,nobyte%)
530CALL outm%,primary%,secondary%,start%,nobyte%
540ENDPROC
550
560DEFPROCinputmemory(primary%,secondary%,start%,nobyte%)
570CALL inm%,primary%,secondary%,start%,nobyte%
580ENDPROC
590
600DEFPROCinitialise(bbcaddress%)
610CALLinit%,bbcaddress%
620ENDPROC
630
640DEFFNserialpoll(primary%,secondary%)
650LOCALstatus%
```

```
660status%=0
670CALL serpoll%,primary%,secondary%,status%
680=status%
690
700DEFPROCaddressedcommand(primary%,secondary%,command%)
710CALLadrcmd%,primary%,secondary%,command%
720ENDPROC
730
740DEFPROCuniversalcommand(command%)
750CALLunicmd%,command%
760ENDPROC
770
780DEFPROCsave(start$,finish$)
790INPUT"Enter filename for saving data from memory "F$
800OSCLI ("SAVE "+F$+" "+start$+" "+finish$)
810ENDPROC
820
830DEFPROCload(fname$,start$)
840 B$=fname$+" "+start$
850 OSCLI ("LOAD "+fname$+" "+start$)
860ENDPROC
870
890DEFPROCopt
890A$=GET$
900IF A$="P"THEN PROCplot ELSE IF A$="P"THEN PROCplot ELSE IF A$="C"THENPROCcl
g ELSE IF A$="S" THENPROCsave("2500","2701")ELSE IF A$="L" GOTO360 ELSE IF A$="T
"THENPROCL ELSE IF A$="H" THEN PROCd ELSE IF A$="R" THEN PROCr
910IFA$="D" THENPROCdiffplot ELSE IF A$="Z" THEN PROCzero ELSEIF ASC(A$)=136 T
HENPROCcurleft ELSE IF ASC(A$)=137 THENPROCcurright ELSE IF A$="E" THEN PROCener
gy ELSE IF A$="F" THENPROCfinn ELSE IF A$="K"THEN PROCreplot ELSE GOTO890
920ENDPROC
930DEFPROCplot
940START=&2500
950 GCOL3,7
960FLAG=0
```

```
 970 MOVE0,550
 980FOR I=1 TO1024 STEP R
 990X=I*1200/1024-1
1000Y=?(START+I)
1010Y=1000-Y*900/256
1020PLOT13,X,Y
1030NEXT
1040PROCbox:PROCbox
1050ENDPROC
1060DEFPROCbox
1070GCOL0,7
1080MOVE0,100:DRAW0,1000:DRAW1200,1000:DRAW1200,100:DRAW0,100:MOVE1200,550:DRAW
0,550
1090GCOL3,7
1100 ENDPROC
1110 DEFPROCclg
1120 CURX=2:CURY=2:CHANNEL=2
1130 CLG:PROCbox
1135PROCpromt
1140 ENDPROC
1150DEFPROCd
1160 CALL &900
1170ENDPROC
1180 DEFPROCr
1190INPUT"R= N  (Plot every Nth point)",R
1200 ENDPROC
1210 DEFPROCt
1220PROCinitialise(0):PROCuniversalcommand(11a%):PROCinputmemory(6,10,&2500,102
4):PROCinitialise(0)
1230ENDPROC
1240DEFPROCdifplot
1250 IF FLAG=1 THEN CURX=LOWLIM
1260 GCOL3,7
1270 MOVE0,550
1280IF FLAG=1 THEN START=&2500+(LOWLIM*1024/1200) ELSE START=&2500
1290 IF FLAG=1 THEN FIN=(HILIM-LOWLIM)*1024/1200 ELSE FIN=1024
```

```
1300FOR I=1 TO FIN
1310 IF FLAG=1 THEN X=I*(1024/1200)*4*(85.3/100) ELSEX=I*1000/1024-1
1320Y=?(START+I)
1330Y1=?(START+(I-5))
1340Y=Y-Y1
1350Y=550-Y*900/128
1360PLOT13,X,Y
1370NEXT
1380PROCbox:PROCbox
1390CURX=1
1400ENDPROC
1410DEFPROCcurright
1420 IF CURX>1277 THEN GOTO 1510
1430IFCURX=1THEN GOTO1470
1440CHANNEL=CHANNEL+1
1450 MOVECURX,CURY
1460 PLOT6,CURX,1023
1470 CURX=CURX+1
1480 MOVE CURX,CURY
1490DRAW CURX,1023
1500 PROCdispcount
1510 ENDPROC
1520DEFPROCcurleft
1530IF CURX<1 THENGOTO1610
1540CHANNEL=CHANNEL-1
1550 MOVECURX,CURY
1560 PLOT6,CURX,1023
1570 CURX=CURX-1
1580 MOVECURX,CURY
1590 DRAW CURX,1023
1600PROCdispcount
1610ENDPROC
1620DEFPROCreplot
1630PROCclg
1640PROCbox :PROCbox
1650START=&2500+(LOWLIM*(1024/1200))
```

```
1660 GCOL3,7
1670 MOVE0,550
1680FOR I=1 TO(HILIM-LOWLIM)*(1024/1200)STEPR
1690X=I*(1024/1200)*4*(85.3/100)
1700Y=?(START+I)
1710Y=1000-Y*900/256
1720PLOT13,X,Y
1730NEXT
1740PROCbox:PROCbox
1750 FLAG=1
1760ENDPROC
1770DEFPROCenergy
1780 IF FLAG<1THEN PRINT:PRINT"SORRY NO CAN DO":FORWT=1TO3000:NEXT:PROCpromt:GO
TO1950
1790 GCOL3,7
1800PROCclg
1810 MOVE1200,550
1815FLAG2=0
1820START=&2500+(LOWLIM*1024/1200)
1830FIN=(HILIM-LOWLIM)*(1024/1200)
1840FOR I=1 TO FIN STEP 1
1850 ENERGY=(TB/1024)
1851ENERGY=ENERGY*I
1855REM PRINT"TIME";ENERGY:FORZZZ=1TO1000:NEXT
1860 ENERGY=ENERGY^2 :ENERGY=1/ENERGY:ENERGY=ENERGY*166.7
1863REM PRINT"ENERGY";ENERGY:FORZZZ=1TO1000:NEXT
1870 X=ENERGY
1880Y=?(START+I):Y1=?(START+(I-5)):Y=Y-Y1
1885Y=ABS(Y):Y=-1*Y
1890Y=550-Y*900/128
1895X=X*100
1900 IFX>1200GOTO1920
1905IFFLAG2=0THENPRINT"HIGH ENERGY ";X/100;" KEV"
1906FLAG2=1
1910PLOT13,X,Y
```

```
50 YCAL=X-Y
170PRINT" CU ENERGY ";X/100;" KEV"
190PROCbox
195ENDPROC
196DEFPROCbox
200HILIN=CURX
210THIN=CURX
220ENDPROC
230DEFPROCdisplay
240MOVE0,0
250IF CHANNEL>1THENMOVE1000,140:DRAWCOLO,0 :PRINT CHANNEL -1
260IF CHANNEL>1THENMOVE1000,140:DRAWCOLO,0 :PRINT CHANNEL +1
270DRAWCOLO,7
280MOVE1000,140
290PRINTCHANNEL
300MOVE975,140:PRINT "CHANNEL"
310DRAWCOL3,7
320MOVE0,4
330ENDPROC
340PROCFPRUDprocess
350OPENIN"T"+STR$1
360PRINT"D)ISP      C)LEAR      M)ES      S)AVE      L)OAD      I)NPUT      H)ard
"
370PRINT"D)ISP      E)NERGY      F)INISH      R)UNCH      Z)ERO      <- -> CURSOR "
380ENDPROC
```

2. Computer Controlled I-V Data Acquisition Program for a Hewlett Packard Model 4140B PicoAmmeter and Hewlett Packard Model 9836 Microcomputer.

```
10    ! PROGRAM "IV"
20    !
30    ! THIS PROGRAM MEASURES I-V CHARACTERISTICS USING THE HP4140B ...
40    ! THE RESULTS ARE PLACED IN A ONE-DIMENSIONAL ARRAY WHICH IS STORED ...
50    ! ON A FILE NAMED BY THE USER
60    !
70    ! THE ORDER OF THE VARIABLES IS   I,V
80    !
90    ! A SCATTER PLOT OF I AGAINST V IS PROVIDED FOR CONFIRMATION ...
100   ! BEFORE FILING IS CARRIED OUT
110   !
120   !
130   !
140   DIM C(1:100)
150   DIM Line$[200]
160   DIM Name$[40]
170   DIM Msg$[150]
180   DIM Blank$[80]
190   INTEGER I,V,Nobs,Ndata,Nlin,Rlen
200   Lp$="LP"
210   Lpmode$="P"
220   Lps$="S"
230   R$="R"
240   LP$="L"
250   Test=99999 99999
260   CLEAR 718
270   PRINT Blank$
280   PRINT "ENTER START,STOP, AND STEP FOR VOLTAGE"
290   PRINT "NOTE- CHECK VOLTAGE POLARITY"
300   ENTER 2;Vbstart,Vbstop,Vbstep
```

```
310   Vb=LOG(Vbstop/Vbstart)/(Nobs-1)
320   Pass=INT(Bstep+.1)+1
330   ALLOCATE A(1:2*Nobs+1)
340   Pow1$=USING$&VAL$(Vbstart)
350   Pwb$=USING$&VAL$(Vb)
360   Pwe$=USING$&VAL$(Vbstop)
370   OUTPUT 710;"F2 PA1 I2 A3 B2 L3 M1"
380   OUTPUT 710;Pow1$,Pwb$,Pwb$,Pwe$,"PI0,1,PD0,1"
390   OUTPUT 710;"SI"
400   PRINT Blank$
410   FOR n=1 TO Nobs
420   ENTER 710;Ps,P,
430   A(2*(n-1)+1)=P,
440   A(2*(n-1)+2)=Ps
450   PRINT USING "SD,4X,2(SD.3DE,3X)";N,P1,Ps
460   NEXT N
470   A(2*Nobs+1)=Test
480   Xmax=-1.0E+308
490   Xmin=+1.0E+308
500   Ymax=-1.0E+308
510   Ymin=+1.0E+308
520   FOR J=1 TO Nobs
530   IF A(2*(J-1)+2)>Xmax THEN Xmax=A(2*(J-1)+2)
540   IF A(2*(J-1)+2)<Xmin THEN Xmin=A(2*(J-1)+2)
550   IF A(2*(J-1)+1)>Ymax THEN Ymax=A(2*(J-1)+1)
560   IF A(2*(J-1)+1)<Ymin THEN Ymin=A(2*(J-1)+1)
570   NEXT J
580   Xmax$="Xmax="
590   Xmin$="Xmin="
600   Ymax$="Ymax="
610   Ymin$="Ymin="
620   PRINT Blank$
630   PRINT USING "5A,X,E9.3DE,5X";Xmax$,Xmax,Xmin$,Xmin
640   PRINT USING "5A,X,E9.3DE,5X",Ymax$,Ymax,Ymin$,Ymin
650   END
660   SUBPROGRAM DM
```

```
570  VIEWPORT 10,114,22,96
600  Xscale=96.1/(Xmax-Xmin)
690  Yscale=72.0/(Ymax-Ymin)
700  WINDOW Xmin*Xscale,Xmax*Xscale,Ymin*Yscale,Ymax*Yscale
710  FRAME
720  CLIP OFF
730  Ds=""
740  FOR J=1 TO Nobs
750  X=A(2*(J-1)+2)*Xscale
760  Y=A(2*(J-1)+1)*Yscale
770  MOVE X-Ds,Y+Ds
780  DRAW X+Ds,Y-Ds
790  MOVE X-Ds,Y-Ds
800  DRAW X+Ds,Y+Ds
810  NEXT J
820  C(1)=2              ! NUMBER OF VARIABLES
830  C(2)=Nobs           ! NUMBER OF OBSERVATIONS
840  C(3)=25.0           ! TEMPERATURE
850  Title$=Test$
860  I=0
870  J=J+1
880  IF C(J)<>0 THEN 870
890  Ncats=J-1
900  ALLOCATE D(1,Ncats)
910  FOR J=1 TO Ncats
920  D(1,J)=C(J)
930  NEXT J
940  PRINT Blanks
950  PRINT "DO YOU WANT STORAGE ON F-HAND OR L-HAND SIDE ? ";
960  INPUT Lorf$
970  IF Lorf$="F" THEN Disc$=Vol$(0)
980  IF Lorf$="L" THEN Disc$="VOL1:"
990  Name$=" DIFFUSN_"&Lorf$&"."&Disc$
1000 Sofs="EOF"
1010 PRINT Blanks
```

```
1020 PRINT "ENTER FILE NAME"
1030 PRINT Blank$
1040 ENTER 2,Name$
1050 J=0
1060 J=J+1
1070 PRINT "ENTER FILE DESCRIPTION LINE"
1080 ENTER 2,Line$(J)
1090 IF Line$(J)(1,3)<>End$ THEN GOTO 1060
1100 N=J-1
1110 ALLOCATE Line$(1:N+1)[80]
1120 FOR J=1 TO N+1
1130 Line$(J)=Line$(J)
1140 NEXT J
1150 !Name$=Name$&Ampus$&".Data":CREATE Name$(1:80),1
1160 !PRINT #1:Name$&Ampus$,1,Rlen
1170 !POSITION #Path TO Name$&Ampus$
1180 !OUTPUT #Path,N,A(*),B(*),Line$(*)
1190 PRINT Blank$
1200 PRINT "DONE - FINISHED"
1210 END
```

3. Computer Controlled C-V Data Acquisition Program for a Hewlett Packard Model 4275A LCR Meter and Hewlett Packard Model 9836 Microcomputer.

```
10    ! PROGRAM "CV"
20    !
30    ! THIS PROGRAM MEASURES C-V CHARACTERISTICS USING THE 4275A LCR METER
40    ! THE RESULTS ARE PLACED IN A ONE-DIMENSIONAL ARRAY WHICH IS STORED
50    ! ON A FILE NAMED BY THE USER
60    !
70    ! THE ORDER OF THE VARIABLES IS:  CAP,R OR G,VBIAS
80    !
90    ! A SCATTER PLOT OF CAP AGAINST VBIAS IS PROVIDED FOR INSPECTION
100   ! BEFORE FILING IS CARRIED OUT
110   !
120   !
130   !
131   CLEAR 717
140   DIM C(1:100)
150   DIM L$(1:20)[80]
160   DIM Name$[10]
170   Dim Msus$[15]
180   INTEGER J,Nb,Ndata,Nlit,Rlen
190   Test=-99999.99999
191   PRINT "SERIES OR PARALLEL REPRESENTATION?   -   ANS C2 OR C3"
192   ENTER 2;Cr$
193   PRINT
194   PRINT "MEASUREMENT FREQUENCY?   -   ANS F1$ TO F20"
195   PRINT "NOTE: 1MHz IS F17"
196   ENTER 2;Fr$
200   OUTPUT 717;"A2 B3"&Cr$&Fr$&"M3 L3$ H0 T3"
201   WAIT .5
205   PRINT
230   PRINT "ENTER START,STOP, AND STEP FOR BIAS VOLTAGE"
```

```
230   PRINT "NOTE: CHECK VOLTAGE POLARITY"
240   PRINT
250   ENTER 2,Vbstart,Vbstop,Vbstep
260   Psteps=ABS((Vbstop-Vbstart)/Vbstep)
270   Nb=INT(Psteps+.1)+1
280   ALLOCATE A(1:3*Nb+1)
290   Vb=Vbstart-Vbstep
300   FOR J=1 TO Nb
310   Vb=Vb+Vbstep
320   Vbias$=VAL$(Vb)
330   OUTPUT 717,"BI"&Vbias$&"E00V"
340   WAIT .1
350   OUTPUT 717;"E"
360   ENTER 717,Cap,Rq
370   PRINT USING "SD.DDDE,XXX";Cap,Rq,Vb
380   A(3*(J-1)+1)=Cap
390   A(3*(J-1)+2)=Rq
400   A(3*(J-1)+3)=Vb
410   WAIT .1
420   NEXT J
430   A(3*Nb+1)=Test
440   Xmax=-1.0E+308
450   Xmin=+1.0E+308
460   Ymax=-1.0E+308
470   Ymin=+1.0E+308
480   FOR J=1 TO Nb
490   IF A(3*(J-1)+3)>Xmax THEN Xmax=A(3*(J-1)+3)
500   IF A(3*(J-1)+3)<Xmin THEN Xmin=A(3*(J-1)+3)
510   IF A(3*(J-1)+1)>Ymax THEN Ymax=A(3*(J-1)+1)
520   IF A(3*(J-1)+1)<Ymin THEN Ymin=A(3*(J-1)+1)
530   NEXT J
540   Capmax=Ymax
550   Capmin=Ymin
560   Xmax$="XMAX="
570   Xmin$="XMIN="
```

```
580   Xmax$="XMAX="
590   Xmin$="XMIN="
591   PRINT
600   PRINT USING "5A,X,SD.3DE,5X";Xmax$,Xmax,Xmin$,Xmin
610   PRINT USING "5A,X,SD.3DE,5X";Ymax$,Ymax,Ymin$,Ymin
620   GINIT
630   GRAPHICS ON
640   VIEWPORT 18.114,22,94
650   Xscale=96.0/(Xmax-Xmin)
660   Yscale=72.0/(Ymax-Ymin)
670   WINDOW Xmin*Xscale,Xmax*Xscale,Ymin*Yscale,Ymax*Yscale
680   FRAME
690   CLIP OFF
700   Ds=.5
710   FOR J=1 TO Nb
720   X=A(3*(J-1)+3)*Xscale
730   Y=A(3*(J-1)+1)*Yscale
740   MOVE X-Ds,Y+Ds
750   DRAW X+Ds,Y-Ds
760   MOVE X+Ds,Y+Ds
770   DRAW X-Ds,Y-Ds
780   NEXT J
790   C(1)=3              ! NUMBER OF VARIABLES
800   C(2)=Nb             ! NUMBER OF OBSERVATIONS
810   C(3)=Vbstart
820   C(4)=Vbstop
830   C(5)=Vbstep
840   C(6)=Capmax
850   C(7)=Capmin
860   C(8)=25.0           ! TEMPERATURE
870   C(9)=Test
880   J=0
890   J=J+1
900   IF C(J)<>Test THEN GOTO 890
910   Ndata=J
920   ALLOCATE D(1:Ndata)
```

```
930  FOR J=1 TO Ndata
940  D(J)=C(J)
950  NEXT J
960  PRINT
970  PRINT "DO YOU WANT STORAGE ON RH OR LH DISC?   -   ANS 0 OR 1"
971  PRINT "TYPE  T  TO TERMINATE"
980  ENTER 2;Disc$
981  IF Disc$="T" THEN GOTO 1190
990  Msus$=":INTERNAL,4,"&Disc$
1000 Eof$="EOF"
1010 PRINT
1020 PRINT "ENTER FILE NAME"
1021 PRINT
1030 ENTER 2;Name$
1040 J=0
1050 J=J+1
1060 PRINT "ENTER FILE DESCRIPTION LINE"
1070 ENTER 2;L$(J)
1080 IF L$(J)[1,3]<>Eof$ THEN GOTO 1050
1090 Nlit=J
1100 ALLOCATE Lit$(1:Nlit)[80]
1110 FOR J=1 TO Nlit
1120 Lit$(J)=L$(J)
1130 NEXT J
1140 Rlen=8*(3*Nb+1)+8*Ndata+(80+4)*Nlit
1150 CREATE BDAT Name$&Msus$,1,Rlen
1160 ASSIGN @Path TO Name$&Msus$
1170 OUTPUT @Path;A(*),D(*),Lit$(*)
1180 PRINT
1181 CLEAR 717
1190 PRINT "JOB FINISHED"
1200 END
```

4. Theoretical Analysis to Determine U_F and D_{it} from High-Frequency C-V Curves for MOS Structures.

The semiconductor capacitance, C_s, in the depletion region for the Si-SiO_2 system is described by LINDNER'S formula[16], thus

$$C_s = C_{s,fb} / \sqrt{2}\,(|U_s| - 1) \qquad -1$$

where $C_{s,fb}$ is the semiconductor capacitance at the flat band condition, and $U_s = q\varnothing_s / kT$ the normalised surface potential.The total capacitance, C, of the MOS system (neglecting the interface trap capacitance) can be expressed by

$$C / C_i = [1 + C_i / C_s]^{-1} \qquad -2$$

where C_i is the insulator capacitance.

The high frequency capacitance of the semiconductor under strong inversion conditions is described by BERMAN and KERR'S formula [16], with an error smaller than 0.02%, thus

$$C_{smin} = \frac{C_{s,fb}}{\sqrt{2}\ \sqrt{2\,|U_F| - 1 + \ln 1.15\,(|U_F| - 1)}} \qquad -3$$

where $|U_F| = \ln [N / n_i]$ is the normalised Fermi potential, $\varnothing_F$.

This formula takes the inversion charge re-distribution effect into account, and its practical approximation has been proposed[256] (with an error smaller than 0.3%) as,

$$C_{smin} = C_{s,fb} / (2.06 \sqrt{|U_F|}) \qquad -4$$

Combining Equations *1*,*2* and *4* one obtains a relationship between the normalised total capacitance and the normalised surface potential which is valid in the range $5 < |U_s| < (2\,|U_F| - 3)$ with an error smaller than 0.5%, thus

$$C / C_i = \frac{1}{\frac{\sqrt{2}\ \sqrt{|U_s| - 1}}{2.06 \sqrt{|U_F|}} \left(\frac{C_i}{C_{min}} - 1\right) + 1} \qquad -5$$

where C_{min} is the high frequency capacitance of the MOS system under strong inversion conditions.

Hence, for the given values of surface potential, one sees that

$$|U_{s1}| = 1 + |U_F| / 2 \text{ and } |U_{s2}| = 1 + 3|U_F| / 2 \qquad -6$$

Then, the corresponding capacitances C_1 and C_2 are

$$C_1 / C_i = \frac{1}{0.485 \left(\frac{C_i}{C_{min}} - 1\right)} \qquad -7$$

and

$$C_2 / C_i = \frac{1}{0.841 \left(\frac{C_i}{C_{min}} - 1\right)} \qquad -8$$

The gate voltage of the ideal structure in the depletion region could be written as

$$V_G = \pm \, {}^{kT}/_{q} \, \{ |U_S| + \sqrt{2 \, |U_F| - 1} \} \qquad -9$$

(the positive sign taken for a p-type substrate, the negative for an n-type substrate).

Taking Equation *4* into consideration gives

$$V_G = \pm \, kT / q \, \frac{\{ |U_S| + 2.06 \sqrt{|U_F| (U_S - 1)} \}}{\frac{C_i}{C_{min}} - 1} \qquad -10$$

The formulas *3* and *10* determine the C-V characteristic of an ideal structure in the depletion region. The parameters measured are C_i and C_{min} and U_F is calculated from theseusing the formulae above.
On the basis of Equation *10* one can determine the difference ΔV_G corresponding to the change in the surface potential, thus

$$|U_{S1}| = 1 + {}^{|U_F|}/_{2} \text{ to } |U_{S2}| = 1 + {}^{3|U_F|}/_{2}$$

as

$$|{}^{U_G}/_{\Phi_F}| = 1 + \frac{1.51}{\frac{C_i}{C_{min}} - 1} \qquad -11$$

For the real MOS structure, the difference in the gate voltages corresponding to the capacitances C_1 and C_2 is ΔV_G'. The values ΔV_G and ΔV_G ' are not equal due to the interface trapped charge Q_{it}.Thus,

$$\Delta V_G - \Delta V_G' = {}^{A}/_{C_i} \, [Q_{it}(U_{S1}) - Q_{it}(U_{S2})]$$

$$= {}^{A}/_{C_i} \int_{U_{S1}}^{U_{S2}} q^2 \, D_{it}(E) \, dU_S \qquad -12$$

where A is the gate area in mm^2, $D_{it}(E)$ is the density of interface traps over the energy gap.
The average value of $D_{it}(E)$ in the range (U_{S1},U_{S2}) is

$$D_{it} = \frac{1}{(|U_{S1}| - |U_{S2}|)} \int_{U_{S1}}^{U_{S2}} D_{it}(E) \, dU_S$$

$$= \frac{C_i}{q^2 A} \frac{(\Delta V_G - \Delta V_G')}{|\Phi_F|} \qquad -13$$

Taking into consideration *11* one obtains

$$D_{it} = C_i/q^2A \left[\left| \frac{\Delta V_G}{\varnothing_F} \right| - 1 - \frac{1.51}{\frac{C_i}{C_{min}} - 1} \right] \qquad -14$$

Thus, a knowledge of the Fermi potential is required and not the dopant concentration, N, and this can be calculated from direct measurement of C_1, C_2 and A. It has already been proposed[256] that U_F can be directly calculated, thus

$$U_F = 1.087 \ln \left(19.2kT / q^2 n_i c_s \right) + 2.174 \ln \left(1/A \right) \left(C_i C_{min} / C_i - C_{min} \right) \qquad -15$$

and hence for a silicon substrate at a typical room temperature of between 290 to 300°K gives, approximately,

$$|\varnothing_F| = \left[T / 296 \right] \left[55.5 \ln \left\{ \left(1/A \right) \left(C_i C_{min} / C_i - C_{min} \right) \right\} - 627 \right] + 658 \text{ mV} \qquad -16$$

The components of Equations *15* and *16* must be in the proper units, that is C (pF), T (°K) and A (mm^2).

Thus the procedure for finding D_{it}, U_F and $|\varnothing_F|$ from the high-frequency C-V curves for a MOS system would be:

1. to measure C_i, C_{min} from the C-V curve (for say gate voltages of ±10V)
2. to calculate values of C_1 and C_2 from Equations *7* and *8*.
3. to find gate voltages corresponding to the capacitances C_1 and C_2 and to calculate $\Delta V_G'$.
4. to calculate the value of U_F from Equation *15*.
5. to calculate the value of $|\varnothing_F|$ from Equation *16*.

and

6. to calculate the value of D_{it} according to *14*.

The errors connected with this form of calculation for D_{it} can be accounted for in three groups:

a. errors connected with the non-ideality of the structure (non-uniform doping, surface potential fluctuations, series resistance, interface trap capacitance, lateral current flow, and bulk traps in the semiconductor.)
b. measurement errors of C_i, C_{min}, A, T, and $\Delta V_G'$.
c. errors due to assumed approximations.

These errors are assumed not to exceed an estimated value of 7% as calculated from the equations with the assumption that the error margins quoted in the text from JAKUBOWSKI and INIEWSKI[256] are fair estimations.

5. Theoretical Analysis to Determine U_F, C_{fb}, Q_{ot}, and the Semiconductor Impurity Concentration from High-Frequency C-V Curves for MOS Structures.

Using the same form of analysis as in Appendix **4**, various approximations to determine U_F, C_{fb}, Q_{ot}, and the semiconductor impurity concentration from the high-frequency C-V curves can be made:
From the analysis by JAKUBOWSKI and INIEWSKI[256], the intrinsic carrier concentration in a silicon substrate with $c_S=11.7c_o$ is given by the approximation

$$n_i = 3.86 * 10^{16} T^{3/2} \; exp \; [^{-7014} / _T] \qquad -17$$

and thus, using Equation *15* one can obtain

$$U_F= -21.494 + 2.174 \ln (^1/_A) (C_iC_{min} / C_i - C_{min}) - 0.544T + ^{7624} / _T \qquad -18$$

and for room temperature of T≈296°K

$$U_F= 1.167 + 2.174 \ln (^1/_A) (C_iC_{min} / C_i - C_{min}) \qquad -19$$

Thus, a second approximation for U_F has been given; this approximation agrees within ±0.14% of that of the previous approximation over the range of U_F 9 to 16.
From Equation *18*, the impurity concentration can be seen to be

$$N_B= 1.786*10^7 T^{0.956} (^1/_A) (C_iC_{min} / C_i - C_{min})^{2.174} \; exp \; (^{610} / _T) \; cm^{-3} \qquad -20$$

and at room temperature of T≈296°K

$$N_B=3.23*10^{10} (^1/_A) (C_iC_{min} / C_i - C_{min})^{2.174} \; cm^{-3} \qquad -21$$

Thus, a relation is presented from the proposals of JAKUBOWSKI and INIEWSKI[256], which gives estimates for U_F for the MOS system and N_B for the semiconductor substrate.

Consider the proposal that the ratio of the maximum high - frequency capacitance of the MOS system in the strong accumulation state, C_{max}, to the minimum high - frequency capacitance of the MOS system in the strong inversion state is determinable from the high - frequency C-V curve as

$$C_{max} / C_{min} = C_i / C_{min} = 1 + [C_i / C_{smin}] \qquad -22$$

Then, considering Equation *4*, the capacitance of the MOS system in the flatband condition C_{fb} can be written as

$$C_{fb} = \frac{C_i}{^1/_{2.06\sqrt{U_F}} \left[\frac{C_i}{C_{min}} - 1\right] + 1} \qquad -23$$

and thus, an approximation for C_{fb} may be made. According to NICOLLIAN and BREWS[16], such an approximation might be accurate to ±1%.
To estimate the trapped oxide charge, Q_{ot}, from the high frequency C-V curve for an MOS system, the assumption that the density of interface traps effecting the midband-voltage voltage-shift is valid, since the majority of interface traps which cause distortion to the C-V characteristic at the flatband condition lie near the conduction band of the interface system and therfore play a minor role in the midgap capacitance for the system.

Thus, since the midgap capacitance at the flatband condition of the MOS system may be approximated to

$$C_{mb} = C_i \; [\, 0.66 \, (C_i / C_{min} - 1) + 1]^{-1} \qquad -24$$

the oxide trapped charge can be calculated from the McLEAN approximation[223] as simply

$$Q_{ot} = C_{mb} \, \Delta V_G'$$

$$Q_{ot} = C_i \; [\, 0.66 \, (C_i / C_{min} - 1) + 1]^{-1} \, \Delta V_G' \qquad -25$$

where $\Delta V_G'$ has been already determined from the C-V characteristic.

Again, the errors connected with this form of analysis for the variuos parameters approximated can be accounted for in three groups:

a. errors connected with the non-ideality of the structure (non-uniform doping, surface potential fluctuations, series resistance, interface trap capacitance, lateral current flow, and bulk traps in the semiconductor.)
b. measurement and calculation errors of C_i, C_{mb}, C_{min}, A, T, and $\Delta V_G'$.

and

c. errors due to assumed approximations.

These errors are assumed not to exceed an estimated value of 2% as calculated from the equations with the assumption that the error margins quoted in the text from JAKUBOWSKI and INIEWSKI[256] and NICOLLIAN and BREWS[16] are fair estimations.

6. A Program for the BBC 'B' Microcomputer to Determine the C-V Characteristics of an MOSC from Its High-Frequency C-V Curve.

```
10 @%=&2030A
20 REM MOS
30 REM A PROGRAM TO CALCULATE BASIC
40 REM PARAMETERS OF MOS DEVICES
50 REM FROM C-V DATA .
60 REM VERSION 1/10/1986 .
70 PRINT:PRINT"      A program to calculate the"
80 PRINT"   basic parameters of MOS devices"
90 PRINT"          from C-V data ."
100 PRINT
110 PRINT
120 PRINT"Enter Device , Thickness , Type"
130 PRINT:PRINT:INPUT DEV$
140 PRINT:INPUT THI$:PRINT
150 INPUT TYP$:PRINT
160 VDU2
170 PRINT"Device              " DEV$
180 PRINT"Oxide thickness     " THI$
190 PRINT"Substrate type      " TYP$ "  Ohm-cm"
200 PRINT:PRINT
210 VDU3
220 PRINT:PRINT"Input Ci in pF"
230 PRINT:INPUT CI:PRINT
240 PRINT"Input Cmin in pF"
250 PRINT:INPUT CMIN
260 VDU2
270 PRINT"Ci ="CI" pF" "    Cmin="CMIN" pF"
280 VDU3
290 A=(CI/CMIN)-1
300 LET C1=CI/(1+0.485*A)
310 LET C2=CI/(1+0.841*A)
320 PRINT:VDU2
330 VDU2
340 PRINT:PRINT
350 PRINT"C1 =" C1 " pF" "    C2=   " C2 " pF"
360 PRINT :VDU3:PRINT
370 PRINT"Input Vg in Volts"
380 PRINT:INPUT VG
390 VDU2
400 PRINT"The Voltage Shift"
410 PRINT" Vg´ is"VG" Volts"
420 PRINT
430 VDU3
440 PRINT
450 PRINT"Input area of device in sq.mm"
460 PRINT:INPUT M
470 VDU2
480 PRINT"The Device Area"
490 PRINT" A is"M"  sq.mm"
```

```
500 LET B=(CI*CMIN)/((CI-CMIN)*M)
510 U=31+(55.5*LN(B))
520 PRINT
530 PRINT"The Normalised Fermi Potential"
540 PRINT" |Uf| is"U " mV"
550 V=1.167+(2.174*LN(B))
560 PRINT:PRINT"The Fermi Potential "
570 PRINT" Uf is  "V
580 LET C=(CI*10^9)/(1.6*M)
590 LET E= (VG*10^3)/U
600 D=C*(E-1-(1.51/A))
610 @%=&1050C
620 PRINT:PRINT"Density of Interface States "
630 PRINT" Dit is  "D"  per eV per sq.cm"
640 PRINT
650 P=1/(2.06*SQR(V))
660 F=CI/((P*A)+1)
670 @%=&2030A
680 PRINT"The Flatband Capacitance"
690 PRINT" Cfb is  "F"  pF"
700 N=(3.23*10^10)*(A^2.174)
710 PRINT
720 PRINT"The Impurity Concentration"
730 @%=&1050C
740 PRINT" Nb is  "N"  per cc"
750 VDU3 :PRINT
760 PRINT"Input Vfb in Volts"
770 INPUT VFB
780 Q=(VFB*CI*10^-12)/(M*10^-2)
790 VDU2
800 PRINT:PRINT"The Flatband Voltage"
810 @%=&2040A
820 PRINT" Vfb is"VFB" Volts":PRINT
830 PRINT:PRINT"The Oxide Charge Density is"
840 @%=&1050C
850 PRINT" Qox is "Q" C per sq.cm"
860 VDU3
870 PRINT:PRINT:PRINT:PRINT:PRINT
880 GOTO 120
```

7. Calibration and Details of the Am^{241} Alpha-Irradiation Source.

All the alpha-radiation exposures were performed using a 0.109 mCi Am^{241} source supplied by Berkeley Nuclear Laboratories, Gloucestershire, UK. This emits alpha particles with a mean energy of 5.5MeV, has a half-life of 433y, and was in the form of a small (≈10mm diameter) disc of material mounted on a short 0BA stud..

This source was calibrated using an Ortec SSB with an active area of $1*10^{-4}m^2$ and an Ortec NIM pulse counting system. The calibration was performed in vacuo at 0.142±0.001m from the SSB; counting periods of 100, 200, and 300 sec were used, and the source activity was found to be 0.1076±1.6% mCi. The associated error in this calibration is due to : counting errors (of less than ±0.3%); distance measurement errors (of less than ±1%); and error in the stated area of the SSB (o less than ±0.3%).

Since 85% of the alpha-particles from Am^{241} are of energy E=5.484 MeV this was considered to be the radiation having the majority of interactions in the SiO_2. Subsequently, the effects of the remaining 15% of alpha-particles with slightly different energies (±1%) have been assumed to produce effects of a similar nature to the most abundant particles and thus the source has been treated as a 100% source of alphas of E=5.484MeV.

The range of the E=5.484MeV alpha-particles in SiO_2 was determined to be 20.4±0.1μm, which implies that all the particles would penetrate into the silicon substrate to some depth and would therefore interact with both the oxide layer and the Si-SiO_2 interface.

The dose rate was determined for SiO_2 as the absorber and ignored the effects of the extremely thin layer of Al overlaying the device oxide layer and acting as a gate electrode and the effects of the underlying silicon substrate since the particles had to traverse the oxide layer initially. The dose rate in the SiO_2 layer was determined to be (46.4±6.6%)Rad(SiO_2)$hour^{-1}$ for devices held at 0.20±0.01m from the Am^{241} source, implying that irradiations in vacuo of up to 9 days were required in order to expose the devices to a total dose of 10KRad(SiO_2).

The device irradiations were performed in vacuum of ≈10^{-2}mbar on either individual basis or on a completed bias-board of devices in the arrangement shown in Figure 184. The boards of devices were irradiated to 10,5, 1, and 0.5 KRad(SiO_2) ±6.6%. The associated errors with the irradiations are due to: distance measurement errors (of less than 1%);the area effect of the device multi-biasboard (the error associated with the difference between the dose at the edge and dose in the centre of the board is ≈±3%);errors in timing of irradiation (of less than ±1%); and errors in the calibration of the source (of less than ±1.6%).

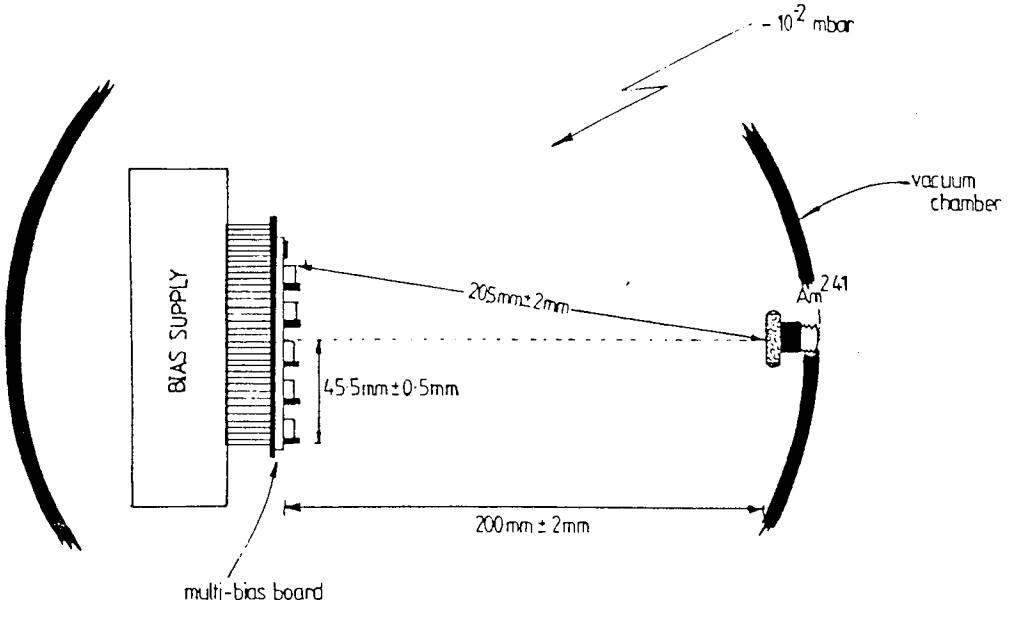

Figure 184: The arrangement of devices in the vacuum irradiation chamber illustrating the dose variation over the device irradiation board.

8. Calibration and Details of the Co^{60} Gamma-Irradiation Sources.

Two gamma-radiation sources were used to perform the gamma-irradiations: a high dose-rate Co^{60} source and a low dose rate Co^{60} source. These both emit gamma-ray photons of energy 1.173 and 1.333MeV, with a half-life of the sources of 5.27y.

The low dose-rate exposures (used to investigate the real-time effects of gamma radiation on the counting characteristics and breakdown effects in devices) were performed in air using a 5.33mCi Co^{60} source supplied by the Amersham Radiochemical Centre, Amersham, UK in 1978. Its activity at the time of the irradiations was calculated to be 1.86±0.11mCi. Thus, individual device exposures to gamma-radiation were made at 0.050±0.001m from the source for long (days) periods since the absorbed dose in the SiO_2 layer of the devices was calculated to be only approximately (0.34±6%)$Rad(SiO_2)hour^{-1}$ and long (days) exposures were necessary these tests. This source was not used for board-mounted device irradiations.

The high dose-rate exposures (used to investigate the effects of relatively low doses of gamma-radiation on the device electrical and physical properties) were performend in air using the gamma-irradiation facility at Birmingham University, UK. The source exposure system used was a Precisa 217 gamma-exposure system, the source-to-target arrangement being illustrated in the main text in Figure102.

The source activity was 950Ci on 1/4/1986, which implied a calculated dose rate at the time of the irradiations of $(1.3751\pm1.1\%)*10^5 Rad(SiO_2)$ $hour^{-1}$ at a source-to-device board distance of 0.240±0.001, the error due to the the uncertainty in the decrease in activity of the source and in measurement of the source-to-device board distance.

Doses of 10, 5, 1, and 0.5 $KRad(SiO_2)$±8% were performed in short time periods; all the dose rate calculations apply to conditions of electronic equilibrium, the state of affairs where the given flux of secondary electrons produced by the interactions of the gamma-rays in the small volume of material is balanced by the flux of electrons leaving that volume.Because of the average forward motion of such electrons, a sheet of perspex of thickness 4mm (density $0.4gcm^{-3}$) was placed in front of the device board to establish electronic equilibrium conditions.

The dose rate distribution at a point greater than 0.1m from the source was assumed to be symmetrical and given by

$$D_o / D = 1 + [x^2 / (d + 1.4)^2] \qquad -25$$

where D_o is the dose at the centre of the distribution, D is the distribution at some point on the device board, x is the distance of the centre point onthe board face to the outer edge of the board, and d is the distance of the centre of the board to the source. With a source-to-device board distance of 0.24m and the board width at maximum of 0.09m, the maximum error in dose at the edge of the board compared with at the centre of the board is -3%.

The associated errors with the irradiations are due to: distance measurement errors (of less than 1%);the area effect of the device multi-biasboard (the error associated with the difference between the dose at the edge and dose in the centre of the board is -3%);errors in timing of irradiation (of less than ±1%); errors in the dose calculations for gamma-rays in SiO_2 (of less than 2%); and errors in the calibration of the source (of less than ±1%).

9. Calibration and details of the National Physical Laboratory Neutron Irradiations.

NATIONAL PHYSICAL LABORATORY
Teddington, Middlesex, England.

Certificate of Measurement

OF THE NEUTRON FLUENCE GIVEN
DURING THE IRRADIATION OF
ARRAYS OF MOS DEVICES

FOR: Mr J L Collins
Department of Electrical & Electronic
Engineering & Applied Physics
Aston University
Aston Triangle
Birmingham B4 7ET

DATE OF IRRADIATIONS: 20 October 1986

IDENTIFICATION: Arrays of MOS devices, individually numbered and mounted by the user.

MEASUREMENTS:

Irradiations of the arrays of MOS devices were carried out in the low-scatter facility associated with the 3 MV Van de Graaff at the National Physical Laboratory, at a known separation distance between the neutron producing layer and the front surface of the board used to mount the MOS devices. The target was mounted at the centre of the facility and the particle beam parameters, target properties and resulting neutron energies are given in Table 1 together with the relevant run numbers.

NATIONAL PHYSICAL LABORATORY

Continuation of Certificate

The neutron fluence was determined using the NPL long counter at 0^{o}, at a distance of (199.3 $\pm$ 0.3)cm, measured from the neutron producing target layer to the long counter moderator front-face. Corrections for inscatter, measured using a shadow-cone, effective centre, dead-time and background effects were made. The neutron fluences at 0^{o} were obtained by assuming that the neutron fluence followed the inverse-square law and by applying a small correction for out-scatter, calculated using the known oxygen and nitrogen cross sections. Individual runs, at the same neutron energy, were related to each other through the NPL "slab-detector", a long counter of enhanced efficiency, used as a monitor of the neutron output. A current integrator was used as a monitor to relate these individual measurement runs to the neutron fluence determinations. A measurement of the ratio of the neutron fluences at 0^{o} and 10^{o} was also made to assist the user in the calculation of the actual fluence given to each sample, and the value for each neutron energy is given in Table 1.

The efficiency of the NPL long counter has previously been determined using radioactive neutron sources calibrated absolutely in the NPL manganese sulphate bath and unfolding the source spectra from the resulting long counter response curve, as described in NPL Report RS5 (April 1976). The efficiency obtained in this manner has been confirmed, relative to the hydrogen scattering cross-section, over the neutron energy range 2.5 MeV to 5.5 MeV using a proton recoil telescope of conventional design, and also, absolutely, over the neutron range 0.55 MeV to 1 MeV using the associated target activity technique.

RESULTS:

The measured neutron fluences, expressed in terms of neutrons per square centimetre, for each of the irradiation runs, are given in Table 2, together with the run number, maximum angle subtended by the chamber, and the angle of incidence of the neutron radiation upon the chamber.

ACCURACY:

The uncertainties associated with these measured neutron fluences are given in Table 3. The only contribution included due to the MOS devices is the systematic uncertainty associated with the irradiation distance. No other contributions to the total uncertainties have been included, as it is felt that the user is a better judge of these components. The first section of Table 3 gives the random uncertainties quoted at 95% confidence limits with the associated number of degrees of freedom essentially infinite. The remaining section gives the component non-random uncertainties estimated at 95% confidence limits.

NATIONAL PHYSICAL LABORATORY

Continuation of Certificate

Table 1

Particle beam parameters, target properties and resulting neutron energies (all in keV).

Date	20.10.86	20.10.86	20.10.86
Run Nos.	1-4	5-8	9-12
Reaction	T(p,n)	^{7}Li(p,n)	T(p,n)
Incident Particle Energy	(1880 ± 3)	(2233 ± 3)	(3296 ± 3)
Target Thickness	(46 ± 5)	(5.8 ± 0.5)	(32 ± 5)
Angle of Detection	0°	0°	0°
Neutron Energy	(1056 ± 24)	(496 ± 5)	(2499 ± 16)
$\frac{\delta E_n}{\delta E_p}$ (0°)	1.030	1.101	1.006
$\frac{\delta E_n}{\delta E_p}$ (10°)	1.020	1.096	0.996
E_n (5°)	(1052 ± 24)	(495 ± 5)	(2491 ± 16)
E_n (10°)	(1040 ± 24)	(491 ± 5)	(2468 ± 16)
E_n (15°)	(1021 ± 24)	(484 ± 5)	(2431 ± 16)
E_n (20°)	(994 ± 24)	(474 ± 5)	(2379 ± 16)
Neutron Fluence Ratio $0^{\circ}/10^{\circ}$	1.04 ± 0.02	1.02 ± 0.02	1.06 ± 0.02

NATIONAL PHYSICAL LABORATORY

Continuation of Certificate

Table 2

Measured neutron fluences for runs 1-12

Run No.	Sample Distance cm	Max. angle Subtended	Angle of Incidence to Normal	Neutron Fluence cm^{-2}
1	(20.0 ± 0.2)	~ 13°	0°	1.00×10^{8}
2	(20.3 ± 0.2)	~ 13°	0°	1.89×10^{7}
3	(20.3 ± 0.2)	~ 13°	0°	1.12×10^{6}
4	(20.3 ± 0.2)	~ 13°	0°	9.6×10^{4}*
5	(20.3 ± 0.2)	~ 13°	0°	1.02×10^{8}
6	(20.3 ± 0.2)	~ 13°	0°	1.05×10^{7}
7	(20.3 ± 0.2)	~ 13°	0°	1.09×10^{6}
8	(20.3 ± 0.2)	~ 13°	0°	1.11×10^{5}*
9	(20.2 ± 0.2)	~ 13°	0°	9.99×10^{7}
10	(20.2 ± 0.2)	~ 13°	0°	9.96×10^{6}
11	(20.2 ± 0.2)	~ 13°	0°	1.00×10^{6}
12	(20.2 ± 0.2)	~ 13°	0°	1.15×10^{5}*

*Runs 4, 8 and 12 are subject to an additional uncertainty of about ± 8% due to difficulties inherent in monitoring very short irradiation runs.

NATIONAL PHYSICAL LABORATORY

Continuation of Certificate
Table 3

Percentage uncertainties associated with the determination of the neutron fluence

UNCERTAINTY	
Random Uncertainties	
Statistical uncertainties associated with the neutron fluence determination. Essentially infinite degrees of freedom.	± 0.3%
Non-random Uncertainties	
Positioning of long counter (± 0.2 cm)	± 0.3%
Positioning of MOS devices (± 0.2 cm)	± 2.0%
Effective centre and $^{1}/r^{2}$ extrapolation	± 0.6%
Outscatter correction	± 0.2%
Dead-time correction	± 0.1%
Long-counter efficiency	± 2.0%
Inscatter correction	± 0.2%
Background effects	± 0.3%
Target scattering effects	± 0.5%
Variation of neutron fluence with incident beam current during irradiations	± 1.5%

10. Calibration and Details of the Am^{241}/Be Neutron-Irradiation Source.

The Am^{241}/Be neutron source (as described in the main text) was used to investigate the real-time effects of neutron radiation on the counting characteristics and breakdown effects in devices and irradiations were performed in air in a thick lead-shielded enclosure. The source activity was 3Ci, equivalent to a flux of $(3.926\pm0.196)*10^{7}$n $cm^{-2}s^{-1}$ at a source-to-device board distance of 0.015±0.005m.

The Am^{241}/Be neutron spectrum is shown in Figure 185, where it can be seen that the mean neutron energy is approximately 5.5MeV with a large number of low energy neutrons below iMeV in energy.

Irradiations were made at source-to-device board distances of 0.150±0.005m to total fluences of 10^{8} to 10^{13}±4% n cm^{-2}, with errors resulting from source-to-device board distance measurements (of less than 3%); in the source activity (of less than 0.5%); and in the exposure times (of less than 0.5%).

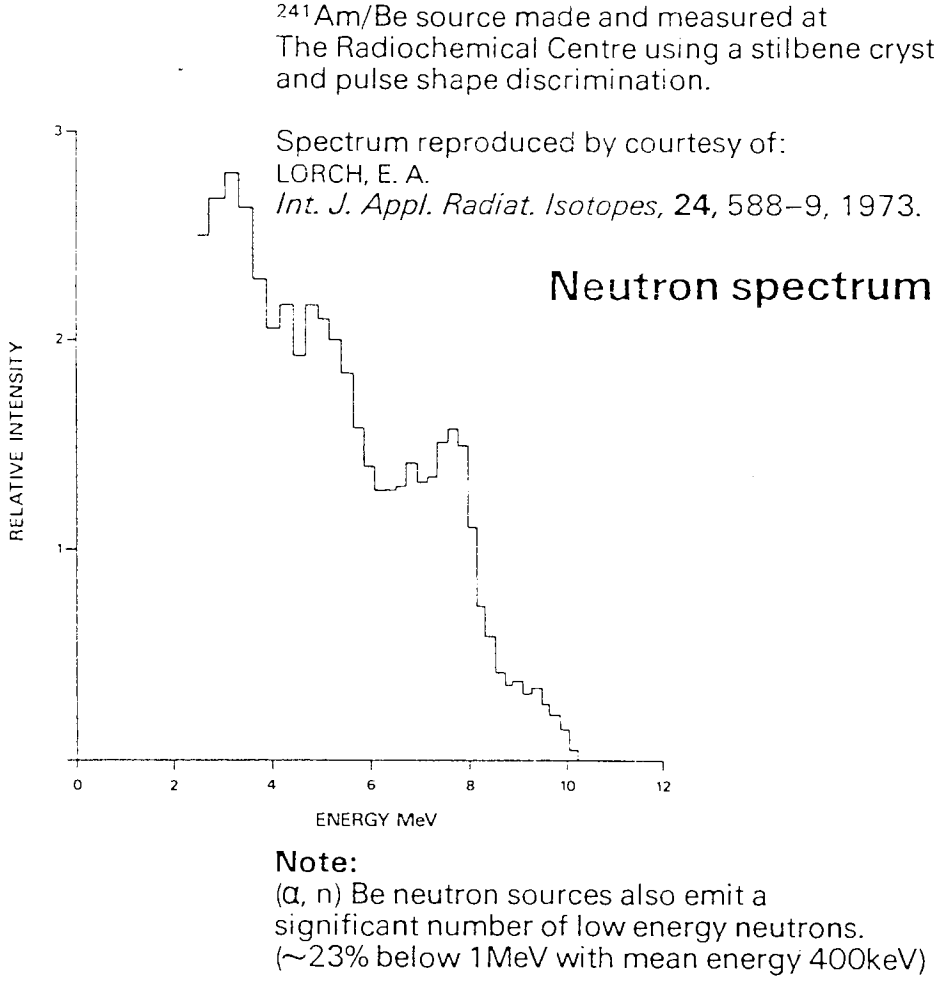

Figure 185: Energy spectrum for an Am^{241} / Be (alpha, neutron) irradiation source.

11. Calibration and Details of the Recoil-Proton Irradiations.

The recoil-proton irradiations were facilitated by the (n,p) rection in a thin hydrogenous radiator placed in close contact with the front gate electrode of the device. The calculations of the number of recoil protons are based on the number of (n,p) interactions occurring in the thin hydrogenous radiator, and all the recoil-protons produced are assumed to leave the radiator and impinge on the device. This assumption is based on two main factors: the first that the thickness of the radiator used was thin enough to prevent large absorption and interactions of the recoil-protons with the nuclei within the hydrogenous radiator, and second that all the recoil-protons produced exit the radiator on the device-side rather than on the source-side of the radiator and therefore no backscattering occurs.
The cross-section for neutron interaction with hydrogenous materials, o_{int}, such as plastic, over the neutron energy range, n_e (in MeV), of 0.5, 1.0, and 2.5 MeV (the energy range of the neutrons used in the combined neutron / recoil-proton irradiations) may be calculated[265] from

$$o_{int} \approx [4.83 / \sqrt{n_e}] - 0.578 \quad \text{barns} \qquad -26$$

and thus;

for neutrons of energy 0.496±0.015MeV $o_{int} \approx 6.25 \pm 0.19$barns
for neutrons of energy 1.056±0.024MeV $o_{int} \approx 4.25 \pm 0.13$barns
for neutrons of energy 2.499±0.016MeV $o_{int} \approx 2.48 \pm 0.07$barns

The number of interactions, N_{int} may be calculated from

$$N_{int} = A\ N_{mol}\ o_{int} \times O_t \qquad -27$$

where A is the area of the sample (m^2); N_{mol} is the number of molecules in the radiator (m^{-3}); x is the thickness of the radiator (m); and O_t is the neutron flux (m^{-2}).
Thus since N_{mol} is $\approx 8.73 * 10^{27}$ m^{-3}, x was $1.13 * 10^{-4}$m, A was $9 * 10^{-6} m^2$ and O_t varied between $10^9$and 10^{12} n m^{-2}, by substitution the results in Table 14 were obtained (Reprinted in this Appendix from the main text).

The errors seen in the relative numbers of recoil-protons are due to: error in the thickness of the hydrogeneous radiator (of less than 0.4%); errors in the neutron energy and fluences (of less than 3% in total); errors in the area of the gate electrode and in the calculation of the cross-section (of less than 0.2%) lead to an overall error in the recoil-proton fluences of approximately 3.6% for devices at the centre of the boards, and approximately 8.6% for devices at the edges of the boards. The relatively low number of recoil-protons compared to the number of neutrons is due maily to the thinness of the hydrogenous material. Had the radiator been any thicker, however, its thickness would have scattered (and possibly absorbed) an appreciable number of the recoil protons away from the devices. Since the effects measured were only for comparison with purely neutron effects the comparitive smallness of the number of interacting recoil-protons (compared with the number of interacting neutrons) is not considered of great importance.

Neutron energy MeV	*Neutron fluence* n cm^{-2}	*Recoil-proton fluence* p cm^{-2}
1.056 ± 0.024	$(1.00\pm0.030)*10^{8}$	$(4.34\pm0.17)*10^{4}$
1.056 ± 0.024	$(1.89\pm0.033)*10^{7}$	$(8.47\pm0.34)*10^{3}$
1.056 ± 0.024	$(1.12\pm0.034)*10^{6}$	$(5.02\pm0.21)*10^{2}$
1.056 ± 0.024	$(9.60\pm0.077)*10^{4}$	$(3.53\pm0.10)*10^{1}$
0.496 ± 0.005	$(1.02\pm0.031)*10^{8}$	$(6.38\pm0.32)*10^{4}$
0.496 ± 0.005	$(1.05\pm0.032)*10^{7}$	$(6.40\pm0.32)*10^{3}$
0.496 ± 0.005	$(1.09\pm0.033)*10^{6}$	$(6.43\pm0.33)*10^{2}$
0.496 ± 0.005	$(1.11\pm0.089)*10^{5}$	$(6.45\pm0.34)*10^{1}$
2.499 ± 0.016	$(9.99\pm0.030)*10^{7}$	$(2.53\pm0.76)*10^{4}$
2.499 ± 0.016	$(9.96\pm0.030)*10^{6}$	$(2.51\pm0.75)*10^{3}$
2.499 ± 0.016	$(1.00\pm0.030)*10^{6}$	$(2.53\pm0.76)*10^{2}$
2.499 ± 0.016	$(1.15\pm0.921)*10^{5}$	$(2.64\pm0.79)*10^{1}$

Neutron and Recoil-Proton Irradiation Parameters.

12. Calibration and Details of the Cf^{252} Fission-Fragment Irradiation Source.

The Cf^{252} source used for fission-fragment irradiations was supplied by the Amersham Radiochemical Centre, Amersham, UK, as a small disc of material of active area ≈ 39 mm^2. On 1 / 5 / 1984 the source had an activity of 1.3μCi, equivalent to $4.81*10^4$ disintegrations s^{-1} of which 3.1% were fission-fragments and the remainder alpha-particles; associated with each spontaneous fission were 4 neutrons.

At the time of the investigations of fssion-fragment effects in the devices, the source had a calculated nominal activity of 2.64 $*10^4$ disintegrations s^{-1} and thus the source emitted approximately 409 fission-fragments s^{-1} forward of the source at the source surface, with the same likelyhood that a particle emerges from the centre as from the edge of the source. This implies that for a device area of 9mm^2 set at (2.51±0.05)mm from the source in vacuo the maximum number of incident fission fragments on the device surface is approximately 55 s^{-1}. For irradiations in air, this figure is reduced somewhat because of attenuation of the fission-fragment flux due to interactions with the surrounding atmosphere.

The source details are listed in Table15 of the main text; inFigure 186 the spectrum for the source is given, and the approximate energies and distribution of energies for the fission-fragments are shown.

The abundance of the mean light fission-fragments (atomic number between 92 and 106, mean approximately 106) and heavy fission-fragments (atomic number between 130 and 160, mean approximately 142) is not easily quantified, but from the shape of the curve in Figure 186 it appears that there are approximately the asme number of light fragments as there are heavy fission-fragments.

The irradiations were performed both in vacuo and in air; the irradiations in air were at various source-to-device distances in order to energy-select fission-fragments. The calculations for the residual energy and stopping powers are shown in Appendix **14**.

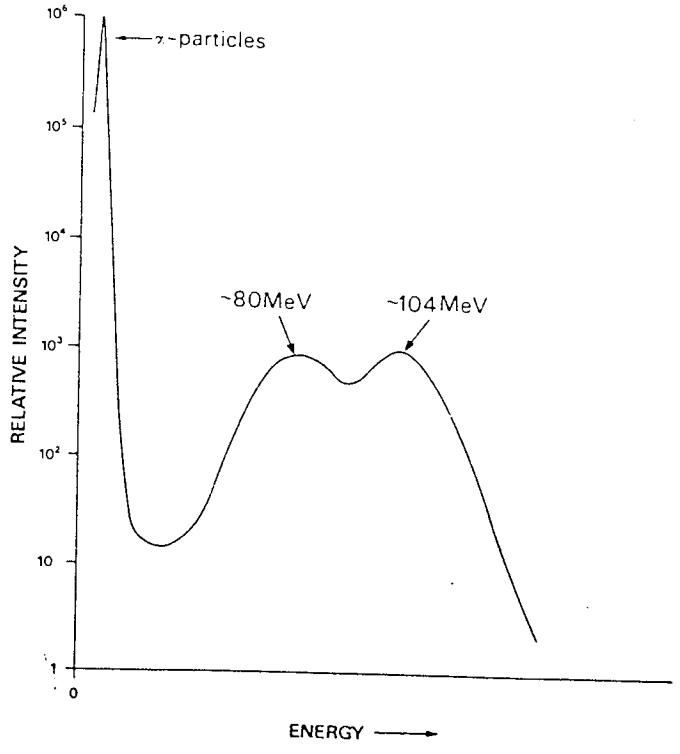

Figure 186: Energy spectrum for a Cf^{252} spontaneous-fission fission-fragment irradiation source.

13. Calculation of the Approximate Number of Displacements in Various Thicknesses of SiO_2 due to Neutron Irradiation in the Energy Range 0.5, 1.0, 2.5, and 5.5 MeV.

The number of interactions that a given neutron fluence (of a particular neutron energy) has with the SiO_2 molecules in a MOSC is a measure of the displacement damage which might occur in the oxide. The assumption that the number of interactions is a direct measure of the displacement damage to the oxide is not valid since it is unknown if each interaction causes one or more than one displacement. However, it can be assumed that each interaction produces at least one displacement and therefore such calculations do give insight into the possible minimum effects of the neutron radiation on the oxide layer.
Using the same analysis as in Appendix 11, the number of interactions in the SiO_2 of the devices is

$$N_{int} = A \{N_{mol,Si}\, o_{int,Si} + N_{mol,O}\, o_{int,O}\} \times O_t \qquad -28$$

where A is the area of the sample (m^2); $N_{mol,Si}$ is the number of atoms of silicon and approximately $1.0624*10^{28}$ m^{-3}; $N_{mol,O}$ is the number of molecules of oxygen and approximately $2.1248*10^{28}$ m^{-3}; x is the thickness of the oxide layer (m); and O_t is the neutron flux (m^{-2}). In this case $o_{int,Si}$ is the interaction cross-section for neutrons with silicon (barns) and $o_{int,O}$ is the interaction cross-section for neutrons with oxygen(barns).
Calculations of the cross-sections for interaction i for the various neutron energies used in the investigations of neutron effects on the MOSCs are shown in tabulated form below:

Neutron Energy MeV	$o_{int,Si}$ barns	$o_{int,O}$ barns
0.496±0.015	4.58±0.14	3.02±0.10
1.056±0.024	8.03±0.24	4.40±0.13
2.499±0.016	4.51±0.14	1.02±0.03
5.5±0.2	2.0±0.06	1.3±0.05

Calculated Cross-sections for the Interaction of Neutrons with silicon and oxygen.
(After NORTHCLIFFE and SCHILLING, Reference 265)

Thus, the number of interactions may easily be calculated using Equation *28*, and the results of these calculations are tabulated below. The smallness of the number of interactions in the devices implies for the low fluences used to irradiate the devices illustrates that the level of displacement damage to the oxide is probably not responsible for the effects seen in the oxide layer and described in the main text. The number of interactions in the silicon substrate however would be approximately $5*10^4$ greater than that for the oxide layer and it is probably in the semiconductor region where displacement damage has most effect. Only calculations for the thinnest and thickest oxide devices are presented.

Neutron Energy	*NeutronFluence*	*Number of Interactions per device of Oxide Thickness*	
MeV	n cm^{-2}	42.5nm	588.3nm
0.496±0.015	10^9	$5*10^{-3}$	$7*10^{-2}$
	10^{10}	$5*10^{-2}$	$7*10^{-1}$
	10^{11}	$5*10^{-1}$	0.7
	10^{12}	0.5	7
1.056±0.024	10^9	$9*10^{-3}$	$1.2*10^{-1}$
	10^{10}	$9*10^{-2}$	1.2
	10^{11}	$9*10^{-1}$	12
	10^{12}	9	120
2.499±0.016	10^9	$2.6*10^{-3}$	$3.6*10^{-2}$
	10^{10}	$2.6*10^{-2}$	26
	10^{11}	$2.6*10^{-1}$	260
	10^{12}	2.6	2600
5.5±0.2	10^{12}	1.8	25.3
	10^{13}	18	253
	10^{14}	180	$2.53*10^3$
	10^{14}	$1.8*10^3$	$2.53*10^4$
	10^{16}	$1.8*10^4$	$2.53*10^5$

The Theoretical Number of Neutron Interactions in the Oxide layer of an MOSC of the Indicated Oxide thicknesses.

14. The Stopping-Power in SiO_2 and Residual energy (range in air at room temperature and pressure) of Light and Heavy Fission-Fragments.

Many fission-fragment irradiations were performed with several source-to-device distances in order to expose the devices to fission-fragments of known energies and thus known stopping powers in the SiO_2; this is described in the main text, section **5.4.5**.

Linear interpolations of available data[265] for the range and stopping power for heavy ions in aluminium to that for SiO_2 have been made in order to gauge the threshold fission-fragment stopping power in SiO_2 for radiation induced dielectric breakdown in the devices.

The stopping powers in SiO_2 have been determined from residual energy curves for average light (A=106, Z=43) and average heavy (A=142, Z=55) fission-fragments, and fission-fragments energy-selected by the source-to-device distance, as described in the main text.

The interpolated data is tabulated below; plots of stopping power versus residual energy (Figures 187) and stopping power versus source-to-device distance (Figure 188) are shown overleaf for average light and average heavy fission-fragments.

Residual Energy of light particle MeV	*Stopping Power in SiO_2* MeV mg^{-1} cm^2 (±3%)
104	39.37
89	43.69
69	40.32
54	38.69
49	35.10
44	31.52
33	29.79
27	24.39
18	20.23
13	18.04

The Residual Energy and Stopping Power in SiO_2 for Average Light (A=106, Z=43) Ions.

Residual Energy of heavy particle MeV	*Stopping Power in SiO_2* MeV mg^{-1} cm^2 (±3%)
80	45.46
63	39.24
45	31.32
35	29.89
31	26.47
27	25.39
21	21.74
17	19.59
12	14.53
8.5	12.57

The Residual Energy and Stopping Power in SiO_2 for Average Heavy (A=142, Z=55) Ions.

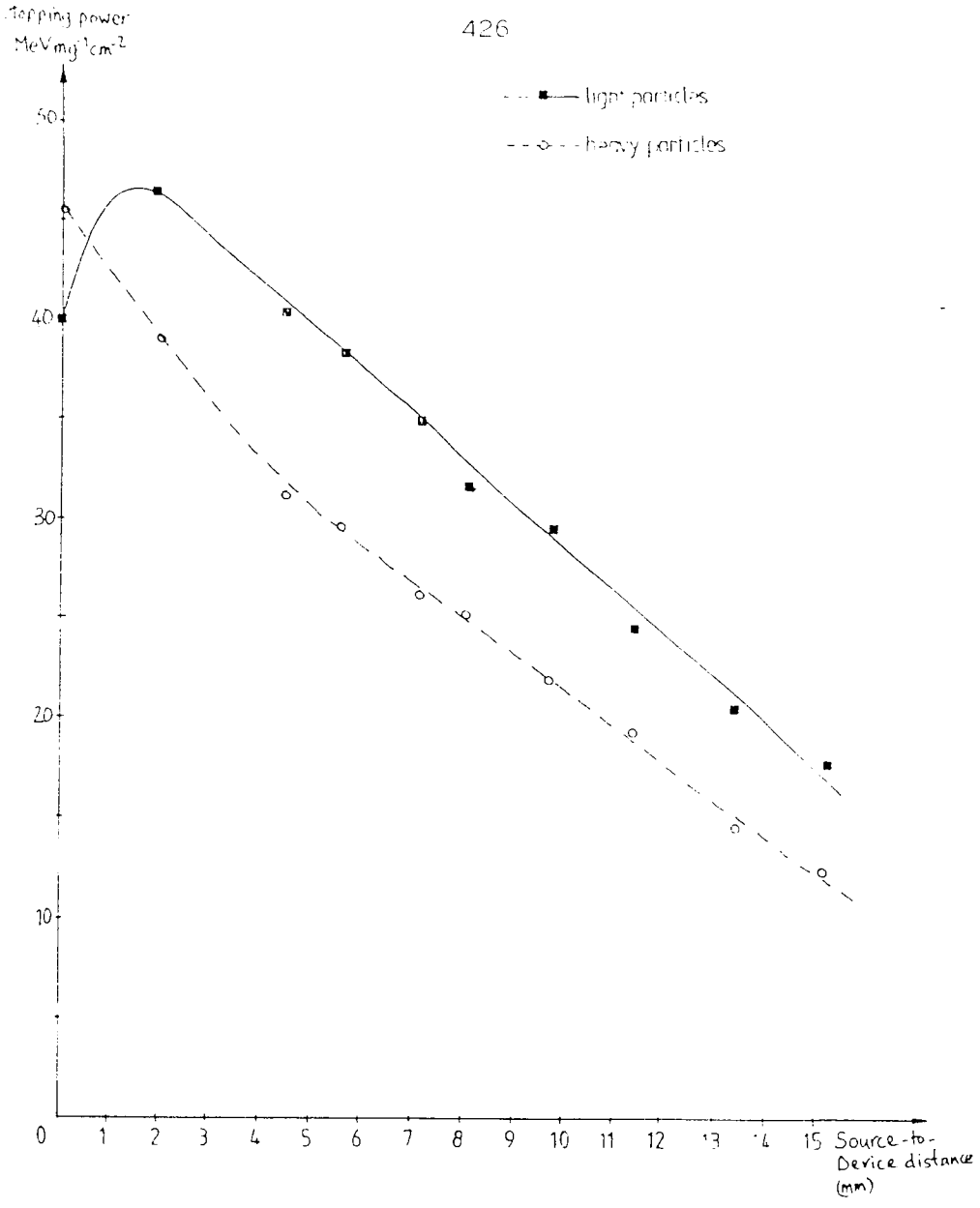

Figure 187: A plot of the residual energy of mean light (A=104, Z=42) and heavy (A=140, Z=55) ions versus their stopping power in SiO_2.

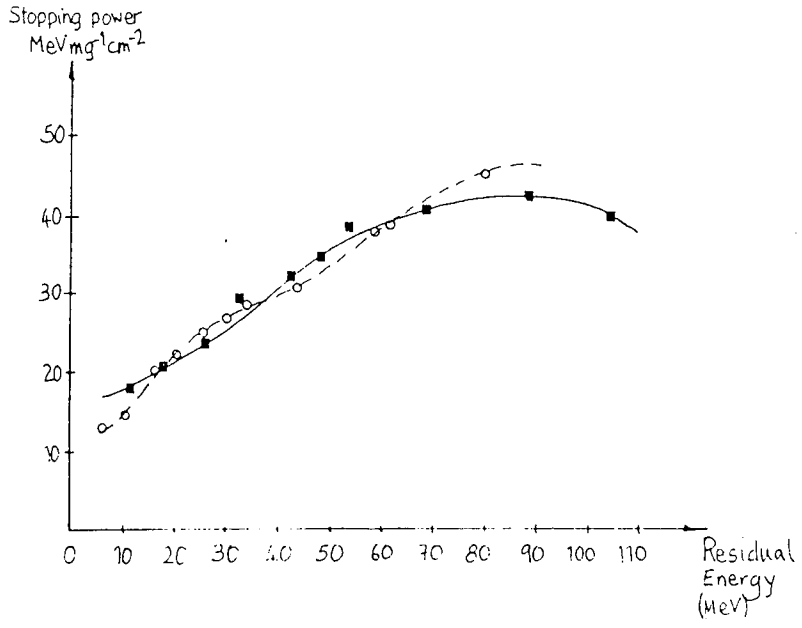

Figure 188: A plot of the stopping power of mean light (A=104, Z=42) and heavy (A=140, Z=55) fission-fragments versus their range in air.

REFERENCES.

1. FRANKL, D. R.
Electrical Properties of Semiconductor Surfaces
Pergammon Press, Oxford, England (1967).

2. MANY, A.; GOLDSTEIN,Y. & GROVER, N.B.
Semiconductor Surfaces
North-Holland Press, Amsterdam, Netherlands (1965).

3. TERMAN, L. M.
An Investigation of Surface States at the Si-SiO_2 Interface Using MOS Diodes.
Solid State Electronics 5(1962)285-

4. LEHOVEC,K. & SLOBODSKOY, A.
Field Effect Capacitance Analysis of Surface States on Silicon.
Phys Stat Solidi 3(1963)447-

5. KLEIN, N.
Electrical Breakdown Mechanical in Thin Insulators.
Thin Solid Films 50 (1978) 223 - 232

6. SOLOMON , P.
Breakdown in SiO_2.
J VacSci Tech 14, 5 (1977) 1122 - 1130

7. KLEIN, N. & GAFNII, H.
Maximum dielectric Strength of Thin SiO_2Films.
IEEE Trans Electron Devices, ED -13 (1966) 281 -

8. O'DWYER, J.J.
The Theory ofElectrical Conduction and Breakdown in Solids
Clarendon Press, Oxford, 1973

9. O'DWYER, J.J.
Theory of High Field Conduction in a Dielectric.
Journal of Applied Physics 40 (1969) 3887 -

10. December issues of the IEEE Transactions on Nuclear Science

11. HOLMES -SIEDLE, A. & FREEMAN, A.
Improving Radiation Tolerance in Space -Born Electronics.
IEEE TRANS NS NS-15 (1978) 1216 - 1227

12. MESSENGER, G.C.; STEEL, E.J. & NEUSTADT, M.
Displacement Damage in MOSTs.
IEEE TRANS NS NS-12 (11965) 78 - 82

13. KLEIN, N. & SOLOMON, P.
Thin Insulator Current Pulse Counter of fission-fragments.
Nuclear Insulation Methods 129 (1975) 119 - 121

14. HARVEY, J.R
The Basis of a Suggested Instrumental approach to the Surveying of Neutron Fields and the Measurement of Personnal Dose from Neutrons.
Phys Med Biol 26,2 (1981) 253 -267

15. McLEAN, F.B.
A Framework for Understanding Radiation Induced Interface States.
IEEE TRANS NS NS-27 (1980) 1651 - 58

16. NICOLLIAN, E.H. & BREWS, J.R.
MOS Physics and Technology
Wiley, USA (1982)

17. SZE, S.M.
Physics of Semiconductor Devices
Wiley, USA (1981)

18. GARRETT,C.G.B. & BRATTAIN,W.H.
Physical Theory of Semiconductor surfaces.
Phys Rev 99 (1955) 376-

19. PIERRET,R.F.
Field Effect Devices: Volume 4 of the Modular Series on Solid State Electronics
Addison-Wesley Publishing Co., USA (1983)

20. HOFSTEIN, S.R. & WARFIELD, G.
The Physical Limitation of the Frequency Response of a Semiconductor Surface Inversion Layer.
Solid State Electronics 8 (1965) 321-

21. GROVE, A.S.; DEAL, B.E.; SNOW,E.H. &SAH, C.T.
Investigation of Thermally Oxidised Si Surfaces Using MOS structures.
Solid State Electronics 8 (1965) 145-

22. GOETZBERGER, A.
Ideal MOS Curves for Silicon.
Bell Systems Technical Journal 45 (1966) 1097-

23. DEAL, B.E.; SNOW, E.H. & MEAD, C.A.
Barrier Energies in Metal-SiO_2-Si Structures.
J Phys Chem Solids 27 (1966) 1873-

24. DEAL, B.E.
Current Understanding of Charge in Thermally Oxidised Si Structures.
J Electrochem Soc 121 (1974) 198-

25. DEAL, B.E.
Standardised Terminology for Oxide Charge associated with Thermally Oxideised Silicon.
IEEE Transactions on Electron Devices ED-27 (1980) 606-

26. KAMIENIECKI,E. & NITECKI, R.
Photocapacity Probing of Si-SiO_2 Interface States.
in The Physics and Chemistry of SiO_2 and Its Interfaces, pp. 417-420
ed. PANTELIDES, S.T., Pergammon Press, New York, USA (1978)

27. GOETZBERGER, A.; KLAUSMANN, E. & SCHULTZ, M.J.
Interface States on Semiconductor- Insulator Surfaces.
CRC Critical Reviews in Solid State Science (1976)

28. DAHLKE, W.E. & GREVE, D.W.
Statistics of Trap Photoemission in MIS Tunnel Diodes.
Solid State Electronics 22 (1979) 893-903

29. WHITE, M.H. & CRICCHI, J.R.
Characterisation of Thin Oxide MNOS Memory Transistors.
IEEE Trans El Dev ED-19 (1972) 1280-

30. SNOW,E.H.; GROVE, A.S. ; DEAL, B.E. & SAH, C.T.
Ion Transport Phenomena in Insulating Films.
J Appl Phys 36 (1965) 1664-

31. YON,E. ; KO, W.H. & KUPER, A.B.
Sodium Distribution in Thermal Oxides on Silicon by Radiochemical and MOS Analysis.
IEEE Trans El Dev ED-13 (1966) 276-

32. CHOPRA, K.L.
Thin Film Phenomena
McGraw-Hill Publishing Co., USA (1969)

33. O'DWYER, J.J.
The Theory of Electrical Conduction and Breakdown in Solid Dielectrics
Clarendon Press, Oxford, UK (1973)

34. FRENKEL,J.
On the Theory of the Breakdown of dielectrics and Electronic Semiconductors.
Technical Physics in the USSR 5 (1938) 685-

35. FRENKEL,J.
On the Pre-Breakdown Phenomena in Insulators and Electronic Semiconductors.
Phys Rev 54 (1938) 647-

36. KLEIN, N.
Electric Breakdown in Solids
Advances in Electronics and Electron Physics, Volume 26
Academic Press, New York, USA (1967)

37. SCHULTZ, M. & PENSL, G.
Insulating Films on Semiconductors
Springer-Verlag Publishing Co., Berlin, FDR (1981)

38. BARBE, D.F.
Very Large Scale Integration: Fundamentals and Applications
Springer-Verlag Publishing Co., Berlin, FDR (1980)

39. SOSMAN, R.B.
The Phases of Silicon
Rutgers University Press, New Brunswick, New Jersey, USA (1975)

40. RAWSON, H.
Inorganic Glass Forming Systems
Academic Press, New York, USA (1967)

41. EITEL, W.
Silicate Science: Volume 2
Academic Press, New York, USA (1965)

42. YEH, T.H.
Thermal Oxidation of Silicon.
J Appl Phys 33(1962) 2849-

43. KARUBE, N.;YAMMAMOTO, K. & KAMIDIYAMA, M
Thermal Oxidation of silicon.
Japanese J Appl Phys 2 (1963) 11-

44. DEAL, B.M.
The Oxidation of Si in Dry O_2, Wet O_2, and Steam.
J Electrochem Soc 110 (1963) 527-

45. EDAGAWA, H. ; MONTIA, Y & MAEKAWA, S.
Growth and Structure of Si O_2 on Si Surfaces.
Japanese J Appl Phys 2 (1963) 765-

46. STEVELS, J.M.
in Non-Crystalline Solids , Chapter 17
ed. FRECHETTE, V.D., Wiley Publishing Co., New York, USA (1960)

47. NAGASIMA, N.
Structure Analysis of Thermal Films of Si O_2 by Electron Diffraction and Infrared Absorption.
Japanese J Appl Phys 9(1970) 879-

48. IRENE, E.A.
Effects of Trace Amounts of Water on the Thermal Oxidation of Si in O_2.
J Electrochem Soc 121 (1974) 1613-

49. KRIVANEK, O.L.; SHENG, T.T. & TSUI, D.C.
High-Resolution Electron Microscopy Study of the Si-SiO_2 Interface.
Appl Phys Letters 32 (1978) 437-

50. WOODS, M.H. & WILLIAMS, R.
High Fields in Si O_2 Produced by Corona Discharge.
J Appl Phys 44 (1973) 5506-

51. PANTELIDES, S.T.
The Physics and Chemistry of SiO_2 and Its Interfaces
ed. PANTELIDES, S.T., Pergammon Press, New York, USA (1978)

52. LUCOVSKY, G.; PANTELIDES, S.T. & GALEENEER, F.L.
The Physics Of MOS Insulators
Pergammon Press, New York, USA (1980)

53. REVESZ, A.G.
Defect Structure of Vitreous SiO_2Films on Si; 1.The Structure of Vitreous SiO_2Films and the Nature of the Si-O Bond.
Physica Status Solidi (a) 58 (1980) 107-113

54. REVESZ, A.G.
Defect Structure of Vitreous SiO_2Films on Si; 2. Defect Structure of Vitreous SiO_2Films on Si.
Physica Status Solidi (a) 58 (1980) 235-43

55. REVESZ, A.G.
Defect Structure of Vitreous SiO_2Films on Si; 3. The Role of Defect Structure in the Growth of SiO_2Films.
Physica Status Solidi (a) 58 (1980) 657-666

56. DEAL, B.E.
Seventeen Drifts of Silicon Dioxide Technology.
J Electrochem Soc 121 (1974) 89c

57. CHANG, C.C & BOULIN, C.
Oxide Measurements on Si Using chemically Shifted Auger Spectra.
Progress in Surface Science 69(1977) 385-

58. PEPPER, M.
Introduction to Silicon Inversion layers.
Contemporary Physics 18(1977) 423 - 454

59. HELMS, C.R.
Morphology and Electronic Structure of the Si-SiO_2 Interface.
J Vac Science Technology 16 (1979) 608-614

60. LAUGHLIN, R.B. ; JOANNOPOLOUS, J.D. & CHADI, D.J.
Bulk Electronic Structure of SiO_2.
Physical Review B-21 (1980) 5728-37

61. SAKUMI, T. & SUGANO, T.
inThe Physics Of MOS Insulators, pp.241-
Pergammon Press, New York, USA (1980)

62. HENAN, F.
Electronic Structure of the Si- SiO_2 Interface.
in Insulating Films on Semiconductors, pp.642-
eds. SCHULTZ, M. & PENSL, G, Springer-Verlag Publishing Co., Berlin, FDR (1981)

63. GRUNTHANER, F.J.; GRUNTHANER, P.J.; VASZUEZ, R.P. & LEWIS, B.F.
High Resolution Photoelectron Spectroscopy as a Probe of Local Atomic Structure and Its Application to a-Si and the Si- SiO_2 Interface.
Phys Rev Letters 43 (1979) 1683-86

64. FEUDMANN, L.C.; SILVERMAN, P.J. & WILLIAMS, J.S.
The Use of Thin Si Crystals in Backscattering Channelling Studies of the Si- SiO_2 Interface.
Phys Rev Letters 41 (1978) 1396

65. MOTT, N.F. & DAVIS, E.A.
Electronic Processes in Non-Crystalline Materials
Clarendon Press, Oxford, UK (1979)

66. ZINAI, J.M.
Models of Disorder
Cambridge University Press, Cambridge, UK (1979)

67. BRODSKY,M.H.
Amorphous Semiconductors.
in Topics in Applied Physics, Volume 36
Springer-Verlag Publishing Co., Berlin, FDR (1979)

68. UHLMAN, D.R.
Polymer Glasses and Oxide Glasses.
J Non-Crystalline Solids 42 (1980) 119 -142

69. PHILLIPS, J.C.
Chemical Bonding, Internal Surfaces and Topology of Non-Crystalline Solids.
Phys Stat Solidi (b) 101 (1980) 473-79

70. PANTELIDES, S.T. & LONG, M.
in The Physics of SiO_2 and Its Interfaces, pp.339-
Pergammon Press, New York, USA (1978)

71. DOHLER, G.H. & DANDOLOFF, R.T.
A Topological-Dynamical Model of Amorphycity.
J Non-Crystalline Solids 42 (1980) 87-95

72. JOHANNESSEN, J.S. & SPICER, W.E.
Auger Depth Profiling of Interfaces of MOS and MNOS Structures.
J Vac Science Technology 13 (1976) 849-855

73. KRIVANEK, O.L. ; SHENG, T.T. & TSUI, D.C.
High-Resolution Studies of the Si-SiO_2 Interface.
Bulletin of American Physics 23,3 (1978) 457-

74. KRIVANEK, O.L. ; TSUI, D.C. & KAMAGAR, A.
in The Physics of SiO_2 and Its Interfaces, pp.356-61
ed. PANTELIDES,S.T., Pergammon Press, New York, USA (1978)

75. BLANC, C.J.; BRIOCCHI, C.J. & ABRAHAMS, M.S.
Revised Model for the Oxidation of Silicon by Oxygen.
Appl Phys Letters 33 (1978) 424-426

76. CHEN, J.J. & SUGANO, T.
in The Physics of SiO_2 and Its Interfaces, pp.351-53
ed. PANTELIDES,S.T., Pergammon Press, New York, USA (1978)

77. OSBURN, C.M. & ORMOND, D.W.
Dielectric Breakdown in SiO_2 Films on Si;
1. Measurement and Interpretation
2. Influence of Processing and Materials.
J Electrochem Soc 119 (1972) 597-

78. HEYNS, M.M.
Trap Generation and Electron Detrapping in SiO_2 During High-Field Stressing of MOS Structures.
Applied Phys Letters 44,2 (1984) 202-5

79. BALK, P & KLEIN, N.
Generation of Interface States in MOS Systems.
Thin Solid Films 89,4 (1982) 329-39

80. SCHULTZ, M.
MOS Interface States.
Institute of Physics Conference Series 50 (1980) Chapter 2

81. GOETZBERGER, A.; KLAUSMAN, E & SCHULTZ, M.J.
Interface States on Semiconductor-Insulator Structures.
CRC Critical Reviews in Solid State Sciences 6,1 (1976) 1-45

82. YOUNG, D.R.; IRENE, E.A. & DiMARIA, D.J.
Electron Trapping in SiO_2 at 295 and 77°K.
J Appl Phys 50,10 (1979) 6366 - 72

83. MIURA, Y.; YAMABE, K.; KOMIYA, Y. & TAURI, Y.
Effect of Hot Electron Injection on the Interface Charge Density at the Si-SiO_2 Interface.
J Electrochem Society 127 (1980) 191 -194

84. SAH, C.T.; SUN, J.Y.C. & TZOU, J.
Generation - Annealing Kinetics of the Interface Donor States in Si O_2.
J Appl Phys 54 (1983) 2547-

85. FISCHETTI, M.V.; GASTALDI, R. & MAGGIONI, F.
Positive Charge Effects on the Flatband Voltage Shift During avalanche Injection On Al-Si O_2-Si Capacitors.
J Appl Phys 53 (1982) 3129-

86. WILLIAMS, R.
Photoemission of Electrons From Si into Si O_2.
Physical Review 140 (1965) A569

87. NICOLLIAN, E.H.; BERGLUND, C.N. & SCHMIDT, P.T.
Electrochemical Charging of Films of Si O_2 by Injected Electron Curents.
J Appl Phys 42 (1971) 5654-

88. JAKUBOWSKI, A. & INIEWSKI, K.
Determination of the Basic Parameters of MOS Structures from High Frequency C-V Characteristics.
Electron Technology 16,1-4 (1983) 45 - 52

89. DEAL, B.E.
Current Understanding of Charges in Thermally Oxidised Silicon.
J Electrochem Soc 121 (1974) 198C

90. LENAHAN, P.M. & DRESSENDORFER, P.V.
Hole Traps and Trivalent Silicon Centres in Al-SiO_2-Si Devices.
J Appl Phys 55, 10 (1984) 3495 - 503

91. FISCHETTI, M.V. & RICCO, B.
Hot Electron Induced Effects at the Si-SiO_2 Interface at High Fields at 295 and 77°K.
J Appl Phys 57,8 (1985) 2854 -2862

92. ZAININGER, K.H. & HERMANN, F.
The C-V Technique as an Analytical Tool.
Solid State Technology 6 (1970) 40 - 53

93. YOUNG, D.R.
Electron Trapping in SiO_2.
Institute of Physics Conference Series 50 (1980) Chapter 1

94. SAH,C.T. ;SUN, J.Y.C. & TZOU,J.J.T.
Study of the Atomic Models of 3 Donor-Like Traps on Oxidised Silicon With Aluminium Gates from Their Processing Dependencies.
J Appl Phys 54,10 (1983) 5864 -84

95. WOLTERS, D.R. & VERWEY, J.F.
Trapping Characteristics in SiO_2.
in Insulating Films On Semiconductors, pp.189-
eds., SCHULTZ & PENSL, Springer-Verlag Publishing Co., Berlin, FDR (1981)

96. DiMARIA, D.J.
in Proceedings of the Topical Conference on the Physics of SiO_2 and its Interfaces, pp.184-
Pergammon Press, New York, USA (1984)

97. YOUNG, D.R.
Electron Trapping in SiO_2.
Institute of Physics Conference Series 50 (1980), pp.28-

98. AHARONI, C. & TOMPKINS, F.C.
Rates of Absorption of Hydrogen in SiO_2.
Advances in Catalysts and Related Subjects 21 (1970)

99. SUZUKI, K.; SAKAGANI, M. & NISHIMURA, E.
Bias Annealing and Bias Induced Positive Charge in n and p-Type MOSCs.
IEEE Trans Nucl Sci NS-32, 6 (1985) 3911 - 3917

100. OSBURN, C.M. & WEITZMANN, E.J.
Electrical Conduction and Dielectric Breakdown in Si O_2 on Si.
J Electrochem Soc 119 (1972) 603-

101. SHATZKES, M. ; AV- RON, M. & ANDERSON, R.M.
Nature of Conduction and Switching in SiO_2.
J Appl Phys 45 (1974) 2065 -

102. SHATZKES, M. & AV- RON, M.
Impact Ionization and Positive Charge in Thin SiO_2 Films.
J Appl Phys 47,7 (1978) 3192-

103. LENZLIGER, M. & SNOW, E.H.
Fowler - Nordheim Tunnelling into Thermally Grown Si O_2.
J Appl Phys 40 (1969) 278 -

104. GOODMAN, A.M.
Electron Hall effect in Si O_2.
Physical Review 164 (1967) 1145-

105. GOODMAN, A.M.
Photoemission of Electrons from Si and Au into SiO_2.
Physical Review 144 (1967) 588-

106. VERWEY, J.F.
Hole Currents in Thermally Grown SiO_2.
J Appl Phys 45 (1972) 2273-

107. HUGHES, R.C.
Hole Mobility and Transport in Thin SiO_2 Films.
Applied Phys Letters 26 (1975) 436 -438

108. MEYER, W.K. & CROOK, D.L.
in Proceedings of the International Reliability Physics Symposium, Phoenix, Arizona, USA 1983.
Reliability Physics, (1983)

109. JENQ, C.S. ; RAGNUTH, T.R. & HUANG, C.H.
High Field Trapping in SiO_2 Films
Institute of Electronics and Devices Meetings 3 (1981) 388 -

110. LIANG, M.S. & FU, S.L.
Characteristics of Polymer Thick Film Resistors: 2 Phenomenological Explanation
IEEE Trans Components 4 (1981) 289 -93

111. ITSUMI, M.
Positive and Negatice Charging of Thermally Grown SiO_2 Induced by Fowler-Nordheim Emission.
J Appl Phys 52 \(1981) 3491 - 97

112. SHIRLEY, C.G.
High Field Phenomena in Thermal SiO_2.
J Electrochem Soc 132,2 (1985) 488 - 500

113. SOLOMON, P.
High Field Electron Trapping in SiO_2.
J Appl Phys 48 (1977) 3843 -

114. DiMARIA, D.J. ; DeMEYER, K.M. & DONG, D.W.
Detection of Impurities on Silicon Surfaces.
J Appl Phys 52 (1981) 1366 - 69

115. NICOLLIAN, E.H. & GOETZBERGER, A.
Avalanche Injection Currents and Charging Phenomena in Thermal SiO_2.
IEEE Trans Electron Devices ED-15 (1969) 174 -

116. ZAKZOUK, A.K. ; STUART, R.A. & ECCLESTON, W.
Nature of Defects in SiO_2.
J Electrochem Soc 123 (1976) 1551 - 1556

117. HARTMAN, U,
Charge Measurements in Thin Insulating Layers of MIS Structures by Means of I-V Characteristics and its Application to the MOS System.
Physica Status Solidi (a) 43 (1977) 103 - 110

118. SZE, S.M.
Physics of Semiconductor Devices
Wiley, USA (1981)

119. 0'DWYER, J.J.
The Theory of Electrical Breakdown in Solid Dielectrics.
Clarendon Press, Oxford, UK (1973)

120. SIMONS, J.G.
Conduction in Dielectrics
J Phys D: Applied Physics 4 (1971) 613 -657

121. WOLTERS, D.R. & VERWEY, J.F.
Electrical Phenomena and Related Instabilities in the Si / SiO_2 Structure.
Noth Holland Physics Publishing Co., Amsterdam, Holland, (1985)

122. KLEIN, N.
Mechanisms of Electrical Breakdown in Thin Insulators - An Open Subject.
Thin Solid Films 100 (1983) 335 - 340

123. AGARWAL, V.K.
Breakdown Conduction in Thin Dielectric films : A Bibliographical Survey.
Thin Solid films 24 (1974) 55 -

124. KERN, W.
Detection and Characterisation of Localised Defects in Dielectric Films.
RCA Review 34 (1973) 655 -

125. SOLOMON, P.
Breakdown in SiO_2 - A Review.
J Vac Science Technology 14, 5 (1977) 1122 - 31

126. HOLWAY, L.H. & FRADIN, D.W.
Electron Avalanche Breakdown By Laser Irradaition In Insulating Crystals.
J Appl Phys 46 (1975) 279 -

127. SMITH, W.L. & BECHTEL, J.H.
Dielectric Breakdown Threshold and Non - Linear Refractive Index Measurements with Picosecond Laser Pulses.
Phys Review B 12 (1975) 706 - 714

128. WILLIAMS, R. & WOODS, M.H.
High Electric fields in SiO_2 by Corona discharge.
J Appl Phys 44 (1973) 1026 -

129. WEINBERG, Z.A. & MATTHIES, D.L.
Measurement of the Steady-State Potential difference Across a Thin Insulating Film in a Corona discharge.
Review of Scientific Instruments 40 (1975) 201 -

130. BUDENSTEIN, P.P
On the Mechanism of Dielectric Breakdown in Solids.
IEEE Trans Electrical Insulation EI-15,3 (1980) 225-

131. JOHNSON, W.C.
Study of Electric Transport and Breakdown in Thin Insulator Films.
RADC-TR-76-158, Princeton University, USA
Final report of May 1976.

132. WILLIAMS, R.
Photoemission of Electrons from Si into SiO_2.
Physical Review 140 (1965) A569

133. WILLIAMS, R.
inSemiconductors and Semimetals, Volume 6
eds., WILLARDSON, R.K. & BEER, A.C.
Academic Press, New York, USA (1970)

134. HUGHES, R.C.
Hot Electrons in SiO_2.
Physical Review Letters 35 (1975) 449 - 452

135. HUGHES, R.C.
Time Resolved Hole Transport in Alpha-SiO_2.
Phys Rev B 15 (1977) 2012 - 2020

136. POWELL, R.J. & DERBENWICK, D.
VUV Radiation Effects In SiO_2.
IEEE Trans Nuclear Science NS-18 (1971) 99 -

137. DiSTEFANO, T.H. & EASTMAN, D.E.
Photoemission Measurements of Valence Levels of AmorphousSiO_2.
Physical Review Letters 27(1971) 1560 -

138. TOMMASINO, L. ; SOLOMON, P. & KLEIN, N.
Thin Film Breakdown Counter of Fission-Fragments.
J Appl Phys 46 (1975) 1484 - 1488

139. KLEIN, N.
Swithching and Breakdown in Films.
Thin Solid films 7 (1971) 149 -

140. KLRIN, N.
Mechanism of Self - Healing Electrical Breakdown in MOS Structures.
IEEE Trans Electron Devices ED - 13 (1966) 788 -

141. OSBURN, C.M. & ORMOND, D.W.
Dielectric Breakdown in SiO_2 Films on Si.
J Electrochem Soc : Solid State Science and Technology 119,5 (1972) 591 - 602

142. YOUNG, D.Y. ; JOHNSON, W.C. & LAMPERT, M.A.
Study of Dielectric Breakdown of Thermally Grown SiO_2 by Self - Quenching Technique.
IEEE Trans Electron Devices ED - 22(1975) 10 - 14

143. SHATZKES, M. ; AV - RON, M. & ANDERSON, R.M.
Conduction and Switching in SiO_2.
J Appl Phys 45 (1974) 2065 -

144. FRITSCHE, C.
Representation of a Lattice Electron in a Uniform Electric Field.
Z Angew Phys 24 (1967) 49 -

145. WORTHING, F.L.
D.C. Dielectric Breakdown of Amorphous SiO_2 Films at Room Temperature.
J Electrochem Soc 115 (1968) 89 -

146. OSBURN, C.M. & WEITZMAN, E.J.
Electrical Conduction and Dielectric Breakdown in SiO_2 on Si
J Electrochem Soc 119(1972) 603 -

147. OSBURN, C.M. & CHOU, N.J.
Accelerated Dielectric Breakdown of SiO_2 Films.
J Electrochem Soc 120(1973) 1377 -

148. SOLOMON, P. ; KLEIN, N. & ALBERT, M.
Statistical Model for Step and Ramp Voltage Breakdown Tests in Thin Insulators.
Thin Solid Films 35 (1976) 321 - 326

149. MEEK, R.L. & BRAUN, R.H.
Devitrification of Steam Grown SiO_2 Films.
J Electrochem Soc 119(1972) 1538-

150. LI, S.P. & MASERJIAN, J.
Effective Defect Densities for MOS Breakdown and its Dependence on Oxide Thickness.
IEEE Trans Electron Devices ED-23 (1976) 525-527

151. PRICE, J.E.
A New Look at Yield of IC's.
Proc IEEE 58 (1970) 1290 -

152. KLEIN, N.
Electrical Breakdown of Insulators by One-Carrier Impact Ionization.
J Appl Phys 53, 88 (1982) 5828 - 5839

153. DiSTEFANO, T.H. & SHATZKES, M.
Dielectric Breakdown Phenomena in SiO_2.
in Proceedings of the 3rd International Symposium on Silicon Materials
Science and Technology Group, Electrochemical Society, Princeton, New Jersey, USA.
Proceedings Volume 77,2 (1977) 332 -

154. OSBURN, C.M. & BASSOUS, E.
Improved Dielectric Breakdown Reliability of SiO_2 Films with Polycrystalline Silicon Electrodes.
J Electrochemical Society 122 (1975) 89 -

155. GARTON, C.G. & STARK, K.H.
Electric strength of Irradiated Polythene.
Nature (London) 176(1955) 1225 -

156. KLEIN, N.
Electrical Breakdown in Thin Dielectric Films.
Advances in Electronics and Electron Physics 26 (1969) 309 - 424

157. KLEIN, N. & GAFNI, H.
Maximum Dielectric Strength of Thin SiO_2 Films.
IEEE Trans Electron Devices ED - 13 (1966) 281 -

158. VON HIPPEL, A.
Electric Breakdown in Solid and Liquid Insulators.
J Appl Phys 8 (1937) 815 -

159. GUNDLACH, K.H. & SCHNUPP, P.
Mechanism of Heavy Ion Interaction in Al_2O_3.
Z Angew Phys 21 (1966) 468 -

160. CHOU, N. & ELDRIDGE, J.
Effects of Materials and Processing Parameters on Dielectric Strength of Thermally Grown SiO_2 Films.
J Electrochem Soc 117 (1970) 1287 -

161. RIDLEY, B.K.
Mechanism of Electrical Breakdown in SiO_2 Films.
J Appl Phys 46 (1975) 998 - 1007

162. JONSCHER, A.K.
-private communication, Chelsea Dielectrcs Group, London, UK.

163. OSBURN, C.M. & RAIDER, R.
Effect of Mobile Na^+ on Field Enhancement Dielectric Breakdown in SiO_2 Films on Si.
J Electrochem Soc 120 (1973) 1369 -

164. HARARI, E.
Dielectric Breakdown in Electrically Stressed Thin Films of Thermal SiO_2.
J Appl Phys 49 (1978) 89 -

165. BARNETT, A.M. & MILNES, A.G.
Filamentary Injection in Semi-Insulating Silicon.
J Appl Phys 37 (1966) 4215 -

166. SCHMIDLIN, F.W.
Electrical Switching Device Based Upon Charge Controlled Double - Injection.
Phys Rev B 1 (1970) 1583 -

167. KLEIN, N.
Electrical Breakdown Mechanisms in Thin Insulators.
Thin Solid Films 50 (1978) 223 - 232

168. KASHAT, I. & KLEIN, N.
Models for Current Runaway in Thin - Insulators by Impact - Ionization.
IEEE Trans Electron Devices ED - 24, 9 (1977) 1208 - 9

169. DiSTEFANO, T.H. & SHATZKES, M.
Dielectric Instability and Breakdown in SiO_2 Thin Films.
J Vacuum Science Technology 13 (1976) 50 - 54

170. KLEIN, N. & SOLOMON, P.
Current Runaway in Insulators Affected by Impact - Ionization and Recombination.
J Appl Phys 47 (1976) 4364 - 72

171. KLEIN, N.
A Theory of Localised Electronic Breakdown in Insulating Films.
Advances in Physics 21 (1972) 605 -

172. BAIDYAROY, S. ; LAMPERT, M.A. ; ZEE, B. & MARTINELLI, R.G.
Studies of Hot Electron Energy Distributions in Thin Insulating Films.
J Appl Phys 47 (1976) 2103 - 2112

173. KADARY, V. & KLEIN, N.
Electroluminescence During Anodic Growth of Ta_2O_5.
J Electrochem Society 128 (1981) 749 - 55

174. FRITZCHE, C.R. ; AXMAN, A. & SEELEWIND, H.
in Proceedings of the European Conference on Ion Implantation , pp123 -
Reading, England (1970)

175. SOLOMON, P. & KLEIN, N.
Impact Ionization in SiO_2 at Fields in the Breakdown Range.
Solid State Communications 17 (1975) 1397 - 1400

176. NISSAN - COHEN, Y.
-private communication via Chelsea Dielectrcs Group, London, UK.

177. FEIGL, F.J.; YOUNG, D.R. & DiMARIA, D.J.
The Effects of Water and Interface Trapped Charge Generation in Thermal SiO_2 Films.
J Appl Phys 52 (1981) 5665 - 5682

178. SOLOMON, P. & AITKEN, J.M.
Current and C-V Instabilities in SiO_2 at High Fields.
Applied Physics Letters 31 (1977) 215 - 217

179. ALBERT, M. & KLEIN, N.
Electrical Breakdown of Al_2O_3 Films Flanked by Metal Electrodes.
J Appl Phys 53 (1982) 5840 - 5850

180. PECK, D.S.; BLAIR, R.R. & BROWN, W.L.
Surface Effects of Radiation on Transistors.
Bell Systems Technical Journal 42 (1963) 95 -

181. NING, T.H.
Electron Trapping in SiO_2 Due to Electron Beam Deposition of Al.
J Appl Phys 49 (1978) 4077 - 4082

182. BRUCKER, G.J.; STASSINOPOLOUS, E.G. ; AUGUST, L.S. & JORDAN, T.M.
The damage Equivalence of Electrons, Protons, and Gamma Rays in MOS Devices.
IEEE Trans Nuclear Science NS - 29, 6 (1982) 1966 - 69

183. STAPOR, W.J.; AUGUST, L.S. & WILSON, D.H.
Proton and Heavy Ion Damage in MOSTs
IEEE Trans Nuclear Science NS - 32, 6 (1985) 4399 - 4404

184. BRUCKER, G.J.
Correlation of Radiation Damage in Si MOSTs Bombarded with Electrons, Protons, and Neutrons.
in Symposium on Radiation Effects in Semiconductor Components
Toulouse, France (1967)

185. SROUR, J.R.; OTHMER, S. & CHEN, S.S.
Investigation of Basic Mechanisms of Radiation Effects on Si MOSTs.
Contract dna 001-78-C-0028
Northrop Corp., Palos Verdes Peninsula, California, USA (1979)

186. SZEDON,J.R. & SANDOR, J.E.
Effects of Low Energy Electron Radiation on MOS Structures.
Appl Phys Leters 6 (1965) 18 -

187. SROUR, J.R. ; CURTIS, O.L. & CHIN, J.Y.
Stable - Damage Comparisons for Neutron Irradiated Silicon.
IEEE Trans Nuclear Science NS - 20 (1974) 190-

188. SMIRNOV, A.N. & EISMONT, V.P.
Thin Film Breakdown Counters (Review)
Translated from: Pribory-i-Teknika Eksperimentia 6 (1983) 5 -13

189. GWYN, C.W.
Ionizing Radiation Effects in the Insulator Region Of MOS Devices.
Sandia Report SLA -73-0013
Sandia Laboratories, USA (1973)

190. SNOW, E.H.; GROVE, A.S. & FITZGERALD, D.J.
Effects of Ionizing Radiation on Oxidised Si Surfaces and Planar Devices.
Proc IEEE 55 (1967) 1168 -

191. MITCHELL, J.P.
A Study of Radiation Effects on SiO_2 and Al_2O_3 Layers Using Thermoluminescence Glow Curve Techniques.
IEEE Trans Electron Devices ED - 14 (1967) 764 -

192. PEEL, J.L. & EDEN, R.C.
Study of Ionizing Radiation Damage in MOS Structures Using Internal Photoemission.
IEEE Trans Nuclear Science NS - 18 (1971) 84 -

193. KNOLL, M. ; BRAUNIG, D. & FAHRNER, W.R.
Generation of Oxide Charge and Interface States by Ionizing Radiation and by Tunnel Injection Experiments.
IEEE Trans Nuclear Science NS - 29(1982) 1473 - 1478

194. SHANFIELD, Z. & MORIWAKI, M.M.
Radiation-Induced Hole Trapping and Interface State Characteristics af Al-gate and Polysilicon Gate MOSCs.
IEEE Trans Nuclear Science NS - 32 (1985) 3929 - 3934

195. ZAININGER, K.H & REVESZ
Electron Bombardment of MOS Capacitors.
Appl Phys Letters 8 (1966) 140 -

196. GROVE, A.S & SNOW, E.H.
A Model for Radiation Damage in MOS Structures.
Proc IEEE 54 (1966) 894 -

197. McLEAN, F.B. ; BOESCH, H.E. & McGARRITY, J.M.
Application of Stochastic Hopping Transport to Hole Conduction in a - Si.
Bulletin American Physics 21 (1976) 315 -

198. PFISTER, G. & SCHER, H.
Dispersive (Non-Gaussian) Transient Transport in Disordered Solids.
Advances in Physics 27 (1978) 747 - 98

199. McLEAN, F.B. & AUSMAN, G.A.
Simple Approximate solutions to Continuous-time Random-walk Transport of Holes in SiO_2.
Physical Review 15 (1977) 1052 - 1061

200. MARSHALL, J.M.
Dispersive Transit Pulses Produced by a Trap Limited Transport Mechanism.
Philosophical Magazine B-38 (1978) 335 -

201. CURTIS, O.L. & SROUR, J.R.
Multiple Trapping Model and Hole Transport in SiO_2.
J Appl Phys 48 (1977) 3919 - 28

202. McGARRITY, J.M.
Considerations for Hardening MOS Devices and Circuitry for Low Radiation Doses.
IEEE Trans Nuclear Science NS - 27 (1980) 1739 - 1744

203. POWELL, R.J & DERBENWICK, G.F.
VUV Radiation Effects in SiO_2.
IEEE Trans Nuclear Science NS - 18,6 (1971) 99 -

204. OLDHAM, T.R.
Analysis of Damage in MOS Devices for Several Radiation Environments.
IEEE Trans Nuclear Science NS - 31(1984) 1236 - 1241

205. BOESCH, H.E. & TAYLOR, T.L.
Charge and Interface State Generation in Field oxides.
IEEE Trans Nuclear Science NS - 31(1984) 1273 - 1279

206. AUSMAN, G.A. & McLEAN, F.B.
Electron -Hole Pair Creation Energy in SiO_2.
Appl Phys Letters 26 (1975) 173-

207. OLDHAM, T.R. & McGARRITY, J.M.
Ionization of SiO_2 by Heavy Charged Particles.
IEEE Trans Nuclear Science NS - 28,6 (1981) 3975 - 3980

208. MAYER, J.W. & ERIKSSON, E.
Ion implantation in Semiconductors
Academic Press, New York, USA (1970)

209. SROUR, J.R. ; CHEN, S.C. ; OTHMER, S & HARTMANN, R.A.
Neutron Damage Mechanisms in Charge Transfer Devices.
IEEE Trans Nuclear Science NS - 25 (1979) 1251 - 1260

210. McLEAN, F.B.
A Framework for Understanding Radiation Induced States in SiO_2 MOS Structures.
IEEE Trans Nuclear Science NS - 27(1980) 1651 - 1260

211. WINOKUR, P.; BOESCH, H. ; McGARRITY, J.M. & McLEAN, F.B.
Two - Stage Process for Buildup of Radiation Induced Interface States.
J Appl Phys 50 (1979) 3492 - 3494

212. WINOKUR, P. & BOESCH, H.
Interface - State Generation in Radiation Hard Oxides.
IEEE Trans Nuclear Science NS - 27 (1980) 1051 - 1058

213. TZOU, J.J. ; SUN, J.Y.C. & SAH, C.T.
Effects of KeV Electron Irradiation on Optical Generation of Hole Traps in Thermal Oxide on Silicon.
J Appl Phys 55, 4 (1984) 846 - 51

214. BOESCH, H.E. & TAYLOR, T.L.
Charge and Interface State Generation in Field Oxides.
IEEE Trans Nuclear Science NS - 31,6 (1984) 1273 - 1279

215. OLDHAM, T.R. & McGARRITY, J.M.
Comparison of Co^{60} Response and 10KeV X - Ray Response in MOSCs.
IEEE Trans Nuclear Science NS - 30,6 (1983) 4377 - 4381

216. BOESCH, H.E.
Interface State Generation in Thermal SiO_2 Layers.
IEEE Trans Nuclear Science NS - 29,6 (1982) 1466 - 1451

217. PEASE, R.L.; TURFLER, R.M. & PLATTEFER, D.
Total Dose Effects in Recessed Oxide Digital Bipolar Microcircuits.
IEEE Trans Nuclear Science NS - 30,6(1983) 4216 - 4225

218. OLDHAM, T.R.
Analysis of Damage in MOS Devices for Several Radiation Environments.
IEEE Trans Nuclear Science NS - 31,6 (1984) 1236 - 1241

219. KNOLL, M.; BRAUNIG, D & FAHRNER, W.R.
Comparitive Studies of Tunnel Injection and Irradiation on MOS Structures.
J Appl Phys 53,10 (1982) 6496 - 52

220. SHANFIELD, Z.
Radiation Induced Hole Trapping and Interface State Characteristics of Al gate and Polysilicon gate MOS Structures.
IEEE Trans Nuclear Science NS - 32,6 (1985) 3929 - 3934

221. KNOLL, M.; BRAUNIG, D & FAHRNER, W.R.
Generation of Oxide Charge and Interface States by Ionizing Radiation and by Tunnel Injection Experiments.
IEEE Trans Nuclear Science NS - 29,6 (1982) 1471 - 1478

222. STASSINOPOLOUS, E.G. ; BRUCKER, G.J.; VAN GUNTEN, O.; KNUDSON, A.R. & JORDAN, T.M.
Radiation Effects on MOS Devices: Dosimetry, Annealing, Irradiation Sequence and Sources.
IEEE Transactions on Nuclear Science NS - 23 (1983) 1880 - 1884

223. McLEAN, F.B.
A Framework for Understanding Radiation Induced Interface Traps in SiO_2 MOS Structures.
IEEE Transactions on Nuclear Science NS - 27 (1980) 1651 - 1658

224. McGARRITY, J. ; WINOKUR, P.S. ; BOESCH, H.E. & McLEAN, F.B.
Interface States Resulting from a Hole Flux Incident on Si-SiO_2 Interface.
in Proceddings of the International Conference of SiO_2 and its Interfaces, pp.428 - 432
Pergammon Press, New York, USA (1978)

225. WINOKUR, P.S. & BOESCH, H.E.
Interface State Generation in Radiation hard Oxides.
IEEE Transactions on Nuclear Science NS - 27 (1980) 1647 - 1650

226. SAH, C.T.
Concentration Profiles of Recombination Centres in Semiconductor Junctions Evaluated from Capacitance Transients.
IEEE Transactions on Electron Devices ED - 23 (1976) 1069 - 1074

227. SVENSSON, C.M.
Defect Structure of Si-SiO_2 Interface: A Model based upon Trivalent Si and its Compounds.
in Proceddings of the International Conference of SiO_2 and its Interfaces, pp.328 - 332
Pergammon Press, New York, USA (1978)

228. REVESZ, A.G.
Role of Hydrogen in SiO_2 Films on Si.
J Electrochem Society 126 (1979) 122 - 30

229. SHIONO, N. ; SHIMAY, M. & SANO, K.
Ionizing Radiation Effects in MOSCs With Very Thin Gate Oxides.
J Appl Phys 22,9 (1983) 1430 - 35

230. HUGHES, R.C.
Excess Electron and Hole Transport in SiO_2.
Bulletin of American Physics 22,3 (1977) 416 -

231. KLEIN, N. ; SOLOMON, P . & TOMMASINO, L.
Thin Insulator Current Pulse Counter of Fission-Fragments.
Nuclear Instruments and Methods 129 (1975) 119 - 121

232. TOMMASINO, L.; KLEIN, N. & SOLOMON, P .
Thin Film Breakdown Counter of Fission-Fragments.
J Appl Phys 46,4 (1975) 1484 - 1488

233. KLEIN, N. ; SOLOMON, P . & TOMMASINO, L.
Fission-Fragment Detection by Thin Film Capacitors: 1. Breakdown Counter.
Nuclear Track Detection 1,1 (1977) 63 - 70

234. KLEIN, N. ; SOLOMON, P . & TOMMASINO, L.
Fission-Fragment Detection by Thin Film Capacitors: 2.Current Pulse Counter and Mechanisms.
Nuclear Track Detection 1,1 (1977) 71 - 74

235. SMIRNOV, A.N. & EISMONT, V.P.
Investigations of Physical Properties of MOS-Structure Heavy Ion Counters.
Nuclear Instruments and Methods 154 (1978) 471 - 476

236. DONICHKIN, A.G. ; SMIRNOV, A.N. & EISMONT, V.P.
Heavy Ion Detection Properties of Thin film Breakdown Counters.
Nuclear tracks 3 (1979) 205 - 211

237. GANGRSKII, Y.P. ; MILLER, M.B. & UTENOV, V.K.
Detection of Fission-Fragments with Thin Film Solid State Capacitors.
Instruments and Experimental Techniques 23,2 (19800 374 - 377

238. SMIRNOV, A.N. ; EISMONT, V.P.; RANJUK, Y.N. & NOGA, V.I.
On the Response of a Breakdown Counter to Pulsed Gamma and Electron radiations.
Nuclear instruments and methods 176 (1980) 601 - 603

239. DORSCHEL, B. ; PFUTZNER, F. ; STRENBEL, G.; KNORR, J. & PAUL, W.
Neutron Detection Using MOS Breakdown Counters Combined With Fissile radiators.
Nuclear instruments and methods 216 (1983) 227 - 229

240. SMIRNOV, A.N. & EISMONT, V.P.
Thin Film breakdown Counters.
Translated from ; Pribory i Teknika Eksperimentia 6 (1983) 5 - 13

241. MILLS, T. & KROGER, F.
Electrical Conduction at Elevated Temperatures in Thermally Grown SiO_2 Films.
J Electrochem Society 120 (1973) 1582 -

242. CHOU, N.J.
Electrical Conduction in SiO_2 at Elevated Temperatures
Journal of Electronic Materials 1 (1973) 1582 -

243. KATZ, R. & KOBETICH, E.
Formation of Etchable Tracks in Dielectrics.
Physical Review 170 (1968) 401 -

244. SWAN, D.
Electrical Breakdown of Liquid Dielectrics.
proceedings of the Physical Society 78 (1961) 423 -

245. KLEIN, N.
The Breakdown Voltages of SiO_2 Breakdown Counters for Fission-Fragments.
Nuclear Instruments and Methods 189 (1981) 569 - 576

246. SOLOMON, P. & KLEIN, N.
Impact Ionization in SiO_2 at Fields in the Breakdown Range.
Solid State Communications 17 (1975) 1397 - 1400

247. SHATZKES, M.
Injection into insulators in the Presence of a Space Charge.
J Applied Physics 49 (1968) 2029 -

248. KLEIN, N.
Dielectric Breakdown in MIM Structures with VeryThin Gate Electrodes.
J Appl Phys 38 (1968) 2029 -

249. KLEIN, N.
Electrical Breakdown Mechanisms in Thin Insulators
Thin Solid Films 50 (1978) 223 - 232

250. PEARCE, C.W.
Crystal Growth and Wafer Preparation.
in VLSI Technology, chapter 3
ed., SZE, S.M. , McGraw- Hill Publishing Co., New York, USA (1983)

251. GHANDI, S.K.
Oxidation of Si and GaAs.
in VLSI Fabrication principles, chapter 2
Wiley Publishing Co., New York, USA (1983)

252. KATZ, L.E.
Thermal Oxidation of Silicon.
in VLSI Technology, chapter 4
ed., SZE, S.M. , McGraw- Hill Publishing Co., New York, USA (1983)

253. YATES, P.
- a private communication with the Production Manager at Plessey semiconductors (UK), Plymouth, UK.

254. FRASER, D.B.
Metallization.
in VLSI Technology, chapter 6
ed., SZE, S.M. , McGraw- Hill Publishing Co., New York, USA (1983)

255. TERMAN, L.
The C-V Technique.
Solid State Electronics 5 (1962) 285 -

256. JAKUBOWSKI, A. & INIEWSKI, K.
Determination of the Basic Parameters of MOS Structures from High Frequency C-V Characteristics.
Electron Technology 16 (1983) 45 - 52

257. CHANG, C.C.
Characterisation of Solid Surfaces.
in Characterisation of Solid Surfaces, chapter 1
eds.,KANE, P.F. & LARRABEE, G.B. , Plenum Press, New York, USA (1972)

258. SHIRLEY, D.A.
AES.
inElectron Spectroscopy, chapter 4
American Elsevier publishing Co., New York, USA (1972)

259. McHUGH, J.A.
ESCA.
in Methods and Phenomena of Surface Analysis, chapter 2
ed., WOLSKY, S.P. , Elsevier, amsterdam, Holland (1975)

260. MAYER, J.W. & ZIEGLER, J.F.
Ion Beam Surface Layer Analysis
Elsevier Sequoia, Lausanne, Switzerland (1974)

261. TOLANSKY, S
Surface Microtopography
John Wiley and Son Publishing Co., New York, USA (1960)

262. JINSHEN, L. & MINGQI, C.
Study of Ellipsometry: The Computation of Elliopsometric Parameters in Non-Uniform Films On Solid Substrates.
in Insulating Films On semiconductors, pp. 174 -178
Proceedings of the 2nd international conference, INFOS'81, Germany 1981
eds., SCHULTZ, M. & PENSL,G. , Springer Verlag publishing Co., Berlin, FDR (1981)

263. MIDDLETON, M.R.
a private communication with the Technical Manager of the Video Technical Centre, 3MSwansea, UK.

264. From The Radiochemical Centre, Amersham, UK, catalogue 1977/78.

265. NORTHCLIFFE, L.C. & SCHILLING, R.F.
Range and Stopping Power Tables for Heavy Ions,
Nuclear Data tables 7 (1970) 233 - 246

266. YAMABE, K. & MIURA,M.
Hot Electron Injection in MOS Structures,
in The Physics of MOS Insulators, pp.336 - 340
Proceedings of the International Conference, Raleigh, New Conneticut, USA (1980)